

Dissertation zur Erlangung des Doktorgrades  
an der Fakultät für Chemie und Pharmazie  
der Ludwig-Maximilians-Universität München

# Photopharmacology of Ion Channels, Adenosine Receptors and Myosin-V

Katharina Hüll

aus

München, Deutschland

**2020**



## Erklärung

Diese Dissertation wurde im Sinne von § 7 der Promotionsordnung vom 28. November 2011 von Herrn Prof. Dr. Dirk Trauner betreut.

## Eidesstattliche Versicherung

Diese Dissertation wurde eigenständig und ohne unerlaubte Hilfe erarbeitet.

München, 24.02.2020

Katharina Hüll

Dissertation eingereicht am:	16.09.2019
1. Gutachterin / 1. Gutachter:	Prof. Dr. Dirk Trauner
2. Gutachterin / 2. Gutachter:	Dr. Oliver Thorn-Seshold
Mündliche Prüfung am:	5.11.2019



## Acknowledgements

First and most importantly, I want to thank Prof. Dr. Dirk Trauner. I appreciated the tremendous amount of freedom and independence we are granted in your lab. Working for you has not only made me become a better scientist, but also the stronger person I am today. Our move to New York City came as a surprise but taking the risk has been the best decision of my life.

Second, I would like to thank Dr. Oliver Thorn-Seshold, who agreed to be the second advisor for this thesis.

I thank my committee: Prof. Dr. Konstantin Karaghiosoff, Prof. Dr. Oliver Trapp, Prof. Dr. Lena Daumann and Prof. Dr. Thomas Klapötke

I thank the Studienstiftung des deutschen Volkes for their financial support and all the training and interaction with other students I was able to enjoy.

None of the work anyone of us does would be possible without the help of the permanent staff. Heike, Aleks, Danielle, Martin, Carrie, Mariia and Luis: thank you so much for making our lives easier.

Along these lines I would also like to thank the following people at LMU: Dr. Werner Spahl, Sonja Kosak, Dr. David Stephenson, Claudia Ober, Oliver Möbus-Ohly, Roland Schürer, Michael Gayer and Heidi Buchholz and at NYU: Dr. Chin Lin, Ron McLurkin and Philip "Pip" Morton.

My work would not have been possible without my mentors and close friends Laura and Matthias. Thank you for your loyalty and your support.

Reliable colleagues and collaborators are extremely important, and I would like to thank Martin Maier, Dr. Bryan Matsuura and Dr. Timm Fehrentz for being so great to work with.

Thank you to all the talented students I had the chance to work with: Lucie Thomas, Benjamin Heinz, Solène Beauchamp, Meike Amma, Mandira Banik and Chris Arp.

Working in the lab is always most enjoyable with the right people around, and I have been lucky to experience both Munich (Green Lab and BioSysM) and NYU labs and I enjoyed and appreciated all of them. The list of people I shared lab space with is endless, but you guys were the reason I came to lab in the morning with a smile on my face.

In particular, thank you, Nina, Felix, Daniel, Philipp, Giulio, Arunas, Julius, Martin M. and Anna I.: You have been more than just colleagues, thank you for being my friends. And most importantly, thank you, Peter, Ally, Dylan, Tom, Max and Steve: you made New York City feel like home.

I would be nothing without my friends. Thank you Krissi, Adri, Krisi, Miri, Angie and Nina: From first year-chemistry students until today, we somehow have grown into adults together. Thank you, Sophia, Caroline and Tanja: I love our trips and

vacations and that you share your world, the real world, with me. Thank you Stufi, Fränzi und May: My school years were much more bearable with you, and now we are in our 30s and life is still better when you are around.

Thank you, Anna. I am so happy we are finally neighbors again.

I am most grateful to my parents. Your unconditional support and love are the reason I am where I am today.

## Project Affiliation Disclosure

Apart from myself, many collaborators, colleagues and students have worked hard for the results presented in this thesis. In this statement I proclaim that the following findings were a team-driven effort and that I am compiling and discussing our findings. Alongside the supervision of Prof. Dr. Dirk Trauner, the following people were involved. Results that have been published in or submitted to a peer-reviewed journal include an author list at the beginning of the subchapter as well.

Chapter I: Johannes Morstein (chapters on transporter/pumps, enzymes and other applications)

Chapter II: Dr. Julie Trads (Synthesis and Electrophysiology), Dr. Bryan Matsuura (Synthesis), Dr. Laura Laprell (Electrophysiology), Dr. Timm Fehrentz (Electrophysiology), Dr. Nicole Görldt (Electrophysiology), Dr. Krystian Kozek (Thallium Flux Assays), Prof. Dr. David Weaver (Supervision), Prof. Dr. Nikolaj Klöcker (Supervision), Dr. David Barber (Synthesis and Supervision), Martin Maier (Synthesis and Computational Analysis), Martin Reynders (Synthesis), Philipp Leippe (Synthesis), Tongil Ko (Synthesis), Lukas Schäffer (Synthesis)

Chapter III: Tyler Benster (Computational Analysis), Prof. Dr. Michael Manookin (Electrophysiology), Prof. Dr. Russell Van Gelder (Supervision), Dr. Laura Laprell (Computational Analysis, Electrophysiology and Supervision)

Chapter IV: Dr. Matthias Schönberger (Synthesis and Supervision), Dr. Daniela Malan (MEA with Cardiomyocytes), Prof. Dr. Philipp Sasse (Supervision), Prof. Dr. David Weaver (Thallium Flux assays and Supervision), Prof. Dr. Bryan Roth (PDSP Binding Studies),

Chapter V: Solène Beauchamp (Synthesis)

Chapter VI: Lucie Thomas (Synthesis), Benjamin Heinz (Synthesis), Georg Merck (Single Molecule Tracking), Prof. Dr. Zeynep Ökten (Supervision)

Chapter VIII: Meike Amma (Synthesis), Kevin Sokol (Synthesis), Christopher Arp (Synthesis)

I am very grateful to have met all these people and that I was able to work with and learn from them.





## Publications

Parts of this doctoral thesis have been published in scientific journals, or are considered for publication, respectively:

1. Maier, M.; **Hüll, K.**<sup>†</sup>; Reynders M.<sup>†</sup>; Matsuura, B.<sup>†</sup>; Leippe, P.; Ko, T. Schäffer, L. and Trauner, D. An Oxidative Approach Enables Efficient Access to Cyclic Azobenzenes, *J. Am. Chem. Soc.* **2019**, *141*, 17295-17304.
2. Trads, J. <sup>†</sup>; **Hüll, K.** <sup>†</sup>; Matsuura, B. <sup>†</sup>; Laprell, L.; Fehrentz, T.; Görltdt, N.; Kozek, K. A.; Weaver, D.; Klöcker, N.; Barber, D.; et al. Sign Inversion in Photopharmacology: Incorporation of Cyclic Azobenzenes in Photoswitchable Potassium Channel Blockers and Openers. *Angew. Chem. Int. Ed.* **2019**, *58*, 15421-15428.
3. **Hüll, K.**; Benster, T.; Manookin M.; Trauner, D., Van Gelder, R. N.; Laprell, L. Photopharmacologic Vision Restoration Reduces Pathological Rhythmic Field Potentials in Blind Mouse Retina, *Sci. Rep.* **2019**, *9*,13561.
4. **Hüll, K.** <sup>†</sup>; Morstein, J.<sup>†</sup>; Trauner, D. In Vivo Photopharmacology. *Chem. Rev.* **2018**, *118*, 10710-10747.

<sup>†</sup>: equal contribution

Further publications in peer-reviewed journals, which are not part of this thesis are:

5. Laprell, L.; **Hüll, K.**; Stawski, P.; Schön, C.; Michalakis, S.; Biel, M.; Sumser, M. P.; Trauner, D. Restoring Light Sensitivity in Blind Retinae Using a Photochromic AMPA Receptor Agonist. *ACS Chem. Neurosci.* **2016**, *7*, 15-20.
6. Damijonaitis, A.; Broichhagen, J.; Urushima, T.; **Hüll, K.**; Nagpal, J.; Laprell, L.; Schonberger, M.; Woodmansee, D. H.; Rafiq, A.; Sumser, M. P.; et al. AzoCholine Enables Optical Control of Alpha 7 Nicotinic Acetylcholine Receptors in Neural Networks. *ACS Chem. Neurosci.* **2015**, *6*, 701-707.



# Contents

ACKNOWLEDGEMENTS	III
PROJECT AFFILIATION DISCLOSURE	V
PUBLICATIONS	VII
CONTENTS	IX
ABSTRACT	XI
<u>I. GENERAL INTRODUCTION</u>	<u>1</u>
IN VIVO PHOTOPHARMACOLOGY	3
<u>II. SIGN INVERSION IN PHOTOPHARMACOLOGY USING DIAZOCINE PHOTOSWITCHES</u>	<u>79</u>
SIGN INVERSION IN PHOTOPHARMACOLOGY: INCORPORATION OF CYCLIC AZOBENZENES IN PHOTOSWITCHABLE POTASSIUM CHANNEL BLOCKERS AND OPENERS.	81
DIAZOCINE DERIVATIVES OF LIDOCAINE, PILSICAINIDE AND QX-314 FOR THE OPTICAL CONTROL OF CARDIAC FUNCTION.	121
OXIDATIVE APPROACH ENABLES EFFICIENT ACCESS TO CYCLIC AZOBENZENES.	129
<u>III. CHEMICAL APPROACHES TO VISION RESTORATION</u>	<u>163</u>
PHOTOPHARMACOLOGIC VISION RESTORATION REDUCES PATHOLOGICAL RHYTHMIC FIELD POTENTIALS IN BLIND MOUSE RETINA	165
<u>IV. PHOTOSWITCHABLE ADENOSINE</u>	<u>213</u>
OPTICAL CONTROL OF ADENOSINE RECEPTORS	215
<u>V. PHOTOSWITCHABLE CAFFEINE</u>	<u>241</u>
PHOTOSWITCHABLE CAFFEINE DERIVATIVES FOR THE OPTICAL CONTROL OF CARDIAC FUNCTION	243
<u>VI. OPTICAL CONTROL OF MYOSIN V</u>	<u>283</u>
A PHOTOSWITCHABLE INHIBITOR OF MYOSIN V TO STUDY THE INTERPLAY OF MYOSIN V AND KINESIN-2 IN SKIN PIGMENTATION	285

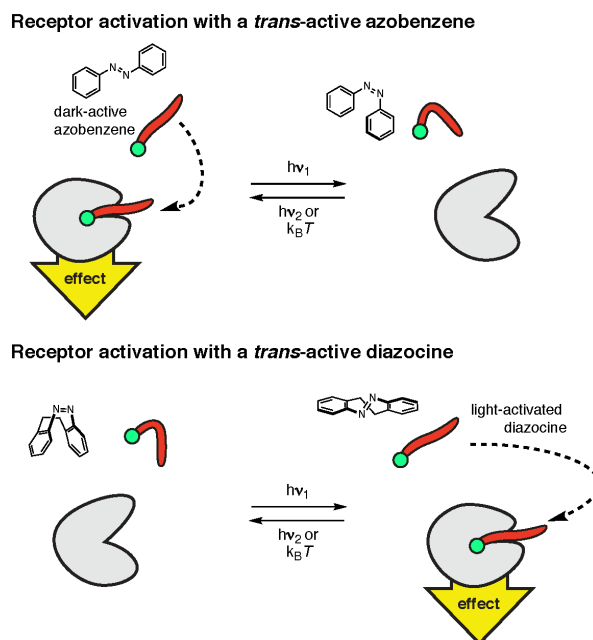
<u>VII. OPEN CHANNEL BLOCKERS FOR THE CO-CRYSTALLIZATION WITH KCSA</u>	<u>305</u>
ARSENIC-DERIVATIVES TO INVESTIGATE THE INTERACTION OF POTASSIUM CHANNELS WITH <i>CIS</i> -AZOBENZENES	307
<u>VIII. KCNQ CHANNEL MODULATORS</u>	<u>327</u>
PHOTOSWITCHABLE AND NON-PHOTOSWITCHABLE RETIGABINE DERIVATIVES TO PROBE KCNQ CHANNEL FUNCTION	329
<u>IX. APPENDIX</u>	<u>355</u>
GENERAL LIST OF ABBREVIATIONS	357
NMR SPECTRA	361

## Abstract

Over the past decade, photopharmacology has become an established method to address biological questions. From the first proof-of-principle that the small molecule azobenzene can be used to control the function of much larger biomolecule like transmembrane receptors, the field has rapidly developed and is now providing tools for medical research.

In this work, we have synthesized and characterized photoswitchable ligands for GPCRs, ion channels, and the cytoskeleton, including adenosine receptors (AzoAdenosines), ryanodine receptors (AzoCaffeines), voltage-gated ion channels (various open channel blockers, KCNQ channel modulators and arsenic analogs for co-crystallization) and myosin V (AzoMyoVIns).

In particular, we have focused on the development and characterization of new photoswitches and their biochemical or medical application. We disclosed an efficient access to cyclic azobenzenes (diazocines) and have thoroughly investigated the effects of different substitution patterns on their photophysical properties. These photoswitches are stable in their bent *cis*-form, and we could show that using these new types of photoswitches, enables inversion of the biological activity of the photoswitch, compared to an azobenzene analog (Figure 1).



**Figure 1: The concept of sign inversion in photopharmacology using diazocine photoswitches.**

This concept was demonstrated with openers of G protein-coupled inwardly rectifying potassium (GIRK) channels and blockers for voltage-gated potassium ( $K_v$ ) channels. While azobenzene-based GIRK-channel openers and  $K_v$  channel blockers bound to their target in the dark-state (*E*-form), our diazocine-based analogs bound upon illumination with light (also *E*-form). This orthogonal toolset will enable researchers to tailor their photoswitch design according to the desired application.

Additionally, we have continued to develop new azobenzene-based photoswitchable ion channel blockers for vision restoration purposes. Our molecules conferred light sensitivity to degenerated and blind mouse retinas, as shown in multi-electrode array studies. Focusing on low-frequency oscillations in the retina (local field potentials, LFPs), which develop during the degeneration process, we discovered a unique property of azobenzene photoswitches. Upon switching, they suppress these detrimental oscillations and lead to an improved signal to noise ratio, a characteristic which makes them unique among other vision restoration approaches, like electrical implants or gene therapy.







# I. General Introduction



# In Vivo Photopharmacology

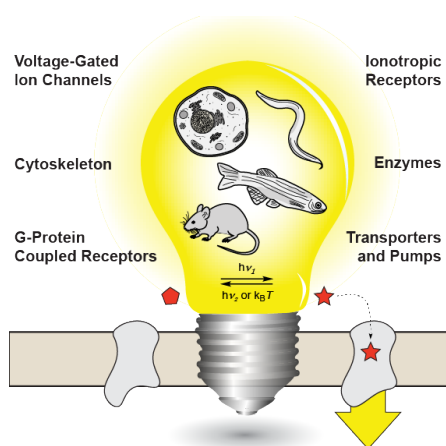
Katharina Hüll<sup>§</sup>, Johannes Morstein<sup>§</sup>, and Dirk Trauner<sup>\*</sup>

Department of Chemistry, New York University, 100 Washington Square East, New York, NY 10003-6699, USA.

<sup>§</sup>These authors contributed equally

Reprinted (adapted) with permission from Hüll, K.; Morstein, J.; Trauner, D. In Vivo Photopharmacology. *Chem. Rev.* **2018**, *118* (21), 10710-10747. Copyright 2018 American Chemical Society

## Abstract



Synthetic photoswitches have been known for many years but their usefulness in biology, pharmacology, and medicine has only recently been systematically explored. Over the last decade photopharmacology has grown into a vibrant field. As the photophysical, pharmacodynamic, and pharmacokinetic properties of photoswitches, such as azobenzenes, have become established, they have been applied to a wide range of biological targets. These include transmembrane proteins (ion channels,

transporters, G protein-coupled receptors, receptor-linked enzymes), soluble proteins (kinases, proteases, factors involved in epigenetic regulation), lipid membranes, and nucleic acids. In this review, we provide an overview of photopharmacology using synthetic switches that have been applied *in vivo*, i.e. in living cells and organisms. We discuss the scope and limitations of this approach to study biological function and the challenges it faces in translational medicine. The relationships between synthetic photoswitches, natural chromophores used in optogenetics, and caged ligands are addressed.

## **Contents - In Vivo Photopharmacology**

### **ABSTRACT**

#### **1 INTRODUCTION**

#### **2 PHOTOSWITCHES FOR ION CHANNELS**

##### 2.1 Ionotropic Glutamate Receptors

###### 2.1.1 AMPA receptors

###### 2.1.2 Kainate Receptors

###### 2.1.3 NMDA Receptors

##### 2.2 Pentameric Ligand-Gated Ion Channels

###### 2.2.1 Nicotinic Acetylcholine Receptors (nAChRs)

###### 2.2.2 GABAA Receptors

##### 2.3 Voltage-Gated Ion Channels

##### 2.4 Other Ion Channels

###### 2.4.1 TRP Channels

###### 2.4.2 ATP-Sensitive Potassium Channels

###### 2.4.3 G Protein-Coupled Inwardly Rectifying Potassium Channels

###### 2.4.4 ENaC/P2X Superfamily

#### **3 PHOTOSWITCHES FOR TRANSPORTERS AND PUMPS**

#### **4 PHOTOSWITCHES FOR GPCRS**

##### 4.1 Class A, Rhodopsin-Like

##### 4.2 Class B, Secretin Receptor Family

##### 4.3 Class C, Metabotropic Glutamate Receptor Family

#### **5 PHOTOSWITCHES FOR ENZYMES**

##### 5.1 Kinases

##### 5.2 Phosphatases

##### 5.3 Proteases

##### 5.4 Histone Deacetylases and Histone Methyltransferases

##### 5.5 Acetylcholinesterases

##### 5.6 RNA Polymerases

##### 5.7 DNA Gyrases and Dihydrofolate Reductases

##### 5.8 Lipoxygenases

5.9	Nitric Oxide Synthases
5.10	Receptor-Linked Enzymes
<b>6</b>	<b>PHOTOSWITCHES THAT TARGET THE CYTOSKELETON</b>
<b>7</b>	<b>OTHER APPLICATIONS OF PHOTOSWITCHES</b>
7.1	Membrane Transport
7.2	Protein Translation
7.3	Cytotoxicity
7.4	Immunobiology
7.5	Cell Adhesion and Cell Communication
<b>8</b>	<b>PHOTOPHARMACOLOGY WITH SYNTHETIC SWITCHES VS. ALTERNATIVE APPROACHES FOR OPTICAL CONTROL</b>
<b>9</b>	<b>CONCLUSION AND OUTLOOK</b>
<b>10</b>	<b>TABLE OF STRUCTURES</b>
10.1	Photoswitches for Ion Channels
10.2	Photoswitches for Transporters/Pumps
10.3	Photoswitches for GPCRs
10.4	Photoswitches for Enzymes
10.5	Photoswitches for Cytoskeleton
10.6	Other Applications of Photoswitches
<b>11</b>	<b>LIST OF ABBREVIATIONS</b>
<b>12</b>	<b>REFERENCES</b>

# 1 Introduction

Light is unsurpassed in its ability to control biological systems with high spatial and temporal resolution. It has the advantages of non-invasive and remote action, reversibility, speed, and facile modulation of the energies involved. This has been recognized in optogenetics, a field that has grown from an attempt to optically control neuronal activity to a broad effort to use light as a precision tool in biology.<sup>1</sup> In its most broadly used form, optogenetics relies on naturally occurring chromophores, such as retinal or flavins, to convey the interaction of light with its receptors on a molecular and cellular level.

Light, however, can also influence the biological activity of *synthetic* molecules by changing their pharmacokinetic or pharmacodynamic properties. This combination of photochemistry and pharmacology is now known as “photopharmacology”. While other names, such as “optopharmacology” and “chemical optogenetics”, have been suggested, in our opinion, photopharmacology is the most suitable one, both for etymological and for esthetic reasons.

The effect of light on small molecules can be irreversible or reversible and both modalities have been used in biology.<sup>2</sup> The irreversible photochemical inactivation of drugs, for instance, has been occasionally applied to probe the functional role of their biological targets (Fig. 1A).<sup>3</sup> Photocleavable protecting groups (“cages”) have enabled the conditional release of biologically active ligands (Fig. 1B). To date, caged ligands are arguably the most widely used photopharmacological tools and new varieties of photocages continue to emerge.<sup>4,5</sup> However, caged ligands have been extensively reviewed elsewhere and are therefore not a subject of this article.<sup>5,6</sup> Other modes of light-activation (e.g. PACT) can be considered but are beyond the scope of this review.<sup>7</sup>

Here, we focus on synthetic *photoswitches* that allow for the fast and reversible optical control of biological systems and we will only cover switches that have been used *in vivo*. As far as this review is concerned, *in vivo* means in a living cell (*‘in cellulo’*) and in an animal (ideally awake and with quantifiable behavior). In comparison to molecular targets investigated *in vitro*, cellular systems exhibit physically permeable barriers, compartmentalization, and a crowded and complex target environment.<sup>8,9</sup> Within the last years, the use of photopharmacology in living systems has grown considerably and its applicability in biology and complementarity to conventional optogenetics has become evident. The timeliness of *in vivo* photopharmacology is also evident by the fact that nearly half of the contributions reviewed here were published in 2015 or thereafter. We refer the reader to other comprehensive reviews on photopharmacology for an overview of *in vitro* studies.<sup>10,11</sup>

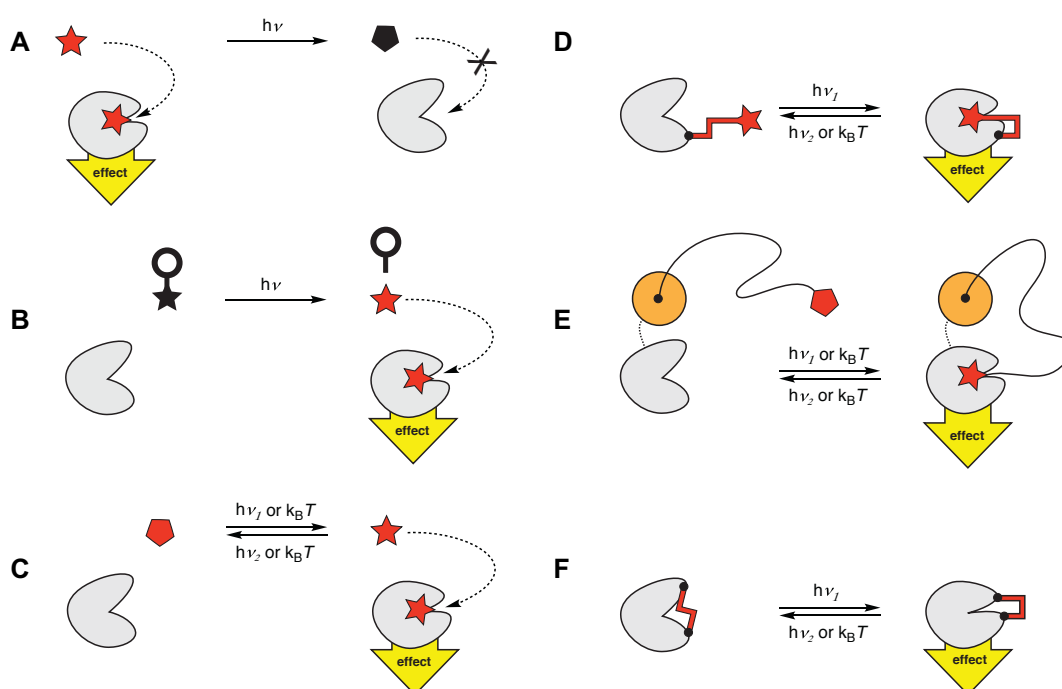
Synthetic photoswitches can be classified by the mechanism with which they interact with their targets (Fig. 1C-F). So-called Photochromic Ligands (PCLs) are freely diffusible molecules that can adopt two (or more) different isomeric forms upon irradiation with light, which exhibit different affinities and/or efficacies towards their biological targets and have different pharmacodynamics (Fig 1C). Switching can also affect the bioavailability (pharmacokinetics) of the PCL.

In a second modality, ligands can be covalently tethered to the receptor through some form of bioconjugation, either to a native or to an engineered residue.<sup>12</sup> This allows for genetic encoding but also accelerates the response due to the high local concentration and the inability of the ligand to diffuse away. In general, tethered photopharmacology is faster than photopharmacology with a freely diffusible ligand, which in turn is faster than normal pharmacology. Tethered ligands can function as agonists, inverse agonists, antagonists, or blockers pending on their pharmacology and/or their site of attachment.

Tethered ligands can be further divided into two subcategories depending on the closeness or remoteness of the covalent attachment site with respect to the ligand binding site: a) Photoswitchable Tethered Ligands (PTLs), and b) Photoswitchable Orthogonal Remotely Tethered Ligands (PORTLs).

If the photoswitch is mounted closely to the binding site and if it constitutes a large portion of the tether, as it is the case in a PTL, switching primarily effects the local concentration of the pharmacophore (Fig. 1 D). Ideally, the ligand cannot reach the binding site in one configuration and binds effectively in the other. Close tethering requires small bioconjugation motifs, e.g. a single cysteine point mutation. By contrast, the photoswitch in a PORTL mostly affects the efficacy of the tethered ligand and has a less pronounced effect on its local concentration (Fig. 1 E).<sup>13</sup> Here, the bioconjugation motif can be much larger, e.g. a self-labeling protein tag that reacts with the speed and selectivity of an enzymatic reaction (Halo, Snap, Clip tag etc.). These orthogonal tags can be fused with a protein of interest but can also be mounted onto an auxiliary protein within the same cell or even in an adjacent cell provided the tether is long enough and the local concentration can be kept high.<sup>14</sup> Of course, the categories of close and remote tethering represent extremes and it is conceivable that there are tethered ligands which fall in between.

Another class of photoswitches covered in this review is light-responsive cross linkers (Fig. 1 F). Here, a photoswitch is covalently attached on both of its ends and, upon isomerization, influences the conformation and activity of a biological target (Fig 1 E). This requires two conjugation motifs on the biomolecule, e.g. two reactive cysteines appropriately spaced.

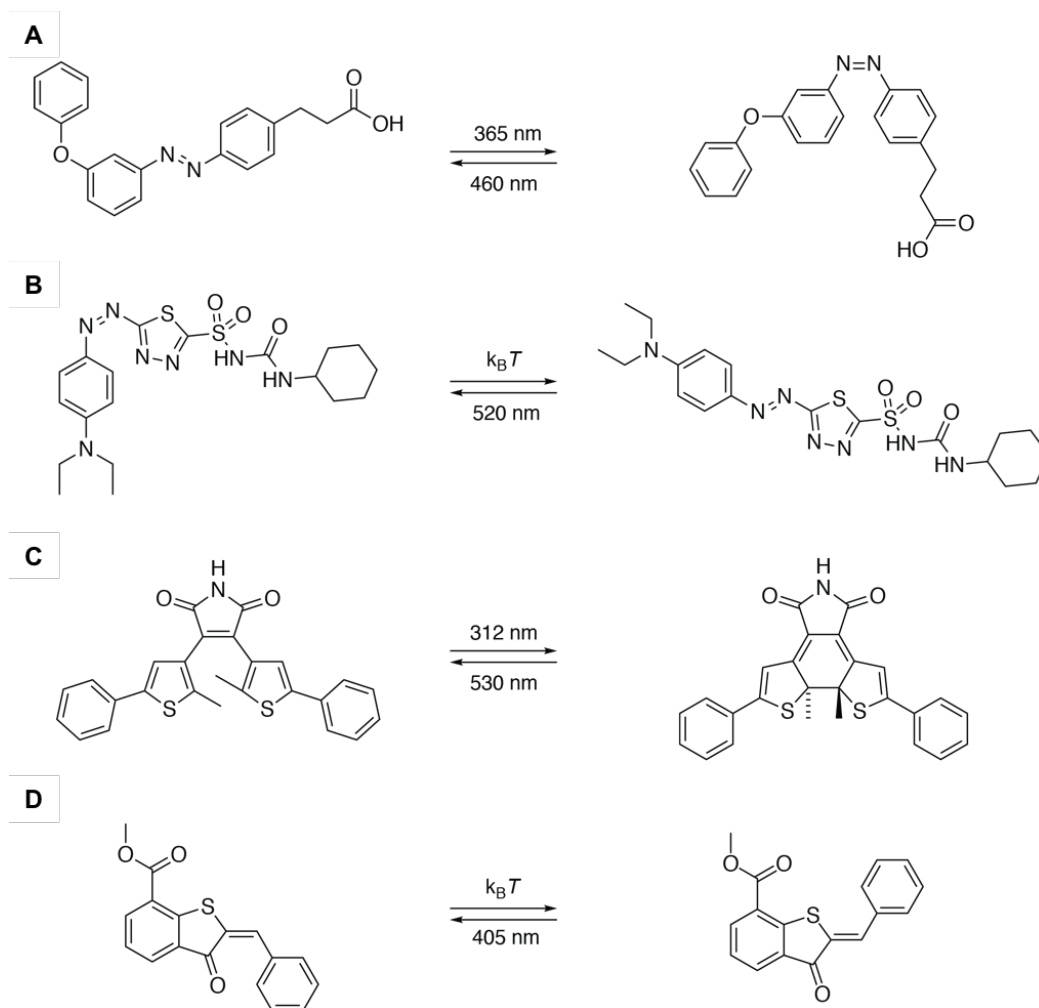


**Figure 1: Modalities of photopharmacology.** (A) Irreversible photoinactivation. (B) Irreversible photoactivation (photo-uncaging). (C) Reversible photoactivation/inactivation using a photochromic ligand (PCL) that toggles between an inactive (pentagon) or active (star) form. (D) A photoswitchable (closely) tethered ligand (PTL). (E) A photoswitchable orthogonal remotely tethered ligand (PORTL). (F) A photoswitchable cross-linker.

Other modalities are possible, such as photoswitches that are incorporated through expansion of the genetic code. Although this is strictly speaking not photopharmacology, the photoswitchable amino acid must be added externally and the photoreceptor so formed is functionally related to those covered in this review.

Having settled on a modality, the question arises as to which synthetic photoswitch to use. It must fulfill several requirements to be applicable *in vivo*: It should have favorable pharmacokinetics and should be metabolically stable in a given milieu. It cannot be phototoxic, which can occur when intersystem crossing competes with photoswitching.<sup>15</sup> Under physiological conditions, this can lead to the formation of singlet oxygen, which bleaches the chromophore and can be damaging to cells.<sup>16,17</sup> Moreover, the photoswitch should exhibit useful photophysical properties, such as high absorbance and quantum yields, and useful thermal relaxation rates.





**Figure 2: Synthetic photoswitches used in photopharmacology.** The active photoisomer is drawn on the left and the inactive photoisomer on the right. (A) An azobenzene that is thermally bistable and can be toggled between the active and inactive form using different wavelengths of light. (B) An azobenzene photoswitch that loses activity in the absence of light. (C) A bistable diarylethene photoswitch. (D) A hemithioindigo switch that is inactive in the dark and can be switched on with light.

Azobenzenes fulfill most of these criteria and therefore account for the majority of switches used to date, although diarylethanes, fulgides, and hemithioindigos have been occasionally employed (Fig. 2).<sup>18-22</sup> Therefore, some functional features of molecular photoswitches are best discussed with azobenzenes. Since the absorption spectra of their isomeric forms overlap to a certain degree one must consider photostationary states, which are a function of the wavelengths used. The isomeric ratio in the photostationary state can approximate 99:1 if the absorption spectra are very well separated but is usually much lower, e.g. 80:20. Due to the inherent non-linearity of biological systems, however, these low ratios can still be

highly consequential. Photoswitches that are ineffective in an *in vitro* enzymatic assay and show considerable background activity can indeed have pronounced and clean effects in a physiological experiment.

The photochemical interconversion of isomers is overlaid by thermal relaxation, i.e. the ability of the switch to fall back into its thermodynamically more stable form. The rate of this thermal relaxation depends on the electronic structure of the azobenzene and is also influenced by temperature and solvent. As far as *in vivo* photopharmacology is concerned, the solvent is an aqueous solution at physiological pH and with high ionic strength, which lowers the barrier for thermal isomerization.<sup>23</sup> Nevertheless, some azobenzene switches remain stable in their high-energy isomeric form for hours or days once the light is turned off,<sup>24-26</sup> whereas others undergo very fast thermal relaxation in the dark.<sup>27,28</sup> Depending on the biological system investigated and its responsiveness, either bistability or the automatic deactivation of a fast relaxing photoswitch can be desirable.<sup>29</sup> The former would be the case, for instance, with photopharmacology that targets gene expression, whereas the latter is applicable in neural systems with millisecond response times, such as the human retina.

With these considerations in mind and a focus on biological applications, we have organized this review according to the biological targets amenable to *in vivo* photopharmacology. These include ion channels, transporters and pumps, GPCRs, enzymes, elements of the cytoskeleton, and a few examples, which go beyond these target classes. In the concluding section, we will compare photopharmacology with other methods for controlling biological activity with light and discuss the advantages and disadvantages of synthetic switches, caged compounds, and optogenetic approaches that involve natural chromophores. Lastly, we will briefly discuss the state of the art and future directions of photopharmacology with respect to clinical applications.

## 2 Photoswitches for Ion Channels

Ion channels are involved in fast synaptic transmission and play a key role in nervous systems. They are also important for secretory processes and the maintenance of body homeostasis. They have highly developed pharmacology and their fast kinetics are well matched to the kinetics of synthetic photoswitches. As such, photopharmacology has been particularly successful with ion channels.

### 2.1 Ionotropic Glutamate Receptors

Ionotropic glutamate receptors (iGluRs) are tetrameric cation channels, which open upon activation with presynaptically released glutamate and trigger action potentials in postsynaptic neurons. Based on their affinity towards certain agonists and their genomic sequence, iGluRs have been divided into AMPA (iGluAs), kainate (iGluKs) and NMDA (iGluNs) receptors. Due to their fundamental role in neural processing and extensive biophysical characterization, iGluRs emerged as one of the first targets for photopharmacology.

#### 2.1.1 AMPA receptors

In 2012, Trauner and colleagues introduced the photoswitchable agonist **ATA** (Table 1, #1), which was characterized in mouse brain slice and HEK293T cells.<sup>30</sup> **ATA** activated GluA2 receptors in its *trans*-form and could be inactivated with blue light. Accordingly, trains of action potentials (APs) were generated in the dark, while AP firing stopped upon irradiation with 480 nm light. In a subsequent study, **ATA** was explored in the context of vision restoration.<sup>31</sup> Multi-electrode-array (MEA) recordings and patch-clamp electrophysiology carried out with degenerated mouse retinæ revealed that **ATA** primarily acts on retinal ganglion cells (RGCs) and amacrine cells. Computational ligand docking studies showed that the *trans* isomer binds tightly and allows for full closure of the clamshell-like ligand binding domain of the receptor, whereas the *cis*-isomer rapidly dissociates.<sup>32</sup>

More recently, a photoswitchable antagonist for AMPA receptors, termed **ShuBQX-3** was developed, complementing the photopharmacology of AMPA receptors (Table 1, #2).<sup>33</sup> **ShuBQX-3** could be used to control action potential firing in hippocampal CA1 neurons with 460 nm/600 nm light. Interestingly, the absorption and action spectrum of **ShuBQX-3** undergoes an unusually large bathochromic shift upon binding to the receptor or interacting with free arginine in solution. This large difference between the UV-Vis spectra in the absence of the receptor and the action spectra has been rarely observed in photopharmacology.

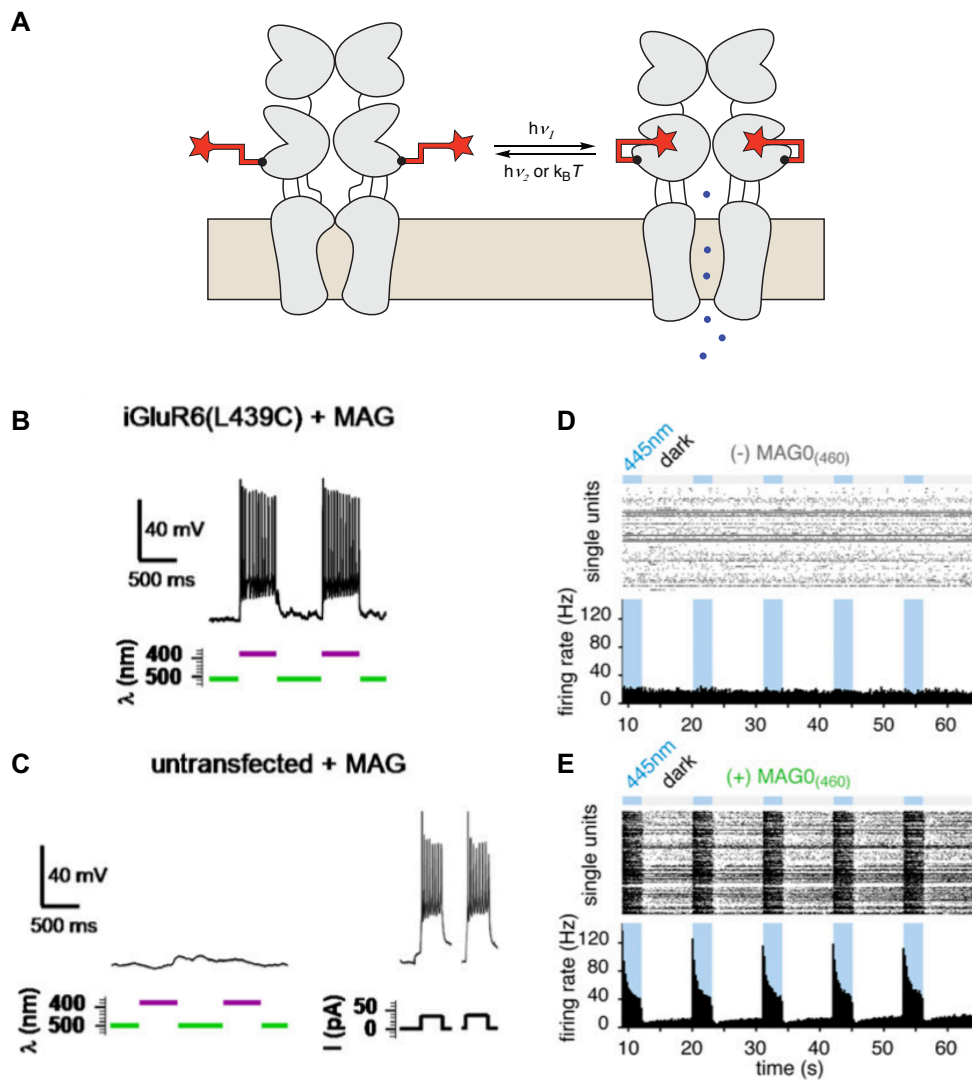
## 2.1.2 Kainate Receptors

Optical control over GluK receptors was achieved with the PCL **GluAzo** (Table 1, #3).<sup>34,35</sup> Signaling through native GluK1 and GluK2 receptors could be controlled with 380 nm/500 nm light. Photoswitching of iGluR-currents was demonstrated in transfected HEK293T cells, dissociated neurons and Purkinje cells.<sup>36</sup>

Covalent attachment of the glutamate photoswitch **L-MAG-1** (Table 1, #4) to a cysteine mutant of GluK2 gave rise to the light-gated glutamate receptor, LiGluR (Fig. 3).<sup>37-39</sup> LiGluR could be monitored with electrophysiology (Fig. 3B and C) but also with calcium imaging due to its Ca<sup>2+</sup>-permeability.<sup>40</sup> PTLs with longer (**L-MAG-2**; Table 1, #4) and shorter linkers (**L-MAG-0**; Table 1, #4) were also developed,<sup>41</sup> as well as versions with red-shifted action spectra (**L-MAG-0<sub>460</sub>**; Table 1 #5 and **toCI-MAG**; Table 1, #6).<sup>42,43</sup> Furthermore, two-photon (2P) switching could be demonstrated with **MAGs**.<sup>44,45</sup> To this end, MAG was modified with a linker (**MAG<sub>2P</sub>**; Table 1, #7) and equipped with a 2P antenna (**MAGA**; Table 1, #8).<sup>45</sup> The biophysical properties of LiGluR and its variants have been investigated in detail. For instance, the PTL was found to function as a photoswitchable full agonist.<sup>39</sup> These studies also provided insights into the function of the native receptor and helped to clarify receptor gating kinetics and its desensitization mechanism.<sup>46</sup> Depending on the point of mutation, **L-MAG-0** can activate the receptor in either its *cis*- or its *trans*-form. This “yin/yang” behavior allows for independent activation of LiGluR in different subsets of neurons.

When expressed in sensory neurons of zebrafish larvae, LiGluR enabled optical control over their escape response. Photostimulation of Kolmer-Agduhr neurons with LiGluR provided insights into their physiological role in zebrafish.<sup>47</sup> The calcium permeability of LiGluR also allowed for the optical control of a variety of calcium-dependent biological processes, such as exocytosis,<sup>48</sup> neurotransmitter release in chromaffin cells,<sup>49</sup> and glutamate release in astrocytes through increased Ca<sup>2+</sup> levels.<sup>50</sup>

In the retina, LiGluR can be selectively expressed *via* transfection with adeno-associated virus (AAV) and labeled with **MAGs**.<sup>51</sup> About five weeks after injection, LiGluR was found exclusively in RGCs. In multielectrode array (MEA) recordings with 5 s light/dark intervals, sustained light responses were observed, which declined in magnitude to reach a plateau after a few cycles. This was sufficient to restore the pupillary light reflex and light-avoidance behavior. With the development of red-shifted **MAG**-derivatives, *in vivo* application became more feasible. As a red-shifted azobenzene, **L-MAG-0<sub>460</sub>** does not require irradiation with UV light and quickly turns off in darkness. MEA recordings with LiGluR-transfected, degenerated retinæ from *rcd1* dog model showed light responses of RGCs. In *rd1* mice, in addition to expression in RGCs (Fig. 3D and E), LiGluR was transfected in ON-bipolar (ON-BP) cells using AAV and an ON-BP specific promoter.<sup>52</sup> Targeting bipolar cells upstream of RGCs makes it possible to exploit



**Figure 3: Ionotropic glutamate receptors.** (A) Schematic depiction of LiGluR. Isomerization of the photoswitch brings the active ligand (red star) in close proximity to the binding site, opening the channel. (B) iGluR6(L439C) transiently expressed in hippocampal neurons with **L-MAG** covalently attached show trains of AP firing upon illumination with 380 nm light. Illumination with 500 nm silences AP firing. Reprinted with permission from reference (38). Copyright 2007 Elsevier Ltd. (C) Neurons lacking LiGluR do not respond to alternating light but do respond to current injections. Reprinted with permission from reference (38). Copyright 2007 Elsevier Ltd. (D)-(E) Multi-electrode-recordings of retinal ganglion cells from blind mouse retinae, overexpressing LiGluR without (D) or with (E) **L-MAG-0<sub>460</sub>**. Alternating dark/445 nm sequences leads to firing of retinal ganglion cells in a blind mouse model. Reprinted with permission from reference (52).

retinal cell processing above the level of RGCs. The resulting signal should resemble the wild type retina signal more closely. Although the **MAGs** worked well in RGCs, their hydrolytic instability limited their use in less accessible cells.<sup>53</sup> This prompted the development of PORTLs (see section 3.3).

Gorostiza and colleagues targeted native kainate receptors in the retina *via* affinity labeling with photoswitchable glutamate derivatives called **TCP-9** and **TCP-10** (Table 1, #9 and #10.) These PTLs bear an *N*-hydroxy succinimide ester (NHS-ester) as an electrophile, which reacted with native lysines close to the ligand binding site.<sup>54</sup> They were used to restore light-dependent electrical activity in a blind mouse retina, as demonstrated with MEA recordings. This approach is related to the photoswitchable affinity label concept (PAL) proposed for potassium channels and demonstrated with the enzyme human carbonic anhydrase.<sup>55,56</sup> Despite the instability of NHS-esters, maleimides, and related electrophiles, it holds promise for imparting light-sensitivity to native receptors with increased selectivity.

In addition to new **MAG**-derivatives, the incorporation of new GluK mutants expanded the repertoire of artificial photoreceptors.<sup>57</sup> The use of an optrode enabled the optical control of such LiGluR variants in awake, adult mice. The modularity of the glutamate receptor family was also exploited to engineer a light-gated K<sup>+</sup>-channel. Combining the K<sup>+</sup>-selective pore domain of the bacterial glutamate receptor sGluR0 with the LBD of the GluK2 cysteine mutant gave rise to HyLighter.<sup>58</sup> HyLighter was expressed in cultured hippocampal neurons and conjugated with **L-MAG-0** (Table 1, #4) to inhibit AP firing upon illumination. Expression in motorneurons of zebrafish larvae allows reversible suppression of escape behavior. Like its predecessor SPARK<sup>59,60</sup> (see below), HyLighter<sup>58</sup> provides a solution to optical inhibition with a light gated potassium-selective channel, which has been difficult to achieve via engineering of channelrhodopsins.<sup>61</sup>

### 2.1.3 NMDA Receptors

With the development of the photoswitchable agonist **ATG** (Table 1, #11), photocontrol over the remaining glutamate receptor class - the NMDA receptors - was achieved in 2015.<sup>62</sup> **ATG** is bistable, active in its *cis*-form, and can be switched on with either UV light (370 nm) or with 740 nm 2P pulses. More recently, a photoswitchable antagonist, termed **PNRA** (Table 1, #12), for GluN receptors, was introduced.<sup>63</sup> This *trans*-active antagonist can be isomerized with 360 nm/420 nm of light and is the first antagonist displaying a higher affinity towards GluN2A and GluN2C over GluN2B and GluN2D.

Adopting the logic of LiGluR (*i.e.* LiGluKR), Isacoff and Trauner established that the photoswitches **L-MAG-0** and **L-MAG-1** (Table 1, #13) can be applied to NMDA receptors, giving rise to LiGluNR.<sup>64</sup> To this end, a small library of LiGluNRs with different cysteine mutants was generated and conjugated to the **MAGs**. Pending on the site of mutation and the PTL used, photo-agonism or photo-antagonism of

GluN2A and GluN2B could be achieved, enabling control of synaptic activation or spine-specific control over calcium levels. Transgenic zebrafish larvae were chronically NMDA-antagonized with short light flashes, leading to increased growth of retinal ganglion cells in their optic tectum.

Paoletti and colleagues incorporated the unnatural photoswitchable amino acid **PSAA** (Table 1, #14) into GluN1, GluN2A, or GluN2B subunits to create light sensitive NMDARs.<sup>65</sup> This work represented the first *in vivo* application of a photoswitchable amino acid integrated *via* genetic code expansion. Both activation and deactivation could be achieved upon UV-illumination, depending on the site of incorporation. Functional studies showed that sensitivity towards glutamate was not affected but the binding affinity of the co-agonist glycine could be modulated with light, thereby raising the open probability of the channel.

## 2.2 Pentameric Ligand-Gated Ion Channels

### 2.2.1 Nicotinic Acetylcholine Receptors (nAChRs)

Nicotinic acetylcholine receptors nAChRs are pentameric ligand-gated ion channels that are primarily permeable to sodium, potassium, and, in some cases, calcium ions. In 1969, the Erlanger group pioneered the photopharmacology of nAChRs, and the entire field of photopharmacology, by perfusing *Electrophorus* electroplaques with the photochromic ligands **AzoCharCh** (Table 1, #15) and **azo-PTA** (Table 1, #16).<sup>66</sup> Two years later, they published the PCL **BisQ** (Table 1, #17) and the covalently attached photochromic ligand **QBr** (Table 1, #18).<sup>67-70</sup> **Trans-BisQ** proved to be a potent activator of *Electrophorus* electroplaques and isomerized to the less active *cis*-isomer upon irradiation with 330 nm light. Erlanger, Lester and colleagues subsequently controlled the membrane potential of the squid giant axon with the azobenzene ammonium ion **EW-1** (Table 1, #19)<sup>71,72</sup> and introduced the symmetrical photoswitchable antagonist **2BQ** (Table 1, #20).<sup>73</sup>

Many years later, Trauner and colleagues introduced a new PTL, **AzoCholine** (Table 1, #21). This compound, which was derived from phenyl choline ether, responded to 360 nm/440 nm light and was found to be a *trans*-active agonist for neuronal  $\alpha 7$  nAChRs.<sup>74</sup> It provided optical control of the thrashing activity of *C. elegans* nematodes. In the same study, **BisQ** was reevaluated and shown to primarily act on muscular nAChRs, but not on neuronal nAChRs. Around the same time, Li and colleagues modified the insecticide imidacloprid, an agonist to insect nAChRs, with an azobenzene.<sup>75</sup> The resulting PCLs were tested for their insecticidal activity against the house fly *Musca domestica*. Under UV light irradiation, a decrease in LD<sub>50</sub> by 80% was observed for the most active compound, **AMI-10** (Table 1, #22).

Applying the PTL concept to nicotinic receptors, Trauner, Kramer, and colleagues designed the light-gated nicotinic acetylcholine receptor LinAChR using based on then available X-ray structure.<sup>76</sup> The PTLs **MAACh** (Table 1, #23) functioned as a photoswitchable agonist, whereas **MAHoCh** (Table 1, #24), proved to be a light-activated antagonist. Both PTLs respond to 380 nm/500 nm light and are bistable under physiological conditions. LinAChR was evaluated in *Xenopus* oocytes but is expected to work well in excitable cells and complex neuronal systems.

## 2.2.2 GABA<sub>A</sub> Receptors

GABA<sub>A</sub> receptors are chloride-selective pentameric ligand gated ion channels that decrease the likelihood of action potential firing upon opening. In 2012, Trauner and colleagues published a light-switchable derivative of propofol, termed **AP-2** (Table 1, #25).<sup>77</sup> This compound functioned as an allosteric modulator that potentiated GABA currents in the dark and could be inactivated upon irradiation. The effect on chloride currents was investigated with *Xenopus* oocytes overexpressing the  $\alpha 1\beta 2\gamma 2$ -GABA<sub>A</sub> variant. Light dependent anesthesia was demonstrated with *Xenopus laevis* tadpoles. Concurrently, Pepperberg and co-workers published a different series of photochromic propofol analogues, including the PCL **MPC-088** (Table 1, #26) and the PTL **MPC-100** (Table 1, #27).<sup>78</sup> They applied these compounds to oocytes and to cerebellar slices and could modulate membrane current and spike firing rate in Purkinje cells using UV/blue light. Shortly thereafter, the Kramer group introduced another light-regulated GABA receptor (LiGABAR) using tethered photopharmacology.<sup>79</sup> In this case, they engineered a GABA<sub>A</sub> receptor bearing a cysteine mutation in its  $\alpha 1$ -subunit that served as conjugation site for the PTL **MAM-6** (Table 1, #28). Although it was derived from muscimol, **MAM-6** does not act as a photoswitchable agonist but as an antagonist. The response of LiGABAR to its endogenous ligand can thus be modulated with light. Illumination at 380 nm allows for greater activation with GABA than at 500 nm, as the ligand antagonist retracted from the binding site in the *cis*-state of the switch. LiGABAR was used in *Xenopus* oocytes, HEK293T cells, and cultured hippocampal neurons, as well as in brain slices. The generation of a LiGABAR knockin mouse line allowed photocontrol of LiGABAR at endogenous expression levels.<sup>80</sup> In the course of this study, new PTLs with higher efficacy were introduced, e.g. the guanidinium analog **PAG-1C** (Table 1, #29). This refined version of LiGABAR enabled the optical control of cortical neurons in awake mice.

## 2.3 Voltage-Gated Ion Channels

Voltage-gated ion channels, which include potassium (K<sub>V</sub>), sodium (Na<sub>V</sub>), and calcium (Ca<sub>V</sub>) channels, play crucial roles in the generation of action potentials and in synaptic transmission and are prime targets for photopharmacology. Not surprisingly, they have played a prominent role in the development of the field. In



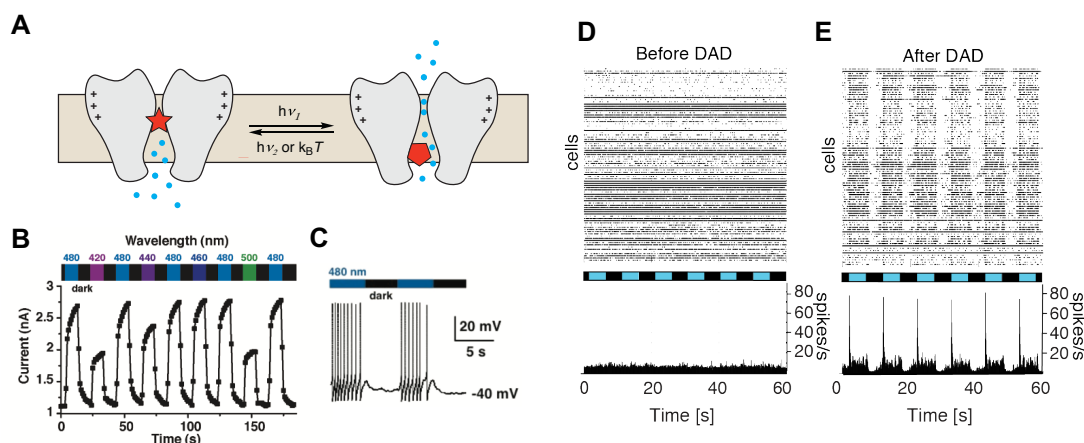
2004, Trauner, Kramer, and Isacoff introduced a light and voltage sensitive potassium channel called SPARK.<sup>59</sup> To this end, they endowed a *Shaker* K<sub>v</sub> with an engineered cysteine, which served as a bioconjugation motif for a tethered quaternary ammonium ion (**MAQ**, Table 1, #30). Isomerization of the photoswitch with 380 nm/500 nm light shortened and lengthened the tether, unblocking and blocking the pore. This translated to the reversible optical control of action potential firing in hippocampal pyramidal neurons. An additional mutation in the channel pore converted the potassium-selective SPARK into a non-selective ion channel (D-SPARK).<sup>60</sup> While SPARK channels led to the optical of neuronal inhibition, the unselective variant enabled light-controlled depolarization and excitation of dissociated neurons.

Photocontrol over the mechanically gated potassium channel TREK1 was achieved by conjugating **MAQ** (Table 1, #31) with a TREK1 cysteine mutant.<sup>81</sup> Isomerization with 380 nm/500 nm light resulted to reversible activation in HEK293T cells. Transfecting hippocampal neurons with the TREK1 mutant and labelling with **MAQ** allowed insights in the formerly unknown role of TREK1 in GABAergic signaling. While no light-elicited TREK1 currents could be detected at resting potential, baclofen-induced GABA currents could be modulated with light.

In addition to PCLs, cationic blockers that function as PTLs have been systematically explored (Fig. 4). Although these compounds are much less selective than **MAQ** as they affect a range of voltage gated ion channels, they have nevertheless proven to be powerful photopharmacological tools *in vivo* and they are on the verge of becoming clinically relevant. The first compound that functioned in this way was **AAQ** (Table 1, #32).<sup>55</sup> Although it was initially designed to attach itself covalently *via* affinity labelling, it proved to be a PCL that binds to the inner cavity of voltage gated ion channels and has long-lasting effects to cells due to its lipophilicity.<sup>82</sup> As such, it is a photoswitchable version of the well-known use-dependent open-channel blocker lidocaine. **AAQ** can be isomerized with 360 nm/500 nm light and is thermally relatively bistable. Suppression of AP firing could be achieved with 380 nm light, whereas 500 nm light restored neuronal activity. In a subsequent study, **AAQ** was used to convey light-sensitivity to blind retinae, where it mainly targets amacrine cells.<sup>83</sup> In addition to **AAQ**, a series of derivatives with different photochemical, thermal, and pharmacological profiles was synthesized and characterized in cells. Amongst these, the highly lipophilic switch **PrAQ** (Table 1, #33) turned out to be *cis*-active, inverting the logic of the otherwise *trans*-active blockers.

The photoswitches discussed above required UV irradiation for *trans/cis* isomerization and were thermally bistable, which limited their utility for applications in vision restoration. To address these issues, a second-generation of red-shifted photochromic ion channel blockers was developed that had absorption maxima in the 420–460 nm range.<sup>84</sup> The lead compounds that emerged from this study, **DENAQ** (Table 1, #34) and **BENAQ** (Table 1, #35) blocked K<sub>v</sub>3.1 and *Shaker*

potassium channels expressed in HEK293T cells in a light-dependent fashion and could be turned on and off with visible light and fast thermal relaxation, respectively (Fig. 4B and C). They worked in hippocampal brain slices and were subsequently used in vision restoration.<sup>85-87</sup> **DENAO** provided sensitivity to white light at relatively low intensities and restored light-guided behavior in blind mice in an open field assay. Like **DENAO**, **BENAO** acted primarily on RGCs and showed long-lasting effects due to its high lipophilicity.



**Figure 4: Photochromic ion channel blockers.** (A) Schematic depiction of a photoswitchable, use-dependent open channel blocker (red star). Upon isomerization to its inactive form (pentagon), the blocker unbinds from the pore. (B) Light-dependent potassium current elicited by isomerization of **DENAO**. Reprinted with permission from reference (84). Copyright 2011 American Chemical Society. (C) optical control of action potential firing in hippocampal neurons with **PhENAO**. Reprinted with permission from reference (84). Copyright 2011 American Chemical Society. (D)-(E) Multi electrode recordings in mouse retinae. Treatment with **DAD** results in light-dependent network activity (blue = 460 nm, black = dark). Figure created by the authors from data in reference (94).

A symmetrically substituted azobenzene with a quaternary ammonium ion on each side, termed **QAO** (Table 1, #36) was introduced shortly after its unsymmetrical predecessors.<sup>88</sup> **QAO** responds to 380 nm/500 nm light, is stable in the dark and can block  $K_v$ ,  $Na_v$  and  $Ca_v$  channels. This bivalent ion channel blocker is not membrane-permeable and needs to be actively transported into the cell via TRPV1 channels or P2X receptors. It was therefore possible to selectively target TRPV1 expressing cells for the optical control of nociception. More bistable and slightly red-shifted *ortho*-substituted derivatives of **QAO** were reported shortly thereafter (Table 1, #37 and #38).<sup>89</sup> The even more red-shifted blocker **QENAO** (Table 1, #39) was developed to combine the pharmacokinetics of **QAO** with the photophysical

properties of **DENAO**.<sup>90</sup> Like **QAO**, **QENAO** blocks  $\text{Na}_V$  and  $\text{K}_V$  and can be used to optically control sensory DRG neurons.

The mechanism of action of **DENAO** and **BENAO** in degenerating retinæ was unraveled in 2016 when Kramer and co-workers could show that they are subject to a similar transport mechanism as **QAO**.<sup>86</sup> Like TRPV1, P2X receptors are known to dilate upon continued activation with ATP. As such, they can serve as an entrance gate in degenerating retinæ. The authors suggested that this mechanism ensures that the photoswitch cannot be taken up into cells of a healthy retina, reducing side-effects. *In vivo* administration of these compounds requires intraocular injection, which is a standard procedure in ophthalmology, but carries a residual infection risk. Therefore, the slow release of **QAO** and **DENAO** from polymeric matrices was investigated.<sup>91</sup>

The permanently charged photoswitchable trimethylammonium ion **AzoTAB** (Table 1, #40) had been used as a photoswitch in material science before it was developed into as photochromic ion channel blocker.<sup>92</sup> **AzoTAB** is isomerized from *trans* to *cis* with UV light and can be switched back with blue light. In cardiomyocytes, the *trans* isomer suppressed spontaneous electric excitability. The shape of action potentials indicated a *trans* block of fast  $\text{Na}_V$  and  $\text{Ca}_V$  channels. In more recent work, **AzoTAB** was shown to potentiate  $\text{K}_V$  currents in the dark.<sup>93</sup>

Further studies culminated in the development of third-generation open-channel blockers, such as **DAD** (Table 1, #41).<sup>94</sup> In contrast to all previously described photoswitches, **DAD** does not bear a permanent charge and can rapidly diffuse across biological barriers in tissues. **DAD** can be isomerized with blue or white light and relaxes quickly in the dark. It mainly acts on bipolar cells exploiting the extant circuitry of a blind retina (Fig. 4D and E).

The photochromic blocker **fotocaine** (Table 1, #42),<sup>95</sup> another compound that is not permanently charged, was developed through “azologization” of the analgesic fomocaine. Azologization refers to the systematic replacement of isosteric motifs in drugs with azobenzenes.<sup>96</sup> **Fotocaine** can be isomerized with 350 nm/450 nm light, allowing and suppressing action potential firing in dissociated mouse hippocampal neurons.

In 2017, Berger and co-workers demonstrated that open-channel blocking of voltage-gated ion channels can also be achieved with guanidinium ions.<sup>97</sup> They synthesized an azobenzene version of the known open-channel blocker 2GBI, **photoGBI** (Table 1, #43) to inhibit the voltage-gated proton channel  $\text{H}_V1$ . The *trans*-active blocker can be removed from the pore by illumination with blue light to induce proton currents in macrophages and sperm.

## 2.4 Other Ion Channels

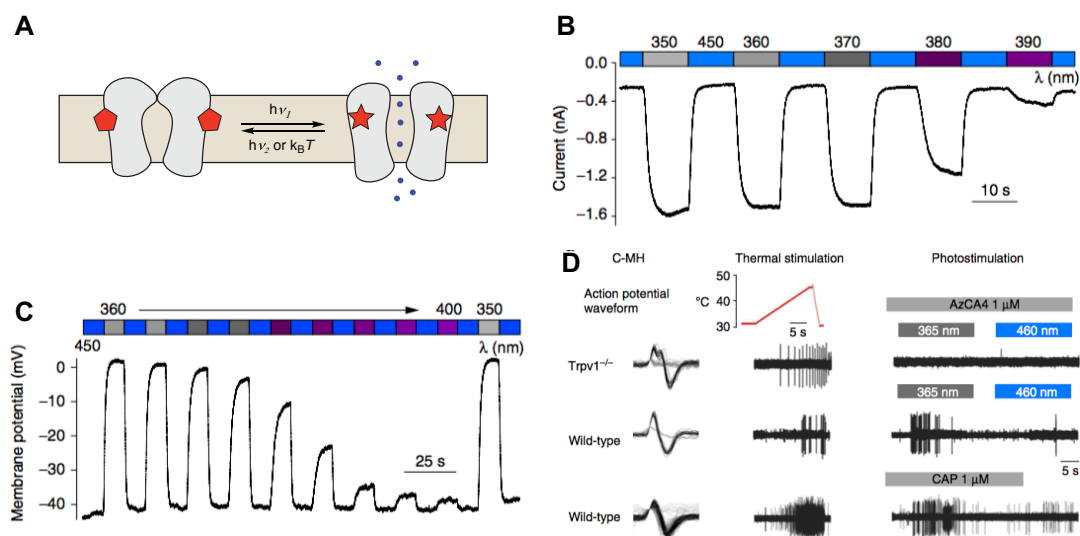
### 2.4.1 TRP Channels

Transient receptor potential (TRP) channels are non-selective cation channels that are involved in the perception of pain, temperature, and pressure. They are multimodal and respond to a variety of input signals with the notable exception of light. The vanilloid receptor 1 (TRPV1) is one of the best studied members of this family (Fig 5). In 2013, Trauner and co-workers published the photoswitchable antagonists **AC-4** (Table 1, #44) and **ABCTC** (Table1, #45), which responded to 360 nm/440 nm and 370 nm/470 nm light respectively.<sup>98</sup> They were evaluated in whole-cell patch-clamp experiments with HEK293T cells transiently transfected with TRPV1. Although both **AC-4** and **ABCTC** inhibited the channel after voltage activation, only **AC-4** antagonized the agonist capsaicin in a light-dependent manner. Moreover, **AC-4** acts as a *trans*-antagonist on the voltage-activated channel and as a *cis*-antagonist in experiments with the agonist capsaicin.

The agonist capsaicin itself could be converted into a photoswitch by incorporating photoswitchable fatty acids (Fig. 5A). This yielded the azo-capsaicins (**AzCAs**) amongst which **AzCA-4** (Table1, #46) turned out to be the most effective compound.<sup>99</sup> **AzCA-4** operates with 350 nm/450 nm light and was used to optically control heterologously expressed TRPV1 in HEK293T cells and endogenous TRPV1 channels in dorsal root ganglions (DRG) cells, as assayed by electrophysiology and calcium imaging (Fig. 5B and C). Paving the way to photoanalgesics, **AzCa-4** affected nociception of mouse C-fibers (Fig. 5D).

Peterson and colleagues achieved the optical control of a second member of the TRP channel family, TRPA1, with a small molecule termed **Optovin** (Table1, #47).<sup>100</sup> This light-responsive rhodanine derivative activated the channel upon irradiation with violet light. The channel deactivated within seconds once the light was gone. **Optovin** bestowed light sensitivity to endogenous TRPA1 channels in zebrafish larvae, stimulating the dorsal fin of a spinalized fish. A subsequent paper presented various analogues that were used to control TRPA1b channels in zebrafish.<sup>101</sup> They provided light-control not only over sensory neurons, but also over the pace rate of zebrafish larvae hearts and human stem cell-derived cardiomyocytes.

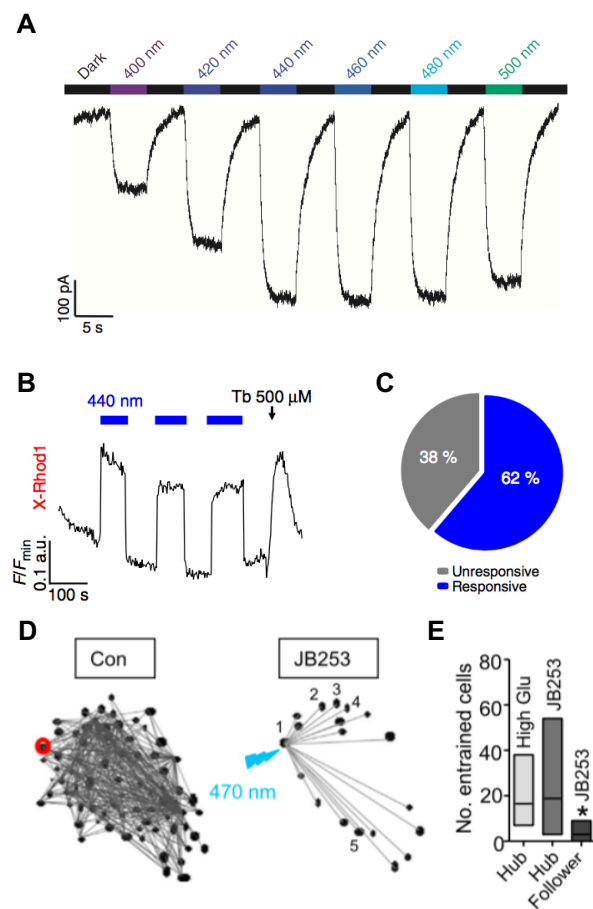
More recently, Zufall and co-workers used photoswitchable diacylglycerols (**PhoDAGs**; Table1, #48) in the optical control of TRPC2 and TRPC6. Photosensitivity of TRPC2 and TRPC6 was demonstrated in cells and tissue slices in combination with Ca<sup>2+</sup>-mapping.<sup>102</sup> For the optical control of TRPC3, Groschner and colleagues developed a new **PhoDAG** variant, termed **OptoDaRG** (Table1, #49), which features two azobenzene containing acyl-chains.<sup>103</sup> It allowed for more efficient photoswitching of TRPC3 than **PhoDAG-1** and provided insights into the lipid gating of this channel.



**Figure 5: Photocontrol of TRPV1 channels.** (A) Schematic depiction of TRPV1, gated by a photochromic agonist (red pentagon/star). Opening occurs upon isomerization to the active isomer (red star). (B)-(C) light-dependent activation of TRPV1-channels expressed in HEK293T cells and treated with **AzCa-4**. Alternating UV and blue light in whole-cell voltage clamp (B) and current clamp (C) results in opening of the channel. The concentration of active photoisomer can be controlled by the wavelength ("color-dosing"). (D) Photocontrol of heat-sensitive C-fiber nociceptors with **AzCA-4** in wild-type and knockout mice. Reprinted with permission from reference (99). Copyright 2015 Nature Publishing Group (<https://doi.org/10.1038/ncomms8118>, <https://creativecommons.org/licenses/by/4.0/>).

## 2.4.2 ATP-Sensitive Potassium Channels

ATP-sensitive Potassium Channels ( $K_{ATP}$ ) consist of two distinct proteins, the sulfonylurea receptor (SUR) and the inwardly rectifying potassium channel 6 (Kir6). Sulfonylureas, such as tolbutamide or glibenclamide, mimic ATP and close  $K_{ATP}$  channels, thus inducing insulin secretion from pancreatic  $\beta$ -cells. The photoswitchable sulfonylurea **JB-253** (Table 1, #50), an azobenzene designed to structurally resemble glibenclamide, closed  $K_{ATP}$  channels upon irradiation with blue light, which was reversed upon thermal relaxation (Fig. 6A).<sup>19</sup> The effect of **JB-253** was only demonstrated in transiently transfected HEK293T cells (Fig. 6B), but also through the optical control of glucose stimulated insulin secretion in pancreatic islets (Fig. 6C and D). Isomerization to the active *cis*-isomer results in an increase of cytosolic  $Ca^{2+}$  levels and insulin secretion. Subsequently, a red-shifted version of **JB-253**, **JB-558** (Table 1, #51) was introduced.<sup>104</sup> This heterocyclic azobenzene absorbed maximally at 526 nm, could be isomerized with green light, and relaxed



**Figure 6: Photopharmacology of  $K_{ATP}$  channels.** (A) Whole-cell patch-clamp recordings show that most efficient blocking of  $K_{ATP}$  with **JB-253** occurred within a range from 440 nm to 500 nm light. Reprinted with permission from reference (19). Copyright 2014 Nature Publishing Group (<https://doi.org/10.1038/ncomms6116>, <https://creativecommons.org/licenses/by/4.0/>) (B)-(C) Optical control of human islets using **JB-253**. (B) Illumination of **JB-253**-treated  $\beta$ -cells resulted in rapid, reversible rises of cytosolic calcium levels in human tissue (Tb, tolbutamide; positive control). (C) Over 60% of cells respond to **JB-253**. (D) Representative cell-cell entrainment with identified hub (red). Reprinted with permission from reference numbers (19). Copyright 2014 Nature Publishing Group (E) Activation of a hub with **JB-253** and 470 nm light shows a larger number of entrained cells than activation of follower. Reprinted with permission from reference (105). Copyright 2016 Elsevier Ltd. (<https://doi.org/10.1016/j.cmet.2016.06.020>, <https://creativecommons.org/licenses/by/4.0/>).

rapidly in the dark. Binding to the SUR was confirmed by [ $^3$ H]-glibenclamide displacement, and Epac2A signaling was optically controlled in FRET assays with an Epac2-camps biosensor. Like **JB-253**, **JB-558** was able to induce glucose stimulated insulin secretion in its *cis*-form. In a combinatorial approach using

photopharmacology and optogenetics, **JB-253** was used to identify a subpopulation of cells in  $\beta$ -cell hubs that is required for regular insulin secretion (Fig. 6E and F).<sup>105</sup> Compounds like **JB-253** could become valuable tools for the investigation of glucose stimulated insulin release and type 2 diabetes *in vivo*.<sup>106</sup>

Toxicological studies in various strains of *S. typhimurium* and *E. coli* with **JB-253** indicated potential mutagenicity, but when administered orally to rats (1000 mg/kg over 7 days), no mortality and no apparent signs of toxicity were observed. Additionally, **JB-253** exhibited metabolic stability, as demonstrated in an azoreductase assay. Light-induced remote activation of glucose homeostasis was demonstrated in mice using 50 mg/kg **JB-253** and a 470 nm fiber optic cable placed in close proximity to the pancreas.

In insects, such as the cockroach *Blattella germanica* or the armyworm *Mythimna seperata*, the SUR plays a crucial role in the inhibition of chitin biosynthesis. Optical control of the SUR in this context was accomplished with a series of benzoylphenylurea (**BPU**) derivatives (Table 1, #52).<sup>107</sup> Insecticidal activity could be modulated with 365 nm and mortality rates increased upon irradiation.

### 2.4.3 G Protein-Coupled Inwardly Rectifying Potassium Channels

G Protein-coupled inwardly rectifying potassium (GIRK) channels are an integral part of inhibitory signal transduction pathways. Opening of GIRK channels mediated by the  $G_{\beta\gamma}$  subunit results in hyperpolarization of the cell membrane, which reduces the activity of excitable cells. The extension of the selective GIRK channel opener ML-297 with an azobenzene led to a small library of light-operated GIRK channel openers (**LOGOs**).<sup>108</sup> These photochromic ligands could be isomerized using 360 nm/440 nm light. The compounds were validated in patch-clamp experiments with HEK293T cells overexpressing GIRK1/2 channels. The lead compound, **LOGO-5** (Table 1, #53), was active in the dark and under 440 nm light and could be inactivated with 360 nm light. It was used to convey light-sensitivity to native GIRK channels and shape behavior in zebrafish larvae. Subsequently, a **LOGO** derivative that fully responded to visible light, termed **VLOGO** (Table 1, #54), was introduced.<sup>109</sup> This tetra-*ortho*-fluoro azobenzene was bistable and alternating illumination with 500 nm/400 nm afforded the optical control of hippocampal neurons.

### 2.4.4 ENaC/P2X Superfamily

Epithelial sodium channels (ENaCs) are heterotrimeric transmembrane proteins that control water transport across epithelia and are targeted by diuretics, such as amiloride. Extension of amiloride with an azobenzene yielded **Photoamiloride-1** (**PA-1**; Table 1, #55), which was selective for the  $\delta\beta\gamma$  subtype of ENaC.<sup>110</sup> **PA-1**

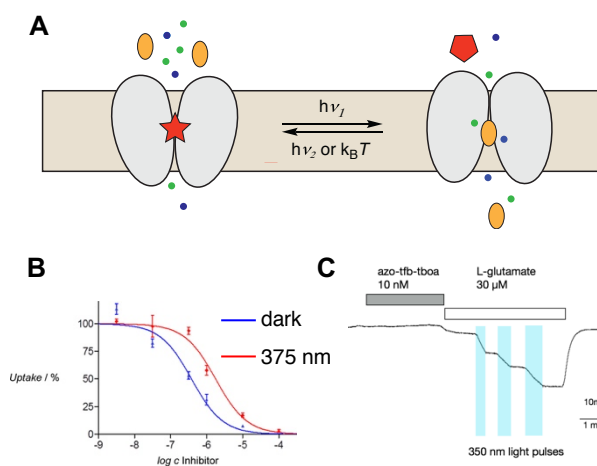
functioned as a photoswitchable blocker in the *trans*-form responding to visible wavelengths of light (400 nm/500 nm). It was characterized using electrophysiology in *Xenopus* oocytes, HEK293T cells, and H441 cell monolayers. Due to its selectivity for  $\delta\beta\gamma$ ENaC, it could be used to distinguish between biological effects mediated by  $\delta\beta\gamma$ ENaC and  $\alpha\beta\gamma$ ENaC.

P2X receptors are cation-permeable, ATP-gated ion channels related to ENaCs. A strategy for their photoactivation exploiting the PTL concept was published by Grutter and co-workers in 2013.<sup>111</sup> Instead of ATP-dependent opening, the channel was endowed with light sensitivity through attachment of the photoswitches **MEA-TMA** and **MEA-TEA** (Table 1, #56 and #57). The receptor could be turned on and off with 365 nm/525 nm light, relying on a retractable ammonium ion to block the pore of the ion channel. Depending on the point of mutation, the channel pore could be blocked in the *trans*- or *cis*-state. Expression in dissociated hippocampal neurons allowed for the optical control of AP firing. North and colleagues crosslinked two subunits of the P2X2 receptor mutant with the azobenzene **BMA** (Table 1, #58) which allowed for rapid and reversible gating of the receptor with UV/blue light.<sup>112</sup> This modular approach was also applied to acid-sensing ion channels (ASICs), which are trimeric channels structurally similar to P2X. To further investigate the pore-opening of P2X channels, Grutter designed the longer photoswitchable cross-linker **MAM** (Table 1, #59), which could be switched with 365 nm/525 nm light.<sup>113</sup>

### 3 Photoswitches for Transporters and Pumps

Like ion channels, transporters and pumps facilitate the translocation of cargo across cell membranes. In contrast to the passive permeation through ion channels, however, this requires energy, which is either provided *via* ATP hydrolysis (primary active transport) or through the discharge of previously established gradients (secondary active transport). Photopharmacological studies have focused on neurotransmitter transporters providing an additional level of control over neural function. In 2014, Wanner and colleagues reported photoswitchable inhibitors of GABA transporters (Fig. 7A).<sup>114</sup> GABA-uptake assays in HEK293T cells showed that most of these are selective for GAT1. The lead-compound of the series (**6e**; Table 1, #60) enabled optical control of GABA<sub>A</sub> receptor-mediated currents in dentate gyrus granule cells (Fig. 7B and C). While the *cis*-isomer prevented current flow, the *trans*-isomer induced current.





**Figure 7: Optical control of a transporter.** (A) Schematic depiction of the optical control of a secondary active transporter with a photoswitchable inhibitor. (B) Light-induced activation of GAT1-mediated GABA uptake. Reprinted with permission from reference (114). Copyright 2014 American Chemical Society (C) Optical control of the excitatory amino acid transporter EAAT2. Reprinted with permission from reference (115). Copyright 2017 American Chemical Society.

In more recent work, a photoswitchable inhibitor of the glutamate transporter EAAT2 (excitatory amino acid transporter 2) was reported.<sup>115</sup> The design of this compound was inspired by the potent EAAT inhibitor of TFB-TBOA. A photoswitchable isoster, termed **ATT** (Table 1, #61), exhibited good selectivity for EAAT2 over other subtypes, as demonstrated with voltage clamp recordings in *Xenopus* oocytes. The *cis*-isomer proved to be significantly less active as a blocker than the *trans*-isomer. Accordingly, irradiation of EAAT2 preincubated with *trans*-**ATT** with 350 nm recovered transport currents.

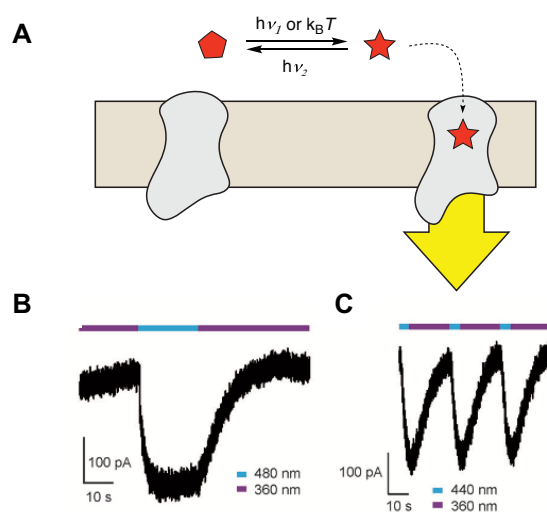
## 4 Photoswitches for GPCRs

G protein-coupled receptors (GPCRs) are the largest class of membrane proteins in the human genome and are critically involved in signal transduction. They are coupled to heterotrimeric G proteins, which, along with  $\beta$ -arrestin, mediate intracellular signaling. GPCRs have proven to be particularly amenable to photopharmacology, which may not be surprising since the only photoreceptors in humans, the opsins, are class A GPCRs that are covalently bound to a photoswitch, viz retinal.

## 4.1 Class A, Rhodopsin-Like

In the 1980s, Erlanger, Wassermann and Lester showed that **BisO** (Table1,#62), which was initially applied to nAChRs, also interacts with muscarinic acetylcholine receptors (mAChR) in frog hearts.<sup>116</sup> In addition to the PCL **BisO**, its congener **QBr** (Table1, #63) was investigated as a tethered ligand.<sup>117,118</sup> Three decades later, the mAChRs were revisited by Decker and colleagues.<sup>119</sup> They developed **BQCAAI** (Table 1, #64), a bitopic (or dualsteric) photoswitchable ligand for M1 receptors based on iperoxo, a highly potent M1 agonist, and BQCA, a positive allosteric modulator. **BQCAAI** functions as a *cis*-antagonist and *trans*-agonist under illumination with 365 nm/455 nm light, respectively, when applied to HEK293T cells that express the receptor.

The optical control of  $\mu$ -opioid receptors was achieved with a photoswitchable derivative of the highly potent agonist fentanyl (Fig. 8A).<sup>120</sup> Photofentanyl-2 (**PF-2**; Table 1, #65) functions as a bistable switch that is active in the dark, can be deactivated with 360 nm light, and reactivated with 480 nm light. The modulation of downstream signaling of the  $\mu$ -opioid receptor *via* GIRK channels was demonstrated using patch-clamp electrophysiology in transiently transfected HEK293T cells (Fig. 8B and C).



**Figure 8: Optical control of GPCRs.** (A) Schematic depiction of the optical control of the  $\mu$ -opioid receptor (a Class A GPCR). Upon isomerization, the ligand (pentagon/star) activates the receptor and triggers a signaling cascade. (B) **PF-2** is isomerized from *cis* to *trans* upon illumination with 480 nm, activating the  $\mu$ -opioid receptor and inducing a GIRK-current via  $G_{\beta\gamma}$ -signaling. Termination of the signal can be achieved with 360 nm irradiation. (C) Repetitive activation of the  $\mu$ -opioid receptor. Reprinted with permission from reference (120). Copyright 2014 Wiley-VCH.

More recently, Isacoff and Trauner disclosed the optical control of dopamine receptors with photopharmacology.<sup>121</sup> Modification of the potent agonist PPHT with an azobenzene yielded tethered (**MAP**, Table 1, #66) and non-tethered (**AP**, Table 1, #67) photochromic ligands. These compounds were used in the reversible control of D1 and D2 dopamine receptors with 360 nm/460 nm light, which was demonstrated in transiently transfected HEK293T cells. Depending on the site of covalent attachment, **MAP** functioned as a neutral antagonist or inverse agonist. The group of König employed dithienylethenes and fulgimide photoswitches to optically control dopamine receptors with light.<sup>122</sup> While their dithienylethene **29** (Table 1, #68) required 312 nm/530 nm light, fulgimide switch **52** (Table 1, #69) could be isomerized between its closed and open state with visible light (400 nm/530 nm). The compounds were evaluated using a *myo*-inositol phosphate (IP) accumulation assay and a  $\beta$ -arrestin assay in HEK293T cells.

In addition, Leurs and colleagues introduced photoswitchable *cis* and *trans*-active agonists for the histamine H3 receptor.<sup>123</sup> The azobenzene-containing photoswitches **VUF-14738** (Table 1, #70) and **VUF-14862** (Table 1, #71) could be isomerized with 360 nm and 434 nm light allowing for reversible control over H3 receptors in *Xenopus* oocytes.

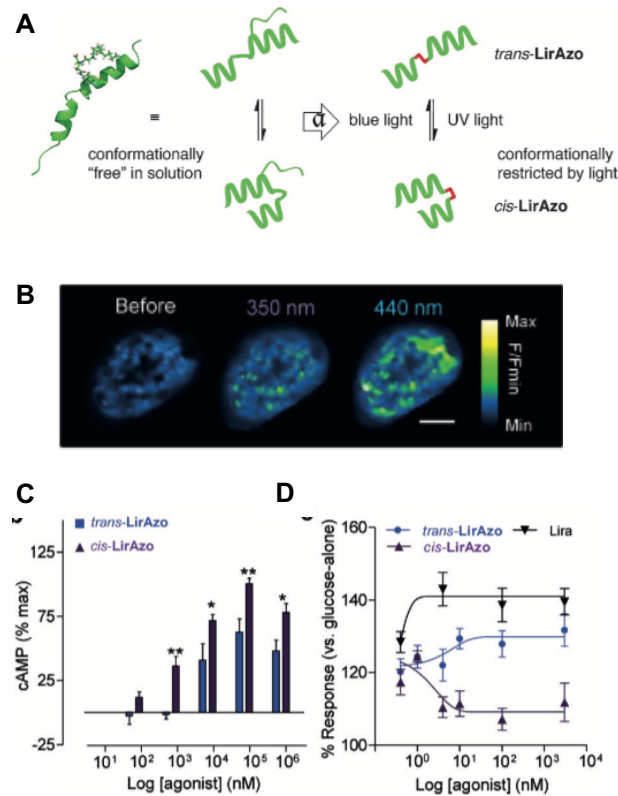
A different member of the class A GPCRs, the adenosine A<sub>2A</sub> receptor, was also rendered light-sensitive with a photoswitchable agonist.<sup>124</sup> The known agonist APNEA was modified with an azobenzene to yield the photoswitchable analog **MRS5543** (Table 1, #72). **MRS5543** could be isomerized with 460 nm light and relaxed quickly in the dark. In its *trans*-state, it acted as a partial agonist, while the *cis*-isomer functioned as an antagonist. Both isomers have been employed in cytotoxicity and cAMP production assays in HEK293T cells.

In addition to aminergic and purinergic receptors, GPCRs that respond to lipid ligands have yielded to photopharmacology. The photoswitchable fatty acid **FAAzo-10** (Table 1, #73) is a photoswitchable derivative of the GPR40 agonist GW-9508. **FAAzo-10** was demonstrated to modulate Ca<sup>2+</sup>-oscillations through GPR40, also known as the free fatty acid receptor 1.<sup>18</sup> In contrast to previously published photoswitchable lipids, **FAAzo-10** proved to be *trans*-active, increasing Ca<sup>2+</sup>-oscillation frequency in pancreatic  $\beta$ -cells under blue light or in the dark. Interestingly, this increase in oscillation frequency did not translate to glucose stimulated insulin secretion, underscoring that the role of GPR40 in insulin secretion is ambiguous. Additionally, **FAAzo-10** was shown to reduce K<sub>V</sub> and K<sub>ATP</sub> potassium currents under blue light.

Finally, Trauner, Carreira, and Frank introduced photoswitchable cannabinoids, termed **azo-THCs**, that enable the optical control of the cannabinoid receptor 1 (CB1).<sup>125</sup> In AtT-20(CB1) cells transiently expressing GIRK channels, the *meta*-substituted ligand **Azo-THC-3** (Table 1, #74) proved to be active under 360 nm light (*i.e.* as *cis* isomer), whereas the *ortho*-substituted **Azo-THC-4** (Table 1, #75) was active when illuminated with 440 nm light (*i.e.* as *trans*-isomer). These

selectivities were validated by computational models based on the crystal structure of activated CB1.

## 4.2 Class B, Secretin Receptor Family



**Figure 9: Optical control of GLP-1.** (A) Conversion of the peptide hormone liraglutide (left, PDB ID: 4apd) into **LirAzo** (right) via incorporation of an azobenzene photoswitch into the backbone. (B) Under 440 nm irradiation, cytosolic  $\text{Ca}^{2+}$  levels exhibit a larger increase than under 350 nm irradiation. (C) *trans*-LirAzo generates significantly less cAMP in MIN6 cells than *cis*-LirAzo. (D) *trans*-LirAzo provides more  $\text{Ca}^{2+}$  mobilization than *cis*-LirAzo. Reprinted with permission from reference (126). Copyright 2015 Wiley-VCH.

The glucagon-like peptide 1 (GLP-1) receptor was the first secretin/class B GPCR to be put under optical control (Fig. 9A).<sup>126</sup> **LirAzo** (Table 1, #76), a peptide derived from the drug liraglutide, was designed by substituting two amino acids with the photoswitchable amino acid AMPP. The azobenzene incorporated in the backbone of the peptide could be isomerized with 350 nm/440 nm light and proved to be bistable (Fig. 9B). Interestingly, **LirAzo** was capable of biased signaling, depending

on the isomerization state (Fig. 9C and D). While *cis*-**LirAzo** in pancreatic  $\beta$ -cells preferentially triggered cAMP generation, *trans*-LirAzo mostly stimulated  $\text{Ca}^{2+}$  influx. It was further shown that **LirAzo** allowed for the optical control of glucose stimulated insulin secretion in pancreatic  $\beta$ -cells. The design principles used in the development of **LirAzo** should be applicable to other peptide hormones and their associated receptors of the secretin family.

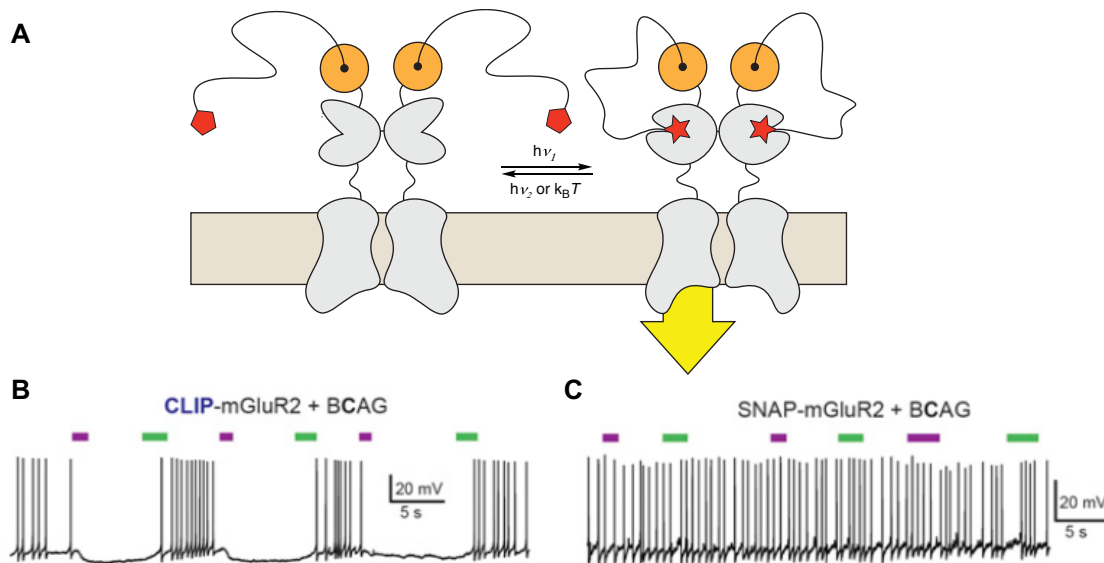
More recently, the groups of Hodson and Trauner introduced a small molecule photoswitch, termed **PhotoETP** (Table 1, #77), that acts as a positive allosteric modulator for the GLP-1 receptor.<sup>127</sup> **PhotoETP** was derived from the small molecule BETP and can be isomerized using 350 nm and 440 nm light. *Trans*-**PhotoETP** increases GLP-induced cAMP generation and results in a light-dependent rise in  $\text{Ca}^{2+}$  levels.

### 4.3 Class C, Metabotropic Glutamate Receptor Family

Class C GPCRs are constitutive dimers and are characterized by a large extracellular ligand binding domain resembling a Venus Fly Trap. The photopharmacology of their most prominent members, the metabotropic glutamate receptors (mGluRs), is now well developed. The first version of a light-gated mGluR (LimGluR) relied on closely mounted photoswitchable ligands, termed **D-MAGs** (Table 1, #78 and #79).<sup>44,128</sup> These compounds are diastereomers of the iGluR-targeting **MAG** switches that match the pharmacology of mGluRs. The LimGluR strategy was implemented with the metabotropic receptors mGluR2, mGluR3 and mGluR6. LimGluR expressed in HEK293T cells together with GIRK channels could be activated with 380 nm and inactivated with 500 nm. It was used to hyperpolarize hippocampal neurons, control action potential firing, and modulate excitatory and inhibitory postsynaptic currents. The escape probability of zebrafish larvae could be optically controlled with LimGluR.<sup>128</sup>

Gorostiza, Llebaria and colleagues used a photoswitchable allosteric modulator for mGluR5, termed **Alloswitch-1** (Table 1, #80), to endow light-sensitivity to mGluR5. It responds to violet (380 - 390 nm) and green (490 - 500 nm) light.<sup>129</sup> Reversible switching has been demonstrated in calcium imaging experiments with rat cortical astrocytes and tadpole motility experiments. The negative allosteric modulator **OptoGluNAM4.1** (Table 1, #81) was discovered through screening of a library of photoisomerizable compounds and found to operate primarily on mGluR4.<sup>130</sup> Calcium responses evoked by a known agonist could be reversibly modulated with blue light in HEK293T cells. In a mouse model for chronic pain, **OptoGluNAM4.1** blocked the analgesic effect of an orthosteric agonist, although not in a light-dependent manner. To demonstrate optical control *in vivo*, zebrafish locomotion assays were performed. Free swimming distance increased with *trans*-

**OptoGluNAM4.1**, whereas *trans*-**Alloswitch-1** inhibited swimming behavior. Both effects could be reversibly controlled with light. Subsequently, additional phenylazopyridine derivatives (Table 1, #80) that resemble **Alloswitch-1** were found to function as photoswitchable allosteric modulators for mGluR5.<sup>131</sup> The most active compounds were evaluated as analgesics in a rodent pain model. Delivery of **Alloswitch-1** to the amygdala restored sensitivity in a light-dependent fashion after inflammatory pain induction.



**Figure 10: PORTLs for metabotropic glutamate receptors:** (A) Schematic depiction of SNAG-mGluR2 with the PORTL attached. (B)-(C) Orthogonality of the PORTL concept demonstrated by optical control of mGluR2 with **BGAG-12** and **BCAG-12**, respectively. Hippocampal neurons became light-sensitive with CLIP-mGluR2 and **BCAG**, but not with SNAP-mGluR2/**BCAG**, due to a lack of labelling. Reprinted with permission from reference (133).

The PORTL approach uses self-labeling protein tags, such as SNAP-, CLIP-, or Halo-tags, to selectively conjugate photoswitches to receptors of interest (Fig. 10A).<sup>132</sup> It was initially introduced by Isacoff and Trauner with an mGluR2 that was N-terminally extended with a SNAP tag and conjugated with photoswitchable glutamate ("SNAG-mGluR2"). In contrast to maleimide-based photoswitches, the benzyl guanines **BGAG-0** to **BGAG-12** used for bioconjugation (Table 1, #82), proved to be stable under physiological conditions. The photoswitches could be isomerized with 380 nm/500 nm light and the constructs were tested in whole-cell patch clamp experiments with HEK293T cells and hippocampal neurons. A red-shifted version, **BGAG-12<sub>460</sub>** (Table 1, #83) could be isomerized to the active form using blue light. In a subsequent report, the PORTL concept was extended to CLIP tags, which

required benzyl cytosines of the **BCAG** series (Table 1, #84 and #85).<sup>133</sup> Both CLIP- and SNAP-tag can be labeled orthogonally, and the right combination of wavelength, photoswitch, and receptor tag resulted in hyperpolarization and silencing of hippocampal neurons (Fig. 10B and C). Exploiting the orthogonality of the approach, the authors could optically control mGluR2 and mGluR7 independently from each other in the same cell. The SNAG-mGluR2 construct could also be used in combination with LiGluR (using **BGAG-12<sub>380</sub>** and **L-MAG-0<sub>460</sub>**; Table 1, #77).<sup>132</sup> This allowed for the dissection of downstream signaling effects triggered by the different receptors.

The SNAG-mGluR2 system was subsequently used for the restoration of vision in blind animals.<sup>134</sup> In MEA experiments with degenerating mouse retinæ, SNAP-tagged mGluR2 with **BGAG-12<sub>460</sub>** (SNAG-mGluR2) responded to light flashes as short as 25 ms. In light avoidance assays, mice were trained to respond to certain light patterns before turning blind. Following treatment with **BGAG-12<sub>460</sub>**, this light-guided behavior was restored. SNAG-mGluR2 enabled animals to discriminate parallel from perpendicular lines and parallel lines at varying spacing. The simultaneous use of SNAG-mGluR2 and LiGluR, both delivered by viral transfection, resulted in ON/OFF responses that resemble the pattern of wild-type retinæ.

Most recently, the PORTL approach was extended to include highly specific non-covalent binders, such as antibodies or nanobodies. To this end, **BGAG-12** was mounted onto a SNAP-tagged anti-GFP nanobody that bound to GFP-tagged mGluR2 and provided photosensitivity to the receptor.<sup>135</sup> Such nanobody-photoswitch-conjugates (NPC) or antibody-photoswitch conjugates (APC) could be applicable to a variety of molecular targets and have great potential for optical control of endogenous receptors at native expression levels.

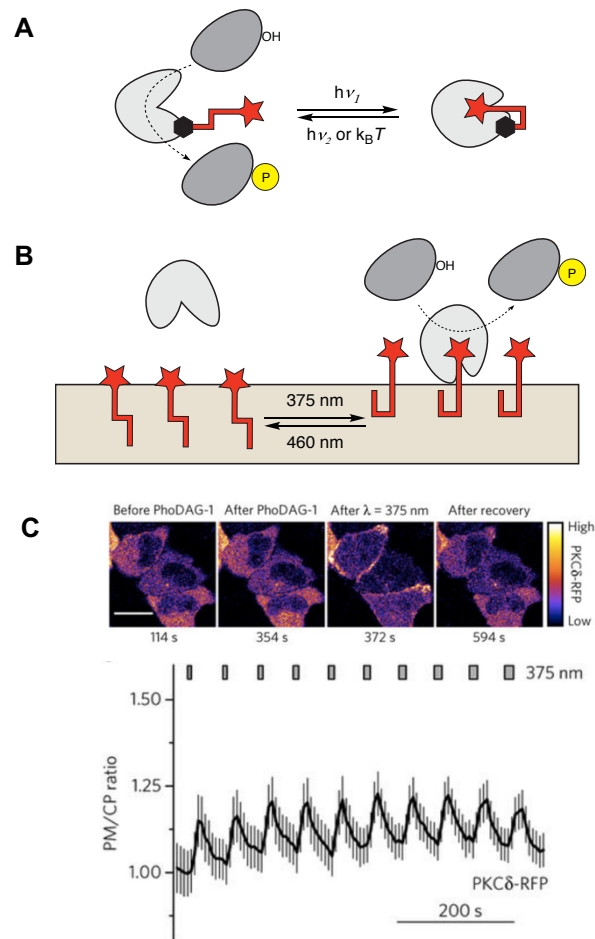
## 5 Photoswitches for Enzymes

Enzymes involved in signaling cascades or other processes that show non-linear biological responses are ideal targets for photopharmacology. A relatively small up- or downregulation of activity can lead to an "all-or-nothing" response. As such, *in vivo* applications of enzyme photopharmacology have been more convincing than *in vitro*-studies, which date back all the way back to the 1960s.<sup>136,137</sup>

### 5.1 Kinases

Kinases are critical to cellular functions, such as growth, proliferation, and mobility. One of the major challenges of kinase pharmacology is the identification of selective inhibitors. Chin and co-workers recently addressed this issue by

combining photopharmacology with genetic code expansion (Fig. 11A).<sup>138</sup> Different MEK isozymes were engineered to express an unnatural amino acid that bears a cyclopropene or strained alkyne. The reactive side chain underwent covalent linkage to a photoswitchable ligand (**photo-X**, Table 1, #86) via bioorthogonal chemistry. This approach, termed photoswitchable bioorthogonal ligand tethering (photo-BOLT) resembles the PTL strategy and allows for isoform-specific, spatiotemporal control of kinase activity.



**Figure 11: Photopharmacological control of kinase activity.** (A) Schematic depiction of photo-BOLT, which relies on an unnatural amino acid (black hexagon) introduced through genetic code expansion. (B) Schematic depiction of the optical control of protein kinase C with **PhoDAG-1**. (C) Illumination of **PhoDAG-1** with 375 nm light induces translocation of RFP-tagged protein kinase C (PKC $\delta$ -RFP) from the cytoplasm (CP) to the plasma membrane (PM). Reprinted with permission from reference (140).



Photochromic ligands that affect kinase function have also been developed. An inhibitor of the kinase RET bearing a stilbene motif was converted to the corresponding azobenzene **4** (Table 1, #87). This molecule allowed for the optical control of RET *in vitro* and *in cellulo*.<sup>139</sup>

Furthermore, diacylglycerol (DAG), which plays a key role as a second messenger in G<sub>q</sub>-coupled GPCR signaling, was rendered photosensitive through incorporation of azobenzenes into one of its fatty acids (Fig. 11B and C).<sup>140</sup> This yielded photoswitchable lipids with varying tail-lengths, termed **PhoDAGs** (Table 1, #88), which allowed for light-dependent translocation and activation of protein kinase C (PKC). No change in localization of PKC and PKC phosphorylation was observed upon addition of *trans*-**PhoDAG-1** to HeLa cells. Photoisomerization to *cis*-**PhoDAG-1** at 375 nm led to rapid translocation and phosphorylation of PKC substrates. **PhoDAG-2** could be applied to the optical control of Munc 13, a protein that is involved in vesicle fusion and neurotransmitter release. The usefulness of **PhoDAGs** was demonstrated in complex systems, including pancreatic  $\beta$ -cell islets, hippocampal neurons, and *C. elegans*. **PhoDAGs** could be used to control the translocation and activation of other proteins that feature a DAG-binding C1 domain.

## 5.2 Phosphatases

To achieve precision control of the immune system, the Fischer group developed photoswitchable versions of the peptide cyclosporin A (e.g., **CsA-AB-CsA**; Table 1, #89).<sup>141</sup> Cyclosporin A is an immunosuppressant, which inhibits the phosphatase calcineurin, an activator of the nuclear factor of activated T cells (NFAT). In addition to calcineurin, cyclosporin A binds to the peptidylprolyl isomerase Cyp18. Photoswitchable cyclosporin A was shown to modulate both Cyp18 and calcineurin in a light-dependent fashion. While optical control of Cyp18 was demonstrated with *in vitro* and in whole blood assays (irradiation with 370 nm or two-photon activation at 740 nm), modulation of calcineurin was demonstrated through a NFAT-coupled transcription activation assay and in  $\gamma$ -irradiated peripheral blood mononuclear cells. In this case, light-dependent inhibition of cell-proliferation was observed.

## 5.3 Proteases

Since the initial reports of Erlanger on photochromic trypsin inhibitors,<sup>136</sup> proteases have been targets for photopharmacology. To date, however, *in vivo* applications are relatively rare despite the importance of these enzymes in biology and medicine. The serine protease thrombin converts fibrinogen into the insoluble protein fibrin, which results in blood clotting. Tan linked an aptamer that targets thrombin to a complementary DNA sequence that contained an azobenzene in its

phosphate backbone (**9c-8azo**; Table 1, #90).<sup>142</sup> Photoswitching influenced the intramolecular hybridization, which affected the affinity of the aptamer and resulted in reversible inhibition of the enzyme. Optical control of blood clotting was demonstrated in human plasma samples.

Proteasomes are responsible for the proteolytic degradation of damaged or unneeded proteins within the cell. Adverse side effects linked to the promiscuity and high toxicity of proteasome inhibitors motivated Szymanski and Feringa to develop photoswitchable versions of bortezomib (**1-6**; Table 1, #91).<sup>143</sup> These compounds were evaluated in activity-based protein profiling assays and in live-cell toxicity assays, establishing light-dependent target inhibition and toxicity. Recently, photoswitchable bortezomib derivatives was further explored by Abell and colleagues (**5**; Table 1, #92 and **4**; Table 1, #93).<sup>144</sup> A cytotoxicity assay in colon colorectal and breast carcinoma cancer cell showed photoreversible toxicity in cancer cells.

These case studies illustrate that the photopharmacology of proteases holds promise for biomedical applications. The approach should be well suited to address a number of proteases implicated in enzymatic cascades, such as caspases.

## 5.4 Histone Deacetylases and Histone Methyltransferases

Histone modifying enzymes such as histone deacetylases (HDACs) and histone methyltransferases (HMTs) play a key role in gene regulation. Aberrant activity leads to epigenetic instability, which is implicated in cancer, neurodegeneration and other diseases. Motivated by their biomedical relevance, the König group developed a photochromic diarylmaimide inhibitor **11** (Table 1, #94), which is structurally related to the bisindolmaleimide Ro31-8220, a potent sirtuin inhibitor.<sup>20</sup> Light-dependent binding of these inhibitors was established *in vitro* and further evaluated with molecular docking simulations. In a cellular assay, the photochromic diarylmaimide showed hyperacetylation of tubulin, similar to the parent compound Ro31-8220. However, the authors conclude that additional experiments are needed to rule out interactions with other enzymes, such as kinases.

Mazitschek, Haggarty, and colleagues demonstrated that photoswitchable HDAC inhibitors can be used for the optical control of epigenetic states.<sup>145</sup> In an approach termed 'chemo-optical modulation of epigenetically regulated transcription' (COMET), the terminal amide of the small molecule HDAC inhibitor CI-994 (tacedinaline) was replaced with an azobenzene (**BG-14**; Table 1, #95). This photoswitchable HDAC inhibitor was used to optically modulate histone deacetylation in MCF-7 cells as shown by immunofluorescence and quantification of mRNA. A series of photoswitchable HDAC inhibitors was developed based on

analogs of the clinically used HDAC inhibitor vorinostat (**12**; Table 1, #96).<sup>146</sup> The potency of these photochromic inhibitors was assessed *in vitro* through HDAC inhibition assays, and their potential as cancer drug was further validated in a HeLa cell viability assay.

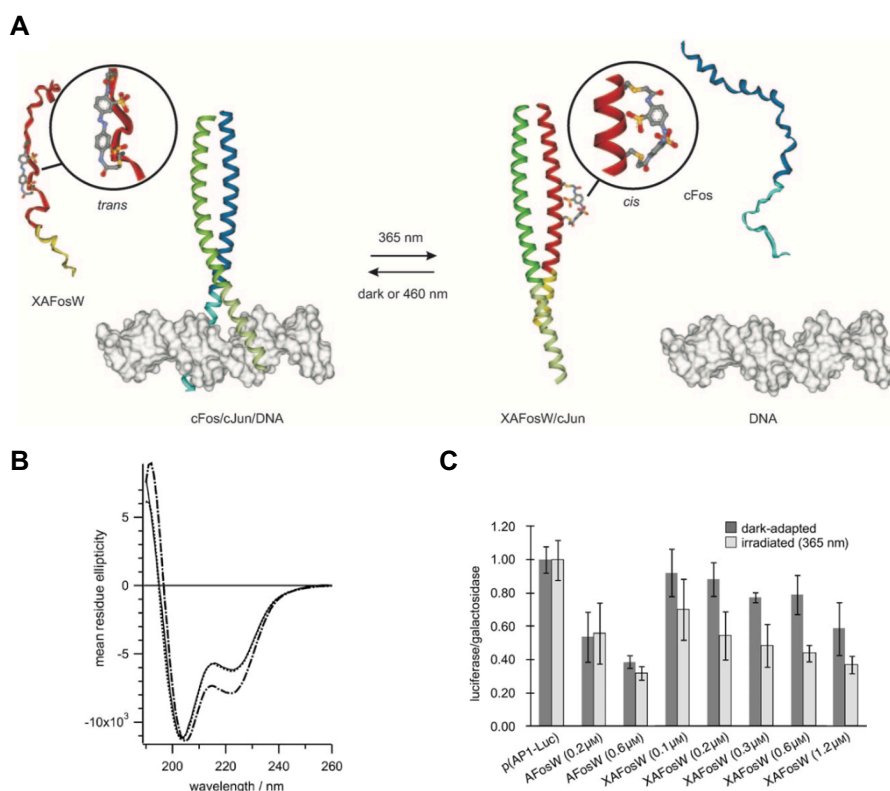
The HDACs inhibitors were recently complemented by photoswitches that indirectly target an HMT implicated in leukemia.<sup>147</sup> The Vasquez group developed a peptide with light-dependent binding affinity to WDR4, which activates the HMT MLL1 (**7**; Table 1, #97). This was achieved by inserting a photoswitchable amino acid into the backbone of a peptide known to disrupt the protein-protein interaction. This switch was used for the photocontrol of a MLL1 target gene in MLL-AF9-transduced mouse bone marrow cells.

## 5.5 Acetylcholinesterases

The photopharmacology of acetylcholinesterase was motivated by the critical role of this enzyme in synaptic transmission. Although some very early *in vitro* photopharmacology studies had addressed this target,<sup>137</sup> its optical control *in vivo* was only demonstrated in 2014 using the tacrine photoswitch **Azo-THA** (Table 1, #98). **Azo-THA** responded to 360 nm/440 nm light and could be used to regulate synaptic transmission at the neuromuscular endplate, as assayed by mouse trachea preparations.<sup>148</sup>

## 5.6 RNA Polymerases

In an early example of *in vivo* enzyme photopharmacology, Woolley and co-workers designed a photoswitchable peptide that could regulate the transcription factor AP-1, which consists of the subunits Fos and Jun.<sup>149</sup> By crosslinking a double cysteine-mutant of this peptide with an azobenzene switch, the authors were able to achieve optical control of helicity and binding affinity (Fig. 12). Light-dependent binding of the resulting peptide **XAFosW** (Table 1, #99) to Jun and replacement of Fos was demonstrated with an electrophoretic mobility shift assay. To probe for the optical control of AP-1 dependent RNA polymerase activity, a luciferase-based reporter gene assay was employed. A significant reduction in luminescence was observed upon irradiation with 365 nm light (Fig. 12C).

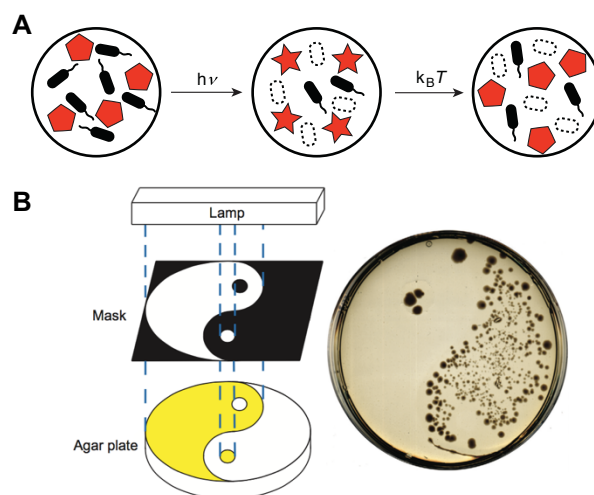


**Figure 12: Optical control of RNA polymerase.** (A) Irradiation of the photoswitchable peptide **XAFosW** with 365 nm light enhances helicity and leads to the inhibition of transcription. (B) Circular Dichroism measurements show helicity increase at 365 nm (---) compared to dark-adapted **XAFosW** (----) and after illumination at 460 nm (---). (C) Reporter gene assay demonstrating the activity of **XAFosW** in HEK293T. Reprinted with permission from reference (149). Copyright 2010 Wiley-VCH.

## 5.7 DNA Gyrases and Dihydrofolate Reductases

DNA-gyrases are bacterial type-II topoisomerases that catalyze DNA-strain relief during replication and transcription. Due to considerable structural deviation from eukaryotic topoisomerases, DNA-gyrases are common targets for antibiotics. To address the issue of antibiotic resistance, Feringa and co-workers developed a series of light-activatable gyrase inhibitors which were derived from the quinolone ciprofloxacin (1-9, Table #100).<sup>150</sup> These compounds could be switched to the more active cis-form with light and deactivated thermally, making them potentially safer and less prone to resistance than conventional antibiotics. The photoswitches exhibited effective inhibition of quinolone sensitive *E. coli* CS1562 growth when activated during the exponential growth phase (Fig. 13). In a subsequent study, coupling of ciprofloxacin itself with an azobenzene or spiropyran yielded the photoresponsive antibiotics **Azofloxacin** and **Spirofloxacin** (Table 1, #101 and

#102).<sup>151</sup> Interestingly, the spiropyranes suffered from photodegradation, whereas the azobenzenes showed little or no fatigue.



**Figure 13: Photocontrol of antimicrobial activity.** (A) Schematic depiction of photoswitchable antibiotics. (B) Optical control of antimicrobial activity enables bacterial patterning with light. Reprinted with permission from reference (150). Copyright 2013 Nature Publishing Group.

Recently, a new class of antibiotics was photosensitized using a similar “azo-extension” approach. The photoswitchable trimethoprim derivative **13** (Table 1, #103) presumably targets dihydrofolate reductase in a light-dependent fashion.<sup>152</sup> Notably, a red-shifted version of this switch which can be isomerized to the *cis*-isomer at 652 nm.

## 5.8 Lipoxygenases

Lipoxygenases (LOXs) mediate lipid-peroxidation and are targets for anti-inflammatory drugs. Kuhn and co-workers developed a photoswitchable hemithioindigo, termed **BODTCM** (Table 1, #104), which was structurally inspired by the LOX inhibitor ebselen.<sup>21</sup> The authors suggest that this photoswitchable drug could be useful for the treatment of inflammatory skin diseases.

## 5.9 Nitric Oxide Synthases

Nitric oxide synthases (NOS) catalyze the production of the gasotransmitter NO from arginine. During muscle contraction, neural NOS is recruited to the plasma membrane through interaction of the  $\beta$ -finger peptide domain of NOS with  $\alpha$ -1-syntrophin. Hoppmann et al. designed a photoswitchable cyclic peptide

mimicking the structure of the neural NOS  $\beta$ -finger peptide domain by integrating a photoswitchable amino acid in the peptide backbone (Table 1, #105).<sup>153</sup> This peptide ligand was membrane permeable and provided photocontrol of neural NOS in both C2C12 myotubes and single skeletal muscle fibers as demonstrated with a fluorescent NO dye. Additionally, optical control of muscle contraction could be observed in skeletal muscle fibers through rapid shortening of sarcomere length upon light irradiation.

## 5.10 Receptor-Linked Enzymes

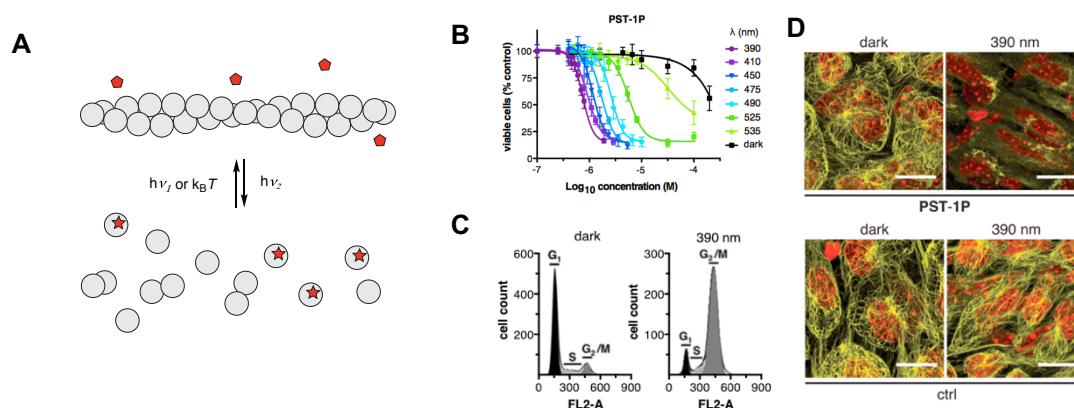
Despite the important role of receptor linked enzymes in signal transduction, their photopharmacology is underdeveloped in comparison with other target classes. However, its feasibility has been demonstrated with a photoswitchable peptide that targets a receptor-linked guanylyl cyclase, the atrial natriuretic peptide (ANP) receptor.<sup>154</sup> Structure-activity relationships of ANP suggested that some variability in the C-terminus of the peptide could be tolerated. Accordingly, a series of photoswitchable peptides with an azobenzene in the backbone replacing either two, three or four amino acids was synthesized. The lead compound of this series **TOP-271** (Table 1, #106) enabled the optical control of the ANP receptor with 365 nm/440 nm light. Light-dependent muscle contraction/dilation in aortic tissue, and  $\text{Ca}^{2+}$  oscillations in rodent islets of Langerhans were demonstrated. Future work should be directed at the photopharmacology of receptor tyrosine kinases (RTKs) to gain precision control over signaling pathways dependent on these enzymes, which are also major drug targets.

## 6 Photoswitches that Target the Cytoskeleton

Small molecules that influence the dynamics of the cytoskeleton are commonly used in cell biology and have found clinical applications as cancer chemotherapeutics. Photopharmacology has great potential for generating research tools for the precise spatiotemporal control of the cytoskeleton and its associated motor proteins and nucleating factors. In addition, photopharmaceuticals may provide a valuable targeted cancer therapy alternative to drugs that are given systemically and cause adverse side effects.

Tubulin is an excellent target for photopharmacology due its dynamic instability and well-developed pharmacology. In 2015, Thorn-Seshold and Trauner introduced a series of photoswitchable inhibitors of microtubule dynamics based on the natural product combrestatin A-4, which they termed "**photostatins**" (Fig. 14A).<sup>155</sup> Cytotoxicity assays revealed that the lead compound, **Photostatin-1 (PST-1)**, Table 1, #107, was approximately 100-fold more toxic in its *cis*-state (at 390 nm) than in its thermodynamically more stable *trans*-form, which predominates

under green light or in the dark (Fig. 14B) and led to cell cycle arrest in the G<sub>2</sub>/M phase (Fig. 14C). Accordingly, **PST-1** allowed for the precision control of cellular functions, such as mitosis and cytokinesis. Mitotic arrest in a single cell within a *C. elegans* embryo could be achieved using millisecond 405 nm light pulses, while neighboring cells under 514 nm continued to divide (see Fig. 16B).<sup>155</sup> The applicability of **photostatins** to tissues was demonstrated with light dependent microtubule disruption in a murine muscle (Fig. 14 D). Studies that use **PST-1** as a cytological tool have begun to appear in the literature shortly after its introduction.<sup>156-158</sup> For example, it was shown that the outgrowth of microtubules at the interface bridge in early embryonic development can be inhibited through **PST-1** at 405 nm light and rescued at 514 nm light.<sup>157</sup> This highlighted the central role of the interface bridge as a microtubule-organizing center in early embryonic mouse development.



**Figure 14: Optical control of cytoskeletal dynamics.** (A) Schematic depiction a photoswitch (red pentagon/star) that affects the dynamic nature of the cytoskeleton via destabilization of the polymer. (B) **PST-1** exhibits wavelength dependent cytotoxicity due to its effect on microtubules. (C) *cis*-**PST-1** induces cell cycle arrest in the G<sub>2</sub>/M phase. (D) Application of **PST-1** (as phosphorylated pro-drug **PST-1P**) to a mouse muscle results in microtubule disruption under 390 nm light. Reprinted with permission from reference (155). Copyright 2015 Elsevier Ltd.

Further investigations by Streu and Hartman validated the usefulness of the **photostatins** and addressed their metabolic stability.<sup>159,160</sup> Recent SAR studies on **photostatins** demonstrated that a minor chemical modification can significantly enhance potency against HeLa and H157 cells (**7**; Table 1, #108).<sup>161</sup>

The success of **PST-1** underscored the usefulness of photopharmacological tools for targeting the cytoskeleton with highly dynamic nature and its non-linear responses. Systematic studies will be required to assess if photoswitchable drugs can be developed into a new form of photodynamic therapy. Efforts should also be

directed towards other elements of the cytoskeleton (actin, microfilaments) and molecular motors (kinesin, dynein etc.), that actin and tubulin filaments for cargo transport or to organize chromosomes.

## 7 Other Applications of Photoswitches

Most examples of *in vivo* photopharmacology reported to date aim at the precision modulation of defined molecular targets. However, some work in the field has been directed at biological processes that do not have a clearly defined target or are based on numerous nonspecific interactions. In addition, there are miscellaneous examples of photopharmacology that involve highly specialized targets not belonging to a larger class. Both types are discussed in this section of the review.

### 7.1 Membrane Transport

The optical control of membrane permeability and cell penetration is an exciting direction in photopharmacology. Möller and colleagues developed a peptide with a photoswitchable penetration profile through incorporation of an azobenzene into the backbone between an oligoarginine and an oligoglutamate sequence (**E<sub>9</sub>R<sub>9</sub>**; Table 1, #109).<sup>162</sup> In its *cis*-isomer, cationic charges of the oligoarginine were effectively neutralized by the aligned oligoglutamate. In the *trans*-isomer of the switch, the oligoarginine side was unmasked, leading to effective uptake of the peptide in HeLa cells after irradiation with 438 nm light. This approach could be used for the optical control of a variety of small molecules conjugated to the peptide.

Optical control of membrane fusion was also explored for clathrin-mediated endocytosis.<sup>163</sup> To this end, an azobenzene was incorporated into the backbone of a cyclic peptide that inhibits the interaction between  $\beta$ -arrestin and the AP2 complex. The resultant photoswitchable peptide **TL-2** (Table 1, #110) allowed for optical control, as shown by FACS analysis of transferrin uptake in HeLa cells with 380 nm/500 nm light.

Liu and co-workers used azobenzene-containing polycations to achieve optical control over gene transfection (**Azo-PDMAEMA**; Table 1, #111).<sup>164</sup> To this end, an azobenzene monomer was incorporated in the middle of a cationic polymer. As demonstrated with a luciferase assay, this allowed for the selective optical control of transfection in mammalian cells.



## 7.2 Protein Translation

The incorporation of a stilbene-modified nucleotide termed **8st-cap** into the 5'-end of a mRNA by Ogasawara enabled the optical control of protein translation (Table 1, #112).<sup>165</sup> Irradiation at 310 nm/410 nm effectively activates/deactivates translation as demonstrated in HeLa cells through the expression of the fluorescent protein Venus. Further experiments showed that this could be achieved with the single cell resolution. Recently, the spatiotemporal resolution of photopharmacology and its usefulness in developmental biology was demonstrated in zebrafish.<sup>166</sup> In contrast to the initial report, the molecular switch employed here was an azobenzene called **mMe-2PA-cap** (Table 1, #113), which could be switched with 370 nm/430 nm light. In a complementary approach, Desaulniers and co-workers incorporated an azobenzene into the backbone of an siRNA.<sup>167</sup> This modified siRNA, termed **siRNAzOs** (Table 1, #114), was used to knockdown firefly luciferase in HeLa cells. The knockdown efficiency was strongly reduced when the respective **siRNAzo** was pre-illuminated with UV-light.

## 7.3 Cytotoxicity

The optical modulation of cytotoxicity holds great potential for targeted cancer therapy. While most studies on photoswitchable cytotoxic agents involve defined molecular target (see section 6), two recent reports describe the development of photoswitchable cytotoxic compounds, which target biomolecules in a less selective manner. This bears resemblance with conventional photodynamic therapy, which relies on the photochemical production of reactive oxygen species. Gamez and co-workers developed a photoswitchable analog of the DNA-intercalating cancer drug *cis*-platin.<sup>168</sup> They synthesized a **(cis[PtCl<sub>2</sub>DMSO])<sub>2</sub>L** complex (Table 1, #115) with a pyridyl-substituted diaryl-ethene ligand (L), which exhibited increased cytotoxicity under UV light, *i.e.* in the closed form. Furthermore, a photoswitchable mimetic of the highly cytotoxic peptide gramicidin S was described (**ES-Sw**; Table 1, #116).<sup>169</sup> Gramicidin S cytotoxicity is exerted through membrane disruption. Incorporation of a dithienylethene into the backbone of the cyclic peptide yielded different levels of cytotoxicity in the closed vs. open form, as demonstrated both in tumor cells and in a Lewis lung carcinoma model in mice.

## 7.4 Immunobiology

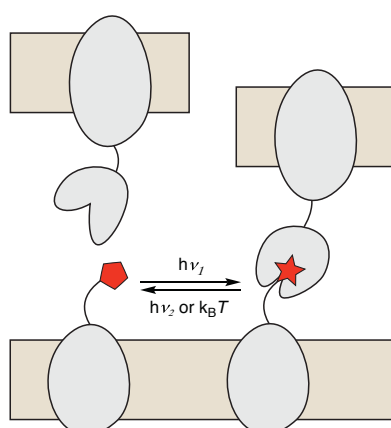
The photopharmacology of non-linear immune responses holds great promise despite being underdeveloped. Feringa and co-workers reported on a photoswitchable inhibitor of mast cell activation. These inhibitors exhibited not only light-dependent activity but also greater potency than other chromone-based

antiallergic agents.<sup>170</sup> The photoswitchable, *cis*-active, inhibitors, termed diazochrome (**DAC**), *meta*-azochrome (**MAC**) and *para*-azochrome (**PAC**, Table 1, #117), resemble the known bivalent inhibitor disodium cromoglycate with an azobenzene incorporated in the spacer region. The compounds were tested in a LAD2 mast cell line. The authors proposed that further optimization could yield highly useful tools for the study of allergic reactions.

## 7.5 Cell Adhesion and Cell Communication

The optical control of cell adhesion has been explored in a variety of settings. In 2005, Kessler and colleagues modified their RGD peptide with an azobenzene to develop a photoswitchable surface-coating system (**1**; Table 1, #118).<sup>171</sup> Upon irradiation with 366 nm light, the adhesion of MC3T3 E1 mouse osteoblasts to a coated polymer was reduced compared to irradiation with 450 nm light. Attaching the photoswitchable RGD to a gold surface in a self-assembled monolayer markedly improved optical control over adhesion.<sup>172</sup> In this study, which employed an azobenzene-thiol (**1**; Table 1, #119), the RGD peptide was embedded in a polyethyleneglycol matrix, which masked it in the *cis*-form of the photoswitch.

Lindhorst and co-workers explored light-dependent lectin binding to carbohydrates.<sup>173</sup> To this end, they prepared azobenzene mannosides and immobilized them on a gold surface via short spacers to suppress unspecific binding (Table 1, #120). Switching between the *cis*- and *trans*-isomer resulted in the optical control of *E. coli* cell adhesion.<sup>174</sup> This approach was further developed to enable reversible control over binding of *E. coli* to human cells (Fig. 15).<sup>175</sup> The authors used modern bioconjugation chemistry to couple an azobenzene glycoside to azide-carbohydrates displayed on the surface HMEC-1 cells (**5**; Table 1, #121).



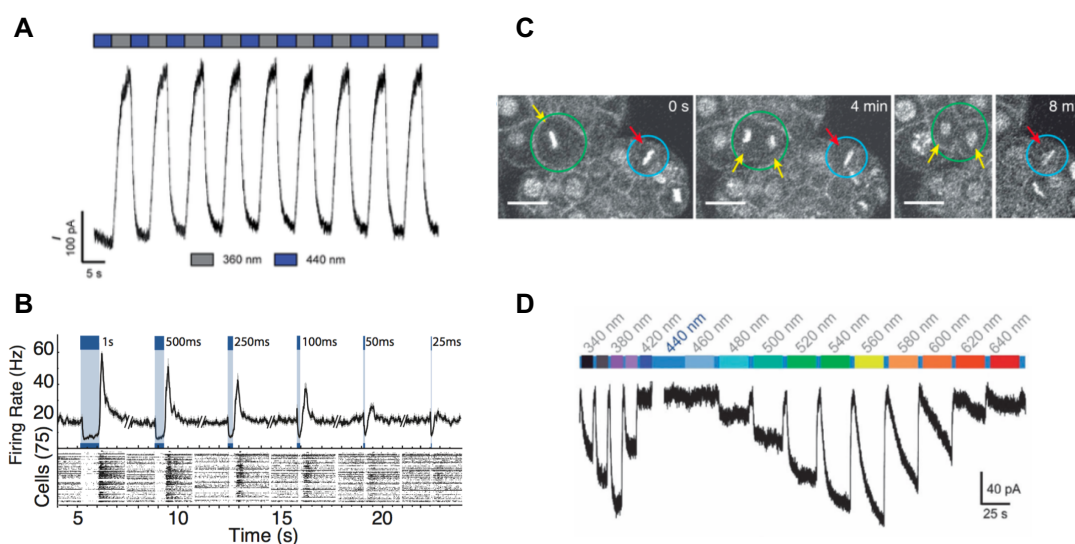
**Figure 15: Cell Adhesion.** Schematic depiction of light-dependent *E. coli* adhesion to a HMEC-1 cells.

Optical control over quorum sensing could be achieved through incorporation of azobenzenes into *N*-acyl homoserine lactones (**2-4**; Table 1, #122).<sup>176</sup> The light-dependent effect of these compounds could be demonstrated in Gram-negative bacteria that express quorum sensing marker genes. Another study concerned the formation of biofilms. It involved azobenzene glycosides that mimic amphiphiles used as antimicrobial and antiadhesive agents (Table 1, #123).<sup>177</sup> The *cis*-isomers of these compounds were shown to be a more potent inhibitors of biofilm formation than the corresponding *trans*-isomers.

## 8 Photopharmacology with Synthetic Switches vs.

### Alternative Approaches for Optical Control

Photocages and photoswitches have unique advantages and disadvantages depending on the biological system for which they are chosen. Caged ligands are somewhat easier to design since the structure of the active species, the original ligand, is clear. Photoswitchable ligands, on the other hand, must accommodate the chromophore and show a sufficient change in activity upon isomerization. Design principles for this have been discussed elsewhere.<sup>96</sup>



**Figure 16: Advantages of synthetic photoswitches.** (A) Temporal precision. Reprinted with permission from reference (108). Copyright 2016 the American Chemical Society (B) Spatial precision. Reprinted with permission from reference (134). Copyright 2017 Nature Publishing Group. (<https://doi.org/10.1038/s41467-017-01990-7>, <https://creativecommons.org/licenses/by/4.0/>) (C) Reversibility. Reprinted with permission from reference (155). Copyright 2014 Elsevier Ltd. (D) Color-dosing. Reprinted with permission from reference (43). Copyright 2014 Published by The Royal Society of Chemistry (<https://doi.org/10.1039/c4cc06612j>, <https://creativecommons.org/licenses/by/3.0/>).

The major advantage of photoswitches is their reversibility (Fig. 16A), which does not depend on diffusive processes, and their favorable off-kinetics (Fig. 16B). This increases the temporal resolution and spatial resolution of switches compared with caged ligands, especially when tethered versions are used (Fig. 16C). With

azobenzenes, reversibility has been demonstrated over many cycles (sometimes thousands) since the photochemical reaction is a very fast and clean process.<sup>178,179</sup> Furthermore, photocages release side products that can be light-absorbent or toxic. By contrast photoswitching does not create an additional chemical species as long as spin exchange and electron transfer processes are avoided.

Photoswitches generally have higher molar extinction coefficients and quantum yields and therefore need lower light intensities. They can be isomerized effectively with standard LEDs (<10 mW/cm<sup>2</sup>)<sup>155</sup> and generally do not require the lasers, mercury or xenon flash lamps, or the high power LEDs used in fluorescence imaging and uncaging.<sup>4</sup> Finally, photoswitches allow for “color-dosing” due to the wavelengths dependence of the photostationary states (Figure 4B, 5B,C, 6A, 14B, 16D). As the photostationary states change with the color (wavelength) of the incident light, the concentration of active pharmacophore can be titrated. This tight control over concentration is difficult, if not impossible to achieve with caged ligands.

Another aspect worthy of exploring is the differences between photopharmacology and conventional optogenetics. Optogenetics relies on endogenous photoswitches, such as retinal and flavins, that are usually present in sufficient quantities, while synthetic photoswitches need to be externally supplied. Therefore, genetically encoded modes of photopharmacology (PTL, PORTL, photoBOLT etc.) are two-component systems, which have practical disadvantages over the fully encoded photoreceptors. On the other hand, photopharmacology aims toward the photosensitization of *native* receptors and does not add entirely foreign genes to cells. In the case of diffusible ligands, these receptors are completely unmodified and expressed at natural physiological levels. When PTLs are employed, their targets are usually overexpressed against a native background but minimally modified. In the PORTL variant, the modifications are large (typically around 25 kDa in molecular mass) and the constructs are also overexpressed, at least in the variants published to date. However, a PORTL can be mounted onto an auxiliary protein, antibody, or nanobody, which leaves the native receptors unmodified and at natural expression levels.<sup>135</sup>

A major point of concern for *in vivo*-photopharmacology is the metabolic stability and toxicity of the photoswitches used. Unfortunately, azobenzenes have a poor reputation in this regard. This is probably due to the historic use of “butter yellow” (4-dimethylamino azobenzene) as a food colorant, which was identified as a carcinogen in the late 1930s.<sup>180</sup> It took a decade for this discovery to become publicly known,<sup>181</sup> resulting in the withdrawal of the compound and its replacement with (synthetic) carotene. Interestingly, other azobenzenes such as tartrazine, sunset yellow, and allura red are still widely used as food-colorants despite understandable concerns and scrutiny surrounding synthetic additives. The identification of the azobenzene prontosil as a prodrug, which releases the active

ingredient sulfanilamide following reduction by bacterial azoreductases further damaged the reputation of azobenzenes as viable drugs.<sup>182</sup>

However, some azobenzenes, such as phenazopyridine, are still in clinical use and many recent studies show that the photoswitches used in photopharmacology exhibit good *in vivo* stability and are non-toxic (e.g. in animal models of vision restoration).<sup>86,87</sup> The stability of azobenzenes towards glutathione or azoreductases, their mutagenic potential, and their stability *in vivo* can be easily assayed.<sup>106,183,184</sup> Long-term toxicity concerns surrounding their reduction products, *viz.* aniline derivatives, could be addressed by turning to heterocyclic azobenzenes, which also increase solubility.<sup>19,106</sup> Therefore, broad generalizations should not be made without considering the individual azobenzene molecule used in photopharmacology. In comparison, the toxicology and biocompatibility of other photoswitches have been studied in much less detail.

## 9 Conclusion and Outlook

The field of photopharmacology is still comparatively young and true *in vivo* applications have only been reported in recent years. It is already clear, however, that synthetic photoswitches are compatible with complex biological systems and that the precise control of biological function can be achieved with this approach. Motivated by this, chemists continue to refine molecular photoswitches and develop improved methods for their synthesis<sup>25,185-189</sup> and strategies for tuning their spectral properties.<sup>190,191</sup>

Many additional targets for *in vivo* photopharmacology can be imagined. For instance, the photosensitization of GPCRs not discussed in this review should be possible and many important classes of ion channels and transporters have not yet been investigated in this regard. Photopharmacology should also work well with enzymes that are involved in cascades, such as caspases, blood clotting factors, or MAP kinases. Transcription factors, nuclear hormone receptors, and other components of the cytoskeleton should be amenable to the approach.

One important goal of photopharmacology is to make it clinically relevant in the near future. Synthetic switches can work with unmodified receptors at native expression levels (as PCLs, PALs, antibody conjugates etc.) and do not necessarily require gene therapy, which could greatly simplify their regulatory approval. Potential therapeutic applications of photopharmacology include microbial infections,<sup>150,152</sup> diabetes,<sup>19,104-106,126</sup> cancer,<sup>155</sup> pain,<sup>98,77,88,99</sup> and blindness.<sup>83,85-87,94</sup> In all cases, efficacy has been demonstrated on the cellular level and some studies have progressed to live animals. Vision restoration is at the forefront of these efforts. Compared to other therapeutic approaches, such as retinal implants and gene therapy, the application of freely diffusible photoswitches has clear

advantages, which are laid out in detail in the accompanying review of Isacoff and Kramer. If successful, vision restoration would pave the way for other applications of photopharmacology in precision medicine.

Vision restoration has an obvious advantage over other potential applications of photopharmacology because light-delivery is not a concern. This is not as much of a problem as it seems, however, for non-transparent tissues.<sup>131</sup> Photopharmacology profits from the enormous progress that has been made elsewhere in photomedicine, for instance in photodynamic therapy, and from imaging techniques adapted to the human body. It will also benefit from the momentum created by optogenetics, which has driven the development of advanced methods for light delivery.<sup>192-194</sup> Sophisticated light guides and micron-sized implantable LEDs are now available and biodegradable remotely powered electronics are on the horizon.<sup>195-197</sup> Therefore, we are optimistic that the combination of light and synthetic photoswitches will eventually find a place in human therapy.

**Author Information****Corresponding Author**

[dirktrauner@nyu.edu](mailto:dirktrauner@nyu.edu)

**Notes**

The authors declare no competing financial interest.

**Biographies**

**Katharina Hüll** is a German Academic Scholarship Foundation Fellow at LMU Munich and New York University. She received her B.S. in Chemistry and Biochemistry from LMU Munich. During her Master's, she worked with Prof. Dr. J Derek Woollins at the University of St. Andrews on chalcogen-P<sub>2</sub>N<sub>2</sub>-scaffolds and with Dirk Trauner at LMU Munich. She joined Dirk Trauner's lab for her Master's thesis on heterocyclic azobenzenes and received her M.S. in Chemistry from LMU Munich in 2013. In 2014, she started her PhD in the group of Dirk Trauner, working on small-molecule photoswitches for the optical control of ion channel and GPCR function.

**Johannes Morstein** is a German Academic Scholarship Foundation and MacCracken Graduate Fellow at New York University. He received his B.S. and M.S. in Chemistry and Biochemistry from Ludwig Maximilian University of Munich. During his Master's, he worked with Prof. Dr. Christopher J. Chang on the development of small-molecule fluorescent sensors and Prof. Dr. John F. Hartwig on the functionalization of C-Si bonds at the University of California in Berkeley. Currently, he is a graduate student in the group of Dirk Trauner, focusing on the development of small-molecule photoswitches to probe different aspects of receptor biology.

**Dirk Trauner** studied in biology and biochemistry at the University of Vienna, Austria, before he joined Prof. Dr. Johann Mulzer's group at the Free University of Berlin, Germany, to pursue natural product synthesis. Subsequently, he became a postdoctoral fellow with Prof. Dr. Samuel J. Danishefsky at the Memorial Sloan-Kettering Cancer Center in New York City, NY, USA. In 2000, he joined the University of California, Berkeley, USA, where he rose through the ranks to become an Associate Professor of chemistry (with tenure). In 2008, he moved to the University of Munich, Germany, as a Professor of Chemistry and Chemical Biology. In March 2017, he has been appointed the Janice Cutler Chair in Chemistry at New York University, where he also resides as adjunct Professor of Neurosciences and Physiology. His research interests range from organic synthesis and natural product chemistry to chemical neurobiology, optogenetics, and photopharmacology.



**Acknowledgments**

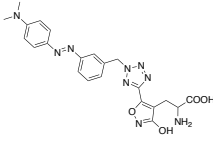
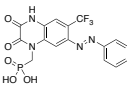
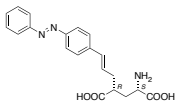
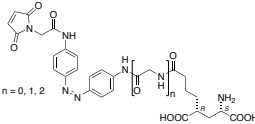
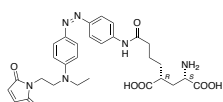
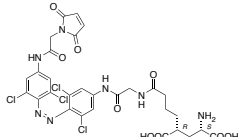
K.H. and J.M. thank the German Academic Scholarship Foundation for a PhD fellowship. J.M. thanks the New York University for a MacCracken fellowship. The authors thank Philipp Leippe, Dr. Bryan Matsuura, Dr. Oliver Thorn-Seshold, Dr. Bichu Cheng, Dr. Benjamin Williams, Dr. Laura Laprell, Martin Reynders, Anna Impastato, and Christopher Arp for critical review of the manuscript. Dr. David Barber and Dr. Nils Winter are acknowledged for their support in the early stages of this review. We thank the European Science Foundation (ERC grant no. 268795 to D.T.) for funding.

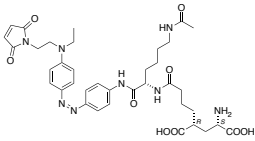
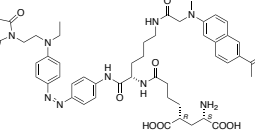
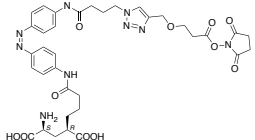
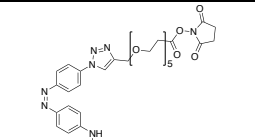
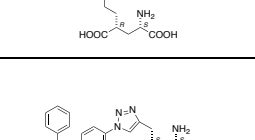
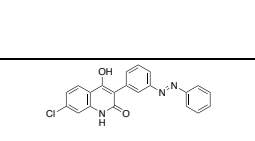
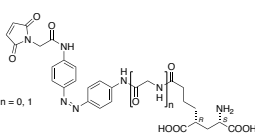
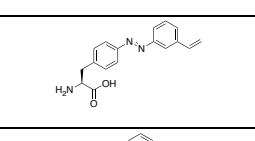
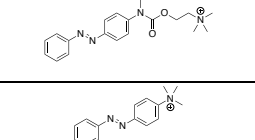
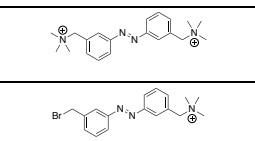
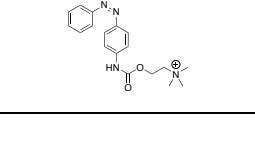




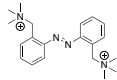
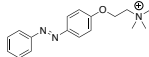
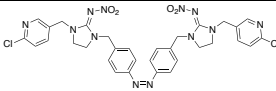
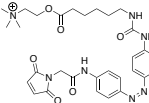
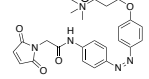
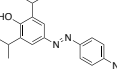
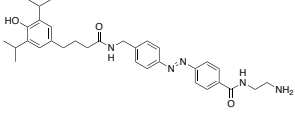
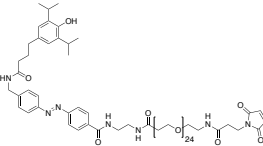
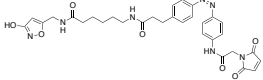
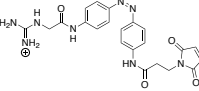
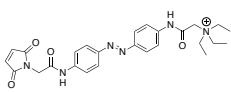
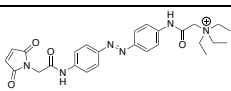
## 10 Table of Structures

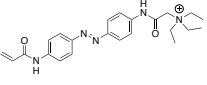
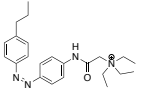
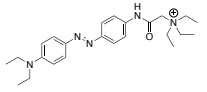
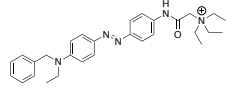
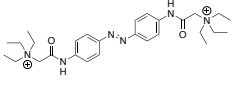
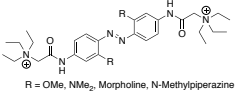
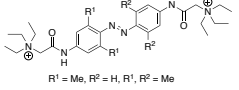
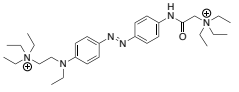
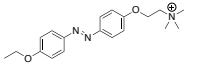
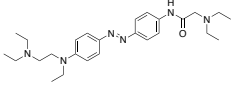
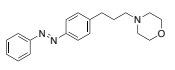
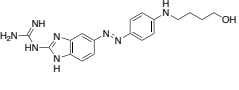
**Table 1:** Photoswitches and their biological targets.

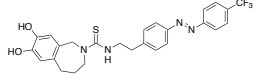
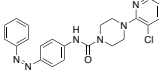
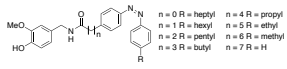
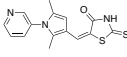
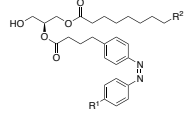
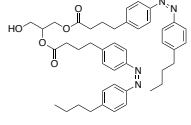
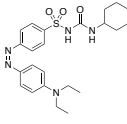
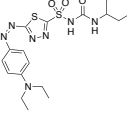
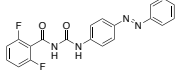
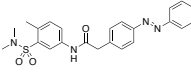
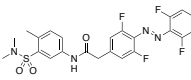
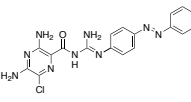
### 10.1 Photoswitches for Ion Channels

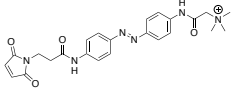
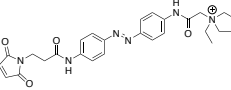
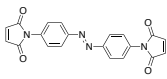
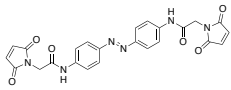
#	Target/ Construct	Compound Name/ Numbering in Original Paper	Compound Structure (Active Form)	Switching Wave- lengths	Model Organism	Ref
1	AMPA	<b>ATA (ATA-3)</b>		440 nm – 480 nm/ dark	HEK293T cells, mouse cortical neurons, hippo- campal neurons, TKO mouse retina	30-32
2	AMPA	<b>ShuBQX-3</b>		460 nm/ 600 nm	HEK293T cells, <i>Xenopus</i> oocytes, hippo- campal neurons	33
3	Kainate	<b>GluAzo</b>		380 nm/ 500 nm	HEK293T cells, rat hippo- campal neurons, purkinje cells,	34-36
4	Kainate Hy- LIGHTER	<b>L-MAG-0, L-MAG (L-MAG-1), L-MAG-2</b>		380 nm or 820 nm (2P)/ 500 nm	HEK293T cells, hippo-campal neurons, astro- cytes, chroma- ffin cells, zebra- fish larvae, <i>rd1</i> mice, TKO mice, AAV transf. wt mice (cortex)	37- 41,44- 51,57, 58
5	Kainate	<b>L-MAG-0<sub>460</sub></b>		460 nm or 840 nm (2P)/ dark	HEK293T cells, hippocampal neurons, <i>rd1</i> mice, wt mice (cortex), <i>rcd1</i> dogs	42,44, 52,57
6	Kainate	<b>toCIMAG</b>		380 nm or 560 nm – 640 nm/ 440 nm	HEK293T cells	43

7	Kainate	<b>MAG<sub>2P</sub></b>		425 nm or 900 nm (2P)/dark	HEK293T cells, hippocampal neurons	45
8	Kainate	<b>MAGA (MAG<sub>2P</sub>)</b>		425 nm or 880 nm (2P)/dark	HEK293T cells	45
9	Kainate	<b>TCP-9</b>		380 nm/ 500 nm	TSA-201 cells, DRG neurons, rd10 mice	54
10	Kainate	<b>TCP-10</b>		380 nm/ 500 nm	tsA201 cells	54
11	NMDA	<b>ATG</b>		370 nm or 700 - 740 nm (2P)/ 420 nm	Mouse cortical neurons, hippocampal slice, <i>Xenopus</i> oocytes	62
12	NMDA	<b>PNRA</b>		360 nm/ 420 nm	<i>Xenopus</i> oocytes	63
13	NMDA	<b>L-MAG-0, L-MAG-1</b>		360 - 405 nm/ 460 - 560 nm	HEK293T cells, hippocampal neurons, hippocampal murine slice, zebrafish larvae	64
14	NMDA	<b>PSAA</b>		365 nm/ 460 nm	HEK293T cells,	65
15	nAChR	<b>AzoCharCh</b>		UV	<i>Electrophorous</i> Electroplaques	66
16	nAChR	<b>Azo-PTA</b>		UV	<i>Electrophorous</i> Electroplaques	66
17	nAChR	<b>BisQ</b>		UV	<i>Electrophorous</i> Electroplaques	67-69,74
18	nAChR	<b>QBr</b>		UV	<i>Electrophorous</i> Electroplaques	67,70
19	nAChR	<b>EW-1</b>		UV	<i>Electrophorous</i> Electroplaques	71,72

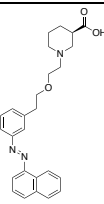
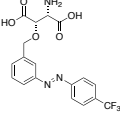
20	nAChR	<b>2BQ</b>		UV	<i>Electrophorous</i> Electroplaques	73
21	nAChR	<b>AzoCholine</b>		360 nm/ 440 nm	HEK293T cells, rat sensory neurons, mouse hippocampal slice, <i>C. elegans</i> nematodes	74
22	insect nAChR	<b>AMI-10</b>		365 nm/ 430 nm	<i>Musca</i> <i>domestica</i>	75
23	nAChR	<b>MAACh</b>		380 nm/ 500 nm or dark	<i>Xenopus</i> oocytes	76
24	nAChR	<b>MAHoCh</b>		380 nm/ 500 nm or dark	<i>Xenopus</i> oocytes	76
25	GABA <sub>A</sub>	<b>AP-2</b>		360 - 400 nm/dark	<i>Xenopus</i> oocytes, HEK293T cells, <i>Xenopus laevis</i> tadpoles	77
26	GABA <sub>A</sub>	<b>MPC-088</b>		365 nm/ white light	<i>Xenopus</i> oocytes, rat RGCs, mice cerebellar purkinje neurons	78
27	GABA <sub>A</sub>	<b>MPC-100</b>		365 nm/ white light	<i>Xenopus</i> oocytes	78
28	GABA <sub>A</sub> (LiGABAR)	<b>MAM-6</b>		380 nm/ 500 nm	HEK293T cells, <i>Xenopus</i> oocytes, hippocampal rat slice	79
29	GABA <sub>A</sub> (LiGABAR)	<b>PAG-1C</b>		380 nm/ 500 nm	HEK293T cells, cortical and hippocampal neurons (slice), knockin mice	80
30	K <sub>v</sub> SPARK, HSPARK	<b>MAQ</b> (Ma-Azo-QA)		380 nm/ 500 nm	<i>Xenopus</i> oocytes, hippocampal neurons, CHO cells,	55,59, 60,81
31	TREK1	<b>MAQ</b>		380 nm/ 500 nm	HEK293T cells, hippocampal neurons	81

32	K <sub>v</sub> , HCN	<b>AAQ</b>		380 nm/ 500 nm	HEK293T cells, hippocampal neurons, rat cerebellar slice, rat RGCs <i>Hirudo medicinalis</i> heart neurons, <i>rd1</i> mice	55,82, 84,83
33	K <sub>v</sub>	<b>PrAQ</b>		380 nm/ 500 nm	HEK293T cells	82
34	K <sub>v</sub> , HCN	<b>DENAQ</b>		460-480 nm or white light /dark	HEK293T cells, <i>rd1</i> mice	84-86, 91
35	K <sub>v</sub> , HCN	<b>BENAQ</b>		460-480 nm or white light/dark	<i>rd1</i> mice	84,86,8 7
36	Nav, K <sub>v</sub> , Cav	<b>QAQ</b>		380 nm/500 nm	HEK293T cells, rat hippocampal neurons, mouse DRG neurons, spinal cord slice	86,88- 91
37	Nav, K <sub>v</sub> , Cav	<b>QAQs</b>	 R = OMe, NMe <sub>2</sub> , Morpholine, N-Methylpiperazine	R = OMe: 420 nm/ dark	HEK293T cells, NG108-15 cells	89
38	Nav, K <sub>v</sub> , Cav	<b>QAQs</b>	 R <sup>1</sup> = Me, R <sup>2</sup> = H, R <sup>3</sup> = Me	380 nm/ 500 nm	HEK293T cells, NG108-15 cells	89
39	Nav, K <sub>v</sub> , (Cav)	<b>QENAQ</b>		480 nm /dark	<i>Xenopus</i> oocytes, mice trigeminal neurons, DRG neurons	90
40	Nav, Cav, K <sub>v</sub>	<b>Azo-TAB</b>		365 nm/ 490 nm	Rat cardiomyocytes	92,93
41	K <sub>v</sub> , HCN, (Nav)	<b>DAD</b>		460 nm or white light/dark	wt mouse cortical neurons (slice), TKO mouse	94
42	Nav	<b>Fotocaine</b>		350 nm/ 450 nm	Mouse hippocampal neuron	95
43	H <sub>v</sub> 1	<b>photoGBI-4</b>		440-480 nm/dark	<i>Xenopus</i> oocytes, human macrophages, sperm, epithelial cells	97

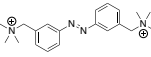
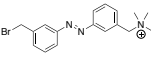
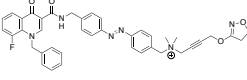
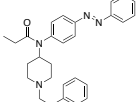
44	TRPV1	<b>AC-4</b>		360 nm/ 440 nm	HEK293T cells	98
45	TRPV1	<b>ABCTC</b>		370 nm/ 470 nm	HEK293T cells	98
46	TRPV1	<b>AzCA-1 to AzCA-8</b>	 <small>n = 0 R = heptyl    n = 4 R = propyl  n = 1 R = heptyl    n = 5 R = ethyl  n = 2 R = pentyl    n = 6 R = methyl  n = 3 R = butyl    n = 7 R = H</small>	350 - 365 nm/ 450 - 460 nm	HEK293T cells, DRG neurons, murine C-fibers	99
47	TRPA1	<b>Optovin</b>		405 nm/ dark	HEK293T cells, DRG neurons, human cardiomyocytes, zebrafish, TRPA1-KO mice	100, 101
48	TRPC2/3/ 6	<b>PhoDAG-1 to PhoDAG-3</b>	 <small>PhoDAG-1: R<sup>1</sup> = C<sub>2</sub>H<sub>5</sub>; R<sup>2</sup> = C<sub>12</sub>H<sub>25</sub>  PhoDAG-2: R<sup>1</sup> = C<sub>2</sub>H<sub>5</sub>; R<sup>2</sup> = H  PhoDAG-3: R<sup>1</sup> = H; R<sup>2</sup> = H</small>	365 nm/ 470 nm	HEK293 cells, mouse vomeronasal sensory neurons, tissue slices, murine vomeronasal organ tissue slices	102
49	TRPC3	<b>OptoDARG</b>		365 nm/ 430 nm	HEK293 cells	103
50	K(ATP)	<b>JB-253</b>		400 - 500 nm/dark	HEK293T cells, rodent and human beta cells, CD1 mice	19,105, 106
51	K(ATP)	<b>JB-558</b>		520-560 nm/dark	HEK293T cells, rodent and human beta cells	104, 106
52	SUR	<b>B3</b>		365 nm	<i>Mythimna separata</i> larvae, <i>Blatella germanica</i>	107
53	GIRK	<b>LOGO-5</b>		360 nm/ 440 nm	HEK293T cells, hippocampal neurons, zebrafish larvae	108
54	GIRK	<b>VLOGO</b>		500 nm/ 400 nm or dark	HEK293T cells, zebrafish larvae	109
55	ENaC	<b>PA-1</b>		400 nm/ 500 nm	<i>Xenopus</i> oocytes, HEK293T cells, H441 cell monolayers	110

56	P2X	<b>MEA-TMA</b>		365 nm/ 525 nm	HEK293T cells, hippocampal neurons	111
57	P2X	<b>MEA-TEA</b>		365 nm/ 525 nm	HEK293T cells	111
58	P2X, ASIC	<b>BMA</b>		360 nm/ 440 nm	HEK293T cells, PC12 cells, CHO-K1 cells	112
59	P2X	<b>MAM</b>		365 nm/ 525 nm	HEK293T cells, TSA-201 cells	113

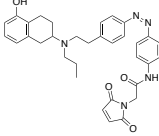
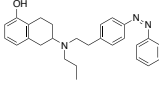
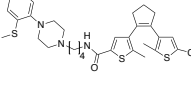
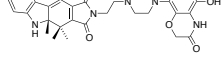
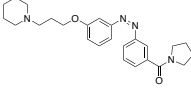
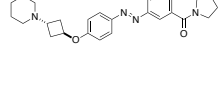
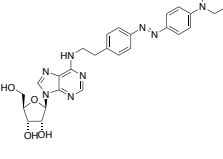
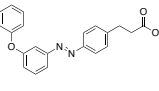
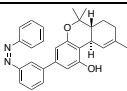
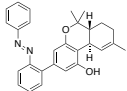
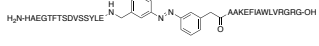
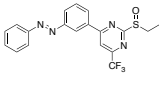
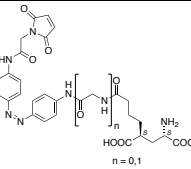
## 10.2 Photoswitches for Transporters/Pumps

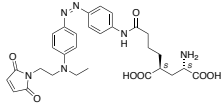
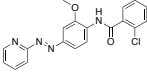
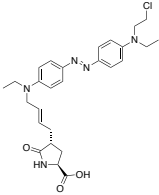
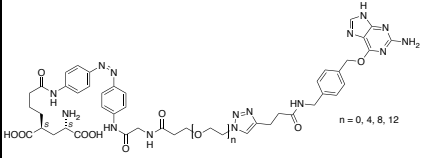
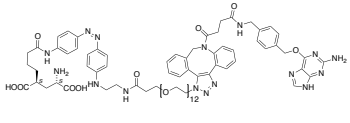
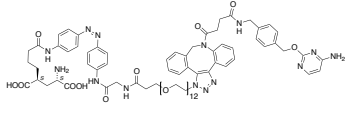
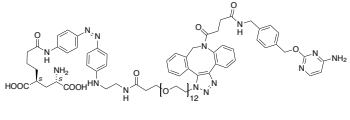
#	Target/ Construct	Compound Name/ Numbering in Original Paper	Compound Structure (Active Form)	Switching Wave- lengths	Model Organism	Ref
60	GAT1	<b>Compound 6e</b>		375 nm/ 450 nm or dark	<i>Xenopus Laevis</i> Oocytes	114
61	EAAT1-3	<b>ATT</b>		350 nm/ 450 nm or dark	HEK293 Cells, Dentate Gyrus Granule Cells	115

## 10.3 Photoswitches for GPCRs

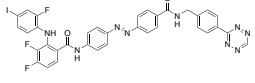
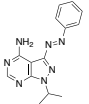
#	Target/ Construct	Compound Name/ Numbering in Original Paper	Compound Structure (Active Form)	Switching Wave- lengths	Model Organism	Ref
62	mAChR	<b>BisQ</b>		360 nm/ 440 nm	Rat myoballs, frog myocardium	116, 117
63	mAChR	<b>QBr</b>		320 nm/ 420 nm	Rat myoballs	118
64	M1	<b>BQCAAI</b>		365 nm/ 455 nm	HEK293 cells	119
65	$\mu$ -Opioid	<b>PF-2</b>		360 nm/ 440 nm	HEK293T cells	120

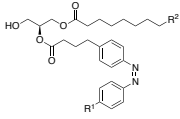
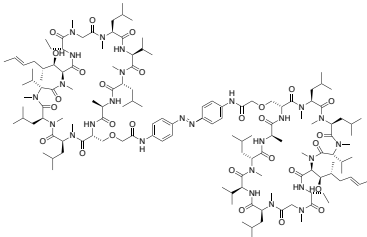
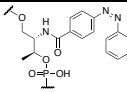
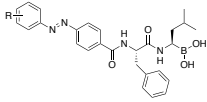
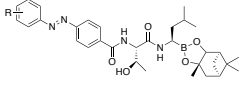
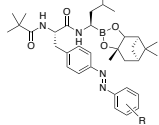
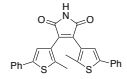
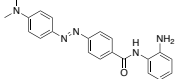
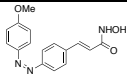
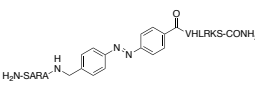
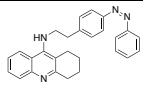


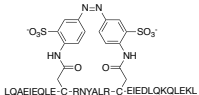
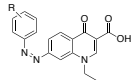
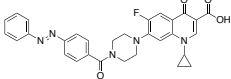
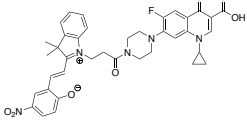
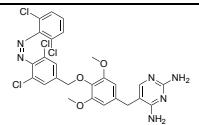
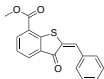
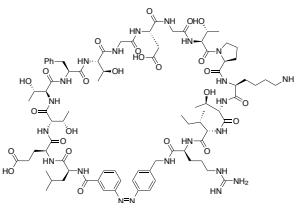
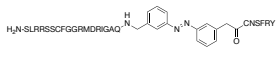
66	D1/D2	<b>MAP</b>		360 nm/ 460 nm	HEK293T cells	121
67	D1/D2	<b>AP</b>		360 nm/ 460 nm	HEK293T cells	121
68	D2	<b>Compound 29</b>		312 nm/ 520 nm	HEK293T cells, CHO-cells	122
69	D2	<b>Compound 52</b>		400 nm/ 530 nm	HEK293T cells, CHO-cells	122
70	H3	<b>VUF-14738</b>		360 nm/ 434 nm	HEK293T cells, CHO cells, <i>Xenopus</i> oocytes	123
71	H3	<b>VUF-14862</b>		360 nm/ 434 nm	HEK293T cells, CHO cells, <i>Xenopus</i> oocytes	123
72	A2a and A3	<b>MRS5543</b>		460 nm	HEK293 cells	124
73	GPR40	<b>FAAzo-10</b>		365 nm/ 460 nm	HeLa Cells, Mouse Pancreatic $\beta$ - Cells	18
74	CB1	<b>Azo-THC-3</b>		360 nm/ 440 nm	AtT-20(CB1) cells	125
75	CB1	<b>Azo-THC-4</b>		360 nm/ 440 nm	AtT-20(CB1) Cells	125
76	GLP-1	<b>LirAzo</b>		330-370 nm/420- 440 nm	CHO-GLP-1R cells, mouse pancreatic $\beta$ - cells, Min6 cells	126
77	GLP-1	<b>PhotoETP</b>		350 nm/ 440 nm	CHO-GLP-1R cells, mouse pancreatic $\beta$ - cells, Min6 cells	127
78	mGluR (LimGluR)	<b>D-MAG-0, D- MAG-1</b>		380 nm/ 500 nm	HEK293 cells, hippocampal neurons	128

79	mGluR (LimGluR)	<b>D-MAG-0<sub>460</sub></b>		470 nm or 850 - 950 nm (2P)/ dark	HEK293 cells, hippocampal neurons	44
80	mGluR	<b>Alloswitch-1 (Azo- pyridines)</b>		390 nm/ 490 nm	HEK293 cells, neonatal rat cortical astrocyte cells, <i>X. tropicalis</i> tadpoles, zebrafish larvae	129, 131
81	mGluR4	<b>OptoGluNA M-4.1</b>		439 nm/ dark	L756S mGluR4 cells, zebrafish larvae	130
82	SNAP- mGluR2, SNAP- mGluR7	<b>BGAG-0, BGAG-4, BGAG-8, BGAG-12</b>		380 nm/ 500 nm	HEK293T cells, hippocampal neurons	132
83	SNAP- mGluR2, SNAP- mGluR7	<b>BGAG-12<sub>460</sub></b>		460 nm/ dark	HEK293T cells, hippocampal neurons	132
84	mGluR2, mGluR3	<b>BCAG-12</b>		380 nm/ 500 nm	HEK293T cells, rod and cone photoreceptor cells, mice	133
85	mGluR2, mGluR3	<b>BCAG-12<sub>460</sub></b>		460 nm/ dark	HEK293T cells, rod and cone photoreceptor cells, mice	133

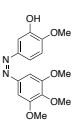
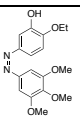
## 10.4 Photoswitches for Enzymes

#	Target/ Construct	Compound Name/ Numbering in Original Paper	Compound Structure (Active Form)	Switching Wave- lengths	Model Organism	Ref
86	MEK Kinase	<b>photo-X</b>		360 nm/ 440 nm	HEK293ET cells	138
87	RET Kinase	<b>Compound 4</b>		365 nm/ 503 nm	PathHunter eXpress receptor tyrosine kinase cells	139

88	PKC	<b>PhoDAG-1 to PhoDAG-3</b>	 <p>PhoDAG-1: R<sup>1</sup> = C<sub>6</sub>H<sub>5</sub>; R<sup>2</sup> = C<sub>10</sub>H<sub>21</sub>  PhoDAG-2: R<sup>1</sup> = C<sub>6</sub>H<sub>5</sub>; R<sup>2</sup> = H  PhoDAG-3: R<sup>1</sup> = H; R<sup>2</sup> = H</p>	360 nm/ 460 nm	HeLa cells, Min6, mouse pancreatic β- cells, mouse pancreatic islets, <i>C.</i> <i>elegans</i>	140
89	Phosphatase - Calcineurin	<b>CsA-AB-CsA</b>		370 nm/ 740 nm or dark	Human PBMC cells, Jurkat cells	141
90	Thrombin	<b>9c-8azo</b>		365 nm/ 553 nm	Human plasma	142
91	Proteasome	<b>Compounds 1-6</b>		365 nm/ white light	RAJI cell lysates, HeLa cells	143
92	Proteasome	<b>Compound 5</b>		365 nm/ dark	MCF-10A Cells	144
93	Proteasome	<b>Compound 4</b>		365 nm/ dark	MCF-10A cells	144
94	HDAC (Sirtuin)	<b>Compound 11</b>		312 nm/ 530 nm	HeLa cells	20
95	HDAC	<b>BG14</b>		470 nm/ dark	MCF-7 cells,	145
96	HDAC	<b>Compound 12</b>		365 nm/ white light	HeLa cells	146
97	HMT (MLL1)	<b>Compound 7</b>		366 nm/ 430 nm	Murine MLL- AF9-transduced mouse bone marrow cells, leukemia cells	147
98	Acetylcholinesterase	<b>AzoTHA</b>		350 nm/ 440 nm	Mouse trachea preparations	148

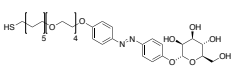
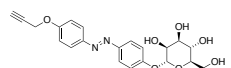
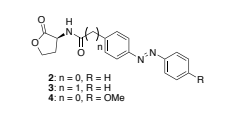
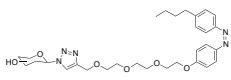
99	RNA Polymerase	<b>XAFosW</b>		365 nm/ 460 nm	HEK293T cells	149
100	DNA Gyrase	<b>Compounds 1-9</b>		365 nm/ dark	<i>E. coli</i> CS1562; <i>M. Luteus</i> ATCC 9341	150
101	DNA Gyrase	<b>Azofloxacin</b>		400 nm/ 530 nm or dark	<i>E. coli</i> CS1562; <i>M. Luteus</i> ATCC 9341	151
102	DNA Gyrase	<b>Spiro-floxacin</b>		365 nm/ 530 nm or dark	<i>E. coli</i> CS1562; <i>M. Luteus</i> ATCC 9341	151
103	Dihydrofolate Reductase	<b>Compound 13</b>		652 nm/ 400 nm or dark	<i>E. coli</i> CS1562	152
104	Lipoxygenase 12/15	<b>BODTCM</b>		405 nm/ dark	U937 cells	21
105	NO Synthase	<b>Photo-switchable Peptide Ligand</b>		366 nm	Mouse skeletal muscle cells	153
106	Guanylyl cyclase	<b>TOP-271</b>		365 nm/ 450 nm	HEK293T cells, mouse pancreatic $\beta$ -cells	154

## 10.5 Photoswitches for Cytoskeleton

#	Target/Construct	Compound Name/Numbering in Original Paper	Compound Structure (Active Form)	Switching Wavelengths	Model Organism	Ref
107	Microtubules	<b>PST-1 (azobestreptatin A4)</b>		388 nm/ 508 nm	HeLa cells, MDA-MB-231 cells, HUVEC cells, HEK293T cells, <i>C. Elegans</i> , C57BL/6 mice	155, 159, 160
108	Microtubules	<b>Compound 7</b>		400 nm/ 500nm or dark	HeLa cells, H157 cells	161

## 10.6 Other Applications of Photoswitches

#	Target/ Construct	Compound Name/Numbe ring in Original Paper	Compound Structure (Active Form)	Switching Waveleng ths	Model Organism	Ref
109	Mem- brane transport	<b>E<sub>9</sub>R<sub>9</sub></b>		366 nm/ 438 nm	HeLa cells	162
110	Mem- brane transport	<b>TL-2</b>		380 nm/ 500 nm	HEK293 cells, HeLa cells	163
111	Mem- brane transport	<b>Azo- PDMAEMA</b>		365 nm	COS-7 cells, HepG-2 cells, CHO-K1 cells	164
112	Protein translation	<b>8ST-cap</b>		310 nm/410 nm	HeLa Cells, PC12 Cells	165
113	Protein translation	<b>mMe-2PA- cap</b>		370 nm/ 430 nm	Zebrafish embryo	166
114	Protein translation	<b>siRNAzo</b>		365 nm/ Vis	HeLa cells	167
115	Cyto- toxicity	<b>[Pt<sub>2</sub>Cl<sub>4</sub>(DMS O)<sub>2</sub>L]</b>		365 nm	A549 cells, A375 cells, DMS53, GLC4, MCF7, PC3	168
116	Cyto- toxicity	<b>GS-Sw</b>		530 nm/ 664 nm	HeLa cells, COLO-205 cells, MAEC cells, human blood serum, LLC mouse model	169
117	Immuno- biology	<b>PAC</b>		365 nm/ Vis	LAD2 cells	170
118	Cell adhesion	<b>Compound 1</b>		366 nm/ 450 nm	MC3T3 E1 mouse osteoblast cells	171
119	Cell adhesion	<b>Compound 1</b>		340-380 nm/ 450- 490 nm	NIH 3T3 cells	172

120	Cell adhesion	<b>Photoswitchable glyco-SAM</b>		365 nm/ 450 nm	Type 1-fimbriated <i>E. coli</i> pPKL1162	174
121	Cell adhesion	<b>Compound 5</b>		365 nm/ 488 nm	Type 1-fimbriated <i>E. coli</i> pPKL1162	175
122	Cell communication	<b>Compounds 2-4</b>		365 nm/ Vis	<i>Staphylococcus aureus</i> ATCC1698, <i>E. coli</i> DH5 $\alpha$ , <i>Pseudomonas aeruginosa</i> MDT283/1-6	176
123	Cell adhesion	<b>AzoGlc, AzoXyl, AzoRha, AzoMan, AzoGlcNAc, AzoAra</b>		361 nm/ 450 nm	Type 1-fimbriated <i>E. coli</i> pPKL1162, HMEC-1 Cells	177

## 11 List of Abbreviations

2P	Two Photon
A2A	Adenosine A2A Receptor
AAV	Adeno-Associated Virus
ABC	ATP Binding Cassette
ANP	Atrial Natriuretic Peptide
AP	Action Potential
APC	Antibody Photoswitch Conjugate
ASIC	Acid-Sensing Ion Channel
BP	Bipolar cell
cAMP	Cyclic Adenosine Monophosphate
Ca <sub>v</sub>	Voltage-Gated Calcium Channel
CNS	Central Nervous System
COMET	Chemo-Optical Modulation of Epigenetically Regulated Transcription
DAG	Diacylglycerol
DRG	Dorsal Root Ganglion
ENaC	Epithelial Sodium Channel
GABA	γ-Aminobutyric Acid
GIRK	G Protein-Coupled Inwardly Rectifying Potassium Channel
GPCR	G Protein-Coupled Receptor
HCN Channels	Hyperpolarization-Activated Cyclic Nucleotide-Gated Channels
HDAC	Histone Deacetylase
HMT	Histone Methyltransferase
iGluA	AMPA Receptor
iGluK	Kainate Receptor
iGluN	NMDA Receptor
iGluR	Ionotropic Glutamate Receptor
K <sub>ATP</sub>	ATP-Sensitive Potassium Channel
K <sub>v</sub>	Voltage-Gated Potassium Channel
LiGABAR	Light-Regulated GABA Receptor
LiGluR	Light-Gated Glutamate Receptor
LinAChR	Light-Gated nAChR
LOX	Lipoxygenase

---

mGluR	Metabotropic Glutamate Receptor
nAChR	Nicotinic Acetylcholine Receptor
Na <sub>v</sub>	Voltage-Gated Sodium Channel
NFAT	Nuclear Factor of Activated T Cells
NOS	Nitric Oxide Synthase
NPC	Nanobody Photoswitch Conjugate
P2X	ATP-Gated Purinoreceptor
PACT	Photodynamic Antimicrobial Cancer Therapy
PAL	Photoswitchable Affinity Labelling
PCL	Photochromic Ligand
photoBOLT	Photoswitchable Bioorthogonal Ligand Tethering
PKC	Protein Kinase C
PORTL	Photoswitchable Orthogonal Remotely Tethered Ligand
PTL	Photoswitchable Tethered Ligand
RGC	Retinal Ganglion Cell
SPARK	Synthetic Photoisomerizable Azobenzene-Regulated Potassium Channel
SUR	Sulfonylurea Receptor
TREK1	Mechano-Gated Potassium Channel
TRP	Transient Receptor Potential
UV	Ultraviolet
VGIC	Voltage-Gated Ion Channels
Vis	Visible



## References

- (1) Fenno, L.; Yizhar, O.; Deisseroth, K. The Development and Application of Optogenetics. *Annu. Rev. Neurosci.* **2011**, *34*, 389-412.
- (2) Gautier, A.; Gauron, C.; Volovitch, M.; Bensimon, D.; Jullien, L.; Vríz, S. How to Control Proteins with Light in Living Systems. *Nat. Chem. Biol.* **2014**, *10*, 533-541.
- (3) Linsmeier, I.; Banerjee, S.; Oakes, P. W.; Jung, W.; Kim, T.; Murrell, M. P. Disordered Actomyosin Networks Are Sufficient to Produce Cooperative and Telescopic Contractility. *Nat. Commun.* **2016**, *7*, No. 12615.
- (4) Ellis-Davies, G. C. R. Caged Compounds: Photorelease Technology for Control of Cellular Chemistry and Physiology. *Nat. Methods* **2007**, *4*, 619-628.
- (5) Klán, P.; Šolomek, T.; Bochet, C. G.; Blanc, A.; Givens, R.; Rubina, M.; Popik, V.; Kostikov, A.; Wirz, J. Photoremovable Protecting Groups in Chemistry and Biology: Reaction Mechanisms and Efficacy. *Chem. Rev.* **2013**, *113*, 119-191.
- (6) Young, D. D.; Deiters, A. Photochemical Control of Biological Processes. *Org. Biomol. Chem.* **2007**, *5*, 999-1005.
- (7) J. Farrer, N.; Salassa, L.; J. Sadler, P. Photoactivated Chemotherapy (PACT): The Potential of Excited-State d-Block Metals in Medicine. *Dalton Trans.* **2009**, *0*, 10690-10701.
- (8) Velema, W. A.; Szymanski, W.; Feringa, B. L. Photopharmacology: Beyond Proof of Principle. *J. Am. Chem. Soc.* **2014**, *136*, 2178-2191.
- (9) Lerch, M. M.; Hansen, M. J.; van Dam, G. M.; Szymanski, W.; Feringa, B. L. Emerging Targets in Photopharmacology. *Angew. Chem. Int. Ed.* **2016**, *55*, 10978-10999.
- (10) Beharry, A. A.; Woolley, G. A. Azobenzene Photoswitches for Biomolecules. *Chem. Soc. Rev.* **2011**, *40*, 4422-4437.
- (11) Szymański, W.; Beierle, J. M.; Kistemaker, H. A. V.; Velema, W. A.; Feringa, B. L. Reversible Photocontrol of Biological Systems by the Incorporation of Molecular Photoswitches. *Chem. Rev.* **2013**, *113*, 6114-6178.
- (12) Hermanson, G. T. *Bioconjugate Techniques, Third Edition*, 3 edition.; Academic Press: London; Waltham, MA, 2013.
- (13) Krishnamurthy, V. M.; Semetey, V.; Bracher, P. J.; Shen, N.; Whitesides, G. M. Dependence of Effective Molarity on Linker Length for an Intramolecular Protein-Ligand System. *J. Am. Chem. Soc.* **2007**, *129*, 1312-1320.
- (14) Leippe, P.; Koehler Leman, J.; Trauner, D. Specificity and Speed: Tethered Photopharmacology. *Biochemistry (Mosc.)* **2017**, *56*, 5214-5220.
- (15) Fredrich, S.; Göstl, R.; Herder, M.; Grubert, L.; Hecht, S. Switching Diarylethenes Reliably in Both Directions with Visible Light. *Angew. Chem. Int. Ed.* **2016**, *55*, 1208-1212.
- (16) DeRosa, M. C.; Crutchley, R. J. Photosensitized Singlet Oxygen and Its Applications. *Coord. Chem. Rev.* **2002**, *233-234*, 351-371.
- (17) Bregnhøj, M.; Blázquez-Castro, A.; Westberg, M.; Breitenbach, T.; Ogilby, P. R. Direct 765 Nm Optical Excitation of Molecular Oxygen in Solution and in Single Mammalian Cells. *J. Phys. Chem. B* **2015**, *119*, 5422-5429.
- (18) Frank, J. A.; Yushchenko, D. A.; Fine, N. H. F.; Duca, M.; Citir, M.; Broichhagen, J.; Hodson, D. J.; Schultz, C.; Trauner, D. Optical Control of GPR40 Signalling in Pancreatic  $\beta$ -Cells. *Chem. Sci.* **2017**, *8*, 7604-7610.

- (19) Broichhagen, J.; Schönberger, M.; Cork, S. C.; Frank, J. A.; Marchetti, P.; Bugliani, M.; Shapiro, A. M. J.; Trapp, S.; Rutter, G. A.; Hodson, D. J.; et al. Optical Control of Insulin Release Using a Photoswitchable Sulfonylurea. *Nat. Commun.* **2014**, *5*, No. 5116.
- (20) Falenczyk, C.; Schiedel, M.; Karaman, B.; Rumpf, T.; Kuzmanovic, N.; Grötli, M.; Sippl, W.; Jung, M.; König, B. Chromo-Pharmacophores: Photochromic Diarylmaaleimide Inhibitors for Sirtuins. *Chem. Sci.* **2014**, *5*, 4794-4799.
- (21) Herre, S.; Schadendorf, T.; Ivanov, I.; Herrberger, C.; Steinle, W.; Rück-Braun, K.; Preissner, R.; Kuhn, H. Photoactivation of an Inhibitor of the 12/15-Lipoxygenase Pathway. *ChemBioChem* **2006**, *7*, 1089-1095.
- (22) Bandara, H. M. D.; Burdette, S. C. Photoisomerization in Different Classes of Azobenzene. *Chem. Soc. Rev.* **2012**, *41*, 1809-1825.
- (23) Bortolus, P.; Monti, S. Cis-Trans Photoisomerization of Azobenzene. Solvent and Triplet Donors Effects. *J. Phys. Chem.* **1979**, *83*, 648-652.
- (24) Weston, C. E.; Richardson, R. D.; Haycock, P. J.; White, A. J. P.; Fuchter, M. J. Arylazopyrazoles: Azoheteroarene Photoswitches Offering Quantitative Isomerization and Long Thermal Half-Lives. *J. Am. Chem. Soc.* **2014**, *136*, 11878-11881.
- (25) Knie, C.; Utecht, M.; Zhao, F.; Kulla, H.; Kovalenko, S.; Brouwer, A. M.; Saalfrank, P.; Hecht, S.; Bléger, D. Ortho-Fluoroazobenzenes: Visible Light Switches with Very Long-Lived Z Isomers. *Chem. - Eur. J.* **2014**, *20*, 16492-16501.
- (26) Calbo, J.; Weston, C. E.; White, A. J. P.; Rzepa, H. S.; Contreras-García, J.; Fuchter, M. J. Tuning Azoheteroarene Photoswitch Performance through Heteroaryl Design. *J. Am. Chem. Soc.* **2017**, *139*, 1261-1274.
- (27) Garcia-Amorós, J.; Díaz-Lobo, M.; Nonell, S.; Velasco, D. Fastest Thermal Isomerization of an Azobenzene for Nanosecond Photoswitching Applications under Physiological Conditions. *Angew. Chem. Int. Ed.* **2012**, *51*, 12820-12823.
- (28) Garcia-Amorós, J.; Castro, M. C. R.; Coelho, P.; Raposo, M. M. M.; Velasco, D. Fastest Non-Ionic Azo Dyes and Transfer of Their Thermal Isomerisation Kinetics into Liquid-Crystalline Materials. *Chem. Commun.* **2016**, *52*, 5132-5135.
- (29) Milo, R.; Phillips, R. *Cell Biology by the Numbers*, 1 edition.; Garland Science: New York, NY, 2015.
- (30) Stawski, P.; Sumser, M.; Trauner, D. A Photochromic Agonist of AMPA Receptors. *Angew. Chem. Int. Ed.* **2012**, *51*, 5748-5751.
- (31) Laprell, L.; Hüll, K.; Stawski, P.; Schön, C.; Michalakis, S.; Biel, M.; Sumser, M. P.; Trauner, D. Restoring Light Sensitivity in Blind Retinae Using a Photochromic AMPA Receptor Agonist. *ACS Chem. Neurosci.* **2016**, *7*, 15-20.
- (32) Wolter, T.; Steinbrecher, T.; Trauner, D.; Elstner, M. Ligand Photo-Isomerization Triggers Conformational Changes in iGluR2 Ligand Binding Domain. *PLOS ONE* **2014**, *9*, e92716.
- (33) Barber, D. M.; Liu, S.-A.; Gottschling, K.; Sumser, M.; Hollmann, M.; Trauner, D. Optical Control of AMPA Receptors Using a Photoswitchable Quinoxaline-2,3-Dione Antagonist. *Chem. Sci.* **2016**, *8*, 611-615.
- (34) Volgraf, M.; Gorostiza, P.; Szobota, S.; Helix, M. R.; Isacoff, E. Y.; Trauner, D. Reversibly Caged Glutamate: A Photochromic Agonist of Ionotropic Glutamate Receptors. *J. Am. Chem. Soc.* **2007**, *129*, 260-261.
- (35) Guo, Y.; Wolter, T.; Kubař, T.; Sumser, M.; Trauner, D.; Elstner, M. Molecular Dynamics Investigation of Gluazo, a Photo-Switchable Ligand for the Glutamate Receptor GluK2. *PLOS ONE* **2015**, *10*, e0135399.

- (36) Abrams, Z. R.; Warriar, A.; Trauner, D.; Zhang, X. A Signal Processing Analysis of Purkinje Cells in Vitro. *Front. Neural Circuits* **2010**, *4*, No. 13.
- (37) Volgraf, M.; Gorostiza, P.; Numano, R.; Kramer, R. H.; Isacoff, E. Y.; Trauner, D. Allosteric Control of an Ionotropic Glutamate Receptor with an Optical Switch. *Nat. Chem. Biol.* **2006**, *2*, 47-52.
- (38) Szobota, S.; Gorostiza, P.; Del Bene, F.; Wyart, C.; Fortin, D. L.; Kolstad, K. D.; Tulyathan, O.; Volgraf, M.; Numano, R.; Aaron, H. L.; et al. Remote Control of Neuronal Activity with a Light-Gated Glutamate Receptor. *Neuron* **2007**, *54*, 535-545.
- (39) Gorostiza, P.; Volgraf, M.; Numano, R.; Szobota, S.; Trauner, D.; Isacoff, E. Y. Mechanisms of Photoswitch Conjugation and Light Activation of an Ionotropic Glutamate Receptor. *Proc. Natl. Acad. Sci. U. S. A.* **2007**, *104*, 10865-10870.
- (40) Wang, S.; Szobota, S.; Wang, Y.; Volgraf, M.; Liu, Z.; Sun, C.; Trauner, D.; Isacoff, E. Y.; Zhang, X. All Optical Interface for Parallel, Remote, and Spatiotemporal Control of Neuronal Activity. *Nano Lett.* **2007**, *7*, 3859-3863.
- (41) Numano, R.; Szobota, S.; Lau, A. Y.; Gorostiza, P.; Volgraf, M.; Roux, B.; Trauner, D.; Isacoff, E. Y. Nanosculpting Reversed Wavelength Sensitivity into a Photoswitchable iGluR. *Proc. Natl. Acad. Sci.* **2009**, *106*, 6814-6819.
- (42) Kienzler, M. A.; Reiner, A.; Trautman, E.; Yoo, S.; Trauner, D.; Isacoff, E. Y. A Red-Shifted, Fast-Relaxing Azobenzene Photoswitch for Visible Light Control of an Ionotropic Glutamate Receptor. *J. Am. Chem. Soc.* **2013**, *135*, 17683-17686.
- (43) Rullo, A.; Reiner, A.; Reiter, A.; Trauner, D.; Isacoff, E. Y.; Woolley, G. A. Long Wavelength Optical Control of Glutamate Receptor Ion Channels Using a Tetra-Ortho-Substituted Azobenzene Derivative. *Chem. Commun.* **2014**, *50*, 14613-14615.
- (44) Carroll, E. C.; Berlin, S.; Levitz, J.; Kienzler, M. A.; Yuan, Z.; Madsen, D.; Larsen, D. S.; Isacoff, E. Y. Two-Photon Brightness of Azobenzene Photoswitches Designed for Glutamate Receptor Optogenetics. *Proc. Natl. Acad. Sci.* **2015**, *112*, E776-E785.
- (45) Izquierdo-Serra, M.; Gascón-Moya, M.; Hirtz, J. J.; Pittolo, S.; Poskanzer, K. E.; Ferrer, È.; Alibés, R.; Busqué, F.; Yuste, R.; Hernando, J.; et al. Two-Photon Neuronal and Astrocytic Stimulation with Azobenzene-Based Photoswitches. *J. Am. Chem. Soc.* **2014**, *136*, 8693-8701.
- (46) Reiner, A.; Isacoff, E. Y. Tethered Ligands Reveal Glutamate Receptor Desensitization Depends on Subunit Occupancy. *Nat. Chem. Biol.* **2014**, *10*, 273-280.
- (47) Wyart, C.; Bene, F. D.; Warp, E.; Scott, E. K.; Trauner, D.; Baier, H.; Isacoff, E. Y. Optogenetic Dissection of a Behavioural Module in the Vertebrate Spinal Cord. *Nature* **2009**, *461*, 407-410.
- (48) Izquierdo-Serra, M.; Trauner, D.; Llobet, A.; Gorostiza, P. Optical Control of Calcium-Regulated Exocytosis. *Biochim. Biophys. Acta BBA - Gen. Subj.* **2013**, *1830*, 2853-2860.
- (49) Izquierdo-Serra, M.; Trauner, D.; Llobet, A.; Gorostiza, P. Optical Modulation of Neurotransmission Using Calcium Photocurrents through the Ion Channel LiGluR. *Front. Mol. Neurosci.* **2013**, *6*, No. 3.
- (50) Li, D.; Héroult, K.; Isacoff, E. Y.; Oheim, M.; Ropert, N. Optogenetic Activation of LiGluR-Expressing Astrocytes Evokes Anion Channel-Mediated Glutamate Release. *J. Physiol.* **2012**, *590*, 855-873.
- (51) Caporale, N.; Kolstad, K. D.; Lee, T.; Tochitsky, I.; Dalkara, D.; Trauner, D.; Kramer, R.; Dan, Y.; Isacoff, E. Y.; Flannery, J. G. LiGluR Restores Visual Responses in Rodent Models of Inherited Blindness. *Mol. Ther.* **2011**, *19*, 1212-1219.

- (52) Gaub, B. M.; Berry, M. H.; Holt, A. E.; Reiner, A.; Kienzler, M. A.; Dolgova, N.; Nikonov, S.; Aguirre, G. D.; Beltran, W. A.; Flannery, J. G.; et al. Restoration of Visual Function by Expression of a Light-Gated Mammalian Ion Channel in Retinal Ganglion Cells or ON-Bipolar Cells. *Proc. Natl. Acad. Sci.* **2014**, *111*, E5574-E5583.
- (53) Fontaine, S. D.; Reid, R.; Robinson, L.; Ashley, G. W.; Santi, D. V. Long-Term Stabilization of Maleimide-Thiol Conjugates. *Bioconjug. Chem.* **2015**, *26*, 145-152.
- (54) Izquierdo-Serra, M.; Bautista-Barrufet, A.; Trapero, A.; Garrido-Charles, A.; Díaz-Tahoces, A.; Camarero, N.; Pittolo, S.; Valbuena, S.; Pérez-Jiménez, A.; Gay, M.; et al. Optical Control of Endogenous Receptors and Cellular Excitability Using Targeted Covalent Photoswitches. *Nat. Commun.* **2016**, *7*, No. 12221.
- (55) Fortin, D. L.; Banghart, M. R.; Dunn, T. W.; Borges, K.; Wagenaar, D. A.; Gaudry, Q.; Karakossian, M. H.; Otis, T. S.; Kristan, W. B.; Trauner, D.; et al. Photochemical Control of Endogenous Ion Channels and Cellular Excitability. *Nat. Methods* **2008**, *5*, 331-338.
- (56) Harvey, J. H.; Trauner, D. Regulating Enzymatic Activity with a Photoswitchable Affinity Label. *ChemBioChem* **2008**, *9*, 191-193.
- (57) Levitz, J.; Popescu, A. T.; Reiner, A.; Isacoff, E. Y. A Toolkit for Orthogonal and in Vivo Optical Manipulation of Ionotropic Glutamate Receptors. *Front. Mol. Neurosci.* **2016**, *9*, No. 2.
- (58) Janovjak, H.; Szobota, S.; Wyart, C.; Trauner, D.; Isacoff, E. Y. A Light-Gated, Potassium-Selective Glutamate Receptor for the Optical Inhibition of Neuronal Firing. *Nat. Neurosci.* **2010**, *13*, 1027-1032.
- (59) Banghart, M.; Borges, K.; Isacoff, E.; Trauner, D.; Kramer, R. H. Light-Activated Ion Channels for Remote Control of Neuronal Firing. *Nat. Neurosci.* **2004**, *7*, 1381-1386.
- (60) Chambers, J. J.; Banghart, M. R.; Trauner, D.; Kramer, R. H. Light-Induced Depolarization of Neurons Using a Modified Shaker K<sup>+</sup> Channel and a Molecular Photoswitch. *J. Neurophysiol.* **2006**, *96*, 2792-2796.
- (61) Mclsaac, R. S.; Bedbrook, C. N.; Arnold, F. H. Recent Advances in Engineering Microbial Rhodopsins for Optogenetics. *Curr. Opin. Struct. Biol.* **2015**, *33*, 8-15.
- (62) Laprell, L.; Repak, E.; Franckevicius, V.; Hartrampf, F.; Terhag, J.; Hollmann, M.; Sumser, M.; Rebola, N.; DiGregorio, D. A.; Trauner, D. Optical Control of NMDA Receptors with a Diffusible Photoswitch. *Nat. Commun.* **2015**, *6*, No. 8076.
- (63) Hartrampf, F. W. W.; Barber, D. M.; Gottschling, K.; Leippe, P.; Hollmann, M.; Trauner, D. Development of a Photoswitchable Antagonist of NMDA Receptors. *Tetrahedron* **2017**, *73*, 4905-4912.
- (64) Berlin, S.; Szobota, S.; Reiner, A.; Carroll, E. C.; Kienzler, M. A.; Guyon, A.; Xiao, T.; Trauner, D.; Isacoff, E. Y. A Family of Photoswitchable NMDA Receptors. *eLife* **2016**, *5*, e12040.
- (65) Klippenstein, V.; Hoppmann, C.; Ye, S.; Wang, L.; Paoletti, P. Optocontrol of Glutamate Receptor Activity by Single Side-Chain Photoisomerization. *eLife* **2017**, *6*, e25808.
- (66) Deal, W. J.; Erlanger, B. F.; Nachmansohn, D. Photoregulation of Biological Activity by Photochromic Reagents, III. Photoregulation of Bioelectricity by Acetylcholine Receptor Inhibitors. *Proc. Natl. Acad. Sci.* **1969**, *64*, 1230-1234.
- (67) Bartels, E.; Wassermann, N. H.; Erlanger, B. F. Photochromic Activators of the Acetylcholine Receptor. *Proc. Natl. Acad. Sci.* **1971**, *68*, 1820-1823.

- (68) Lester, H. A.; Won Chang, H. Response of Acetylcholine Receptors to Rapid Photochemically Produced Increases in Agonist Concentration. *Nature* **1977**, *266*, 373-374.
- (69) Nass, M. M.; Lester, H. A.; Krouse, M. E. Response of Acetylcholine Receptors to Photoisomerizations of Bound Agonist Molecules. *Biophys. J.* **1978**, *24*, 135-160.
- (70) Lester, H. A.; Krouse, M. E.; Nass, M. M.; Wassermann, N. H.; Erlanger, B. F. A Covalently Bound Photoisomerizable Agonist: Comparison with Reversibly Bound Agonists at Electrophorus Electroplaques. *J. Gen. Physiol.* **1980**, *75*, 207-232.
- (71) Lester, H. A.; Krouse, M. E.; Nass, M. M.; Wassermann, N. H.; Erlanger, B. F. Light-Activated Drug Confirms a Mechanism of Ion Channel Blockade. *Nature* **1979**, *280*, 509-510.
- (72) Lester, H. A.; Nass, M. M.; Krouse, M. E.; Nerbonne, J. M.; Wassermann, N. H.; Erlanger, B. F. Electrophysiological Experiments With Photoisomerizable Cholinergic Compounds: Review and Progress Report \*. *Ann. N. Y. Acad. Sci.* **1980**, *346*, 475-490.
- (73) Krouse, M. E.; Lester, H. A.; Wassermann, N. H.; Erlanger, B. F. Rates and Equilibria for a Photoisomerizable Antagonist at the Acetylcholine Receptor of Electrophorus Electroplaques. *J. Gen. Physiol.* **1985**, *86*, 235-256.
- (74) Damijonaitis, A.; Broichhagen, J.; Urushima, T.; Hüll, K.; Nagpal, J.; Laprell, L.; Schonberger, M.; Woodmansee, D. H.; Rafiq, A.; Sumser, M. P.; et al. AzoCholine Enables Optical Control of Alpha 7 Nicotinic Acetylcholine Receptors in Neural Networks. *ACS Chem. Neurosci.* **2015**, *6*, 701-707.
- (75) Xu, Z.; Shi, L.; Jiang, D.; Cheng, J.; Shao, X.; Li, Z. Azobenzene Modified Imidacloprid Derivatives as Photoswitchable Insecticides: Steering Molecular Activity in a Controllable Manner. *Sci. Rep.* **2015**, *5*, No. 13962.
- (76) Tochitsky, I.; Banghart, M. R.; Mourot, A.; Yao, J. Z.; Gaub, B.; Kramer, R. H.; Trauner, D. Optochemical Control of Genetically Engineered Neuronal Nicotinic Acetylcholine Receptors. *Nat. Chem.* **2012**, *4*, 105-111.
- (77) Stein, M.; Middendorp, S. J.; Carta, V.; Pejo, E.; Raines, D. E.; Forman, S. A.; Sigel, E.; Trauner, D. Azo-Propofols: Photochromic Potentiators of GABAA Receptors. *Angew. Chem. Int. Ed.* **2012**, *51*, 10500-10504.
- (78) Yue, L.; Pawlowski, M.; Dellal, S. S.; Xie, A.; Feng, F.; Otis, T. S.; Bruzik, K. S.; Qian, H.; Pepperberg, D. R. Robust Photoregulation of GABAA Receptors by Allosteric Modulation with a Propofol Analogue. *Nat. Commun.* **2012**, *3*, No. 1095.
- (79) Lin, W.-C.; Davenport, C. M.; Mourot, A.; Vytila, D.; Smith, C. M.; Medeiros, K. A.; Chambers, J. J.; Kramer, R. H. Engineering a Light-Regulated GABAA Receptor for Optical Control of Neural Inhibition. *ACS Chem. Biol.* **2014**, *9*, 1414-1419.
- (80) Lin, W.-C.; Tsai, M.-C.; Davenport, C. M.; Smith, C. M.; Veit, J.; Wilson, N. M.; Adesnik, H.; Kramer, R. H. A Comprehensive Optogenetic Pharmacology Toolkit for In Vivo Control of GABAA Receptors and Synaptic Inhibition. *Neuron* **2015**, *88*, 879-891.
- (81) Sandoz, G.; Levitz, J.; Kramer, R. H.; Isacoff, E. Y. Optical Control of Endogenous Proteins with a Photoswitchable Conditional Subunit Reveals a Role for TREK1 in GABAB Signaling. *Neuron* **2012**, *74*, 1005-1014.
- (82) Banghart, M. R.; Mourot, A.; Fortin, D. L.; Yao, J. Z.; Kramer, R. H.; Trauner, D. Photochromic Blockers of Voltage-Gated Potassium Channels. *Angew. Chem. Int. Ed.* **2009**, *48*, 9097-9101.
- (83) Polosukhina, A.; Litt, J.; Tochitsky, I.; Nemargut, J.; Sychev, Y.; De Kouchkovsky, I.; Huang, T.; Borges, K.; Trauner, D.; Van Gelder, R. N.; et al. Photochemical Restoration of Visual Responses in Blind Mice. *Neuron* **2012**, *75*, 271-282.

- (84) Mouroto, A.; Kienzler, M. A.; Banghart, M. R.; Fehrentz, T.; Huber, F. M. E.; Stein, M.; Kramer, R. H.; Trauner, D. Tuning Photochromic Ion Channel Blockers. *ACS Chem. Neurosci.* **2011**, *2*, 536–543.
- (85) Tochitsky, I.; Polosukhina, A.; Degtyar, V. E.; Gallerani, N.; Smith, C. M.; Friedman, A.; Van Gelder, R. N.; Trauner, D.; Kaufer, D.; Kramer, R. H. Restoring Visual Function to Blind Mice with a Photoswitch That Exploits Electrophysiological Remodeling of Retinal Ganglion Cells. *Neuron* **2014**, *81*, 800–813.
- (86) Tochitsky, I.; Helft, Z.; Meseguer, V.; Fletcher, R. B.; Vessey, K. A.; Telias, M.; Denlinger, B.; Malis, J.; Fletcher, E. L.; Kramer, R. H. How Azobenzene Photoswitches Restore Visual Responses to the Blind Retina. *Neuron* **2016**, *92*, 100–113.
- (87) Tochitsky, I.; Trautman, J.; Gallerani, N.; Malis, J. G.; Kramer, R. H. Restoring Visual Function to the Blind Retina with a Potent, Safe and Long-Lasting Photoswitch. *Sci. Rep.* **2017**, *7*, No. 45487.
- (88) Mouroto, A.; Fehrentz, T.; Le Feuvre, Y.; Smith, C. M.; Herold, C.; Dalkara, D.; Nagy, F.; Trauner, D.; Kramer, R. H. Rapid Optical Control of Nociception with an Ion-Channel Photoswitch. *Nat. Methods* **2012**, *9*, 396–402.
- (89) Fehrentz, T.; Kuttruff, C. A.; Huber, F. M. E.; Kienzler, M. A.; Mayer, P.; Trauner, D. Exploring the Pharmacology and Action Spectra of Photochromic Open-Channel Blockers. *ChemBioChem* **2012**, *13*, 1746–1749.
- (90) Mouroto, A.; Herold, C.; Kienzler, M. A.; Kramer, R. H. Understanding and Improving Photo-control of Ion Channels in Nociceptors with Azobenzene Photo-switches. *Br. J. Pharmacol.* **2017**, DOI: 10.1111/bph.13923.
- (91) Groynom, R.; Shoffstall, E.; Wu, L. S.; Kramer, R. H.; Lavik, E. B. Controlled Release of Photoswitch Drugs by Degradable Polymer Microspheres. *J. Drug Target.* **2015**, *23*, 710–715.
- (92) Magome, N.; Kanaporis, G.; Moisan, N.; Tanaka, K.; Agladze, K. Photo-Control of Excitation Waves in Cardiomyocyte Tissue Culture. *Tissue Eng. Part A* **2011**, *17*, 2703–2711.
- (93) Frolova, S. R.; Gaiko, O.; Tselaya, V. A.; Pimenov, O. Y.; Agladze, K. I. Photocontrol of Voltage-Gated Ion Channel Activity by Azobenzene Trimethylammonium Bromide in Neonatal Rat Cardiomyocytes. *PLOS ONE* **2016**, *11*, e0152018.
- (94) Laprell, L.; Tochitsky, I.; Kaur, K.; Manookin, M. B.; Stein, M.; Barber, D. M.; Schön, C.; Michalakis, S.; Biel, M.; Kramer, R. H.; et al. Photopharmacological Control of Bipolar Cells Restores Visual Function in Blind Mice. *J. Clin. Invest.* **2017**, *127*, 2598–2611.
- (95) Schoenberger, M.; Damijonaitis, A.; Zhang, Z.; Nagel, D.; Trauner, D. Development of a New Photochromic Ion Channel Blocker via Azologization of Fomocaine. *ACS Chem. Neurosci.* **2014**, *5*, 514–518.
- (96) Broichhagen, J.; Frank, J. A.; Trauner, D. A Roadmap to Success in Photopharmacology. *Acc. Chem. Res.* **2015**, *48*, 1947–1960.
- (97) Rennhack, A.; Grahn, E.; Kaupp, U. B.; Berger, T. K. Photocontrol of the Hv1 Proton Channel. *ACS Chem. Biol.* **2017**, *12*, 2952–2957.
- (98) Stein, M.; Breit, A.; Fehrentz, T.; Gudermann, T.; Trauner, D. Optical Control of TRPV1 Channels. *Angew. Chem. Int. Ed.* **2013**, *52*, 9845–9848.
- (99) Frank, J. A.; Moroni, M.; Moshourab, R.; Sumser, M.; Lewin, G. R.; Trauner, D. Photoswitchable Fatty Acids Enable Optical Control of TRPV1. *Nat. Commun.* **2015**, *6*, No. 7118.

- (100) Kokel, D.; Cheung, C. Y. J.; Mills, R.; Coutinho-Budd, J.; Huang, L.; Setola, V.; Sprague, J.; Jin, S.; Jin, Y. N.; Huang, X.-P.; et al. Photochemical Activation of TRPA1 Channels in Neurons and Animals. *Nat. Chem. Biol.* **2013**, *9*, 257-263.
- (101) Lam, P.-Y.; Mendu, S. K.; Mills, R. W.; Zheng, B.; Padilla, H.; Milan, D. J.; Desai, B. N.; Peterson, R. T. A High-Conductance Chemo-Optogenetic System Based on the Vertebrate Channel Trpa1b. *Sci. Rep.* **2017**, *7*, No. 11839.
- (102) Leinders-Zufall, T.; Storch, U.; Bleyemehl, K.; Schnitzler, M. M. y; Frank, J. A.; Konrad, D. B.; Trauner, D.; Gudermann, T.; Zufall, F. PhoDAGs Enable Optical Control of Diacylglycerol-Sensitive Transient Receptor Potential Channels. *Cell Chem. Biol.* **2018**, *25*, 215-223.e3.
- (103) Lichtenegger, M.; Tiapko, O.; Svobodova, B.; Stockner, T.; Glasnov, T. N.; Schreibmayer, W.; Platzer, D.; Cruz, G. G.; Krenn, S.; Schober, R.; et al. An Optically Controlled Probe Identifies Lipid-Gating Fenestrations within the TRPC3 Channel. *Nat. Chem. Biol.* **2018**, *14*, 396-404.
- (104) Broichhagen, J.; Frank, J. A.; Johnston, N. R.; Mitchell, R. K.; Šmid, K.; Marchetti, P.; Bugliani, M.; Rutter, G. A.; Trauner, D.; Hodson, D. J. A Red-Shifted Photochromic Sulfonylurea for the Remote Control of Pancreatic Beta Cell Function. *Chem. Commun.* **2015**, *51*, 6018-6021.
- (105) Johnston, N. R.; Mitchell, R. K.; Haythorne, E.; Pessoa, M. P.; Semplici, F.; Ferrer, J.; Piemonti, L.; Marchetti, P.; Bugliani, M.; Bosco, D.; et al. Beta Cell Hubs Dictate Pancreatic Islet Responses to Glucose. *Cell Metab.* **2016**, *24*, 389-401.
- (106) Mehta, Z. B.; Johnston, N. R.; Nguyen-Tu, M.-S.; Broichhagen, J.; Schultz, P.; Lerner, D. P.; Leclerc, I.; Trauner, D.; Rutter, G. A.; Hodson, D. J. Remote Control of Glucose Homeostasis in Vivo Using Photopharmacology. *Sci. Rep.* **2017**, *7*, 291.
- (107) Tian, X.; Zhang, C.; Xu, Q.; Li, Z.; Shao, X. Azobenzene-Benzoylphenylureas as Photoswitchable Chitin Synthesis Inhibitors. *Org. Biomol. Chem.* **2017**, *15*, 3320-3323.
- (108) Barber, D. M.; Schönberger, M.; Burgstaller, J.; Levitz, J.; Weaver, C. D.; Isacoff, E. Y.; Baier, H.; Trauner, D. Optical Control of Neuronal Activity Using a Light-Operated GIRK Channel Opener (LOGO). *Chem. Sci.* **2016**, *7*, 2347-2352.
- (109) Trads, J. B.; Burgstaller, J.; Laprell, L.; Konrad, D. B.; Rosa, L. de la O. de la; Weaver, C. D.; Baier, H.; Trauner, D.; Barber, D. M. Optical Control of GIRK Channels Using Visible Light. *Org. Biomol. Chem.* **2016**, *15*, 76-81.
- (110) Schönberger, M.; Althaus, M.; Fronius, M.; Clauss, W.; Trauner, D. Controlling Epithelial Sodium Channels with Light Using Photoswitchable Amilorides. *Nat. Chem.* **2014**, *6*, 712-719.
- (111) Lemoine, D.; Habermacher, C.; Martz, A.; Méry, P.-F.; Bouquier, N.; Diverchy, F.; Taly, A.; Rassendren, F.; Specht, A.; Grutter, T. Optical Control of an Ion Channel Gate. *Proc. Natl. Acad. Sci.* **2013**, *110*, 20813-20818.
- (112) Browne, L. E.; Nunes, J. P. M.; Sim, J. A.; Chudasama, V.; Bragg, L.; Caddick, S.; North, R. A. Optical Control of Trimeric P2X Receptors and Acid-Sensing Ion Channels. *Proc. Natl. Acad. Sci.* **2014**, *111*, 521-526.
- (113) Habermacher, C.; Martz, A.; Calimet, N.; Lemoine, D.; Peverini, L.; Specht, A.; Cecchini, M.; Grutter, T. Photo-Switchable Tweezers Illuminate Pore-Opening Motions of an ATP-Gated P2X Ion Channel. *eLife* **2016**, *5*, e11050.
- (114) Quandt, G.; Höfner, G.; Pabel, J.; Dine, J.; Eder, M.; Wanner, K. T. First Photoswitchable Neurotransmitter Transporter Inhibitor: Light-Induced Control of  $\gamma$ -

- Aminobutyric Acid Transporter 1 (GAT1) Activity in Mouse Brain. *J. Med. Chem.* **2014**, *57*, 6809–6821.
- (115) Cheng, B.; Shchepakin, D.; Kavanaugh, M. P.; Trauner, D. Photoswitchable Inhibitor of a Glutamate Transporter. *ACS Chem. Neurosci.* **2017**, *8*, 1668–1672.
- (116) Nargeot, J.; Lester, H. A.; Birdsall, N. J. M.; Stockton, J.; Wassermann, N. H.; Erlanger, B. F. A Photoisomerizable Muscarinic Antagonist. Studies of Binding and of Conductance Relaxations in Frog Heart. *J. Gen. Physiol.* **1982**, *79*, 657–678.
- (117) Chabala, L. D.; Gurney, A. M.; Lester, H. A. Dose-Response of Acetylcholine Receptor Channels Opened by a Flash-Activated Agonist in Voltage-Clamped Rat Myoballs. *J. Physiol.* **1986**, *371*, 407–433.
- (118) Chabala, L. D.; Lester, H. A. Activation of Acetylcholine Receptor Channels by Covalently Bound Agonists in Cultured Rat Myoballs. *J. Physiol.* **1986**, *379*, 83.
- (119) Agnetta Luca; Kauk Michael; Canizal Maria Consuelo Alonso; Messerer Regina; Holzgrabe Ulrike; Hoffmann Carsten; Decker Michael. A Photoswitchable Dualsteric Ligand Controlling Receptor Efficacy. *Angew. Chem. Int. Ed.* **2017**, *56*, 7282–7287.
- (120) Schonberger, M.; Trauner, D. A Photochromic Agonist for Mu-Opioid Receptors. *Angew. Chem. Int. Ed.* **2014**, *53*, 3264–3267.
- (121) Donthamsetti, P. C.; Winter, N.; Schönberger, M.; Levitz, J.; Stanley, C.; Javitch, J. A.; Isacoff, E. Y.; Trauner, D. Optical Control of Dopamine Receptors Using a Photoswitchable Tethered Inverse Agonist. *J. Am. Chem. Soc.* **2017**, *139*, 18522–18535.
- (122) Lachmann, D.; Studte, C.; Männel, B.; Hübner, H.; Gmeiner, P.; König, B. Photochromic Dopamine Receptor Ligands Based on Dithienylethenes and Fulgides. *Chem. – Eur. J.* **2017**, *23*, 13423–13434.
- (123) Hauwert, N. J.; Mocking, T. A. M.; Da Costa Pereira, D.; Kooistra, A. J.; Wijnen, L. M.; Vreeker, G. C. M.; Verweij, E. W. E.; De Boer, A. H.; Smit, M. J.; De Graaf, C.; et al. Synthesis and Characterization of a Bidirectional Photoswitchable Antagonist Toolbox for Real-Time GPCR Photopharmacology. *J. Am. Chem. Soc.* **2018**, *140*, 4232–4243.
- (124) Bahamonde, M. I.; Taura, J.; Paoletta, S.; Gakh, A. A.; Chakraborty, S.; Hernando, J.; Fernández-Dueñas, V.; Jacobson, K. A.; Gorostiza, P.; Ciruela, F. Photomodulation of G Protein-Coupled Adenosine Receptors by a Novel Light-Switchable Ligand. *Bioconjug. Chem.* **2014**, *25*, 1847–1854.
- (125) Westphal, M. V.; Schafroth, M. A.; Sarott, R. C.; Imhof, M. A.; Bold, C. P.; Leippe, P.; Dhopeswarkar, A.; Grandner, J. M.; Katritch, V.; Mackie, K.; et al. Synthesis of Photoswitchable  $\Delta^9$ -Tetrahydrocannabinol Derivatives Enables Optical Control of Cannabinoid Receptor 1 Signaling. *J. Am. Chem. Soc.* **2017**, *139*, 18206–18212.
- (126) Broichhagen, J.; Podewin, T.; Meyer-Berg, H.; von Ohlen, Y.; Johnston, N. R.; Jones, B. J.; Bloom, S. R.; Rutter, G. A.; Hoffmann-Röder, A.; Hodson, D. J.; et al. Optical Control of Insulin Secretion Using an Incretin Switch. *Angew. Chem. Int. Ed.* **2015**, *54*, 15565–15569.
- (127) Broichhagen, J.; Johnston, N. R.; von Ohlen, Y.; Meyer-Berg, H.; Jones, B. J.; Bloom, S. R.; Rutter, G. A.; Trauner, D.; Hodson, D. J. Allosteric Optical Control of a Class B G-Protein-Coupled Receptor. *Angew. Chem. Int. Ed.* **2016**, *55*, 5865–5868.
- (128) Levitz, J.; Pantoja, C.; Gaub, B.; Janovjak, H.; Reiner, A.; Hoagland, A.; Schoppik, D.; Kane, B.; Stawski, P.; Schier, A. F.; et al. Optical Control of Metabotropic Glutamate Receptors. *Nat. Neurosci.* **2013**, *16*, 507–516.
- (129) Pittolo, S.; Gómez-Santacana, X.; Eckelt, K.; Rovira, X.; Dalton, J.; Goudet, C.; Pin, J.-P.; Llobet, A.; Giraldo, J.; Llebaria, A.; et al. An Allosteric Modulator to Control



- Endogenous G Protein-Coupled Receptors with Light. *Nat. Chem. Biol.* **2014**, *10*, 813-815.
- (130) Rovira, X.; Trapero, A.; Pittolo, S.; Zussy, C.; Faucherre, A.; Jopling, C.; Giraldo, J.; Pin, J.-P.; Gorostiza, P.; Goudet, C.; et al. OptoGluNAM4.1, a Photoswitchable Allosteric Antagonist for Real-Time Control of MGlu4 Receptor Activity. *Cell Chem. Biol.* **2016**, *23*, 929-934.
- (131) Gómez-Santacana, X.; Pittolo, S.; Rovira, X.; Lopez, M.; Zussy, C.; Dalton, J. A. R.; Faucherre, A.; Jopling, C.; Pin, J.-P.; Ciruela, F.; et al. Illuminating Phenylazopyridines To Photoswitch Metabotropic Glutamate Receptors: From the Flask to the Animals. *ACS Cent. Sci.* **2017**, *3*, 81-91.
- (132) Broichhagen, J.; Damijonaitis, A.; Levitz, J.; Sokol, K. R.; Leippe, P.; Konrad, D.; Isacoff, E. Y.; Trauner, D. Orthogonal Optical Control of a G Protein-Coupled Receptor with a SNAP-Tethered Photochromic Ligand. *ACS Cent. Sci.* **2015**, *1*, 383-393.
- (133) Levitz, J.; Broichhagen, J.; Leippe, P.; Konrad, D.; Trauner, D.; Isacoff, E. Y. Dual Optical Control and Mechanistic Insights into Photoswitchable Group II and III Metabotropic Glutamate Receptors. *Proc. Natl. Acad. Sci.* **2017**, *114*, E3546-E3554.
- (134) Berry, M. H.; Holt, A.; Levitz, J.; Broichhagen, J.; Gaub, B. M.; Visel, M.; Stanley, C.; Aghi, K.; Kim, Y. J.; Cao, K.; et al. Restoration of Patterned Vision with an Engineered Photoactivatable G Protein-Coupled Receptor. *Nat. Commun.* **2017**, *8*, 1862.
- (135) Farrants, H.; Ruiz, A. A.; Gutzeit, V. A.; Trauner, D.; Johnsson, K.; Levitz, J.; Broichhagen, J. SNAP-Tagged Nanobodies Enable Reversible Optical Control of a G Protein-Coupled Receptor via a Remotely Tethered Photoswitchable Ligand. *bioRxiv* **2018**, 266247.
- (136) Wainberg, M. A.; Erlanger, B. F. Investigation of the Active Center of Trypsin Using Photochromic Substrates. *Biochemistry (Mosc.)* **1971**, *10*, 3816-3819.
- (137) Bieth, J.; Vratsanos, S. M.; Wassermann, N.; Erlanger, B. F. Photoregulation of Biological Activity by Photochromic Reagents, II. Inhibitors of Acetylcholine Esterase\*. *Proc. Natl. Acad. Sci. U. S. A.* **1969**, *64*, 1103-1106.
- (138) Tsai, Y.-H.; Essig, S.; James, J. R.; Lang, K.; Chin, J. W. Selective, Rapid and Optically Switchable Regulation of Protein Function in Live Mammalian Cells. *Nat. Chem.* **2015**, *7*, 554-561.
- (139) Ferreira, R.; Nilsson, J. R.; Solano, C.; Andréasson, J.; Grøtli, M. Design, Synthesis and Inhibitory Activity of Photoswitchable RET Kinase Inhibitors. *Sci. Rep.* **2015**, *5*, No. 9769.
- (140) Frank, J. A.; Yushchenko, D. A.; Hodson, D. J.; Lipstein, N.; Nagpal, J.; Rutter, G. A.; Rhee, J.-S.; Gottschalk, A.; Brose, N.; Schultz, C.; et al. Photoswitchable Diacylglycerols Enable Optical Control of Protein Kinase C. *Nat. Chem. Biol.* **2016**, *12*, 755-762.
- (141) Zhang, Y.; Erdmann, F.; Fischer, G. Augmented Photoswitching Modulates Immune Signaling. *Nat. Chem. Biol.* **2009**, *5*, 724-726.
- (142) Kim, Y.; Phillips, J. A.; Liu, H.; Kang, H.; Tan, W. Using Photons to Manipulate Enzyme Inhibition by an Azobenzene-Modified Nucleic Acid Probe. *Proc. Natl. Acad. Sci.* **2009**, *106*, 6489-6494.
- (143) Hansen, M. J.; Velema, W. A.; de Bruin, G.; Overkleeft, H. S.; Szymanski, W.; Feringa, B. L. Proteasome Inhibitors with Photocontrolled Activity. *ChemBioChem* **2014**, *15*, 2053-2057.

- (144) Blanco, B.; Palasis, K. A.; Adwal, A.; Callen, D. F.; Abell, A. D. Azobenzene-Containing Photoswitchable Proteasome Inhibitors with Selective Activity and Cellular Toxicity. *Bioorg. Med. Chem.* **2017**, *25*, 5050-5054.
- (145) Reis, S. A.; Ghosh, B.; Hendricks, J. A.; Szantai-Kis, D. M.; Törk, L.; Ross, K. N.; Lamb, J.; Read-Button, W.; Zheng, B.; Wang, H.; et al. Light-Controlled Modulation of Gene Expression by Chemical Optoepigenetic Probes. *Nat. Chem. Biol.* **2016**, *12*, 317-323.
- (146) Szymanski, W.; Ourailidou, M. E.; Velema, W. A.; Dekker, F. J.; Feringa, B. L. Light-Controlled Histone Deacetylase (HDAC) Inhibitors: Towards Photopharmacological Chemotherapy. *Chem. - Eur. J.* **2015**, *21*, 16517-16524.
- (147) Albert, L.; Xu, J.; Wan, R.; Srinivasan, V.; Dou, Y.; Vázquez, O. Controlled Inhibition of Methyltransferases Using Photoswitchable Peptidomimetics: Towards an Epigenetic Regulation of Leukemia. *Chem. Sci.* **2017**, *8*, 4612-4618.
- (148) Broichhagen, J.; Jurastow, I.; Iwan, K.; Kummer, W.; Trauner, D. Optical Control of Acetylcholinesterase with a Tacrine Switch. *Angew. Chem. Int. Ed.* **2014**, *53*, 7657-7660.
- (149) Zhang, F.; Timm, K. A.; Arndt, K. M.; Woolley, G. A. Photocontrol of Coiled-Coil Proteins in Living Cells. *Angew. Chem. Int. Ed.* **2010**, *49*, 3943-3946.
- (150) Velema, W. A.; van der Berg, J. P.; Hansen, M. J.; Szymanski, W.; Driessen, A. J. M.; Feringa, B. L. Optical Control of Antibacterial Activity. *Nat. Chem.* **2013**, *5*, 924-928.
- (151) Velema, W. A.; Hansen, M. J.; Lerch, M. M.; Driessen, A. J. M.; Szymanski, W.; Feringa, B. L. Ciprofloxacin-Photoswitch Conjugates: A Facile Strategy for Photopharmacology. *Bioconjug. Chem.* **2015**, *26*, 2592-2597.
- (152) Wegener, M.; Hansen, M. J.; Driessen, A. J. M.; Szymanski, W.; Feringa, B. L. Photocontrol of Antibacterial Activity: Shifting from UV to Red Light Activation. *J. Am. Chem. Soc.* **2017**, *139*, 17979-17986.
- (153) Hoppmann, C.; Schmieder, P.; Domaing, P.; Vogelreiter, G.; Eichhorst, J.; Wiesner, B.; Morano, I.; Rück-Braun, K.; Beyermann, M. Photocontrol of Contracting Muscle Fibers. *Angew. Chem. Int. Ed.* **2011**, *50*, 7699-7702.
- (154) Podewin, T.; Broichhagen, J.; Frost, C.; Groneberg, D.; Ast, J.; Meyer-Berg, H.; Fine, N. H. F.; Friebe, A.; Zacharias, M.; Hodson, D. J.; et al. Optical Control of a Receptor-Linked Guanylyl Cyclase Using a Photoswitchable Peptidic Hormone. *Chem. Sci.* **2017**, *8*, 4644-4653.
- (155) Borowiak, M.; Nahaboo, W.; Reynders, M.; Nekolla, K.; Jalinot, P.; Hasserodt, J.; Rehberg, M.; Delattre, M.; Zahler, S.; Vollmar, A.; et al. Photoswitchable Inhibitors of Microtubule Dynamics Optically Control Mitosis and Cell Death. *Cell* **2015**, *162*, 403-411.
- (156) Eguchi, K.; Taoufiq, Z.; Thorn-Seshold, O.; Trauner, D.; Hasegawa, M.; Takahashi, T. Wild-Type Monomeric  $\alpha$ -Synuclein Can Impair Vesicle Endocytosis and Synaptic Fidelity via Tubulin Polymerization at the Calyx of Held. *J. Neurosci.* **2017**, *37*, 6043-6052.
- (157) Zenker, J.; White, M. D.; Templin, R. M.; Parton, R. G.; Thorn-Seshold, O.; Bissiere, S.; Plachta, N. A Microtubule-Organizing Center Directing Intracellular Transport in the Early Mouse Embryo. *Science* **2017**, *357*, 925-928.
- (158) Chen, C.; Zhao, J.; Gao, M.; Meng, X.; Fan, A.; Wang, Z.; Zhao, Y. Photo-Triggered Micelles: Simultaneous Activation and Release of Microtubule Inhibitors for on-Demand Chemotherapy. *Biomater. Sci.* **2018**, *6*, 511-518.

- (159) Engdahl, A. J.; Torres, E. A.; Lock, S. E.; Engdahl, T. B.; Mertz, P. S.; Streu, C. N. Synthesis, Characterization, and Bioactivity of the Photoisomerizable Tubulin Polymerization Inhibitor Azo-Combretastatin A4. *Org. Lett.* **2015**, *17*, 4546–4549.
- (160) E. Sheldon, J.; Michael Dcona, M.; E. Lyons, C.; C. Hackett, J.; T. Hartman, M. C. Photoswitchable Anticancer Activity via Trans – Cis Isomerization of a Combretastatin A-4 Analog. *Org. Biomol. Chem.* **2016**, *14*, 40–49.
- (161) Rastogi, S. K.; Zhao, Z.; Barrett, S. L.; Shelton, S. D.; Zafferani, M.; Anderson, H. E.; Blumenthal, M. O.; Jones, L. R.; Wang, L.; Li, X.; et al. Photoresponsive Azo-Combretastatin A-4 Analogues. *Eur. J. Med. Chem.* **2018**, *143*, 1–7.
- (162) Prestel, A.; Möller, H. M. Spatio-Temporal Control of Cellular Uptake Achieved by Photoswitchable Cell-Penetrating Peptides. *Chem. Commun.* **2015**, *52*, 701–704.
- (163) Nevola, L.; Martín-Quirós, A.; Eckelt, K.; Camarero, N.; Tosi, S.; Llobet, A.; Giralt, E.; Gorostiza, P. Light-Regulated Stapled Peptides to Inhibit Protein-Protein Interactions Involved in Clathrin-Mediated Endocytosis. *Angew. Chem. Int. Ed.* **2013**, *52*, 7704–7708.
- (164) Li, Y.; Yang, J.; Sun, L.; Wang, W.; Liu, W. UV Light-Triggered Unpacking of DNA to Enhance Gene Transfection of Azobenzene-Containing Polycations. *J. Mater. Chem. B* **2014**, *2*, 3868–3878.
- (165) Ogasawara, S. Control of Cellular Function by Reversible Photoregulation of Translation. *Chembiochem Eur. J. Chem. Biol.* **2014**, *15*, 2652–2655.
- (166) Ogasawara, S. Duration Control of Protein Expression in Vivo by Light-Mediated Reversible Activation of Translation. *ACS Chem. Biol.* **2017**, *12*, 351–356.
- (167) Hammill, M. L.; Isaacs-Trépanier, C.; Desaulniers, J.-P. SiRNAzOs: A New Class of Azobenzene-Containing SiRNAs That Can Photochemically Regulate Gene Expression. *ChemistrySelect* **2017**, *2*, 9810–9814.
- (168) Presa, A.; Brissos, R. F.; Caballero, A. B.; Borilovic, I.; Korrodi-Gregório, L.; Pérez-Tomás, R.; Roubeau, O.; Gamez, P. Photoswitching the Cytotoxic Properties of Platinum(II) Compounds. *Angew. Chem. Int. Ed.* **2015**, *54*, 4561–4565.
- (169) Babii, O.; Afonin, S.; Garmanchuk, L. V.; Nikulina, V. V.; Nikolaienko, T. V.; Storozhuk, O. V.; Shelest, D. V.; Dasyukevich, O. I.; Ostapchenko, L. I.; Iurchenko, V.; et al. Direct Photocontrol of Peptidomimetics: An Alternative to Oxygen-Dependent Photodynamic Cancer Therapy. *Angew. Chem.* **2016**, *128*, 5583–5586.
- (170) Velema, W. A.; van der Toorn, M.; Szymanski, W.; Feringa, B. L. Design, Synthesis, and Inhibitory Activity of Potent, Photoswitchable Mast Cell Activation Inhibitors. *J. Med. Chem.* **2013**, *56*, 4456–4464.
- (171) Auernheimer, J.; Dahmen, C.; Hersel, U.; Bausch, A.; Kessler, H. Photoswitched Cell Adhesion on Surfaces with RGD Peptides. *J. Am. Chem. Soc.* **2005**, *127*, 16107–16110.
- (172) Liu, D.; Xie, Y.; Shao, H.; Jiang, X. Using Azobenzene-Embedded Self-Assembled Monolayers To Photochemically Control Cell Adhesion Reversibly. *Angew. Chem. Int. Ed.* **2009**, *48*, 4406–4408.
- (173) Chandrasekaran, V.; Kolbe, K.; Beiroth, F.; Lindhorst, T. K. Synthesis and Testing of the First Azobenzene Mannobioside as Photoswitchable Ligand for the Bacterial Lectin FimH. *Beilstein J. Org. Chem.* **2013**, *9*, 223–233.
- (174) Weber, T.; Chandrasekaran, V.; Stamer, I.; Thygesen, M. B.; Terfort, A.; Lindhorst, T. K. Switching of Bacterial Adhesion to a Glycosylated Surface by Reversible Reorientation of the Carbohydrate Ligand. *Angew. Chem. Int. Ed.* **2014**, *53*, 14583–14586.

- (175) Möckl, L.; Müller, A.; Bräuchle, C.; Lindhorst, T. K. Switching First Contact: Photocontrol of *E. coli* Adhesion to Human Cells. *Chem. Commun.* **2016**, *52*, 1254–1257.
- (176) Berg, J. P. V. der; A. Velema, W.; Szymanski, W.; M. Driessen, A. J.; L. Feringa, B. Controlling the Activity of Quorum Sensing Autoinducers with Light. *Chem. Sci.* **2015**, *6*, 3593–3598.
- (177) Hu, Y.; Zou, W.; Julita, V.; Ramanathan, R.; F. Tabor, R.; Nixon-Luke, R.; Bryant, G.; Bansal, V.; L. Wilkinson, B. Photomodulation of Bacterial Growth and Biofilm Formation Using Carbohydrate-Based Surfactants. *Chem. Sci.* **2016**, *7*, 6628–6634.
- (178) Holme, N. C. R.; Ramanujam, P. S.; Hvilsted, S. 10,000 Optical Write, Read, and Erase Cycles in an Azobenzene Sidechain Liquid-Crystalline Polyester. *Opt. Lett.* **1996**, *21*, 902–904.
- (179) Shishido, A.; Kanazawa, A.; Shiono, T.; Ikeda, T.; Tamai, N. Enhancement of Stability in Optical Switching of Photosensitive Liquid Crystal by Means of Reflection Mode Analysis. *J. Mater. Chem.* **1999**, *9*, 2211–2213.
- (180) Butenandt, A. Neuere Beiträge Der Biologischen Chemie Zum Krebsproblem. *Angew. Chem.* **1940**, *53*, 345–352.
- (181) Hartmann, F. 55. Tagung der Deutschen Gesellschaft für Innere Medizin. *Naturwissenschaften* **1949**, *36*, 245–249.
- (182) Brock, T. E.; Fred, E. B.; Domagk, G. A Contribution to the Chemotherapy of Bacterial Infections. *Rev. Infect. Dis.* **1986**, *8*, 163–166.
- (183) Beharry, A. A.; Wong, L.; Tropepe, V.; Woolley, G. A. Fluorescence Imaging of Azobenzene Photoswitching In Vivo. *Angew. Chem. Int. Ed.* **2011**, *50*, 1325–1327.
- (184) Samanta, S.; Beharry, A. A.; Sadowski, O.; McCormick, T. M.; Babalhavaeji, A.; Tropepe, V.; Woolley, G. A. Photoswitching Azo Compounds in Vivo with Red Light. *J. Am. Chem. Soc.* **2013**, *135*, 9777–9784.
- (185) Hammerich, M.; Schütt, C.; Stähler, C.; Lentjes, P.; Röhricht, F.; Höppner, R.; Herges, R. Heterodiazocines: Synthesis and Photochromic Properties, Trans to Cis Switching within the Bio-Optical Window. *J. Am. Chem. Soc.* **2016**, *138*, 13111–13114.
- (186) Konrad, D. B.; Frank, J. A.; Trauner, D. Synthesis of Redshifted Azobenzene Photoswitches by Late-Stage Functionalization. *Chem. – Eur. J.* **2016**, *22*, 4364–4368.
- (187) Lundgren, R. J.; Stradiotto, M. Palladium-Catalyzed Cross-Coupling of Aryl Chlorides and Tosylates with Hydrazine. *Angew. Chem. Int. Ed.* **2010**, *49*, 8686–8690.
- (188) Hansen, M. J.; Lerch, M. M.; Szymanski, W.; Feringa, B. L. Direct and Versatile Synthesis of Red-Shifted Azobenzenes. *Angew. Chem. Int. Ed.* **2016**, *55*, 13514–13518.
- (189) Bléger, D.; Hecht, S. Visible-Light-Activated Molecular Switches. *Angew. Chem. Int. Ed.* **2015**, *54*, 11338–11349.
- (190) Samanta, S.; Babalhavaeji, A.; Dong, M.; Woolley, G. A. Photoswitching of Ortho-Substituted Azonium Ions by Red Light in Whole Blood. *Angew. Chem. Int. Ed.* **2013**, *52*, 14127–14130.
- (191) Wang, D.; Wagner, M.; Butt, H.-J.; Wu, S. Supramolecular Hydrogels Constructed by Red-Light-Responsive Host-guest Interactions for Photo-Controlled Protein Release in Deep Tissue. *Soft Matter* **2015**, *11*, 7656–7662.
- (192) Montgomery, K. L.; Yeh, A. J.; Ho, J. S.; Tsao, V.; Mohan Iyer, S.; Grosenick, L.; Ferenczi, E. A.; Tanabe, Y.; Deisseroth, K.; Delp, S. L.; et al. Wirelessly Powered, Fully Internal Optogenetics for Brain, Spinal and Peripheral Circuits in Mice. *Nat. Methods* **2015**, *12*, 969–974.

- (193) Park, S. I.; Brenner, D. S.; Shin, G.; Morgan, C. D.; Copits, B. A.; Chung, H. U.; Pullen, M. Y.; Noh, K. N.; Davidson, S.; Oh, S. J.; et al. Soft, Stretchable, Fully Implantable Miniaturized Optoelectronic Systems for Wireless Optogenetics. *Nat. Biotechnol.* **2015**, *33*, 1280-1286.
- (194) McCall, J. G.; Qazi, R.; Shin, G.; Li, S.; Ikram, M. H.; Jang, K.-I.; Liu, Y.; Al-Hasani, R.; Bruchas, M. R.; Jeong, J.-W.; et al. Preparation and Implementation of Optofluidic Neural Probes for *in Vivo* Wireless Pharmacology and Optogenetics. *Nat. Protoc.* **2017**, *12*, 219-237.
- (195) Canales, A.; Park, S.; Kiliyas, A.; Anikeeva, P. Multifunctional Fibers as Tools for Neuroscience and Neuroengineering. *Acc. Chem. Res.* **2018**, *51*, 829-838.
- (196) Lei, T.; Guan, M.; Liu, J.; Lin, H.-C.; Pfattner, R.; Shaw, L.; McGuire, A. F.; Huang, T.-C.; Shao, L.; Cheng, K.-T.; et al. Biocompatible and Totally Disintegrable Semiconducting Polymer for Ultrathin and Ultralightweight Transient Electronics. *Proc. Natl. Acad. Sci.* **2017**, *114*, 5107-5112.
- (197) Salvatore, G. A.; Sülzle, J.; Dalla Valle, F.; Cantarella, G.; Robotti, F.; Jokic, P.; Knobelspies, S.; Daus, A.; Büthe, L.; Petti, L.; et al. Biodegradable and Highly Deformable Temperature Sensors for the Internet of Things. *Adv. Funct. Mater.* **2017**, *27*, No. 1702390.



## II. Sign Inversion in Photopharmacology Using Diazocine Photoswitches





# Sign Inversion in Photopharmacology: Incorporation of Cyclic Azobenzenes in Photoswitchable Potassium Channel Blockers and Openers.

Julie B. Trads,<sup>[a,b],†</sup> Katharina Hüll,<sup>[a,c],†</sup> Bryan S. Matsuura,<sup>[a,c],†</sup> Laura Laprell,<sup>[a]</sup> Timm Fehrentz,<sup>[d]</sup> Nicole Görldt,<sup>[d]</sup> Krystian A. Kozek,<sup>[e]</sup> C. David Weaver,<sup>[f]</sup> Nikolaj Klöcker,<sup>[d]</sup> David M. Barber<sup>[a]\*</sup> and Dirk Trauner<sup>[c]\*</sup>

<sup>[a]</sup> Department of Chemistry and Center for Integrated Protein Science (CIPSM), Ludwig Maximilian University Munich, Butenandtstr. 5-13, 81377 Munich, Germany

<sup>[b]</sup> Center for DNA Nanotechnology, Department of Chemistry and iNANO, Aarhus University Gustav Wieds Vej 14, 8000 Aarhus C, Denmark

<sup>[c]</sup> Department of Chemistry, New York University, 100 Washington Square East, New York, NY 10003-6699, USA

<sup>[d]</sup> Institute of Neural and Sensory Physiology, Medical Faculty, University of Düsseldorf, Düsseldorf, Germany

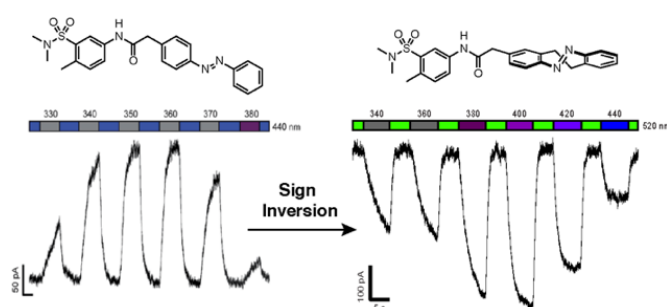
<sup>[e]</sup> Departments of Pharmacology and Chemistry, Institute of Chemical Biology, Vanderbilt University School of Medicine, Nashville, TN, USA

<sup>[f]</sup> Department of Pharmacology, Vanderbilt University School of Medicine, Nashville, TN, USA

<sup>†</sup>these authors contributed equally

Reprinted (adapted) with permission from Trads, J. B. et al. Sign Inversion in Photopharmacology: Incorporation of Cyclic Azobenzenes in Photoswitchable Potassium Channel Blockers and Openers. *Angew. Chem. Int. Ed.* **2019** 58, 15421-15428. Copyright 2019 Wiley-VCH.

## Abstract



Photopharmacology relies on ligands that change their pharmacodynamics upon photoisomerization. Many of these ligands are azobenzenes that are thermodynamically more stable in their elongated *trans*-configuration. Often, they are biologically active in this form and lose activity upon irradiation and photoisomerization to their *cis*-isomer. Recently, cyclic azobenzenes, so-called diazocines, have emerged, which are thermodynamically more stable in their bent *cis*-form. Incorporation of these switches into a variety of photopharmaceuticals

could convert dark-active ligands into dark-inactive ligands, which is preferred in most biological applications. This “pharmacological sign-inversion” is demonstrated for a photochromic blocker of voltage-gated potassium channels, termed CAL, and a photochromic opener of G protein-coupled inwardly rectifying potassium (GIRK) channels, termed CLOGO.

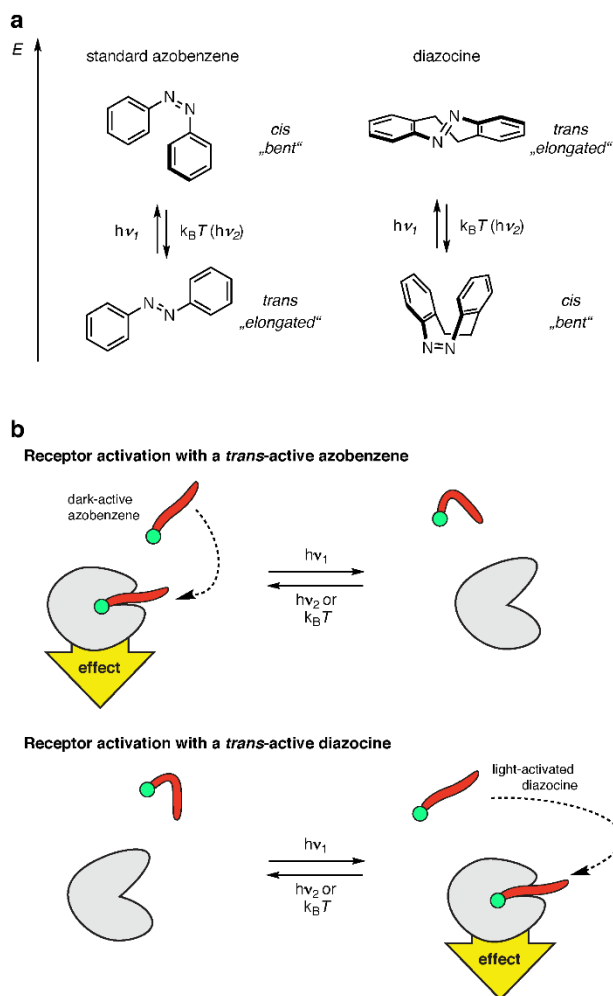
## Introduction

Photopharmacology endeavors to bestow light sensitivity to a multitude of biological targets using synthetic photoswitches.<sup>[1-5]</sup> Its scope has been demonstrated with a vast array of biological targets ranging from enzymes<sup>[6-9]</sup> to elements of the cytoskeleton,<sup>[10]</sup> voltage- and ligand-gated ion channels,<sup>[11-16]</sup> G protein-coupled receptors (GPCRs),<sup>[17-20]</sup> and transporters.<sup>[21-23]</sup> Amongst other photoswitchable molecules, azobenzenes have emerged as the photoswitch of choice due to a variety of reasons, including fast photoswitching, good photostationary states, lack of phototoxicity, a large change in dipole moment and steric bulk upon switching, compatibility with physiological conditions, fatigue-resistance, tunability, and the relative ease of their chemical synthesis.<sup>[1]</sup> Several research groups have developed a number of ingenious ways to red-shift the photoswitching of azobenzenes and modulate their thermal bistability and conformational preferences.<sup>[24,25]</sup>

Standard azobenzenes are thermodynamically more stable in their elongated *trans*-form and can be isomerized to their bent *cis*-form with light (Fig. 1). Depending on their electronic nature and substitution pattern, they can thermally isomerize back to their *trans*-form in a tunable fashion, with thermal half-lives ranging from nanoseconds to days under physiological conditions. Although several azobenzene photoswitches have been reported to be biologically active in their thermodynamically less stable *cis*-form,<sup>[10,26-28]</sup> the majority are more active in the dark, i.e. as their thermodynamically more stable *trans*-isomers. This is, in part, because their parent compounds tend to bind in elongated or stretched conformations, as demonstrated by a recent computational analysis of drug-like molecules that are suitable to azologization.<sup>[29]</sup>

Cyclic azobenzene photoswitches, also known as diazocines, wherein the diazene unit is embedded in an eight-membered ring, have been known for many years but were only recently photophysically and conformationally characterized by Temps and Herges.<sup>[30-34]</sup> In contrast to standard azobenzenes, their bent *cis*-isomer is thermodynamically more stable and predominates in the dark, while exposure to light in the violet or deep blue range of the visible light spectrum promotes the formation of the thermodynamically less stable, elongated *trans*-isomer. We postulated that the stable *cis*-isomer of the diazocine could effectively mimic the *cis*-isomer of a standard azobenzene, whereas the elongated *trans*-diazocine would sterically resemble the *trans*-isomer of a standard azobenzene. Similar to

azobenzenes, diazocines undergo a large change in dipole moment upon isomerization.<sup>[35]</sup> These features could allow for an inversion of the intrinsic dark-activity of a photoswitch (Fig. 1). Furthermore, diazocines photoisomerize in both directions with visible light, therefore circumventing the need to use potentially harmful UV light.



**Figure 1. The logic of standard azobenzenes and diazocines.** a: Conventional azobenzenes are thermodynamically more stable in their elongated *trans*-forms whereas diazocines are more stable in their bent, *cis*-forms. Both can be switched back and forth with a combination of irradiation and thermal relaxation. The wavelengths needed for photoisomerization and the kinetics of thermal relaxation can be tuned. b: Schematic depiction how the exchange of a dark-active azobenzene for a dark-inactive diazocine influences the induction of a biological effect.

In 2008, we introduced photoswitchable azobenzene blockers to control the function of voltage-gated ion channels with light.<sup>[11]</sup> These compounds, which were derived from lidocaine and its permanently charged congener QX-314, have been

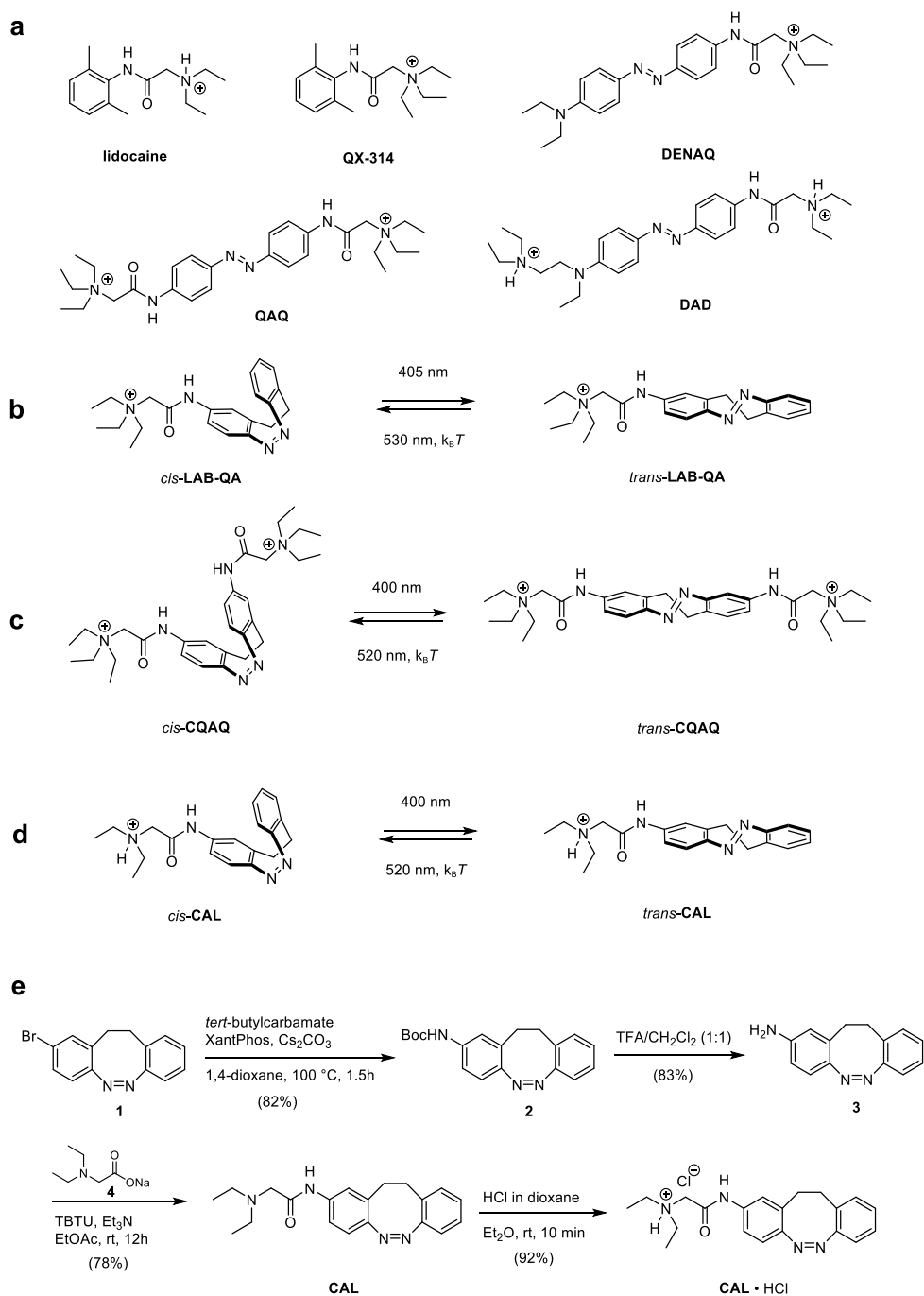
continuously refined and have been used in a broad effort to restore vision with photopharmacology<sup>[38-41]</sup> (Fig. 2). Representative examples include the permanently charged blocker DENAQ,<sup>[13,39,40]</sup> the bis-quaternary ammonium ion QAQ,<sup>[12,42,43]</sup> and the red-shifted lidocaine derivative DAD.<sup>[41]</sup> Ion channel blockers of this type have also been employed in a program that aims to control nociception with light.<sup>[43]</sup> With one exception, these azobenzenes were more active blockers in their elongated *trans*-form, i.e. in the dark-adapted form.<sup>[12]</sup> This elongated *trans* isomer appears to be a better fit for the binding site of use-dependent ion channel blockers in the inner cavity of voltage-gated ion channels than the bent *cis*-form. Incorporation of a diazocine should overcome the issue of dark-activity and provide compounds that are inactive in their dark-adapted form.<sup>[44]</sup> While this manuscript was in preparation, Ellis-Davies introduced a version of DENAQ that incorporates a diazocine as a photoswitch.<sup>[36]</sup> This compound, termed LAB-QA (Fig. 2b) was designed to be inactive or less active in the dark, where the bent *cis*-form predominates, and becomes an active blocker upon isomerization to the elongated *trans*-form. We now present similar photoswitchable blockers of voltage-gated potassium channels and extend the concept of sign inversion in photopharmacology to openers of inwardly rectifying potassium channels.

## Results and Discussion

Substituting standard azobenzenes with diazocines, we designed CQAQ, a Cyclic version of QAQ, as well as CAL, a Cyclic Azobenzene version of Lidocaine (Fig. 2c,d). CQAQ is permanently charged and presumably requires the presence of additional import channels, such as P2X or TPV1-channels, to reach its binding site, whereas CAL can exist as a charged ammonium ion or in a neutral form that enables it to cross biological barriers and partition effectively into membranes. The synthesis of CQAQ was achieved in one step from the known diazocine dianiline<sup>[45]</sup> and the respective carboxylic acid **12** through a peptide coupling with TBTU in DMF (Fig. S1). HPLC purification yielded the molecule as a formate salt.

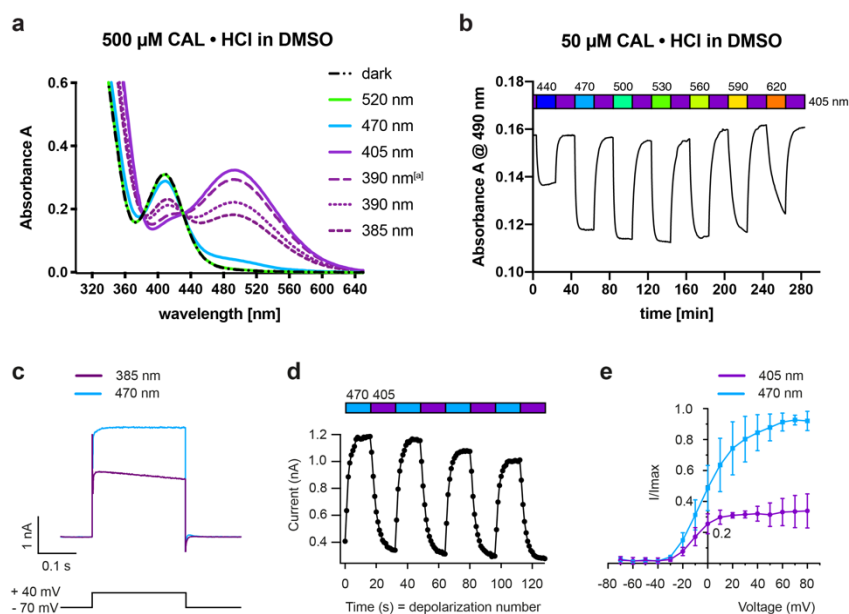
The synthesis of CAL started from the known bromodiazocine **1** and is shown in Fig. 2e. It involved a high-yielding Buchwald-Hartwig cross-coupling of **1** with *tert*-butylcarbamate, followed by deprotection, peptide coupling with diethyl sodium glycinate (**4**) and formation of the quaternary ammonium salt. To enhance solubility, CAL was prepared as a hydrochloride salt (CAL·HCl).

Given the importance of lidocaine as an antiarrhythmic agent and local analgesic and the pharmacokinetic intricacies of CQAQ, we decided to focus our photophysical and biological investigations on CAL. In the dark, under ambient light conditions, and under 520 nm light, CAL exists almost exclusively in its *cis*-form (> 98%), as determined by UV-Vis spectroscopy and NMR spectroscopy (Fig. 3a,b; Fig. S2). Upon irradiation with 385 – 405 nm light, we were able to enrich the *trans*-isomer (Fig. 3a). At 390 nm, using a high-power LED, we observed a PSS



**Figure 2. Previously synthesized photoswitchable open-channel blockers and design strategy.** a) Structure of lidocaine, QX-314, photoswitchable  $K_v$  blockers DENAQ, QAQ and DAD. b) Structure and photoisomerization of LAB-QA. c) Structure and photoisomerization of CQAQ. d) Structure and photoisomerization of CAL. e) Synthesis of CAL·HCl.

of 41:59 = *cis:trans* in buffered, aqueous solution as determined by NMR spectroscopy (Fig. S2a). Upon illumination with 470 - 560 nm light CAL could be quickly reverted into the thermodynamically more stable *cis*-form (Fig. 3b).

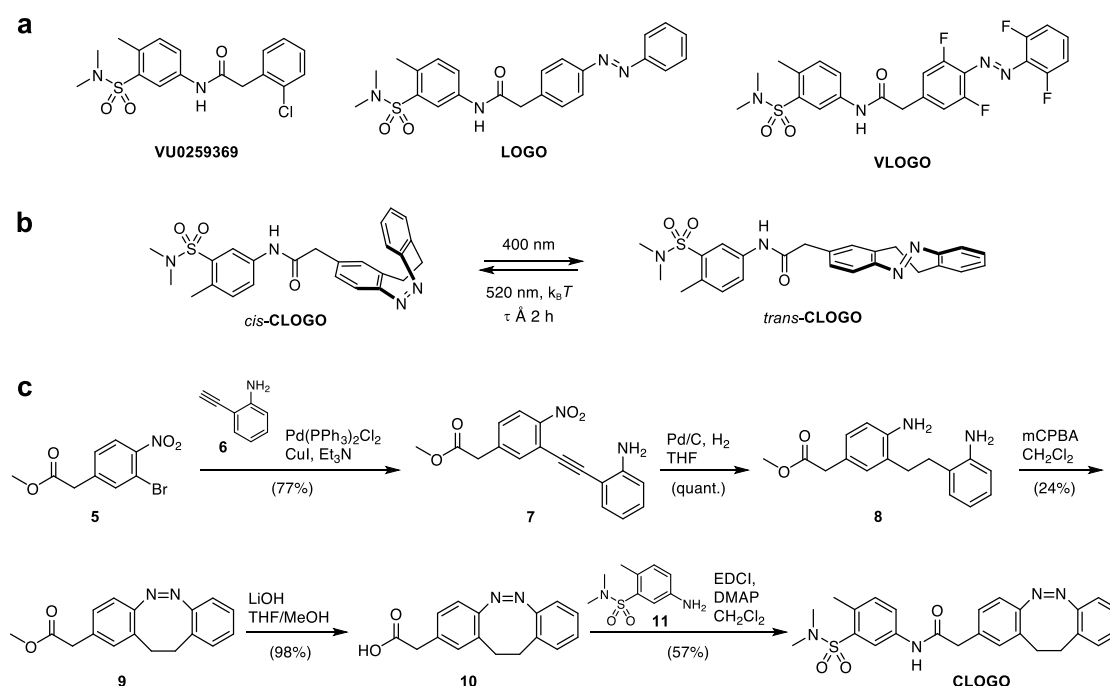


**Figure 3. Photophysical characterization and electrophysiological characterization of CAL.**

a) Photophysical characterization of 500  $\mu\text{M}$  CAL in DMSO solution. The absorption spectra after illumination with 385 nm, 390 nm, 405 nm, 470 nm, and 520 nm light. b) CAL can be isomerized from *trans* to *cis* with a wide range of wavelengths. c) Reversible optical control of Shaker  $\text{K}^+$  channel currents with CAL. Representative current traces in the presence of CAL (500  $\mu\text{M}$ ) at 385 nm and 470 nm illumination, respectively, are shown. Outward  $\text{K}^+$  currents were elicited by depolarizing cells from  $-70$  mV to  $+40$  mV at 1 Hz for time intervals of 250 ms. The last triggered current responses after 16 depolarizations at respective illuminations are shown. d)  $\text{K}^+$  currents under 405 nm and 470 nm illumination demonstrating reversible optical control. e) I-V relationship of Shaker  $\text{K}^+$  channel under 405 nm and 470 nm illumination.  $\text{K}^+$  currents were elicited by stepping from  $-70$  mV to  $+80$  mV, in 10 mV intervals, at 1 Hz for 250 ms. <sup>[a]</sup> Illumination with a high-intensity LED (Prizmatix).

Next, we investigated the effect of CAL on inactivation-removed Shaker  $\text{K}^+$  channel<sup>[46]</sup> heterologously expressed in HEK293T cells using patch-clamp recordings in the voltage-clamp mode. For technical reasons, we employed 385 nm and 405 nm light to enrich the *trans*-form and 470 nm light to revert to the thermodynamically more stable *cis*-form. Under 385 nm illumination, where there is a substantial concentration of the elongated *trans*-isomer (ca. 50%), we observed robust channel block by CAL (500  $\mu\text{M}$ ). This block was greatly diminished under

470 nm illumination, where the switch is exclusively in the bent *cis*-form (Fig. 3c). The photoswitch index of CAL was determined to be  $40.4 \pm 4.9\%$  ( $n = 4$  cells at 470 nm and 405 nm light; see SI).<sup>[38]</sup> The block was reversible with light, as demonstrated in Fig. 3d. Optical control of the current-voltage (IV) relationships is shown in Fig. 3e ( $n = 3$  cells). Thus, CAL shows robust photoswitching of Shaker K<sup>+</sup> channel currents with the opposite sign of previous use-dependent photoswitchable blockers, such as DENAQ and DAD.



**Figure 4. Design and synthesis of the GIRK channel agonist CLOGO.** a) Chemical structures of the GIRK channel agonists VU0259369<sup>[50]</sup> and the photoswitchable GIRK channel openers LOGO and VLOGO b) Isomerization of CLOGO upon illumination. Thermal half-life in the dark was determined at 37°C in 50% DMSO/PBS. c) Synthesis of CLOGO using a Sonogashira/reduction/cyclization strategy.

Having successfully demonstrated the concept of sign-inversion with one of our photoswitchable ion channel blockers, we turned our attention to photochromic channel openers. In recent years, we have developed a series of photoswitchable openers of G protein-coupled inwardly rectifying potassium channels (GIRK channels). GIRK channels are attractive biological targets since they play key roles in neuronal silencing and are involved in a wide range of complex biological processes, including nociception, cognition and cardiac output. Moreover, they are associated with numerous neurological and cardiovascular (patho-)physiological conditions.<sup>[47,48]</sup> We envisioned that our previous photoswitchable GIRK-activator,

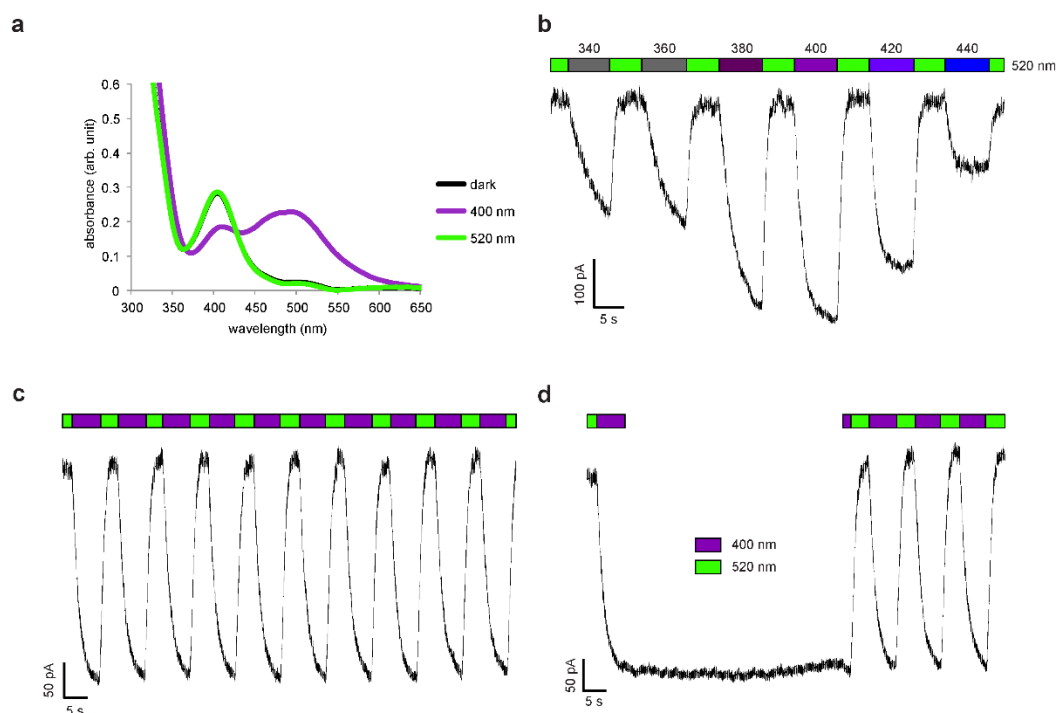
termed LOGO<sup>[49,50]</sup> (Fig. 4a), would be a suitable candidate for sign inversion, because it behaves as a potent agonist in the dark (*trans*-isomer), whilst the *cis*-isomer is significantly less active. The same was true for a red-shifted tetrafluoro-derivative that operated with visible light and was named VLOGO<sup>[51]</sup> (Fig. 4a). Substitution of the regular azobenzene or tetrafluoro azobenzene in these compounds with a diazocine afforded the Cyclic azobenzene Light Operated GIRK channel Opener (CLOGO), the structure and basic switching behavior of which is shown in Fig. 4b.

The synthesis of CLOGO is shown in Fig. 4c. Various syntheses of cyclic azobenzenes have been reported.<sup>[52]</sup> However, these methods are often hampered by poor yields and many of them only afford cyclic azobenzenes bearing symmetrical substitution patterns. We therefore envisaged that a Sonogashira/reduction/cyclization strategy could be a viable route to afford key diazocine acid **10**, with a subsequent amide coupling with aniline **11** affording our desired product (Fig. 4c). Sonogashira cross-coupling of nitro bromide **5** with aniline **6** efficiently provided nitro alkyne **7** in 77% yield. Subsequent reduction in the presence of palladium on carbon followed by cyclization using *m*CPBA afforded diazocine **9** in acceptable yield. Hydrolysis of the methyl ester then provided the acid **10** and an amide coupling with aniline **11** yielded CLOGO.

With CLOGO in hand, we evaluated its potential as a photochromic agonist of GIRK channels. We determined its optimal photoswitching wavelengths to be violet (400 nm, *trans*-isomer) and green light (520 nm, *cis*-isomer) using UV-Vis spectroscopy (Fig. 5a). We then applied this information to our electrophysiological experiments conducted in HEK293T cells heterologously expressing recombinant GIRK1/2 channels. Gratifyingly, we found that at high external potassium concentrations and a membrane potential of -60 mV, CLOGO is an excellent photoswitchable agonist of GIRK1/2 channels, whilst exhibiting the desired reversal in intrinsic activity.

The *cis*-isomer (dark-state or green light) proved to be a significantly less active GIRK channel agonist than the *trans*-isomer (violet light). By changing the wavelength of illumination between green light (520 nm) and different wavelengths of UV, violet and blue light (340 - 440 nm, Fig. 5b), we were able to confirm that switching between 400 nm and 520 nm provided the largest change in observed current (Fig. S4). We next established that photoactivation of CLOGO (10  $\mu$ M) is highly reversible and robust, with nearly no loss of photocurrent over several switching cycles (Fig. 5c). Similar results were also obtained when operating in current clamp mode (Fig. S5). We then examined the stability of *trans*-CLOGO in the dark in a biological system (Fig. 5d). After illumination at 400 nm light, the cell treated with CLOGO was exposed to darkness, which kept the channel open. Deactivation of GIRK channels could then be achieved using green light (520 nm). These results demonstrate that constant illumination of CLOGO is not required to maintain the maximum *trans*-isomer content.



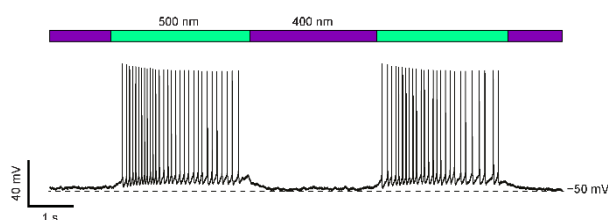


**Figure 5. UV-Vis spectroscopy and whole-cell patch clamp electrophysiology characterization of CLOGO.** a) UV-Vis absorption spectrum of CLOGO (500  $\mu\text{M}$  in DMSO) in the dark and after illumination with violet (400 nm) and green light (520 nm). b) Action spectrum of CLOGO (10  $\mu\text{M}$ ) showing the accurate control of currents in HEK293T cells, heterologously expressing recombinant GIRK1/2 channels, by switching the irradiation wavelength between 520 nm and 340 – 440 nm. c) Highly reproducible photoswitching of CLOGO (10  $\mu\text{M}$ ) recorded in voltage-clamp mode. d) The *trans*-isomer of CLOGO was shown to be relatively stable on the second timescale when there was no light stimulus. Traces representative of  $n = 5$  cells.

Having shown that the cyclic azobenzene photoswitch in the molecule CLOGO can effectively alter the intrinsic agonist activity when compared to the photoswitch LOGO, we next wanted to quantify the efficacy of the *cis*- and *trans*-isomers of CLOGO against a saturating concentration of the non-photoswitchable GIRK channel agonist VU0259369 (Fig. S6) using patch clamp electrophysiology. To accomplish this, we first washed in a known concentration of CLOGO and converted it to its *cis*- and *trans*-isomers. We then washed in VU0259369 (30  $\mu\text{M}$ ) and compared the inward current observed to the inward current obtained for each of the *cis*- and *trans*-isomers of CLOGO. The data show that *cis*-CLOGO (10  $\mu\text{M}$ ) exhibited 23% of VU0259369 (30  $\mu\text{M}$ ) activation on GIRK1/2 channels. This is significantly different from the 65% activation exhibited by *trans*-CLOGO (10  $\mu\text{M}$ ). Increasing the concentration of CLOGO (30  $\mu\text{M}$ ) led to an increase of GIRK channel opening as was the case for *cis*-CLOGO (34%). In comparison, the *trans*-isomer

exhibited no significant increase in GIRK channel opening (68%), showing that at saturating *trans*-CLOGO concentration had almost been attained when using 10  $\mu\text{M}$ .

To evaluate the potency, efficacy and selectivity of CLOGO between different GIRK channel subunit combinations, CLOGO was evaluated using the fluorescence-based thallium influx assay as previously described.<sup>[49,51]</sup> When various concentrations of CLOGO were tested on the predominantly neuronal GIRK subunit combination, GIRK1 + GIRK2, the predominantly cardiac subunit combination GIRK1 + GIRK4 and homomeric GIRK2 we found the compound to be completely inactive on homomeric GIRK2 channels while CLOGO activated GIRK1 + GIRK2 channels with a potency of 6.7 (6.0 – 7.4 95% CI)  $\mu\text{M}$  and GIRK1 + GIRK2 channels with a potency of 7.1  $\mu\text{M}$  (5.8 – 8.7 95% CI) (Fig. S7). Further, we observed that CLOGO is a more effective activator of GIRK1 + GIRK2 channels compared to GIRK1 + GIRK4 channels. Our findings are in accordance with the GIRK subunit selectivity profile of the parent molecule VU0259369; the ability to activate GIRK1-containing GIRK channels but not non-GIRK1-containing channels.



**Figure 6. Optical control of action potential firing in CA1 mouse hippocampal neurons after preincubation for 5 - 10 min and subsequent washout of 100  $\mu\text{M}$  CLOGO.** Switching between the *cis*- and *trans*-isomers of CLOGO in current clamp mode enables the optical control of spontaneous action potential firing at depolarizing holding currents. Trace representative of  $n = 5$  neurons.

Finally, we wanted to investigate if CLOGO could be used to control GIRK channels in excitable cells. As shown in Fig. 6, CLOGO silenced spontaneous action potential firing in mouse CA1 hippocampal neurons in its elongated *trans*-state at 400 nm illumination. Firing was, however, reversibly restored by isomerization into bent *cis*-CLOGO by illuminating with blue/green light (500 nm).

## Conclusion

Photopharmacology greatly benefits from the development of new types of photoswitches. Although the improvement of their photophysical properties remains an important aspect, their structure can also have a profound effect on pharmacology. In some cases, the photopharmacological sign of the biological

effect, i.e. active (+) vs. inactive (-), can be “inverted”, as we have demonstrated here with a photoswitchable potassium channel blocker and a photoswitchable potassium channel opener.<sup>[53]</sup>

The substitution of standard azobenzenes with diazocines enabled us to convert a dark-active channel blocker, such as DENAQ or DAD, into one that shows little if any activity in the dark, like CAL. The approach also proved successful for LOGO and VLOGO, two GIRK-channel openers that could be used to control neuronal activity with light but had a functional feature that may have prevented them from being widely adopted: they were active in the dark. We have overcome this drawback with a diazocine version, *viz.* CLOGO, that is inactive in the dark or at 500 nm but can be activated with violet light (400 nm) and used to effectively silence neuronal activity. As such, CAL and CLOGO are complementary tools to optically control neural networks with minimal effect in the absence of light.

The high concentrations needed for CAL and related channel blockers are not a major concern since the dark-adapted form is the pharmacologically inactive one. The active form is generated upon irradiation and its concentration can be fine-tuned with the wavelength of the light used (“color-dosing”). Like all diazocines reported to date, CAL thermally reverts slowly to the *cis*-form, but can be quickly and quantitatively switched back with a longer wavelength (Fig. S3). The photoswitch index of CAL, i.e. the strength of the photoswitching effect, is higher than that of the permanently charged compound LAB-QA. Whereas CAL could be simply added to the extracellular solution, LAB-QA needed to be applied via a patch pipette to be effective.<sup>[36]</sup> We anticipate that thermally bistable diazocines, such as CAL, CQAQ, and LAB-QA will be more useful as switchable analgesics and antiarrhythmics than as use-dependent channel blockers in vision restoration. Compared with red-shifted standard azobenzenes, which have been employed in this context, diazocines have slow relaxation kinetics, which limits their application where fast thermal back-isomerization to the default form is important. Whether the relaxation kinetics can be tuned through substitution of the diazocine remains to be determined. The pharmacokinetics of diazocine blockers, in particular with respect to the duration of their effect, is another point of concern that needs to be investigated in the future. It is likely that lipophilic cations of this type interact with membranes and serum differently than their conventional azobenzene counterparts.

Freely diffusible azobenzene photoswitches that are active in their *trans*-form have been developed for a variety of targets. These include GPCRs, such as the  $\mu$ -opioid receptor,<sup>[17]</sup> the M1 muscarinic receptor,<sup>[54]</sup> the sphingosine phosphate receptor S1PR1,<sup>[55]</sup> and the metabotropic glutamate receptor mGluR5,<sup>[18]</sup> and ion channels, such as GABA<sub>A</sub>,<sup>[56,57]</sup>  $\alpha 7$  nAChR,<sup>[14]</sup> and ionotropic glutamate receptors.<sup>[15,37,58]</sup> Dark active photopharmaceuticals have also been used to optically control transporters, such as GAT1,<sup>[21]</sup> EAAT1-3,<sup>[22,23]</sup> and F1F0-ATPase,<sup>[59]</sup> as well as enzymes.<sup>[60]</sup> Given the success of CAL, LAB-QA, CLOGO, and the glutamate diazocine derivatives

LAB-Glu<sup>[36]</sup> and Glu\_brAzo1/2,<sup>[61]</sup> which target NMDA receptors and kainate receptors, respectively, it seems likely that the photopharmacological sign inversion of trans-active azobenzenes through substitution with diazocines is a generally applicable concept. The incorporation of diazocines into covalently tethered photoswitches (PTLs) is also likely to expand the reach of photopharmacology. In any case, the optimization of biologically active diazocine switches and their systematic incorporation in photopharmaceuticals will require efficient synthetic access to diazocines with various substitution patterns. Efforts in this direction are currently underway in our laboratories and will be reported in due course.

## **Acknowledgements**

J.B.T. thanks the Danish National Research Foundation Center for DNA Nanotechnology (DNRF81) and Aarhus University, Faculty of Science and Technology for financial support. K.H. thanks the Studienstiftung des deutschen Volkes for a PhD scholarship. B.S.M. thanks the Alexander von Humboldt Foundation for a postdoctoral research fellowship. N.K. was supported by the SFB1116, TPA01 (Deutsche Forschungsgemeinschaft). D.M.B. thanks the European Commission for a Marie Skłodowska-Curie Intra-European Fellowship (PIEF-GA-2013-627990). D.T. was supported by the European Research Council (Advanced Grant 268795) and thanks the Centre for Integrated Protein Science Munich (CIPSM). We thank Dr. Martin Sumser for helpful discussions during the preparation of this manuscript and Christopher Arp for programming the MATLAB interface to control the monochromator.

## **Live subject statement**

Animal procedures were in accord with EU and national law and were licensed by the Regierung Oberbayern.

## **Conflict of Interest**

CDW is an owner of WaveFront Biosciences, maker of the thallium-sensitive fluorescent dye, Thallos, and the kinetic imaging plate reader, Panoptic, used in this manuscript. No other authors have any conflicts of interest to declare.

## **Keywords**

diazocines • GIRK channels • photopharmacology • photoswitchable molecules • potassium channels

## References

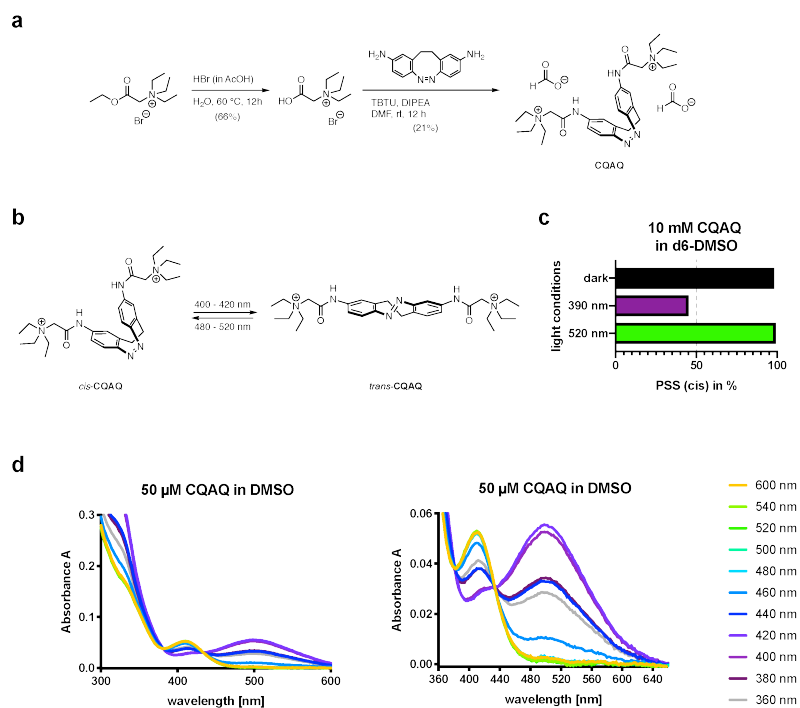
- [1] K. Hüll, J. Morstein, D. Trauner, *Chem. Rev.* **2018**, *118*, 10710–10747.
- [2] T. Fehrentz, M. Schönberger, D. Trauner, *Angew. Chem. Int. Ed.* **2011**, *50*, 12156–12182.
- [3] A. A. Beharry, G. A. Woolley, *Chem. Soc. Rev.* **2011**, *40*, 4422–4437.
- [4] W. Szymański, J. M. Beierle, H. A. V. Kistemaker, W. A. Velema, B. L. Feringa, *Chem. Rev.* **2013**, *113*, 6114–6178.
- [5] M. M. Lerch, M. J. Hansen, G. M. van Dam, W. Szymanski, B. L. Feringa, *Angew. Chem. Int. Ed.* **2016**, *55*, 10978–10999.
- [6] J. Broichhagen, I. Jurastow, K. Iwan, W. Kummer, D. Trauner, *Angew. Chem. Int. Ed.* **2014**, *53*, 7657–7660.
- [7] C. Falencyk, M. Schiedel, B. Karaman, T. Rumpf, N. Kuzmanovic, M. Grøtli, W. Sippl, M. Jung, B. König, *Chem. Sci.* **2014**, *5*, 4794–4799.
- [8] B. Reisinger, N. Kuzmanovic, P. Löffler, R. Merkl, B. König, R. Sterner, *Angew. Chem. Int. Ed.* **2014**, *53*, 595–598.
- [9] X. Chen, S. Wehle, N. Kuzmanovic, B. Merget, U. Holzgrabe, B. König, C. A. Sotriffer, M. Decker, *ACS Chem. Neurosci.* **2014**, *5*, 377–389.
- [10] M. Borowiak, W. Nahaboo, M. Reynders, K. Nekolla, P. Jalinot, J. Hasserodt, M. Rehberg, M. Delattre, S. Zahler, A. Vollmar, et al., *Cell* **2015**, *162*, 403–411.
- [11] D. L. Fortin, M. R. Banghart, T. W. Dunn, K. Borges, D. A. Wagenaar, Q. Gaudry, M. H. Karakossian, T. S. Otis, W. B. Kristan, D. Trauner, et al., *Nat. Methods* **2008**, *5*, 331–338.
- [12] M. R. Banghart, A. Mourot, D. L. Fortin, J. Z. Yao, R. H. Kramer, D. Trauner, *Angew. Chem. Int. Ed.* **2009**, *48*, 9097–9101.
- [13] A. Mourot, M. A. Kienzler, M. R. Banghart, T. Fehrentz, F. M. E. Huber, M. Stein, R. H. Kramer, D. Trauner, *ACS Chem. Neurosci.* **2011**, *2*, 536–543.
- [14] A. Damijonaitis, J. Broichhagen, T. Urushima, K. Hüll, J. Nagpal, L. Laprell, M. Schonberger, D. H. Woodmansee, A. Rafiq, M. P. Sumser, et al., *ACS Chem. Neurosci.* **2015**, *6*, 701–7.
- [15] D. M. Barber, S.-A. Liu, K. Gottschling, M. Sumser, M. Hollmann, D. Trauner, *Chem. Sci.* **2017**, *8*, 611–615.
- [16] F. W. W. Hartrampf, D. M. Barber, K. Gottschling, P. Leippe, M. Hollmann, D. Trauner, *Tetrahedron* **2017**, *73*, 4905–4912.
- [17] M. Schonberger, D. Trauner, *Angew. Chem. Int. Ed.* **2014**, *53*, 3264–7.
- [18] S. Pittolo, X. Gómez-Santacana, K. Eckelt, X. Rovira, J. Dalton, C. Goudet, J.-P. Pin, A. Llobet, J. Giraldo, A. Llebaria, et al., *Nat. Chem. Biol.* **2014**, *10*, 813–815.
- [19] J. A. Frank, D. A. Yushchenko, N. H. F. Fine, M. Duca, M. Citir, J. Broichhagen, D. J. Hodson, C. Schultz, D. Trauner, *Chem. Sci.* **2017**, *8*, 7604–7610.
- [20] J. Broichhagen, N. R. Johnston, Y. von Ohlen, H. Meyer-Berg, B. J. Jones, S. R. Bloom, G. A. Rutter, D. Trauner, D. J. Hodson, *Angew. Chem. Int. Ed.* **2016**, *55*, 5865–5868.
- [21] G. Quandt, G. Höfner, J. Pabel, J. Dine, M. Eder, K. T. Wanner, *J. Med. Chem.* **2014**, *57*, 6809–6821.
- [22] B. Cheng, D. Shchepakina, M. P. Kavanaugh, D. Trauner, *ACS Chem. Neurosci.* **2017**, *8*, 1668–1672.
- [23] M. W. H. Hoorens, H. Fu, R. H. Duurkens, G. Trinco, V. Arkhipova, B. L. Feringa, G. J. Poelarends, D. J. Slotboom, W. Szymanski, *Adv. Ther.* **2018**, *1*, 1800028.

- [24] D. Bléger, J. Schwarz, A. M. Brouwer, S. Hecht, *J. Am. Chem. Soc.* **2012**, *134*, 20597–20600.
- [25] S. Samanta, A. A. Beharry, O. Sadovski, T. M. McCormick, A. Babalhavaeji, V. Tropepe, G. A. Woolley, *J. Am. Chem. Soc.* **2013**, *135*, 9777–9784.
- [26] J. Broichhagen, M. Schönberger, S. C. Cork, J. A. Frank, P. Marchetti, M. Bugliani, A. M. J. Shapiro, S. Trapp, G. A. Rutter, D. J. Hodson, et al., *Nat. Commun.* **2014**, *5*, No. 5116.
- [27] L. Laprell, E. Repak, V. Franckevicius, F. Hartrampf, J. Terhag, M. Hollmann, M. Sumser, N. Rebola, D. A. DiGregorio, D. Trauner, *Nat. Commun.* **2015**, *6*, No. 8076.
- [28] J. A. Frank, M. Moroni, R. Moshourab, M. Sumser, G. R. Lewin, D. Trauner, *Nat. Commun.* **2015**, *6*, No. 7118.
- [29] J. Morstein, M. Awale, J.-L. Reymond, D. Trauner, *ACS Cent. Sci.* **2019**, *5*, 607–618.
- [30] W. W. Paudler, A. G. Zeiler, *J. Org. Chem.* **1969**, *34*, 3237–3239.
- [31] R. Siewertsen, H. Neumann, B. Buchheim-Stehn, R. Herges, C. Näther, F. Renth, F. Temps, *J. Am. Chem. Soc.* **2009**, *131*, 15594–15595.
- [32] R. Siewertsen, J. B. Schönborn, B. Hartke, F. Renth, F. Temps, *Phys. Chem. Chem. Phys.* **2010**, *13*, 1054–1063.
- [33] M. Hammerich, C. Schütt, C. Stähler, P. Lentjes, F. Röhricht, R. Höppner, R. Herges, *J. Am. Chem. Soc.* **2016**, *138*, 13111–13114.
- [34] M. Schehr, C. Ianes, J. Weisner, L. Heintze, M. P. Müller, C. Pichlo, J. Charl, E. Brunstein, J. Ewert, M. Lehr, et al., *Photochemical & Photobiological Sciences* **2019**, *18*, 1398–1407.
- [35] H. Sell, C. Näther, R. Herges, Beilstein *J. Org. Chem.* **2013**, *9*, 1–7.
- [36] E. R. Thapaliya, J. Zhao, G. C. R. Ellis-Davies, *ACS Chem. Neurosci.* **2019**, *10*, 2481–2488.
- [37] M. Volgraf, P. Gorostiza, S. Szobota, M. R. Helix, E. Y. Isacoff, D. Trauner, *J. Am. Chem. Soc.* **2007**, *129*, 260–261.
- [38] A. Polosukhina, J. Litt, I. Tochitsky, J. Nemargut, Y. Sychev, I. De Kouchkovsky, T. Huang, K. Borges, D. Trauner, R. N. Van Gelder, et al., *Neuron* **2012**, *75*, 271–282.
- [39] I. Tochitsky, A. Polosukhina, V. E. Degtyar, N. Gallerani, C. M. Smith, A. Friedman, R. N. Van Gelder, D. Trauner, D. Kaufer, R. H. Kramer, *Neuron* **2014**, *81*, 800–813.
- [40] I. Tochitsky, Z. Helft, V. Meseguer, R. B. Fletcher, K. A. Vessey, M. Telias, B. Denlinger, J. Malis, E. L. Fletcher, R. H. Kramer, *Neuron* **2016**, *92*, 100–113.
- [41] L. Laprell, I. Tochitsky, K. Kaur, M. B. Manookin, M. Stein, D. M. Barber, C. Schön, S. Michalakakis, M. Biel, R. H. Kramer, et al., *J. Clin. Invest.* **2017**, *127*, 2598–2611.
- [42] T. Fehrentz, C. A. Kuttruff, F. M. E. Huber, M. A. Kienzler, P. Mayer, D. Trauner, *ChemBioChem* **2012**, *13*, 1746–1749.
- [43] A. Mourot, T. Fehrentz, Y. Le Feuvre, C. M. Smith, C. Herold, D. Dalkara, F. Nagy, D. Trauner, R. H. Kramer, *Nat. Methods* **2012**, *9*, 396–402.
- [44] A. J. Damijonaitis, Photoswitchable molecules for the optical control of GPCRs and ion channels, PhD Thesis, Ludwig-Maximilians-Universität München, 2015, deposited 22. Oct 2018, <https://edoc.ub.uni-muenchen.de/23011/>.
- [45] S. Samanta, C. Qin, A. J. Lough, G. A. Woolley, *Angew. Chem. Int. Ed.* **2012**, *51*, 6452–6455.
- [46] T. Hoshi, W. N. Zagotta, R. W. Aldrich, *Science* **1990**, *250*, 533–8.
- [47] H. Hibino, A. Inanobe, K. Furutani, S. Murakami, I. Findlay, Y. Kurachi, *Physiol. Rev.* **2010**, *90*, 291–366.

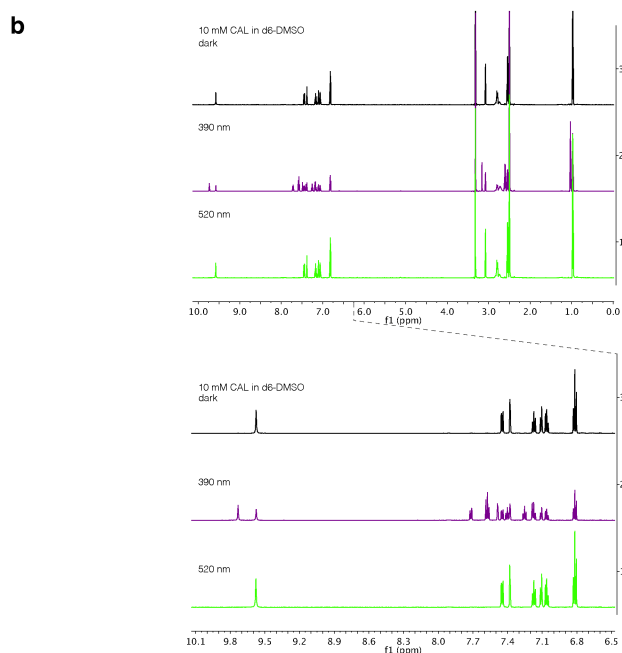
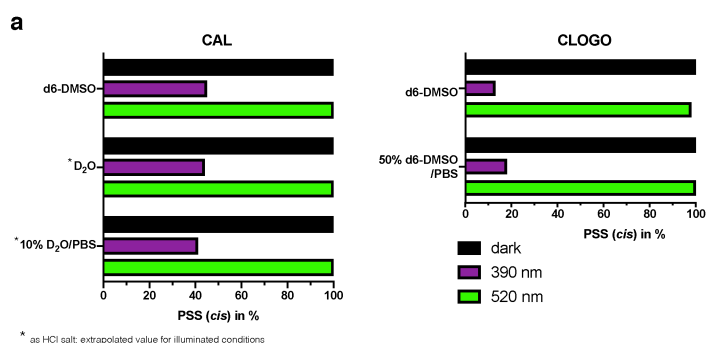
- [48] R. Luján, E. Marron Fernandez de Velasco, C. Aguado, K. Wickman, *Trends Neurosci.* **2014**, *37*, 20-29.
- [49] D. M. Barber, M. Schönberger, J. Burgstaller, J. Levitz, C. D. Weaver, E. Y. Isacoff, H. Baier, D. Trauner, *Chem. Sci.* **2016**, *7*, 2347-2352.
- [50] S. J. Ramos-Hunter, D. W. Engers, K. Kaufmann, Y. Du, C. W. Lindsley, C. D. Weaver, G. A. Sulikowski, *Bioorg. Med. Chem. Lett.* **2013**, *23*, 5195-5198.
- [51] J. B. Trads, J. Burgstaller, L. Laprell, D. B. Konrad, L. de la Osa de la Rosa, C. D. Weaver, H. Baier, D. Trauner, D. M. Barber, *Org. Biomol. Chem.* **2016**, *15*, 76-81.
- [52] D. K. Joshi, M. J. Mitchell, D. Bruce, A. J. Lough, H. Yan, *Tetrahedron* **2012**, *68*, 8670-8676.
- [53] Replacement of an azobenzene with a hemithioindigo switch was recently used to invert the pharmacology of antimetabolic agents targeting tubulin: A. Sailer, F. Ermer, Y. Kraus, F. H. Lutter, C. Donau, M. Bremerich, J. Ahlfeld, O. Thorn-Seshold, *ChemBioChem* **2019**, *20*, 1305-1314.
- [54] L. Agnetta, M. Kauk, M. C. A. Canizal, R. Messerer, U. Holzgrabe, C. Hoffmann, M. Decker, *Angew. Chem. Int. Ed.* **2017**, *56*, 7282-7287.
- [55] J. Morstein, R. Z. Hill, A. J. E. Novak, S. Feng, D. D. Norman, P. C. Donthamsetti, J. A. Frank, T. Harayama, B. M. Williams, A. L. Parrill, et al., *Nat. Chem. Biol.* **2019**, *15*, 623-631.
- [56] L. Yue, M. Pawlowski, S. S. Dellal, A. Xie, F. Feng, T. S. Otis, K. S. Bruzik, H. Qian, D. R. Pepperberg, *Nat. Commun.* **2012**, *3*, No. 1095.
- [57] M. Stein, S. J. Middendorp, V. Carta, E. Pejo, D. E. Raines, S. A. Forman, E. Sigel, D. Trauner, *Angew. Chem. Int. Ed.* **2012**, *51*, 10500-10504.
- [58] L. Laprell, K. Hüll, P. Stawski, C. Schön, S. Michalakakis, M. Biel, M. P. Sumser, D. Trauner, *ACS Chem. Neurosci.* **2016**, *7*, 15-20.
- [59] B. Eisel, F. W. W. Hartrampf, T. Meier, D. Trauner, *FEBS Lett.* **2018**, *592*, 343-355.
- [60] Y.-H. Tsai, S. Essig, J. R. James, K. Lang, J. W. Chin, *Nat. Chem.* **2015**, *7*, 554-561.
- [61] G. Cabré, A. Garrido-Charles, À. González-Lafont, W. Moormann, D. Langbehn, D. Egea, J. M. Lluch, R. Herges, R. Alibés, F. Busqué, et al., *Org. Lett.* **2019**, *21*, 3780-3784.



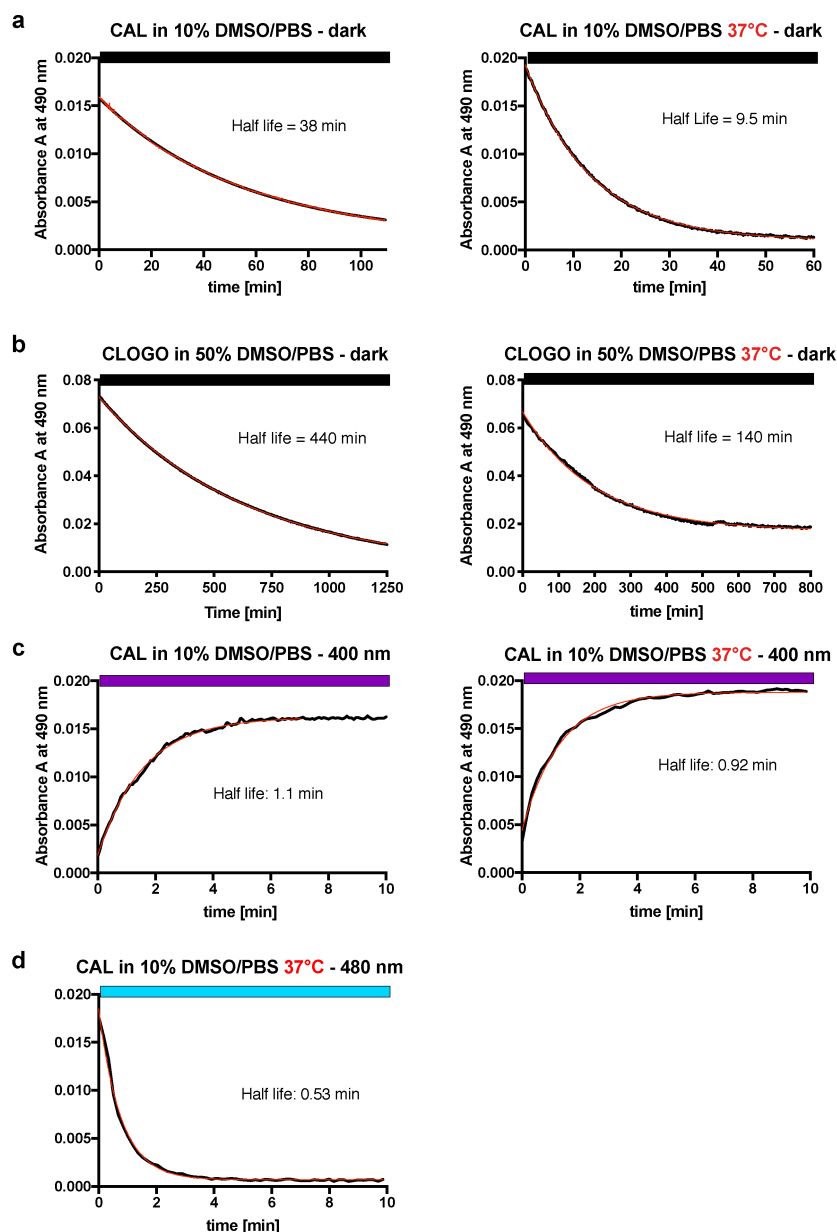
## Supplementary Figures



**Fig. S1: Synthesis and photophysical characterization of CQAQ.** a: Synthesis of CQAQ. b: Isomerization of CQAQ upon illumination is best achieved with 400 – 420 nm and 480 – 520 nm. Half-life time was measured in DMSO at room temperature at 50  $\mu$ M concentration. c: Photostationary states of 10 mM CQAQ in  $d_6$ -DMSO upon 30 sec. illumination with a 390 nm high-power LED. d: UV-Vis spectra of CQAQ at 50  $\mu$ M in DMSO. Illumination with distinct wavelengths took place for 10 min before collection of the spectrum.

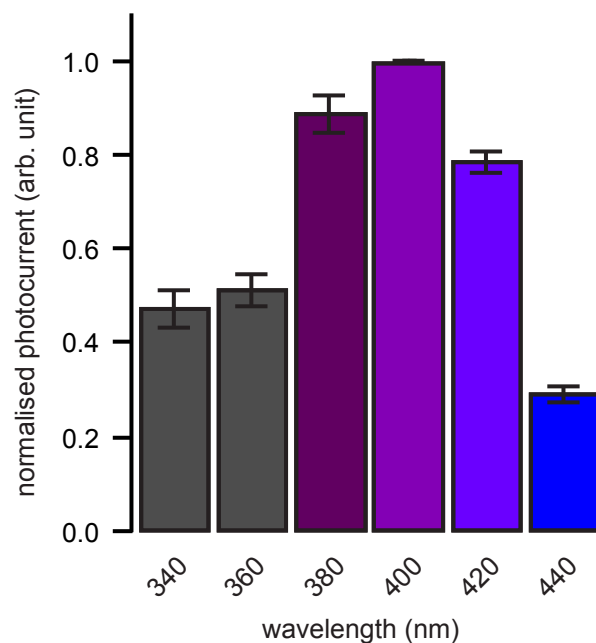


**Fig. S2: PSS-determination of CAL and CLOGO by NMR.** a: PSS of CAL or CAL · HCl and CLOGO as determined by NMR spectroscopy in dark and after illumination of the NMR sample with a 390 nm and 520 nm high powered LED (by Prizmatix®). In protic solvents, the PSS of CAL was determined through extrapolation to the theoretical value from ten data points collected over 5 min. Due to low solubility of CLOGO in PBS, d<sub>6</sub>-DMSO was used as a co-solvent. b: the NMR spectrum in d<sub>6</sub>-DMSO shows the appearance of *trans*-peaks after 390 nm illumination and complete isomerization to the *cis*-compound after 520 nm illumination.

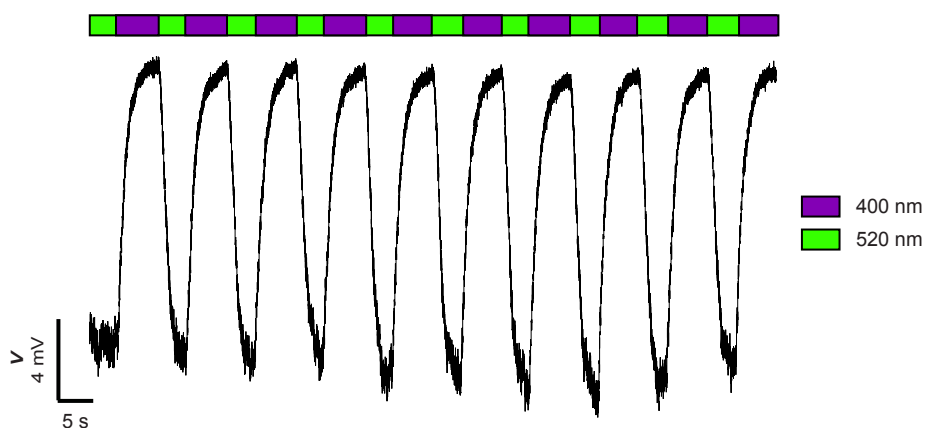


**Fig. S3: Isomerization kinetics of CAL and CLOGO in aqueous medium.**

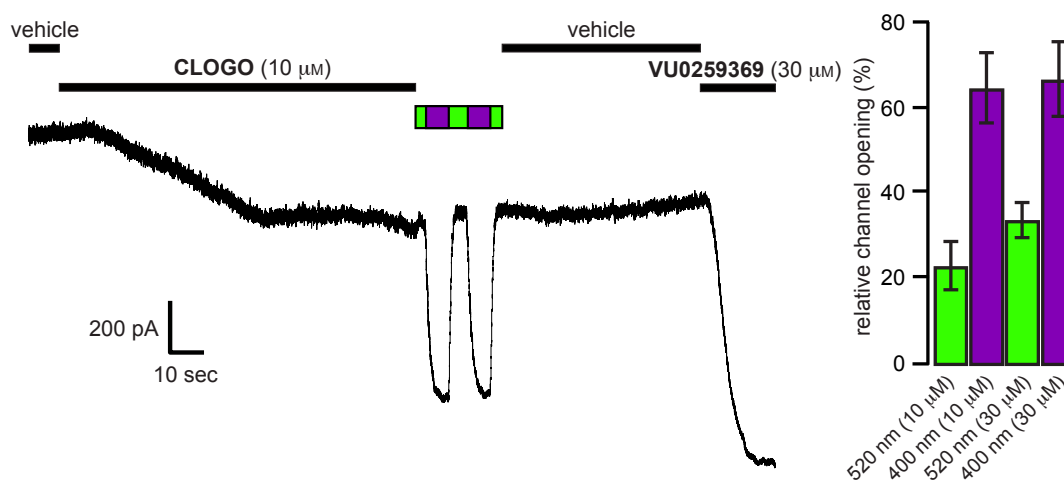
a: thermal relaxation of CAL in 10% DMSO/PBS at room temperature and 37°C.  
 b: thermal relaxation of CLOGO in 50% DMSO/PBS at room temperature and 37°C.  
 c: isomerization rate with light is not affected by the increase of temperature. d: *trans* to *cis* isomerization with light has a similar half-life than *cis* to *trans* isomerization. Light illumination was performed with the optoscan monochromator.



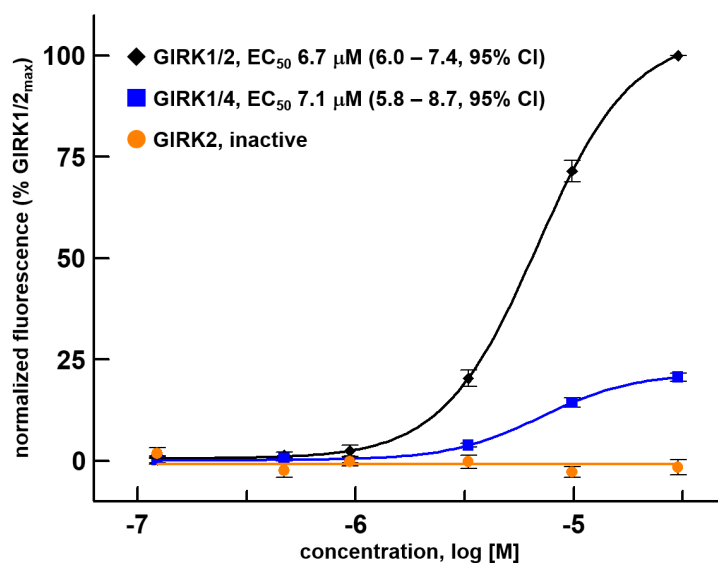
**Fig. S4: Action spectrum of CLOGO in voltage-clamp mode.** When using 520 nm as the OFF wavelength, CLOGO (10  $\mu\text{m}$ ) consistently showed the largest change in current in combination with 400 nm. Error bars represent mean  $\pm$  SEM ( $n = 6$  cells). HEK293T cells, transiently transfected with GIRK1/2 and YFP, 24 - 48 h post transfection.



**Fig. S5: Photoswitching of CLOGO in the current clamp mode.** The photoswitching of CLOGO (10  $\mu\text{m}$ ) is highly reproducible whilst in current clamp mode.



**Fig. S6: Comparison of GIRK1/2 channel opening using the non-photoswitchable agonist VU0259369 (30  $\mu\text{M}$ ) and the *cis*- and *trans*-isomers of CLOGO (10  $\mu\text{M}$  and 30  $\mu\text{M}$ ).** Trace representative of  $n=5$  cells. Error bars represent mean  $\pm$  SEM ( $n=5$  cells).



**Fig. S7. Potency and efficacy of CLOGO for various combinations of GIRK channel subunits.** Fluorescence-based thallium flux measurements were made using a series of concentrations of CLOGO applied to HEK-293 cells stably expressing heteromeric GIRK1 + GIRK2 ( $\blacklozenge$ ), GIRK1 + GIRK4 ( $\blacksquare$ ) or homomeric GIRK2 channels ( $\bullet$ ). Error bars shown represent standard errors of the mean (SEM). Potency values and 95% confidence intervals (CI) were calculated from a fit to a four-parameter logistic equation. Efficacy values were normalized to the maximum effect of CLOGO on GIRK1/2 channels. All data shown were obtained from three independent experiments.



## Methods

### Electrophysiology

**CAL: Cell culture and electrophysiology.** HEK293T (tsA-201) cells were cultured in DMEM supplemented with 5% fetal bovine solution and split upon 70% confluency as described elsewhere<sup>1</sup>. Cells were transiently transfected with inactivation-removed *Shaker* K<sup>+</sup> channel by the calcium phosphate method<sup>1</sup> and recorded 12 - 24 h later.

Electrophysiological recordings were performed in whole cell mode by using a standard patch clamp setup including a HEKA Patch Clamp EPC10 USB amplifier and patch master software (V2X90, HEKA). Recordings were low-pass-filtered at 2 kHz. Igor Pro using the Patcher's Power Tools (MPI for Biophysical Chemistry, Göttingen) plugin and FitMaster (HEKA) were applied to analyze data. Patch pipettes (Science Products) showed a resistance of 5 - 10 MΩ. Sample illumination was performed as described elsewhere.<sup>2</sup> To record voltage-gated K<sup>+</sup> currents, the voltage-clamp protocol depolarized transfected cells from a holding potential of -70 mV to +40 mV for 250 ms at a frequency of 1 Hz. Illumination wavelength of the sample was changed every 16<sup>th</sup> depolarization step. I-V relationships were recorded by stepping from a holding potential of -70 mV up to +80 mV in 10 mV increments for 250 ms at a frequency of 1 Hz and under simultaneous illumination of a defined wavelength. I-V recordings were corrected for leak current. External recording solution contained (in mM): 138 NaCl, 1.5 KCl, 5 HEPES, 1.2 MgCl<sub>2</sub>, 2.5 CaCl<sub>2</sub>, 10 glucose, and the pH was adjusted to 7.4 using NaOH. The internal patch solution contained (in mM): 10 NaCl, 135 K<sup>+</sup> gluconate, 10 HEPES, 2 MgCl<sub>2</sub>, 2 MgATP, 1 EGTA and the pH was adjusted to 7.4 using NaOH. CAL was dissolved in DMSO before adding to external solutions, whereas DMSO concentration did not exceed 0.1%. Photoswitching was quantified as outward current amplitudes in the initial two consecutive recorded cycles (one at 385 nm and one at 470 nm): photoswitch index =  $((I_{470\text{nm}} - I_{385/405\text{nm}}) / I_{470\text{nm}}) * 100$ . Photoswitching data are expressed as mean ± standard error of the mean (s.e.m).

**CLOGO: Cell culture and electrophysiology in HEK293T cells.** HEK293T cells were incubated in Dulbecco's MEM supplemented with 10% FBS and split at 80 - 90% confluency. For detachment, the growth medium was removed, the cells were washed with calcium and magnesium free PBS and then treated with trypsin solution 2 min at 37 °C. The detached cells were diluted with growth medium and singularized by pipetting. For transfection, acid-etched coverslips were coated with poly-L-lysine and placed in a 24-well plate. 40,000 cells were added to each well in 500 μL standard growth medium. DNA (per coverslip: 350 ng GIRK1/2 and 50 ng YFP) was mixed with 1 μL polyplus jetprime in 50 μL jetprime buffer. After standing at room temperature for 10 - 15 min, the DNA-mix was added to the cells shortly after seeding them into the abovementioned 24-well-plate. After 3 - 5 h, the

medium was exchanged for standard growth medium. Cells were used for electrophysiological recordings 24 – 48 h post transfection.

Whole-cell patch clamp experiments were performed using a standard electrophysiology setup equipped with a HEKA Patch Clamp EPC10 USB amplifier and PatchMaster software (HEKA Elektronik). Micropipettes were generated from a Science Products GB200-F-8P with filament pipettes using a vertical puller. Resistance varied between 3 – 7 M $\Omega$ . The extracellular solution contained in mM: 115 NaCl, 50 KCl, 2 CaCl<sub>2</sub>, 1 MgCl<sub>2</sub>, 11 glucose and 5 HEPES (KOH to pH 7.4). The intracellular solution contained in mM: 4 NaCl, 107 KCl, 1 CaCl<sub>2</sub>, 1 MgCl<sub>2</sub>, 10 EGTA, 2 MgATP, 0.3 Na<sub>2</sub>GTP and 5 HEPES (KOH to pH 7.2). The holding potential for voltage-clamp experiments was –60 mV. All compounds were diluted into the extracellular solution from 100 mM DMSO stock solutions. Illumination during electrophysiology experiments was provided by a TILL Photonics Polychrome 5000 monochromator.

**Thallium Flux.** HEK-293 cells expressing GIRK1 + GIRK2 or GIRK1 + GIRK4 were cultured in:  $\alpha$ -MEM (Corning, Corning, NY) supplemented with glutagro (Corning) and 10% (v/v) fetal bovine serum (Thermo Fisher Scientific, Waltham, MA) henceforth referred to as cell culture medium. Twenty thousand cells per well in 20  $\mu$ L of cell culture medium were plated into 384-well, black-wall, clear-bottom, PureCoat Amine plates (Corning) and incubated overnight in a humidified 5% CO<sub>2</sub> incubator at 37 °C. For testing CLOGO, cell culture medium replaced with 20  $\mu$ L/well of a Hank's Balanced Salt Solution (HBSS, Thermo Fisher), with the addition of 10 mM HEPES-NaOH pH 7.3 (Thermo Fisher), 0.02% (w/v) Pluronic F-127, and 1.5  $\mu$ M Thallos-AM (WaveFront Biosciences, Austin, TX). The dye-loading solution was replaced with 20  $\mu$ L/well HBSS containing 10 mM HEPES-NaOH, pH 7.3 (assay buffer) after 1 h of incubation at room temperature. A 30 mM solution of CLOGO was prepared and serially diluted in DMSO. CLOGO was further diluted in assay buffer to 2-fold over their final test concentration. Thallos-loaded cell plates were imaged using a Panoptic kinetic imaging plate reader (WaveFront Biosciences, Franklin, TN) at 5 Hz, excitation 482/35 nm and emission 536/40 nm. After 10 s of baseline collection 20  $\mu$ L/well diluted compounds were added and imaging continued for 2 min at which time 10  $\mu$ L/well of a solution containing (in mM) 125 NaHCO<sub>3</sub>, 1.8 CaSO<sub>4</sub>, 1 MgSO<sub>4</sub>, 5 glucose, 1.6 Tl<sub>2</sub>SO<sub>4</sub> and 10 HEPES-NaOH pH 7.3 was added and imaging continued for an additional 2 minutes.

**Hippocampal Neuron Electrophysiology.** All animal procedures were performed in accordance with the guidelines of the Regierung Oberbayern. Horizontal slices were prepared from C57Bl6JRj mice (postnatal day 10 – 13). Following decapitation, the brain was rapidly removed and transferred to an ice-cold saline solution composed of (in mM) 87 NaCl, 75 sucrose, 25 NaHCO<sub>3</sub>, 2.5 KCl, 1.25 NaH<sub>2</sub>PO<sub>4</sub>, 0.5 CaCl<sub>2</sub>, 7 MgCl<sub>2</sub>, 25 glucose saturated with carbogen (95% O<sub>2</sub>/5% CO<sub>2</sub>). Slices (300  $\mu$ m thick) were cut with a vibratome (NPI Electronic), incubated at 34 °C for 1 h in saline solution and then kept at room temperature for up to 6 h



before being used in patch-clamp recordings. Experiments were carried out in ACSF composed of (in mM) 125 NaCl, 26 NaHCO<sub>3</sub>, 2.5 KCl, 1.25 NaH<sub>2</sub>PO<sub>4</sub>, 2 CaCl<sub>2</sub>, 1 MgCl<sub>2</sub> and 20 glucose saturated with carbogen at room temperature.

Hippocampal neurons were patched using glass electrodes (Science Products) with a resistance of 6 – 9 MΩ. Current-clamp recordings were carried out using the following intracellular solution (in mM): 140 K-gluconate, 10 HEPES, 12 KCl, 4 NaCl, 4 MgATP, 0.4 Na<sub>2</sub>GTP. Recordings were made with an EPC 10 USB amplifier, controlled by the Patchmaster software (HEKA). Data was filtered at 2.9 and 10 kHz. Data was analyzed using the Patcher's Power Tools (MPI Göttingen) and IgorPro (Wavemetrics). CLOGO was diluted into the extracellular solution from a 100 mM DMSO stock solution. Photoswitching was achieved through a microscope coupled monochromator (Polychrome V, FEI).

## Experimental Procedures for Chemical Synthesis

**General Experimental Techniques.** All reactions were conducted using dried glassware (120 °C) under a positive pressure of nitrogen with magnetic stirring unless otherwise stated. Liquid reagents and solvents were added via syringe or oven-dried stainless-steel cannulas through rubber septa. Solids were added under inert gas counter flow or were dissolved in specified solvents prior to addition. Low temperature reactions were carried out in a Dewar vessel filled with the appropriate cooling agent e.g. H<sub>2</sub>O/ice (0 °C). Reactions using temperatures above room temperature were conducted using a heated oil bath. Yields refer to spectroscopically pure compounds unless otherwise stated.

**Solvents and Reagents.** Tetrahydrofuran (THF) was distilled under a nitrogen atmosphere from Na/benzophenone prior to use. Triethylamine (Et<sub>3</sub>N) was distilled under a nitrogen atmosphere from CaH<sub>2</sub> prior to use. Dichloromethane (CH<sub>2</sub>Cl<sub>2</sub>), 1,2-dichloroethane (DCE), ethyl acetate (EtOAc), dimethylformamide (DMF) and methanol (MeOH) were purchased from commercial suppliers (Acros Organics) and used as received. Solvents for extraction and flash column chromatography were purchased in technical grade purity and distilled under reduced pressure prior to use. All other reagents and solvents were purchased from commercial suppliers and used as received, except stated otherwise.

**Chromatography.** Reactions and chromatography fractions were monitored by qualitative thin-layer chromatography (TLC) on silica gel F<sub>254</sub> TLC plates from Merck KGaA. Analytes on the glass plates were visualized by irradiation with UV light and by immersion of the TLC plate in KMnO<sub>4</sub>, CAM or ninhydrin staining solution, followed by heating with a hot-air gun. Flash column chromatography was performed using silica gel, particle size 40–63 μm (eluents are given in parenthesis).

**Melting Points.** Melting points were measured on an EZ-Melt apparatus from Stanford Research Systems and are uncorrected.

**NMR Spectra.** NMR spectra were measured on a Bruker Avance III HD 400 MHz spectrometer equipped with a CryoProbe™ operating at 400 MHz for proton nuclei and 100 MHz for carbon nuclei. The  $^1\text{H}$  and  $^{13}\text{C}$  NMR shifts are reported in ppm related to the chemical shift of tetramethylsilane.  $^1\text{H}$  NMR shifts were calibrated to residual solvent resonances:  $\text{CDCl}_3$  (7.26 ppm).  $^{13}\text{C}$  NMR shifts were calibrated to the center of the multiplet signal of the residual solvent resonance:  $\text{CDCl}_3$  (77.16 ppm).  $^1\text{H}$  NMR spectroscopic data are reported as follows: Chemical shift in ppm (multiplicity, coupling constants, integration). The multiplicities are abbreviated with s (singlet), br s (broad singlet), d (doublet), t (triplet), q (quartet) and m (multiplet) and their respective combinations. Except for multiplets, the chemical shift of all signals is reported as the center of the resonance range. In addition to  $^1\text{H}$  and  $^{13}\text{C}$  NMR measurements, 2D NMR techniques as homonuclear correlation spectroscopy (COSY), heteronuclear single quantum coherence (HSQC) and heteronuclear multiple bond coherence (HMBC) were used to assist the compound identification process. Coupling constants  $J$  are reported in Hz. All raw fid files were processed, and the spectra analyzed using the program MestReNova 11.0 from Mestrelab Research S. L.

**Mass Spectra.** High-resolution mass spectra (HRMS) were recorded by the LMU Mass Spectrometry Service on a MAT 90 (ESI) spectrometer from Thermo Finnigan GmbH or using an Agilent 6224 Accurate-Mass time-of-flight spectrometer with electrospray ionization at the New York University Shared Instrumentation Facility (NYU-SIF).

**Infrared Spectra.** IR spectra were recorded on a PerkinElmer Spectrum BX II FT-IR or Thermo Nicolet AVATAR FT-IR equipped with an ATR unit. The measured wave numbers are reported in  $\text{cm}^{-1}$ .

**UV/Vis Spectra.** CAL UV/Vis spectra were recorded on a Varian Cary 60 Scan UV/Vis spectrometer equipped with an 18-cell holder using Brandtech Scientific Inc. UV cuvettes (70-850  $\mu\text{L}$ , 10 mm light path). Sample preparation and all experiments were performed under red light conditions in a dark room. The stock solution was prepared at 50 mM in DMSO and diluted to 500  $\mu\text{M}$  in DMSO prior to the experiment. For the wavelength scan, photoswitching was achieved using an Optoscan Monochromator with an Optosource (75 mW lamp), which was controlled through a program written in Matlab. Irradiation to establish PSS took place from the top through a fiber-optic cable. Illumination was screened from 360-540 nm in 20 nm steps, also including the wavelengths used in the electrophysiological experiments, going from higher to lower wavelengths, illuminating 10 min for each wavelength. Illumination conditions that afforded the highest *trans*-isomer and *cis*-isomer enrichment are shown in Fig. 2a

CLOGO UV/Vis spectra were recorded on a Varian Cary 50 Scan UV/Vis spectrometer using Helma SUPRASIL precision cuvettes (10 mm light path). A solution of CLOGO in DMSO (500  $\mu\text{M}$ ) was placed in the 1 mL cuvette and a light-fibre cable connected to a Till Photonics Polychrome V monochromator was

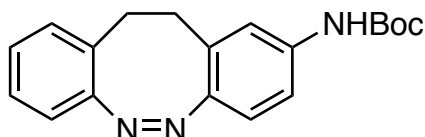
placed in the cuvette until it penetrated the surface of the solution. Illumination was screened from 340–600 nm in 20 nm steps going from higher to lower wavelengths. Every wavelength was applied for 5 min before a UV-Vis spectrum was recorded. Illumination conditions that afforded the highest *trans*-isomer and *cis*-isomer enrichment are shown in Fig. 4a.

**PSS Determination by NMR spectroscopy.** One pulse proton NMR spectroscopy to determine photostationary states was performed on a Bruker Avance 600 with Cryoprobe at 10 mM concentration, to ensure a low optical density and good signal to noise ratio. The samples were illuminated for 30 to 60 s with a Prizmatix high power LED (390 nm and 520 nm), prior to collection of the spectrum. The spectrum was referenced to the solvent  $d_6$ -DMSO (2.500 ppm) or  $D_2O$  (4.790 ppm) and signals integrated using MestReNova 11.0 from Mestrelab Research S. L. Spectra in 10%  $D_2O$ /PBS were recorded with solvent suppression and the spectra referenced to the *trans*-isomer. In  $D_2O$  and PBS, spectra were collected every 20–30 s over 5 min and the values extrapolated to the time when illumination of the sample was switched off.



## Experimental Procedures

### Synthesis and characterization of *tert*-butyl (Z)-(11,12-dihydrodibenzo[*c,g*][1,2]diazocin-2-yl)carbamate (**2**)



To a Schlenk tube was added **1**<sup>3</sup> (580 mg, 2.02 mmol, 1.0 equiv), *tert*-butyl carbamate (592 mg, 5.05 mmol, 2.5 equiv), XantPhosG3 palladium pre-catalyst (47.9 mg, 0.05 mmol, 0.025 equiv), and Cs<sub>2</sub>CO<sub>3</sub> (987 mg, 3.03 mmol, 1.5 equiv). The reaction headspace was evacuated and backfilled with nitrogen, upon which degassed 1,4-dioxane (3.5 mL) was added. The reaction was sealed and put into an oil bath preheated to 100 °C and allowed to react for 1.5 h. After this period, the reaction was cooled to room temperature, diluted with EtOAc, and washed with sat. aq. NH<sub>4</sub>Cl. The aqueous layer was extracted three times with EtOAc, the organic layers were combined and successively washed with sat. aq. NaHCO<sub>3</sub> and sat. NaCl. The organic layer was washed with sat. NaCl, dried over Na<sub>2</sub>SO<sub>4</sub> and concentrated in vacuo. Purification by flash column chromatography on silica gel eluting with *i*-Hexanes/EtOAc (9:1 → 7:3) afforded compound **2** (537 mg, 1.66 mmol, 82%) as a yellow, amorphous solid.

**TLC** (*i*-Hex/EtOAc, 8:2): R<sub>f</sub> = 0.4 (UV/CAM).

**<sup>1</sup>H NMR** (400 MHz, CDCl<sub>3</sub>): δ = 7.20 – 7.06 (m, 2H), 7.01 (ddt, *J* = 9.8, 7.6, 4.2 Hz, 3H), 6.87 – 6.71 (m, 2H), 6.37 (s, 1H), 2.85 (s, 4H), 1.47 (s, 9H).

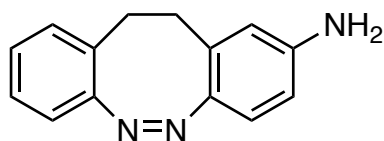
Note: *t*-Bu-carbamate impurity peaks at δ = 4.36 (br s, 2H), 1.36 (s, 9H),

**<sup>13</sup>C NMR** (100 MHz, CDCl<sub>3</sub>): δ = 155.6, 152.6, 150.9, 137.3, 129.7, 129.2, 128.2, 127.2, 126.8, 120.3, 119.0, 116.6, 80.9, 32.3, 31.6, 28.4.

Note: *t*-Bu-carbamate impurity peaks at δ = 79.8, 28.4.

**HRMS** (ESI, *m/z*): [(M+H)<sup>+</sup>] calcd. for C<sub>19</sub>H<sub>22</sub>N<sub>3</sub>O<sub>2</sub>: 324.1707; found 324.1721;

**IR** (thin film): 3314, 2977, 1722, 1586, 1516, 1234, 1153, 1058, 911, 752, 730 cm<sup>-1</sup>.

**Synthesis and characterization of (Z)-11,12-dihydrodibenzo[c,g][1,2]diazocin-2-amine (3)**

To a solution of 2 (300 mg, 0.927 mmol, 1.0 equiv) in DCM (3.5 mL) was added TFA (3.5 mL) at room temperature. The reaction was allowed to stir for 30 min at room temperature and was concentrated in vacuo to afford a red oil (259 mg, 0.77 mmol, 83%, based on MW of TFA salt) which was used without further purification. An analytical sample was purified by silica gel flash column chromatography (30% → 60% EtOAc/hexanes).

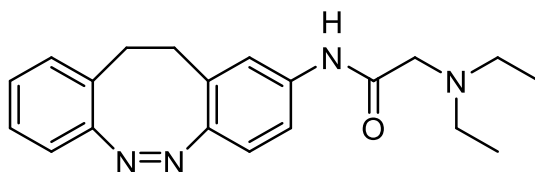
**TLC** (Hex/EtOAc, 1:1):  $R_f$  = 0.41 (UV/CAM).

**$^1\text{H NMR}$**  (400 MHz,  $\text{CDCl}_3$ ):  $\delta$  = 7.13 (ddd,  $J$  = 7.8, 6.8, 2.0 Hz, 1H), 7.02 (ddd,  $J$  = 15.9, 7.6, 1.2 Hz, 1H), 7.01 (s, 1H), 6.81 (dd,  $J$  = 7.7, 1.2 Hz, 1H), 6.72 (d,  $J$  = 8.3 Hz, 1H), 6.44 (dd,  $J$  = 8.3, 2.5 Hz, 1H), 6.27 (d,  $J$  = 2.4 Hz, 1H), 3.56 (s, 2H), 2.82 (br s, 4H).

**$^{13}\text{C NMR}$**  (101 MHz,  $\text{CDCl}_3$ ):  $\delta$  = 155.8, 147.9, 145.4, 129.4, 129.3, 128.6, 126.9, 126.7, 121.4, 119.0, 115.6, 113.4, 32.5, 31.5.

**HRMS** (ESI,  $m/z$ ): calcd. for  $\text{C}_{14}\text{H}_{14}\text{N}_3^+$   $[\text{M}+\text{H}]^+$ : 224.1188; found: 224.1178.

**IR** (thin film): 3444, 3346, 3220, 2896, 1604, 1503, 1437, 1308, 1255, 906, 727  $\text{cm}^{-1}$ .

**Synthesis and characterization of (Z)-2-(diethylamino)-N-(11,12-dihydrodibenzo[c,g][1,2]diazocin-2-yl) acetamide (CAL)**

To a solution of **3** (700 mg, 3.14 mmol, 1.0 equiv) in EtOAc (34 mL) was added sodium diethylglycinate **4** (528 mg, 3.45 mmol, 1.1 equiv), TBTU (1.21 g, 3.76 mmol, 1.2 equiv), and Et<sub>3</sub>N (0.48 mL, 349 mg, 3.45 mmol, 1.1 equiv) sequentially at room temperature. The heterogenous reaction mixture was allowed to stir at room temperature overnight. The reaction was washed with sat. aq. NaHCO<sub>3</sub> and sat. NaCl, dried over Na<sub>2</sub>SO<sub>4</sub>, filtered and concentrated *in vacuo*. The red residue was purified by flash column chromatography over silica gel eluting with 8:1.5:0.5 DCM/acetone/MeOH to afford the desired product (822 mg, 2.44 mmol, 78%) as a viscous dark red oil.

**TLC** (EtOAc): R<sub>f</sub> = 0.47 (UV/CAM).

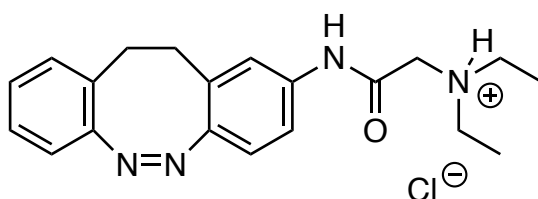
**<sup>1</sup>H NMR** (400 MHz, CDCl<sub>3</sub>): δ = 10.01 (s, 1H), 7.33 (d, *J* = 7.1 Hz, 2H), 7.14 (ddd, *J* = 7.8, 6.9, 1.8 Hz, 1H), 7.05 – 6.97 (m, 2H), 6.86 – 6.79 (m, 2H), 3.44 (s, 2H), 2.95 (s, 2H), 2.89 (q, *J* = 7.2 Hz, 4H), 2.78 (s, 2H), 1.18 (t, *J* = 7.2 Hz, 6H).

**<sup>13</sup>C NMR** (101 MHz, CDCl<sub>3</sub>): δ = 166.6, 155.6, 151.9, 136.6, 129.8, 129.2, 128.1, 127.3, 126.9, 120.4, 120.2, 119.0, 117.9, 56.9, 48.4, 32.2, 31.6, 10.9.

**HRMS (ESI)**: calcd for C<sub>20</sub>H<sub>25</sub>N<sub>4</sub>O<sup>+</sup> [M+H]<sup>+</sup>: 337.2023 found: 337.2011.

**UV-Vis**: λ<sub>max</sub> = 421 nm (500 μM in DMSO).

**IR** (thin film): 3275, 2969, 1687, 1506, 1456, 1415, 1348, 1204, 1088, 894, 751, cm<sup>-1</sup>.

**Synthesis and characterization of (Z)-2-((11,12-dihydrodibenzo[c,g][1,2]diazocin-2-yl)amino)-N,N-diethyl-2-oxoethan-1-aminium (CAL·HCl)**

CAL (950 mg, 2.82 mmol, 1.0 equiv) was dissolved in diethylether (56.5 mL) and HCl in dioxane (4.0 M, 0.777 mL, 1.1 equiv) was added and stirred for 10 min. The protonated product precipitated and was filtered through a fritted glass funnel. The solid residue was washed with cold diethyl ether (50 mL) and dried *in vacuo* to yield CAL · HCl (970 mg, 2.60 mmol, 92%) as yellow powder.

**TLC** (EtOAc):  $R_f = 0.35$  (UV/CAM).

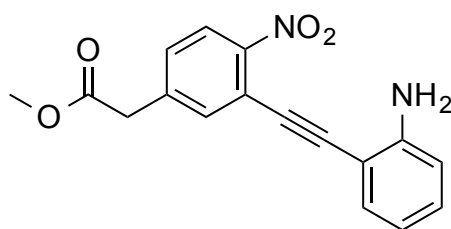
**$^1\text{H NMR}$**  (400 MHz,  $\text{CDCl}_3$ ):  $\delta = 10.96$  (s, 1H), 10.83 (s, 1H), 7.58 (d,  $J = 8.4$  Hz, 1H), 7.40 (s, 1H), 7.10 (t,  $J = 7.4$  Hz, 1H), 6.98 (t,  $J = 7.3$  Hz, 1H), 6.91 (d,  $J = 7.5$  Hz, 1H), 6.78 (t,  $J = 8.5$  Hz, 2H), 4.17 (s, 2H), 3.45 (s, 2H), 3.31 (s, 2H), 2.88 (s, 2H), 2.68 (s, 2H), 1.38 (t,  $J = 7.0$  Hz, 6H).

**$^{13}\text{C NMR}$**  (100 MHz,  $\text{CDCl}_3$ ):  $\delta = 161.6, 155.6, 152.3, 136.6, 129.8, 129.2, 128.1, 127.2, 126.8, 120.6, 120.0, 118.9, 118.3, 67.3, 66.0, 52.5, 48.7, 32.0, 31.6, 9.9$ .

**HRMS (ESI)**: calcd for  $\text{C}_{20}\text{H}_{25}\text{N}_4\text{O}^+$   $[\text{M}+\text{H}]^+$ : 337.2023, found: 337.2037.

**IR** (thin film): 2988, 1693, 1613, 1595, 1550, 1484, 1410, 1318, 1268, 819, 756, 732  $\text{cm}^{-1}$ .



**Synthesis and characterization of methyl {3-[(2-aminophenyl)ethynyl]-4-nitrophenyl} acetate (**7**)**

To a stirred solution of compound **5** (400 mg, 1.46 mmol, 1.0 equiv) and compound **6** (171 mg, 1.46 mmol, 1.0 equiv) in Et<sub>3</sub>N (3.5 mL) at room temperature was added Pd(PPh<sub>3</sub>)<sub>2</sub>Cl<sub>2</sub> (20.5 mg, 0.029 mmol, 0.02 equiv) and CuI (11.1 mg, 0.058 mmol, 0.04 equiv). The resulting mixture was stirred at room temperature for 18 h. The reaction mixture was diluted with sat. aq. NH<sub>4</sub>Cl and extracted three times with EtOAc. The combined organic extracts were washed with sat. NaCl, dried over Na<sub>2</sub>SO<sub>4</sub>, filtered and concentrated under reduced pressure. Purification by flash column chromatography on silica gel eluting with *i*-hexanes/EtOAc (7:1 → 1:1) afforded compound **7** (351 mg, 1.13 mmol, 77%) as a red solid.

**mp:** 82 – 84 °C.

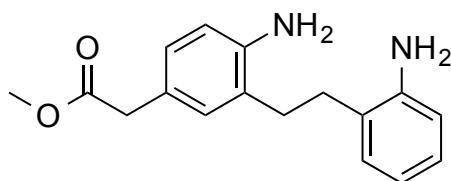
**TLC** (*i*-Hex/EtOAc, 1:1): R<sub>f</sub> = 0.50 (UV/KMnO<sub>4</sub>).

**<sup>1</sup>H NMR** (400 MHz, CDCl<sub>3</sub>): δ = 8.12 (d, *J* = 8.5 Hz, 1H), 7.64 (s, 1H), 7.41 – 7.32 (m, 2H), 7.18 (t, *J* = 7.7 Hz, 1H), 6.75 – 6.66 (m, 2H), 4.72 (br s, 2H), 3.74 (s, 3H), 3.71 (s, 2H).

**<sup>13</sup>C NMR** (100 MHz, CDCl<sub>3</sub>): δ = 170.5, 149.7, 147.2, 140.1, 135.2, 132.6, 131.2, 129.2, 125.5, 119.7, 117.5, 114.4, 106.2, 95.6, 91.0, 52.6, 40.5.

**HRMS** (ESI): calcd. for C<sub>17</sub>H<sub>15</sub>N<sub>2</sub>O<sub>4</sub><sup>+</sup> [M+H]<sup>+</sup>: 311.1026; found: 311.1028.

**IR** (thin film): 3350, 2952, 1727, 1510, 1334, 1171, 747 cm<sup>-1</sup>.

**Synthesis and characterization of methyl {4-amino-3-[2-(2-aminophenyl)ethyl]phenyl} acetate (**8**)**

To a stirred solution of compound **7** (142 mg, 0.458 mmol) in THF at room temperature was added Pd/C (10% w/w, 31.4 mg). The reaction vessel was purged three times with hydrogen and the resulting mixture was stirred at room temperature for 20 h. The reaction mixture was filtered through a plug of celite, washing with MeOH and the filtrate was concentrated under reduced pressure to afford compound **8** (130 mg, 0.458 mmol, quant.) as an orange oil.

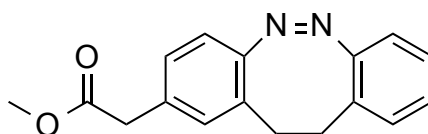
**TLC** (*i*-Hex/EtOAc, 1:1):  $R_f$  = 0.27 (UV/KMnO<sub>4</sub>);

**<sup>1</sup>H NMR** (400 MHz, CDCl<sub>3</sub>):  $\delta$  = 7.11 – 7.04 (m, 2H), 7.02 – 6.95 (m, 2H), 6.77 (td,  $J$  = 7.6, 1.1 Hz, 1H), 6.68 (d,  $J$  = 7.6 Hz, 1H), 6.63 (d,  $J$  = 7.6 Hz, 1H), 3.70 (s, 3H), 3.66 – 3.46 (m, 6H), 2.85 – 2.72 (m, 4H).

**<sup>13</sup>C NMR** (100 MHz, CDCl<sub>3</sub>):  $\delta$  = 172.8, 144.5, 143.5, 130.5, 129.6, 128.2, 127.4, 126.6, 126.3, 124.4, 119.2, 116.2, 116.0, 52.1, 40.5, 31.1 Note: two carbon signals overlap at 31.1 ppm.

**HRMS** (ESI): calcd. for C<sub>17</sub>H<sub>21</sub>N<sub>2</sub>O<sub>2</sub><sup>+</sup> [M+H]<sup>+</sup>: 285.1598; found: 285.1598.

**IR** (thin film): 3366, 2924, 1729, 1625, 1505, 1269, 1155, 752 cm<sup>-1</sup>.

**Synthesis and characterization of methyl (11,12-dihydrodibenzo[c,g][1,2]-diazocin-2-yl)acetate (9)**

To a stirred solution of compound **8** (33.0 mg, 0.116 mmol, 1.0 equiv) in CH<sub>2</sub>Cl<sub>2</sub> (1.7 mL) at room temperature was added *m*CPBA (77%, 26.0 mg, 0.135 mmol, 1.2 equiv). The reaction mixture was protected from light and stirred at room temperature for 22 h. The reaction mixture was diluted with CH<sub>2</sub>Cl<sub>2</sub> and washed with sat. aq. NaHCO<sub>3</sub> and sat. NaCl. The organic phase was dried over Na<sub>2</sub>SO<sub>4</sub>, filtered and concentrated under reduced pressure. Purification by flash column chromatography on silica gel eluting with *i*-Hex/EtOAc (9:1) afforded compound **9** (7.80 mg, 0.0278 mmol, 24%) as an orange oil.

**TLC** (*i*-Hex/EtOAc, 9:1): R<sub>f</sub> = 0.32 (UV/KMnO<sub>4</sub>).

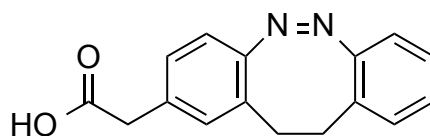
**<sup>1</sup>H NMR** (400 MHz, CDCl<sub>3</sub>): δ = 7.14 (t, *J* = 7.4 Hz, 1H), 7.07 - 6.96 (m, 3H), 6.89 (s, 1H), 6.84 (d, *J* = 7.8 Hz, 1H), 6.80 (d, *J* = 8.0 Hz, 1H), 3.66 (s, 3H), 3.47 (s, 2H), 3.07 - 2.87 (m, 2H), 2.85 - 2.65 (m, 4H).

Note: acetone at 1.17 ppm.

**<sup>13</sup>C NMR** (100 MHz, CDCl<sub>3</sub>): δ = 171.8, 155.5, 154.5, 132.8, 130.7, 129.7, 128.4, 128.1, 127.7, 127.2, 126.9, 119.4, 118.9, 52.2, 40.6, 32.0, 31.6.

**HRMS** (ESI): calcd. for C<sub>17</sub>H<sub>17</sub>N<sub>2</sub>O<sub>2</sub><sup>+</sup> [M+H]<sup>+</sup>: 281.1285; found: 281.1286.

**IR** (thin film): 2950, 1733, 1484, 1257, 1150, 1013, 753 cm<sup>-1</sup>.

**Synthesis and characterization of (11,12-dihydrodibenzo[*c,g*][1,2]diazocin-2-yl)acetic acid (**10**)**

To a stirred solution of compound **9** (15 mg, 0.054 mmol) in a mixture of THF (1.0 mL) and MeOH (0.5 mL) at room temperature was added aq. LiOH (1.0 M, 0.5 mL). The resulting mixture was stirred at room temperature for 17 h. An extra portion of aq. LiOH (1.0 M, 0.5 mL) was added and the reaction mixture was stirred for an additional 1 h. The reaction mixture was acidified with HCl (10% aq. solution) and extracted twice with EtOAc. The combined organic extracts were washed with sat. NaCl, dried over Na<sub>2</sub>SO<sub>4</sub>, filtered and concentrated under reduced pressure to afford compound **10** (14.0 mg, 0.053 mmol, 98%) as a pale yellow solid. The crude product was used in the next step without further purification.

**mp:** 168 - 170 °C.

**TLC** (CH<sub>2</sub>Cl<sub>2</sub>/MeOH, 19:1): R<sub>f</sub> = 0.52 (UV/KMnO<sub>4</sub>).

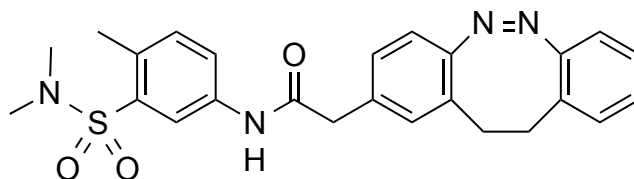
**<sup>1</sup>H NMR** (400 MHz, CDCl<sub>3</sub>): δ = 7.16 - 7.10 (m, 1H), 7.08 - 6.95 (m, 3H), 6.89 (d, J = 1.5 Hz, 1H), 6.84 (d, J = 8.6 Hz, 1H), 6.81 (d, J = 8.0 Hz, 1H), 3.50 (s, 2H), 3.07 - 2.87 (m, 2H), 2.87 - 2.45 (m, 2H).

**<sup>13</sup>C NMR** (100 MHz, CDCl<sub>3</sub>): δ = 176.2, 132.1, 130.8, 130.8, 129.7, 128.5, 128.0, 127.8, 127.8, 127.3, 126.9, 119.5, 119.0, 40.3, 32.0, 31.6.

**HRMS** (ESI): calcd. for C<sub>16</sub>H<sub>13</sub>N<sub>2</sub>O<sub>2</sub><sup>-</sup> [M-H]<sup>-</sup>: 265.0983; found: 265.0984.

**IR** (thin film): 2923, 1709, 1260, 1153, 755 cm<sup>-1</sup>.

**Synthesis and characterization of 2-(11,12-dihydrodibenzo[*c,g*][1,2]diazocin-2-yl)-*N*-[3-(dimethylsulfamoyl)-4-methylphenyl]acetamide (CLOGO)**



To a solution of compound **10** (14.0 mg, 0.053 mmol, 1.0 equiv) and compound **11**<sup>4</sup> (13.5 mg, 0.0630 mmol, 1.2 equiv) in CH<sub>2</sub>Cl<sub>2</sub> (4 mL) at room temperature was added EDCI hydrochloride (40.3 mg, 0.210 mmol, 4.0 equiv) and DMAP (32.1 mg, 0.263 mmol, 5.0 equiv). The resulting mixture was stirred at room temperature for 29 h. The reaction mixture was diluted with CH<sub>2</sub>Cl<sub>2</sub>, washed with HCl (5% aq. solution), sat. aq. NaHCO<sub>3</sub> and sat. NaCl. The organic layer was dried over Na<sub>2</sub>SO<sub>4</sub>, filtered and concentrated under reduced pressure. Purification by flash column chromatography on silica gel eluting with *i*-Hex/EtOAc (7:3 → 1:1) afforded compound CLOGO (14.0 mg, 0.030 mmol, 57%) as a pale yellow solid.

**TLC** (*i*-Hex/EtOAc, 1:1): R<sub>f</sub> = 0.26 (UV/KMnO<sub>4</sub>).

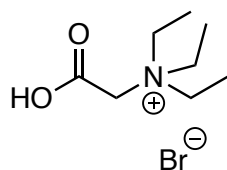
**<sup>1</sup>H NMR** (400 MHz, CDCl<sub>3</sub>): δ = 7.75 (d, *J* = 2.2 Hz, 1H), 7.62 (dd, *J* = 8.3, 2.2 Hz, 1H), 7.25 – 7.20 (m, *J* = 8.2 Hz, 2H), 7.15 (td, *J* = 7.6, 1.5 Hz, 1H), 7.10 (dd, *J* = 8.0, 1.5 Hz, 1H), 7.02 (td, *J* = 8.0, 2.2 Hz, 1H), 7.00 – 6.94 (m, 2H), 6.88 – 6.81 (m, 2H), 3.59 (s, 2H), 3.07 – 2.89 (m, 2H), 2.86 – 2.70 (m, 8H), 2.55 (s, 3H).

**<sup>13</sup>C NMR** (100 MHz, CDCl<sub>3</sub>): δ = 169.1, 155.6, 155.0, 136.3, 135.9, 133.7, 133.5, 132.9, 130.9, 129.8, 129.5, 128.1, 127.9, 127.4, 127.0, 124.1, 120.9, 119.9, 118.9, 44.1, 37.3, 31.9, 31.6, 20.2.

**HRMS** (ESI, *m/z*): calcd. for C<sub>25</sub>H<sub>27</sub>N<sub>4</sub>O<sub>3</sub>S<sup>+</sup> [(M+H)<sup>+</sup>], 463.1798; found 463.1800.

**UV-Vis**: λ<sub>max</sub> = 405 nm (500 μM in DMSO).

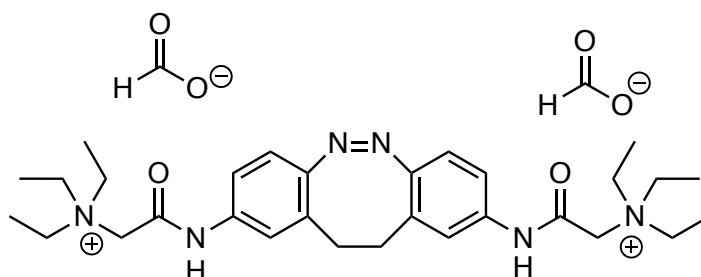
**IR** (thin film): 3312, 2923, 1668, 1592, 1526, 1489, 1389, 1322, 1142, 956, 733, cm<sup>-1</sup>.

***N*-(carboxymethyl)-*N,N*-diethylethanammonium bromide (12)**

2-Ethoxy-*N,N,N*-triethyl-2-oxoethan-1-ammonium bromide<sup>5</sup> (3.00 g, 11.2 mmol) was dissolved in water (20 mL) and HBr (33% in acetic acid, 12 mL) was added. The reaction mixture was heated to 60°C for 12 h and conversion was monitored by NMR spectroscopy. The solvent was removed *in vacuo*. To the crude mixture of white crystals and an orange oil, was added DCM, which dissolved the orange oil under sonication. The white crystalline solid was filtered off. This process was repeated once to yield **12** (1.77 g, 7.39 mmol, 66%) as white crystalline solid.

**<sup>1</sup>H NMR** (400 MHz, CDCl<sub>3</sub>): δ = 14.00 (s, br, 1H), 4.22 (s, 2H), 3.49 (q, J = 7.2 Hz, 6H), 1.21 (t, J = 7.2 Hz, 9H). Note: the broad singlet at 14.00 only integrates to 0.5.

**<sup>13</sup>C NMR** (100 MHz, CDCl<sub>3</sub>): δ = 166.5, 54.9, 53.6, 7.4.

**(Z)-2,2'-((11,12-dihydrodibenzo[c,g][1,2]diazocine-2,9-diyl)bis(azanediy))-bis(*N,N,N*-triethyl-2-oxoethan-1-amonium) bisformate (**CQAQ** • 2FA)**

**12** (54.4 mg, 0.227 mmol, 2.0 equiv) and TBTU (76.4 mg, 0.238 mmol, 2.1 equiv) were dissolved in DMF (2.5 mL) and DIPEA (200  $\mu$ L, 148 mg, 1.15 mmol, 10.2 equiv) was added. 11,12-dihydrodibenzo[c,g][1,2]diazocine-2,9-diamine<sup>6</sup> (27.0 mg, 0.113 mmol, 1.0 equiv) in DMF (0.5 mL) was added and the reaction mixture was stirred overnight. Due to incomplete conversion a premixed solution of **12** (40.8 mg, 0.170 mmol, 1.5 equiv), TBTU (54.6 mg, 0.170 mmol, 1.5 equiv) and DIPEA (80  $\mu$ L, 59.4 mg, 0.459 mmol, 4.1 equiv) was added to the reaction mixture and stirred for 5 h. The crude reaction mixture was passed over a C-18 column (H<sub>2</sub>O + 0.1% FA, then MeCN + 0.1% FA) to remove the DMF. The product containing fractions were combined, the solvent evaporated, and the crude material was purified by reverse phase HPLC (5  $\rightarrow$  20% H<sub>2</sub>O/MeCN + 0.1% FA) to yield **CQAQ** • 2FA (14.0 mg, 22.8  $\mu$ mol, 21%) as a dark yellow solid.

**LCMS** (5  $\rightarrow$  100% MeCN/H<sub>2</sub>O, 5 min):  $R_t$  = 2.2 min ( $m/z$  = 261.2).

**<sup>1</sup>H NMR** (400 MHz, d<sub>6</sub>-DMSO):  $\delta$  = 11.87 (s, 2H), 8.36 (s, 4H), 7.45 - 7.42 (m, 4H), 6.86 (d,  $J$  = 9.0 Hz, 2H), 4.31 (s, 4H), 3.49 (q,  $J$  = 7.2 Hz, 12H), 2.91 - 2.65 (m, 4H), 1.23 (t,  $J$  = 7.1 Hz, 19H). Note: MeCN at 2.1 ppm and the integral of the formate is integrating to 4.

**<sup>13</sup>C NMR** (100 MHz, d<sub>6</sub>-DMSO):  $\delta$  = 164.8, 162.2, 151.4, 137.0, 128.7, 120.3, 119.5, 118.2, 56.2, 53.9, 31.2, 7.4. Note: MeCN at 1.0 ppm.

**HRMS** (ESI,  $m/z$ ): calcd. for C<sub>30</sub>H<sub>46</sub>N<sub>6</sub>O<sub>2</sub><sup>2+</sup> [ $M^{2+}$ ], 261.1836; found 261.1848.

**UV-Vis**:  $\lambda_{max}$  = 410 nm (50  $\mu$ M in DMSO).

**IR** (thin film): 2985, 1687, 1594, 1483, 1400, 1343, 1011, 900, 814 cm<sup>-1</sup>.

## References

- (1) Mourof, A.; Fehrentz, T.; Le Feuvre, Y.; Smith, C. M.; Herold, C.; Dalkara, D.; Nagy, F.; Trauner, D.; Kramer, R. H. Rapid Optical Control of Nociception with an Ion-Channel Photoswitch. *Nat. Methods* **2012**, *9*, 396–402.
- (2) Fehrentz, T.; Huber, F. M. E.; Hartrampf, N.; Bruegmann, T.; Frank, J. A.; Fine, N. H. F.; Malan, D.; Danzl, J. G.; Tikhonov, D. B.; Sumser, M.; et al. Optical Control of L-Type Ca<sup>2+</sup> Channels Using a Diltiazem Photoswitch. *Nat. Chem. Biol.* **2018**, *1*.
- (3) Joshi, D. K.; Mitchell, M. J.; Bruce, D.; Lough, A. J.; Yan, H. Synthesis of Cyclic Azobenzene Analogues. *Tetrahedron* **2012**, *68*, 8670–8676.
- (4) Barber, D. M.; Schönberger, M.; Burgstaller, J.; Levitz, J.; Weaver, C. D.; Isacoff, E. Y.; Baier, H.; Trauner, D. Optical Control of Neuronal Activity Using a Light-Operated GIRK Channel Opener (LOGO). *Chem. Sci.* **2016**, *7*, 2347–2352.
- (5) Messadi, A.; Mohamadou, A.; Boudesocque, S.; Dupont, L.; Fricoteaux, P.; Nguyen-Van-Nhien, A.; Courty, M. Syntheses and Characterisation of Hydrophobic Ionic Liquids Containing Trialkyl(2-Ethoxy-2-Oxoethyl)Ammonium or N-(1-Methylpyrrolidyl-2-Ethoxy-2-Oxoethyl)Ammonium Cations. *J. Mol. Liq.* **2013**, *184*, 68–72.
- (6) Samanta, S.; Qin, C.; Lough, A. J.; Woolley, G. A. Bidirectional Photocontrol of Peptide Conformation with a Bridged Azobenzene Derivative. *Angew. Chem. Int. Ed.* **2012**, *51*, 6452–6455.

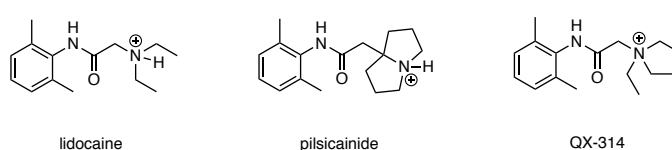


## Diazocine Derivatives of Lidocaine, Pilsicainide and QX-314 for the Optical Control of Cardiac Function.

### Introduction

The term arrhythmia describes irregularities in the heartbeat frequency. Tachycardia (too fast) and bradycardia (too slow) describe the two phenomenological antipodes.<sup>1</sup> Arrhythmias can also be categorized by the site of origin, which are mainly atrial, ventricular or occurring on junctions and nodes. They can be caused by a variety of factors, like genetic predispositions,<sup>2</sup> environmental conditions,<sup>3</sup> or through prescription or non-prescription drugs.<sup>4</sup> Likewise, treatment of arrhythmia can be accomplished with drugs that block, activate or antagonize ionotropic and metabotropic receptors or ion channels. These include, but are not limited to: adrenergic receptors, adenosine receptors (ARs), acetylcholine receptors, sodium channels, inwardly rectifying potassium (GIRK) channels, and L-type calcium channels.<sup>5</sup> The choice of pharmacological therapy is usually indicated by the type of arrhythmia, the site of origin, and disease-related contraindications.<sup>5</sup>

Lidocaine (Figure II.1) is a well-known local anesthetic and has antiarrhythmic properties. Its congener pilsicainide (Figure II.1), is also a marketed drug for the latter indication.<sup>5,6</sup> The basic tertiary amines makes them open-channel blockers, meaning the ammonium ion is able to block the pore after initial voltage-gated opening of Na<sup>+</sup> and K<sup>+</sup> channels.<sup>7</sup> With its fast on- and off-kinetics, lidocaine and related open-channel blockers are well-suited for use in photopharmacology, which has already been successfully demonstrated.<sup>8-11</sup>



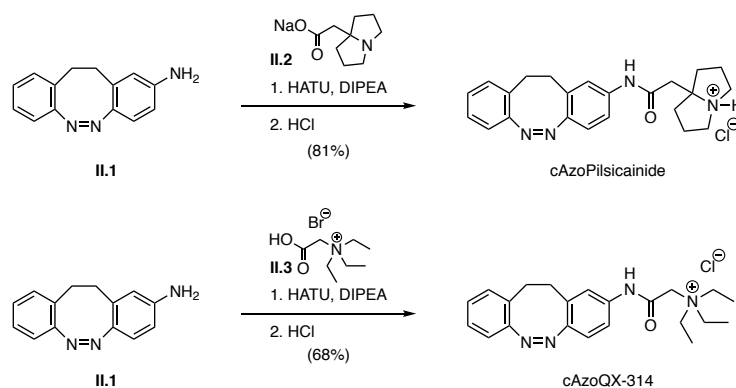
**Figure II.1: Molecular structures of the open-channel blockers lidocaine, pilsicainide and QX-314.** Lidocaine and pilsicainide are protonated under physiological conditions at pH = 7.4

Optical control of cardiac function, however, has so far been mainly investigated using agonists of the muscarinic acetylcholine receptors<sup>12</sup> and L-type calcium channels.<sup>13</sup> The use of photoswitchable ion channel blockers<sup>14-16</sup> in Langendorff preparations<sup>17</sup> or cardiomyocytes has been hampered by their activity in the dark. We wanted to overcome this limitation through the incorporation of a diazocine

photoswitch.<sup>18</sup> We envisaged to synthesize photoswitchable sodium channel blockers for the control of cardiac function. In addition to a cyclic azobenzene version of lidocaine (CAL), we sought to synthesize a diazocine derivative of pilsicainide and an analog based on the known tool-compound QX-314 (Figure II.1),<sup>19</sup> like it has recently been published by Ellis-Davies and co-workers.<sup>20</sup>

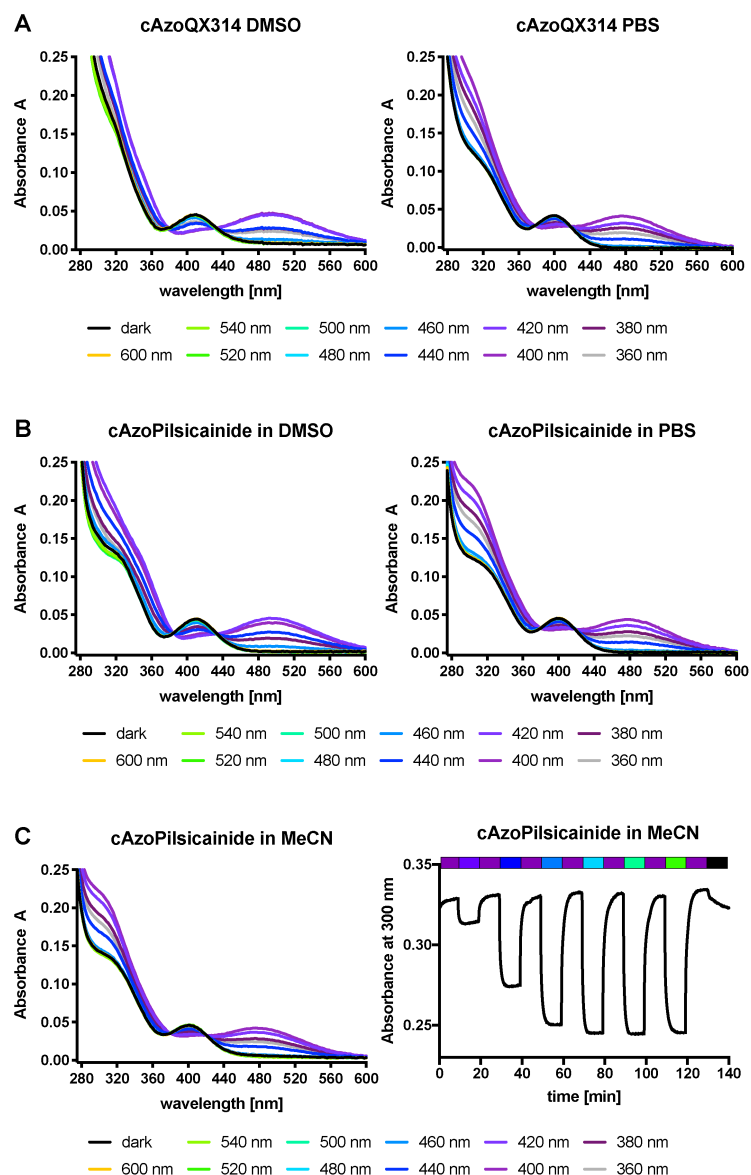
## Results and Discussion

Our cyclic azobenzene derivative of lidocaine (CAL) has been published recently.<sup>18</sup> cAzoPilsicainide was synthesized in two steps from the aniline **II.1**<sup>21</sup> by HATU mediated peptide coupling reaction with the corresponding acid **II.2**. cAzoQX-314 was synthesized analogously (Scheme II.1). The acid coupling partner **II.3** was synthesized in two steps starting from ethylbromoacetate and triethylamine.<sup>18,22</sup> Both cAzoPilsicainide and cAzoQX-314 were isolated as chloride salts in good yield.



**Scheme II.1: chemical synthesis of cAzoQX-314 and cAzoPilsicainide.**

The optimal wavelength to isomerize cAzoQX-314 and cAzoPilsicainide to their thermodynamically less favored *E*-isomer, was determined in DMSO and PBS at room temperature. Both diazocine photoswitches are most effectively isomerized using 400 nm light, in MeCN (cAzoPilsicainide only), DMSO and PBS (Figure II.2). Alternating 400 nm with ascending wavelengths ( $x + 20$  nm) in MeCN, showed that wavelengths between 480 nm and at least 520 nm are suitable to isomerize the compound back into its thermodynamically favored *Z*-state. These results are in coherence with other diazocine photoswitches.<sup>18,20,23</sup> Both compounds are now under investigation by Dr. Timm Fehrentz and Dr. Nicole Gördlt in the lab of Prof. Dr. Nikolaj Klöcker, where they are tested in Langendorff Heart preparations, together with CAL.



**Figure II.2: Determination of the optimal switching wavelength of cAzo-QX-314 and cAzoPilsicainide.** A: cAzoQX-314 is best isomerized to the *E*-isomer with 400 nm light (50  $\mu$ M in DMSO and PBS) B: cAzoPilsicainide is best isomerized to the *E*-somer with 400 nm light. C: cAzoPilsicainide is best isomerized to the *E*-isomer with 400 nm light. Isomerization to the *Z*-isomer is best achieved with 480 nm to 520 nm light (50  $\mu$ M, light illumination in DMSO and PBS for 10 min, in MeCN for 5 min).

## References

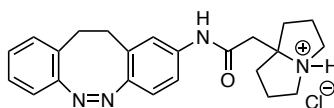
- (1) Spodick, D. H.; Raju, P.; Bishop, R. L.; Rifkin, R. D. Operational Definition of Normal Sinus Heart Rate. *Am. J. Cardiol.* **1992**, *69*, 1245–1246.
- (2) Bennett, P. B.; Yazawa, K.; Makita, N.; George, A. L. Molecular Mechanism for an Inherited Cardiac Arrhythmia. *Nature* **1995**, *376*, 683–685.
- (3) Peters, A.; Liu, E.; Verrier, R. L.; Schwartz, J.; Gold, D. R.; Mittleman, M.; Baliff, J.; Oh, J. A.; Allen, G.; Monahan, K.; et al. Air Pollution and Incidence of Cardiac Arrhythmia. *Epidemiology* **2000**, *11*, 11.
- (4) Barnes, B. J.; Hollands, J. M. Drug-Induced Arrhythmias. *Crit. Care Med.* **2010**, *38*, 188.
- (5) Roden, D. M.; Darbar, D.; Kannankeril, P. J. Antiarrhythmic Drugs. In *Cardiovascular Medicine*; Willerson, J. T., Wellens, H. J. J., Cohn, J. N., Holmes, D. R., Eds.; Springer London: London, **2007**; 2085–2102.
- (6) Strupczewski, J. D.; Ellis, D. B. Chapter 33. To Market, To Market - 1991. In *Annual Reports in Medicinal Chemistry*; Bristol, J. A., Ed.; Academic Press, **1992**; *27*, 321–337.
- (7) Xia, Y.; Chen, E.; Tibbits, D. L.; Reilley, T. E.; McSweeney, T. D. Comparison of Effects of Lidocaine Hydrochloride, Buffered Lidocaine, Diphenhydramine, and Normal Saline after Intradermal Injection. *J. Clin. Anesth.* **2002**, *14*, 339–343.
- (8) Tochitsky, I.; Helft, Z.; Meseguer, V.; Fletcher, R. B.; Vessey, K. A.; Talias, M.; Denlinger, B.; Malis, J.; Fletcher, E. L.; Kramer, R. H. How Azobenzene Photoswitches Restore Visual Responses to the Blind Retina. *Neuron* **2016**, *92*, 100–113.
- (9) Tochitsky, I.; Polosukhina, A.; Degtyar, V. E.; Gallerani, N.; Smith, C. M.; Friedman, A.; Van Gelder, R. N.; Trauner, D.; Kaufer, D.; Kramer, R. H. Restoring Visual Function to Blind Mice with a Photoswitch That Exploits Electrophysiological Remodeling of Retinal Ganglion Cells. *Neuron* **2014**, *81*, 800–813.
- (10) Polosukhina, A.; Litt, J.; Tochitsky, I.; Nemargut, J.; Sychev, Y.; De Kouchkovsky, I.; Huang, T.; Borges, K.; Trauner, D.; Van Gelder, R. N.; et al. Photochemical Restoration of Visual Responses in Blind Mice. *Neuron* **2012**, *75*, 271–282.
- (11) Laprell, L.; Tochitsky, I.; Kaur, K.; Manookin, M. B.; Stein, M.; Barber, D. M.; Schön, C.; Michalakis, S.; Biel, M.; Kramer, R. H.; et al. Photopharmacological Control of Bipolar Cells Restores Visual Function in Blind Mice. *J. Clin. Invest.* **2017**, *127*, 2598–2611.
- (12) Riefolo, F.; Matera, C.; Garrido-Charles, A.; Gomila, A. M. J.; Sortino, R.; Agnetta, L.; Claro, E.; Masgrau, R.; Holzgrabe, U.; Batlle, M.; et al. Optical Control of Cardiac Function with a Photoswitchable Muscarinic Agonist. *J. Am. Chem. Soc.* **2019**, *141*, 7628–7636.
- (13) Fehrentz, T.; Huber, F. M. E.; Hartrampf, N.; Bruegmann, T.; Frank, J. A.; Fine, N. H. F.; Malan, D.; Danzl, J. G.; Tikhonov, D. B.; Sumser, M.; et al. Optical Control of L-Type Ca<sup>2+</sup> Channels Using a Diltiazem Photoswitch. *Nat. Chem. Biol.* **2018**, 764–767.
- (14) Banghart, M. R.; Mourot, A.; Fortin, D. L.; Yao, J. Z.; Kramer, R. H.; Trauner, D. Photochromic Blockers of Voltage-Gated Potassium Channels. *Angew. Chem. Int. Ed.* **2009**, *48*, 9097–9101.
- (15) Mourot, A.; Kienzler, M. A.; Banghart, M. R.; Fehrentz, T.; Huber, F. M. E.; Stein, M.; Kramer, R. H.; Trauner, D. Tuning Photochromic Ion Channel Blockers. *ACS Chem. Neurosci.* **2011**, *2*, 536–543.

- (16) Leippe, P.; Winter, N.; Sumser, M.; Trauner, D. Optical Control of a Delayed Rectifier and a Two-Pore Potassium Channel with a Photoswitchable Bupivacaine. *ACS Chem. Neurosci.* **2018**, *9*, 2886-2891.
- (17) Bell, R. M.; Mocanu, M. M.; Yellon, D. M. Retrograde Heart Perfusion: The Langendorff Technique of Isolated Heart Perfusion. *J. Mol. Cell. Cardiol.* **2011**, *50*, 940-950.
- (18) Trads, J.; Hüll, K.; Matsuura, B. S.; Laprell, L.; Fehrentz, T.; Görltdt, N.; Kozek, K. A.; Weaver, C. D.; Klöcker, N.; Barber, D. M.; et al. Sign Inversion in Photopharmacology: Incorporation of Cyclic Azobenzenes in Photoswitchable Potassium Channel Blockers and Openers. *Angew. Chem. Int. Ed.* **2019**, *58*, 15421-15428.
- (19) Strichartz, G. R. The Inhibition of Sodium Currents in Myelinated Nerve by Quaternary Derivatives of Lidocaine. *J. Gen. Physiol.* **1973**, *62*, 37-57.
- (20) Thapaliya, E. R.; Zhao, J.; Ellis-Davies, G. C. R. Locked-Azobenzene: Testing the Scope of a Unique Photoswitchable Scaffold for Cell Physiology. *ACS Chem. Neurosci.* **2019**, *10*, 2481-2488.
- (21) Samanta, S.; Qin, C.; Lough, A. J.; Woolley, G. A. Bidirectional Photocontrol of Peptide Conformation with a Bridged Azobenzene Derivative. *Angew. Chem. Int. Ed.* **2012**, *51*, 6452-6455.
- (22) Messadi, A.; Mohamadou, A.; Boudesocque, S.; Dupont, L.; Fricoteaux, P.; Nguyen-Van-Nhien, A.; Courty, M. Syntheses and Characterisation of Hydrophobic Ionic Liquids Containing Trialkyl(2-Ethoxy-2-Oxoethyl)Ammonium or N-(1-Methylpyrrolidyl-2-Ethoxy-2-Oxoethyl)Ammonium Cations. *J. Mol. Liq.* **2013**, *184*, 68-72.
- (23) Cabré, G.; Garrido-Charles, A.; González-Lafont, À.; Moormann, W.; Langbehn, D.; Egea, D.; Lluch, J. M.; Herges, R.; Alibés, R.; Busqué, F.; et al. Synthetic Photoswitchable Neurotransmitters Based on Bridged Azobenzenes. *Org. Lett.* **2019**, *21*, 3780-3784.



## Experimental Procedures

### cAzoPilsicainide



Tetrahydro-1H-pyrrolizine-7a(5H)-acetic acid (**II.2**) (227 mg, 1.34 mmol, 1.5 eq) was dissolved in DMF (4.5 mL), and TBTU (575.2 mg, 1.79 mmol, 2.0 eq) was added followed by DIPEA (390  $\mu$ L, 2.24 mmol, 2.5 eq). The solution was stirred for 30 min at room temperature and subsequently added to a solution of aniline **II.1** (200 mg, 0.896 mmol, 1.0 eq) in DMF (4.5 mL). The reaction was stirred at room temperature overnight. The reaction was diluted with 10% aq. NaCl (100 mL) and extracted with EtOAc (4 x 50 mL). The combined organic layers were washed with 10% aq. NaCl to remove remaining DMF followed by sat. NaHCO<sub>3</sub> (1 x 50 mL), dried over Na<sub>2</sub>SO<sub>4</sub> and concentrated *in vacuo*. The crude material was purified by silica gel column chromatography (0  $\rightarrow$  10 % MeOH/DCM) to yield the target molecule with minor impurities as yellow oil. The oil was dissolved in dioxane (4.0 mL) and HCl in dioxane (4 M, 269  $\mu$ L, 4.0 eq) was added and the mixture was stirred for 30 min. the solvent was removed under reduced pressure and the material was purified by column chromatography (0  $\rightarrow$  20% MeOH/DCM) to yield cAzoPilsicainide (297 mg, 0.723 mmol, 81%) as a yellow solid.

**<sup>1</sup>H-NMR:** (400 MHz, CDCl<sub>3</sub>)  $\delta$  = 10.62 (s, 1H), 7.60 (dd, J = 8.4, 1.7 Hz, 1H), 7.45 (d, J = 1.8 Hz, 1H), 7.16 - 7.08 (m, 1H), 7.05 - 6.95 (m, 2H), 6.81 (dd, J = 11.2, 8.3 Hz, 2H), 3.73 (dt, J = 11.9, 6.9 Hz, 2H), 3.07 (s, 2H), 2.98 - 2.67 (m, 6H), 2.42 - 2.26 (m, 2H), 2.10 - 1.86 (m, 7H).

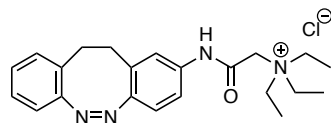
**<sup>13</sup>C-NMR:** (100 MHz, CDCl<sub>3</sub>)  $\delta$  = 166.9, 155.5, 151.6, 137.3, 129.7, 128.8, 128.1, 127.0, 126.6, 120.3, 119.9, 118.9, 118.0, 79.5, 55.7, 44.3, 37.0, 32.0, 31.4, 24.1.

**HRMS:** (ESI) calcd. for C<sub>23</sub>H<sub>27</sub>N<sub>4</sub>O<sup>+</sup> [M+H]<sup>+</sup>: 375.2179, found: 375.2179.

**IR** (neat, cm<sup>-1</sup>): 3386, 3047, 2957, 2641, 1681, 1591, 1609, 1485, 1904, 1312, 1247, 1199, 1154, 1030, 894, 823, 755.

**R<sub>f</sub>** = 0.4 (10%MeOH/DCM)

**R<sub>t</sub>** = 2.64 min (5  $\rightarrow$  100% MeCN/H<sub>2</sub>O; + 0.1% FA; 5 min)

**cAzoQX-314**

Betaine **II.3** (323 mg, 1.34 mmol, 1.5 eq) was dissolved in DMF (4.5 mL) and TBTU (575.2 mg, 1.79 mmol, 2.0 eq) was added followed by DIPEA (780  $\mu$ L, 4.48 mmol, 5.0 eq). The solution was stirred for 30 min at room temperature and subsequently added to a solution of aniline **II.1** (200 mg, 0.896 mmol, 1.0 eq) in DMF (4.5 mL). The reaction was stirred at room temperature overnight. The reaction mixture was passed over a short C-18 reverse phase silica gel column (10  $\rightarrow$  50 % MeCN/H<sub>2</sub>O; + 0.1% formic acid). The solvent was removed under reduced pressure and the crude material was purified by RP-HPLC (5  $\rightarrow$  35% MeCN/H<sub>2</sub>O; + 0.1% formic acid). Product containing fractions were combined and the solvent was removed under reduced pressure. An excess of HCl (4 M in MeOH) was added and all volatiles were removed *in vacuo*. The obtained residue was purified by silica gel column chromatography (0  $\rightarrow$  20% MeOH/DCM) to yield cAzoQX-314 (243 mg, 0.606 mmol, 68%) as a yellow solid.

**<sup>1</sup>H-NMR:** (400 MHz, MeOD)  $\delta$  = 7.38 (dd,  $J$  = 8.5, 2.0 Hz, 1H), 7.34 (d,  $J$  = 2.0 Hz, 1H), 7.21 - 7.13 (m, 1H), 7.06 (d,  $J$  = 4.0 Hz, 2H), 6.87 - 6.78 (m, 2H), 4.07 (s, 2H), 3.63 (q,  $J$  = 7.3 Hz, 6H), 2.99 - 2.79 (m, 4H), 1.36 (t,  $J$  = 7.2 Hz, 9H).

**<sup>13</sup>C-NMR:** (100 MHz, MeOD)  $\delta$  = 162.9, 156.8, 153.5, 137.7, 130.8, 129.5, 128.4, 127.9, 122.0, 120.7, 119.6, 119.5, 57.5, 55.8, 32.9, 32.2, 8.0.

**HRMS:** (ESI) calcd. for C<sub>22</sub>H<sub>29</sub>N<sub>4</sub>O<sup>+</sup> [M]<sup>+</sup>: 365.2336, found: 365.2330.

**IR** (neat, cm<sup>-1</sup>): 2990, 1987, 1594, 1548, 1480, 1401, 1314, 1265, 1221, 1155, 1057, 9501, 822, 730.

**R<sub>f</sub>** = 0.7 (20% MeOH/DCM)

**R<sub>t</sub>** = 2.63 min (5  $\rightarrow$  100% MeCN/H<sub>2</sub>O; + 0.1%; FA, 5 min)



## Oxidative Approach Enables Efficient Access to Cyclic Azobenzenes.

Martin S. Maier,<sup>†,‡</sup> Katharina Hüll,<sup>†,‡,a</sup> Martin Reynders,<sup>†,‡,a</sup> Bryan S. Matsuura,<sup>†,‡,a</sup> Philipp Leippe,<sup>†,§</sup> Tongil A. Ko,<sup>‡</sup> Lukas Schäffer<sup>†</sup> and Dirk Trauner<sup>\*,†,‡</sup>

<sup>†</sup>Department of Chemistry and Center for Integrated Protein Science (CIPSM), Ludwig Maximilian University Munich, 81377 Munich, Germany

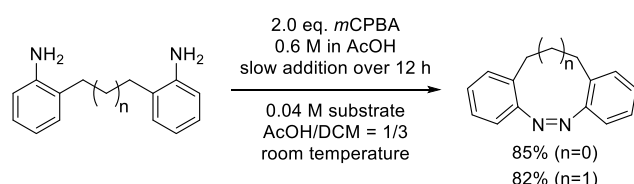
<sup>‡</sup>Department of Chemistry, New York University, New York, New York 10003, United States  
Present Addresses

<sup>§</sup> Present address: Department of Chemical Biology, Max Planck Institute for Medical Research, 69120 Heidelberg, Germany

<sup>a</sup>: these authors contributed equally

Reprinted (adapted) with permission from Maier, M. S.; Hüll, K.; Reynders, M.; Matsuura, B. S.; Leippe, P.; Ko, T.; Schäffer, L.; Trauner, D. Oxidative Approach Enables Efficient Access to Cyclic Azobenzenes. *J. Am. Chem. Soc.* **2019**, *141* (43), 17295-17304. Copyright 2019 American Chemical Society.

### Abstract

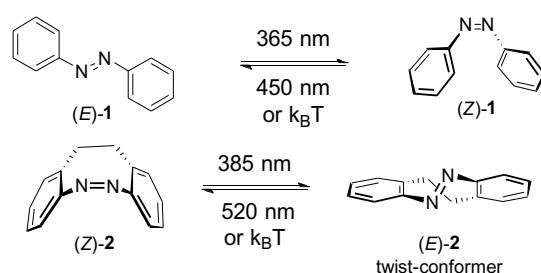


Azobenzenes are versatile photoswitches that have found widespread use in a variety of fields, ranging from photopharmacology to the material sciences. In addition

to regular azobenzenes, the cyclic diazocines have recently emerged. Although diazocines have fascinating conformational and photophysical properties, their use has been limited by their synthetic accessibility. Herein, we present a general, high-yielding protocol that relies on the oxidative cyclization of dianilines. In combination with a modular substrate synthesis, it allows for rapid access to diversely functionalized diazocines on gram scales. Our work systematically explores substituent effects on the photoisomerization and thermal relaxation of diazocines. It will enable their incorporation into a wide variety of functional molecules, unlocking the full potential of these emerging photoswitches. The method can be applied to the synthesis of a new cyclic azobenzene with a nine-membered central ring and distinct properties.

## Introduction

Azobenzene photoswitches contain a diaryl diazene moiety that can exist either in an (*E*) or in a (*Z*) configuration. In general, the elongated (*E*) or *trans*-form is thermodynamically preferred and the bent (*Z*) or *cis* form is subject to gradual thermal isomerization (Scheme 1). The half-lives for this thermal relaxation range from picoseconds to days,<sup>1</sup> and photoswitches whose thermal relaxation is comparatively slow are often designated as “bistable”. Irradiation of azobenzenes with monochromatic light establishes a photostationary state (PSS) that depends on both the extinction coefficients of the two isomers at a particular wavelength and their respective isomerization quantum yields. Photostationary states as high as (*Z*)/(*E*)  $\approx$  90/10 can be achieved, but are generally lower.<sup>2</sup> Because of their photostability, facile synthesis, and relatively low molecular weight, azobenzenes have become the photoswitch of choice in many applications. They have been successfully incorporated in photopharmaceuticals, in photoresponsive functional materials, such as polymers and hydrogels, or in catalysts that can be controlled with light.<sup>3</sup>

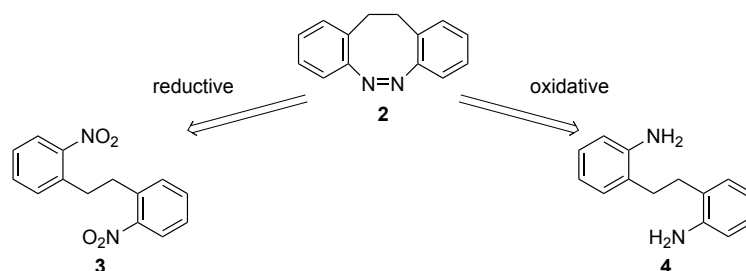


**Scheme 1. Photoswitching of azobenzene (1)<sup>1</sup> compared to diazocine (2)<sup>5a</sup>**

Despite their long history and popularity, there is still a need to tailor the properties of azobenzenes. One important direction is red shifting the action spectra while maintaining thermal bistability.<sup>4</sup> Significant progress toward this goal has been made by developing tetra-ortho-substituted azobenzenes, but these are marked by increased steric bulk and changes in dipole moment, which can interfere with their function. Another desirable feature are highly biased PSS, for both wavelengths that favor the (*Z*) isomer and those that give preference to the (*E*) isomer. Although thermal relaxation can revert azobenzenes fully to their (*E*) form, this process can be slow with bistable variants and the faster photochemical conversion to the (*E*) isomer is generally incomplete. Lastly, it can be useful to employ photoswitches that are bent in their default form, that is, in the absence of light, and become elongated upon irradiation. This is especially true in photopharmacology where tonic “dark activity” is often undesirable.

Cyclic azobenzenes, wherein the diazene unit is embedded in an eight-membered ring, meet many of these challenges. The parent compound of this class is

5,6-dihydrodibenzo[*c,g*]-[1,2]diazocine (“diazocine”), which had already been discovered at the beginning of the last century.<sup>6a</sup> It received little attention, until recently, when its remarkable photophysical properties were recognized by Herges, Temps, and co-workers.<sup>5</sup> Contrary to regular azobenzenes, the thermodynamically preferred form of diazocines is the (*Z*) isomer because of the increased strain that the ring system imposes on the (*E*) isomer (Scheme 1). In addition, diazocines can be switched to more than 90% of the (*E*) isomer and quantitatively back to the (*Z*) isomer by irradiation with visible wavelengths around 400 and 520 nm, respectively.<sup>5a</sup>



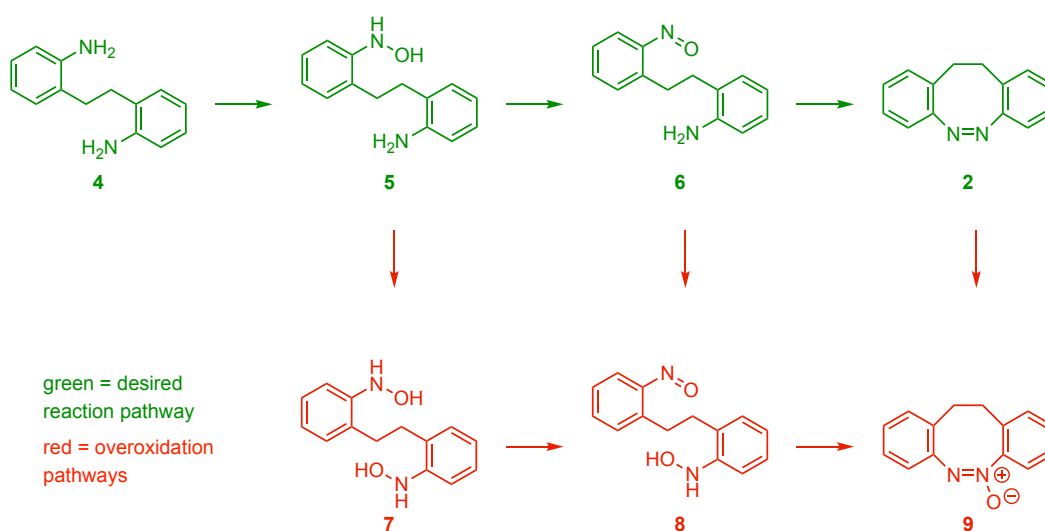
**Scheme 2. Synthetic approaches towards the diazocine core.**

Despite these remarkable photophysical properties, diazocines have found relatively few applications to date. The reason for this has been their limited availability due to lack of effective synthetic methods.<sup>5a,6-9</sup> Most reported diazocines have been synthesized by a reductive cyclization of 2,2'-dinitrodibenzyls (Scheme 2).<sup>6,7,9a-c</sup> Apart from low yields, a major limitation of the reductive cyclization is that it does not give straightforward access to unsymmetrical diazocines.<sup>7,9a-c</sup> In addition to the reductive cyclization approach, conditions based on oxidation of 2,2'-ethylenedianilines or hydroxyl-amine-aniline analogs have been reported, albeit with low-to-mediocre yields.<sup>8,9cd</sup> Very recently, an oxidative strategy has been applied in a synthesis of a photoswitchable glutamate derivative.<sup>8b</sup> However, the potential of the oxidative cyclization of 2,2'-ethylenedianilines has not been investigated systematically and a practical, generally applicable, and high-yielding protocol for the synthesis diazocines has been lacking.

## Results and Discussion

**1. Mechanistic Considerations.** Our investigation commenced with the optimization of reaction conditions for the oxidative cyclization of the commercially available 2,2'-ethylenedianiline **4** to the corresponding diazocine **2**. We considered four key requirements which needed to be fulfilled to make this an effective process (Scheme 3). First, it would be necessary to selectively oxidize 2,2'-ethylenedianiline **4** to 2-amino-2'-nitrosodibenzyl **6**, without formation of the dihydroxylamine **7** from intermediate **5**. Second, the cyclization of the nitrosoaniline **6** to diazocine **2** via a

Baeyer-Mills reaction has to be faster than the oxidation to nitrosohydroxylamine **8**. Third, the product diazocine **2** must not be oxidized further to form the azoxy compound **9**. Fourth, intermolecular reactions leading to oligomeric or polymeric structures need to be suppressed. While temperature, concentration, and rate of addition of the oxidant are important considerations for optimization with respect to the second and fourth conditions, the other two conditions are more dependent on the inherent reactivity of the substrates. On the basis of our mechanistic scheme, we expected slow addition of the oxidant to be the most important parameter.



**Scheme 3. Mechanistic considerations for an oxidative cyclization approach towards diazocines.**

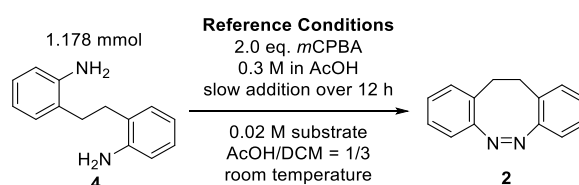
*2. Development of Reaction Conditions.* Most commonly, the oxidation of anilines to nitrosobenzenes is performed in a biphasic system of dichloromethane (DCM)/water using oxone as an oxidant. The ensuing Baeyer-Mills reaction is typically performed in acetic acid and mixtures of acetic acid with DCM or toluene. As these two sets of conditions are not compatible, we decided to use typical solvent systems of the Baeyer-Mills reaction, such as pure acetic acid or acetic acid/DCM, as the solvent and peroxycarboxylic acids as the oxidant. To simplify the workup, we initially focused on peracetic acid.

After optimization of oxidant addition rate, stoichiometry, and substrate concentrations, we were able to obtain diazocine **2** by the slow addition of 2 equiv of peracetic acid in acetic acid to a dilute solution of 2,2'-ethylenediamine **4** within a 12 hour period in a yield of more than 70%, which was already substantially superior to any previously reported value.<sup>5a,6-9</sup> However, we noticed several inconsistencies during the course of this initial optimization. The most important observations were a noticeably fluctuating yield, a highly detrimental effect of

copper salts, and an unexpected relation between the obtained yields and the equivalents of peracetic acid that were employed.

We suspected the underlying issue to be the presence of considerable amounts of hydrogen peroxide in the commercial peracetic acid solutions. This “dormant oxidant” may either directly participate in the oxidation or slowly be transformed to peracetic acid, thus resulting in an incorrect stoichiometry. The effect can be expected to be more prominent under conditions that should activate the hydrogen peroxide (e.g., the presence of transition metal ions), which agrees with the observed results. Additionally, we confirmed the reactivity of hydrogen peroxide in acetic acid by treatment of 2,2'-ethylenedianiline with urea hydrogen peroxide as a source of “dry” hydrogen peroxide. This led to the slow formation of diazocine but could unfortunately not be developed into a synthetically practical procedure.

**Table 1. Optimization of the oxidative cyclization of 2,2'-ethylenedianiline - selected examples**



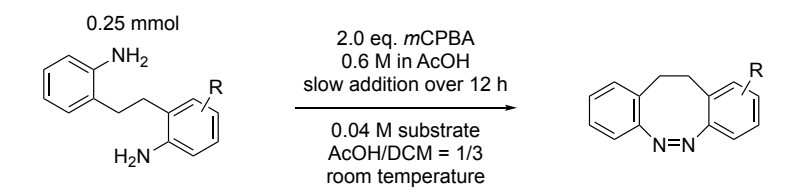
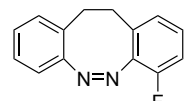
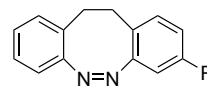
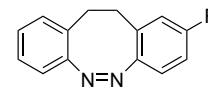
Entry	Variation from Reference Conditions	Yield <sup>a</sup>
1	none	86%
2	Solvent AcOH	75%
3	Solvent AcOH/DCM = 1/1	86%
4	Solvent AcOH/PhMe = 1/1	84%
5	Solvent AcOH/DCM = 1/9	81%
6	Entry 4 + 40 °C	82%
7	Entry 4 + 60 °C	76%
8	0.01 M substrate	85%
9	0.04 M substrate	85%
10	Entry 9 + 0.6 M <i>m</i> CPBA	86%
11	Entry 10 + 0.06 M substrate	79%
12	Entry 10 + catalytic Cu(II)	59%

<sup>a</sup>Determined by <sup>1</sup>H-NMR spectroscopy with dimethyl terephthalate as internal standard.

Building on the knowledge gained from our initial optimization with peracetic acid, we continued our search for optimal reaction conditions (Table 1). We did not perform an additional screening on the rate of addition as well as equivalents of oxidant and continued with the theoretically ideal stoichiometry of 2 equiv of oxidant and the addition of oxidant within 12 hours. To identify a more reliable oxidant, we compared the most commonly employed commercially available

percarboxylic acids. Among peracetic acid, *meta*-chloroperoxybenzoic acid (*m*CPBA), and magnesium monoperoxyphthalate (MMPP), we found that *m*CPBA performed best. The use of *m*CPBA to prepare nitrosobenzenes from anilines is well precedented.<sup>10</sup> A screen of solvent mixtures revealed that diluting acetic acid with DCM or toluene resulted in a further increased yield, although a sizable fraction of acetic acid was necessary for optimal results. Increasing the temperature proved to be slightly detrimental to the reaction outcome, while higher concentrations of the *m*CPBA solution (0.6 M) and substrate (0.04 M) were tolerated without a negative effect on the yield.

**Table 2. Oxidative cyclization yields of monosubstituted 2,2'-ethylene-dianilines**

		
 <p><b>19</b>, 46%</p>	 <p><b>2</b>, 85% R = H</p> <p><b>10</b>, 85% R = Me</p> <p><b>11</b>, 82% R = CH<sub>2</sub>CO<sub>2</sub>Me</p> <p><b>12</b>, 74% R = CH<sub>2</sub>NHBoc</p> <p><b>13</b>, 58% R = CF<sub>3</sub></p> <p><b>14</b>, 74% R = CO<sub>2</sub>Me</p> <p><b>15</b>, 39% R = CN</p> <p><b>16</b>, 68% R = OMe</p> <p><b>17</b>, 73% R = OAc</p> <p><b>18</b>, 62% R = F</p>	 <p><b>20</b>, 82% R = Me</p> <p><b>21</b>, 82% R = CH<sub>2</sub>CO<sub>2</sub>Me</p> <p><b>22</b>, 69% R = CH<sub>2</sub>NHBoc</p> <p><b>23</b>, 37% R = CF<sub>3</sub></p> <p><b>24</b>, 32% R = CO<sub>2</sub>Me</p> <p><b>25</b>, n.d.<sup>c</sup> R = CN</p> <p><b>26</b>, 29% R = OMe</p> <p><b>27</b>, 61% R = OAc</p> <p><b>28</b>, 77% R = F</p> <p><b>29</b>, 81% R = Br</p> <p><b>30</b>, 76% R = I</p>

<sup>a</sup>Isolated yields are reported. <sup>b</sup>4.28 mmol scale. <sup>c</sup>Not determined. <sup>d</sup>7.90 mmol scale. <sup>e</sup>7.69 mmol scale.

Copper salts were reported to be beneficial to the formation of azobenzenes by oxidative dimerization of anilines with peroxy acids.<sup>11</sup> However, we observed that addition of copper acetate reduced the yield and an increased amount of unreacted starting material remained. This supports our theory that our reaction does not depend on trace amounts of metal salts. Finally, we confirmed that the undesired overoxidation of diazocine **2** to azoxy compound **9** does not occur in the presence of unreacted dianiline **4** (see Supporting Information). This finding supports our initial reasoning about the importance of slow addition. Azoxy

compound **9** does not primarily result from oxidation of desired product **2**, but forms through nitroso-hydroxylamine **8** (see Scheme 3).

**3. Investigation of Reaction Scope.** After optimizing reaction conditions for the parent system, we applied our best protocol to various monosubstituted 2,2'-ethylenedianilines (compounds **10–30**, Table 2). For a majority of these compounds, we obtained the cyclization products in yields similar to or only slightly lower than those observed for the parent system. Substituents that only weakly affect the electronic nature of the arenes, such as most halogens and alkyl groups, had virtually no effect on the yield of the cyclization. The yields observed for the fluorinated compounds followed a trend, decreasing from *para*- to *meta*- to *ortho*-fluoro substitution.

**Table 2. Oxidative cyclization yields of monosubstituted 2,2'-ethylenedianilines**

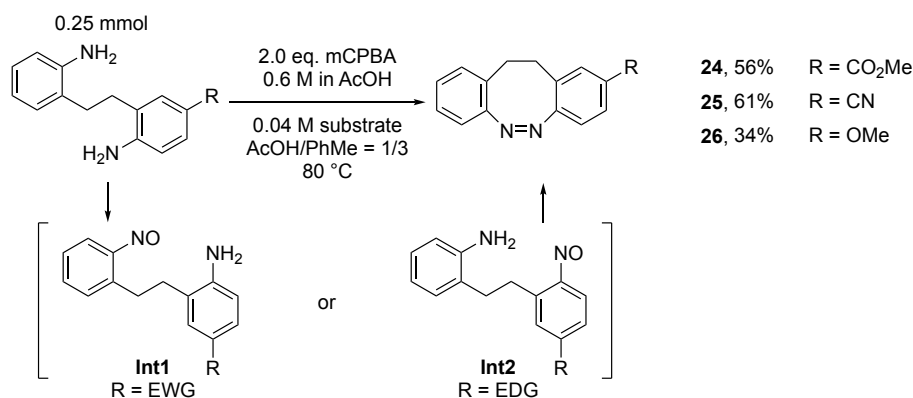
<p><b>19</b>, 46%</p>	<p><b>2</b>, 85% R = H</p> <p><b>10</b>, 85% R = Me</p> <p><b>11</b>, 82% R = CH<sub>2</sub>CO<sub>2</sub>Me</p> <p><b>12</b>, 74% R = CH<sub>2</sub>NHBoc</p> <p><b>13</b>, 58% R = CF<sub>3</sub></p> <p><b>14</b>, 74% R = CO<sub>2</sub>Me</p> <p><b>15</b>, 39% R = CN</p> <p><b>16</b>, 68% R = OMe</p> <p><b>17</b>, 73% R = OAc</p> <p><b>18</b>, 62% R = F</p>	<p><b>20</b>, 82% R = Me</p> <p><b>21</b>, 82% R = CH<sub>2</sub>CO<sub>2</sub>Me</p> <p><b>22</b>, 69% R = CH<sub>2</sub>NHBoc</p> <p><b>23</b>, 37% R = CF<sub>3</sub></p> <p><b>24</b>, 32% R = CO<sub>2</sub>Me</p> <p><b>25</b>, n.d.<sup>c</sup> R = CN</p> <p><b>26</b>, 29% R = OMe</p> <p><b>27</b>, 61% R = OAc</p> <p><b>28</b>, 77% R = F</p> <p><b>29</b>, 81% R = Br</p> <p><b>30</b>, 76% R = I</p>

<sup>a</sup>Isolated yields are reported. <sup>b</sup>4.28 mmol scale. <sup>c</sup>Not determined. <sup>d</sup>7.90 mmol scale. <sup>e</sup>7.69 mmol scale.

Notably, the presence of both strongly electron-withdrawing and electron-donating substituents resulted in a significant reduction in yield. *para*-Substituted substrates gave generally lower yields than the corresponding *meta*-substituted ones, both for electron-withdrawing and electron-donating substituents. We reasoned that low-yielding substrates would undergo a highly selective oxidation

of one of the two amino groups (see Scheme 4). In the corresponding intermediates **Int1** and **Int2**, the more nucleophilic aniline moiety is now oxidized, which leaves a deactivated aniline moiety in **Int1** and a deactivated nitrosobenzene moiety in **Int2**. This would make the subsequent Baeyer-Mills cyclization comparatively slow in both cases. Additionally, the tendency for intermolecular, instead of intramolecular, reactions would be increased, as the unreacted substrates (not shown) carry a more reactive amino group than the corresponding intermediates **Int1** and **Int2**. These considerations led us to explore whether, instead of the slow addition protocol, one-batch addition and increased temperatures might be beneficial in these cases.

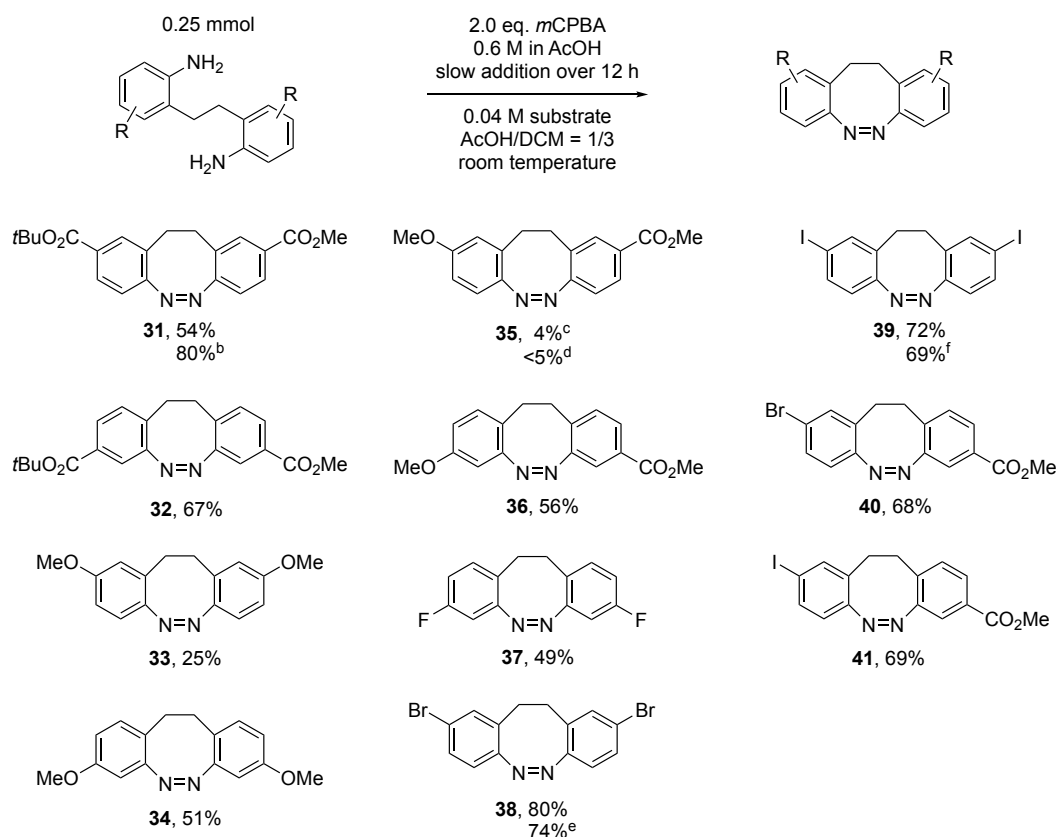
**Scheme 4. Synthesis of diazocines using a one-batch addition protocol and presumed intermediates due to oxidation selectivity**



We tested this alternative protocol for the three compounds that were the most problematic for our slow addition method (Scheme 4). Gratifyingly, we now obtained the known<sup>7a</sup> *para*-cyano diazocine **25** in a respectable yield of 61%. The yield of the *para*-methyl ester diazocine **24** also was improved substantially to 56%. However, the *para*-methoxy product **26** was obtained only with slightly increased yield. A different factor seems to affect the yield in this case. The most probable explanation is the reactivity of *para*-alkoxy-nitrosobenzenes toward nucleophilic aromatic substitution.<sup>12</sup>

Next, we turned our attention toward disubstituted diazocines (compounds **31–41**, Table 3). Considering the large amount of combinatorial possibilities, we selected only a small number of examples. Our main goals were to obtain an appropriate set of disubstituted diazocines to investigate the photophysical properties of substituted diazocines, to determine the limitations of our approach, and to explore how substituent effects of the monosubstituted substrates extend to disubstituted substrates.



**Table 3. Oxidative cyclization yields<sup>a</sup> of disubstituted 2,2'-ethylenedianilines**

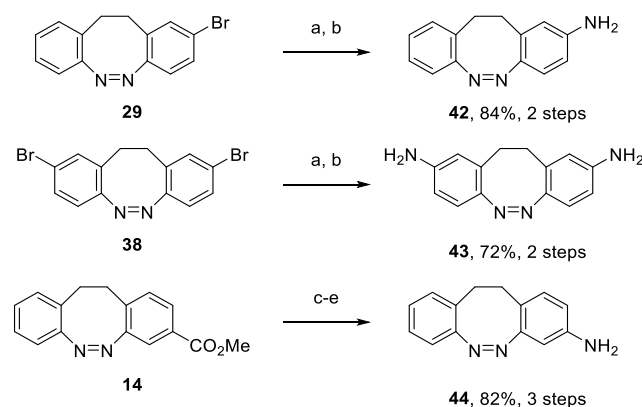
<sup>a</sup>Isolated yields are reported. <sup>b</sup>80 °C. <sup>c</sup>0.832 mmol scale, 0.03 M substrate. <sup>d</sup>0.156 mmol scale, batch addition protocol. <sup>e</sup>7.16 mmol scale. <sup>f</sup>7.87 mmol scale.

Employing our standard slow addition protocol, we observed that for most compounds the substituent effects were additive. The yields decreased compared to those of the corresponding monosubstituted analogs but remained in a synthetically useful range. A clear exception was found in the *para*-diester compound **31**, where the yield was significantly increased compared to that of the *para*-ester **24**. Performing the reaction at higher temperature further increased the yield to 80%, a level similar to that of the parent compound **5**. An example that shows a limitation of our approach, for both the slow and batch addition protocols, is the push–pull diazocine **35**. Still, we were able to obtain a sufficient quantity for photophysical characterization of this diazocine.

**4. Late-Stage Derivatization.** Despite the large number of mono- and disubstituted diazocines accessible with our oxidative method, it could not readily deliver amino-substituted diazocines. Therefore, we developed a practical late-stage derivatization (Scheme 5). The known *para*-amino-diazocine **42**<sup>7c</sup> was synthesized in 84% yield from the *para*-bromo diazocine **29**<sup>7a</sup> by Buchwald-Hartwig coupling with *tert*-butyl carbamate, followed by deprotection of the *tert*-butyloxycarbonyl (Boc) group by treatment with tetra-*N*-butylammonium fluoride (TBAF).<sup>13</sup> Although

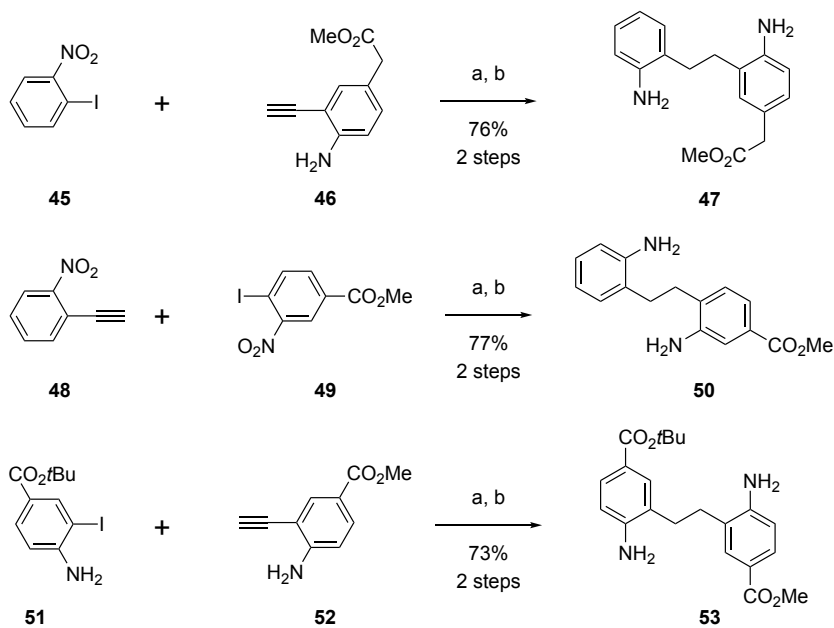
the trifluoro-acetic acid (TFA) protocol could be used, TBAF afforded a cleaner product and avoided side reactions resulting from the presence of *tert*-butyl cations. The known *para*-diamino diazocine **43**<sup>6e</sup> was prepared in 72% yield in an identical fashion to the monoamino compound **42**. To access the *meta*-amino diazocine **44**, we started from *meta*-ester **14**. Ester hydrolysis followed by Curtius rearrangement in the presence of allyl alcohol, followed by removal of the allyloxycarbonyl (Alloc) group, gave the desired product **44** in 82% yield.

### Scheme 5. Late-stage diversification



a) BocNH<sub>2</sub>, Cs<sub>2</sub>CO<sub>3</sub>, XanthPhos Pd G3, 1,4-dioxane, 100 °C; b) TBAF·3H<sub>2</sub>O, Me-THF, 70 °C; c) LiOH, THF/MeOH/H<sub>2</sub>O; d) Allyl alcohol, DPPA, Et<sub>3</sub>N, PhMe, RT to 80 °C; e) pyrrolidine, Pd(PPh<sub>3</sub>)<sub>4</sub>, DCM.

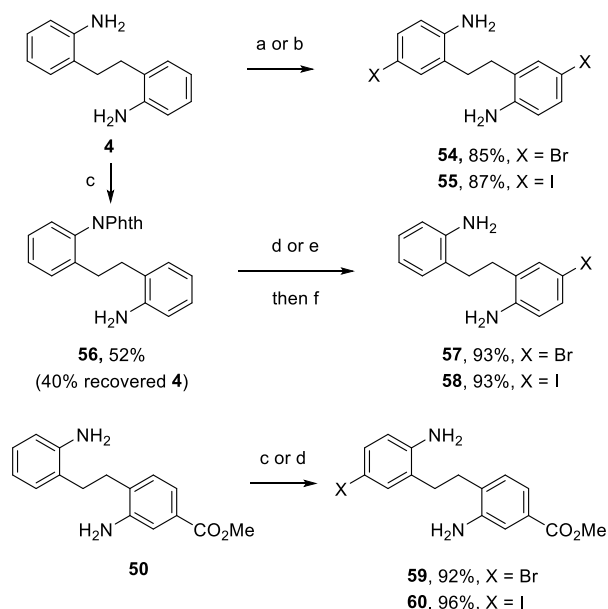
### Scheme 6. Example 2,2'-ethylenedianiline syntheses by Sonogashira coupling/hydrogenation



a) PdCl<sub>2</sub>(PPh<sub>3</sub>)<sub>2</sub>, CuI, Et<sub>3</sub>N, THF, RT; then TMS-acetylene; b) H<sub>2</sub>, Pd/C, MeOH/DCM.

**5. Cyclization Substrate Synthesis.** A major advantage of the oxidative cyclization approach is the relative ease with which the requisite 2,2'-ethylenedianilines can be accessed. To this end, we developed a Sonogashira coupling strategy, which is exemplified in Scheme 6. Several combinations of alkynes and aryl halides are possible, pending on the nature of the coupling partners and their oxidation states. The first and most useful variant is based on the coupling of a 2-aminophenylacetylene with 2-iodonitrobenzene, as depicted for dianiline **47**. The second route proceeds through the coupling of a 2-nitrophenylacetylene with a 2-iodonitrobenzene, which is exemplified for compound **50**. In some cases, however, considerable decomposition of the 2-nitrophenylacetylenes was observed under the conditions of the Sonogashira coupling.<sup>14</sup> The third route involved the coupling of a 2-amino-phenylacetylene with a 2-iodoaniline as shown for dianiline **53**. This route is less general, as 2,2'-diamino-diphenylacetylenes tend to undergo cyclization to indoles.<sup>15</sup> Regarding the hydrogenation of the diarylacetylenes, we found that substrates must not contain any contaminants remaining from the Sonogashira reaction. Otherwise, we observed significant catalyst poisoning, resulting in unreasonably high catalyst loading. Since our cross-coupling approach involves a hydrogenation step that is not compatible with aryl halides, we prepared several halo-substituted dianilines via electrophilic aromatic substitution (Scheme 7).

### Scheme 7. Halogenation of 2,2'-ethylenedianilines

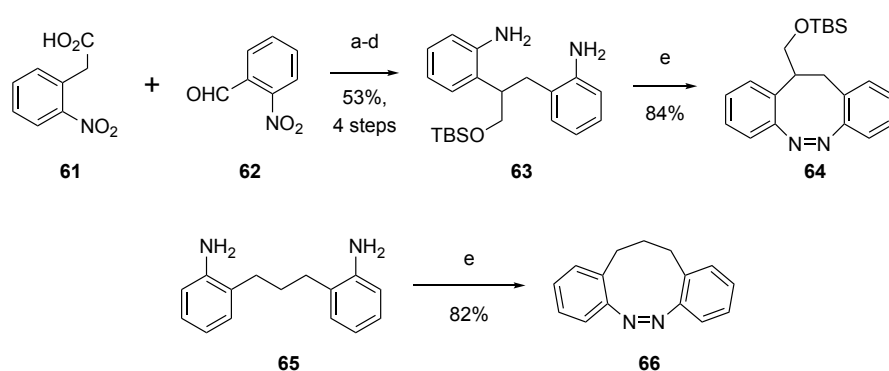


a) NBS (2 equiv), DMSO; b) NIS (2 equiv), DMSO; c) phthalic anhydride, BSA, PhMe, reflux; d) NBS (1 equiv), DMSO; e) NIS (1 equiv), DMSO; f)  $\text{N}_2\text{H}_4 \cdot \text{H}_2\text{O}$ , THF, reflux.

While the synthesis of the precursors leading to the symmetrical *para*-dihalogenated compounds **54** and **55** was straightforward, access to precursors of monohalo diazocines was more difficult. We initially used an unselective, statistical halogenation followed by purification *via* chromatography and precipitation. However, to avoid the tedious separation of mono- and dihalogenation products, as well as unreacted substrate, we developed a more scalable and practical sequence. Desymmetrization of the commercially available dianiline **4** by protection of one amino group as the phthalimide, followed by highly selective halogenation of phthalimide **56** and deprotection, allowed to access the desired products **57** and **58** without any chromatographic purification. Selective halogenation could also be achieved by exploiting electronic differences in substituted dianilines. We tested this on ester **50**, which afforded the halogenation products **59** and **60** in high yield and without any undesired isomers.

6. *New Cyclic Azobenzenes*. Cyclic azobenzenes may be substituted not only on their arene moieties but also on their central ring.<sup>7f,8b</sup> Indeed, several heterodiazocines have recently emerged.<sup>9</sup> Confident in our new methodology, we have begun to explore cyclic azobenzenes with substitutions on the central bridge and with an increased ring size (Scheme 8).

**Scheme 8. Synthesis of new cyclic azobenzenes**



a)  $\text{Ac}_2\text{O}$ ,  $\text{Et}_3\text{N}$ , neat,  $50\text{ }^\circ\text{C}$ ; b)  $\text{EtOCOCl}$ ,  $\text{Et}_3\text{N}$ , THF then  $\text{NaHB}_4$ ,  $\text{H}_2\text{O}$ ; c) TBSOTf, 2,6-lutidine, DCM; d)  $\text{H}_2$ , Pd/C, MeOH/DCM; e) *m*CPBA in AcOH (2 equiv, slow addition), AcOH/DCM = 1/3.

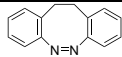
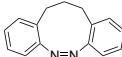
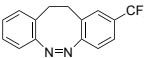
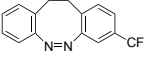
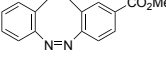
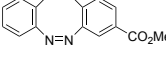
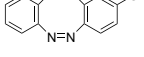
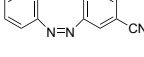
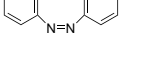
Condensation<sup>16</sup> of aldehyde **62** with acid **61**, followed by carboxylic acid reduction, *tert*-butyldimethylsilyl (TBS) protection, and hydrogenation afforded cyclization precursor **63** in 53% yield over four steps. The oxidative cyclization of the dianiline **63** to diazocine **64** proceeded in 84% yield, which is virtually the same efficiency as that for the unsubstituted parent system. The dianiline **65**<sup>17</sup> could be cyclized equally well to diazocine **66**, affording the first cyclic azobenzene that features a propylene bridge in the central ring.

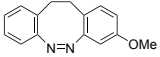
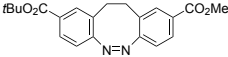
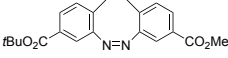
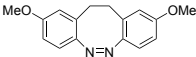
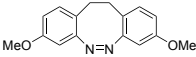
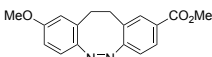
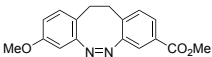
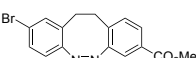
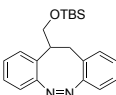
Both syntheses of dianilines **63** and **65** can in principle be adapted to allow access to symmetric and nonsymmetric substitution on the aromatic rings as well as to the halogenation strategy that we described in the previous section. Thus, the syntheses of diazocine **64** and diazonine **66** may be used as blueprints for new types of azobenzenes with interesting photophysical and pharmacological features.

**7. Ultraviolet–Visible (UV–Vis) Spectroscopic Characterization.** With more than 40 cyclic azobenzenes in hand, we turned toward their photophysical characterization to gain insight into the effects of substituents and backbone modifications on UV–vis spectra and photoswitching behavior. To determine the optimal wavelength ( $\lambda_{\text{opt}}$ ) for a high (*Z*)/(*E*) ratio, we illuminated a 50  $\mu\text{M}$  DMSO solution of each compound for 10 min in 20 nm increments from 540 to 360 nm and measured the resulting absorption spectra (Figures S4–S8).

For all diazocines, the lowest energy absorption was not significantly affected by substitution and typically centered around 400 nm for the (*Z*) isomer and around 490 nm for the (*E*) isomer. Like the parent compound **2**, the majority of the diazocines can be isomerized most efficiently to their thermodynamically less stable (*E*) form with 400 nm light (Table 4 and Table S1). A slightly longer wavelength of 420 nm or even 440 nm was required in the case of several electron-rich diazocines. The backbone-substituted compound **64** also did not show special features compared to the parent system **2**.

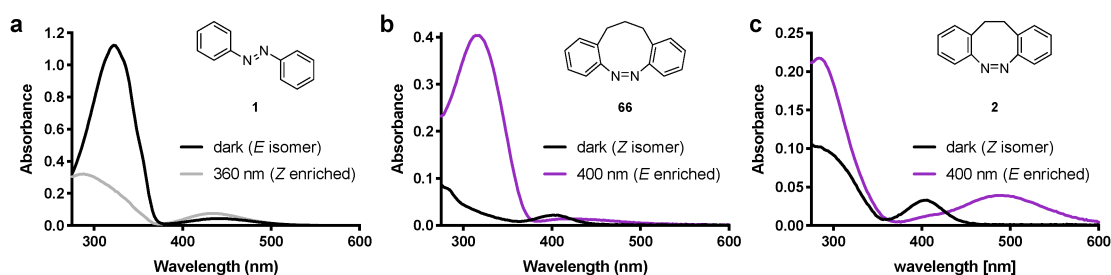
**Table 4. Photophysical properties of selected cyclic azobenzenes.**

Compound	$\lambda_{\text{opt}}^{\text{a}}$	$T_{1/2}$	PSS ( <i>Z</i> / <i>E</i> ) <sup>b</sup>
 <b>2</b>	400 nm	9.4 h	12/88 <sup>c</sup>
 <b>66</b>	400 nm	n.d. <sup>e</sup>	14/86 <sup>c</sup>
 <b>23</b>	400 nm	51 min	12/88 <sup>c</sup>
 <b>13</b>	400 nm	4.3 h	14/86 <sup>c</sup>
 <b>24</b>	400 nm	14 min	14/86 <sup>c</sup>
 <b>14</b>	380 nm	6.7 h	14/86 <sup>c</sup>
 <b>25</b>	400 nm	6 min	15/85 <sup>c</sup>
 <b>15</b>	400 nm	3.3 h	14/86 <sup>c</sup>
 <b>26</b>	420 nm	3.0 h	33/67 <sup>c</sup>

	<b>16</b>	420 nm	10.4 h	45/55 <sup>d</sup>
	<b>31</b>	400 nm	24 min	14/86 <sup>c</sup>
	<b>32</b>	400 nm	6.0 h	15/85 <sup>c</sup>
	<b>33</b>	420 nm	3.5 h	32/68 <sup>c</sup>
	<b>34</b>	420 nm	11.2 h	55/45 <sup>d</sup>
	<b>35</b>	420 nm	2.2 min	55/45 <sup>c</sup>
	<b>36</b>	420 nm	7.5 h	52/48 <sup>d</sup>
	<b>40</b>	400 nm	4.7 h	14/86 <sup>c</sup>
	<b>64</b>	400 nm	14.2 h	19/81 <sup>c</sup>

<sup>a</sup>For (*Z*) to (*E*) switching, determined by UV-Vis spectroscopy. <sup>b</sup>For (*Z*) to (*E*) switching, determined by <sup>1</sup>H-NMR spectroscopy in DMSO-*d*<sub>6</sub>. <sup>c</sup>390 nm. <sup>d</sup>415 nm. <sup>e</sup>Not determined, no measurable isomerization within two weeks

Finally, we also investigated the spectra and switching of the nine-membered diazocine **66**. Analogously to the eight-membered system, it could be isomerized to the (*E*) isomer with 400 nm irradiation and back to the (*Z*) isomer using 520 nm light. Interestingly, compared to that of the (*E*) isomer of diazocine **2**, the spectrum of the (*E*) isomer of diazocine **66** exhibits a notably higher absorbance for the band corresponding to the  $\pi\pi^*$ -transition, which also is found at a longer wavelength of 316 nm. Therefore, the spectrum of (*E*) diazocine resembles that of a regular (*E*) azobenzene, while the (*Z*) diazocine spectrum is similar to that of (*Z*) diazocine (Figure 1 and Table S3).



**Figure 1. Comparison of UV-Vis spectra** of a) azobenzene **1** b) diazocine **66** and c) diazocine **2** in the dark and under illumination. All spectra in DMSO, 50  $\mu$ m.

The comparatively small effect of substituents on the lowest energy absorption band of diazocines are not surprising since it results from a  $n\pi^*$ -excitation. A stronger effect was observed for the next absorption band at shorter wavelengths, which corresponds to a  $\pi\pi^*$ -transition. This band was notably red-shifted for diazocines carrying electron-donating substituents (e.g., compounds **16** and **26**) or with a push–pull substitution. Increased overlap of the bands corresponding to  $\pi\pi^*$ -transitions of the (*E*) forms with the  $n\pi^*$ -transitions of the (*Z*) forms might be contributing to the poorer switching behavior observed for these diazocines (see PSS investigation by NMR spectroscopy below).

**8. Thermal Relaxation.** In respect to thermal relaxation, we observed broad variability (Table 4 and Table S1) with trends similar to regular azobenzenes. Thermal relaxation was monitored in 50  $\mu\text{M}$  DMSO solution at 25 °C over a period of 24 h. Reduced half-lives for the (*E*) isomer were observed with electron-withdrawing groups in the *meta*-position as well as both electron-withdrawing and electron-donating groups in the *para*-position. Strong electron-withdrawing groups and push–pull substitution in *para*-position resulted in rapidly relaxing photoswitches. When comparing the effect of a substituent in *meta*-position to that of the same substituent in *para*-position, we found that *para*-substituted compounds were generally more affected than their *meta*-substituted counterparts. To determine the effect of water on the relaxation rates, we also investigated solutions in phosphate-buffered saline (PBS)/DMSO mixtures for three selected compounds (see Table S2). Surprisingly, we observed up to 2 or 3 times longer half-lives upon increasing the fraction of the aqueous component in the solvent mixture.

None of the aromatic substitutions resulted in a major increase in relaxation times compared to the parent system **2**. However, improved bistability could be achieved by changes in the central ring system. An increased thermal stability of the (*E*) form was observed for the ethylene-bridge-substituted diazocine **64**. For diazocine **66** no relaxation could be observed at room temperature after enrichment of the (*E*) isomer by both UV–vis (40 h) as well as NMR measurements (2 weeks). Still, diazocine **66** did fully relax to the (*Z*) isomer upon prolonged storage in the solid state in the dark. The high bistability of diazocine **66** is expected to be connected to the low energy difference between (*E*) and (*Z*) isomer, which is a consequence of the longer three-carbon bridge ( $\Delta G_{Z \rightarrow E} = 10.6$  kJ/mol in the gas phase and 17.4 kJ/mol in DMSO, see Tables S14 and S15).

**9. PSS Investigation by NMR Spectroscopy.** Having determined the best switching wavelengths and relaxation times, we turned toward determination of the PSS compositions (Table 4 and Table S1, Figure S3). We chose to determine the PSS as (*Z*)/(*E*) ratio observed with one-pulse  $^1\text{H}$  NMR spectroscopy measurements of 10 mM solutions in  $\text{DMSO-d}_6$ . The samples were first measured before illumination, then after 30 s of illumination with a 390 nm high-power light-emitting diode (LED), and after successive 30 s of illumination with a 520 nm high-power LED (Prizmatix).

We additionally tested the (*Z*)-to-(*E*) isomerization with a 460 nm high-power LED and a 415 nm Mic-LED (Prizmatix) for the compounds either where we had determined an optimal switching wavelength higher than 400 nm in our UV–vis experiments or where we observed poor (*Z*)/(*E*) ratios (>20/ 80) after 390 nm illumination.

Despite handling the samples without precautions to avoid exposure to ambient light, most samples contained no detectable (*E*) isomer and all diazocines showed an initial (*Z*)/(*E*) ratio of at least 97/3. For the (*Z*)-to-(*E*) isomerization upon irradiation with violet/blue light, we observed distinct differences between individual groups of diazocines. With the majority of the compounds, we were able to establish a PSS between 12/88 and 19/81. This included compounds with electron-withdrawing substituents, backbone substitution, some electron-donating substituents, and weakly interacting substituents, such as alkyl or halogen, which all showed excellent PSS. However, methoxy and most amino substituents lowered the (*E*) isomer fraction and more of the (*Z*) isomer remained. Furthermore, the push–pull combination of methoxy and methyl ester led to a drastic PSS deterioration, regardless of their position on the ring.

The photoisomerization from the (*E*) to the (*Z*) form was found to be highly effective for all diazocines. In all cases illumination with 520 nm led to quantitative isomerization to the thermodynamically favored (*Z*) form. This is an important distinction from regular azobenzenes. In summary, all tested diazocines can be reversibly isomerized with visible light.

For diazonine **66** we observed no (*E*) isomer before illumination and a PSS of 14/86 after illumination with 390 nm light. While this result for the (*Z*)-to-(*E*) isomerization was virtually identical to that of the unsubstituted diazocine **2**, a nonquantitative conversion was observed for the (*E*)-to-(*Z*) photoisomerization of diazonine **66** and only a (*Z*)/(*E*) ratio of 89/11 could be achieved with 520 nm light. Still, the value for the photoisomerization to the thermodynamically preferred form is better for diazonine **66** than for azobenzene **1**, which exhibited at best a PSS of 83/17 for (*Z*)-to-(*E*) isomerization in DMSO (Table S4).

Finally, it is important to mention that we had to reduce the concentration of azobenzene **1** for our NMR experiments from 10 to 1 mM, as we had observed a very low (*E*)-to-(*Z*) conversion at 10 mM. Probably this issue results from incomplete sample penetration during irradiation due to complete absorption of light. This issue is alleviated by the lower extinction coefficients of diazocine and diazonine. Thus, at least at the present concentrations, both diazocines and the diazonine allow for a more rapid and efficient establishment of the PSS than regular azobenzenes.



## Conclusion

The broad implementation of diazocines as photoswitches with useful new functional properties has been limited by their poor synthetic accessibility. With this work, we have shown that the oxidative cyclization of dianilines can largely overcome this limitation. In combination with a modular cross-coupling approach to furnish the cyclization substrates, as well as late-stage functionalization, the oxidative protocol gives access to a wide variety of diazocines that are substituted on one or both aromatic rings. Additionally, we were able to prepare a diazocine with a nine-membered ring and a diazocine substituted on the ethylene bridge, which we consider the vanguard of new types of photoswitches.

Furthermore, we have compared the photophysical properties and thermal relaxation data of diazocines. This allowed us to identify substitution patterns that are tolerated without affecting the useful photoswitch characteristics of the parent system as well as the patterns that should be avoided because of their detrimental effects. On the basis of our results, it is also possible to tune the thermal relaxation of diazocines over a broad range. This knowledge will facilitate the choice of diazocines in a variety of applications.

**Supporting Information.**

Synthetic procedures and characterization data; Photophysical characterization; Optimization of reaction conditions; Synthetic recommendations; Computational data; X-ray crystallographic data for **38**.

"This material is available free of charge via the Internet at <http://pubs.acs.org>."

**Notes**

The authors declare no competing financial interest.

**Acknowledgements**

K.H. thanks the Studienstiftung des deutschen Volkes for a PhD scholarship. B.S.M. thanks the Alexander von Humboldt Foundation for a postdoctoral research fellowship. D.T. was supported by the European Research Council (Advanced Grant 268795) and thanks the Centre for Integrated Protein Science Munich (CIPSM). M.R. and D.T. thank the German Research Foundation (DFG) for financial support (SFB749). We further acknowledge National Institutes of Health (NIH) support (OD016343). T.A.K. thanks New York University for a MacCracken fellowship. The Shared Instrumentation Facility at the New York University Department of Chemistry was supported by a NIH Research Facilities Improvement Award (C06 RR-16572-01) and a NIH S10 grant (OD016343). The authors thank Dr. Chin Lin for his assistance with NMR spectroscopy and mass spectrometry and Christopher Arp for programming the MATLAB interface to control the monochromator.

**Abbreviations**

DCM, dichloromethane; THF, tetrahydrofuran; DMSO, dimethyl sulfoxide; *m*CPBA, *meta*-chloroperoxybenzoic acid; MMPP, magnesium monoperoxyphthalate; TBAF, tetra-*N*-butylammonium fluoride; NIS, *N*-iodosuccinimide; NBS, *N*-bromosuccinimide; TFA, trifluoroacetic acid; BSA, Bis(trimethylsilyl)acetamide; Boc, *tert*-butyloxycarbonyl; TBS, *tert*-butyldimethylsilyl; Alloc, allyloxycarbonyl; EWG, electron-donating group; EDG, electron-withdrawing group; PSS, photostationary state; UV, ultraviolet; Vis, visible; NMR, nuclear magnetic resonance; LED, light-emitting diode.

## References

- (1) (a) Broichhagen, J.; Frank, J. A.; Trauner, D. A Roadmap to Success in Photopharmacology. *Acc. Chem. Res.* **2015**, *48*, 1947. (b) Garcia-Amoròs, J.; Mearz, B.; Reig, M.; Cuadrado, A.; Blancafort, L.; Samoylova, E.; Velasco, D. Picosecond Switchable Azo Dyes. *Chem. Eur. J.* **2019**, *25*, 7726.
- (2) (a) Bortolus, P.; Monti, S. Cis-Trans Photoisomerization of Azobenzene. Solvent and Triplet Donors Effects. *J. Phys. Chem.* **1979**, *83*, 648. (b) Ito, Y.; Ito, H.; Matsuura, T. Trans-Cis Photoisomerization of *Meta*-(Phenylazo)Azobenzenes. *Tetrahedron Lett.* **1988**, *29*, 563. (c) Fisher, E. Temperature Dependence of Photoisomerization Equilibria. Part I. Azobenzene and the Azonaphthalenes. *J. Am. Chem. Soc.* **1960**, *82*, 3249.
- (3) (a) Beharry, A. A.; Woolley, G. A. Azobenzene Photoswitches for Biomolecules. *Chem. Soc. Rev.* **2011**, *40*, 4422. (b) Szymanski, W.; Beierle, J. M.; Kistemaker, H. A. V.; Velema, W. A.; Feringa, B. L. Reversible Photocontrol of Biological Systems by the Incorporation of Molecular Photoswitches. *Chem. Rev.* **2013**, *113*, 6114. (c) Hüll, K.; Morstein, J.; Trauner, D. In Vivo Photopharmacology. *Chem. Rev.* **2018**, *118*, 10710. (d) Natansohn, A.; Rochon, P. Photoinduced Motions in Azo-Containing Polymers. *Chem. Rev.* **2002**, *102*, 4139. (e) Tomatsu, I.; Peng, K.; Kros, A. Photoresponsive Hydrogels for Biomedical Applications. *Adv. Drug Delivery Rev.* **2011**, *63*, 1257. (f) Blanco, V.; Leigh, D. A.; Marcos, V. Artificial Switchable Catalysts. *Chem. Soc. Rev.* **2015**, *44*, 5341. (g) Göstl, R.; Senf, A.; Hecht, S. Remote-Controlling Chemical Reactions by Light: Towards Chemistry with High Spatio-Temporal Resolution. *Chem. Soc. Rev.* **2014**, *43*, 1982.
- (4) (a) Bléger, D.; Schwarz, J.; Brouwer, A. M.; Hecht, S. O-Fluoroazobenzenes as Readily Synthesized Photoswitches Offering Nearly Quantitative Two-Way Isomerization with Visible Light. *J. Am. Chem. Soc.* **2012**, *134*, 20597. (b) Wendler, T.; Schütt, C.; Näther, C.; Herges, R. Photoswitchable Azoheterocycles via Coupling of Lithiated Imidazoles with Benzenediazonium Salts. *J. Org. Chem.* **2012**, *77*, 3284. (c) Samanta, S.; Babalhavaeji, A.; Dong, M.; Woolley, G. A. Photoswitching of Ortho-Substituted Azonium Ions by Red Light in Whole Blood. *Angew. Chem. Int. Ed.* **2013**, *52*, 14127. (d) Samanta, S.; Beharry, A. A.; Sadovski, O.; McCormick, T. M.; Babalhavaeji, A.; Tropepe, V.; Woolley, G. A. Photoswitching Azo Compounds in Vivo with Red Light. *J. Am. Chem. Soc.* **2013**, *135*, 9777. (e) Weston, C. E.; Richardson, R. D.; Haycock, P. R.; White, A. J. P.; Fuchter, M. J. Arylazopyrazoles: Azoheteroarene Photoswitches Offering Quantitative Isomerization and Long Thermal Half-Lives. *J. Am. Chem. Soc.* **2014**, *136*, 11878. (f) Dong, M.; Babalhavaeji, A.; Samanta, S.; Beharry, A. A.; Woolley, G. A. Red-Shifting Azobenzene Photoswitches for in Vivo Use. *Acc. Chem. Res.* **2015**, *48*, 2662. (g) Konrad, D. B.; Frank, J. A.; Trauner, D. Synthesis of Redshifted Azobenzene Photoswitches by Late-Stage Functionalization. *Chem. Eur. J.* **2016**, *22*, 4364. (h) Calbo, J.; Weston, C. E.; White, A. J. P.; Rzepa, H. S.; Contreras-García, J.; Fuchter, M. J. Tuning Azoheteroarene Photoswitch Performance through Heteroaryl Design. *J. Am. Chem. Soc.* **2017**, *139*, 1261. (i) Dong, M.; Babalhavaeji, A.; Collins, C. V.; Jarrah, K.; Sadovski, O.; Dai, Q.; Woolley, G. A. Near-Infrared Photoswitching of Azobenzenes under Physiological Conditions. *J. Am. Chem. Soc.* **2017**, *139*, 13483.
- (5) (a) Siewertsen, R.; Neumann, H.; Buchheim-Stehn, B.; Herges, R.; Näther, C.; Renth, F.; Temps, F. Highly Efficient Reversible Z–E Photoisomerization of a Bridged Azobenzene with Visible Light through Resolved S<sub>1</sub>(nπ\*) Absorption Bands. *J. Am.*

- Chem. Soc.* **2009**, *131*, 15594. (b) Siewertsen, R.; Schönborn, J. B.; Hartke, B.; Renth, F.; Temps, F. Superior Z → E and E → Z Photoswitching Dynamics of Dihydrodibenzodiazocine, a Bridged Azobenzene, by S<sub>1</sub>(nn\*) Excitation at λ = 387 and 490 nm. *Phys. Chem. Chem. Phys.* **2011**, *13*, 1054.
- (6) (a) Duval, H. Recherches Su La Benzidination. *Bull. Soc. Chim. Fr.* **1910**, *7*, 727. (b) Gerson, F.; Heilbronner, E.; van Veen, A.; Wepster, B. M. Elektronenstruktur und physikalisch-chemische Eigenschaften von Azo-Verbindungen. Teil VIII: Die konjugaten S#uren des trans- und des cis-Azobenzols. *Helv. Chim. Acta* **1960**, *43*, 1889. (c) Paudler, W. W.; Zeiler, A. G. Diazocine Chemistry. VI. Aromaticity of 5,6-Dihydrodibenzo-[b,f][1,2]Diazocine. *J. Org. Chem.* **1969**, *34*, 3237. (d) Sell, H.; Näther, C.; Herges, R. Amino- Substituted Diazocines as Pincer-Type Photochromic Switches. *Beilstein J. Org. Chem.* **2013**, *9*, 1. (e) Samanta, S.; Qin, C.; Lough, A. J.; Woolley, G. A. Bidirectional Photocontrol of Peptide Conformation with a Bridged Azobenzene Derivative. *Angew. Chem. Int. Ed.* **2012**, *51*, 6452. (f) Deo, C.; Bogliotti, N.; Métivier, R.; Retailleau, P.; Xie, J. A Visible-Light-Triggered Conformational Diastereomer Photoswitch in a Bridged Azobenzene. *Chem. Eur. J.* **2016**, *22*, 9092. (g) Moormann, W.; Langbehn, D.; Herges, R. Solvent-Free Synthesis of Diazocine. *Synthesis* **2017**, *49*, 3471. (h) Li, S.; Han, G.; Zhang, W. Concise Synthesis of Photoresponsive Polyureas Containing Bridged Azobenzenes as Visible-Light-Driven Actuators and Reversible Photopatterning. *Macromolecules* **2018**, *51*, 4290. (i) Zhu, Q.; Wang, S.; Chen, P. Diazocine Derivatives: A Family of Azobenzenes for Photochromism with Highly Enhanced Turn-On Fluorescence. *Org. Lett.* **2019**, *21*, 4025. (j) Moormann, W.; Langbehn, D.; Herges, R. Synthesis of Functionalized Diazocines for Application as Building Blocks in Photo- and Mechanoresponsive Materials. *Beilstein J. Org. Chem.* **2019**, *15*, 727.
- (7) (a) Joshi, D. K.; Mitchell, M. J.; Bruce, D.; Lough, A. J.; Yan, H. Synthesis of Cyclic Azobenzene Analogues. *Tetrahedron* **2012**, *68*, 8670. (b) Tellkamp, T.; Shen, J.; Okamoto, Y.; Herges, R. Diazocines on Molecular Platforms. *Eur. J. Org. Chem.* **2014**, *2014*, 5456. (c) Eljabu, F.; Dhruval, J.; Yan, H. Incorporation of Cyclic Azobenzene into Oligodeoxynucleotides for the Photo-Regulation of DNA Hybridization. *Bioorg. Med. Chem. Lett.* **2015**, *25*, 5594. (d) Jun, M.; Joshi, D. K.; Yalagala, R. S.; Vanloon, J.; Simionescu, R.; Lough, A. J.; Gordon, H. L.; Yan, H. Confirmation of the Structure of TransCyclic Azobenzene by X-Ray Crystallography and Spectroscopic Characterization of Cyclic Azobenzene Analogs. *ChemistrySelect* **2018**, *3*, 2697. (e) Albert, L.; Peñalver, A.; Djokovic, N.; Werel, L.; Hoffarth, M.; Ruzic, D.; Xu, J.; Essen, L.-O.; Nikolic, K.; Dou, Y.; Vázquez, O. Modulating Protein–Protein Interactions with Visible-Light-Responsive Peptide Backbone Photoswitches. *ChemBioChem* **2019**, *20*, 1417. (f) Thapaliya, E. R.; Zhao, J.; Ellis-Davies, G. C. R. Locked Azobenzene: Testing the Scope of a Unique Photoswitchable Scaffold for Cell Physiology. *ACS Chem. Neurosci.* **2019**, *10*, 2481. (g) Löw, R.; Rusch, T.; Röhricht, F.; Magnussen, O.; Herges, R. Diazocine-Functionalized TATA Platforms. *Beilstein J. Org. Chem.* **2019**, *15*, 1485.
- (8) (a) Wang, J.; He, J.; Zhi, C.; Luo, B.; Li, X.; Pan, Y.; Cao, X.; Gu, H. Highly Efficient Synthesis of Azos Catalyzed by the Common Metal Copper(0) through Oxidative Coupling Reactions. *RSC Adv.* **2014**, *4*, 16607. (b) Cabré, G.; Garrido-Charles, A.; González-Lafont, À.; Moormann, W.; Langbehn, D.; Egea, D.; Lluch, J. M.; Herges, R.; Alibés, R.; Busqueé, F.; Gorostiza, P.; Hernando, J. Synthetic Photoswitchable Neurotransmitters Based on Bridged Azobenzenes. *Org. Lett.* **2019**, *21*, 3780.

- (9) (a) Hammerich, M.; Schütt, C.; Stahler, C.; Lentjes, P.; Röhrich, F.; Höppner, R.; Herges, R. Heterodiazocines: Synthesis and Photochromic Properties, Trans to Cis Switching within the BioOptical Window. *J. Am. Chem. Soc.* **2016**, *138*, 13111. (b) Schehr, M.; Ianes, C.; Weisner, J.; Heintze, L.; Müller, M. P.; Pichlo, C.; Charl, J.; Brunstein, E.; Ewert, J.; Lehr, M.; Baumann, U.; Rauh, D.; Knippschild, U.; Peifer, C.; Herges, R. 2-Azo-, 2-Diazocine-Thiazols and 2-Azo-Imidazoles as Photoswitchable Kinase Inhibitors: Limitations and Pitfalls of the Photoswitchable Inhibitor Approach. *Photochem. Photobiol. Sci.* **2019**, *18*, 1398. (c) Lentjes, P.; Stadler, E.; Röhrich, F.; Brahm, A.; Groebner, J.; Sonnichsen, F. D.; Gescheidt, G.; Herges, R. Nitrogen Bridged Diazocines: Photochromes Switching within the Near-Infrared Region with High Quantum Yields in Organic Solvents and in Water. *J. Am. Chem. Soc.* **2019**, *141*, 13592. (d) Schehr, M.; Hugenbusch, D.; Moje, T.; Näther, C.; Herges, R. Synthesis of Mono-Functionalized S-Diazocines via Intramolecular Baeyer–Mills Reactions. *Beilstein J. Org. Chem.* **2018**, *14*, 2799.
- (10) (a) Kajimoto, T.; Yahiro, K.; Nohara, T. A Short Step Synthesis of AV-toxin D. *Chem. Lett.* **1988**, *17*, 1113. (b) Bleasdale, C.; Ellis, M. K.; Farmer, P. B.; Golding, B. T.; Handley, K. F.; Jones, P.; McFarlane, W. Synthesis and spectroscopic characterisation of 3-chloroperbenzoic acid-17O,18O, nitrosobenzene-17O,18O and nitrosobenzene-15N. *J. Labelled Compd. Radiopharm.* **1993**, *33*, 739. (c) Reuter, R.; Wegner, H. A. meta-Oligoazobiphenyls – synthesis via site-selective Mills reaction and photochemical properties. *Beilstein J. Org. Chem.* **2012**, *8*, 877.
- (11) Pfeil, E.; Schmidt, K. H. Über die Katalytische Wirkung von Metallsalzen bei der Oxydation primärer aromatischer Amine mit Peressigsäure. *Liebigs Ann.* **1964**, *675*, 36.
- (12) Hays, J. T.; Young, H. L.; Espy, H. H. P-Nitrosophenol Chemistry. II. Amination of p-Nitrosophenol Ethers with Primary Aromatic Amines. *J. Org. Chem.* **1967**, *32*, 158.
- (13) Routier, S.; Saugé, L.; Ayerbe, N.; Coudert, G.; Mérour, J.-Y. A Mild and Selective Method for N-Boc Deprotection. *Tetrahedron Lett.* **2002**, *43*, 589.
- (14) (a) Hooper, M.; Imam, S. H. 11H-Isoindolo[2,1-a]Indol-11-Ones: Novel Rearrangement Products from the Attempted Preparation of 2-(2-Diethylaminomethylphenyl)Isatogens. *J. Chem. Soc., Perkin Trans. 1* **1985**, 1583. (b) Söderberg, B. C. G.; Gorugantula, S. P.; Howerton, C. R.; Petersen, J. L.; Dantale, S. W. A Palladium-Catalyzed Synthesis of Isatins (1H-Indole-2,3-Diones) from 1-(2-Haloethynyl)-2-Nitrobenzenes. *Tetrahedron* **2009**, *65*, 7357. (c) Liu, R.-R.; Ye, S.-C.; Lu, C.-J.; Zhuang, G.-L.; Gao, J.-R.; Jia, Y.-X. Dual Catalysis for the Redox Annulation of Nitroalkynes with Indoles: Enantioselective Construction of Indolin-3-Ones Bearing Quaternary Stereocenters. *Angew. Chem. Int. Ed.* **2015**, *54*, 11205. (d) Marien, N.; Brigou, B.; Pinter, B.; De Proft, F.; Verniest, G. Synthesis of 2-Spiropseudoindoxyls via an Intramolecular Nitroalkyne Redox–Dipolar Cycloaddition Cascade. *Org. Lett.* **2015**, *17*, 270. (e) Maduli, E. J. M.; Edeson, S. J.; Swanson, S.; Procopiu, P. A.; Harrity, J. P. A. 2-Iodoisatogens: Versatile Intermediates for the Synthesis of Nitrogen Heterocycles. *Org. Lett.* **2015**, *17*, 390. (f) Peng, H.; Ma, J.; Duan, L.; Zhang, G.; Yin, B. CuH-Catalyzed Synthesis of 3-Hydroxyindolines and 2-Aryl-3H-indol-3-ones from o-Alkylnitroarenes, Using Nitro as Both the Nitrogen and Oxygen Source. *Org. Lett.* **2019**, *21*, 6194. (g) Dhote, P. S.; Ramana, C. V. One-Pot Au[III]-/Lewis Acid Catalyzed Cycloisomerization of Nitroalkynes and [3 + 3]Cycloaddition with Donor-Acceptor Cyclopropanes. *Org. Lett.* **2019**, *21*, 6221.

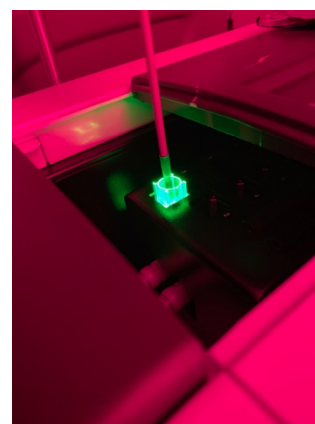
- (15) (a) Arcadi, A.; Cacchi, S.; Fabrizi, G.; Ghirga, F.; Goggiamani, A.; Iazzetti, A.; Marinelli, F. Synthesis of Indolo[1,2-c]Quinazolines from 2-Alkynylaniline Derivatives through Pd-Catalyzed Indole Formation/Cyclization with N,N-Dimethylformamide Dimethyl Acetal. *Beilstein J. Org. Chem.* **2018**, *14*, 2411. (b) Rodriguez, A. L.; Koradin, C.; Dohle, W.; Knochel, P. Versatile Indole Synthesis by a 5-Endo-Dig Cyclization Mediated by Potassium or Cesium Bases. *Angew. Chem. Int. Ed.* **2000**, *39*, 2488. (c) Perea-Buceta, J. E.; Wirtanen, T.; Laukkanen, O.-V.; Mäkelä, M. K.; Nieger, M.; Melchionna, M.; Huittinen, N.; Lopez-Sanchez, J. A.; Helaja, J. Cycloisomerization of 2-Alkynylanilines to Indoles Catalyzed by Carbon-Supported Gold Nanoparticles and Subsequent Homocoupling to 3,3'-Biindoles. *Angew. Chem. Int. Ed.* **2013**, *52*, 11835. (d) Abbiati, G.; Arcadi, A.; Chiarini, M.; Marinelli, F.; Pietropaolo, E.; Rossi, E. An Alternative One-Pot Gold-Catalyzed Approach to the Assembly of 11H-Indolo[3,2-c]Quinolines. *Org. Biomol. Chem.* **2012**, *10*, 7801. (e) Koradin, C.; Dohle, W.; Rodriguez, A. L.; Schmid, B.; Knochel, P. Synthesis of Polyfunctional Indoles and Related Heterocycles Mediated by Cesium and Potassium Bases. *Tetrahedron* **2003**, *59*, 1571.
- (16) Pailer, M.; Schleppe, A.; Meller, A. Die Synthese von  $\alpha$ -(o-Nitroaryl)-zimtsäuren. *Monatsh. Chem.* **1958**, *89*, 211.
- (17) Molina, P.; Alajarín, M.; Sánchez-Andrada, P.; Carrió, J. S.; Martínez-Ripoll, M.; Anderson, J. E.; Jimeno, M. L.; Elguero, J. New Models for the Study of the Racemization Mechanism of Carbodiimides. Synthesis and Structure (X-Ray Crystallography and  $^1\text{H}$  NMR) of Cyclic Carbodiimides. *J. Org. Chem.* **1996**, *61*, 4289.

## Supporting Information - Photophysical Characterization

This thesis only includes the supporting information for the photophysical characterization. Synthetic recommendations, procedures and spectra can be found under <https://doi.org/10.1021/jacs.9b08794>.

**UV-Vis Spectroscopy.** UV-Vis spectra were recorded on a Varian Cary 60 Scan UV-Vis spectrometer equipped with a Peltier PCB-1500 Thermostat and an 18-cell holder using Brand disposable UV cuvettes (70-850  $\mu\text{L}$ , 10 mm light path) by Brandtech Scientific Inc.. Sample preparation and all experiments were performed under red light conditions in a dark room. All UV-Vis measurements were performed with dimethyl sulfoxide (DMSO) as the solvent.

wavelength	time
600 nm	10 s (dummy time at resting wavelength)
540 nm	600 s
520 nm	600 s
500 nm	600 s
480 nm	600 s
460 nm	600 s
440 nm	600 s
420 nm	600 s
400 nm	600 s
380 nm	600 s
360 nm	600 s



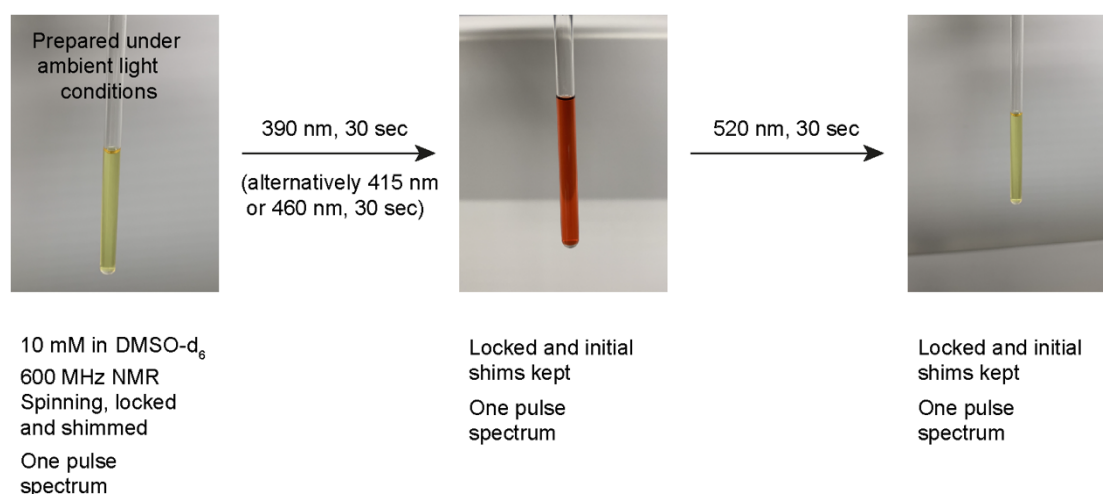
**Figure SI-1:** Left: Protocol for the determination of the optimal switching wavelength. Right: Picture of a sample being illuminated in the UV-Vis spectrometer.

Determination of optimal switching wavelength: Light at different wavelengths was provided by an Optoscan Monochromator with an Optosource (75 mW lamp), which was controlled through a program written in Matlab (Figure SI-1). Irradiation to establish the photostationary state took place from the top through a fiber-optic cable. For each compound a 25 or 100 mM stock solution in DMSO was prepared and diluted to a 50  $\mu\text{M}$  concentration prior to the experiment. First, a spectrum of the non-irradiated sample was acquired, then a spectrum with irradiation at 600 nm. If these two spectra did not overlap, the measurement was aborted and the light fiber readjusted, then a new run was started. Otherwise, spectra with illumination were acquired from 540 to 360 nm in 20 nm steps going from higher to lower wavelengths and illuminating 10 minutes for each wavelength.

**Thermal relaxation.** All samples were prepared by dilution of a 100 mM stock solution in DMSO to a 50  $\mu\text{M}$  concentration. Thermal isomerization half-lives at

25 °C were determined by measuring the absorption decay at 490 nm. The samples were irradiated for 1 minute with a 390 nm Prizmatix high power LED from the top, then data points were collected for 24 hours. For compounds **23**, **24**, **31**, **35**, **42** and **43**, the collection of data points was stopped earlier, due to their short relaxation times. Each sample was measured at least twice.

**Photostationary state investigation by NMR spectroscopy.** To determine the photostationary state compositions, one pulse proton  $^1\text{H}$ -NMR spectroscopy was performed on a Bruker Avance 600 spectrometer with Cryoprobe<sup>1</sup> at 10 mM concentration in DMSO- $d_6$  to ensure a low optical density and good signal-to-noise ratio. Samples were prepared by diluting 100 mM stock solutions in DMSO- $d_6$  and were handled without precautions under ambient light. Spectra were collected before illumination and after illumination for 30 seconds with Prizmatix high power LEDs (390, 460 and 520 nm) or Prizmatix Mic-LEDs (365 and 415 nm). Each sample was first illuminated at 390 nm followed by 520 nm<sup>2</sup> (see Figure SI-2). If necessary (see Table 4, main text and Figure SI-3) the samples were also irradiated with 415 nm or 460 nm light. Diazonine 66 was additionally irradiated at 365 nm. For the irradiation sequence of azobenzene 1 see Table SI-3.



**Figure SI-2:** Workflow for the investigation of the photostationary states by  $^1\text{H}$ -NMR spectroscopy.

The (*Z*)/(*E*)-ratio was determined by integration of baseline separated signals in the aromatic region. For compounds with a relaxation time shorter than 100 minutes (established through UV-Vis spectroscopy), ten spectra were collected every 20–60 seconds and the values extrapolated to the timepoint when the illumination of the sample was stopped.

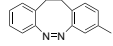
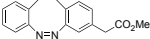
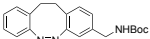
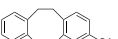
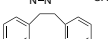
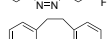
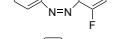
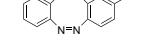
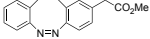
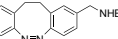
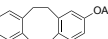
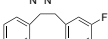
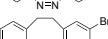
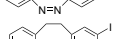
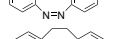
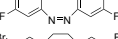
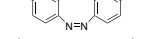
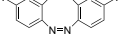
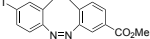
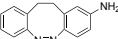

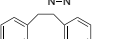
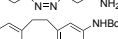
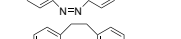
<sup>1</sup>For more details on NMR spectroscopy see section General Information in Supporting Information – Synthetic procedures.

<sup>2</sup>The most suitable range of wavelengths for (*E*) to (*Z*) switching of diazocine **2** was determined to lie between 480 nm and 540 nm by UV-Vis spectroscopy (see Figure SI-4).



## Summary of photophysical properties for characterization by UV-Vis and NMR spectroscopy

**Table SI-1: Photophysical properties of diazocines**

Compound	$\lambda_{\text{opt}}^{\text{a}}$	$T_{1/2}$	PSS (Z/E) <sup>b</sup>	
	<b>10</b>	400 nm	9.3 h	17/83 <sup>c</sup>
	<b>11</b>	400 nm	8.9 h	14/86 <sup>c</sup>
	<b>12</b>	400 nm	8.9 h	17/83 <sup>c</sup>
	<b>17</b>	400 nm	8.0 h	15/85 <sup>c</sup>
	<b>18</b>	400 nm	5.7 h	13/87 <sup>c</sup>
	<b>19</b>	400 nm	11.0 h	15/85 <sup>c</sup>
	<b>20</b>	400 nm	6.8 h	15/85 <sup>c</sup>
	<b>21</b>	400 nm	7.9 h	14/86 <sup>c</sup>
	<b>22</b>	400 nm	7.9 h	14/86 <sup>c</sup>
	<b>27</b>	400 nm	8.7 h	17/83 <sup>c</sup>
	<b>28</b>	400 nm	9.5 h	13/87 <sup>c</sup>
	<b>29</b>	400 nm	5.6 h	14/86 <sup>c</sup>
	<b>30</b>	400 nm	4.9 h	15/85 <sup>c</sup>
	<b>37</b>	400 nm	5.9 h	15/85 <sup>c</sup>
	<b>38</b>	400 nm	4.0 h	15/85 <sup>c</sup>
	<b>39</b>	400 nm	3.2 h	19/81 <sup>c</sup>
	<b>41</b>	400 nm	4.3 h	17/83 <sup>c</sup>
	<b>42</b>	400 and 360 nm	16 min	85/15 <sup>c</sup>
	<b>43</b>	440 nm	14 min	73/27 <sup>c</sup>
	<b>44</b>	360 - 420 nm	13.2 h	61/39 <sup>c</sup>
	<b>SI-95</b>	420 nm	2.1 h	44/56 <sup>d</sup>
	<b>SI-96</b>	420 nm	11.3 h	61/39 <sup>c</sup>
	<b>SI-97</b>	400 nm	8.6 h	12/88 <sup>c</sup>
	<b>SI-98</b>	420 nm	3.0 h	15/85 <sup>e</sup>

<sup>a</sup>For (Z) to (E) switching, determined by UV-Vis spectroscopy. <sup>b</sup>For (Z) to (E) switching, determined by <sup>1</sup>H-NMR spectroscopy in DMSO-*d*<sub>6</sub>. <sup>c</sup>390 nm. <sup>d</sup>415 nm. <sup>e</sup>460 nm.

**Table SI-2:  $\pi\pi^*$ - and  $n\pi^*$ -absorption maxima of azobenzene 1, diazonine 66 and diazocine 2 in DMSO (50  $\mu\text{M}$ ).**

Transition	(E)-1a	(Z)-1b	(E)-66c	(Z)-66a	(E)-2c	(Z)-2a
$\pi\pi^*$	322 nm	280 nm	316 nm	280 nm	284 nm	286 nm
$n\pi^*$	444 nm	430 nm	426 nm	406 nm	494 nm	405 nm

<sup>a</sup>Non-irradiated sample. <sup>b</sup>After 360 nm illumination. <sup>c</sup>After 400 nm illumination.

**Table SI-3: (Z)/(E) ratios of 1 mM azobenzene 1 in DMSO-d<sub>6</sub> determined by 1H-NMR spectroscopy after 30 seconds of irradiation at different wavelengths.**

Entry <sup>a</sup>	$\lambda$	PSS (Z/E)
1 <sup>b,c</sup>	365 nm	17/83
2	non-irradiated sample	3/97
3 <sup>c</sup>	365 nm	60/40
4 <sup>d</sup>	415 nm	17/83 <sup>c</sup>
5	390 nm	18/82
6	460 nm	23/77
7	520 nm	35/65

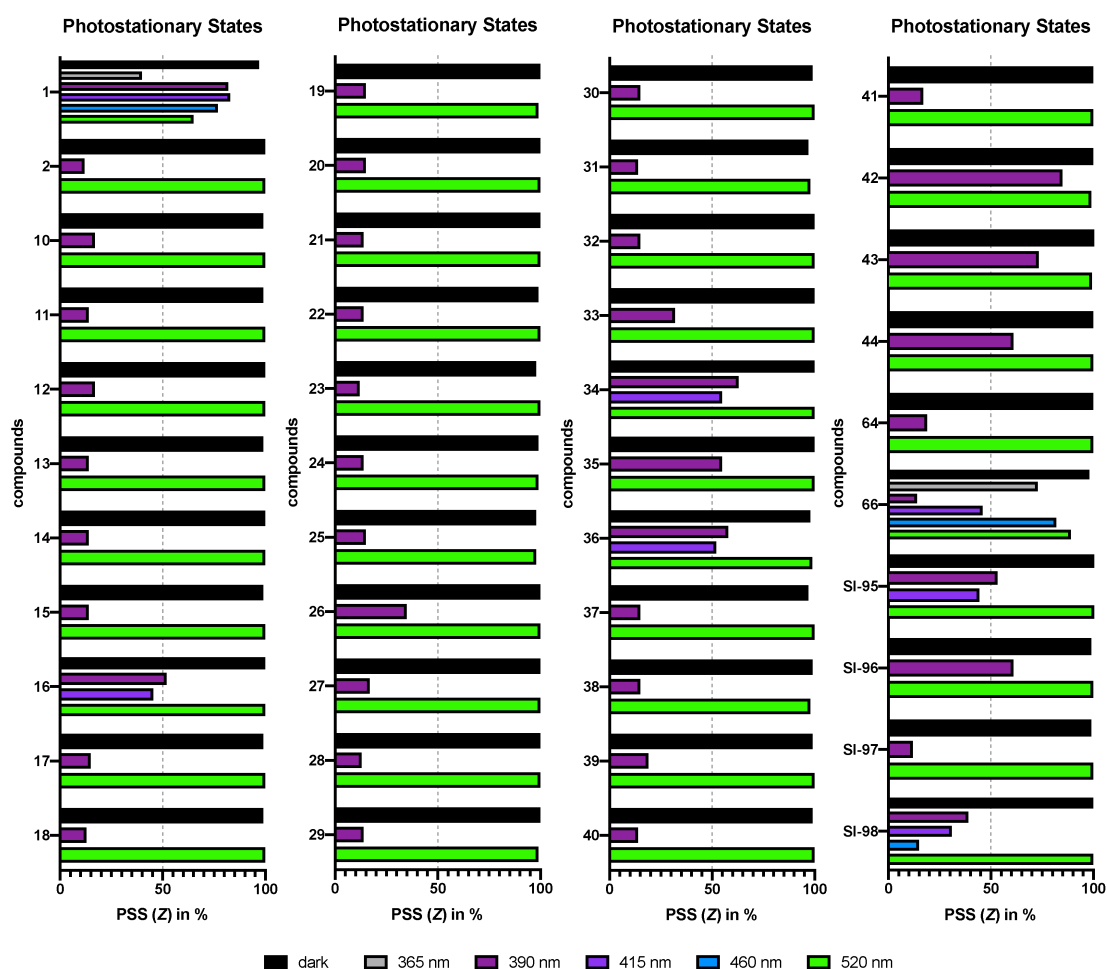
<sup>a</sup>The entries in this table refer to the same sample and are ordered from top to bottom according to the sequence of irradiation, except for the entry 1, which refers to a more concentrated sample that was measured separately.

<sup>b</sup>10 mM.

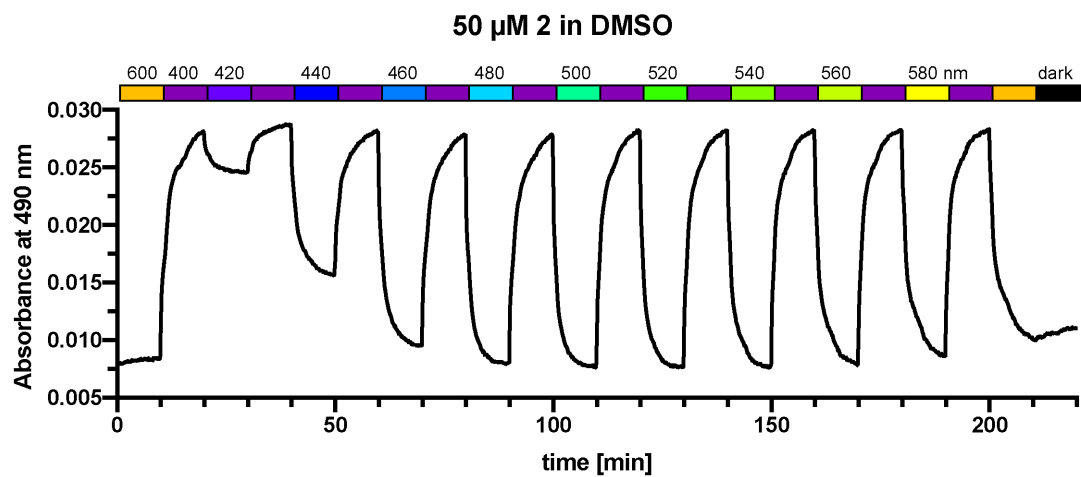
<sup>c</sup>The determination of the optimal wavelength for switching to (Z)-1 by UV-Vis spectroscopy (see Figure SI-5) did not include wavelengths below 360 nm. Thus, at shorter wavelengths a higher conversion from (E)/(Z) may be possible.

<sup>d</sup>The optimal wavelength for switching to (E)-1 determined by UV-Vis spectroscopy (see Figure SI-5) was 420 nm.

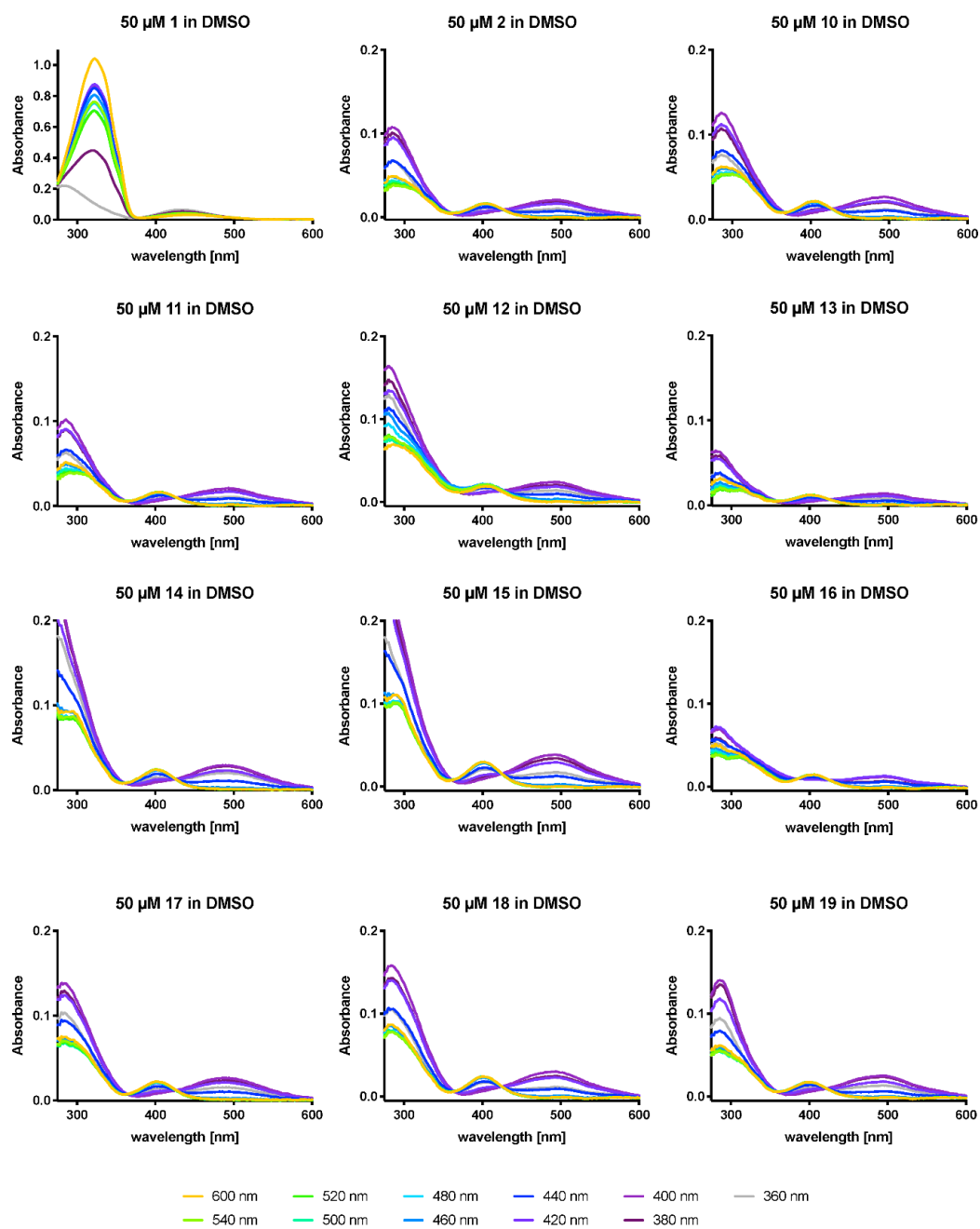
## Supplementary figures



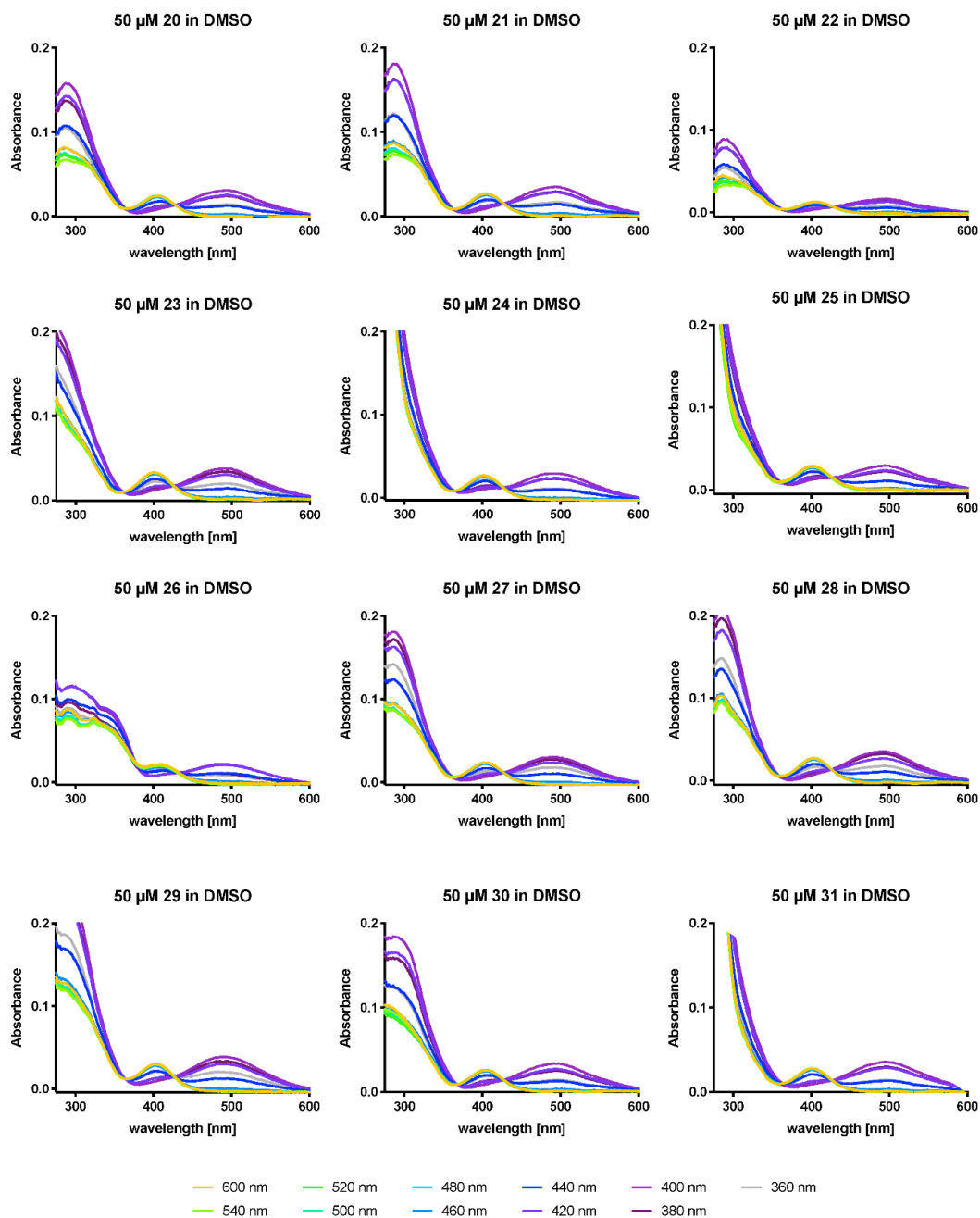
**Figure SI-3:** Overview of the fraction of (Z)-isomer determined by  $^1\text{H-NMR}$  spectroscopy for the non-irradiated sample (prepared under ambient light conditions, labeled as "dark") and the PSS at different wavelengths. Values for 390 and 520 nm irradiation are depicted for all compounds and values for 365, 415 and 460 nm irradiation are shown for selected compounds or if a better PSS composition was obtained.



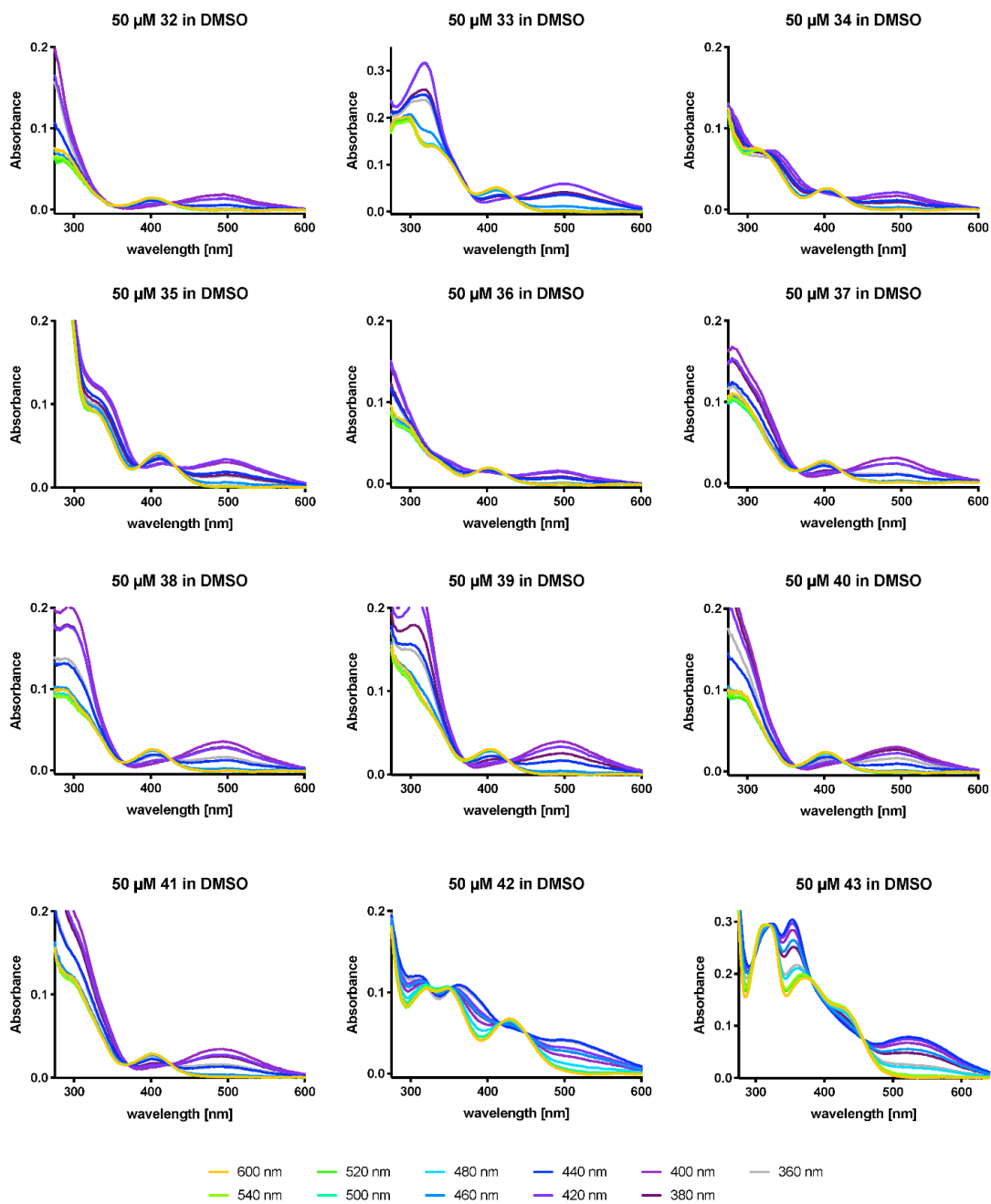
**Figure SI-4:** Determination of the ideal wavelength to switch diazocine **2** from (*E*) to (*Z*).



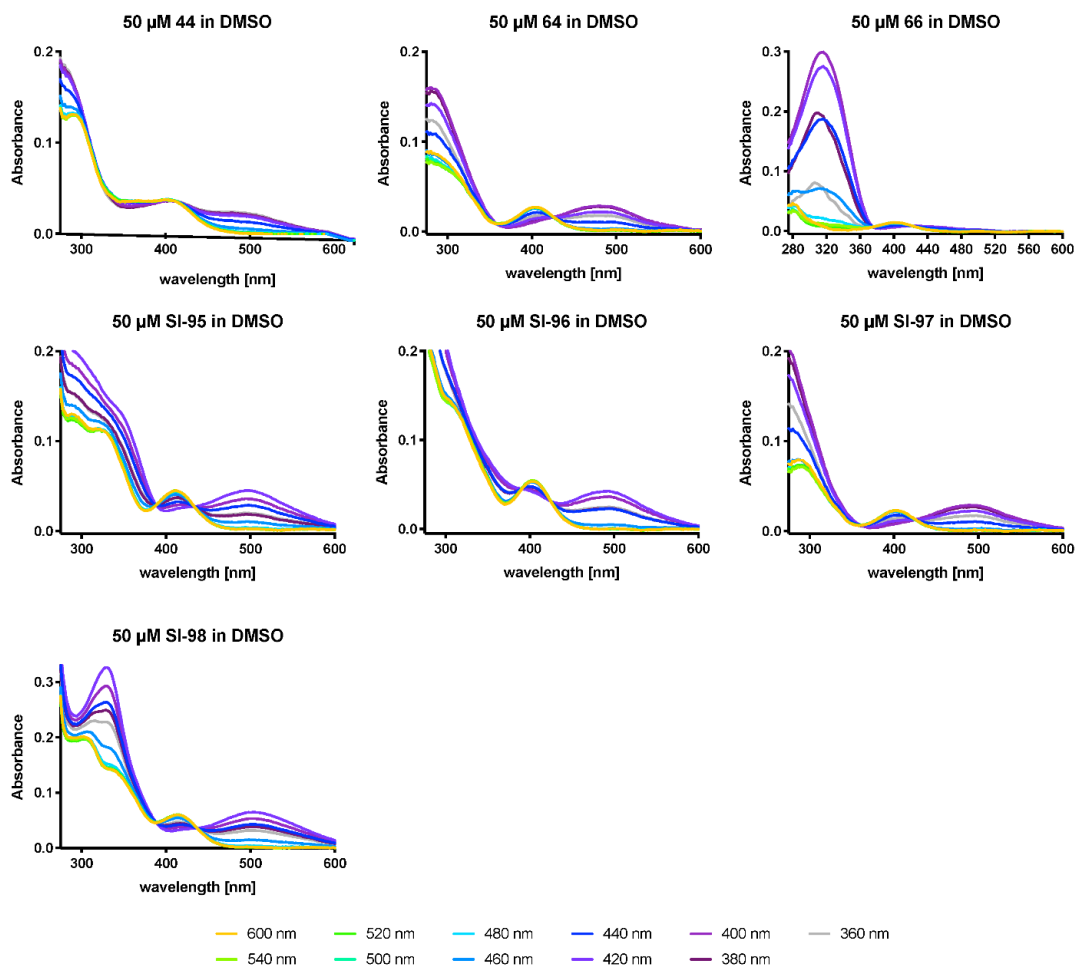
**Figure SI-5:** UV-Vis spectra of compounds **1**, **2**, **10-19**.



**Figure SI-6:** UV-Vis spectra of compounds **20-31**.



**Figure SI-7:** UV-Vis spectra of compounds **32-43**.



**Figure SI-8:** UV-Vis spectra of compounds **44**, **64**, **66**, **SI-95-SI-98**.







### III. Chemical Approaches to Vision Restoration



# Photopharmacologic Vision Restoration Reduces Pathological Rhythmic Field Potentials in Blind Mouse Retina

Katharina Hüll<sup>1,2</sup>, Tyler Benster<sup>3,4</sup>, Michael B. Manookin<sup>3</sup>, Dirk Trauner<sup>2</sup>, Russell N. Van Gelder<sup>\*3,5</sup> and Laura Laprell<sup>\*3,6</sup>

<sup>1</sup> Center for Integrated Protein Science Munich and Department of Chemistry, Ludwig-Maximilians-Universität München, Munich, Germany.

<sup>2</sup> Department of Chemistry, New York University, 100 Washington Square East, New York, New York 10003-6699, United States

<sup>3</sup> Department of Ophthalmology, University of Washington School of Medicine, Seattle, Washington, USA.

<sup>4</sup> Present address: Neurosciences Graduate Program, Stanford University, Stanford, CA 94305, USA

<sup>5</sup> Departments of Biological Structure and Pathology, University of Washington School of Medicine, Seattle, Washington, USA.

<sup>6</sup> Department of Synaptic Physiology, Center for Molecular Neurobiology, ZMNH, University Medical Center Hamburg-Eppendorf, Hamburg, Germany.

\*Corresponding authors

Reprinted (adapted) with permission from Hüll, K., Benster, T., Manookin, M.B., Trauner, D., Van Gelder R.N., Laprell, L., Photopharmacologic Vision Restoration Reduces Pathological Rhythmic Field Potentials in Blind Mouse Retina. *Sci Rep* **2019**, *9*, 13561. Copyright 2019 Springer Nature (CC BY license).

## Abstract

Photopharmacology has yielded compounds that have potential to restore impaired visual responses resulting from outer retinal degeneration diseases such as retinitis pigmentosa. Here we evaluate two photoswitchable azobenzene ion channel blockers, DAQ and DAA for vision restoration. DAQ exerts its effect primarily on RGCs, whereas DAA induces light-dependent spiking primarily through amacrine cells activation. Degeneration-induced local field potentials remain a major challenge common to all vision restoration approaches. These 5-10 Hz rhythmic potentials increase the background firing rate of retinal ganglion cells (RGCs) and overlay the stimulated response, thereby reducing signal-to-noise ratio. Along with the bipolar cell-selective photoswitch DAD and second-generation RGC-targeting photoswitch PhENAQ, we investigated the effects of DAA and DAQ on rhythmic local field potentials (LFPs) occurring in the degenerating retina. We found that photoswitches targeting neurons upstream of RGCs, DAA (amacrine cells) and DAD (bipolar cells) suppress the frequency of LFPs,

while DAO and PhENAO (RGCs) had negligible effects on frequency or spectral power of LFPs. Taken together, these results demonstrate remarkable diversity of cell-type specificity of photoswitchable channel blockers in the retina and suggest that specific compounds may counter rhythmic LFPs to produce superior signal-to-noise characteristics in vision restoration.

## Introduction

Outer retinal degenerative diseases, such as retinitis pigmentosa and age-related macular degeneration, affect millions of people worldwide. While in these diseases the photoreceptor cell layer degenerates, the rest of the retinal circuitry remains largely intact, undergoing slow remodeling. Restoration of impaired vision is a long-sought goal<sup>1</sup>.

Recently, we and others have pursued photopharmacological approaches for vision restoration, utilizing small freely diffusible azobenzene photoswitches that target intrinsic neuronal receptors in different retinal cell types<sup>2,3</sup>. Photoswitches can be reversibly switched between two configurations, a thermodynamically stable *trans*- and a less stable *cis*-configuration, using light of visible wavelengths (Fig. 1). Whereas in one configuration

the photoswitch blocks its target channel, the other configuration leads to release of the photoswitch from the pore (Fig. 1 inset). By switching between the two configurations using visible (blue/white) light and darkness, light-dependent ganglion cell firing can be restored in the remaining circuitry of the blind retina<sup>2,4-7</sup>.

Retinal reanimation using photopharmacology is a promising approach for the restoration of vision. However, being a pharmacological approach, the optimization of cell specificity, membrane permeability, and kinetics becomes a major challenge in further development. Cell specificity of photoswitches becomes especially important when considering the progression of retinal degeneration. While in early stages of disease the intermediate layers of the retina (i.e. bipolar and amacrine cells) are still in place and can be pharmacologically targeted; in late stage retinas, death of bipolar and amacrine cells leads to remodeling of the retina. Therefore, at late stage retinal degeneration targeting RGCs might be the only option<sup>8-10</sup>. Having a toolbox at hand that targets different stages of disease becomes therefore desirable.

The onset of photoreceptor cell loss is accompanied by strong spontaneous oscillatory activity in the retina arising in the bipolar-amacrine cell network<sup>11,12</sup>. This oscillatory activity represents a major challenge to all vision restoration approaches as it increases background firing rate and may overlay the stimulated response, thereby reducing the signal-to-noise ratio. In mouse models for retinal degeneration, e.g. *rd1* and *rd10*, spontaneous oscillations become evident about the age of first eye opening<sup>13</sup>. In *rd10* mice, a mouse model for slow retinal



degeneration, rhythmic local field potentials (LFPs) occur first at frequencies around ~5 Hz and increase in frequency with disease progression. In *rd1* mice, disease onset occurs earlier, and strong 5 and 10 Hz LFPs are observed a few weeks after birth<sup>14</sup>. LFPs coincide with rhythmic bursting activity in RGCs in both *rd1* and *rd10* mouse models for retinal degeneration<sup>14,15</sup>.

One approach that has been investigated for reduction of LFPs is the application of GAP-junction blockers, such as meclofenamic acid (MFA)<sup>16</sup>. Blocking gap-junctions between bipolar and All amacrine cells lead to the reduction of this pathological hyperactivity and underlying LFPs. When applied in *rd1* retinas rescued with ganglion cell expression of Chr2 this in turn lead to a significant increase in signal-to-noise of RGC output. However, this strategy has its limitations: MFA is a non-specific agent (it was originally approved as a COX inhibitor) and influences the entire retinal circuitry, thus limiting its use to approaches that target RGCs<sup>17</sup>.

To date, apart from the third-generation photoswitch DAD, which targets bipolar cells, most studied fast-relaxing photochromic open-channel blockers primarily target retinal ganglion cells (RGCs)<sup>3-5</sup>. Here we extend the photopharmacological toolbox for vision restoration approaches with two novel compounds and show that targeting cells upstream from RGCs leads to a reduction in LFPs. Furthermore, we demonstrate that photoswitches that target bipolar and amacrine cells suppress oscillatory activity when activated by light, even well after onset of strong ~5 Hz oscillations.

Both photoswitches are derivatives of the sodium channel blockers lidocaine or QX-314 (Fig. 1B). It has been previously shown that azobenzene-derivatives of QX-314 do not primarily target sodium channels but exert their effects mainly through voltage-gated potassium channels<sup>18</sup>. Since potassium channels are widely expressed in a variety of cell types, and particularly in neurons, these photoswitches should in principle target all cells in the remaining retinal circuitry of a blind mouse. However, we recently discovered that the non-permanently charged lidocaine derivative DAD primarily targets bipolar cells in the degenerating retina, but not in the wild-type or in the morphologically intact but blind retina and has only negligible effects on amacrine or retinal ganglion cells<sup>6</sup>. The permanently charged QX-314 derivatives DENAQ and BENAQ, in contrast, primarily target RGCs, relying on an uptake mechanism through dilated P2X channels<sup>3,5</sup>. In the current study we developed intermediate compounds between DAD and BENAQ to study their functionality in the degenerating retina and to address the optimization process for photoswitch pharmacology in respect to target cell type and effect on LFPs.



## Results

**Open-channel blocker design, synthesis and characterization.** To better understand the pharmacology and mechanism-of-action of open-channel blockers, we synthesized derivatives of the soluble azobenzene DAD, named DAQ and DAA (Scheme S1 and 2)<sup>6</sup>. In an attempt to change characteristics of the molecules such as membrane permeability, we modified both sides of the azobenzene in DAD. In comparison to previously published photoswitches applied in blind retina, DAD has two possible, but structurally different pharmacophores (Fig. 1). Under physiological conditions both amines in DAD are protonated<sup>19</sup>. Although not initially considered as a pharmacophore, we wanted to investigate if the common motif in DAD and DAQ, the aminoethylaniline functionality alone (truncated blocker: DAA, Fig. 1B) can induce light-dependent responses in blind retina and how it influences LFPs. We also sought to determine if the presence of a permanent charge (DAQ) is sufficient to influence cell subtype selectivity. This effect is suggested by the previously studied charged open-channel blockers DENAQ and BENAQ, which are RGC-specific<sup>3,5</sup>, but otherwise share similarities with the non-permanently charged DAD.

DAQ and DAA were synthesized in 6 steps using a divergent approach, following the synthetic route of DAD. UV-Vis characterization showed similar properties for all three compounds (Fig. S1): DAD, DAQ and DAA could be isomerized by blue light and are fast-relaxing in the dark. All compounds were prepared as HCl salts to improve solubility. PhENAQ, a 'second-generation' charged photoswitch, was synthesized for comparison as previously described<sup>18</sup>.

DAD, DAQ and DAA were initially characterized in layer 2/3 cortical neurons of acute mouse brain slice preparations. Like DAD, DAQ blocks and unblocks potassium channels in cortical neurons<sup>6</sup>. The optimal switching wavelengths were determined to be 460 nm and 540 nm for unblock and block, respectively, and the kinetics of block and unblock are comparable to those of DAD ( $\tau_{\text{on}} = 16.0 \pm 0.49$  ms,  $\tau_{\text{off}} = 93.5 \pm 2.12$  ms<sup>6</sup>) (Fig. S2). In addition, sodium channel currents in layer 2/3 neurons of acute brain slice preparations were not affected by DAQ application, similar to what has been shown for DAD (Fig. S2G,H). Taken together, DAQ's photoswitching properties closely resemble those of DAD in acute brain slice preparation.

Characterization of DAA in murine brain slice also showed light-induced  $K_V$ -channel currents in depolarized cortical cells upon blue light illumination (Fig. S3). In addition, the wavelength sensitivity was comparable to DAD and DAQ with a maximum near 460 nm (consistent with the respective UV-Vis spectra in Figure S1). The major difference between DAD, DAQ and DAA in layer 2/3 neurons was detected in the photoswitch off-kinetics. Whereas DAQ has a relatively fast  $\tau_{\text{off}}$  similar to DAD ( $\tau_{\text{off(DAD)}} = 72.1 \pm 8.7$  ms<sup>6</sup>), DAA was significantly slower when illuminated with 540 nm light ( $\tau_{\text{off}} = 204 \pm 20.3$  ms) (Fig. S3F).

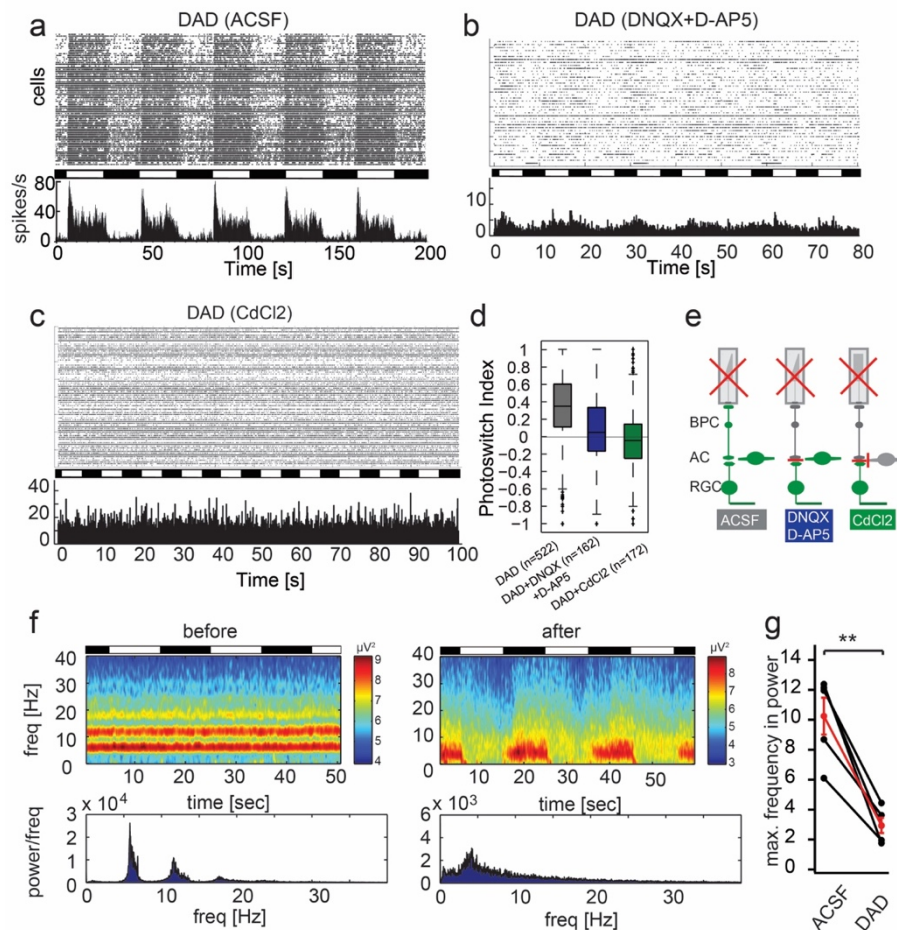
In summary, all three molecules, DAD, DAQ and DAA act as open-channel blocker in their *trans* state and unblock the pore upon isomerization with blue light to *cis*, making all three compounds suitable candidates for application to vision restoration of degenerated retina.

**DAD targets bipolar cells and reduces local field potentials in the degenerating retina.** DAD (Fig. 1A) is a non-permanently charged, third-generation photoswitch that primarily targets bipolar cell in retinas undergoing degeneration<sup>6</sup>. DAD has increased solubility compared to second-generation photoswitch compounds such as DENAQ and BENAQ, which allows for good tissue penetration *in vitro* as well as *in vivo*. We have previously demonstrated that DAD can be reversibly switched using blue or white light, and it restores light-dependent ganglion cell firing and behavioral responses to light in blind mice (Fig. 2A)<sup>6</sup>. As shown previously, DAD exerts its effects on bipolar cells rather than on RGCs (Fig. 2A-D), which is confirmed by application of blockers for either the excitatory retinal pathway (DNQX and D-AP5) or all synaptic transmission onto RGCs (CdCl<sub>2</sub>) (graphic representation Fig. 2E). We have also demonstrated that application of DAD leads to significant reduction in spontaneous activity in retinal ganglion cells in blind retina, thereby increasing signal to noise ratio of restored light responses. We were interested whether this silencing effect on background firing rate is mediated by reduction of LFPs in general<sup>6</sup>.

To investigate whether photoswitches are able to influence LFP in retina undergoing degeneration, we measured the power spectrum of field potentials using multielectrode array recording and analyzed oscillatory activity from 0 to 40 Hz using the Chronux Matlab Package to calculate the multitaper spectrum over a moving window<sup>20,21</sup>. In wildtype retinas in darkness, only very weak, low frequency oscillatory activity was observed (Fig. S4). A similar low frequency and amplitude oscillatory activity was seen in retinas lacking the light sensitive protein melanopsin in the intrinsically photosensitive retinal ganglion cells (Fig. S4). LFPs were also nearly absent in a model of stationary night blindness, in which the photoreceptor cells are morphologically intact, but lack light-sensing function (*Gnat1*<sup>-/-</sup>, *Gnat2*<sup>-/-</sup>, *Opn4*<sup>-/-</sup>) (Fig. S4)<sup>22-24</sup>. In retina undergoing photoreceptor degeneration, however, strong local field potentials at 5 and 10 Hz are detected (Fig. 2E *before application of photoswitch*). Taken together, these results suggest LFPs are specific to models featuring outer retinal degeneration.

When DAD was applied to blind, degenerated *rd1/rd1, Opn4*<sup>-/-</sup> retina in darkness, LFPs were significantly reduced to frequencies lower than 10 Hz (Fig. S5A,B), which was then similar to wildtype retinas. Additional application of MFA only led to a minor additional decrease in frequency (Fig. S5C-E), but significantly attenuated the light response of DAD itself (Fig. S5D-F). This result was expected as we previously demonstrated that DAD requires the active bipolar-amacrine cell network to function<sup>6</sup>. Interestingly, however, LFPs were nearly completely suppressed when light is switched on in the presence of DAD (Fig. 2E,F).

To establish that this effect is not strain-specific, we also measured local field potential rhythms in the *rd1/rd1,Opn4<sup>-/-</sup>* mouse on a different genetic background (C57Bl6JRj) (Fig. S6). In this mouse line the same effects of reduced LFPs in darkness and elimination of LFP in light were observed.



**Figure 2. DAD suppresses LFPs in degenerating retina.** (a) Raster plot and histogram of representative MEA recording in an *rd1/rd1,Opn4<sup>-/-</sup>* retina after treatment with 200  $\mu\text{M}$  DAD. (b) Same as in A, with additional application of DNQX and D-AP5. (c) Same as in A, with additional application of CdCl<sub>2</sub>. (d) Quantification of light responses using the photoswitch index. (e) Graphical overview of pharmacological experiments. (f) Power spectrum of rhythmic firing due to oscillatory local field potentials before and after application of DAD. Heat plot represents spectral power at noted frequency in Hz. (g) Quantification of maximal frequency response before and after application of DAD (average intensities of complete time range). Maximum frequency with significant power is defined by the peak of the highest frequency reaching a threshold of 4 SD. Each data point refers to the power average of local field potentials in one retina. (n=4 retinas). The average change in power is depicted in red with error bars (mean $\pm$ SEM).

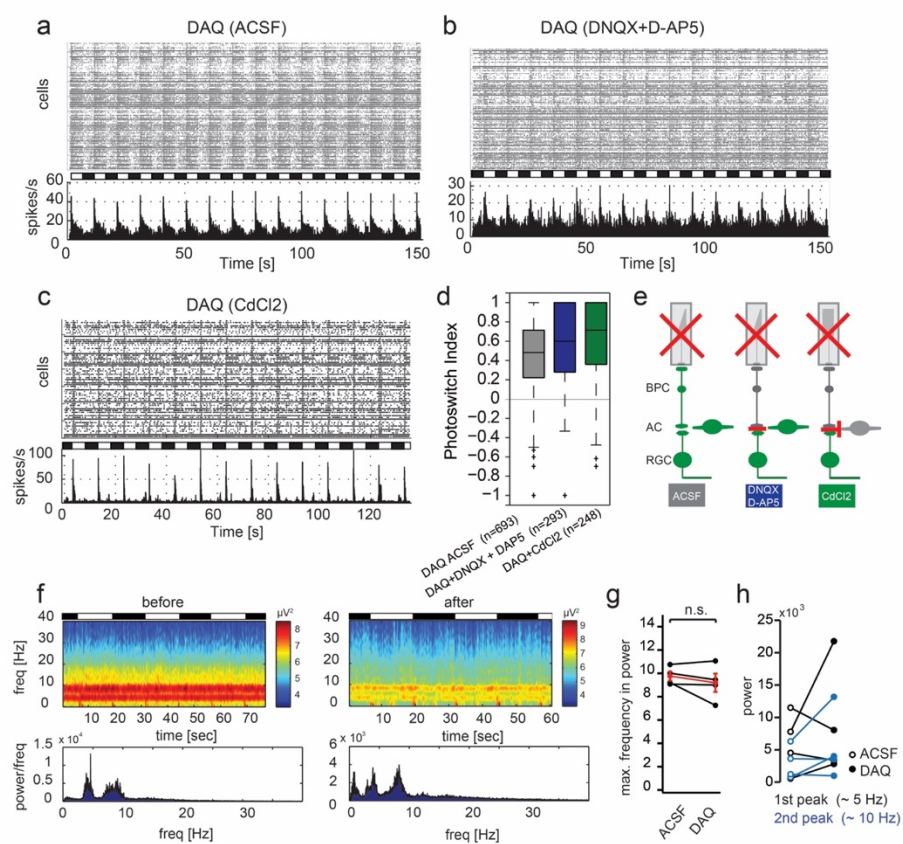
Taken together, these results support the finding that DAD reduces the overall spiking activity by reduction of LFPs in retinas undergoing degeneration and that DAD exerts its effects in the upstream retinal circuitry, where the oscillations arise.

**DAQ: a charged version of DAD acts on retinal ganglion cells and has no effect on LFP frequency.** DAQ (Diethylamino-Azo-Quaternary ammonium, Fig. 1B) is a permanently charged version of DAD. After initial characterization of DAQ in layer 2/3 cortical neurons (Fig. S2), we sought to determine DAQ's properties in blind retina of the *rd1/rd1, Opn4<sup>-/-</sup>* mouse model. We previously demonstrated that the non-permanently charged photoswitch derivative DAD acts primarily on bipolar cells. Although DAD is not permanently charged, the diethyl-groups of DAD are largely protonated in physiological pH (Fig. S7). We therefore expected similar properties of DAQ in blind retina, since DAQ resembles the charged version of DAD. As with DAD, the primary response was observed when light was switched on, and no activation occurred after switching light off (Fig. 2 and Fig. 3). However, the pharmacological profile of DAQ was markedly different from that of DAD. Unlike with DAD, blocking bipolar-to-retinal ganglion cell input by application of DNQX and D-AP5 did not abolish light-dependent activity in the retina (Fig. 3B-D, Table 1). In addition, application of CdCl<sub>2</sub> (blocking all synaptic transmission) showed a similar result (i.e. persistent light-dependent spiking), thereby demonstrating that neither bipolar cells nor amacrine cells are the primary target cell type affected by DAQ (Fig. 3C, Table 1). These results were unexpected and are in strong contrast to the previously reported pharmacological characterization of DAD, which shows little activation of RGCs but acts primarily through bipolar cells.

To confirm our MEA results we also performed patch-clamp experiments in bipolar cells from *rd1/rd1* retinas. DAQ was applied with the extracellular solution and patch recordings were performed with no additional blockers present. Cells were filled with a fluorescent dye for post-hoc identification of the patched cell (Fig. S8F). At a holding potential of -54 mV, no light-induced currents could be detected (Fig. S8). When we performed current-voltage relationships on the other hand, a strong sustained light-dependent outward current was observed (Fig. S8C-E). This current, however, is unlikely to be the cause of the light induced firing responses seen in RGCs in MEA recordings, as bipolar cell resting potentials lie below -50 mV in degenerated retina<sup>25</sup>. However, these patch clamp experiments demonstrate that lack of light-induced excitatory currents at membrane resting potential is not due to limited accessibility of the photoswitch within the tissue. Light-dependent outward currents were detectable above holding potential of -20 mV and size of these currents are comparable to currents mediated by DAD (80.86±11.64 pA and 64.96±13.19 pA at 40 mV holding potential, respectively,  $p = 0.44$ ).

Previous studies using these types of photoswitches indicated that these compounds elicited their effects on cellular excitability by modulating voltage-gated K<sup>+</sup> channels<sup>6</sup>. To determine whether the observed light-evoked spiking in

the presence of DAQ was mediated by the same mechanism, we recorded spike responses from individual RGCs after applying DAQ (control condition) and after blocking voltage-gated  $K^+$ -channels (200  $\mu$ M TEA-Cl). Consistent with the



**Figure 3. DAQ primarily activates retinal ganglion cells and has minimal effect on LFPs.** (a) Raster plot and histogram of representative MEA recording in an *rd1/rd1, Opn4<sup>-/-</sup>* retina after treatment with 200  $\mu$ M DAQ. (b) Same as in a, with additional application of DNQX and D-AP5. (c) Same as in a, with additional application of CdCl<sub>2</sub>. (d) Quantification of light-on responses using the photoswitch index. (e) Graphical overview of pharmacological experiments. (f) Heat map of rhythmic RGC firing power spectrum before and after application of DAQ. (g) Quantification of maximal frequency response before and after application of DAQ (average intensities of complete time range). Maximum frequency with significant power is defined by the peak of the highest frequency reaching a threshold of 4 SD. Each data point refers to the power average of local field potentials in one retina (n=4 retinas). The average change in power is depicted in red with error bars (mean $\pm$ SEM). (h) Quantification of maximum power at frequency peaks around 5 Hz (black) and 10 Hz (blue) before and after application of DAQ (empty and filled circles, respectively)

hypothesized site of action at voltage-gated  $K^+$ -channels, this pharmacological manipulation strongly suppressed light-evoked spike responses in ganglion cells, resulting in a significant decrease in photoswitch index (Fig S9A, B). To gain further

insight into the circuit mechanisms mediating the observed light responses, we performed whole-cell, voltage-clamp recordings from individual RGCs following DAQ application. Excitatory and inhibitory synaptic inputs to the cells were isolated by holding a cell's membrane voltage at the reversal potential for inhibition (-70 mV) or excitation (0 mV), respectively. Light-evoked excitatory synaptic currents were small (<20 pA) and changes in inhibitory synaptic currents were undetectable relative to the leak currents (Fig. S9C). Further, blocking excitatory synaptic input with ionotropic glutamate receptor antagonists (25  $\mu$ M NBQX; 50  $\mu$ M D-AP5) slightly, but insignificantly, suppressed light-evoked spike responses in ganglion cells and did not significantly affect the measures photoswitch index relative to control (Fig. S9D,E). Together, these data are consistent with a relatively weak effect of DAQ at the level of retinal bipolar cells, suggesting that the principal site of action within the retinal circuit occurs at the level of the ganglion cells. Furthermore, the results from these patch experiments are consistent with the outcome of the pharmacological experiments on MEA.

**Table 1** - Summary of photoswitch indices for DAD, DAQ, DAA and PhENAQ in absence and presence of pharmacological blockers. Data is represented as mean $\pm$ sem.

Compound+condition	PI (mean $\pm$ sem)	n retinas (RGCs)
DAD	0.42 $\pm$ 0.04	5 (522)
DNQX+AP5	0.06 $\pm$ 0.03	3 (162)
CdCl <sub>2</sub>	-0.03 $\pm$ 0.04	3 (172)
DAQ	0.46 $\pm$ 0.04	8 (693)
DNQX+D-AP5	0.55 $\pm$ 0.07	4 (293)
CdCl <sub>2</sub>	0.62 $\pm$ 0.1	3 (248)
DAA	-0.09 $\pm$ 0.06	12 (970)
DAA off response	0.29 $\pm$ 0.06	12 (970)
DNQX+D-AP5	0.19 $\pm$ 0.04	6 (543)
CdCl <sub>2</sub>	0.07 $\pm$ 0.14	5 (463)
PhENAQ	0.21 $\pm$ 0.02	7 (709)
DNQX+AP5	0.33 $\pm$ 0.06	3 (260)
CdCl <sub>2</sub>	0.46 $\pm$ 0.06	4 (268)

Taken together, these results demonstrate that DAQ has a different pharmacological and cell-specificity profile compared to DAD, likely attributable to the permanent charge in the molecule. In this regard, DAQ seems more similar to DENAQ, a second-generation photoswitch. However, DAQ has a much higher solubility in water and buffer than DENAQ (up to 200 mM in H<sub>2</sub>O, comparable to DAD). We therefore consider DAQ as an intermediate between second (DENAQ, BENAQ, PhENAQ) and the third-generation photoswitch (DAD).

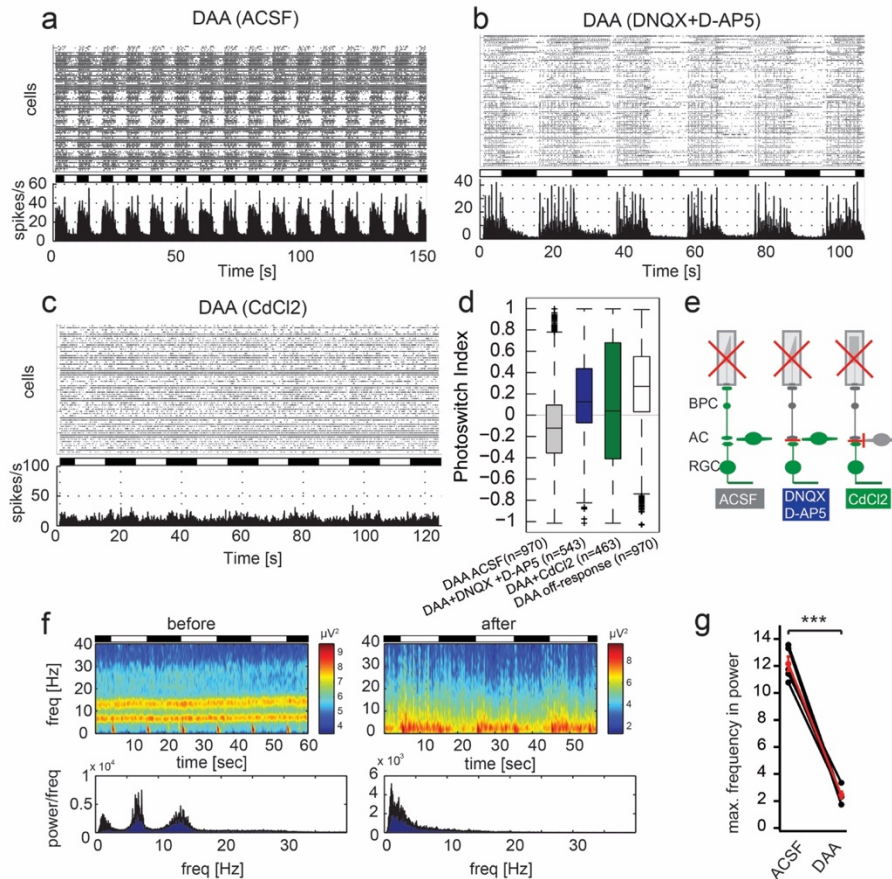
We next wanted to investigate whether DAQ reduces LFPs in absence or presence of light. When washed onto the retina in the dark or switching between light and dark, DAQ had no effect on LFP frequencies (Fig. 3F,G) and overall power (Fig. 3F,H). This result can most likely be attributed to DAQ targeting retinal ganglion cells and not influencing the upstream circuitry, which is responsible for generating the oscillatory activity.

### **DAA: A truncated version of DAD acts upstream of retinal ganglion cells and suppresses rhythmic LFPs**

Although DAA and DAQ showed relatively similar properties in layer 2/3 neurons of murine brain slice preparations, DAA had strikingly different functionality when applied to blind mouse retina (Fig. 4A-D and Table 1). Unlike all other photoswitches studied to date, the strongest firing was observed when light was switched off (sustained off-response), though a transient light-on response was also detected (Fig. 4D). Because of this unique light response, we next set out to investigate DAA's action on bipolar and amacrine cells selectively. First, we performed pharmacological experiments blocking bipolar cell input onto retinal ganglion cells using DNQX and D-AP5. Interestingly, application of these blockers led to a full inversion in light response, with emergence of a sustained light-on response. The main spiking activity in presence of these blockers was detected during the light phase and only a transient response was seen when light was switched off (Fig. 4B). This inversion of the photo-response under glutamergic blockage strongly suggests a dominant action of DAA on amacrine cells, analogously to the first-generation photoswitch AAQ<sup>4</sup>. Conversely, application of CdCl<sub>2</sub> nearly completely abolished light-dependent firing (Fig. 4C,D). These results demonstrate that DAA targets primarily amacrine cells and partially bipolar cells, and that it has only a minor effect on RGCs. It is notable that both uncharged photoswitch compounds (DAA and DAD) have primary effect upstream of retinal ganglion cells while all fast-relaxing charged compounds to date (DAQ, DENAQ, and BENAQ) appear to primarily target retinal ganglion cells directly.

To further substantiate the finding that photoswitches acting upstream from retinal ganglion cells, at the site of LFP origin, reduce the oscillatory activity, we investigated the effect of DAA on rhythmic LFPs (Fig. 4E,F). Similar to DAD, DAA reduced LFPs, with an even stronger reduction than induced by DAD application (Fig. 2E,F). This may be explained by DAA largely targeting amacrine cells, the

primary source of the LFPs in the degenerating retina, whereas DAD exerts its effects primarily on bipolar cells.



**Figure 4. Pharmacological profile of DAA and effect on LFPs in blind retinæ.** (a) Raster plot and histogram of representative MEA recording in an *rd1/rd1, Opn4<sup>-/-</sup>* retina after treatment with 200  $\mu\text{M}$  DAA. (b) Same as in a, with additional application of DNQX and D-AP5. (c) Same as in a, with additional application of  $\text{CdCl}_2$ . (d) Quantification of light-on responses using the photoswitch index. (e) Graphical overview of pharmacological experiments. (f) Heat map of power spectrum of local field potentials before and after application of DAA. (g) Quantification of maximal frequency response before and after application of DAA. Maximum frequency with significant power is defined by the peak of the highest frequency reaching a threshold of 4 SD. Each data point refers to the power average of local field potentials in one retina (n=5 retinas). The average change in power is depicted in red with error bars (mean $\pm$ SEM).



**PhENAO: A second-generation photoswitch targets retinal ganglion cells and has no effect on LFPs.**

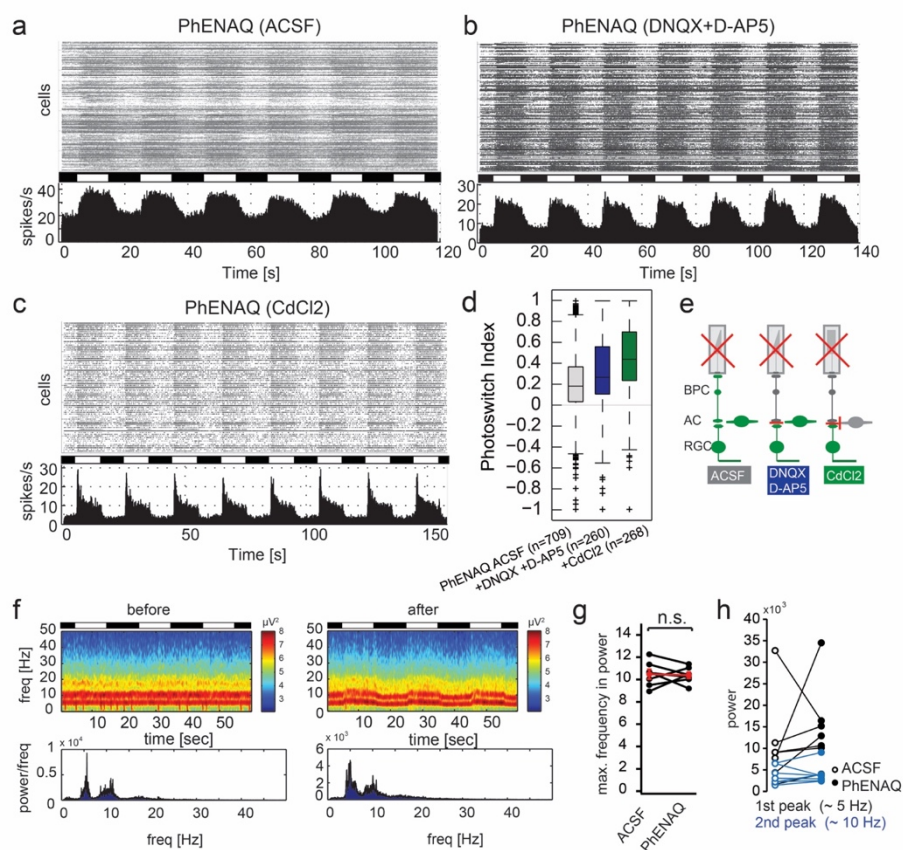
To extend our knowledge further regarding structure-activity relationships and repression of LFPs by application of photochromic blockers, we also analyzed PhENAO (Fig. 1B). PhENAO is a 'second-generation' photoswitch similar to DENAO and BENAQ with a permanent charge and a large hydrophobic group<sup>18</sup>. As shown previously, PhENAO has a rather slow and sustained effect on neuronal firing<sup>18</sup>. When applied to *rd1* retinas, PhENAO showed primarily sustained light on responses (Fig. 5). Application of DNQX and D-AP5 had no effect on light responses; however, spontaneous activity was reduced (Fig. 5B,D). Application of CdCl<sub>2</sub>, on the other hand, led to transient light on responses (Fig. 5C,D) and strongly decreased spontaneous activity, thereby significantly increasing the signal to noise ratio (Table 1,  $p = 0.0015$ ). These MEA experiments demonstrate that retinal output is primarily dominated by direct light responses in retinal ganglion cells. However, the fact that light responses were significantly improved upon block of all upstream inputs (i.e. application of CdCl<sub>2</sub>) indicates some effect of PhENAO on amacrine and bipolar cells. Therefore, we conclude that PhENAO acts in a similar fashion as the other second-generation photoswitches DENAO and BENAQ (Fig. 1B)<sup>3,26</sup>.

We further investigated the action of PhENAO on LFPs. As expected for a photoswitch primarily targeting RGCs, application of PhENAO in darkness had no effect on LFPs (Fig. 5E,F). However, when light stimulation was applied, a mild modulating effect on LFPs became visible (Fig. 5E), consistent with PhENAO acting on both RGCs and to a minor extent on cells upstream of RGCs. However, no effect on maximal frequency response or overall power was detected (Fig. 5F,H).

**Discussion**

Although the pharmacological profiles of DAQ, DAD and DAA in brain slice are very similar, there are marked differences in their cell-type selectivity in retinal tissue. The mechanism of uptake into RGCs has been studied by Tochitsky et al. for various second-generation open-channel blockers, such as DENAO<sup>5</sup>. In contrast to second-generation compounds, membrane-permeable, photoswitchable open-channel blockers appear to target different cell types (bipolar for DAD and amacrine cells for DAA) and do not appear to rely on an uptake through dilated channels. Although Tochitsky et al. have demonstrated how second-generation open-channel blockers enter into retinal ganglion cells of degenerated retinas (via P2X receptors), the important question of what prevents the supposedly membrane-permeable photoswitches such as DAD and DAA from diffusing through all cell types' membranes, remains to be answered<sup>6</sup>.

Rhythmic LFPs arising in blind retinas are an obstacle for vision restoration approaches, as the oscillatory activity increases the general background activity and therefore decreases the signal-to-noise ratio for restored signals<sup>16</sup>.



**Figure 5. Pharmacological profile of PhENAO and effect on rhythmic LFPs in blind retinas.** (a) Raster plot and histogram of representative MEA recording in an *rd1/rd1, Opn4<sup>-/-</sup>* retina after treatment with 200 μM PhENAO. (b) Same as in a, with additional application of DNQX and D-AP5. (c) Same as in a, with additional application of CdCl<sub>2</sub>. (d) Quantification of light-on responses using the photoswitch index. (e) Graphical overview of pharmacological experiments. (f) Power spectrum of local field potentials before and after application of PhENAO. (g) Quantification of maximal frequency response before and after application of PhENAO (average intensities of complete time range). Maximum frequency with significant power is defined by the peak of the highest frequency reaching a threshold of 4 SD. Each data point refers to the power average of local field potentials in one retina (n=7 retinas). The average change in power is depicted in red with error bars (mean±SEM). (h) Quantification of maximum power at frequency peaks around 5 (black) and 10 Hz (blue) before and after application of PhENAO (empty and filled circles, respectively).

Interestingly, in wild-type retina, in a melanopsin knock-out model and in a model for stationary night-blindness, in which rod and cones are not light-responsive, rhythmic LFPs around 5 and 10 Hz were not detected. In contrast, in two studied retinal degenerate mouse models (*rd1* and *rd10*), these characteristic LFPs were present, even at an early stage of the degenerative process<sup>13</sup>. These results indicate that although not fully functional, the presence of morphologically intact photoreceptor cells can prevent the induction of LFPs and that LFPs are primarily related to the degeneration of photoreceptor cells. However, after partial bleaching of healthy retina, which leaves photoreceptor cells intact, some electrophysiological features of LFPs comparable to *rd10* mice can be mimicked<sup>27</sup>.

The majority of the pathological hyperactivity in degenerated retinas is thought to arise from All amacrine - bipolar cell coupling and from a second network in the outer retina, which has been recently described by Euler and Schubert<sup>28</sup>. These multiple sources of LFPs may complicate the elucidation and understanding of a possible mode of action of pharmaceuticals to target them<sup>28-30</sup>. Pharmacological intervention by blocking GAP-junctions eliminates most of the aberrant activity and improves optogenetically evoked light responses<sup>16,31</sup>. While blocking GAP-junction coupling between All amacrine and bipolar cells might be beneficial for approaches targeting RGCs directly, it will not be applicable for strategies targeting the retinal network upstream from RGCs. However, restoring vision in the upper retinal network is able to induce light on and off responses, which might be advantageous for the perceived spatial and temporal resolution in blind patients<sup>6,32,33</sup>.

We have now investigated the effect of different classes of photoswitches on these LFPs. MEA recordings of degenerated retina with photoswitches were filtered for low frequencies. In combination with pharmacological evaluation of the photoswitches, we conclude that molecules that exert their effect via RGCs (i.e. PhENAQ and DAQ) have no effect on the magnitude and frequency of LFPs, while photoswitches that act on cell types upstream of RGCs can be used to suppress LFPs. Furthermore, DAA, which primarily exerts its effect on amacrine cells, reduces LFPs to a greater extent than DAD, which primarily acts on bipolar cells. This is further supported by the fact, that light stimulation has opposing effects on LFP modulation, i.e. light stimulation depresses LFP further in presence of DAD but increases with DAA (Fig. 2F and 4F, respectively). This data is in line with the current understanding that LFPs arise from ON bipolar cells and All amacrine cells, which is further supported by the finding that blockage of glutamatergic input onto RGCs decreases local field potentials, however, fails to abolish the high spontaneous firing rates<sup>13,15,25,29</sup>.

PhENAQ, a photoswitch with strong actions on RGCs, fails to decrease overall LFPs, however, light dependent modulation is observed. In addition, the pharmacological experiments also indicate light-dependent activation in amacrine and bipolar cells (Fig 5). This lack of overall LFP reduction could partially be

explained, if bipolar and amacrine cell responses cancel each other out. To investigate the exact specificity and functionality of PhENAQ further studies need to be performed.

To determine if these conclusions are generalizable to all outer retinal degeneration models further testing in other retinal degenerate models will be required. In addition, it remains to be seen, whether optogenetic stimulation of the upstream retinal circuitry or photochromic ligands targeting synaptic receptors rather than ion channels are also able to suppress local field potentials<sup>34</sup>. Furthermore, photoswitches targeting cells upstream from RGCs induce slight modulations in LFP generation depending on light application. These modulations are probably due to different binding affinities of the photoswitches in light and darkness; whereby incomplete depression of LFPs is induced in one state and not the other. It remains to be seen whether these fluctuations may present further challenges to the visual processing in higher brain areas.

Chemical modification of azobenzene-derivatives of QX-314 and lidocaine demonstrate the remarkable sensitivity of the retina to small structural changes of these compounds. Different derivatives appear to target different cell types, with DAD targeting bipolar cells primarily, DAA targeting amacrine cells, and DAQ primarily targeting retinal ganglion cells. The retinal ganglion cell outputs of blind retinas treated with these compounds are distinct, with DAD-treated retinas showing strong transient on- and off- responses, DAA retinas showing a sustained off-response to alternating light-dark stimuli, and DAQ showing responses similar to second-generation compounds PhENAQ and DENAQ, with primarily sustained-on responses. However, even within a group targeting the same cell class, compounds may show distinctly different physical properties, such as PhENAQ and DAQ, with DAQ being much more soluble than PhENAQ. The substantial variety of responses and physical properties of closely related photoswitch derivatives of QX-314 and lidocaine suggest that additional medicinal chemistry may result in compounds further optimized for use in vision restoration in outer retinal degeneration.

Our results confirm that photochromic ligands are a potentially powerful pharmacological approach for the restoration of vision lost to outer retinal degeneration. The strong suppression of rhythmic local potentials by DAA and DAD indicate that members of this class may be particularly useful for vision restoration by providing higher signal-to-noise output as well as potentially recapitulating retinal processing by circuitry upstream of the ganglion cell.

## Methods

**Chemicals.** Photoswitch derivatives were synthesized as HCl salts in accordance with the synthetic routes described in the *Supplementary Methods*. All other chemicals were purchased from Abcam or Tocris Bioscience.

**Animals and retina and acute brain slice preparation.** For all MEA and retina patch clamp recordings we used 3- to 7-month-old homozygous *rd1/rd1 Opn4<sup>-/-</sup>* mice (C3H/HeJ strain, Charles River Laboratories), if not otherwise indicated. Furthermore, we investigated local field potentials in *rd1/rd1 Opn4<sup>-/-</sup>* mice (C57Bl6JRj background), in wild type (C57Bl6JRj) and *Opn4<sup>-/-</sup>* mice [gift of Satchin Panda, Salk Institute, La Jolla, California, USA] animals as well as in the blind, but nondegenerating mouse line (*Gnat1<sup>-/-</sup> Gnat2<sup>-/-</sup> Opn4<sup>-/-</sup>*, derived from *Gnat1<sup>tm1Clma</sup>* and B6.Cg-*Gnat2<sup>cpfl3/Boc</sup>*, The Jackson Laboratory). Mice were sacrificed by cervical dislocation. Retinas were dissected and kept in artificial cerebrospinal fluid (ACSF) at room temperature containing 125 mM NaCl, 2.5 mM KCl, 1.25 mM NaH<sub>2</sub>PO<sub>4</sub>, 1 mM MgCl<sub>2</sub>, 2 mM CaCl<sub>2</sub>, 26 mM NaHCO<sub>3</sub>, and 20 mM D-glucose; aerated with 95% O<sub>2</sub>/5% CO<sub>2</sub>.

All animal use procedures were approved by the University of Washington Institutional Animal Care and Use Committees. All experiments were performed in accordance with relevant guidelines and regulations.

**Coronal slice preparation.** For basic characterization of photoswitches acute coronal brain slices were prepared from C57Bl6JRj mice (postnatal day 10–13, both male and female animals were used without known experimenter bias). Mice were decapitated and the brain was rapidly removed and kept in ice-cold saline solution composed of (in mM): 87 NaCl, 2.5 KCl, 1.25 NaH<sub>2</sub>PO<sub>4</sub>, 25 NaHCO<sub>3</sub>, 0.5 CaCl<sub>2</sub>, 7 MgCl<sub>2</sub>, 25 glucose, 75 sucrose saturated with carbogen (95% O<sub>2</sub>/5% CO<sub>2</sub>). Coronal brain slices (250 μm) were prepared using a Campden vibratome 7000 smz<sup>2</sup> (NPI Electronic). Slices were incubated at 34 °C for 30 min in ACSF and further stored at room temperature from 1 to 5 h before recordings were started.

**Retina slice preparation.** Retinal slice preparations were performed as previously described in<sup>6</sup>. Briefly, retinas were embedded in 3% low-melting agarose and cut into a small block. The agar block with the retina was glued to the specimen disc. A Campden vibratome 7000 smz<sup>2</sup> (NPI Electronic) was used to cut slices with a thickness of 400–450 μm, which were directly transferred to the recording chamber. A slice anchor was mounted to hold down the agar, while the retina was unobstructed.

**Patch-Clamp recordings of layer 2/3 cortical neurons.** All experiments were performed at room temperature and in presence of 1 μM TTX unless stated otherwise. Photoswitch solutions were prepared in ACSF was prepared from a 200 mM stock solutions (ddH<sub>2</sub>O), except for DENAQ, which was prepared in DMSO. Holding potential was set to -60 mV. To evaluate blocking/unblocking K<sub>v</sub> channels kinetics of photoswitches, cells were depolarized from a holding potential of -

60 mV to +50 mV. During the depolarization, pulse the photoswitch was switched from *trans* (dark) to *cis* (460 nm) and back. Light-induced currents were corrected for desensitization, and  $t$  was calculated from this photoswitch-mediated current trace. For investigation of photoswitch-mediated effects on  $\text{Na}_v$ -channels, a voltage jump from -70mV to -40mV was performed in the absence of TTX, but in presence of TEA and cesium. Cells were patched using glass electrodes with a resistance of 6–7 M $\Omega$  and an intracellular solution containing (in mM): 140 K-gluconate, 10 HEPES, 12 KCl, 4 NaCl, 4 Mg-ATP, 0.4 Na<sub>2</sub>-GTP. Recordings were made with an EPC 10 USB amplifier, which was controlled by the Patchmaster software (HEKA). Data was filtered at 2.9–10 kHz and digitized at 50 kHz. Cells with leak currents were >200 pA for hippocampal neurons or with a series resistance >15 M $\Omega$  were rejected from analysis. Data was analyzed using the Patcher's Power Tools (MPI Göttingen) and routines written in IgorPro (Wavemetrics).

**Patch-clamp recordings in whole mount retinas.** Retinal Ganglion Cells: Patch-clamp recordings were performed using borosilicate glass pipettes containing Ames medium for extracellular spike recording or, for whole-cell recording, a cesium-based internal solution containing: 105 mM Cs-methansulfonate, 10 mM TEA-Cl, 20 mM HEPES, 10 mM EGTA, 2 mM QX-314, 5 mM Mg-ATP, and 0.5 mM Tris-GTP, pH ~7.3 with CsOH, ~280 mOsm. Series resistance (~3-9 M $\Omega$ ) was compensated online by 50%. Excitatory and inhibitory synaptic currents were isolated by holding cells at the reversal potentials for inhibition/chloride (-70 mV) and excitation (0 mV), respectively. Data were acquired at 10 kHz using a Multiclamp 700B amplifier (Molecular Devices), Bessel filtered at 3 kHz, digitized using an ITC-18 analog-digital board (HEKA Instruments), and acquired using the Symphony acquisition software package (<http://symphony-das.github.io>).

**Patch-clamp recordings in retinal slices.** Retinal slices were transferred to the recording chamber immediately after slicing. Electrodes with a resistance of 12-14 M $\Omega$  and with an intracellular solution containing either 140 mM K-gluconate, 10 mM HEPES, 12 mM KCl, 4 mM NaCl, 4 mM Mg-ATP, 0.4 mM Na-GTP, and 1% Lucifer Yellow, pH 7.3, with KOH or 120 mM Cs-methansulfonate, 5 mM TEA-Cl, 10 mM HEPES, 3 mM NaCl, 10 mM EGTA, 2 mM QX-314, 2 mM Mg-ATG, 0.3 mM Na-GTP, and 1% Lucifer Yellow were used for patch clamp recordings in retinal bipolar cells. Bipolar cells were patched with the same amplifier and settings used as for cortical slice patch clamp recordings. Bipolar cell recordings with >50 pA and >25 M $\Omega$  were excluded from analysis.

**Multielectrode Array (MEA) electrophysiology.** For extracellular recordings, a whole-mount retina was placed onto a multielectrode-array (MEA 1060-inv-BC, Multi-Channel Systems) with the retinal ganglion cell layer down. We used 8 × 8 rectangular arranged MEA electrodes with a diameter of 30  $\mu\text{m}$  and a spacing of 200  $\mu\text{m}$  (200/30 ITO, Multichannel Systems). After mounting on the MEA, retinas were washed for at least 20 min and recordings were made at 34 °C, while constantly perfusing ACSF without photoswitch. Retinas were then perfused with

200  $\mu\text{M}$  photoswitch solution for up to 10 minutes and afterwards again with ACSF. Recordings of spiking as well as LFP recordings were continued for up to 4 hours post photoswitch application. Effects on firing rate and LFPs were constant during this time. Extracellular spikes were high-pass filtered at 300 Hz and digitized at 20 kHz. A spike threshold of 4 SD (standard deviation) was set for each channel. Typically, electrodes with a width of 30  $\mu\text{m}$  record from one to three RGCs. Analysis of spike waveforms was performed using Plexon Offline Sorter (version 3) analyzing principle component analysis of spike waveforms. Blocking excitatory input on retinal ganglion cells is achieved by perfusion of 25  $\mu\text{M}$  DNQX and 50  $\mu\text{M}$  D-AP5. In order to completely block all synaptic transmission in the retina and isolate retinal ganglion cell responses 500  $\mu\text{M}$   $\text{CdCl}_2$  was applied. Blockade of gap junctions in the retina was achieved by perfusion of meclofenamic acid (MFA).

**Light Stimulation.** MEA recordings were performed using a xenon light source (Sutter Instruments) through a liquid light guide and diffusing filter (Thorlabs Inc.). Light stimuli were delivered and monitored by a computer-controlled shutter (Vincent Associates). In patch clamp recordings light was applied using a Polychrome V (Till Photonics) controlled through the Patchmaster software.

**Data Analysis.** RGC firing rate was calculated in 100 ms bins for individual retinas in light and in darkness. The Photoswitch Index was calculated in order to normalize light-elicited changes in firing rate of individual retinal ganglion cells and plotted as interquartile range (Boxplot).  $\text{PI} = (\text{firing rate in the light} - \text{firing rate in darkness}) / (\text{firing rate in the light} + \text{firing rate in darkness})$ . Data analysis was performed using custom routines in IgorPro software (Wavemetrics) or Matlab. In order to analyze oscillatory activity between 0 to 40 Hz we used the Chronux Matlab Package to calculate the multitaper spectrum over a moving window (`mtspeggramc`)<sup>20,21</sup>. Raw data was converted to hdf5-files with no further preprocessing. Settings parameters were set to ('tapers',<sup>5,9</sup>, 'Fs', 40000, 'fpass'<sup>1,40</sup>, 'pad', 'trialave'<sup>1</sup>). Power is represented as  $\mu\text{V}^2$ .

For analysis of 'maximum frequency in power' the peak of the highest frequency reaching a threshold of 4 SD was measured.

**Statistics.** Statistical significance was calculated using the Wilcoxon rank sum test in Matlab. Results were considered significant with \* $p < 0.05$ , \*\* $p < 0.01$ , and \*\*\* $p < 0.001$ . Error bars are presented as mean  $\pm$  standard error of the mean (sem).

**Data Availability Statement**

The datasets generated during and/or analyzed during the current study are available from the corresponding author on reasonable request.

**Acknowledgements**

We thank Florian Huber for providing PhENAQ. Luis de la Osa de la Rosa is acknowledged for the determination of the  $pK_A$  of DAD. Katharina Hüll thanks the German Academic Scholarship foundation for a PhD scholarship. This work was supported by NIH P30EY001730 (Department of Ophthalmology, University of Washington), R24EY023937 (RVG), an unrestricted grant from Research to Prevent Blindness, and the Mark J. Daily, MD Research Fund. We acknowledge the European Research Council (ERC advanced grant 268795 to DT) and NIH (NEI R01-EY027323 to M.B.M) for financial support.

**Author Contributions**

L.L., R.N.V.G., D.T. and K.H. designed the experiments and conceived the study. K.H performed chemical synthesis and patch-clamp in acute brain slices, L.L., performed all MEA and patch-clamp experiments in retinal and brain slices, M.B.M. performed patch-clamp experiments in whole-mount retinal preparations, T.B. and L.L. performed data analysis on local field potential data, K.H., L.L. and R.N.V.G. wrote the manuscript with input from all other co-authors.

**Author Information**

The authors declare no competing interests.



## References

- [1] Roska, B. & Sahel, J. A. Restoring vision. *Nature* **557**, 359–367 (2018).
- [2] Tochitsky, I., Kienzler, M. A., Isacoff, E. & Kramer, R. H. Restoring Vision to the Blind with Chemical Photoswitches. *Chem. Rev.* **118**, 10748–10773 (2018).
- [3] Tochitsky, I., Trautman, J., Gallerani, N., Malis, J. G. & Kramer, R. H. Restoring visual function to the blind retina with a potent, safe and long-lasting photoswitch. *Sci. Rep.* **7**, 45487 (2017).
- [4] Polosukhina, A. *et al.* Photochemical Restoration of Visual Responses in Blind Mice. *Neuron* **75**, 271–282 (2012).
- [5] Tochitsky, I. *et al.* Restoring Visual Function to Blind Mice with a Photoswitch that Exploits Electrophysiological Remodeling of Retinal Ganglion Cells. *Neuron* **81**, 800–813 (2014).
- [6] Laprell, L. *et al.* Photopharmacological control of bipolar cells restores visual function in blind mice. *J. Clin. Invest.* **127**, (2017).
- [7] Hüll, K., Morstein, J. & Trauner, D. In Vivo Photopharmacology. *Chem. Rev.* **118**, 10710–10747 (2018).
- [8] Marc, R. E. & Jones, B. W. Retinal Remodeling in Inherited Photoreceptor Degenerations. *Mol. Neurobiol.* **28**, 139–148 (2003).
- [9] Jones, B. W. *et al.* Retinal remodeling triggered by photoreceptor degenerations. *J. Comp. Neurol.* **464**, 1–16 (2003).
- [10] Jones, B. W. *et al.* Retinal remodeling in human retinitis pigmentosa. *Exp. Eye Res.* **150**, 149–165 (2016).
- [11] Choi, H. *et al.* Intrinsic bursting of All amacrine cells underlies oscillations in the rd1 mouse retina. *J. Neurophysiol.* **112**, 1491–504 (2014).
- [12] Margolis, D. J., Gartland, A. J., Singer, J. H. & Detwiler, P. B. Network Oscillations Drive Correlated Spiking of ON and OFF Ganglion Cells in the rd1 Mouse Model of Retinal Degeneration. *PLoS One* **9**, e86253 (2014).
- [13] Stasheff, S. F., Shankar, M. & Andrews, M. P. Developmental time course distinguishes changes in spontaneous and light-evoked retinal ganglion cell activity in rd1 and rd10 mice. *J. Neurophysiol.* **105**, 3002–3009 (2011).
- [14] Goo, Y. S. *et al.* Spontaneous oscillatory rhythm in retinal activities of two retinal degeneration (rd1 and rd10) mice. *Korean J. Physiol. Pharmacol.* **15**, 415–422 (2011).
- [15] Ye, J. H. & Goo, Y. S. The slow wave component of retinal activity in rd/rd mice recorded with a multi-electrode array. *Physiol. Meas.* **28**, 1079–88 (2007).
- [16] Barrett, J. M., Degenaar, P. & Sernagor, E. Blockade of pathological retinal ganglion cell hyperactivity improves optogenetically evoked light responses in rd1 mice. *Front. Cell. Neurosci.* **9**, 330 (2015).
- [17] Meade, E. A., Smith, W. L. & DeWitt, D. L. Differential inhibition of prostaglandin endoperoxide synthase (cyclooxygenase) isozymes by aspirin and other non-steroidal anti-inflammatory drugs. *J. Biol. Chem.* **268**, 6610–4 (1993).
- [18] Mourot, A. *et al.* Tuning Photochromic Ion Channel Blockers. *ACS Chem. Neurosci.* **2**, 536–543 (2011).
- [19] Dipin, D. & Evans, D. Evans pKa Table. [http://evans.rc.fas.harvard.edu/pdf/evans\\_pKa\\_table.pdf](http://evans.rc.fas.harvard.edu/pdf/evans_pKa_table.pdf)
- [20] Mitra, P. & Bokil, H. *Observed Brain Dynamics*. (Oxford University Press, 2007). doi:10.1093/acprof:oso/9780195178081.001.0001

- [21] Bokil, H., Andrews, P., Kulkarni, J. E., Mehta, S. & Mitra, P. P. Chronux: a platform for analyzing neural signals. *J. Neurosci. Methods* **192**, 146-51 (2010).
- [22] Chang, B. *et al.* Cone Photoreceptor Function Loss-3, a Novel Mouse Model of Achromatopsia Due to a Mutation in Gnat2. *Investig. Ophthalmology Vis. Sci.* **47**, 5017 (2006).
- [23] Lyubarsky, A. L. *et al.* Functionally rodless mice: transgenic models for the investigation of cone function in retinal disease and therapy. *Vision Res.* **42**, 401-15 (2002).
- [24] Panda, S. *et al.* Melanopsin (Opn4) requirement for normal light-induced circadian phase shifting. *Science* **298**, 2213-6 (2002).
- [25] Borowska, J., Trenholm, S. & Awatramani, G. B. An intrinsic neural oscillator in the degenerating mouse retina. *J. Neurosci.* **31**, 5000-5012 (2011).
- [26] Tochitsky, I. *et al.* How Azobenzene Photoswitches Restore Visual Responses to the Blind Retina. *Neuron* **92**, 100-113 (2016).
- [27] Menzler, J., Channappa, L. & Zeck, G. Rhythmic Ganglion Cell Activity in Bleached and Blind Adult Mouse Retinas. *PLoS One* **9**, e106047 (2014).
- [28] Euler, T. & Schubert, T. Multiple Independent Oscillatory Networks in the Degenerating Retina. *Front. Cell. Neurosci.* **9**, 444 (2015).
- [29] Menzler, J. & Zeck, G. Network Oscillations in Rod-Degenerated Mouse Retinas. *J. Neurosci.* **31**, 2280-2291 (2011).
- [30] Yee, C. W., Toychiev, A. H. & Sagdullaev, B. T. Network deficiency exacerbates impairment in a mouse model of retinal degeneration. *Front. Syst. Neurosci.* **6**, 8 (2012).
- [31] Toychiev, A. H., Ivanova, E., Yee, C. W. & Sagdullaev, B. T. Block of gap junctions eliminates aberrant activity and restores light responses during retinal degeneration. *J. Neurosci.* **33**, 13972-7 (2013).
- [32] van Wyk, M., Pielecka-Fortuna, J., Löwel, S. & Kleinlogel, S. Restoring the ON Switch in Blind Retinas: Opto-mGluR6, a Next-Generation, Cell-Tailored Optogenetic Tool. *PLoS Biol.* **13**, e1002143 (2015).
- [33] Buskamp, V. *et al.* Genetic reactivation of cone photoreceptors restores visual responses in retinitis pigmentosa. *Science* **329**, 413-417 (2010).
- [34] Laprell, L. *et al.* Restoring Light Sensitivity in Blind Retinae Using a Photochromic AMPA Receptor Agonist. *ACS Chem. Neurosci.* **7**, 15-20 (2016).

## Supplementary Methods - Chemical Synthesis

**General Experimental Techniques.** Unless stated otherwise all reactions were carried out with magnetic stirring using oven-dried glassware (160 °C) under inert gas atmosphere (nitrogen or argon). Syringes used to transfer reagents and solvents were purged with nitrogen prior to use. Low temperature reactions were carried out in a Dewar vessel filled with the appropriate cooling agent e.g. H<sub>2</sub>O/ice (0 °C). Heating was conducted using a heated oil bath. Yields refer to spectroscopically pure compounds unless otherwise stated.

**Solvents and Reagents.** Reaction solvents were purchased from Acros Organics as 'extra dry' over molecular sieves and handled under inert gas atmosphere. Tetrahydrofuran (THF) was distilled from Na/benzophenone prior to use. Dichloromethane (DCM), triethylamine (TEA) and diisopropylethylamine (DIPEA) were distilled from calcium hydride. Ethanol was purchased from commercial suppliers and used as received. Solvents for extraction and flash column chromatography were purchased in technical grade purity and distilled under reduced pressure on a rotary evaporator prior to use. All other reagents and solvents were purchased from commercial suppliers and used as received.

**Chromatography.** Reactions and chromatography fractions were monitored by qualitative thin-layer chromatography (TLC) on silica gel F254 TLC plates from Merck KGaA. Analytes were visualized by irradiation with UV light and/or by immersion of the TLC plate in ninhydrin or potassium permanganate solution followed by heating with a hot-air gun. Flash column chromatography was performed Geduran® Si60 (40-63 µm) silica gel from Merck KGaA (eluents are given in parenthesis). Reverse Phase column chromatography was performed on Waters C18 (C18; 55-105 µm, 125 Å) as stationary phase (eluents are given in parenthesis). LC-MS was performed on an Agilent 1260 Infinity HPLC System, MS-Agilent 1100 Series, Type: 1946D, Model: SL, equipped with a Agilent Zorbax Eclipse Plus C18 (100 x 4.6 mm, particle size 3.5 micron) reverse phase column with a constant flow-rate of 1 mL/min and a 10 → 100% MeCN/H<sub>2</sub>O + 0.1% FA gradient over 10 min.

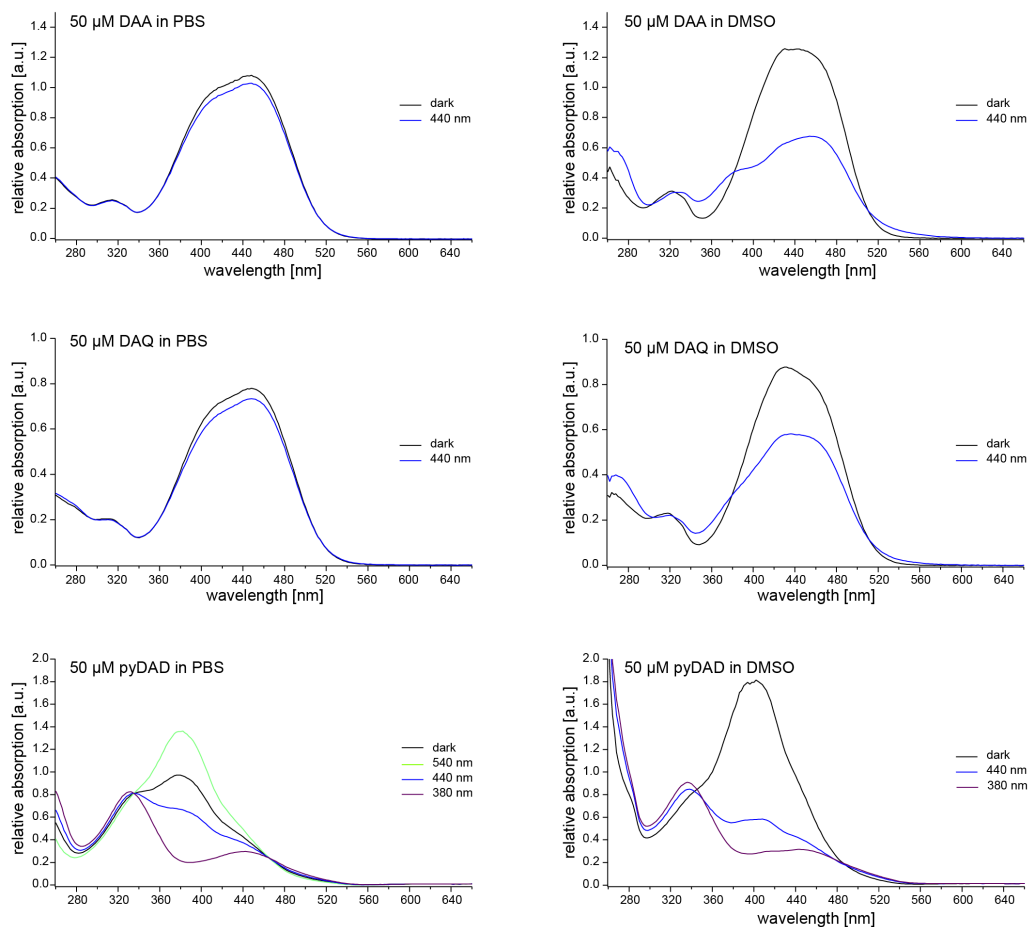
**NMR Spectra.** NMR spectra were measured on Varian 400 MHz Bruker AVIII HD (cryoprobe) for proton nuclei (100 MHz for carbon nuclei respectively). The <sup>1</sup>H NMR shifts are reported in parts per million (ppm) related to the chemical shift of tetramethylsilane. <sup>1</sup>H and <sup>13</sup>C NMR shifts were calibrated to the residual solvent signals: CDCl<sub>3</sub> (7.26 ppm/77.16 ppm) and DMSO (2.50 ppm/39.5 ppm). <sup>1</sup>H NMR spectroscopic data are reported as follows: Chemical shift in ppm (multiplicity, coupling constants (Hz), integration). The multiplicities are abbreviated as follows: s (singlet), d (doublet), t (triplet), q (quartet) and m (multiplet) and are reported as observed. Except for multiplets, the chemical shift of all signals is reported as the centre of the resonance range. Additionally, to <sup>1</sup>H and <sup>13</sup>C NMR measurements, 2D NMR techniques as homonuclear correlation spectroscopy (COSY), heteronuclear single quantum coherence (HSQC) and heteronuclear multiple bond coherence

(HMBC) were used to assist signal assignment. All raw fid files were processed, and the spectra analyzed using the program MestReNova from Mestrelab Research S.L.

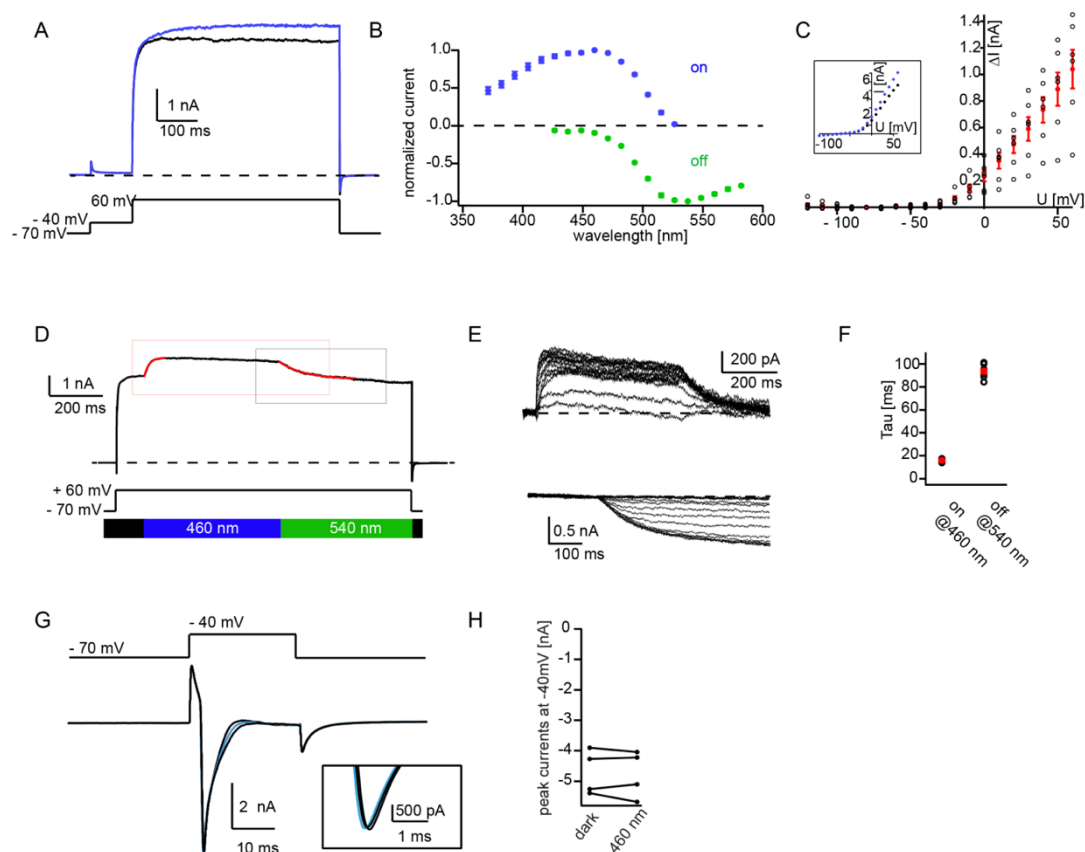
**Mass Spectra.** All high-resolution mass spectra (HRMS) were recorded by the LMU Mass Spectrometry Service. HRMS were recorded on a MAT 90 from Thermo Finnigan GmbH using electrospray ionisation (ESI) or a MAT 90 from Jeol Ltd. using electron ionization (EI).

**UV/Vis Spectra.** UV/Vis spectra were recorded on a Varian Cary 50 Scan UV/Vis spectrometer using Helma SUPRASIL precision cuvettes (10 mm light path). All compound stock solutions were prepared under benchtop light conditions at 50 mM in DMSO and diluted to the right concentration in the final solvent (DMSO or PBS). Photoswitching was achieved using a Polychrome V (Till Photonics) Monochromator, or a Prizmatix ultra high-power LED (460 nm), connected to a fiber-optic cable through which the sample in the spectrophotometer was irradiated from the top.

## Supplementary Figures

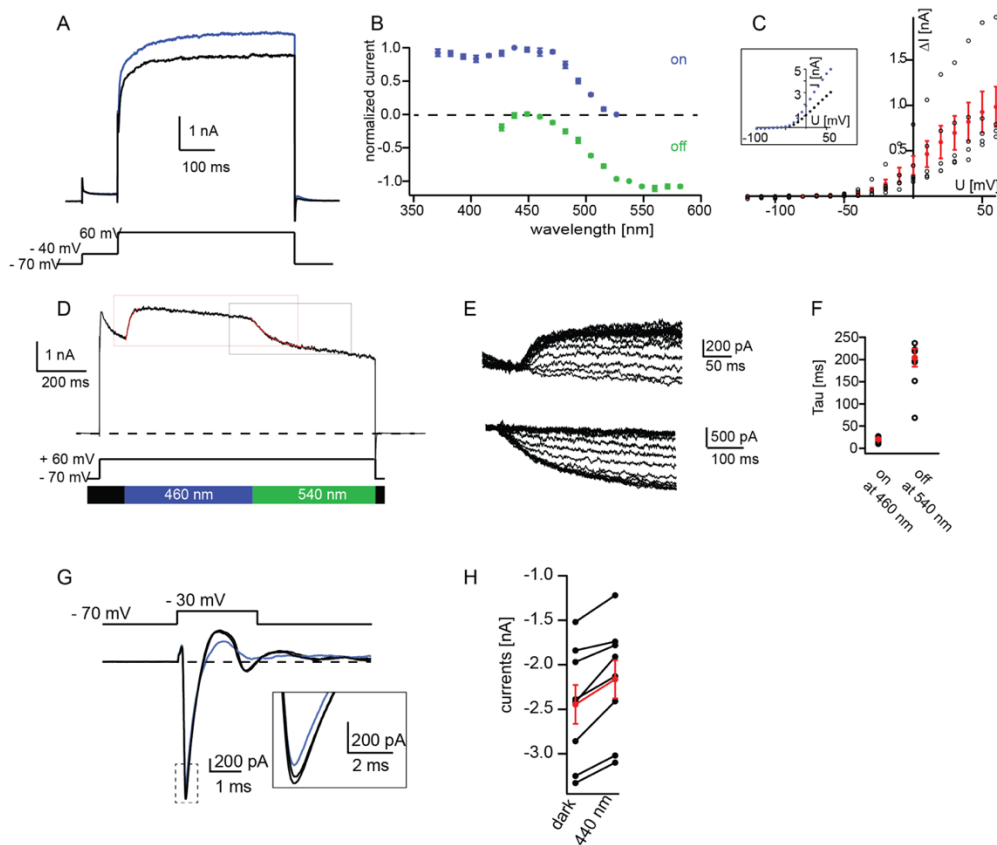


**Supplementary Figure 1. UV Vis spectra of DAA, DAQ and pyDAD in PBS and DMSO.** Spectra were collected at 50  $\mu\text{M}$  concentration and samples were irradiated for 3 min with monochromatic light of the respective wavelength before collecting the spectrum.

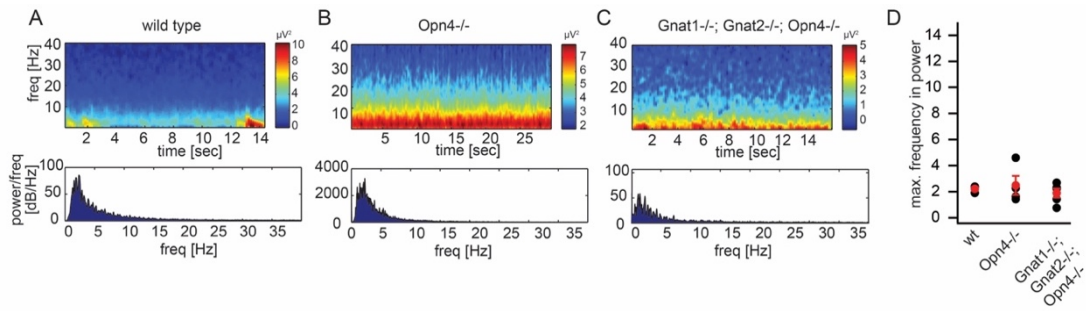


**Supplementary Figure 2. Characterization of DAQ in layer 2/3 cortical neurons of an acute brain slice of wild type mice.**

(A) Whole-cell recording after incubation with 200  $\mu\text{M}$  DAQ in the presence of 1  $\mu\text{M}$  TTX. Potassium ( $K_v$ ) outward currents were activated by a step from  $-70$  mV to  $+60$  mV. Currents in darkness (black) are compared to currents in the presence of 460 nm light. (B) Normalized change in  $K_v$  current in DAQ-treated cortical neurons in response to stimulation with light of different wavelengths. (C) Difference in current-voltage relationship between darkness and 460 nm light. Inset: Representative raw data traces in darkness (black) and in 460 nm light (blue). (D) Example trace for determining the kinetics of unblocking the pore of  $K_v$ -channels. (E) Top: Raw data currents at  $+60$  mV holding potential, while switching between different wavelengths of light and darkness. Bottom: Raw data traces of decay time by different wavelengths of light (F) Quantification of on- and off-kinetics in response to different wavelengths.  $\tau_{\text{unblock}} = 16.0 \pm 0.49$  ms ( $n = 7$  cells). Fastest off-responses were achieved at 520 nm light ( $\tau_{\text{block}} = 93.51 \pm 2.12$  ms,  $n = 7$  cells). (G) Recording in cortical neurons in presence of Cesium and TEA. Voltage jump from  $-70$  mV resting potential to  $-40$  mV induces sodium channel currents. (H) Quantification of peak sodium currents in darkness and under blue light illumination.

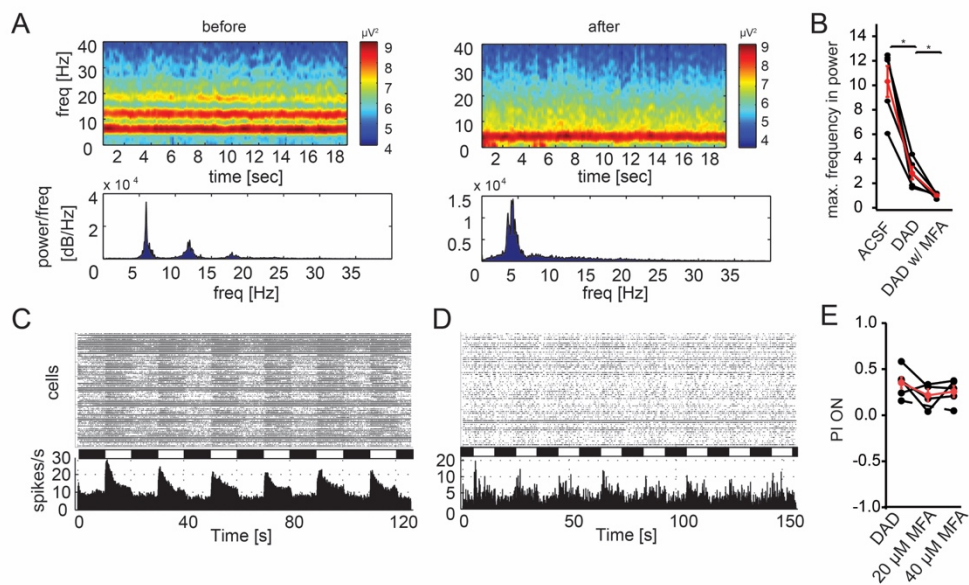


**Supplementary Figure 3. Characterization of DAA in layer 2/3 cortical neurons of an acute brain slice of wild type mice.** (A) Whole-cell recording after incubation with 200  $\mu\text{M}$  DAA in the presence of 1  $\mu\text{M}$  TTX. Potassium ( $\text{K}_v$ ) outward currents were activated by a step from  $-70$  mV to  $+60$  mV. Currents in darkness (black) are compared to currents in the presence of 460 nm light. (B) Normalized change in  $\text{K}_v$  current in DAA-treated cortical neurons in response to stimulation with light of different wavelengths. (C) Difference in current-voltage relationship between darkness and 460 nm light. Inset: Representative raw data traces in darkness (black) and in 460 nm light (blue). (D) Example trace for determining the kinetics of unblocking the pore of  $\text{K}_v$ -channels. (E) Top: Raw data currents at  $+60$  mV holding potential, while switching between different wavelengths of light. Bottom: Raw data traces of decay time by different wavelengths of light. (F) Quantification of on- and off-kinetics in response to different wavelength.  $\tau_{\text{unblock}} = 20.4 \pm 1.75$  ms ( $n = 9$  cells). Fastest off-responses were achieved at 520 nm light ( $\tau_{\text{block}} = 204 \pm 20.3$  ms,  $n = 9$  cells). (G) Recording in cortical neurons in presence of Cesium and TEA. Voltage jump from  $-70$  mV resting potential to 0 mV induces sodium channel currents. (H) Quantification of peak sodium currents in darkness and under blue light illumination.

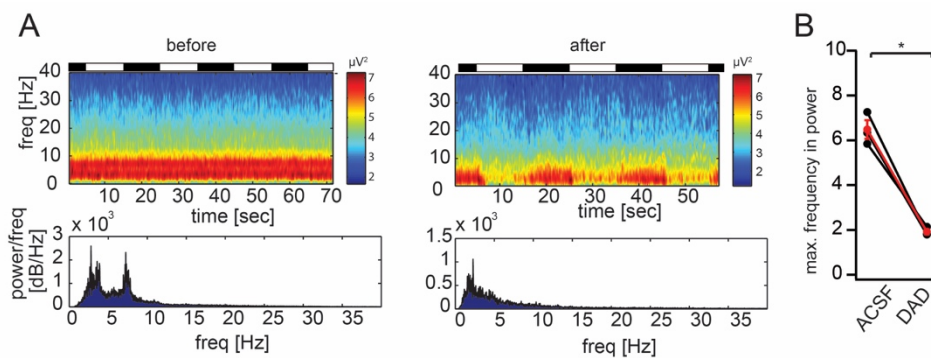


**Supplementary Figure 4.** Power spectrum of rhythmic LFP in non-degenerating retinas. (A) Local field potentials in wild type animals, (B) *Opn4*<sup>-/-</sup> and (C) *gnat1*<sup>-/-</sup>; *gnat2*<sup>-/-</sup>; *Opn4*<sup>-/-</sup> animals. (D) Quantification of maximal frequency response (average intensities of complete time range).

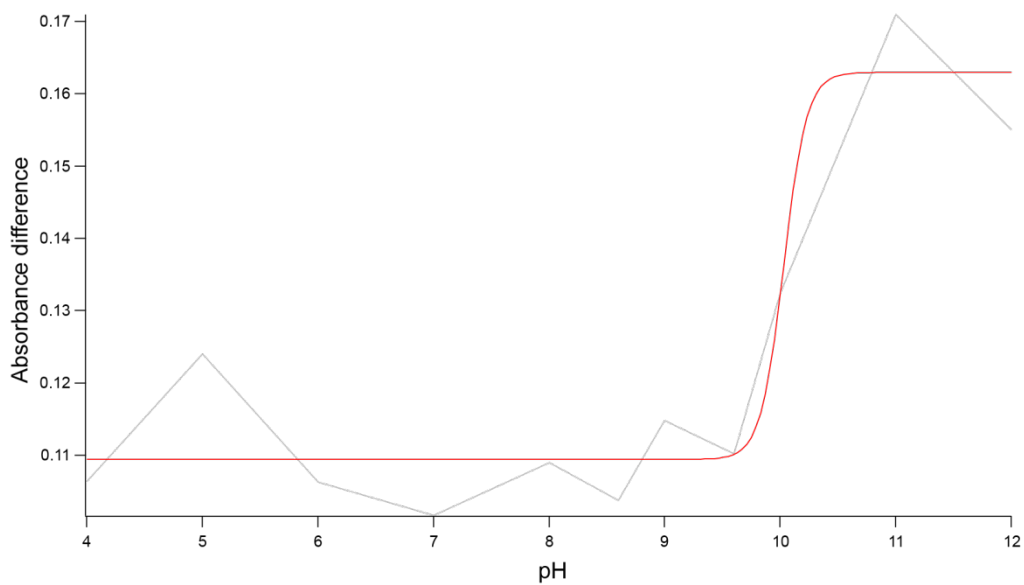




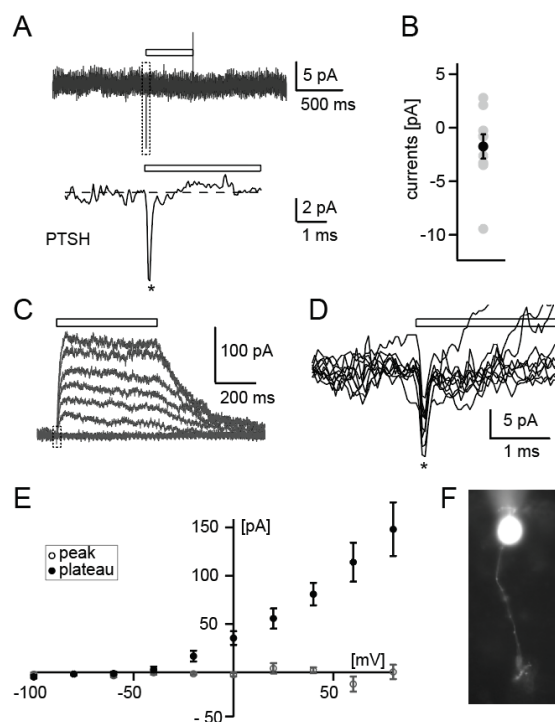
**Supplementary Figure 5.** DAD represses LFPs in retina undergoing degeneration. (A) Power spectrum of local field potentials before and after application of DAD without light stimulation. (B) Quantification of maximal frequency response before and after application of DAD and after application of meclofenamic acid (MFA) (average intensities of complete time range). (C) Raster plot and histogram of representative MEA recording in a *rd1/rd1; Opn4<sup>-/-</sup>* retina after treatment with 200  $\mu M$  DAD. (D) Same as in a, with additional application of MFA. (E) Quantification of light-on responses using the photoswitch index.



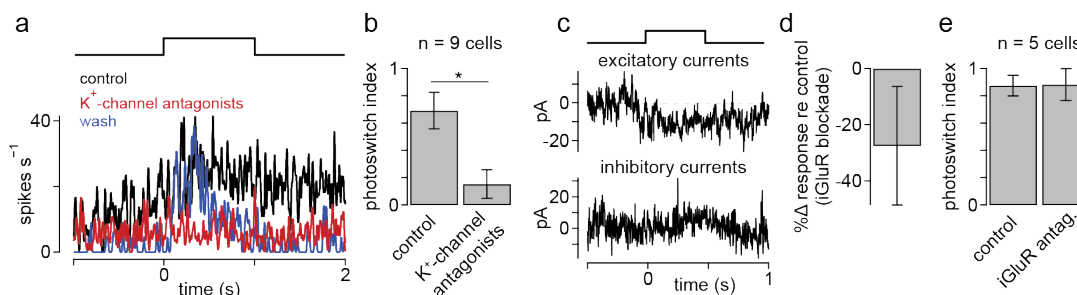
**Supplementary Figure 6.** DAD represses local field potentials in a *rd1* mouse model with C57Bl/6 genetic background. (A) Power spectrum of oscillatory local field potentials before and after application of DAD. (B) Quantification of maximal frequency response before and after application of DAD. (average intensities of complete time range).



**Supplementary Figure 7.**  $pK_A$  determination of DAD according to a procedure by Ríos Martínez and Dardonville.<sup>2</sup> Sigmoidal fit using Igor 6.37 estimated a  $pK_A$  of 10 for DAD. Data was collected as a single measurement.



**Supplementary Figure 8. DAQ has no effect in retinal bipolar cells from *rd1/rd1,Opn4<sup>-/-</sup>* retinas** (A) Voltage-clamp recording of a bipolar cell in presence of DAQ. Top: Full trace, peristimulus time histogram (PTSH) of 5 sweeps. Asterix (\*) marks a light artefact induced by the LED. Bottom: Enlargement of dotted box on top. Bar above the trace marks the light stimulation with 460 nm light. (B) Peak-currents measured at 0.5 ms after light onset (average time to peak for DAQ-mediated light responses in bipolar cells<sup>1</sup>) (C) Raw data traces of an IV-relationship of DAQ mediated currents in the absence of blockers. (D) Raw data trace for voltages from  $-100$  to  $+40$  mV. Enlargement of box in C. (E) Analysis of IV relationships. Empty circles: Transient peak current. Filled circles: Late  $K_v$ -channel component. ( $n = 8$ ). (F) Fluorescence image of a bipolar cell filled with Lucifer Yellow after whole cell patch clamp configuration. Data is represented as mean $\pm$ sem.

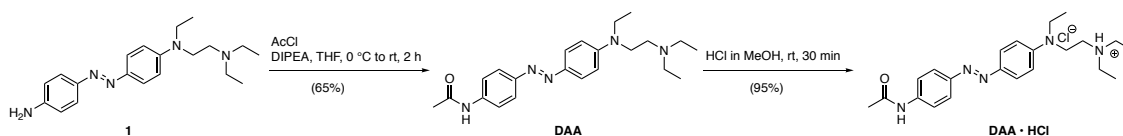


**Supplementary Figure 9. K<sup>+</sup>-channel antagonists attenuate DAQ-mediated light responses.**

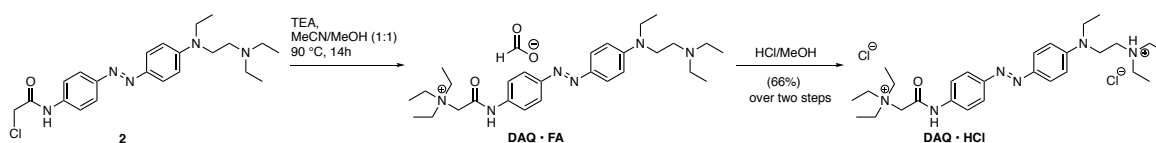
(A) Spike rate from a ganglion cell recorded to a 1-s light flash following DAQ application. Recordings were made under control conditions (black), following the application of K<sup>+</sup>-channel antagonists (red), and after washing out the drugs (blue). Spike rate was strongly attenuated during the light flash following drug application. (B) The photoswitch index was significantly suppressed following application of K<sup>+</sup>-channel antagonists ( $n = 9$  cells;  $p = 2.0 \times 10^{-2}$ ). (C) Excitatory and inhibitory synaptic current recordings in the same cell following application of DAQ. Synaptic currents were relatively small. (D) On average, the ionotropic glutamate receptor antagonists suppressed ganglion cell spike responses by ~25%, but this effect was not statistically significant ( $n = 5$  cells;  $p = 0.16$ ). (E) The photoswitch index was not significantly decreased following application of ionotropic glutamate receptor antagonists that attenuated excitatory synaptic input to the recorded ganglion cells ( $n = 5$  cells;  $p = 0.25$ ). Bars indicate mean  $\pm$  SEM. All statistical tests were paired and were performed using the Wilcoxon signed rank test. Control conditions refer to conditions where only the photoswitch DAQ is applied.



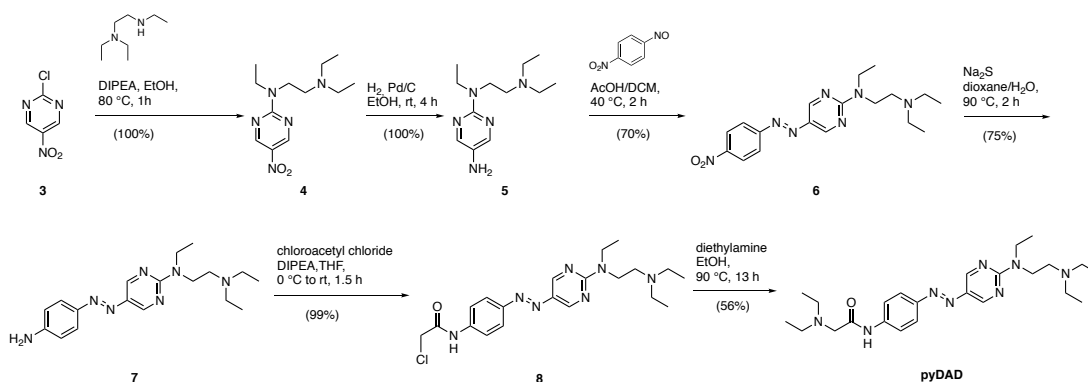
## Experimental Procedures



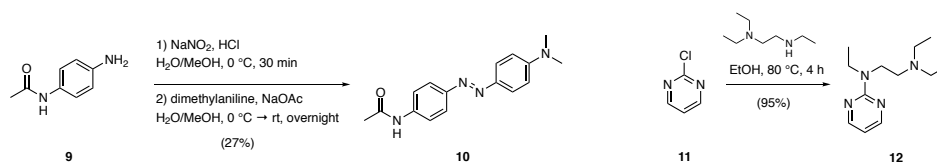
**Supplementary Scheme 1.** Synthesis of DAA·HCl, starting from the known precursor **1**<sup>1</sup>.



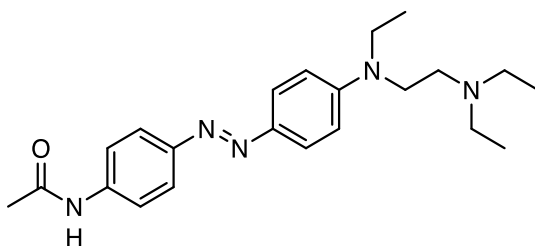
**Supplementary Scheme 2.** Synthesis of DAQ·HCl, starting from the known precursor **2**<sup>1</sup>.



**Supplementary Scheme 3.** Synthesis of pyDAD.



**Supplementary Scheme 4.** Synthesis of 10 and 12.

**(E)-N-(4-((4-((2-(diethylamino)ethyl)(ethyl)amino)phenyl)diazenyl)phenyl)-acet-amide (DAA)**

(E)-N1-(4-((4-aminophenyl)diazenyl)phenyl)-N<sup>1</sup>,N<sup>2</sup>,N<sup>2</sup>-triethylethane-1,2-diamine (**1**) was synthesized according to literature.<sup>1</sup> **1** (20.0 mg, 58.9 μM, 1.0 eq) was dissolved in THF (1 mL) and DIPEA (12.2 μL, 70.7 μmol, 1.2 eq) and acetyl chloride (6.31 μL, 88.4 μmol, 1.5 eq) were added at 0°C. The reaction mixture was stirred for 2 h upon which it was allowed to warm up to room temperature. The reaction mixture was concentrated under reduced pressure and the crude mixture was purified by silica gel column chromatography (0.1% TEA + 0 → 5% MeOH/DCM). **DAA** (14.7 mg, 38.9 μmol, 65%) was gained as orange solid.

**<sup>1</sup>H NMR:** (400 MHz, CDCl<sub>3</sub>) δ = 7.87 – 7.75 (m, 4H), 7.62 (d, J = 8.8 Hz, 2H), 7.40 (s, 1H), 6.77 – 6.69 (m, 2H), 3.48 (m, 4H), 2.63 (m, 6H), 2.20 (s, 3H), 1.22 (t, J = 7.1 Hz, 3H), 1.07 (t, J = 7.1 Hz, 6H).

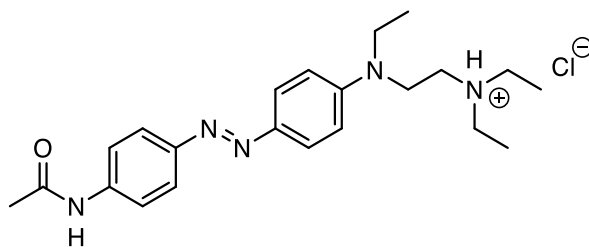
**<sup>13</sup>C NMR:** (100 MHz, CDCl<sub>3</sub>) δ = 168.4, 150.1, 149.8, 143.4, 139.0, 125.3, 123.2, 119.9, 111.1, 50.3, 49.5, 47.7, 45.8, 24.9, 12.6, 12.0.

**HRMS** (ESI): calcd for C<sub>22</sub>H<sub>32</sub>N<sub>5</sub>O<sup>+</sup> [M+H]<sup>+</sup>: 382.2601, found: 382.2607.

**R<sub>f</sub>** = 0.14 (5% MeOH/DCM)

**λ<sub>max</sub>** = 448 nm



**(E)-2-((4-((4-acetamidophenyl)diazenyl)phenyl)(ethyl)amino)-N,N-diethylethan-1-aminium chloride (DAA · HCl)**

HCl in MeOH (1.25 M, 180  $\mu$ L, 0.224 mmol, 1.5 eq) was added dropwise to a solution of **DAA** (57.1 mg, 0.150 mmol, 1.0 eq) in MeOH (1 mL) at rt, upon which the reaction mixture turned purple and was stirred for 5 min. The solvent was removed under reduced pressure and the product was dried under high vacuum to yield **DAA · HCl** (62.1 mg, 0.149 mmol, 99%) as dark orange solid.

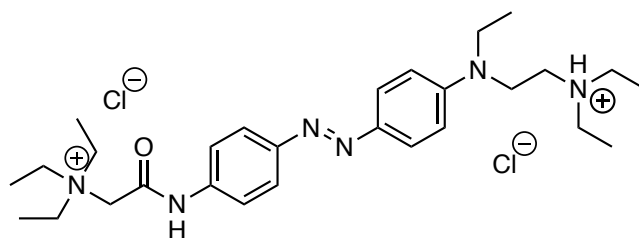
**$^1\text{H NMR}$** : (400 MHz, DMSO- $d_6$ )  $\delta$  = 10.79 (s, 1H), 10.29 (s, 1H), 7.79 – 7.71 (m, 6H), 6.99 – 6.92 (m, 2H), 3.87 (t,  $J$  = 7.9 Hz, 2H), 3.50 (q,  $J$  = 6.9 Hz, 2H), 3.25 – 3.08 (m, 6H), 2.08 (s, 3H), 1.25 (t,  $J$  = 7.2 Hz, 6H), 1.15 (t,  $J$  = 6.9 Hz, 3H).

**$^{13}\text{C NMR}$** : (100 MHz, DMSO- $d_6$ )  $\delta$  = 168.7, 149.3, 147.8, 142.9, 141.0, 124.7, 122.7, 119.15, 111.8, 47.6, 46.2, 44.6, 44.2, 24.2, 12.2, 8.4.

**HRMS** (ESI): calcd for  $\text{C}_{22}\text{H}_{32}\text{N}_5\text{O}^+$  [ $\text{M}+\text{H}$ ] $^+$ : 382.2601, found: 382.2598.

**$R_t$**  = 4.848 min (10  $\rightarrow$  100% MeCN/ $\text{H}_2\text{O}$  + 0.1% FA, 10 min)

**$\lambda_{\text{max}}$**  = 448 nm

**(E)-2-((4-((4-((2-(diethylamino)ethyl)(ethyl)amino)phenyl)diazenyl)phenyl)amino)-N,N,N-triethyl-2-oxoethan-1-aminium (DAQ · HCl)**

(E)-2-chloro-N-(4-((4-((2-(diethylamino)ethyl)(ethyl)amino)phenyl)diazenyl)phenyl)-acetamide (**2**) was prepared according to the literature.<sup>1</sup> **2** (41.0 mg, 98.6  $\mu\text{mol}$ , 1.0 eq) was dissolved in MeCN/MeOH (1.5 mL, 1:1), triethylamine (690  $\mu\text{L}$ ) was added and the reaction mixture was heated to 90  $^{\circ}\text{C}$  in a sealed flask overnight. All solvents were removed under reduced pressure and the crude material was purified by reverse-phase flash column chromatography (10%  $\rightarrow$  100% MeCN/H<sub>2</sub>O + 0.1% FA) to yield DAQ as the formate salt. Addition of HCl in MeOH (1.25 M, 790  $\mu\text{L}$ , 10 eq) followed by removal of the solvent in vacuo yielded DAQ · HCl (35.8 mg, 0.0647 mmol, 66%) as deep purple solid.

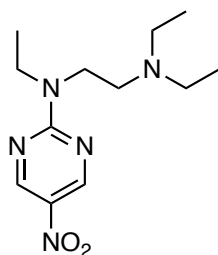
**<sup>1</sup>H NMR:** (400 MHz, DMSO-*d*<sub>6</sub>)  $\delta$  = 11.98 (s, 1H), 11.30 (s, 1H), 7.89 (d, *J* = 8.9 Hz, 2H), 7.82 - 7.76 (m, 4H), 7.00 (d, *J* = 9.2 Hz, 2H), 4.46 (s, 2H), 3.96 - 3.89 (m, 2H), 3.56 - 3.49 (m, 8H), 3.24 - 3.12 (m, 6H), 1.32 - 1.24 (m, 15H), 1.15 (t, *J* = 6.9 Hz, 3H).

**<sup>13</sup>C NMR:** (100 MHz, DMSO-*d*<sub>6</sub>)  $\delta$  = 162.2, 149.6, 148.7, 142.9, 139.5, 124.9, 122.7, 120.0, 111.8, 56.5, 54.2, 47.5, 46.0, 44.6, 44.2, 12.2, 8.3, 7.6.

**HRMS** (ESI): calcd for C<sub>28</sub>H<sub>45</sub>N<sub>6</sub>O<sup>+</sup> [M]<sup>+</sup>: 481.3649, found: 481.3659.

**R<sub>t</sub>** = 4.972 min (10  $\rightarrow$  100% MeCN/H<sub>2</sub>O + 0.1% FA, 10 min)

**$\lambda_{\text{max}}$**  = 448 nm

***N*<sup>1</sup>,*N*<sup>1</sup>,*N*<sup>2</sup>-triethyl-*N*<sup>2</sup>-(5-nitropyrimidin-2-yl)ethane-1,2-diamine (**4**)**

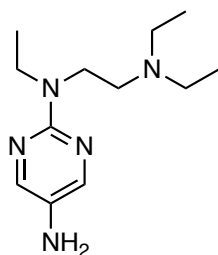
2-Chloro-5-nitropyrimidine (**3**) (100 mg, 0.627 mmol, 1.0 eq.) was dissolved in EtOH (2 mL). *N*<sup>1</sup>,*N*<sup>2</sup>,*N*<sup>2</sup>-triethylethane-1,2-diamine (124  $\mu$ L, 0.690 mmol, 1.1 eq.) and DIPEA (119  $\mu$ L, 0.690 mmol, 1.1 eq.) were added and heated to 80  $^{\circ}$ C for 2 h in a sealed flask. The reaction mixture was diluted with NaHCO<sub>3</sub> (20 mL) and extracted with EtOAc (3 x 20 mL). The combined organic layers were washed with NaOH (1M, 2 x 20 mL) and sat. NaCl (20 mL) and dried over Na<sub>2</sub>SO<sub>4</sub>. The solvent was removed *in vacuo*. The product (**4**) (168 mg, 0.627 mmol, quant.) was obtained as a pale, yellow oil and used without further purification.

**<sup>1</sup>H NMR:** (400 MHz, CDCl<sub>3</sub>)  $\delta$  = 9.05 (s, 2H), 3.79 – 3.69 (m, 4H), 2.69 – 2.63 (m, 2H), 2.58 (q, *J* = 7.1 Hz, 4H), 1.22 (t, *J* = 7.1 Hz, 3H), 1.03 (t, *J* = 7.1 Hz, 6H).

**<sup>13</sup>C NMR:** (100 MHz, CDCl<sub>3</sub>)  $\delta$  = 161.6, 154.9, 133.4, 50.4, 47.7, 47.1, 44.4, 12.8, 12.2.

**HRMS** (ESI): calcd for C<sub>12</sub>H<sub>22</sub>N<sub>5</sub>O<sub>2</sub><sup>+</sup> [M+H]<sup>+</sup>: 268.1768, found: 268.1768.

**R<sub>f</sub>** = 0.6 (10% MeOH/DCM, TLC deactivated with ammonia)

***N*<sup>2</sup>-(2-(diethylamino)ethyl)-*N*<sup>2</sup>-ethylpyrimidine-2,5-diamine (**5**)**

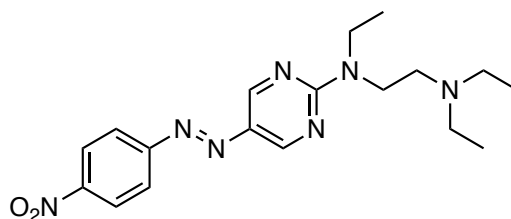
Pd/C (33.4 mg, 0.313 mmol, 0.5 eq.) was wetted with EtOH and **4** (168 mg, 0.627 mmol, 1.0 eq.) dissolved EtOH (5 mL) was added. The reaction vessel was purged with H<sub>2</sub> and a H<sub>2</sub> balloon was placed on top. The reaction was stirred at room temperature for 4 h. The crude material was filtered over celite and the solvent was removed under reduced pressure. The product (**5**) (148 mg, 0.624 mmol, quant) was obtained as a brown oil and used without further purification.

**<sup>1</sup>H NMR:** (400 MHz, CDCl<sub>3</sub>) δ = 7.96 (s, 2H), 3.66 – 3.53 (m, 4H), 3.02 (s, 2H), 2.67 – 2.60 (m, 6H), 1.15 (t, J = 7.0 Hz, 3H), 1.08 (t, J = 7.1 Hz, 6H).

**<sup>13</sup>C NMR:** (100 MHz, CDCl<sub>3</sub>) δ = 157.2, 147.0, 129.8, 50.5, 47.6, 45.8, 43.1, 13.3, 11.8.

**HRMS** (ESI): calcd for C<sub>12</sub>H<sub>24</sub>N<sub>5</sub><sup>+</sup> [M+H]<sup>+</sup>: 238.2026, found: 238.2031.

**R<sub>f</sub>** = 0.2 (10% MeOH/DCM, TLC deactivated with ammonia)

**(E)-N<sup>1</sup>,N<sup>1</sup>,N<sup>2</sup>-triethyl-N<sup>2</sup>-(5-((4-nitrophenyl)diazenyl)pyrimidin-2-yl)ethane-1,2-diamine (6)**

**5** (150 mg, 0.632 mmol, 1.0 eq) and 1-nitro-4-nitrosobenzene (111 mg, 0.632 mmol, 1.15 eq.) were dissolved in DCM/AcOH (1:1, 6 mL) and stirred at 40 °C for 4 h. The reaction mixture was neutralized with NaOH (1M) and extracted with EtOAc. The combined organic layers were washed with sat. NaCl, dried over Na<sub>2</sub>SO<sub>4</sub> and the solvent was removed *in vacuo*. The crude material was purified by silica gel column chromatography (NH<sub>3</sub> deactivated silica gel, 0% → 1% → 10% MeOH/DCM) to yield the product (**6**) (164 mg, 0.440 mmol, 70%) as red solid.

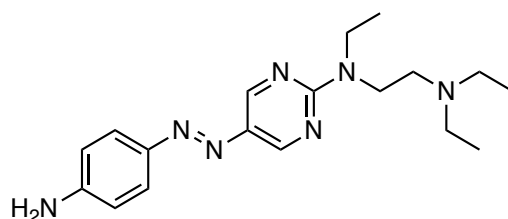
**<sup>1</sup>H NMR:** (400 MHz, CDCl<sub>3</sub>) δ = 8.91 (s, 2H), 8.35 (d, J = 9.0 Hz, 2H), 7.94 (d, J = 9.0 Hz, 2H), 3.80 - 3.75 (m, 4H), 2.77 - 2.69 (m, 2H), 2.63 (q, J = 7.1 Hz, 4H), 1.26 (t, J = 7.1 Hz, 4H), 1.08 (t, J = 7.1 Hz, 6H).

**<sup>13</sup>C NMR:** (100 MHz, CDCl<sub>3</sub>) δ = 161.8, 156.3, 154.5, 153.9, 148.1, 137.9, 124.9, 123.1, 50.5, 47.7, 46.7, 44.1, 13.1, 12.1.

Note: carbons at 154.5 and 153.9 couple to the proton signal at 8.91.

**HRMS** (ESI): calcd for C<sub>18</sub>H<sub>26</sub>N<sub>7</sub>O<sub>2</sub><sup>+</sup> [M+H]<sup>+</sup>: 372.2142, found: 372.2151.

**R<sub>f</sub>** = 0.4 (10% MeOH/DCM).

**(E)-N<sup>1</sup>-(5-((4-aminophenyl)diazenyl)pyrimidin-2-yl)-N<sup>1</sup>,N<sup>2</sup>,N<sup>2</sup>-triethylethane-1,2-diamine (7)**

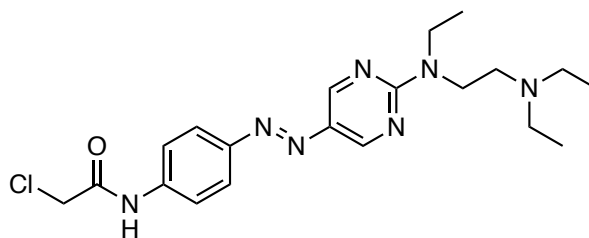
**6** (160 mg, 0.431 mmol, 1.0 eq.) was dissolved in 1,4-dioxane (12 mL), Na<sub>2</sub>S (84.1 mg, 1.08 mmol, 2.5 eq.) in water (1 mL) was added and the reaction was heated to 95 °C for 3 h. The reaction mixture was diluted with EtOAc (30 mL) and washed with water (2 x 10 mL), 10% NaCl (2 x 10 mL), aq. NaOH (1M, 2 x 10 mL) and sat. NaCl (1 x 10 mL). The organic phase was dried over Na<sub>2</sub>SO<sub>4</sub> and the solvent was removed *in vacuo*. The crude material was purified by silica gel column chromatography (NH<sub>3</sub> deactivated silica gel, 0% → 5% MeOH/DCM) to yield the product (**7**) (139 mg, 0.407 mmol, 95%) as orange solid.

**<sup>1</sup>H NMR:** (400 MHz, CDCl<sub>3</sub>) δ = 8.80 (s, 2H), 7.71 (d, J = 8.7 Hz, 2H), 6.72 (d, J = 8.8 Hz, 2H), 4.03 (s, 2H), 3.82 - 3.68 (m, 4H), 2.80 - 2.73 (m, 2H), 2.69 (q, J = 7.1 Hz, 4H), 1.23 (t, J = 7.0 Hz, 3H), 1.12 (t, J = 7.1 Hz, 6H).

**<sup>13</sup>C NMR:** (100 MHz, CDCl<sub>3</sub>) δ = 161.1, 152.8, 149.1, 145.8, 137.9, 124.6, 114.8, 50.3, 47.6, 46.0, 43.8, 13.2, 11.7.

**HRMS** (ESI): calcd for C<sub>18</sub>H<sub>28</sub>N<sub>7</sub><sup>+</sup> [M+H]<sup>+</sup>: 342.2401, found: 342.2400.

**R<sub>f</sub>** = 0.2 (10% MeOH/DCM)

**(E)-2-chloro-N-(4-((2-((2-(diethylamino)ethyl)(ethyl)amino)pyrimidin-5-yl)diazenyl)phenyl)acetamide (8)**

**7** (136 mg, 0.398 mmol, 1.0 eq) was dissolved in THF (20 mL) and cooled to 0 °C. DIPEA (103  $\mu$ L, 0.597 mmol, 1.2 eq.) was added and chloroacetyl chloride (38.0  $\mu$ L, 0.478 mmol, 1.5 eq.) was added dropwise. The reaction was stirred at 0 °C for 30 min, upon which it was allowed to warm up to room temperature and stirred for 1.5 h. The reaction was quenched by addition of NaHCO<sub>3</sub> (10 mL) and extracted with EtOAc (3 x 10 mL). The combined organic layers were washed with NaOH (1M, 2 x 10 mL), NaHCO<sub>3</sub> (1 x 10 mL) and sat. NaCl (1 x 10 mL) and dried over Na<sub>2</sub>SO<sub>4</sub>. The solvent was removed *in vacuo* and the crude material was purified by column chromatography (NH<sub>3</sub> deactivated silica, 1%  $\rightarrow$  10% MeOH/DCM) to yield the product (**8**) (84.2 mg, 0.201 mmol, 51%) as orange solid.

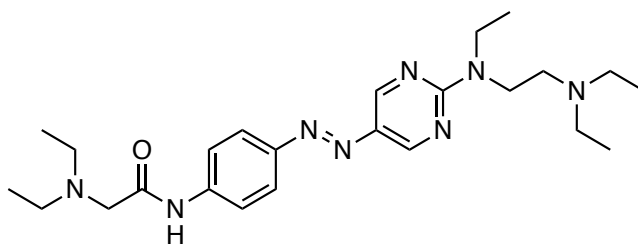
**<sup>1</sup>H NMR:** (400 MHz, CDCl<sub>3</sub>)  $\delta$  = 8.86 (s, 2H), 8.40 (s, 1H), 7.86 (d, J = 8.8 Hz, 2H), 7.70 (d, J = 8.9 Hz, 2H), 4.23 (s, 2H), 3.75 (q, J = 8.6, 7.1 Hz, 4H), 2.77 - 2.68 (m, 2H), 2.64 (q, J = 7.1 Hz, 4H), 1.25 (t, J = 7.1 Hz, 3H), 1.09 (t, J = 7.1 Hz, 6H).

**<sup>13</sup>C NMR:** (100 MHz, CDCl<sub>3</sub>)  $\delta$  = 163.9, 161.5, 153.3, 150.0, 138.5, 137.8, 123.6, 120.3, 50.5, 47.7, 46.5, 43.9, 43.1, 13.1, 12.0.

Note: the signal at 153.3 was extracted from the HSQC spectrum.

**HRMS** (ESI): calcd for C<sub>20</sub>H<sub>29</sub>ClN<sub>7</sub>O<sup>+</sup> [M+H]<sup>+</sup>: 418.2117, found: 418.2120.

**R<sub>f</sub>** = 0.2 (10% MeOH/EtOAc)

**(E)-2-(diethylamino)-N-(4-((2-((2-(diethylamino)ethyl)(ethyl)amino)pyrimidin-5-yl)diazenyl)phenyl)acetamide (pyDAD)**

**8** (33.8 mg, 80.8  $\mu\text{mol}$ , 1.0 eq) was dissolved in EtOH (1 mL), diethylamine (83.2  $\mu\text{L}$ , 0.808 mmol, 10 eq.) was added and the reaction was heated to 100  $^{\circ}\text{C}$  in a sealed flask overnight. The solvent was removed under reduced pressure and the crude material was purified by column chromatography ( $\text{NH}_3$  deactivated silica gel, 25% acetone/ $\text{CHCl}_3$ ) to yield **pyDAD** (20.4 mg, 44.9  $\mu\text{mol}$ , 56%) as orange solid.

**$^1\text{H NMR}$** : (400 MHz,  $\text{CDCl}_3$ )  $\delta$  = 9.60 (s, 1H), 8.85 (s, 2H), 7.84 (d,  $J$  = 8.8 Hz, 2H), 7.71 (d,  $J$  = 8.9 Hz, 2H), 3.77 - 3.60 (m, 4H), 3.18 (s, 2H), 2.71 - 2.53 (m, 10H), 1.24 (t,  $J$  = 7.1 Hz, 3H), 1.17 - 1.00 (m, 12H).

Note: Due to overlap of the signals, *trans* and *cis* (ratio 10:1) have been integrated here.

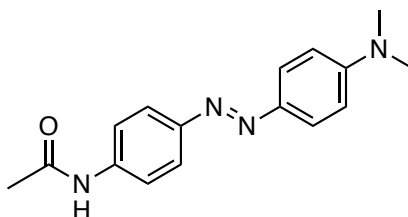
**$^{13}\text{C NMR}$** : (100 MHz,  $\text{CDCl}_3$ )  $\delta$  = 170.5, 161.4, 153.2, 149.3, 139.7, 137.8, 123.6, 119.5, 58.3, 50.6, 49.0, 47.8, 46.6, 43.9, 13.2, 12.6, 12.2.

**HRMS** (ESI): calcd for  $\text{C}_{24}\text{H}_{39}\text{N}_8\text{O}^+$  [ $\text{M}+\text{H}$ ] $^+$ : 455.3241, found: 455.3248.

**$R_f$**  = 0.7 (20% MeOH/DCM)

**$\lambda_{\text{max}}$**  = 382 nm



**(E)-N-(4-((4-(dimethylamino)phenyl)diazenyl)phenyl)acetamide**

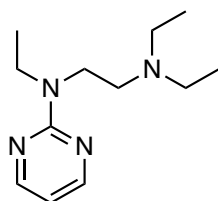
*p*-Aminoacetaniline (**9**) (200 mg, 1.33 mmol, 1.0 eq.) was dissolved in water/MeOH (1:1, 50 mL), aq. HCl (1M, 4.00 mL, 3.99 mmol, 3.0 eq) was added and the solution was cooled to 0 °C. NaNO<sub>2</sub> (110 mg, 1.46 mmol, 1.1 eq.) was added and the reaction was stirred at 0 °C for 30 min. This solution was then added dropwise to a solution of dimethylaniline and NaOAc (655 mg, 7.99 mmol, 6.0 eq.) in water/MeOH (1:1, 50 mL). The solution was stirred at 0 °C and allowed to warm up to room temperature overnight. The organic solvent was removed under reduced pressure and the aqueous phase was extracted with EtOAc (4 x 50 mL). The combined organic layers were washed with NaHCO<sub>3</sub> (3 x 50 mL) and sat. NaCl (1 x 50 mL). The organic layer was dried over Na<sub>2</sub>SO<sub>4</sub> and the solvent was removed *in vacuo*. The crude material was purified by silica gel column chromatography (60% EtOAc/hexanes) to yield the product **10** (99.8 mg, 0.353 mmol, 27%) as orange solid.

**<sup>1</sup>H NMR:** (400 MHz, CDCl<sub>3</sub>) δ = 7.84 (t, 4H), 7.62 (d, 2H), 7.33 (s, 1H), 6.75 (d, 2H), 3.08 (s, 6H), 2.21 (s, 3H).

**<sup>13</sup>C NMR:** (100 MHz, CDCl<sub>3</sub>) δ = 168.3, 152.4, 149.8, 143.7, 139.1, 124.9, 123.3, 119.9, 111.7, 40.5, 24.9.

**HRMS** (ESI): calcd for C<sub>24</sub>H<sub>39</sub>N<sub>3</sub>O<sup>+</sup> [M+H]<sup>+</sup>: 455.3241, found: 455.3248.

**R<sub>f</sub>** = 0.7 (20% MeOH/DCM)

***N*<sup>1</sup>,*N*<sup>1</sup>,*N*<sup>2</sup>-triethyl-*N*<sup>2</sup>-(pyrimidin-2-yl)ethane-1,2-diamine**

2-Chloropyrimidine (**11**) (100 mg, 0.873 mmol, 1.0 eq.) and *N*<sup>1</sup>,*N*<sup>2</sup>,*N*<sup>2</sup>-triethylethane-1,2-diamine (783  $\mu$ L, 4.37 mmol, 5.0 eq.) were dissolved in EtOH (2 mL) and heated to 80 °C for 4 h in a sealed flask. The solvent was removed under reduced pressure and the crude material was purified by silica gel column chromatography (0  $\rightarrow$  5% MeOH/DCM) to yield the product (**12**) (185 mg, 0.832 mmol, 95%) as a pale white oil.

**<sup>1</sup>H NMR:** (400 MHz, CDCl<sub>3</sub>)  $\delta$  = 8.27 (d, *J* = 4.7 Hz, 2H), 6.40 (t, *J* = 4.7 Hz, 1H), 3.68 - 3.58 (m, 4H), 2.68 - 2.56 (m, 6H), 1.18 (t, *J* = 7.1 Hz, 3H), 1.06 (t, *J* = 7.1 Hz, 6H).

**<sup>13</sup>C NMR:** (100 MHz, CDCl<sub>3</sub>)  $\delta$  = 161.3, 157.8, 109.0, 50.5, 47.7, 45.9, 43.0, 13.1, 12.1.

**HRMS** (ESI): calcd for C<sub>12</sub>H<sub>23</sub>N<sub>4</sub><sup>+</sup> [M+H]<sup>+</sup>: 223.1917, found: 223.1919.

**R<sub>f</sub>** = 0.3 (3% MeOH/DCM)

### Supplementary References

1. Laprell, L. et al. Photopharmacological control of bipolar cells restores visual function in blind mice. *J. Clin. Invest.* **2017**, *127*, 2598-2611.
2. Martínez, C. H. R.; Dardonville, C. Rapid Determination of Ionization Constants ( $pK_a$ ) by UV Spectroscopy Using 96-Well Microtiter Plates. *ACS Medicinal Chemistry Letters* **2013**, *4*, 142-145.



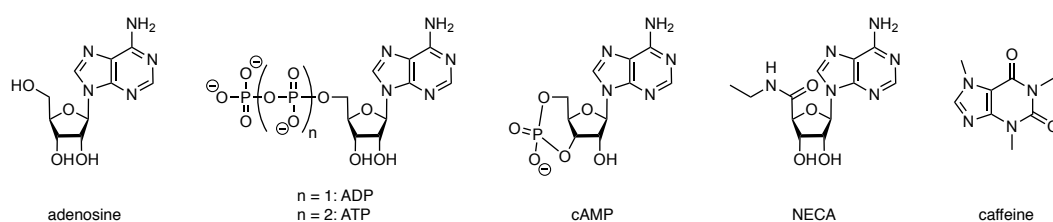
## IV. Photoswitchable Adenosine



## Optical Control of Adenosine Receptors

### Introduction

Adenosine and its related signaling molecules, ADP, ATP and cAMP, are some of the most important second messengers and ligands in signal transduction (Figure IV.1).<sup>1-3</sup> Adenosine receptors (ARs) are G protein-coupled receptors and belong to the purinergic receptor family, and consist of four subtypes,  $A_1$ ,  $A_{2A}$ ,  $A_{2B}$  and  $A_3$ , with  $A_{2A}$  and  $A_3$  showing lower affinity of adenosine than  $A_1$  and  $A_{2A}$ .<sup>4-6</sup>



**Figure IV.1: molecular structures of adenosine, ADP, ATP, cAMP, NECA and caffeine.**

While  $A_1$  and  $A_3$  mainly exert their effects through  $G_{i/o}$ -mediated opening of G protein-coupled inwardly rectifying potassium (GIRK) channels, agonizing  $A_{2A}$  or  $A_{2B}$  mainly activates adenylyl cyclase through  $G_s$  signaling to increase cAMP levels. To date, agonist and antagonist bound structures of the  $A_{2A}$ , and an agonist bound structure of the  $A_1$  receptor are available.<sup>7-11</sup> Nevertheless, and even though the effects of extracellular adenosine have been studied for many decades, development of selective ligands and their translation into the clinic has been facing challenges.<sup>12,13</sup> This is even more tragic as ARs play an important role in many medical disorders, including neurodegenerative diseases like Parkinson's<sup>14</sup> and Alzheimer's,<sup>15</sup> where multiple studies point out beneficial effects of caffeine (Figure IV.1 and Chapter V) or other  $A_{2A}$  antagonists, mediated by combined  $D_2$  and  $A_{2A}$  signaling.<sup>12</sup> Due to their ubiquitous expression, adenosine receptors play a role not only in the central nervous system, but also in cardiac protection,<sup>16-18</sup> tissue protection<sup>19</sup> and nociception.<sup>20,21</sup> Intravenous adenosine is used as a cardiac stress test, for example in myocardial perfusion imaging with patients, who are unable to perform exercise. However, the use of adenosine stress tests is debated due to arrhythmogenic effects in some individuals.

Involvement of ARs in pain perception has first been observed in the 1970s.<sup>22</sup> The underlying mechanisms is still poorly understood, and some studies are contradicting each other.<sup>21</sup> Initial investigations focused on  $A_1$  receptors, but more recently the potential of all subtypes as targets in pain treatment has been

recognized.  $A_1$  and  $A_{2A}$  are the best studied ARs in this context, and while  $A_1$  reportedly is antinociceptive, the effects of  $A_{2A}$  agonism are still under debate.<sup>21,23</sup> Early studies reported pronociceptive effects, but recent work indicated that these effects could be due to inflammation caused by the cannula used for administration.<sup>21</sup> Little is known about the role of  $A_{2B}$  receptor, but in general its effects are pronociceptive, as antagonists lead to antinociception.<sup>24,25</sup> Lastly, reported effects of  $A_3$  receptors are also contradicting. Latest studies, however, indicate that  $A_3$  is involved in reducing inflammation and therefore reduction of pain.<sup>26,27</sup>

The expression patterns of the four subtypes are critical for their mode of action. In general, animal models distinguish between peripheral, spinal and supraspinal mechanisms.<sup>21,23</sup> Due to the ubiquitous expression of ARs, selective targeting of a specific region is often considered problematic. Light can add the spatiotemporal precision to an experiment, which is needed to investigate physiological processes that take place on a second to millisecond timescale in a confined area of the organism. In contrast to genetic engineering (knock-out animals, CRISPR-CAS9), photopharmacology is not only faster and reversible, but can also be used to study a native system.<sup>28-30</sup>

In 2014, optical control of the  $A_{2A}$  receptor with a photoswitchable ligand, has been achieved.<sup>31</sup> The authors used the non-selective AR agonist APNEA and extended the terminal aniline to an azobenzene. Upon isomerization, the photoswitch toggles between an antagonistic and a partially agonistic state. Most recently, a photoactivatable antagonist for  $A_{2A}$  has been reported as well,<sup>32</sup> but to our knowledge, photomodulation of  $G_{i/o}$ -coupled signal transmission through  $A_1$  or  $A_3$  receptors has not yet been demonstrated.

## Results and Discussion

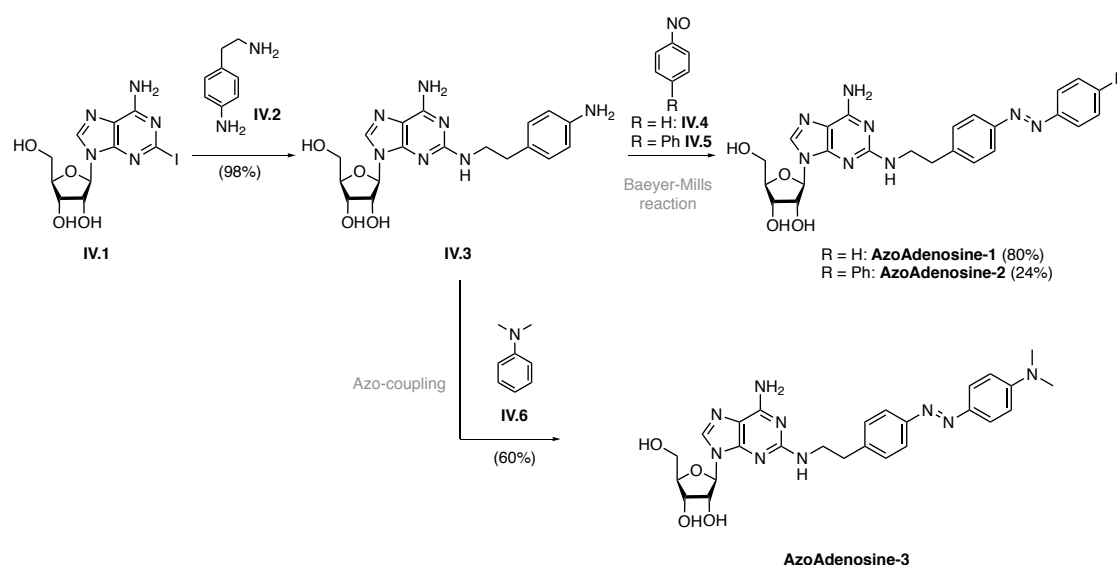
**Design.** Subtype selective drugs for ARs are still underdeveloped despite their potential for treating cardiac and neurological diseases and in the treatment of pain. The recently disclosed X-ray structure of the human  $A_1R$  covalently bound to the antagonist DU172, however, provided valuable insights into the general architecture of the ligand binding pocket (pdb 5UEN).<sup>11</sup> Even though the majority of amino acid residues compounding the ligand binding pocket of  $A_1$  are conserved compared to  $A_{2A}$ , there is a major difference in topology. Most interestingly,  $A_1$  displays a wide cavity with a secondary hydrophobic binding pocket that extends from the primary binding site.

We designed our photoswitchable ligands with the azobenzene functional group extending from 2-position of the purine heterocycle, hypothesizing that the two azobenzene isomers would interact differently with the extracellular loops. We further decided to install agonist properties. While antagonists carry hydrophobic substituents such as propyl or furanyl groups in 8-position of the purine core,



agonists are usually furnished with a ribose moiety, or derivatives thereof, in 9-position. Keeping in mind that strongly binding ligands with slow unbinding kinetics can impede efficient photoswitching, we settled on the native ribose functional group, rather than, for instance, secondary amide-derivatives as found in NECA (Figure IV.1).<sup>33</sup>

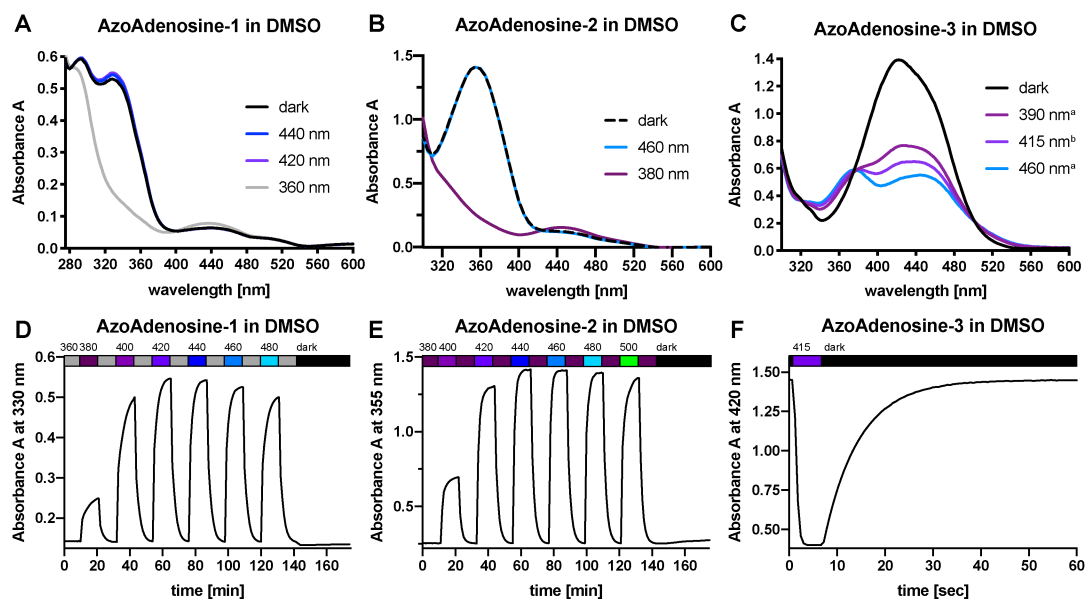
**Chemical Synthesis.** The initial target structures included the unsubstituted AzoAdenosine, AA-1, its biphenyl derivative AA-2, and the red-shifted dimethylamino substituted AA-3.



**Scheme IV.1: Synthetic access to AzoAdenosine-1, -2 and -3 via Baeyer-Mills reaction or azo coupling.**

AA-1 and AA-2 have been synthesized before.<sup>34</sup> The syntheses of all three AzoAdenosines started from commercially available 2-iodo-adenosine (**IV.1**) which gave the common precursor **IV.3** after  $S_NAr$  with aminophenethylamine (**IV.2**).<sup>34</sup> The resulting aniline underwent chemo-selective Baeyer-Mills reaction<sup>35,36</sup> without protection of the ribose moiety or the aminopurine, yielding AzoAdenosine-1 (AA-1) and AzoAdenosine-2 (AA-2). Nitrosoaryl **IV.4** and **IV.5** were purchased (**IV.4**) or freshly prepared by oxidation with oxone. Our attempts to engage adenosine in Baeyer-Mills reactions to furnish 6-(phenyldiazenyl)-purines were unsuccessful. Likewise, the electron-rich dimethylaniline was not amenable to Baeyer-Mills reactions. Instead, **IV.3** underwent diazotization and subsequent azo coupling, yielding the red-shifted derivative AzoAdenosine-3 (AA-3).

**Photophysical Characterization.** UV-Vis spectrophotometry was used to determine the optimal isomerization wavelengths and the isomerization properties in different solvents and with different light-sources (Figure IV.2).

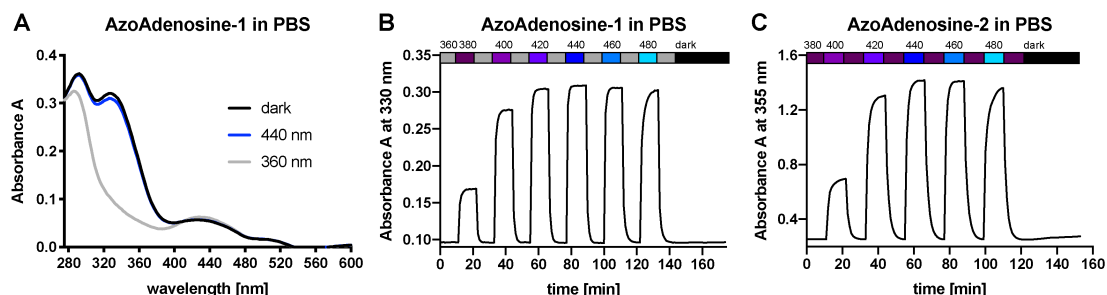


**Figure IV.2: UV-Vis studies of three AzoAdenosines in DMSO.** A-C: illumination-dependent UV-Vis spectra of AA-1 (A), AA-2 (B) and AA-3 (C) D-F: Alternating illumination shows PSSs of AA-1 (D) and AA-2 (E). Both compounds are stable in the dark over 30 min, while AA-3 (F) is fast-relaxing ( $\tau_{\text{on}} = 0.5$  s,  $\tau_{\text{off}} = 7.4$  s). <sup>a</sup>: ultra-high-power LED by Prizmatix. <sup>b</sup>: Mic-LED by Prizmatix

AA-1 was most efficiently isomerized by irradiation with 360 nm (*trans* to *cis*) and 420 – 440 nm (*cis* to *trans*) leading to distinct absorption spectra in DMSO, with clearly visible absorption maxima of the  $\pi$ - $\pi^*$  and  $n$ - $\pi^*$  transitions (Figure IV.2A). The isomerization was fully reversible with 440 nm illumination. Moreover, a wide range of blue light (400 – 460 nm) can be used to facilitate *cis* to *trans* isomerization (Figure IV.2D). By comparison, the  $\lambda_{\text{max}}$  of AA-2 displayed a bathochromic shift by 20 nm due to resonance to the aryl-substituent in 4'-position (Figure IV.2B). AA-2 could be isomerized with 380 nm (*cis* to *trans*) and 460 nm (*trans* to *cis*) light. The  $\lambda_{\text{max}}$  of AA-3, showed a more pronounced red-shift to 420 nm and no obvious separation of the  $\pi$ - $\pi^*$  and  $n$ - $\pi^*$  transitions, attributed to the electron-pushing effect of the dimethylamino moiety in 4'-position. (Figure IV.2C). Only violet to blue light with higher intensity (390 nm and 460 nm ultra-high-power LED and 415 Mic-LED by Prizmatix) in combination with polar aprotic solvents led to an observable PSS change (Figure IV.2C). As previously observed with red-shifted azobenzenes, we measured accelerated dark-relaxation for AA-3 in DMSO (Figure IV.2F), ( $\tau_{\text{on}} = 0.5$  s,  $\tau_{\text{off}} = 7.4$  s). Experiments in protic solvents did not result in an observable change in *trans/cis* ratio (not shown). Still, we assumed isomerization to occur, although it cannot be observed with the employed UV-Vis spectrophotometer.<sup>37,38</sup>

PSS quantification in DMSO was achieved by NMR spectroscopy (SI Figure IV.1.).<sup>39</sup> Under ambient light conditions, a DMSO solution of AA-1 to -3 contained 85 – 90% *trans*-isomer. Illumination with the respective wavelengths (AA-1: 360 nm, AA-2:

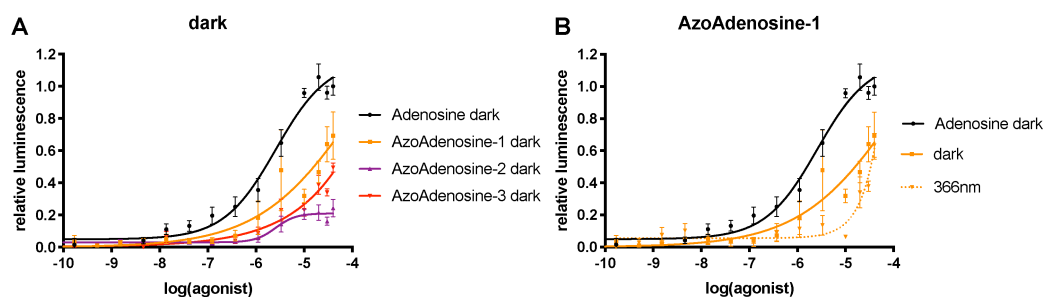
380 nm, AA-3: 415 nm) enriched the *cis*-content to 85%, 68% and 74% respectively. Isomerization to the thermodynamically favored isomer was incomplete, with residual 10 – 30% *cis*-isomer.



**Figure IV.3 UV Vis studies of AzoAdenosine-1 and -2 in PBS.**

PSS establishment was highly solvent dependent, with faster kinetics in PBS solution compared to DMSO. In contrast, thermostability of AA-1 and AA-2 was less affected by the solvent. AA-1 and AA-2 were *cis*-stable in the dark for at least 30 min, in both DMSO and PBS (Figure IV.2D/E and Figure IV.3.B/C), which is desirable to minimize exposure to UV light during physiological experiments.

**Adenosine A<sub>1</sub> and A<sub>2</sub> Receptor Radioligand Binding Studies.** Radioligand binding studies with AA-1 to -3 that were conducted by the psychoactive drug screen program (PDSP) in the laboratories of Prof. Dr. Bryan Roth, revealed that all three compounds are binding A<sub>1</sub>, A<sub>2A</sub> and A<sub>2B</sub>, with weak selectivity for A<sub>2A</sub> over A<sub>2B</sub> over A<sub>1</sub> (SI Table IV.1). In secondary binding studies, displacing ZM241385 bound A<sub>2A</sub>, K<sub>i</sub> values in the nanomolar (AA-1 and AA-3) and low micromolar (AA-2) range were determined (SI Table IV.2). Binding was also confirmed for A<sub>1</sub>Rs, albeit with lower affinity. Secondary binding experiments with A<sub>2B</sub> are scheduled.

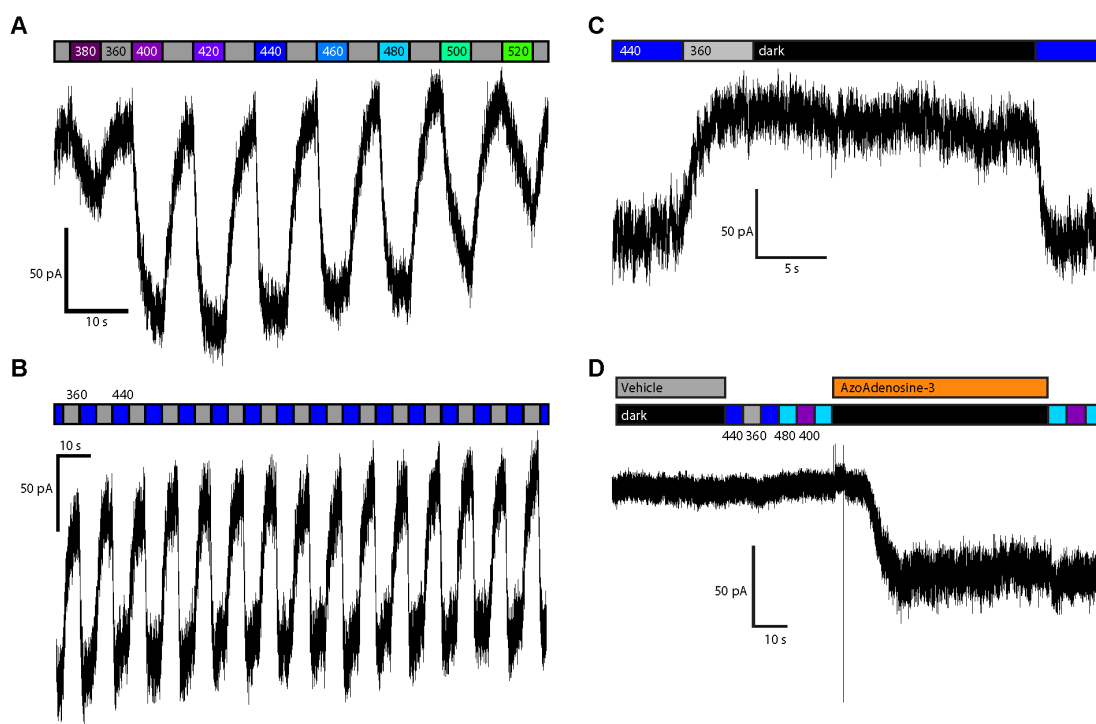


**Figure IV.4: Dose-dependent activation of A<sub>1</sub>Rs by AA-1, AA-2 and AA-3.**

A: Dose-response curves of the photoswitches were measured under dark-adapted conditions. B: AA-1 in its dark-adapted and 366 nm illuminated state. (Values represent mean  $\pm$  SEM.)

To evaluate if our dark-adapted, *trans*-enriched compounds are agonists for A<sub>1</sub>Rs like the parent molecule, we performed DiscoverX<sup>®</sup> β-arrestin signaling assays, with adenosine as reference agonist (Figure IV.4). Even though solubility limits did not allow us to reach saturation and calculation of EC-50 values, we gained valuable insights into the relative efficacies of our new compounds. AA-1 was the most efficacious agonist, reaching 70% of the maximal activation by adenosine at 40 mM. In comparison, the lipophilic compound AA-2 reached 24% activation, and the red-shifted compound AA-3 50% (Figure IV.4A). Irradiation with UV light during the incubation phase, decreased the potency of AA-1, indicating that the molecule is more active in its *trans*-state. (Figure IV.4B).

**Photocontrol of the Adenosine A<sub>1</sub> Receptor.** To further characterize the ability of our compounds to manipulate the G protein-mediated A<sub>1</sub> receptor pathway with light, we employed a heterogeneous expression system including co-expression with GIRK1/2 channels in CHO-K1 cells (Figure IV.5).



**Figure IV.5: Optical control of adenosine A<sub>1</sub> receptors in CHO-K1 cells.** A: Action spectrum of AA-1 shows that all wavelengths from 420 nm to 480 nm effectively switch the molecule from *trans* to *cis*. B: Reversible switching of AA-1 over 15 cycles. C: AA-1 is bistable on a second time scale in aqueous medium. AA-1 is switched to *cis* with a short light pulse. Reactivation occurs under blue light. D: AA-3 (30 μM) acts as an agonist but photocontrol cannot be achieved.

GIRK1/2 channels are a physiological signaling partner of A<sub>1</sub>Rs and present a link between the cAMP-mediated metabotropic communication pathways and

potassium-current-mediated electrical signaling.<sup>12</sup> In addition to the physiological relevance, e.g. in cardiac myocytes<sup>17,40,41</sup> and neuronal tissue,<sup>42,43</sup> the GIRK1/2-based read-out allows investigation of reversible photopharmacological stimuli with high temporal resolution. Action spectra were recorded to determine the optimal isomerization wavelengths. Confirming our UV-Vis results, termination of AA-1-induced GPCR signaling can be achieved with a broad range of blue light (Figure IV.5A). Receptor activation is reversible over many cycles without decreasing amplitude (fatigue resistance, Figure IV.5B). In our UV-Vis experiments, AA-1 exhibited high *cis*-stability, even in aqueous medium. This translated into our patch-clamp experiments, which allowed us to decrease illumination times and therefore exposure to UV light (Figure IV.5C). While AA-3 proved to be a potent agonist, photocontrol at 30  $\mu$ M could not be achieved (Figure IV.5D). This lack of photocontrol might be attributed to the fast, thermal relaxation.

Similar action spectra were obtained from experiments with HEK293T cells, transiently transfected with A1 and GIRK1/2 (SI Figure IV.2). Even though the current evoked by the photoswitch could be blocked upon addition of an antagonist (caffeine or DPCPX), the light-response persisted (SI Figure IV.2D/E). Additionally, AA-1 was also active in cells transiently transfected with only GIRK1/2 and YFP (SI Figure IV.3).

**Frequency Modulation in Human Stem Cell-Derived Cardiomyocytes.** As ARs play a major role in cardiac physiology, we wanted to evaluate if our compounds would be suitable to control the beating frequency in human stem cell-derived cardiomyocytes (SI Figure VII.4). Application of AA-3 resulted in a weak but reversible decrease in beating frequency under green/blue light. To our surprise, AA-1 reduced beating frequency under 360 nm illumination, in the *cis*-form, which was unexpected as the *trans*-isomer was the better agonist in our patch-clamp experiments. However, in our patch-clamp experiments we had focused on A<sub>1</sub> receptors (Figure IV.4 and IV.5), and not on other, G<sub>s</sub>-coupling, receptor subtypes.

**Possible Off-Target Effects.** Thallium flux assays in HEK293T cells (no co-expression of adenosine receptors) showed only minor direct effects on GIRK channels, which were not suppressed by an AR antagonist (SI Figure IV.5). We therefore attribute this current to off-target effects, stemming from a different receptor family, which is endogenously expressed in HEK293T cells. We then wanted to know if the unknown receptors are transmembrane receptors with an extracellular ligand binding domain, or if our molecules enter the cell and activate from the intracellular side. In whole-cell patch-clamp experiments in GIRK1/2 expressing HEK293T cells, we therefore applied AA-1 via the patch pipette to find that the compound was not active (SI Figure IV.6). However, external application led to receptor activation. This led us to believe that the compound acts on other transmembrane receptors (like GPCRs) and does not block or interact with channels from the intracellular side. Next, we looked into endogenously expressed GPCRs in HEK293T cells. A<sub>2A</sub> and A<sub>2B</sub> receptors are reported to be endogenously

expressed in HEK293T cells,<sup>44-46</sup> but as these are G<sub>s</sub>-coupled and therefore don't signal via GIRK channels, we did not attribute our current to these receptors.<sup>47</sup> In 2011, Atwood et al. performed microarray studies to detect mRNA levels in HEK293 cells.<sup>46</sup> Apart from A<sub>2A</sub> and A<sub>2B</sub> mRNA, they were also able to detect A<sub>1</sub> mRNA, although not on a statistically significant level. This is in coherence with our results, as we were able to block the agonist-evoked current with an antagonist (SI Figure IV.2D/E).

Searching for another lead, we examined additional results received from the psychoactive drug screen program (PDSP).<sup>48</sup> Results from the PDSP showed that all three molecules bind to a small number of receptors and transporters. The highest binding affinity, apart from ARs (SI Table IV.3), was found towards the dopamine transporter (DET) with sub-micromolar affinity. DETs are responsible for dopamine re-uptake from the synaptic cleft into presynaptic neurons.<sup>49,50</sup> Lower binding affinity was also determined for the norepinephrine transporter (NET). However, to the best of our knowledge, both transporters are not endogenously expressed in HEK cells. Additionally, AA-1 was found to bind 5-hydroxytryptamine 2B receptors (5-HT2B; 0.64 mM) and alpha-2A adrenergic receptors (Alpha2A; 4.1 mM), AA-2 to 5-hydroxytryptamine 2A receptors (5-HT2A; 6.4 mM) and Sigma1 receptors (1.5 mM). From this short list, 5-HT2B receptors were found to be endogenously expressing in HEK293T cells, however, the mRNA levels did not reach significance.<sup>46</sup> Nevertheless, these low expression levels of 5-HT2B could be sufficient to lead to the off-target effects detected in our control experiments.

## Conclusion

In this study we present three photoswitchable derivatives of the nucleoside adenosine, including one red-shifted derivative. In radioligand binding studies, Azo-Adenosine-1 to -3 showed binding to all ARs tested (A<sub>2</sub> and A<sub>1</sub>), with little selectivity for A<sub>2A</sub> over the other subtypes. In functional  $\beta$ -arrestin assays, we determined agonistic behavior of AA-1 and AA-3, which in case of AA-1, was shown to be reversible in patch-clamp experiments in CHO-K1 cells. Whole-cell patch-clamp experiments in HEK293T cells, however, revealed off-target effects of AA-1. MEA experiments with human stem cell derived cardiomyocytes disclosed inverse effects of AA-1 and AA-3 upon isomerization, which are, in case of AA-1, not in coherence with our patch-clamp experiments. This could possibly be attributed to other subtypes of ARs, or other receptor families. Binding studies by the psychoactive drug screen program (PDSP) disclosed possible targets of all Azo-Adenosines and additional whole-cell patch-clamp experiments could help verifying the target.

## References

- (1) Tsuda, M.; Tozaki-Saitoh, H.; Inoue, K. Pain and Purinergic Signaling. *Brain Res Rev* **2010**, *63*, 222-232.
- (2) Burnstock, G.; Ralevic, V. Purinergic Signaling and Blood Vessels in Health and Disease. *Pharmacol Rev* **2014**, *66*, 102-192.
- (3) Burnstock, G. An Introduction to the Roles of Purinergic Signalling in Neurodegeneration, Neuroprotection and Neuroregeneration. *Neuropharmacology* **2016**, *104*, 4-17.
- (4) Fredholm, B. B.; IJzerman, A. P.; Jacobson, K. A.; Klotz, K.-N.; Linden, J. International Union of Pharmacology. XXV. Nomenclature and Classification of Adenosine Receptors. *Pharmacol Rev* **2001**, *53*, 527-552.
- (5) Fredholm, B. B.; IJzerman, A. P.; Jacobson, K. A.; Linden, J.; Müller, C. E. International Union of Basic and Clinical Pharmacology. LXXXI. Nomenclature and Classification of Adenosine Receptors—An Update. *Pharmacol Rev* **2011**, *63*, 1-34.
- (6) Fredholm, B. B. Adenosine—a Physiological or Pathophysiological Agent? *J Mol Med* **2014**, *92*, 201-206.
- (7) Jaakola, V.-P.; Griffith, M. T.; Hanson, M. A.; Cherezov, V.; Chien, E. Y. T.; Lane, J. R.; IJzerman, A. P.; Stevens, R. C. The 2.6 Angstrom Crystal Structure of a Human A2A Adenosine Receptor Bound to an Antagonist. *Science* **2008**, *322*, 1211-1217.
- (8) Doré, A. S.; Robertson, N.; Errey, J. C.; Ng, I.; Hollenstein, K.; Tehan, B.; Hurrell, E.; Bennett, K.; Congreve, M.; Magnani, F.; et al. Structure of the Adenosine A2A Receptor in Complex with ZM241385 and the Xanthines XAC and Caffeine. *Structure* **2011**, *19*, 1283-1293.
- (9) Lebon, G.; Warne, T.; Edwards, P. C.; Bennett, K.; Langmead, C. J.; Leslie, A. G.; Tate, C. G. Agonist-Bound Adenosine A2A Receptor Structures Reveal Common Features of GPCR Activation. *Nature* **2011**, *474*, 521-525.
- (10) Xu, F.; Wu, H.; Katritch, V.; Han, G. W.; Jacobson, K. A.; Gao, Z. G.; Cherezov, V.; Stevens, R. C. Structure of an Agonist-Bound Human A2A Adenosine Receptor. *Science* **2011**, *332*, 322-327.
- (11) Glukhova, A.; Thal, D. M.; Nguyen, A. T.; Vecchio, E. A.; Jörg, M.; Scammells, P. J.; May, L. T.; Sexton, P. M.; Christopoulos, A. Structure of the Adenosine A1 Receptor Reveals the Basis for Subtype Selectivity. *Cell* **2017**, *168*, 867-877
- (12) Jacobson, K. A.; Gao, Z.-G. Adenosine Receptors as Therapeutic Targets. *Nature Reviews Drug Discovery* **2006**, *5*, 247-264.
- (13) Chen, J.-F.; Eltzschig, H. K.; Fredholm, B. B. Adenosine Receptors as Drug Targets - What Are the Challenges? *Nature Reviews Drug Discovery* **2013**, *12*, 265-286.
- (14) Cieślak, M.; Komoszyński, M.; Wojtczak, A. Adenosine A2A Receptors in Parkinson's Disease Treatment. *Purinergic Signal* **2008**, *4*, 305-312.
- (15) Rahman, A. The Role of Adenosine in Alzheimer's Disease. *Current Neuropharmacology* **2009**, *7*, 207-216.
- (16) Thornton, J. D.; Liu, G. S.; Olsson, R. A.; Downey, J. M. Intravenous Pretreatment with A1-Selective Adenosine Analogues Protects the Heart against Infarction. *Circulation* **1992**, *85*, 659-665.
- (17) Conti, A.; Monopoli, A.; Gamba, M.; Borea, P. A.; Ongini, E. Effects of Selective A1 and A2 Adenosine Receptor Agonists on Cardiovascular Tissues. *Naunyn-Schmiedeberg's Arch Pharmacol* **1993**, *348*, 108-112.

- (18) Matherne, G. P.; Linden, J.; Byford, A. M.; Gauthier, N. S.; Headrick, J. P. Transgenic A1 Adenosine Receptor Overexpression Increases Myocardial Resistance to Ischemia. *PNAS* **1997**, *94*, 6541-6546.
- (19) Linden, J. Adenosine in Tissue Protection and Tissue Regeneration. *Mol Pharmacol* **2005**, *67*, 1385.
- (20) Sawynok, J. Adenosine Receptor Activation and Nociception. *European Journal of Pharmacology* **1998**, *347*, 1-11.
- (21) Sawynok, J. Adenosine Receptor Targets for Pain. *Neuroscience* **2016**, *338*, 1-18.
- (22) Vapaatalo, H.; Onken, D.; Neuvonen, P. J.; Westermann, E. Stereospecificity in Some Central and Circulatory Effects of Phenylisopropyl-Adenosine (PIA). *Arzneimittelforschung* **1975**, *25*, 407-410.
- (23) Zylka, M. J. Pain-Relieving Prospects for Adenosine Receptors and Ectonucleotidases. *Trends in Molecular Medicine* **2011**, *17*, 188-196.
- (24) Abo-Salem, O. M.; Hayallah, A. M.; Bilkei-Gorzo, A.; Filipek, B.; Zimmer, A.; Müller, C. E. Antinociceptive Effects of Novel A2B Adenosine Receptor Antagonists. *J Pharmacol Exp Ther* **2004**, *308*, 358-366.
- (25) Bilkei-Gorzo, A.; Abo-Salem, O. M.; Hayallah, A. M.; Michel, K.; Müller, C. E.; Zimmer, A. Adenosine Receptor Subtype-Selective Antagonists in Inflammation and Hyperalgesia. *Naunyn-Schmied Arch Pharmacol* **2008**, *377*, 65-76.
- (26) Baraldi, P. G.; Cacciari, B.; Romagnoli, R.; Merighi, S.; Varani, K.; Borea, P. A.; Spalluto, G. A3 Adenosine Receptor Ligands: History and Perspectives. *Medicinal Research Reviews* **2000**, *20*, 103-128.
- (27) Chen, Z.; Janes, K.; Chen, C.; Doyle, T.; Bryant, L.; Tosh, D. K.; Jacobson, K. A.; Salvemini, D. Controlling Murine and Rat Chronic Pain through A3 Adenosine Receptor Activation. *The FASEB Journal* **2012**, *26*, 1855-1865.
- (28) Beharry, A. A.; Woolley, G. A. Azobenzene Photoswitches for Biomolecules. *Chem. Soc. Rev.* **2011**, *40*, 4422-4437.
- (29) Szymański, W.; Beierle, J. M.; Kistemaker, H. A. V.; Velema, W. A.; Feringa, B. L. Reversible Photocontrol of Biological Systems by the Incorporation of Molecular Photoswitches. *Chem. Rev.* **2013**, *113*, 6114-6178.
- (30) Hüll, K.; Morstein, J.; Trauner, D. In Vivo Photopharmacology. *Chem. Rev.* **2018**, *118*, 10710-10747.
- (31) Bahamonde, M. I.; Taura, J.; Paoletta, S.; Gakh, A. A.; Chakraborty, S.; Hernando, J.; Fernández-Dueñas, V.; Jacobson, K. A.; Gorostiza, P.; Ciruela, F. Photomodulation of G Protein-Coupled Adenosine Receptors by a Novel Light-Switchable Ligand. *Bioconjugate Chemistry* **2014**, *25*, 1847-1854.
- (32) Taura, J.; Nolen, E. G.; Cabré, G.; Hernando, J.; Squarzialupi, L.; López-Cano, M.; Jacobson, K. A.; Fernández-Dueñas, V.; Ciruela, F. Remote Control of Movement Disorders Using a Photoactive Adenosine A2A Receptor Antagonist. *Journal of Controlled Release* **2018**, *283*, 135-142.
- (33) Cusack, N. J.; Hourani, S. M. O. 5'-N-Ethylcarboxamidoadenosine: A Potent Inhibitor of Human Platelet Aggregation. *British Journal of Pharmacology* **1981**, *72*, 443-447.
- (34) Schönberger, M. Developing Photoswitchable Ligands for Transmembrane Receptors. Ph.D. Thesis, Ludwig-Maximilian-University, Munich, 2014.
- (35) Baeyer, A. Nitrosobenzol Und Nitrosonaphtalin. *Berichte der deutschen chemischen Gesellschaft* **1874**, *7*, 1638-1640.
- (36) Mills, C. XCIII. –Some New Azo-Compounds. *J. Chem. Soc., Trans.* **1895**, *67*, 925-933.



- (37) Garcia-Amorós, J.; Díaz-Lobo, M.; Nonell, S.; Velasco, D. Fastest Thermal Isomerization of an Azobenzene for Nanosecond Photoswitching Applications under Physiological Conditions. *Angew. Chem. Int. Ed.* **2012**, *51*, 12820–12823.
- (38) Garcia-Amorós, J.; Castro, M. C. R.; Coelho, P.; Raposo, M. M. M.; Velasco, D. Fastest Non-Ionic Azo Dyes and Transfer of Their Thermal Isomerisation Kinetics into Liquid-Crystalline Materials. *Chem. Commun.* **2016**, *52*, 5132–5135.
- (39) Barber, D. M.; Schönberger, M.; Burgstaller, J.; Levitz, J.; Weaver, C. D.; Isacoff, E. Y.; Baier, H.; Trauner, D. Optical Control of Neuronal Activity Using a Light-Operated GIRK Channel Opener (LOGO). *Chem. Sci.* **2016**, *7*, 2347–2352.
- (40) Ma, J.; Guo, L.; Fiene, S. J.; Anson, B. D.; Thomson, J. A.; Kamp, T. J.; Kolaja, K. L.; Swanson, B. J.; January, C. T. High Purity Human-Induced Pluripotent Stem Cell-Derived Cardiomyocytes: Electrophysiological Properties of Action Potentials and Ionic Currents. *American Journal of Physiology-Heart and Circulatory Physiology* **2011**, *301*, H2006–H2017.
- (41) Bett, G. C. L.; Kaplan, A. D.; Lis, A.; Cimato, T. R.; Tzanakakis, E. S.; Zhou, Q.; Morales, M. J.; Rasmusson, R. L. Electronic “Expression” of the Inward Rectifier in Cardiocytes Derived from Human-Induced Pluripotent Stem Cells. *Heart Rhythm* **2013**, *10*, 1903–1910.
- (42) Haas, H. L.; Selbach, O. Functions of Neuronal Adenosine Receptors. *Naunyn-Schmied Arch Pharmacol* **2000**, *362*, 375–381.
- (43) Mogul, D. J.; Adams, M. E.; Fox, A. P. Differential Activation of Adenosine Receptors Decreases N-Type but Potentiates P-Type Ca<sup>2+</sup> Current in Hippocampal CA3 Neurons. *Neuron* **1993**, *10*, 327–334.
- (44) Thomas, P.; Smart, T. G. HEK293 Cell Line: A Vehicle for the Expression of Recombinant Proteins. *Journal of Pharmacological and Toxicological Methods* **2005**, *5*, 187–200.
- (45) Cooper, J.; Hill, S. J.; Alexander, S. P. H. An Endogenous A<sub>2B</sub> Adenosine Receptor Coupled to Cyclic AMP Generation in Human Embryonic Kidney (HEK 293) Cells. *British Journal of Pharmacology* **1997**, *122*, 546–550.
- (46) Atwood, B. K.; Lopez, J.; Wager-Miller, J.; Mackie, K.; Straiker, A. Expression of G Protein-Coupled Receptors and Related Proteins in HEK293, AtT20, BV2, and N18 Cell Lines as Revealed by Microarray Analysis. *BMC Genomics* **2011**, *12*, 14.
- (47) Feoktistov, I.; Biaggioni, I. Adenosine A<sub>2B</sub> Receptors. *Pharmacol Rev* **1997**, *49*, 381–402.
- (48) Besnard, J.; Ruda, G. F.; Setola, V.; Abecassis, K.; Rodriguiz, R. M.; Huang, X.-P.; Norval, S.; Sassano, M. F.; Shin, A. I.; Webster, L. A.; et al. Automated Design of Ligands to Polypharmacological Profiles. *Nature* **2012**, *492*, 215–220.
- (49) Penmatsa, A.; Wang, K. H.; Gouaux, E. X-Ray Structure of Dopamine Transporter Elucidates Antidepressant Mechanism. *Nature* **2013**, *503*, 85–90.
- (50) Vaughan, R. A.; Foster, J. D. Mechanisms of Dopamine Transporter Regulation in Normal and Disease States. *Trends in Pharmacological Sciences* **2013**, *34*, 489–496.



## Supplementary Tables

SI Table VI.1: Primary binding studies.

Compound	Receptor	Inhibition 1	Inhibition 2	Inhibition 3	Inhibition 4	Mean %
AA-1	A <sub>1</sub>	36.16	15189	28.50	30.15	25.81
AA-1	A <sub>2A</sub>	33.73	71.54	70.96	103.28	69.88
AA-1	A <sub>2B</sub>	63.95	55.90	50.27	47.85	54.49
AA-2	A <sub>1</sub>	6.24	-4.12	9.65	-0.08	2.92
AA-2	A <sub>2A</sub>	46.71	37.48	79.33	85.68	62.30
AA-2	A <sub>2B</sub>	43.71	17.38	56.13	17.61	25.19
AA-3	A <sub>1</sub>	33.78	21.66	29.33	17.01	25.45
AA-3	A <sub>2A</sub>	94.34	76.73	97.80	100.97	92.46
AA-3	A <sub>2B</sub>	71.22	65.90	56.13	61.21	63.62

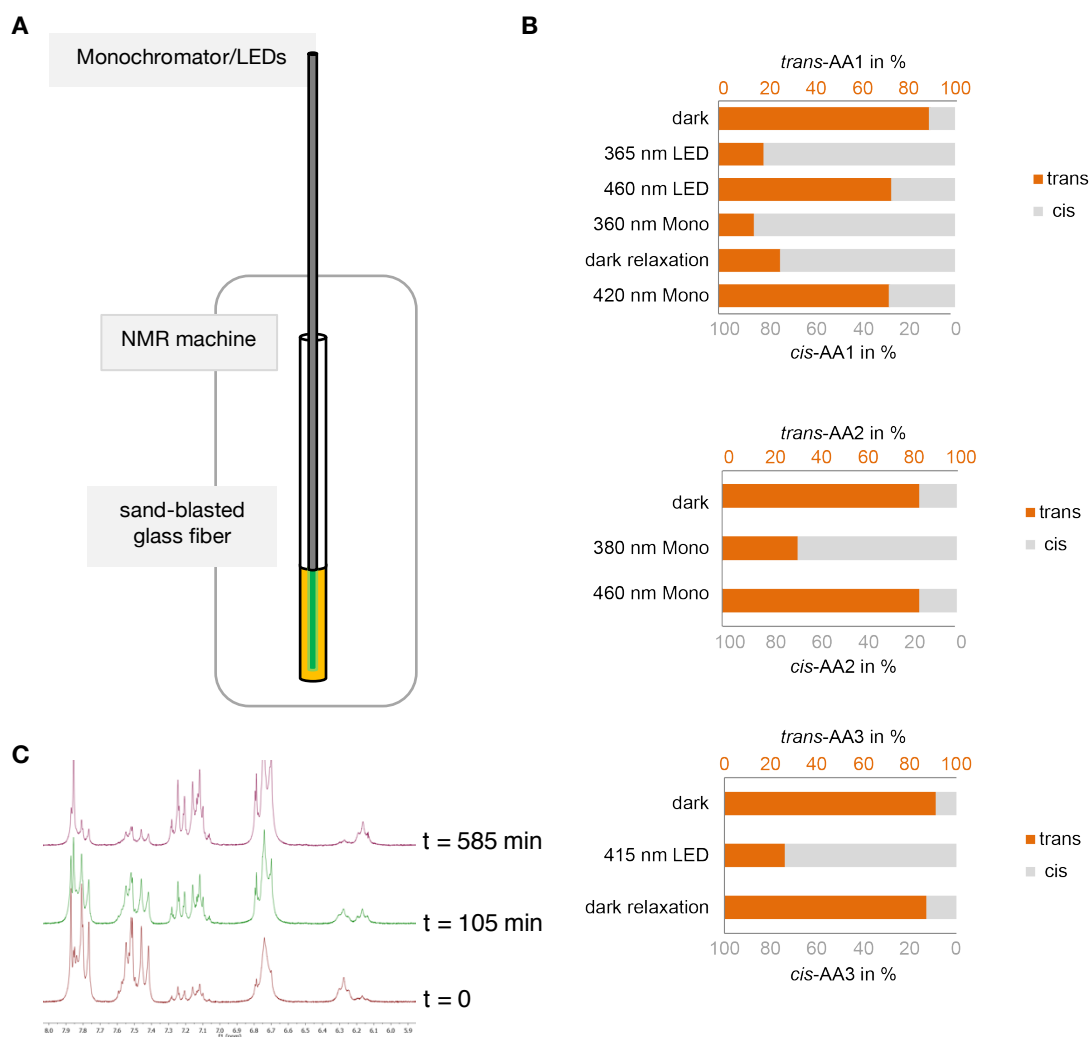
SI Table IV.2: Secondary Binding studies. Binding constants of AA-2, AA-2 and AA-3 for A<sub>2A</sub> and A<sub>1</sub> receptors

Compound	Receptor	Hot ligand	LogK <sub>i</sub>	K <sub>i</sub> (nM)
AA-1	A <sub>2A</sub>	ZM241385	-6.13	740.97
AA-1	A <sub>2A</sub>	ZM241385	-6.81	155.35
AA-1	A <sub>2A</sub>	ZM241385	-6.32	481.95
AA-1	A <sub>2A</sub>	ZM241385	-6.42	376.01
AA-2	A <sub>2A</sub>	ZM241385	-5.56	2777.15
AA-2	A <sub>2A</sub>	ZM241385	-5.97	1079.20
AA-2	A <sub>2A</sub>	ZM241385	-5.75	1758.33
AA-3	A <sub>2A</sub>	ZM241385	-6.37	425.11
AA-3	A <sub>2A</sub>	ZM241385	-6.16	686.44
AA-3	A <sub>2A</sub>	ZM241385	-6.67	212.08
AA-3	A <sub>2A</sub>	ZM241385	-6.23	594.57
AA-1	A <sub>1</sub>	CCPA	> -5	> 10,000
AA-2	A <sub>1</sub>	CCPA	> -5	> 10,000
AA-3	A <sub>1</sub>	CCPA	-5.52	3023.43

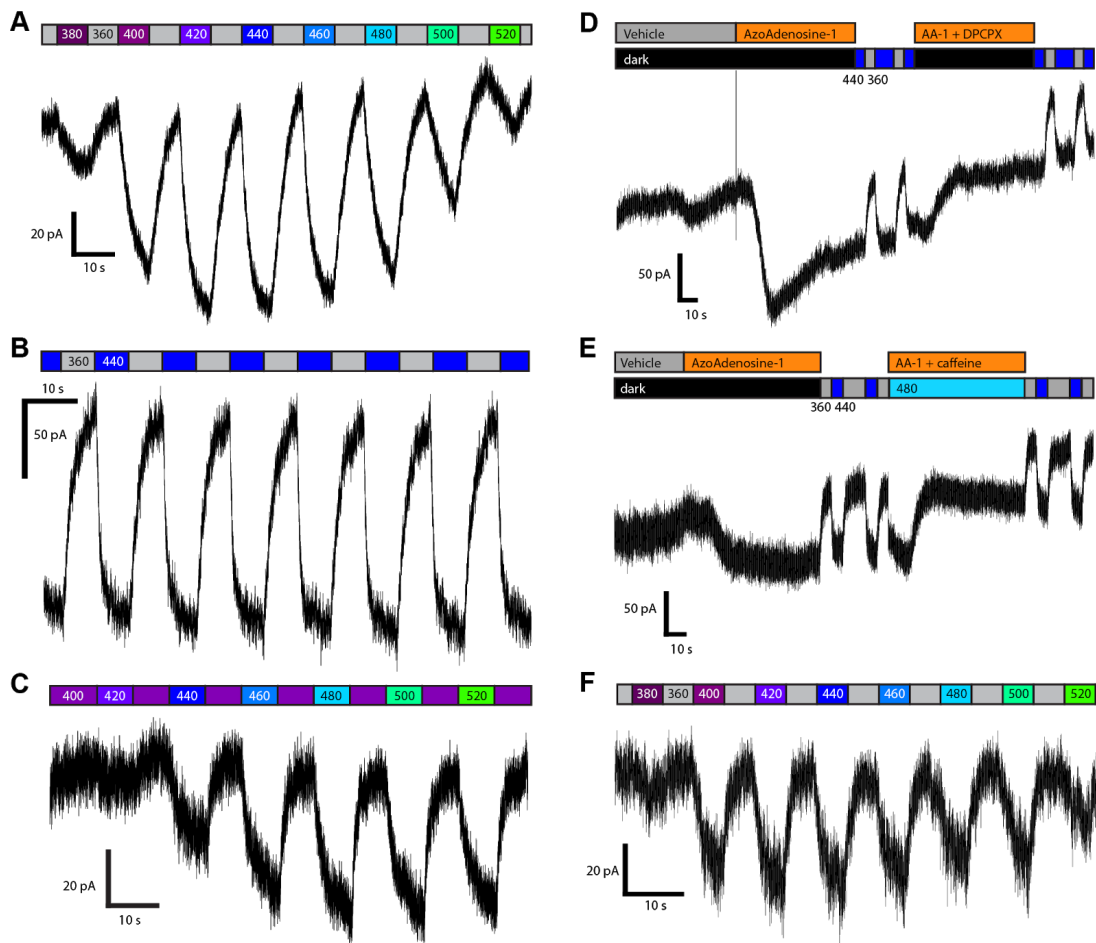
**Si Table VI.3: Secondary binding studies.** Binding constants of AA-1, AA-2 and AA-3 for other GPCRs and transporters than ARs.

Compound	Receptor	Hot Ligand	K <sub>i</sub> (nM)	pK <sub>i</sub> Error
AA-1	5-HT <sub>2B</sub>	[ <sup>3</sup> H]LSD	640	±0.07
AA-1	NET	[ <sup>3</sup> H]Nisoxetine	2153	±0.1
AA-1	DAT	[ <sup>3</sup> H]WIN35428	295	±0.07
AA-1	Alpha <sub>2A</sub>	[ <sup>3</sup> H]-Rauwolscine	4145	±0.1
AA-2	5-HT <sub>2A</sub>	[ <sup>3</sup> H]Ketanserin	6375	±0.06
AA-2	NET	[ <sup>3</sup> H]Nisoxetine	2466	±0.1
AA-2	DAT	[ <sup>3</sup> H]WIN35428	187	±0.08
AA-2	Sigma 1	[ <sup>3</sup> H]Pentazocine(+)	1451	±0.1
AA-3	NET	[ <sup>3</sup> H]Nisoxetine	2276	±0.1
AA-3	DAT	[ <sup>3</sup> H]WIN35428	407	±0.07

## Supplementary Figures

**Supplementary Figure IV.1: Determination of photostationary states (PSSs).**

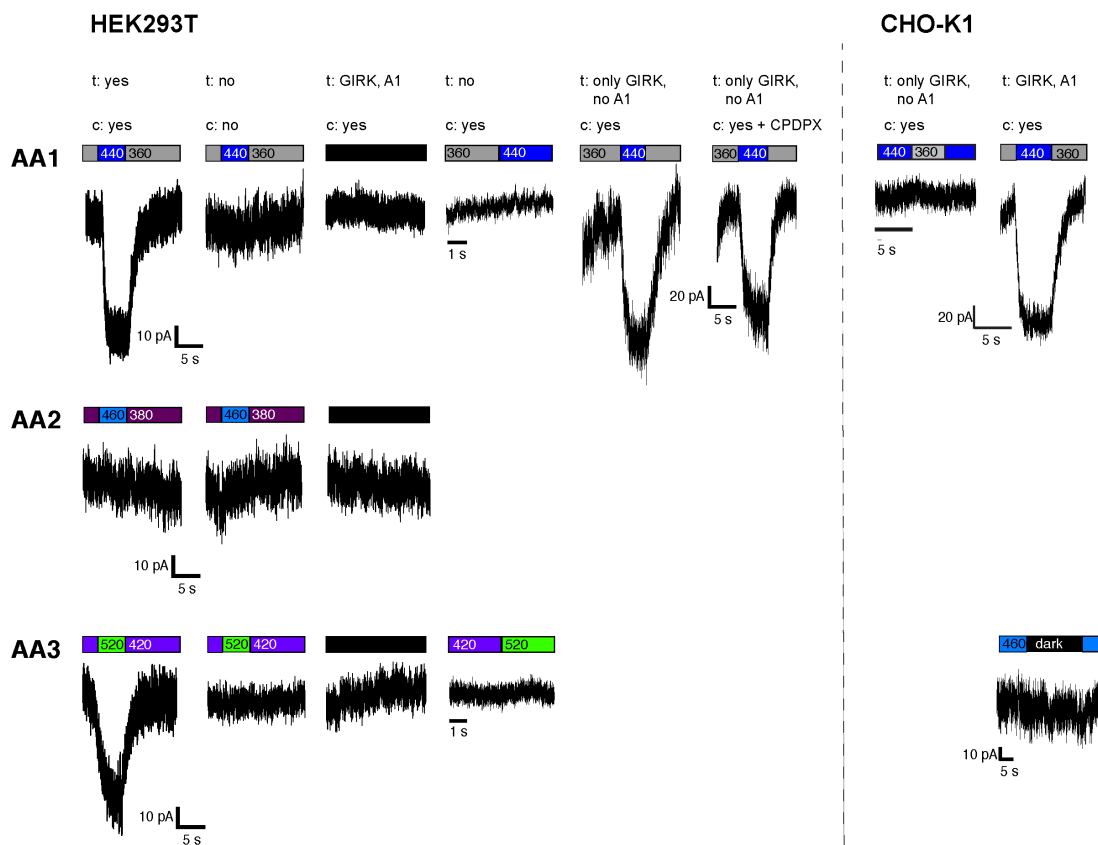
A: schematic depiction of the NMR with glass-fiber and light source to determine photostationary states by NMR. B: Determination of PSS for all three AzoAdenosines determined by NMR. Dark adapted state: wrapped in tin foil prior to measurement immediately after preparation of NMR sample. Illumination: 12-14 h, until PSS was established. Dark relaxation: no illumination for 12 h. (note: for the red-shifted derivative, an illumination inside the NMR was not practical. The sample was irradiated outside the NMR machine and the maximum *cis*-content of the PSS was extrapolated.) C:  $^1\text{H}$ -NMR (200 MHz) cutout, showing *trans* to *cis* isomerization over time. C:  $^1\text{H}$ -NMR (200 MHz) spectrum of AzoAdenosine-1 at different time points.



**Supplementary Figure IV.2: Light-dependent GIRK currents evoked by**

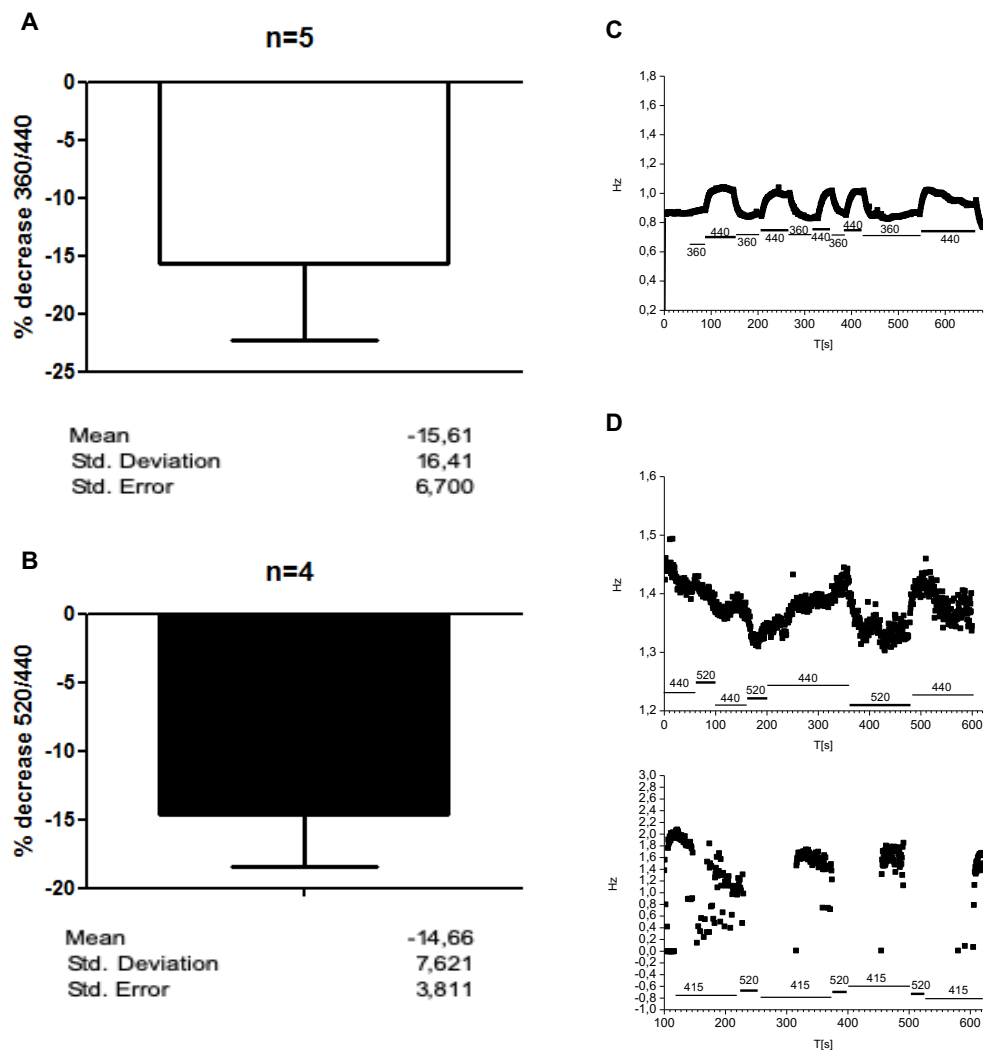
**AzoAdenosine-1 and AzoAdenosine-3.**

A-C: HEK293T cells were transiently transfected with A1, GIRK1/2 and YFP. A: Illumination with 360 nm can deactivate the receptor repeatedly over many cycles. B: action spectrum of AA-1 (50 μM) shows activation is possible with violet to blue light. C: action spectrum of AA-3 shows activation is possible with blue to green light. D-F: HEK293T cells were transiently transfected with GIRK1/2 and YFP D: Switching in presence and absence of the A1 antagonist DPCPX (AA-1: 20 μM, DPCPX: 10 μM, top bar: perfusion, bottom bar: light protocol). E: Switching in presence and absence of the adenosine receptor antagonist caffeine (AA-1: 20 μM, caffeine: 200 μM, top bar: perfusion, bottom bar: light protocol). F: Action spectrum of AA-1 (50 μM).



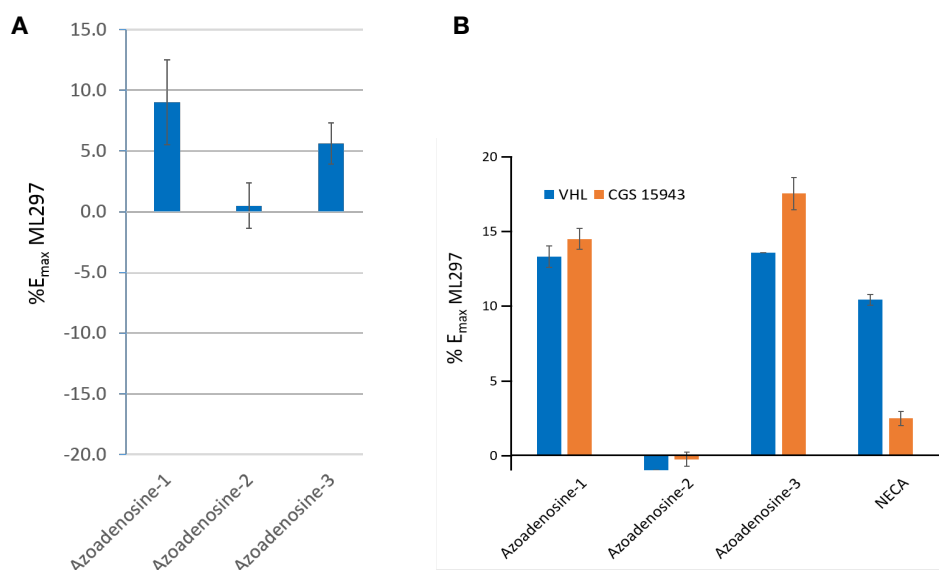
amounts used for transfection: 50ng A1, 400 ng GIRK, 50 ng YFP, 24 h post-transfection  
 t: transfection  
 c: compound

**Supplementary Figure IV.3: Overview of all control experiments.**



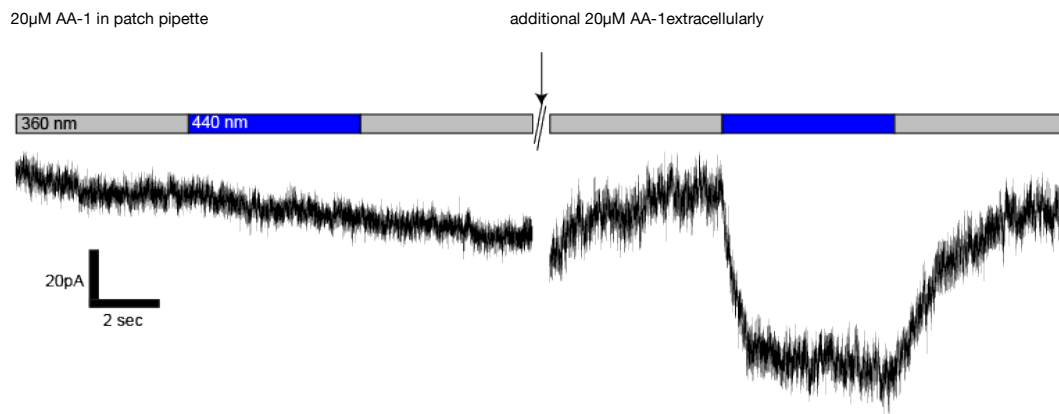
**Supplementary Figure IV.4: Recordings in human stem cell derived cardiomyocytes by MEA.** A and B: mean frequency decrease upon light illumination with AzoAdenosine-1 (A) and AzoAdenosine-3 (B) applied. C: representative example of spontaneous beating frequency in the presence of AA-1. Isomerization to the *cis* state (360 nm) results in a reduction, which can be reversed with 440 nm light. D: Representative examples of spontaneous beating frequency presence of AA-3. Isomerization to the *trans*-state (520 nm) results in a reduction (above) or complete block (below) of spontaneous beating with could be reverted by illumination with 440 - 415 nm light.





**Supplementary Figure IV.5: TI<sup>+</sup> flux assay after activation with AzoAdenosines.**

A: TI<sup>+</sup> flux evoked through AA-1 to -3. B: Ion flux could not be blocked with adenosine receptor antagonists. (ML297: GIRK Opener, CGS 15943: adenosine receptor antagonist, NECA: adenosine receptor agonist)



**Supplementary Figure IV.6: Comparison of AA-1 applied through the patch pipette and in the bath solution in HEK 293T cells (350 ng GIRK1/2, 50 ng YFP, no A1).**

## Methods

**General Experimental Techniques.** Unless stated otherwise all reactions were carried out with magnetic stirring using oven-dried glassware (160 °C) under inert gas atmosphere (nitrogen or argon). Syringes used to transfer reagents and solvents were purged with nitrogen prior to use. Low temperature reactions were carried out in a Dewar vessel filled with the appropriate cooling agent e.g. H<sub>2</sub>O/ice (0 °C). Heating was conducted using a heated oil bath. Yields refer to spectroscopically pure compounds unless otherwise stated.

**Solvents and Reagents.** Reaction solvents were purchased from Acros Organics as 'extra dry' over molecular sieves and handled under inert gas atmosphere. Tetrahydrofuran (THF) was distilled from Na/benzophenone prior to use. Dichloromethane (DCM), triethylamine (TEA) and diisopropylethylamine (DIPEA) were distilled from calcium hydride. Ethanol and acetic acid were purchased from commercial suppliers and used as received. Solvents for extraction and flash column chromatography were purchased in technical grade purity and distilled under reduced pressure on a rotary evaporator prior to use. All other reagents and solvents were purchased from commercial suppliers and used as received. **IV.3**, AA-1 was synthesized as reported elsewhere,<sup>34</sup> AA-2 was synthesized by Matthias Schönberger.<sup>34</sup>

**Chromatography.** Reactions and chromatography fractions were monitored by qualitative thin-layer chromatography (TLC) on silica gel F254 TLC plates from Merck KGaA. Analytes were visualized by irradiation with UV light and/or by immersion of the TLC plate in ninhydrin or potassium permanganate solution followed by heating with a hot-air gun. Flash column chromatography was performed Geduran® Si60 (4063 µm) silica gel from Merck KGaA (eluents are given in parentheses). Reverse Phase column chromatography was performed on Waters C<sub>18</sub> (C<sub>18</sub>; 55-105 µm, 125 Å) as stationary phase (eluents are given in parentheses). LCMS was performed on an Agilent 1260 Infinity HPLC System, MS-Agilent 1100 Series, Type: 1946D, Model: SL, equipped with a Agilent Zorbax Eclipse Plus C<sub>18</sub> (100 x 4.6 mm, particle size 3.5 micron) reverse phase column with a constant flowrate of 1 mL/min and a 10 → 100% MeCN/H<sub>2</sub>O + 0.1% FA gradient over 10 min.

**NMR Spectra.** NMR spectra were measured on Varian 400 MHz Bruker AVIII HD (cryoprobe) for proton nuclei (100 MHz for carbon nuclei respectively). The <sup>1</sup>H NMR shifts are reported in parts per million (ppm) related to the chemical shift of tetramethylsilane. <sup>1</sup>H and <sup>13</sup>C NMR shifts were calibrated to the residual solvent signal: DMSO (2.50 ppm/39.5 ppm). <sup>1</sup>H NMR spectroscopic data are reported as follows: Chemical shift in ppm (multiplicity, coupling constants (Hz), integration). The multiplicities are abbreviated as follows: s (singlet), d (doublet), t (triplet), q (quartet) and m (multiplet) and are reported as observed. Except for multiplets, the chemical shift of all signals is reported as the center of the resonance range. Additionally, to <sup>1</sup>H and <sup>13</sup>C NMR measurements, 2D NMR techniques as homonuclear correlation spectroscopy (COSY), heteronuclear single quantum

coherence (HSQC) and heteronuclear multiple bond coherence (HMBC) were used to assist signal assignment. All raw fid files were processed, and the spectra analyzed using the program MestReNova 11.0 from Mestrelab Research S. L.

**Mass Spectra.** All high-resolution mass spectra (HRMS) were recorded by the LMU Mass Spectrometry Service. HRMS were recorded on a MAT 90 from Thermo Finnigan GmbH using electrospray ionisation (ESI) or a MAT 90 from Jeol Ltd. using electron ionization (EI).

**UV/Vis Spectra.** UV/Vis spectra were recorded on a Varian Cary 50 Scan UV/Vis spectrometer using Helma SUPRASIL precision cuvettes (10 mm light path). All compound stock solutions were prepared under benchtop light conditions at 50 mM in DMSO and diluted to 50  $\mu$ M in the final solvent (DMSO or PBS). Photoswitching was achieved using a Polychrome V (Till Photonics) monochromator, or a Prizmatix ultra high power LED (460 nm), connected to a fiber-optic cable through which the sample in the spectrophotometer was irradiated from the top.

**Determination of *trans/cis*-ratios.** NMR samples of 5 mM concentration were prepared, wrapped in tin foil and a sand-blasted glass fiber was adjusted to the correct height of 1 cm above the bottom of the NMR tube in the sample solution. A test-spectrum was measured to ensure no interfering with the measurement. The sample was inserted in a 200 MHz NMR machine and  $^1\text{H}$  NMRs were collected, every 5-10 min (in the first hour) to every hour (for 12-14 h). Corresponding *trans*- and *cis*-signals were integrated, and the percentage was calculated.

**DiscoverX  $\beta$ -arrestin assay.** DiscoverX assays were performed according to the protocol provided by the manufacturer (DiscoverX Pathhunter  $\beta$ -arrestin cell line and detection kit catalog number 93-0001). Light control was achieved through illumination of the well-plate in the incubator.

**Cell-culture.** CHO-K1 cells were incubated in Ham's F12 medium + 10% FBS + 1% Penicillin-Streptomycin and split at 80 to 90% confluency. For detachment, growth medium was removed, cells were washed with calcium free PBS buffer and cells were treated with trypsin solution at 37  $^{\circ}$ C for 1 min. Detached cells were diluted with growth medium and singularized by pipetting. For transfection, acid etched coverslips were coated with monomeric collagen A according to protocol (Merck Millipore) and placed in a 24-well plate. 40.000 cells were added to each well in 1.5 mL standard growth medium. The following day, the cells were transfected with the respective DNA (per coverslip: 50 ng A1, 350 ng GIRK1/2 and 50 ng YFP) using TransIT-X2 (MirusBio LLC), according to protocol, with the exception of using 1  $\mu$ L transfection reagent per cover slip. After 3-5 hours, medium was exchanged for standard growth medium. Cells were used for electrophysiological recordings 24 to 48 hours post transfection.

HEK293T cells were incubated in dulbecco's minimal essential medium (DMEM) + 10% FBS and split at 80 to 90% confluency. For detachment, growth medium was

removed, cells were washed with calcium free PBS buffer and cells were treated with trypsin solution at 37 °C for 1 min. Detached cells were diluted with DMEM and singularized by pipetting. For transfection, acid etched coverslips were coated with poly-L-lysine and placed in a 24-well plate. 50,000 cells were added to each well in 500  $\mu$ L standard growths medium. The following day, the cells were transfected with the respective DNA (per coverslip: 50 ng A1, 350 ng GIRK1/2 and 50 ng YFP) following the polyplus jetprime protocol with 1  $\mu$ L transfection reagent in 50  $\mu$ L jetprime buffer. After 3-5 hours, medium was exchanged for standard growth medium. Cells were used for electrophysiological recordings 24 to 48 hours post transfection.

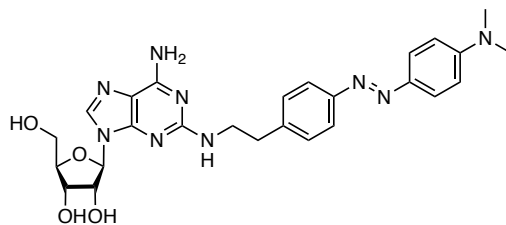
**Patch-Clamp Electrophysiology.** Whole cell patch clamp experiments were performed using a standard electrophysiology setup equipped with a HEKA Patch Clamp EPC10 USB amplifier and patch master software. Micropipettes were generated from "Science Products GB200-F-8P with filament" pipettes using a vertical puller. Resistance varied between 5-7 M $\Omega$ . Bath solution contained in mM: 140 KCl, 2.6 CaCl<sub>2</sub>, 1.2 MgCl<sub>2</sub>, 5 HEPES (KOH to pH 7.4). Pipette solution contained in mM: 107 KCl, 1.2 MgCl<sub>2</sub>, 1 CaCl<sub>2</sub>, 10 EGTA, 5 HEPES, 2 MgATP, 0.3 Na<sub>2</sub>GTP (KOH to pH 7.2). Photoswitchable ligands and reference agonist were dissolved in bath solution from a 1000 x DMSO stock. Irradiation during electrophysiology and UV/Vis experiments was performed using a TILL Photonics Polychrome 5000 monochromator.

**Thallium Flux** HEK-293 cells expressing GIRK1 + GIRK2 were cultured in:  $\alpha$ -MEM (Corning, Corning, NY) supplemented with glutagro (Corning) and 10% (v/v) fetal bovine serum (Thermo Fisher Scientific, Waltham, MA) henceforth referred to as cell culture medium. 20,000 cells per well in 20  $\mu$ L of cell culture medium were plated into 384-well, black-wall, clear-bottom, PureCoat Amine plates (Corning) and incubated overnight in a humidified 5% CO<sub>2</sub> incubator at 37 °C. For testing, cell culture medium was replaced with 20  $\mu$ L/well of a Hank's Balanced Salt Solution (HBSS, Thermo Fisher), with the addition of 10 mM HEPES-NaOH pH 7.3 (Thermo Fisher), 0.02% (w/v) Pluronic F-127, and 1.5  $\mu$ M Thallos-AM (WaveFront Biosciences, Austin, TX). The dye-loading solution was replaced with 20  $\mu$ L/well HBSS containing 10 mM HEPES-NaOH, pH 7.3 (assay buffer) after 1 hour of incubation at room temperature. A 30 mM solution of AzoAdenosine-1, -2 or -3 was prepared and serially diluted in DMSO. The solutions were further diluted in assay buffer to 2-fold over their final test concentration. Thallos-loaded cell plates were imaged using a Panoptic kinetic imaging plate reader (WaveFront Biosciences, Franklin, TN) at 5 Hz, excitation 482/35 nm and emission 536/40 nm. After 10 s of baseline collection 20  $\mu$ L/well diluted compounds were added and imaging continued for 2 min at which time 10  $\mu$ L/well of a solution containing (in mM) 125 NaHCO<sub>3</sub>, 1.8 CaSO<sub>4</sub>, 1 MgSO<sub>4</sub>, 5 glucose, 1.6 TI<sub>2</sub>SO<sub>4</sub> and 10 HEPES-NaOH pH 7.3 was added and imaging continued for an additional 2 min.

**Cell culture, coating and frequency recording on multi electrode arrays (MEAs).** Human stem cell-derived cardiomyocytes were used for MEA analysis. MEA (Multichannels systems) (60MEA200/30iRTi) were coated with a 2  $\mu$ L drop of 10  $\mu$ g/ml fibronectin (Sigma Aldrich) covering the field of electrodes and  $2 \times 10^4$  cardiomyocytes were plated. After 2-3 days of culture field potentials (FP) were recorded with the MC Rack software (Multichannel Systems) at 10 kHz sampling rate. The recording area was illuminated with 520, 440 or 360 nm light generated by a monochromator (Polychrome V, Till Photonics), controlled with the Powerlab 8/35 and the Chart 7.1 software (AD Instruments). The recording was conducted before and after incubation of the drugs in a Tyrode's external solution with 142 mM NaCl, 4.4 mM KCl, 2.0 mM  $MgCl_2$ , 1.8 mM  $CaCl_2$ , 10.0 mM glucose, 10.0 mM HEPES (pH 7.4 NaOH). The frequency was extrapolated using the MC\_Rack software (multichannel systems) to determine the values. The values were then plotted with the Origin Pro 8G software (OriginLab) for further analysis.

## Experimental procedures

### AzoAdenosine-3



**IV.3** (100 mg, 0.249 mmol, 1.0 eq) was dissolved in methanol/water (50 mL, 1:1), cooled to 0 °C and aq. HCl (1 M, 747  $\mu$ L, 0.747 mmol, 3.0 eq) was added. NaNO<sub>2</sub> was dissolved in a water (0.5 mL) and added dropwise to the stirred aniline solution. The reaction mixture was stirred for 30 min and the resulting solution of diazonium salt was added dropwise to a pre-cooled (0 °C) mixture of dimethylaniline (**VI.6**) (47.7  $\mu$ L, 45.3 mg, 0.374 mmol, 1.5 eq.) and sodium acetate (123 mg, 1.49 mmol, 6.0 eq.) and in methanol. The resulting solution was slowly allowed to warm up to room temperature and stirred for 3 h. Ethyl acetate (110 mL) was added and the majority of the methanol was removed under reduced pressure. The organic phase was washed with sat. NaHCO<sub>3</sub> and sat. NaCl and dried over MgSO<sub>4</sub>. The solvent was removed *in vacuo* and the crude material was purified by silica gel column chromatography (10% MeOH/DCM) and **AzoAdenosine-3** (80.0 mg, 0.249 mmol, 60%) was isolated as orange solid.

**<sup>1</sup>H NMR** (400 MHz, DMSO-*d*<sub>6</sub>):  $\delta$  = 7.90 (s, 1H, CH), 7.75 (d, *J* = 8.7 Hz, 2H, CH<sub>2</sub>), 7.69 (d, *J* = 7.9 Hz, 2H, CH<sub>2</sub>), 7.38 (d, *J* = 8.0 Hz, 2H, CH<sub>2</sub>), 6.85 - 6.69 (m, 4H, NH<sub>2</sub> and CH<sub>2</sub>), 6.28 (s, 1H, OH), 5.73 (d, *J* = 5.9 Hz, 1H, CH), 5.38 (d, *J* = 6.1 Hz, 1H, OH), 5.12 (d, *J* = 4.6 Hz, 2H, OH, overlapping with 1H, NH), 4.61 (s, 1H, CH), 4.16 - 4.08 (m, 1H, CH), 3.88 (d, *J* = 3.4 Hz, 1H, CH), 3.61 (dt, *J* = 8.7, 4.3 Hz, 1H,  $\frac{1}{2}$  CH<sub>2</sub>), 3.55 - 3.42 (m, 3H,  $\frac{1}{2}$  CH<sub>2</sub> and CH<sub>2</sub>), 3.02 (s, 6H, 2 CH<sub>3</sub>), 2.88 (t, *J* = 7.1 Hz, 2H, CH<sub>2</sub>).

**<sup>13</sup>C NMR** (100 MHz, DMSO-*d*<sub>6</sub>):  $\delta$  = 159.2, 156.1, 152.4, 151.5, 150.8, 142.6, 142.2, 136.5, 129.6, 124.6, 121.9, 113.7, 111.6, 87.2, 85.3, 72.9, 70.7, 61.8, 42.8, 39.7 (extracted from HSQC), 35.2.

**HRMS** (ESI): calcd. for C<sub>26</sub>H<sub>32</sub>N<sub>9</sub>O<sub>4</sub> [M+H]<sup>+</sup>: 534.2572; found: 534.2572.

**R<sub>t</sub>**: 2.866 min (5  $\rightarrow$  100% MeCN/H<sub>2</sub>O + 0.1% FA)

**$\lambda_{\max}$**  (DMSO): 422 nm ( $\pi$ - $\pi^*$ ).





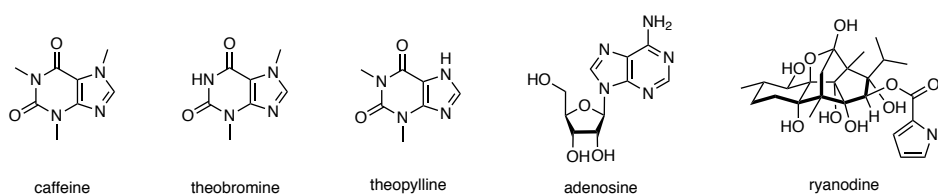
## V. Photoswitchable Caffeine



## Photoswitchable Caffeine Derivatives for the Optical Control of Cardiac Function

### Introduction

Methylxanthines like caffeine, theobromine and theophylline, (Figure V.1) are naturally occurring alkaloids, which are found in many plant components commonly consumed by humans in forms such as tea, coffee, energy drinks, and carbonated soft drinks.<sup>1</sup> Pure caffeine is a white, crystalline solid, and its isolation from black tea leaves is a popular undergraduate laboratory experiment.<sup>2</sup> It is likely the most commonly consumed neurostimulant and in the late 1990s, it was estimated that almost 90% of the US population consumed an average daily dose of close to 200 mg, mainly in the form of liquid coffee.<sup>3,4</sup> Since then, caffeine consumption in the US has slightly decreased, but coffee still remains the major source.<sup>1</sup> Caffeine consumption can cause insomnia, restlessness, and heart burn, but also help with daytime fatigue.



**Figure V.1: molecular structures of caffeine, theobromine, theophylline, adenosine, ryanodine.**

The beneficial effects of caffeine are mainly attributed to its antagonizing effect on adenosine  $A_1$  and  $A_{2A}$  receptors (Chapter IV).<sup>3</sup> Adenosine (Figure V.1) receptors are G protein-coupled receptors, which belong to the purinergic receptor family. The adenosine receptor family comprises four receptor subtypes,  $A_1$ ,  $A_{2A}$ ,  $A_{2B}$  and  $A_3$ . Their most widely known antagonist is caffeine. If activation of  $A_1$  receptors is inhibited, GIRK channels are less likely to be open and neuronal excitability is increased. Antagonism of  $A_{2A}$  also prevents inhibition of postsynaptic  $D_2$  receptors, which overall increases their activity in the brain.<sup>5</sup>

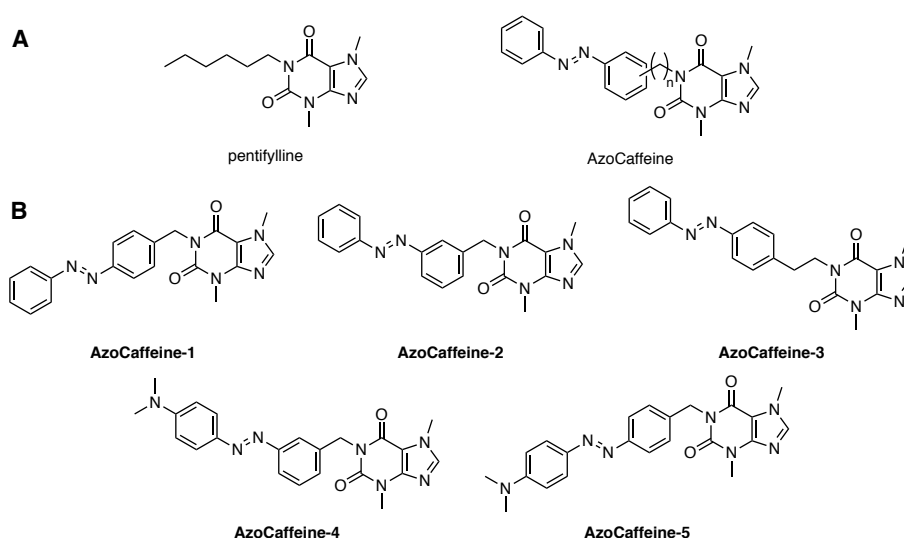
Adenosine receptors are ubiquitously expressed in the human body. Antagonism of ARs is considered to have effects on the cardiovascular system, however, arrhythmias in particular are often linked to an imbalance in calcium levels. Two distinct receptor classes are mainly responsible for calcium homeostasis in heart muscle cells: inositol triphosphate (IP3) receptors and ryanodine receptors (RyRs), the latter of which can be activated by caffeine as well. RyRs received their name

from the poisonous diterpenoid ryanodine (Figure V.1), which stabilizes the receptor in an open, but not yet conducting state.<sup>6</sup> RyRs are localized in the endoplasmic reticulum (ER) and the sarcoplasmic reticulum (SR).<sup>7</sup> Upon depolarization, L-type voltage-gated calcium channels open and  $\text{Ca}^{2+}$  is able to enter the cytoplasm.  $\text{Ca}^{2+}$  then binds to RyRs and  $\text{Ca}^{2+}$  is released from the ER or SR, a process called calcium induced calcium release (CICR).<sup>6</sup> Binding of caffeine or other methylxanthines activates RyRs, but many details of the mechanism are still under debate.<sup>7-10</sup> A caffeine overdose can be fatal, due to severe arrhythmias,<sup>11,12</sup> but consumption through beverages and food is usually considered safe.<sup>13</sup> As a tool compound to study RyRs, caffeine is used from structural biology to medical sciences. For example, it was used to elucidate the structural basis of gating and activation mechanisms,<sup>14</sup> to study the pacemaker mechanism in embryonic heart cells<sup>15</sup> and the role of  $\text{Ca}^{2+}$  leaks in tachycardia.<sup>16</sup>

A photoswitchable version of caffeine could enable the optical control of RyRs, to study cardiac function (arrhythmias, myocardial ischemia, etc). Spatiotemporal control over the activity of the proarrhythmic agent could give valuable insights into basic receptor function and the effects of localized activation in model systems like Langendorff heart preparations.<sup>17,18</sup>

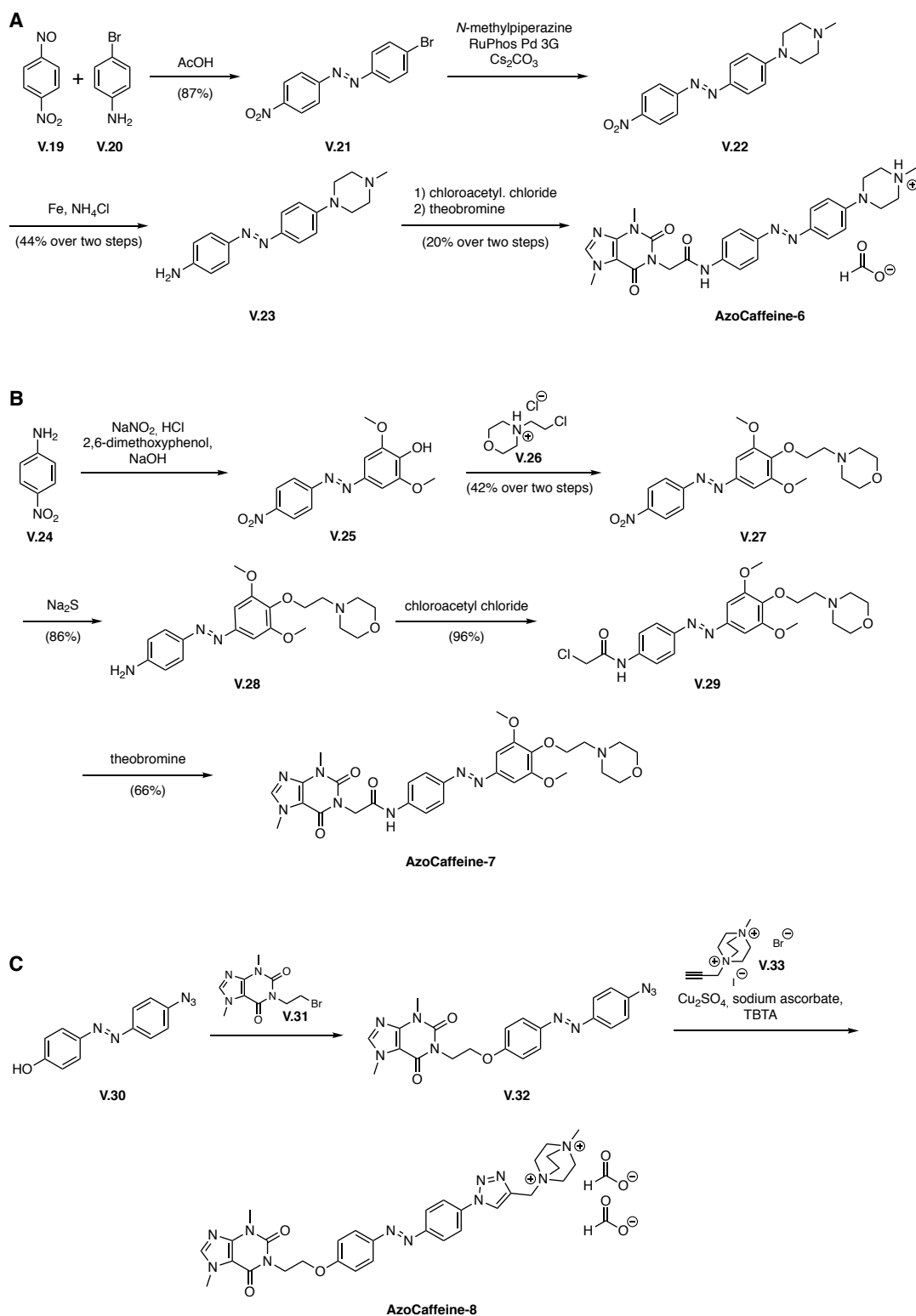
## Results and Discussion

*Design.* The methylxanthine pentifylline (Figure V.2) shows increased binding affinity towards RyRs, compared to caffeine.<sup>19</sup> It was shown that hydrophobic residues in 1-, 3- and 7-position in general enhance potency.



**Figure V.2: Molecular structure of pentifylline and caffeine-photoswitches.** A: Structure of pentifylline and general azologization approach. B: Molecular structures of target molecules AzoCaffeine-1 to -5.



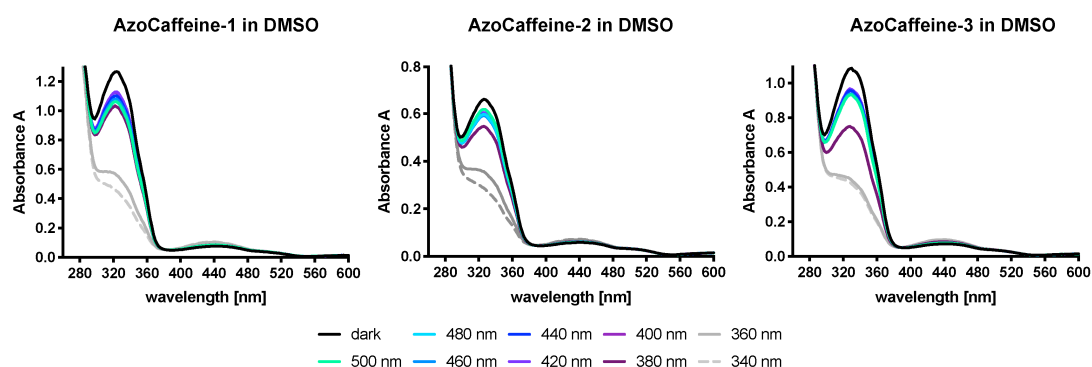


As especially the red-shifted compounds (AzoCaffeine-4 and -5) showed poor solubility, we envisioned to synthesize AzoCaffeine derivatives, decorated with solubility-enhancing, polar substituents (Scheme V.2). As an azo-coupling reaction of *para*-nitroaniline to 1-methyl-4-phenylpiperazine proved to be unsuccessful, the azobenzene core was accessed through Baeyer-Mills reaction of *para*-nitro-nitrosobenzene (**V.19**) and *para*-bromoaniline (**V.20**), followed by Buchwald-Hartwig cross-coupling of *N*-methylpiperazine using RuPhos Pd 3G. Low solubility hampered purification of **V.22**, which was subsequently reduced to the aniline **V.23** using iron powder in presence of ammonium chloride. Amide formation with chloroacetyl chloride followed by S<sub>N</sub>Ar with theobromine yielded AzoCaffeine-6. Interestingly, the *N*-methylpiperazino substituent did not enhance solubility, instead adhesion to glass walls in combination with poor solubility prevented isolation of AzoCaffeine-6 in significant quantities and will likely limit future applications.

AzoCaffeine-7 was therefore designed bearing a morpholine, which extends from the azobenzene through an alkyl linker, making the molecule more flexible.<sup>21</sup> Azo-coupling to yield phenol **V.25** was followed by substitution with alkyl chloride **V.26** in good yield. The resulting substituted nitroazobenzene **V.27** was reduced to the aniline **V.28** by sodium sulfide and the substitution precursor **V.29** was formed through amide bond formation with chloroacetyl chloride. Substitution with theobromine was then performed in DMF to yield AzoCaffeine-7.

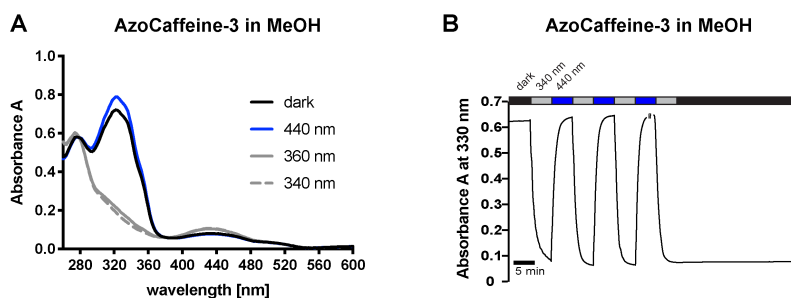
AzoCaffeine-8 was synthesized following a procedure used to synthesize diltiazem photoswitches,<sup>22</sup> which bear the same azobenzene photoswitch. Azobenzene **V.30** and di-cation **V.32** were provided by Dr. Nina Hartrampf (diltiazem project). Substitution with alkyl bromide **V.31** followed by click reaction yielded AzoCaffeine-8.

*UV-Vis Characterization.* Having seven AzoCaffeine derivatives at hand, we characterized their photophysical properties.



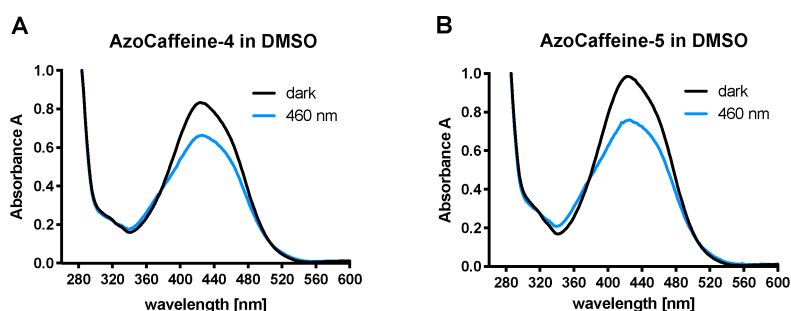
**Figure V.3: First-generation AzoCaffeines in DMSO.** Optimal wavelength to enrich the *cis*-state is 340 nm for benzyl linked AzoCaffeine-1 and -2, and 360 nm for the phenethyl linked AzoCaffeine-3. All spectra recorded at 50  $\mu$ M.

The absorption spectra of AzoCaffeine-1, -2 and -3 in DMSO show a maximum in absorption attributed to the  $\pi$ - $\pi^*$  transition at 320-330 nm (Figure V.3). In coherence with this, enrichment of the *cis*-state is most efficiently achieved with UV light (340 - 360 nm). The optimal wavelengths determined in DMSO translated into protic solvents (MeOH, Figure V.4) and switching between the two isomer-enriched states was reversible over many cycles. AzoCaffeine-3 was bistable in the darkness over 30 min, after irradiation with 340 nm light.



**Figure V.4: Phenethyl substituted AzoCaffeine-3.** A: Absorption spectra in MeOH under 440 nm, 360 nm and 340 nm illumination. B: repetitive isomerization with 340 nm and 440 nm light. Compound is stable in its thermodynamically unfavored *cis*-form over 30 min. All spectra recorded at 50  $\mu$ m.

AzoCaffeine-4 and -5, bearing a dimethylamino-substituent in 4'-position, showed red-shifted absorption spectra and fast-relaxation kinetics. Enrichment of the thermodynamically unstable *cis*-state was only achievable upon irradiation with a high-intensity light source (Figure V.5).

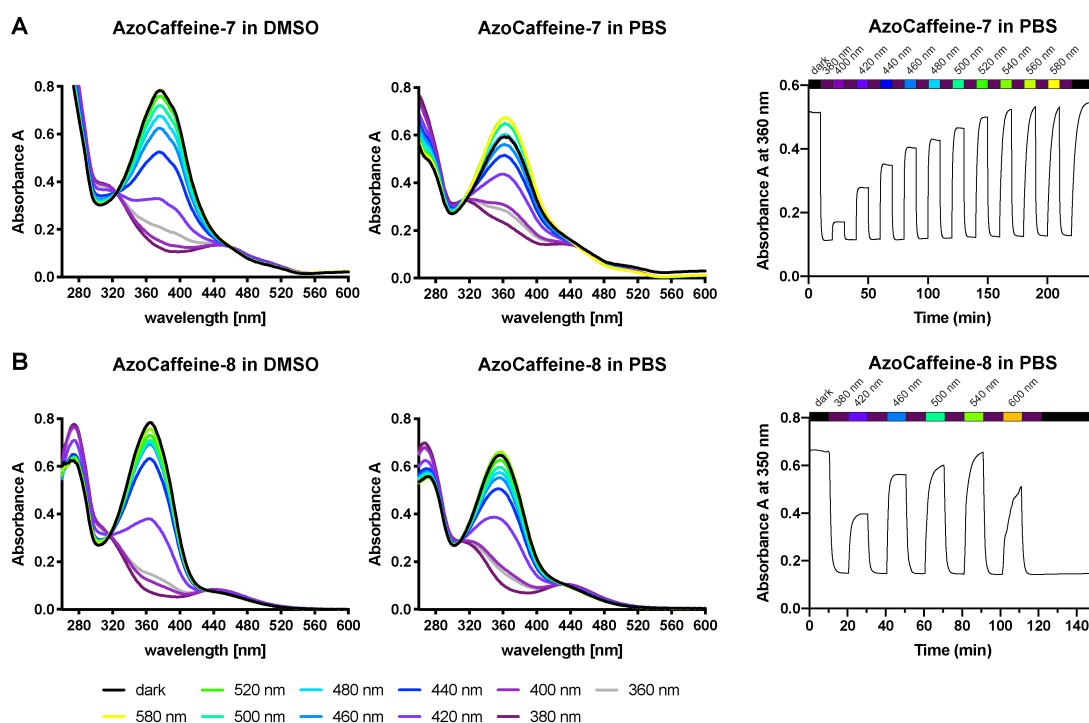


**Figure V.5: UV-Vis spectra of red-shifted AzoCaffeines-4 and -5.** A: AzoCaffeine-4 and B: AzoCaffeine-5 in DMSO, only show isomerization upon illumination with a high-powered LED (UHP-LED by Prizmatix). All spectra recorded at 50  $\mu$ m.

Due to their improved solubility, we had identified AzoCaffeine-7 and -8 as our lead compounds and characterized their photophysical properties in more detail



(Figure V.6). The spectra of both compounds show small bathochromic shifts, with absorption maxima at 374 nm (AzoCaffeine-7) and 367 nm (AzoCaffeine-8). This translates into red-shifting of the optimal wavelengths for isomerization, which were determined to be 380 nm in both cases. Back-isomerization to the thermodynamically favored *trans*-state can be achieved with a range of blue to green light. While AzoCaffeine-7 relaxes back to its *trans*-state within minutes in PBS (half-life = 2.2 min, see experimental procedures section for curve fit), AzoCaffeine-8 is stable in the dark over 30 min in this solvent.



**Figure V.6: UV-Vis spectra of second-generation AzoCaffeines.** A: absorption spectra under various wavelengths of light illumination of AzoCaffeine-7 in DMSO and in PBS and observation of PSSs under wavelengths ranging from 380 nm to 580 nm in PBS. B: absorption spectra under various wavelengths of illumination of AzoCaffeine-8 in DMSO and in PBS and observation of PSSs under wavelengths ranging from 380 nm to 600 nm in PBS. All spectra recorded at 50  $\mu\text{M}$ .

## Conclusion

In summary, we have successfully synthesized seven AzoCaffeine derivatives and characterized their photophysical properties. Compared to caffeine, the solubility in water, DMSO and PBS decreased significantly upon attachment of an azobenzene, and the first-generation compounds were not suitable for testing in Langendorff hearts. Attachment of polar substituents enhanced solubility and AzoCaffeine-7 and -8 are also red-shifted by 40 nm, compared to regular

azobenzenes. They can be isomerized in both directions using visible light. Their thermal relaxation properties are, however, distinct and could enable different applications. Thermal bistability enables pre-illumination, which is desirable, if light penetration through skin and muscle is not sufficient, which might likely be the case in Langendorff heart preparations. If tissue penetration is not the limiting factor, fast thermal relaxation would be useful as spatial localization can be important. A half-life of 2.2 min might, however, not yet be fast enough to ensure deactivation as soon as the molecule perfuses out of the light beam.

## References

- (1) Mitchell, D. C.; Knight, C. A.; Hockenberry, J.; Teplansky, R.; Hartman, T. J. Beverage Caffeine Intakes in the U.S. *Food Chem. Toxicol.* **2014**, *63*, 136-142.
- (2) Gatterman, L.; Wieland, H. *Laboratory Methods of Organic Chemistry*, 24th ed.; The MacMillan Company: New York, NY, 1937.
- (3) Addicott, M. A.; Yang, L. L.; Peiffer, A. M.; Burnett, L. R.; Burdette, J. H.; Chen, M. Y.; Hayasaka, S.; Kraft, R. A.; Maldjian, J. A.; Laurienti, P. J. The Effect of Daily Caffeine Use on Cerebral Blood Flow: How Much Caffeine Can We Tolerate? *Hum. Brain Mapp.* **2009**, *30*, 3102-3114.
- (4) Frary, C. D.; Johnson, R. K.; Wang, M. Q. Food Sources and Intakes of Caffeine in the Diets of Persons in the United States. *J. Acad. Nutr. Diet.* **2005**, *105*, 110-113.
- (5) Fredholm, B. B. Adenosine, Adenosine Receptors and the Actions of Caffeine\*. *Pharmacol. Toxicol.* **1995**, *76*, 93-101.
- (6) Petegem, F. V. Ryanodine Receptors: Structure and Function. *J. Biol. Chem.* **2012**, *287*, 31624-31632.
- (7) Meissner, G. The Structural Basis of Ryanodine Receptor Ion Channel Function. *J. Gen. Physiol.* **2017**, *149*, 1065-1089.
- (8) Kong, H.; Jones, P. P.; Koop, A.; Zhang, L.; Duff, H. J.; Chen, S. R. W. Caffeine Induces Ca<sup>2+</sup> Release by Reducing the Threshold for Luminal Ca<sup>2+</sup> Activation of the Ryanodine Receptor. *Biochem. J.* **2008**, *414*, 441-452.
- (9) Porta, M.; Zima, A. V.; Nani, A.; Diaz-Sylvester, P. L.; Copello, J. A.; Ramos-Franco, J.; Blatter, L. A.; Fill, M. Single Ryanodine Receptor Channel Basis of Caffeine's Action on Ca<sup>2+</sup> Sparks. *Biophys. J.* **2011**, *100*, 931-938.
- (10) Murayama, T.; Ogawa, H.; Kurebayashi, N.; Ohno, S.; Horie, M.; Sakurai, T. A Tryptophan Residue in the Caffeine-Binding Site of the Ryanodine Receptor Regulates Ca<sup>2+</sup> Sensitivity. *Commun. Biol.* **2018**, *1*, 1-12.
- (11) Poussel, M.; Kimmoun, A.; Levy, B.; Gambier, N.; Dudek, F.; Puskarczyk, E.; Poussel, J.-F.; Chenuel, B. Fatal Cardiac Arrhythmia Following Voluntary Caffeine Overdose in an Amateur Body-BUILDER Athlete. *Int. J. Cardiol.* **2013**, *166*, e41-e42.
- (12) Baraldi, P. G.; Tabrizi, M. A.; Gessi, S.; Borea, P. A. Adenosine Receptor Antagonists: Translating Medicinal Chemistry and Pharmacology into Clinical Utility. *Chem. Rev.* **2008**, *108*, 238-263.
- (13) Heckman, M. A.; Weil, J.; de Mejia, E. G. Caffeine (1, 3, 7-Trimethylxanthine) in Foods: A Comprehensive Review on Consumption, Functionality, Safety, and Regulatory Matters. *J. Food Sci.* **2010**, *75*, R77-R87.
- (14) Georges, A. des; Clarke, O. B.; Zalk, R.; Yuan, Q.; Condon, K. J.; Grassucci, R. A.; Hendrickson, W. A.; Marks, A. R.; Frank, J. Structural Basis for Gating and Activation of RyR1. *Cell* **2016**, *167*, 145-157.e17.
- (15) Sasse, P.; Zhang, J.; Cleemann, L.; Morad, M.; Hescheler, J.; Fleischmann, B. K. Intracellular Ca<sup>2+</sup> Oscillations, a Potential Pacemaking Mechanism in Early Embryonic Heart Cells. *J. Gen. Physiol.* **2007**, *130*, 133-144.
- (16) Lehnart, S. E.; Terrenoire, C.; Reiken, S.; Wehrens, X. H. T.; Song, L.-S.; Tillman, E. J.; Mancarella, S.; Coromilas, J.; Lederer, W. J.; Kass, R. S.; et al. Stabilization of Cardiac Ryanodine Receptor Prevents Intracellular Calcium Leak and Arrhythmias. *Proc. Natl. Acad. Sci.* **2006**, *103*, 7906-7910.
- (17) Bell, R. M.; Mocanu, M. M.; Yellon, D. M. Retrograde Heart Perfusion: The Langendorff Technique of Isolated Heart Perfusion. *J. Mol. Cell. Cardiol.* **2011**, *50*, 940-950.

- (18) Skrzypiec-Spring, M.; Grotthus, B.; Szeląg, A.; Schulz, R. Isolated Heart Perfusion According to Langendorff–Still Viable in the New Millennium. *J. Pharmacol. Toxicol. Methods* **2007**, *55*, 113–126.
- (19) Liu, W.; Meissner, G. Structure-Activity Relationship of Xanthines and Skeletal Muscle Ryanodine Receptor/Ca<sup>2+</sup> Release Channel. *Pharmacology* **1997**, *54*, 135–143.
- (20) Eidebenz, E. D.; Schuh, H. G. V. D. Verfahren Zur Herstellung von 1-Hexyl-3, 7-Dimethylxanthin. DE860217 (C), December 18, 1952.
- (21) Walker, M. A. Improving Solubility via Structural Modification. In *Tactics in Contemporary Drug Design*; Meanwell, N. A., Ed.; Topics in Medicinal Chemistry; Springer Berlin Heidelberg, 2015; pp 69–106.
- (22) Fehrentz, T.; Huber, F. M. E.; Hartrampf, N.; Bruegmann, T.; Frank, J. A.; Fine, N. H. F.; Malan, D.; Danzl, J. G.; Tikhonov, D. B.; Sumser, M.; et al. Optical Control of L-Type Ca<sup>2+</sup> Channels Using a Diltiazem Photoswitch. *Nat. Chem. Biol.* **2018**, *1*.
- (23) Sarkar, S.; Sarkar, P.; Ghosh, P. Selective Single-Step Oxidation of Amine to Cross-Azo Compounds with an Unhampered Primary Benzyl Alcohol Functionality. *Org. Lett.* **2018**, *20*, 6725–6729.
- (24) Fatás, P.; Longo, E.; Rastrelli, F.; Crisma, M.; Toniolo, C.; Jiménez, A. I.; Cativiela, C.; Moretto, A. Bis(Azobenzene)-Based Photoswitchable, Prochiral, C $\alpha$ -Tetrasubstituted  $\alpha$ -Amino Acids for Nanomaterials Applications. *Chem. - Eur. J.* **2011**, *17*, 12606–12611.
- (25) Yu, B.-C.; Shirai, Y.; Tour, J. M. Syntheses of New Functionalized Azobenzenes for Potential Molecular Electronic Devices. *Tetrahedron* **2006**, *62*, 10303–10310.

## Methods

**General Experimental Techniques.** All reactions were conducted using dried glassware (160 °C) under a positive pressure of nitrogen with magnetic stirring unless otherwise stated. Liquid reagents and solvents were added *via* syringe through rubber septa. Solids were added under inert gas counter flow or were dissolved in specified solvents prior to addition. Low temperature reactions were carried out in a Dewar vessel filled with the appropriate cooling agent e.g. H<sub>2</sub>O/ice (0 °C). Reactions using temperatures above room temperature were conducted using a heated oil bath. Solutions are aqueous, unless otherwise stated. Yields refer to spectroscopically pure compounds unless otherwise stated.

**Solvents and Reagents.** Anhydrous solvents were prepared with a solvent purification system by filtration of HPLC grade solvents through alumina or distilled as followed: Tetrahydrofuran (THF) was distilled under a nitrogen atmosphere from Na/benzophenone prior to use. Triethylamine (Et<sub>3</sub>N) was distilled under a nitrogen atmosphere from CaH<sub>2</sub> prior to use. Dichloromethane (CH<sub>2</sub>Cl<sub>2</sub>), 1,2-dichloroethane (DCE), ethyl acetate (EtOAc), dimethylformamide (DMF) and methanol (MeOH) were purchased from commercial suppliers (Acros Organics) and used as received. Solvents and additives for extraction and flash column chromatography were purchased in technical grade purity and distilled under reduced pressure prior to use. All other reagents and solvents were purchased from commercial suppliers and used as received, except stated otherwise.

**Chromatography.** Reactions and chromatography fractions were monitored by qualitative thin-layer chromatography (TLC) on silica gel F<sub>254</sub> TLC plates from Merck KGaA. Analytes on the glass plates were visualized by irradiation with UV light and/or by immersion of the TLC plate in ninhydrin staining solution, followed by heating with a hot-air gun. Flash column chromatography was performed using silica gel, particle size 40–63 μM (eluents are given in parenthesis) Additives (FA and TEA) were added to all components of the eluent mixture and constantly kept at 0.1%, unless stated otherwise.

**NMR Spectra.** NMR spectra were measured on a Bruker Avance III (600/150 MHz) Bruker Avance III HD (400/100 MHz) spectrometer, both equipped with a CryoProbe™. The <sup>1</sup>H and <sup>13</sup>C NMR shifts are reported in ppm related to the chemical shift of tetramethylsilane. NMR shifts were calibrated to residual solvent resonances: CDCl<sub>3</sub> (7.26 ppm, 77.16 ppm), DMSO (2.50 ppm, 39.52 ppm) and MeOD (3.31 ppm, 49.00 ppm). <sup>1</sup>H NMR spectroscopic data are reported as follows: Chemical shift in ppm (multiplicity, coupling constants, integration). The multiplicities are abbreviated with s (singlet), br s (broad singlet), d (doublet), t (triplet), q (quartet) and m (multiplet) and their respective combinations. Except for multiplets, the chemical shift of all signals is reported as the center of the resonance range. In addition to <sup>1</sup>H and <sup>13</sup>C NMR measurements, 2D NMR techniques as homonuclear correlation spectroscopy (COSY), heteronuclear single quantum coherence (HSQC) and heteronuclear multiple bond coherence (HMBC) were used

to assist the compound identification process. Coupling constants  $J$  are reported in Hz. All raw fid files were processed, and the spectra analyzed using the program MestReNova 11.0 from Mestrelab Research S. L.

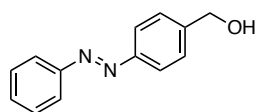
**Mass Spectra.** High-resolution mass spectra (HRMS) were recorded by the LMU Mass Spectrometry Service on a Thermo Finnigan LTQ FT Ultra Fourier (ESI), a Finnigan MAT 95 (EI, DEI), a JEOL MS station JMS-700 (FAB) or using an Agilent 6224 Accurate-Mass time-of-flight spectrometer with electrospray ionization (ESI) at the New York University Shared Instrumentation Facility (NYU-SIF).

**Infrared Spectra.** IR spectra were recorded on a Thermo Nicolet AVATAR FT-IR equipped with an ATR unit. The measured wave numbers are reported in  $\text{cm}^{-1}$ .

**UV/Vis Spectra.** UV-Vis spectra were recorded on a Varian Cary 50 Scan UV-Vis spectrometer (AzoCaffeine-1 to -5) using Helma SUPRASIL precision cuvettes (10 mm light path) or a Varian Cary 60 Scan UV-Vis (AzoCaffeine-7 and -8) spectrometer equipped with an 18-cell holder using Brandtech Scientific Inc. UV cuvettes (70-850  $\mu\text{L}$ , 10 mm light path),. The stock solution was prepared at 50 mM in DMSO and diluted to 50  $\mu\text{M}$  in DMSO, PBS or MeOH prior to the experiment. For the wavelength scan, photoswitching was achieved using an Optoscan Monochromator (AzoCaffeine-7 and -8) with an Optosource (75 mW lamp), which was controlled through a program written in Matlab or a Till Photonics Polychrome V monochromator (AzoCaffeine-1 to -5). Irradiation to establish PSS took place from the top through a fiber-optic cable. Illumination was screened from 360 - 540 nm in 20 nm steps, going from higher to lower wavelengths, illuminating 5 to 10 min for each wavelength. Illumination conditions that afforded the highest *trans*-isomer and *cis*-isomer enrichment are shown. Spectra were processed using Microsoft Excel 16 and Prism 8 and the figures were generated in Adobe Illustrator 23.

## Experimental Procedures

### (4-(phenyldiazenyl)phenyl)methanol (**V.3**)



Nitrosobenzene (**V.1**) (1.06 g, 9.90 mmol, 1.0 eq) and 4-aminobenzyl alcohol (**V.2**) (1.22 g, 9.90 mmol, 1.0 eq) were dissolved in DCM (25 mL) at room temperature and acetic acid (3.4 mL) was added. After 4 h the reaction mixture was neutralized with NaHCO<sub>3</sub>. The aqueous phase was extracted with EtOAc (2 x 30 mL) and the combined organic phase was washed with sat. NaHCO<sub>3</sub> (30 mL), and sat. NaCl (30 mL), and dried over Na<sub>2</sub>SO<sub>4</sub>. The solvent was removed *in vacuo*. The crude product was purified by silica gel flash column chromatography (30% EtOAc/hexanes) to yield (4-(phenyldiazenyl)phenyl)methanol (1.56 g, 7.36 mmol, 74%) as orange solid.

**<sup>1</sup>H NMR** (400 MHz, CDCl<sub>3</sub>): δ = 7.92 (d, *J* = 8.1 Hz, 4H), 7.57 - 7.44 (m, 5H), 4.79 (s, 2H), 1.88 (s, 1H).

**<sup>13</sup>C NMR** (100 MHz, CDCl<sub>3</sub>): δ = 152.7, 152.2, 144.0, 131.2, 129.2, 127.6, 123.2, 123.0, 65.0.

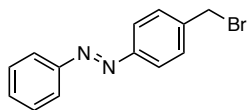
**Note:** For reasons of clarity, only *trans*-signals are reported. The spectroscopic data match those reported.<sup>23</sup>

**HRMS** (ESI): calcd for C<sub>13</sub>H<sub>11</sub>N<sub>2</sub>O [M+H]<sup>+</sup>: 212.0950. Found: 212.0950.

**IR** (neat, cm<sup>-1</sup>): 3312, 3066, 2917, 2856, 2361, 2339, 1595, 1521, 1503, 1487, 1465, 1442, 1413, 1349, 1303, 1221, 1150, 1108, 1071, 1026, 1009, 922, 850, 831, 763, 717.

**R<sub>f</sub>** = 0.29 (30% EtOAc/hexanes)

**R<sub>t</sub>** = 5.66 min (0.1% FA + 10 → 100% MeCN/H<sub>2</sub>O; 10 min)

**1-(4-(bromomethyl)phenyl)-2-phenyldiazene (V.4)**

4-(phenyldiazenyl)phenyl)methanol (**V.3**) (1.30 g, 6.12 mmol, 1.0 eq) and  $\text{CBr}_4$  (2.44 g, 7.35 mmol, 1.2 eq) were dissolved in DCM (70 mL) at room temperature and  $\text{PPh}_3$  (2.41 g, 9.19 mmol, 1.5 eq) was added. After 1.5 h, sat.  $\text{NaHCO}_3$  was added, the phases were separated, and the aqueous phase was extracted with DCM (2 x 20 mL). The combined organic layers were washed with  $\text{NaHCO}_3$  (20 mL) and sat.  $\text{NaCl}$  (20 mL), dried over  $\text{Na}_2\text{SO}_4$  and concentrated *in vacuo*. The crude product was purified by silica gel flash column chromatography (1% EtOAc/hexanes) to yield 1-(4-(bromomethyl)phenyl)-2-phenyldiazene (**V.4**) (1.29 g, 4.70 mmol, 77%) as orange solid.

**$^1\text{H NMR}$**  (400 MHz,  $\text{CDCl}_3$ ):  $\delta$  = 7.95 - 7.87 (m, 4H), 7.57 - 7.46 (m, 5H), 4.56 (s, 2H).

**$^{13}\text{C NMR}$**  (101 MHz,  $\text{CDCl}_3$ ):  $\delta$  = 152.7, 152.5, 140.7, 131.4, 130.0, 129.3, 123.4, 123.1, 32.9.

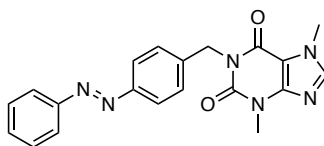
**Note:** *cis* and *trans* signal of the methylene have been integrated as the aromatic signals of both isomers overlap. In the carbon spectrum, the *cis* methylene signal is visible at 45.8 ppm.

**HRMS** (ESI): calcd for  $\text{C}_{13}\text{H}_{11}\text{BrN}_2$   $[\text{M}+\text{H}]^+$ : 275.0185. Found: 275.0183.

**IR** (neat,  $\text{cm}^{-1}$ ): 3040, 2921, 2161, 1956, 1811, 1698, 1582, 1499, 1485, 1464, 1442, 1413, 1302, 1261, 1218, 1194, 1151, 1090, 1071, 1017, 1010, 1000, 921, 873, 853, 833, 783, 768.

**$R_f$**  = 0.48 (1% EtOAc/hexanes)



**3,7-dimethyl-1-(4-(phenyldiazenyl)benzyl)-3,7-dihydro-1H-purine-2,6-dione (AzoCaffeine-1)**

Azobenzene bromide **V.4** (100 mg, 0.363 mmol, 1.0 eq), theobromine (65.5 mg, 0.363 mmol, 1.0 eq),  $K_2CO_3$  (65.3 mg, 0.472 mmol, 1.3 eq) and KI (6.03 mg, 0.0363 mmol, 0.1 eq) were dissolved in DMF (15 mL). The reaction was heated to 110 °C for 2 h. Sat.  $NaHCO_3$  (10 mL) was added and the aqueous phase was extracted with EtOAc (3 x 20 mL). The combined organic layers were washed with 10% NaCl (3 x 15 mL) and sat. NaCl (1 x 15 mL), dried over  $Na_2SO_4$ , and concentrated under reduced pressure. The crude product was purified by silica gel flash column chromatography (5% EtOAc/hexanes) to yield AzoCaffeine-1 (122.1 mg, 0.326 mmol, 90%) as orange solid.

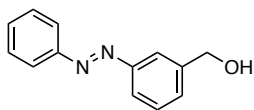
**$^1H$  NMR** (400 MHz,  $CDCl_3$ ):  $\delta$  = 7.95 – 7.81 (m, 4H), 7.63 (d,  $J$  = 8.3 Hz, 2H), 7.57 – 7.41 (m, 4H), 5.26 (s, 2H), 4.00 (s, 3H), 3.59 (s, 3H).

**$^{13}C$  NMR** (100 MHz,  $CDCl_3$ ):  $\delta$  = 155.3, 152.8, 152.1, 151.7, 149.1, 141.8, 140.4, 136.8, 131.1, 129.7, 129.2, 127.5, 123.1, 122.9, 107.8, 44.3, 33.8, 30.0.

**HRMS** (ESI): calcd for  $C_{20}H_{18}N_6O_2$   $[M+H]^+$ : 375.1570. Found 375.1573.

**IR** (neat,  $cm^{-1}$ ): 2949, 1702, 1655, 1604, 1548, 1485, 1454, 1430, 1414, 1369, 1351, 1323, 1287, 1234, 1185, 1154, 1127, 1097, 1071, 1015, 949, 861, 789, 761, 743.

**$R_f$**  = 0.18 (5% EtOAc/hexanes)

**(3-(phenyldiazenyl)phenyl)methanol (V.6)**

Nitrosobenzene (**V.1**) (1.04 g, 9.74 mmol, 1.0 eq) and 3-aminobenzyl alcohol (**V.5**) (1.20 g, 9.74 mmol, 1.0 eq) were dissolved in DCM (25 mL) at room temperature and acetic acid (3.4 mL) was added. After 4 h the reaction mixture was neutralized with  $\text{NaHCO}_3$ , the phases were separated, and the aqueous phase was extracted with EtOAc (2 x 30 mL). The combined organic layers were washed with sat.  $\text{NaHCO}_3$  (30 mL), and sat.  $\text{NaCl}$  (30 mL), dried over  $\text{Na}_2\text{SO}_4$  and concentrated under reduced pressure. The crude product was purified by silica gel flash column chromatography (20% EtOAc/hexanes) to yield (3-(phenyldiazenyl)phenyl)methanol (**V.6**) (1.61 g, 7.59 mmol, 78%) as orange solid.

**$^1\text{H NMR}$**  (400 MHz,  $\text{CDCl}_3$ ):  $\delta$  = 7.98 - 7.82 (m, 4H), 7.57 - 7.45 (m, 5H), 4.81 (s, 2H).

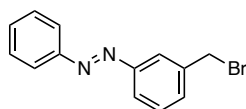
**$^{13}\text{C NMR}$**  (100 MHz,  $\text{CDCl}_3$ ):  $\delta$  = 153.0, 152.7, 142.2, 131.2, 129.5, 129.5, 129.3, 123.0, 122.8, 120.7, 65.1.

**Note:** the spectroscopic data match those reported.<sup>16</sup>

**HRMS** (ESI): calcd for  $\text{C}_{14}\text{H}_{14}\text{N}_2\text{O}$   $[\text{M}+\text{H}]^+$ : 212.0949. Found 212.0946.

**IR** (neat,  $\text{cm}^{-1}$ ): 3324, 3051, 2874, 2361, 1955, 1889, 1704, 1653, 1586, 1552, 1471, 1447, 1364, 1304, 1236, 1195, 1150, 1125, 1070, 1019, 922, 884, 793.

**R<sub>f</sub>** = 0.65 (40% EtOAc/hexanes)

**1-(3-(bromomethyl)phenyl)-2-phenyldiazene (V.7)**

(3-(phenyldiazenyl)phenyl)methanol (**V.6**) (1.58 g, 7.44 mmol, 1.0 eq) and  $\text{CBr}_4$  (2.96 g, 8.93 mmol, 1.2 eq) were dissolved in DCM (70 mL) at room temperature.  $\text{PPh}_3$  (2.93 g, 11.2 mmol, 1.5 eq) was added and the reaction was stirred for 1.5 h. Sat.  $\text{NaHCO}_3$  (20 mL) was added, the phases separated, and the aqueous phase was extracted with DCM (2 x 20 mL). The combined organic layers were washed with  $\text{NaHCO}_3$  (20 mL), and sat.  $\text{NaCl}$  (20 mL), dried over  $\text{Na}_2\text{SO}_4$ , filtered and concentrated *in vacuo*. The crude product was purified by silica gel flash column chromatography (3% EtOAc/hexanes) to yield 1-(3-(bromomethyl)phenyl)-2-phenyldiazene (**V.7**) (1.33 g, 4.82 mmol, 65%) as red liquid.

**$^1\text{H NMR}$**  (400 MHz,  $\text{CDCl}_3$ ):  $\delta$  = 7.98 - 7.84 (m, 4H), 7.58 - 7.45 (m, 5H), 4.72 - 4.57 (s, 2H).

**$^{13}\text{C NMR}$**  (100 MHz,  $\text{CDCl}_3$ ):  $\delta$  = 153.0, 152.7, 139.0, 138.7, 131.5, 131.4, 131.4, 131.1, 129.7, 129.7, 129.3, 123.5, 123.5, 123.1, 123.0, 122.6, 45.9, 33.0.

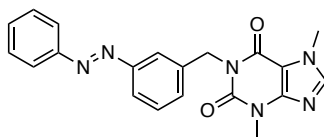
**Note:** the compound was obtained as a 1:1 mixture of *cis*- and *trans*-isomers. The spectroscopic data match those reported.<sup>17</sup>

**HRMS** (ESI): calcd for  $\text{C}_{13}\text{H}_{11}\text{BrN}_2$   $[\text{M}+\text{H}]^+$ : 275.0184. Found 275.0182.

**IR** (neat,  $\text{cm}^{-1}$ ): 3058, 2962, 2329, 1955, 1892, 1803, 1702, 1585, 1481, 1445, 1295, 1267, 1238, 1212, 1149, 1126, 1070, 1020, 1000, 9922, 837, 796, 762, 710.

**R<sub>f</sub>** = 0.29 (1% EtOAc/hexanes)

**3,7-dimethyl-1-(3-(phenyldiazenyl)benzyl)-3,7-dihydro-1H-purine-2,6-dione (AzoCaffeine-2)**



Azobenzene bromide **V.7** (100 mg, 0.363 mmol, 1.0 eq), theobromine (65.5 mg, 0.363 mmol, 1.0 eq),  $K_2CO_3$  (65.3 mg, 0.472 mmol, 1.3 eq) and KI (6.0 mg, 0.036 mmol, 0.1 eq) were dissolved in DMF (15 mL). The reaction was heated to 110 °C for 2 h. Sat.  $NaHCO_3$  (10 mL) was added, the phases separated, and the aqueous phase was extracted with EtOAc (3 x 20 mL). The combined organic layers were washed with 10% NaCl (3 x 15 mL) and sat. NaCl (1 x 15 mL), dried over  $Na_2SO_4$ , and concentrated under reduced pressure. The crude product was purified by silica gel flash column chromatography (5% EtOAc/hexanes) to yield AzoCaffeine-2 (132 mg, 0.353 mmol, 97%) as orange solid.

**$^1H$  NMR** (400 MHz,  $CDCl_3$ )  $\delta$  = 8.02 (s, 1H), 7.90 (d,  $J$  = 8.5 Hz, 2H), 7.80 (d,  $J$  = 7.9 Hz, 1H), 7.60 (d,  $J$  = 7.5 Hz, 1H), 7.56 – 7.42 (m, 5H), 5.30 (s, 2H), 4.00 (s, 3H), 3.59 (s, 3H).

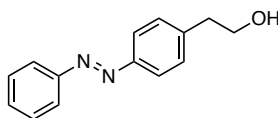
**$^{13}C$  NMR** (100 MHz,  $CDCl_3$ )  $\delta$  = 155.2, 152.8, 152.6, 151.6, 149.0, 141.6, 138.5, 131.3, 131.0, 129.1, 129.1, 124.0, 122.9, 121.1, 107.7, 44.3, 33.7, 29.9.

Note for reasons of clarity, only *trans*-signals are reported.

**HRMS** (ESI): calcd for  $C_{20}H_{18}N_6O_2$   $[M+H]^+$ : 375.1570. Found 375.1575.

**IR** (neat,  $cm^{-1}$ ): 3568, 3060, 2947, 2361, 1700, 1653, 1603, 1548, 1483, 1448, 1429, 1413, 1370, 1351, 1322, 1233, 1186, 1150, 1128, 1021, 1000, 965, 926, 844, 803, 775, 749, 741.

**R<sub>f</sub>** = 0.19 (5% EtOAc/hexanes)

**2-(4-(phenyldiazenyl)phenyl)ethan-1-ol (V.9)**

Nitrosobenzene (**V.1**) (1.04 g, 9.74 mmol, 1.1 eq) and 4-aminophenethyl alcohol (**V.8**) (1.20 g, 8.75 mmol, 1.0 eq) were dissolved in DCM (25 mL) at room temperature and acetic acid (3.4 mL) was added. After 4 h, the reaction was neutralized with sat.  $\text{NaHCO}_3$  and the phases were separated. The aqueous phase was extracted with EtOAc (2 x 30 mL). The combined organic layers were washed with  $\text{NaHCO}_3$  (30 mL) and sat.  $\text{NaCl}$  (30 mL), dried over  $\text{Na}_2\text{SO}_4$ , and concentrated under reduced pressure. The crude product was purified by silica gel flash column chromatography (30% EtOAc/hexanes) to yield 2-(4-(phenyldiazenyl)phenyl)ethanol (**V.9**) (1.62 g, 7.16 mmol, 82%) as orange solid.

**$^1\text{H NMR}$**  (400 MHz,  $\text{CDCl}_3$ ):  $\delta$  = 7.94 - 7.85 (m, 4H), 7.56 - 7.45 (m, 3H), 7.39 (d,  $J$  = 8.5 Hz, 2H), 3.93 (t,  $J$  = 6.5 Hz, 2H), 2.96 (t,  $J$  = 6.5 Hz, 2H).

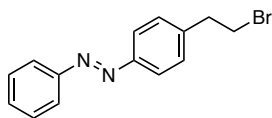
**$^{13}\text{C NMR}$**  (100 MHz,  $\text{CDCl}_3$ ):  $\delta$  = 152.8, 151.6, 142.1, 131.0, 129.9, 129.2, 123.2, 122.9, 63.6, 39.2.

**Note:** the spectroscopic data match those reported.<sup>25</sup>

**HRMS** (ESI): calcd for  $\text{C}_{14}\text{H}_{14}\text{N}_2\text{O}$   $[\text{M}+\text{H}]^+$ : 226.1106. Found 226.1099.

**IR** (neat,  $\text{cm}^{-1}$ ): 3309, 3021, 2936, 2916, 2862, 2360, 2340, 1703, 1656, 1603, 1582, 1549, 1500, 1486, 1466, 1442, 1413, 1331, 1303, 1221, 1151, 1106, 1039, 1018, 1011, 922, 869, 840, 823, 795, 764, 727.

**R<sub>f</sub>** = 0.33 (60% EtOAc/hexanes)

**1-(3-(bromomethyl)phenyl)-2-phenyldiazene (V.10)**

2-(4-(phenyldiazenyl)phenyl)ethan-1-ol (**V.9**) (1.60 g, 7.02 mmol, 1.0 eq) and  $\text{CBr}_4$  (2.81 g, 8.49 mmol, 1.2 eq) were dissolved in anhydrous DCM (70 mL) at room temperature.  $\text{PPh}_3$  (2.78 g, 10.6 mmol, 1.5 eq) was added. After 1.5 h, sat.  $\text{NaHCO}_3$  was added and the aqueous phase was extracted with DCM (2 x 20 mL). The combined organic layers were washed with  $\text{NaHCO}_3$  (20 mL) and sat.  $\text{NaCl}$  (20 mL), dried over  $\text{Na}_2\text{SO}_4$ , and concentrated under reduced pressure. The crude product was purified with silica gel flash column chromatography (1% EtOAc/hexanes) to yield 1-(3-(bromomethyl)phenyl)-2-phenyldiazene (**V.10**) (1.86 g, purity: 75% judged by  $^1\text{H}$  NMR) as orange solid, which was used without further purification.

Note: Separation of the byproducts, presumably the alkene and chlorinated product, was not possible.

**$^1\text{H}$  NMR** (400 MHz,  $\text{CDCl}_3$ )  $\delta$  = 7.93 - 7.86 (m, 4H), 7.55 - 7.47 (m, 3H), 7.39 - 7.35 (m, 2H), 3.62 (t,  $J$  = 7.5 Hz, 2H), 3.25 (t,  $J$  = 7.5 Hz, 2H).

**$^{13}\text{C}$  NMR** (100 MHz,  $\text{CDCl}_3$ )  $\delta$  = 152.6, 151.6, 142.0, 131.0, 129.4, 129.1, 123.1, 122.8, 39.1, 32.5.

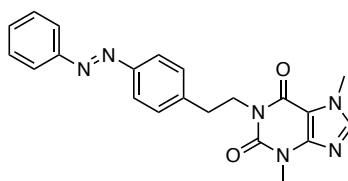
**Note:** signals were assigned using 2D NMR data.

**HRMS** (EI): calc for  $\text{C}_{14}\text{H}_{13}\text{BrN}_2$   $[\text{M}]^+$ : 288.0262, found 288.0257.

**$R_f$**  = 0.29 (1% EtOAc/hexanes)

**$R_t$**  = 8.28 min (LC-MS: 0.1% FA, 10  $\rightarrow$  100% MeCN/ $\text{H}_2\text{O}$  over 10 min)

**3,7-dimethyl-1-(4-(phenyldiazenyl)phenethyl)-3,7-dihydro-1H-purine-2,6-dione (AzoCaffeine-3)**



Azobenzene bromide (**V.10**) (92.1 mg, 0.331 mmol, 1.0 eq), theobromine (62.3 mg, 0.346 mmol, 1.1 eq),  $K_2CO_3$  (62.1 mg, 0.450 mmol, 1.4 eq) and KI (5.7 mg, 0.035 mmol, 0.1 eq) were dissolved in DMF (15 mL) to 110 °C for 3.5 h. Sat.  $NaHCO_3$  (10 mL) was added and the aqueous phase was extracted with EA (3 x 20 mL). The combined organic layers were washed with 10% NaCl (3 x 15 mL) and sat. NaCl, dried over  $Na_2SO_4$ , and concentrated under reduced pressure. The crude product was purified by silica gel flash column chromatography (5% → 100% EtOAc/hexanes) to yield AzoCaffeine-3 (42.4 mg, 0.109 mmol, 31% over two steps) as orange solid.

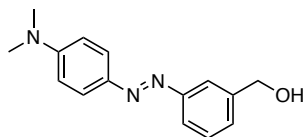
**$^1H$  NMR** (400 MHz,  $CDCl_3$ )  $\delta$  = 7.95 – 7.83 (m, 4H), 7.56 – 7.44 (m, 6H), 4.33 – 4.23 (m, 2H), 4.00 (s, 3H), 3.60 (s, 3H), 3.10 – 2.99 (m, 2H).

**$^{13}C$  NMR** (100 MHz,  $CDCl_3$ )  $\delta$  = 155.3, 152.8, 151.5, 149.0, 142.2, 141.7, 131.0, 129.9, 129.2, 127.4, 123.2, 122.9, 107.8, 42.6, 34.3, 33.8, 29.9.

**HRMS** (ESI): calcd for  $C_{20}H_{18}N_6O_2$   $[M+H]^+$ : 389.1727. Found 389.1730.

**IR** (neat,  $cm^{-1}$ ): 2952, 2361, 1703, 1656, 1604, 1550, 1485, 1453, 1414, 1356, 1326, 1288, 1188, 1155, 1121, 1071, 1014, 980, 851, 763, 749.

**R<sub>f</sub>** = 0.16 (5% EtOAc/hexanes)

**(3-((4-(dimethylamino)phenyl)diazenyl)phenyl)methanol (V.15)**

3-aminobenzyl alcohol (**V.13**) (1.17 g, 9.50 mmol, 1.0 eq) was dissolved in water (20 mL) and methanol (40 mL) and cooled to 0 °C. HCl 2 M (14.3 mL, 28.5 mmol, 3.0 eq) and NaNO<sub>2</sub> (0.721 g, 10.5 mmol, 1.1 eq) were added the reaction was stirred for 30 min. The resulting reaction mixture was then added to a pre-cooled (0 °C) solution of sodium acetate (4.68 g, 57.0 mmol, 6.0 eq) and *N,N*-dimethylaniline (**V.11**) (1.15 g, 9.50 mmol, 1.0 eq) in methanol (30 mL) The reaction was allowed to warm to room temperature for 3 h and thereafter stirred for 1 h. EtOAc (20 mL) was added and the bulk of the methanol was removed under reduced pressure. Sat. NaHCO<sub>3</sub> (40 mL) was added, the phases were separated, and the aqueous phase was extracted with EtOAc (2 x 40 mL). The organic layers were combined and washed with sat. NaHCO<sub>3</sub> (2 x 30 mL), and sat. NaCl (30 mL), dried over Na<sub>2</sub>SO<sub>4</sub>, and concentrated under reduced pressure. The crude product was purified by silica gel (deactivated with NH<sub>3</sub>) flash column chromatography (0% → 10% MeOH/DCM; +0.1% TEA) to yield (3-((4-(dimethylamino)phenyl)diazenyl)phenyl)methanol (**V.15**) (1.92 g, 7.51 mmol, 79%) as orange solid.

**<sup>1</sup>H NMR** (400 MHz, CDCl<sub>3</sub>): δ = 7.89 (d, J = 9.1 Hz, 2H), 7.83 (s, 1H), 7.78 (d, J = 7.9 Hz, 1H), 7.47 (t, J = 7.7 Hz, 1H), 7.39 (d, J = 7.5 Hz, 1H), 6.76 (d, J = 9.2 Hz, 2H), 4.78 (s, 2H), 3.09 (s, 6H).

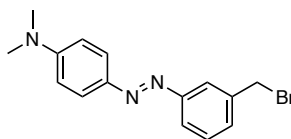
**<sup>13</sup>C NMR** (100 MHz, CDCl<sub>3</sub>): δ = 153.5, 152.6, 143.7, 142.0, 129.3, 127.9, 125.2, 122.2, 120.1, 111.6, 65.3, 40.5.

**HRMS** (ESI): calcd for C<sub>15</sub>H<sub>17</sub>N<sub>3</sub>O [M+H]<sup>+</sup>: 256.1451. Found 256.1446.

**IR** (neat, cm<sup>-1</sup>): 3356, 2910, 2361, 1598, 1563, 1518, 1481, 1444, 1405, 1362, 1310, 1228, 1149, 1124, 1063, 945, 885, 821, 798, 777, 726.

**R<sub>f</sub>** = 0.53 (60% EtOAc/hexanes)



**4-((3-(bromomethyl)phenyl)diazenyl)-*N,N*-dimethylaniline (V.17)**

**V.15** (1.00 g, 3.92 mmol, 1.0 eq) and  $\text{CBr}_4$  (1.56 g, 4.70 mmol, 1.2 eq) were dissolved in DCM (45 mL) at room temperature and  $\text{PPh}_3$  (1.54 g, 5.87 mmol, 1.5 eq) was added. After 1.5 h, sat.  $\text{NaHCO}_3$  (20 mL) was added, the phases were separated, and the aqueous phase was extracted with DCM (3 x 20 mL). The combined organic layers were washed with sat.  $\text{NaHCO}_3$  (1 x 20 mL) and sat.  $\text{NaCl}$  (1 x 20 mL), dried over  $\text{Na}_2\text{SO}_4$ , and concentrated under reduced pressure. The crude product was purified by silica gel (deactivated with  $\text{NH}_3$ ) flash column chromatography (6%  $\rightarrow$  100% EtOAc/hexanes; + 0.1% TEA) to yield 4-((3-(bromomethyl)phenyl)diazenyl)-*N,N*-dimethylaniline (**V.17**) (0.402 g, 1.26 mmol, 32%) as orange solid.

**$^1\text{H NMR}$**  (400 MHz,  $\text{CDCl}_3$ ):  $\delta$  = 7.89 (d,  $J$  = 9.1 Hz, 2H), 7.83 (s, 1H), 7.77 (d,  $J$  = 7.9 Hz, 1H), 7.47 (t,  $J$  = 7.7 Hz, 1H), 7.39 (d,  $J$  = 7.6 Hz, 1H), 6.76 (d,  $J$  = 9.2 Hz, 2H), 4.78 (s, 2H), 3.09 (s, 6H).

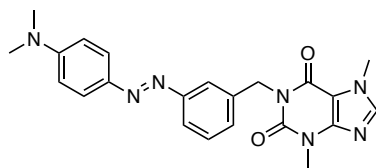
**$^{13}\text{C NMR}$**  (100 MHz,  $\text{CDCl}_3$ ):  $\delta$  = 153.5, 152.6, 143.7, 142.0, 129.3, 127.9, 125.2, 122.2, 120.1, 111.6, 65.3, 40.5.

**HRMS** (ESI): calcd for  $\text{C}_{15}\text{H}_{16}\text{BrN}_3$   $[\text{M}+\text{H}]^+$ : 318.0607, found 318.0607.

**IR** (neat,  $\text{cm}^{-1}$ ): 2904, 2813, 2361, 1599, 1563, 1518, 1480, 1444, 1405, 1364, 1310, 1229, 1151, 1125, 1064, 998, 945, 906, 822, 798.

**R<sub>f</sub>** = 0.20 (95% EtOAc/hexanes)

**1-(4-((4-(dimethylamino)phenyl)diazenyl)benzyl)-3,7-dimethyl-3,7-dihydro-1H-purine-2,6-dione (AzoCaffeine-4)**



Azobenzene bromide **V.17** (100 mg, 0.314 mmol, 1.0 eq), theobromine (56.6 mg, 0.314 mmol, 1.0 eq),  $K_2CO_3$  (56.5 mg, 0.409 mmol, 1.3 eq) and KI (5.20 mg, 31.4  $\mu$ mol, 0.1 eq) were dissolved in DMF (15 mL). The reaction was heated to 110 °C for 3 h. Upon cooling to room temperature, sat.  $NaHCO_3$  (10 mL) was added, the phases were separated, and the aqueous phase was extracted with EtOAc (3 x 20 mL). The combined organic layers were washed with 10% NaCl (3 x 15 mL) and sat. NaCl (1 x 15 mL), dried over  $Na_2SO_4$ , and concentrated under reduced pressure. The crude product was purified by silica gel (deactivated with  $NH_3$ ) flash column chromatography (100% EtOAc) to yield AzoCaffeine-4 (118 mg, 0.283 mmol, 90%) as orange solid.

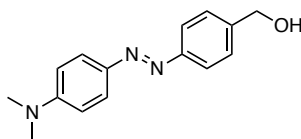
**$^1H$  NMR** (400 MHz,  $CDCl_3$ ):  $\delta$  = 7.93 (s, 1H), 7.86 (d,  $J$  = 9.1 Hz, 2H), 7.71 (d,  $J$  = 8.0 Hz, 1H), 7.53 – 7.47 (m, 2H), 7.40 (t,  $J$  = 7.7 Hz, 1H), 6.74 (d,  $J$  = 9.1 Hz, 2H), 5.28 (s, 2H), 3.99 (s, 3H), 3.59 (s, 3H), 3.08 (s, 6H).

**$^{13}C$  NMR** (100 MHz,  $CDCl_3$ ):  $\delta$  = 155.4, 153.4, 152.5, 151.8, 149.0, 143.7, 141.7, 138.3, 129.8, 129.1, 125.1, 123.5, 120.6, 111.6, 107.8, 44.5, 40.5, 33.8, 30.0.

**HRMS** (ESI): calcd for  $C_{22}H_{23}N_7O_2$   $[M+H]^+$ : 418.1992. Found 418.1994.

**IR** (neat,  $cm^{-1}$ ): 3467, 2922, 2853, 2361, 1700, 1655, 1598, 1548, 1518, 1482, 1445, 1406, 1323, 1286, 1231, 1150, 1123, 1065, 998, 945, 823, 781, 762, 734.

**$R_f$**  = 0.16 (95% EtOAc/hexanes)

**(4-((4-(dimethylamino)phenyl)diazenyl)phenyl)methanol (V.16)**

4-aminobenzyl alcohol (**V.14**) (1.22 g, 9.90 mmol, 1.0 eq) was dissolved in water (20 mL) and methanol (40 mL) at 0 °C and 2 M HCl (15 mL, 29.7 mmol, 3.0 eq) and NaNO<sub>2</sub> (0.751 g, 10.9 mmol, 1.1 eq) were added. The reaction was stirred for 30 min at 0 °C and then added dropwise to a precooled (0 °C) solution of NaOAc (4.87 g, 59.4 mmol, 6.0 eq) and *N,N*-dimethylaniline (**V.11**) (1.20 g, 9.90 mmol, 1.0 eq) in methanol (30 mL). After 3 h, the reaction was allowed to warm up to room temperature, stirred for 1 h at room temperature and then diluted with EtOAc (20 mL) and the bulk of the methanol was removed under reduced pressure. NaHCO<sub>3</sub> (40 mL) was added, the phases separated, and the aqueous phase was extracted with EtOAc (2 x 40 mL). The organic layers were combined and washed with sat. NaHCO<sub>3</sub> (2 x 30 mL) and sat. NaCl (30 mL), dried over Na<sub>2</sub>SO<sub>4</sub>, and concentrated under reduced pressure. The crude product was purified by silica gel flash column chromatography (30% → 70% EtOAc/hexanes) to yield 4-((4-(dimethylamino)phenyl)diazenyl)phenyl)methanol (**V.16**) (1.96 g, 7.67 mmol, 78%) as orange solid.

**<sup>1</sup>H NMR** (400 MHz, CDCl<sub>3</sub>) δ = 7.90 (d, *J* = 8.4 Hz, 2H), 7.85 (d, *J* = 8.2 Hz, 2H), 7.47 (d, *J* = 8.2 Hz, 2H), 6.78 (d, *J* = 8.8 Hz, 2H), 4.76 (s, 2H), 3.10 (s, 6H).

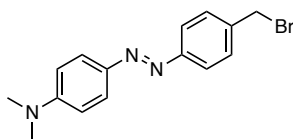
**<sup>13</sup>C NMR** (100 MHz, CDCl<sub>3</sub>) δ = 152.6, 143.7, 142.2, 127.6, 125.4, 122.5, 111.9, 65.2, 40.6.

**Note:** the carbon signal at 143.7 was extracted from HMBC data, another quaternary carbon is not visible.

**HRMS** (ESI): calcd for C<sub>15</sub>H<sub>17</sub>N<sub>3</sub>O [M+H]<sup>+</sup>: 256.1451. Found 256.1446.

**IR** (neat, cm<sup>-1</sup>): 3352, 2895, 2360, 1608, 1557, 1522, 1442, 1424, 1396, 1374, 1315, 1250, 1231, 1198, 1157, 1142, 1104, 1070, 1051, 1007, 990, 969, 945, 846, 825, 798, 727, 705.

**R<sub>f</sub>** = 0.25 (30% EtOAc/hexanes)

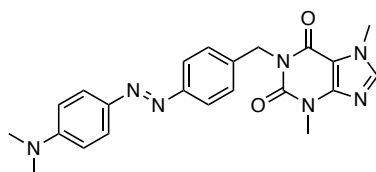
**4-((4-(bromomethyl)phenyl)diazenyl)-N,N-dimethylaniline phenyldiazene (V.18)**

4-((4-(dimethylamino)phenyl)diazenyl)phenyl)methanol (**V.16**) (1.68 g, 6.58 mmol, 1.0 eq) and  $\text{CBr}_4$  (2.62 g, 7.90 mmol, 1.2 eq) were dissolved in DCM (70 mL) at room temperature and  $\text{PPh}_3$  (2.59 g, 7.9 mmol, 1.5 eq) was added. The reaction was stirred for 1.5 h.  $\text{NaHCO}_3$  (20 mL) was added, the phases were separated, and the aqueous phase was extracted with DCM (2 x 20 mL). The combined organic layers were washed with  $\text{NaHCO}_3$  (20 mL) and sat.  $\text{NaCl}$  (20 mL), dried over  $\text{Na}_2\text{SO}_4$ , and concentrated under reduced pressure. The crude product was purified by silica gel flash column chromatography (2% EtOAc/hexanes) to yield 4-((4-(bromomethyl)phenyl)diazenyl)-N,N-dimethylaniline phenyldiazene (**V.18**) (79 mg) as red solid with remaining impurities, which was used without further purification.

**HRMS** (ESI): calcd for  $\text{C}_{15}\text{H}_{16}\text{BrN}_3$   $[\text{M}+\text{H}]^+$ : 318.0607, found 318.0606.

**R<sub>f</sub>** = 0.47 (20% EtOAc/hexanes)

**1-(4-((4-(dimethylamino)phenyl)diazenyl)benzyl)-3,7-dimethyl-3,7-dihydro-1H-purine-2,6-dione (AzoCaffeine-5)**



Azobenzene bromide **V.18** (40.3 mg, 0.127 mmol, 1.0 eq), theobromine (22.8 mg, 0.127 mmol, 1.0 eq),  $K_2CO_3$  (22.8 mg, 0.165 mmol, 1.3 eq) and KI (2.1 mg, 12.7  $\mu$ mol, 0.1 eq) were dissolved in DMF (8 mL) and the reaction was heated to 110 °C for 2 h. Sat.  $NaHCO_3$  (10 mL) was added and the aqueous phase was extracted with EtOAc (3 x 15 mL). The combined organic layers were washed with 10% NaCl (3 x 15 mL) and sat. NaCl (1 x 15 mL), dried over  $Na_2SO_4$ , and concentrated under reduced pressure. The crude product was purified by silica gel (deactivated with  $NH_3$ ) flash column chromatography (100% EtOAc) to yield AzoCaffeine-5 (20.8 mg, 49.8  $\mu$ mol, 16% over two steps) as orange solid.

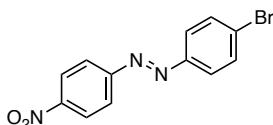
**$^1H$  NMR** (400 MHz,  $CDCl_3$ ):  $\delta$  = 7.85 (d,  $J$  = 8.8 Hz, 2H), 7.77 (d,  $J$  = 8.3 Hz, 2H), 7.58 (d,  $J$  = 8.4 Hz, 2H), 7.50 (s, 1H), 6.75 (d,  $J$  = 9.0 Hz, 2H), 5.24 (s, 2H), 3.99 (s, 3H), 3.58 (s, 3H), 3.08 (s, 6H).

**$^{13}C$  NMR** (100 MHz,  $CDCl_3$ ):  $\delta$  = 155.4, 152.7, 152.5, 151.7, 149.0, 143.8, 141.7, 138.6, 129.7, 125.1, 122.4, 111.6, 107.8, 44.4, 40.5, 33.8, 30.0.

**HRMS** (ESI): calcd for  $C_{22}H_{23}N_7O_2$   $[M+H]^+$ : 418.1991. Found 418.1996.

**IR** (neat,  $cm^{-1}$ ): 2926, 2854, 2361, 2340, 1704, 1660, 1601, 1549, 1518, 1488, 1448, 1428, 1403, 1365, 1314, 1288, 1234, 1156, 1140, 946, 824, 762, 744.

**$R_f$**  = 0.24 (95% EtOAc/hexanes)

**(E)-1-(4-bromophenyl)-2-(4-nitrophenyl)diazene (V.21)**

4-Bromoaniline (**V.20**) (500 mg, 2.91 mmol, 1.0 eq) was dissolved in DCM (75 mL) and 4-nitronitrosobenzene (**V.19**) (442 mg, 2.91 mmol, 1.0 eq) was added. Acetic acid (75 mL) was added and the reaction was stirred overnight at room temperature. The orange precipitate was filtered, washed with DCM (10 mL) and cold water (200 mL), and dried *in vacuo* to yield **V.21** (779 mg, 2.54 mmol, 87%) as an orange solid.

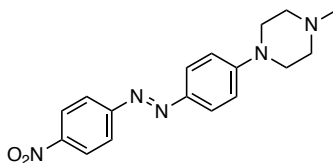
**<sup>1</sup>H NMR** (600 MHz, CDCl<sub>3</sub>): δ = 8.39 (d, *J* = 9.0 Hz, 2H), 8.03 (d, *J* = 9.0 Hz, 2H), 7.85 (d, *J* = 8.7 Hz, 2H), 7.70 (d, *J* = 8.7 Hz, 2H).

**<sup>13</sup>C NMR** (150 MHz, CDCl<sub>3</sub>): δ = 155.6, 151.2, 149.0, 132.8, 127.3, 125.0, 124.9, 123.7.

**HRMS** (ESI): calcd. [M]<sup>+</sup>: 304.9805. Found: 304.9805.

**IR** (neat, cm<sup>-1</sup>): 3108, 1606, 1581, 1572, 1519, 1475, 1454, 1408, 1395, 1341, 1325, 1281, 1218, 1142, 1107, 1062, 1007, 963, 920, 856, 833, 819, 811, 753.

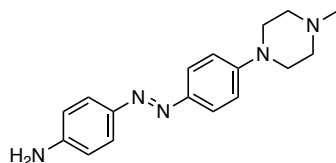
**R<sub>f</sub>** = 0.15 (1% MeOH/DCM)

**(E)-1-methyl-4-(4-((4-nitrophenyl)diazenyl)phenyl)piperazine (V22)**

This reaction was performed under argon and <sup>t</sup>BuOH was degassed beforehand. Azobenzene **V21** (500 mg, 1.63 mmol, 1.0 eq), *N*-methylpiperazine (164 mg, 1.63 mmol, 1.0 eq) and RuPhos Pd 3G (27.3 mg, 32.7 μmol, 2 mol%) were dissolved in <sup>t</sup>BuOH (15 mL) and Cs<sub>2</sub>CO<sub>3</sub> (585 mg, 1.80 mmol, 1.1 eq.) was added. The reaction was heated to 70 °C overnight. Upon cooling to room temperature, the reaction was diluted with DCM (50 mL) and the organic layer was washed with 5 M NaOH (1 x 20 mL), sat. NaHCO<sub>3</sub> (2 x 20 mL) and sat. NaCl (1 x 20 mL). The organic layer was dried over Na<sub>2</sub>SO<sub>4</sub> and the solvent was removed *in vacuo*. The crude material was passed over a large plug of silica (elution with 5% MeOH/DCM) and the material (242 mg) was used without further purification.

**<sup>1</sup>H NMR** (400 MHz, CDCl<sub>3</sub>): δ = 8.34 (d, *J* = 8.9 Hz, 2H), 8.01 - 7.87 (m, 4H), 6.97 (d, *J* = 9.1 Hz, 2H), 3.50 - 3.38 (m, 4H), 2.64 - 2.54 (m, 4H), 2.37 (s, 3H).

**HRMS** (ESI): calcd C<sub>17</sub>H<sub>20</sub>N<sub>5</sub>O<sub>2</sub><sup>+</sup> [M+H]<sup>+</sup>: 326.1612. Found: 326.1603.

**(E)-4-((4-(4-methylpiperazin-1-yl)phenyl)diazenyl)aniline (V.23)**

Azobenzene **V.22** (184 mg, 0.566 mmol, 1.0 eq) was dissolved in dioxane/EtOH/water (2:1.5:1, 30 mL total). Iron powder (158 mg, 2.83 mmol, 5.0 eq) was added followed by sat.  $\text{NH}_4\text{Cl}$  (121 mg, 2.26 mmol, 4.0 eq). The reaction was heated to 90 °C for 1.5 h. Upon cooling to room temperature, the reaction mixture was filtered over celite, the plug washed with EtOAc. The filtrate was washed with 5 M NaOH (1 x 30 mL) and sat.  $\text{NaHCO}_3$  (3 x 30 mL). The organic layer was dried over  $\text{Na}_2\text{SO}_4$  and the solvent was removed *in vacuo*. The crude material was purified by silica gel flash column chromatography (1% → 5% MeOH/EtOAc; +0.1% TEA) to yield **V.23** (90.0 mg, 0.305 mmol, 25% over two steps) as orange solid.

**$^1\text{H NMR}$**  (400 MHz,  $\text{CDCl}_3$ ):  $\delta$  = 7.80 (d,  $J$  = 8.9 Hz, 2H), 7.75 (d,  $J$  = 8.6 Hz, 2H), 6.97 (d,  $J$  = 9.0 Hz, 2H), 6.73 (d,  $J$  = 8.6 Hz, 2H), 3.96 (s, 2H), 3.39 – 3.32 (m, 4H), 2.62 – 2.56 (m, 4H), 2.37 (s, 3H).

**$^{13}\text{C NMR}$**  (100 MHz,  $\text{CDCl}_3$ ):  $\delta$  = 152.5, 148.7, 146.0, 145.9, 124.6, 124.0, 55.1, 48.3, 46.3.

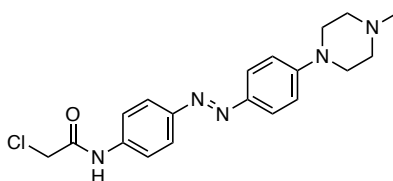
**HRMS** (DEI): calcd for  $\text{C}_{17}\text{H}_{20}\text{N}_5^+$   $[\text{M}]^+$ : 295.1713. Found: 295.1790

**IR** (neat,  $\text{cm}^{-1}$ ): 3340, 3218, 2964, 2829, 1636, 1594, 1506, 1449, 1396, 1378, 1343, 1318, 1299, 1287, 1258, 1236, 1157, 1140, 1051, 1004, 948, 917, 852, 827, 794, 731.

**$R_f$**  = 0.29 (10% MeOH/DCM;  $\text{NH}_3$  deactivated)

**$R_t$**  = 1.45 min (10 → 100% MeCN/ $\text{H}_2\text{O}$ , 10 min)

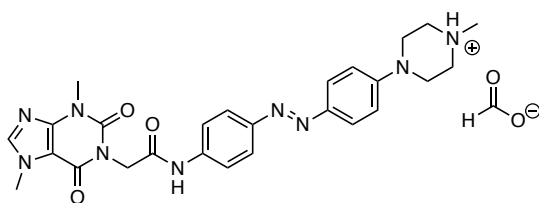


**(E)-2-chloro-N-(4-((4-(4-methylpiperazin-1-yl)phenyl)diazenyl)phenyl)acetamide (V.33)**

Aminoazobenzene **V.23** (40.0 mg, 0.135 mmol, 1.0 mg) was dissolved in THF (5 mL) and cooled to 0 °C. DIPEA (35.1  $\mu$ L, 0.203 mmol, 1.5 eq) was added and chloroacetyl chloride (11.8  $\mu$ L, 0.149 mmol, 1.1 eq) was dissolved in THF (2 mL) and then added dropwise to the solution. The reaction was stirred at 0 °C for 1 h, followed by 3 h at room temperature. Sat. NaHCO<sub>3</sub> (15 mL) was added to the reaction and the mixture was extracted with EtOAc (3 x 10 mL). The combined organic layers were washed with sat. NaCl (1 x 15 mL), dried over Na<sub>2</sub>SO<sub>4</sub> and the solvent was removed *in vacuo*. The crude product (30.4 mg) was used without further purification.

**R<sub>t</sub>** = 5.2 min (5 → 100% MeCN/H<sub>2</sub>O; 10 min)

**(E)-4-(4-((4-(2-(3,7-dimethyl-2,6-dioxo-2,3,6,7-tetrahydro-1H-purin-1-yl)-acetamido)phenyl)diazenyl)phenyl)-1-methylpiperazin-1-ium formate (AzoCaffeine-6 formate)**



Azobenzene **V.33** (20.0 mg, 53.8  $\mu\text{mol}$ , 1.0 eq), theobromine (11.6 mg, 64.5  $\mu\text{mol}$ , 1.2 eq),  $\text{K}_2\text{CO}_3$  (8.92 mg, 64.5  $\mu\text{mol}$ , 1.2 eq) and KI (0.893 mg, 5.38  $\mu\text{mol}$ , 0.1 eq) were dissolved in DMF (2 mL) and heated to 60  $^\circ\text{C}$  for 2 h. Upon cooling to room temperature, the reaction was diluted with EtOAc (10 mL) and the organic phase was washed with 10% NaCl (10 mL) and sat. NaCl (10 mL). The solvent was removed *in vacuo* and the crude material was purified by HPLC (10%  $\rightarrow$  27.5% MeCN/ $\text{H}_2\text{O}$  with + 0.1% FA over 8 min; 100% MeCN/ $\text{H}_2\text{O}$  with + 0.1% FA over 2 min) to yield AzoCaffeine-6 formate (10.1 mg, 18.0  $\mu\text{mol}$ , 20% over two steps) as orange solid.

**$^1\text{H NMR}$**  (600 MHz,  $\text{DMSO-}d_6$ )  $\delta$  10.55 (s, 1H), 8.42 (s, 1H), 8.09 (s, 1H), 7.82 - 7.71 (m, 6H), 7.07 (d,  $J = 9.2$  Hz, 2H), 6.83 (s, 1H), 4.72 (s, 2H), 3.90 (s, 3H), 3.45 (s, 3H), 2.48 - 2.43 (m, 4H), 2.23 (s, 3H).

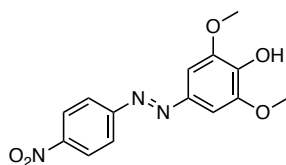
**$^{13}\text{C NMR}$**  (150 MHz,  $\text{DMSO-}d_6$ )  $\delta$  187.7, 161.9, 154.6, 149.0, 148.5, 144.5, 143.8, 141.0, 124.6, 123.4, 119.8, 114.6, 110.8, 107.1, 54.8, 47.3, 46.2, 44.0, 33.7, 29.9.

**Note:** the second set of 4H from the piperazine overlaps with the water signal. The signal can be extracted from COSY data at 3.34 ppm.

Due to the poor solubility, not all signals are visible in the  $^{13}\text{C}$  spectrum.

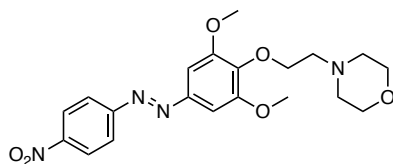
**HRMS** (ESI): calcd for  $\text{C}_{26}\text{H}_{30}\text{N}_9\text{O}_3^+$   $[\text{M}+\text{H}]^+$ : 516.2466. Found: 516.2470.

**$R_t$**  = 2.39 min (5  $\rightarrow$  100% MeCN/ $\text{H}_2\text{O}$ ; 5 min).

**(E)-2,6-dimethoxy-4-((4-nitrophenyl)diazenyl)phenol (V.25)**

4-nitroaniline (**V.24**) (500 mg, 3.62 mmol, 1.0 eq) was dissolved in methanol (150 mL) and 1 M HCl (10.9 mL, 10.9 mmol, 3.0 eq) and the mixture was cooled to 0 °C. NaNO<sub>2</sub> (275 mg, 3.98 mmol, 1.1 eq) was added and the reaction was stirred for 30 min, upon which the diazonium salt precipitates. The suspension was slowly added to a precooled (0 °C) solution of 2,6-dimethoxyphenol (558 mg, 3.62 mmol, 1.0 eq) in methanol and 1 M NaOH (21.7 mL, 21.7 mmol, 6.0 eq) and the reaction was stirred for 12 h, during which time it was allowed to warm up to room temperature. The reaction was neutralized through addition of 1 M HCl. EtOAc (100 mL) was added and most of the methanol was removed by rotary evaporation. The aqueous phase was extracted with EtOAc (3 x 150 mL), and the combined organic layers were washed with 1 M HCl (3 x 100 mL) and sat. NaCl (1 x 100 mL). The solvent was removed *in vacuo* and the crude product **V.25** (597 mg) was used without further purification for the next step.

**R<sub>t</sub>** = 7.17 min (10 → 100 % MeCN/H<sub>2</sub>O +0.1% FA, 10 min)

**(E)-4-(2-(2,6-dimethoxy-4-((4-nitrophenyl)diazenyl)phenoxy)ethyl)morpholine (V.27)**

In a pressure tube, phenol **V.25** (500 mg, 1.65 mmol, 1.0 eq), 4-(2-chloroethyl)morpholin-4-ium chloride (**V.26**) (614 mg, 3.30 mmol, 2.0 eq.),  $K_2CO_3$  (798 mg, 5.77 mmol, 3.5 eq), and KI (27.4 mg, 165  $\mu$ mol, 0.1 eq) were dissolved in DMF (30 mL). The reaction was heated to 110 °C for 5 h. After cooling to room temperature down, the reaction mixture was diluted with EtOAc (300 mL), washed with 10% NaCl (3 x 100 mL), 1 M NaOH (3 x 100 mL) and sat. NaCl (1 x 100 mL). The solvent was removed *in vacuo* and the crude material was purified by silica gel flash column chromatography (0%  $\rightarrow$  1% MeOH/EtOAc) to yield **V.27** (523 mg, 1.26 mmol, 42% over two steps) as orange solid.

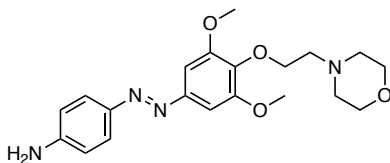
**$^1H$  NMR** (400 MHz,  $CDCl_3$ ):  $\delta$  = 8.38 (d,  $J$  = 8.9 Hz, 2H), 8.01 (d,  $J$  = 8.9 Hz, 2H), 7.29 (s, 2H), 4.22 (t,  $J$  = 5.6 Hz, 2H), 3.95 (s, 6H), 3.80 - 3.73 (m, 4H), 2.83 (t,  $J$  = 5.5 Hz, 2H), 2.63 (br s, 4H).

**$^{13}C$  NMR** (100 MHz,  $CDCl_3$ ):  $\delta$  = 155.8, 153.9, 148.7, 148.5, 141.1, 124.9, 123.4, 101.1, 70.4, 67.0, 58.6, 56.3, 54.0.

**HRMS** (ESI): calcd for  $C_{20}H_{25}N_4O_6^+$   $[M+H]^+$ : 417.1769. Found: 417.1769.

**IR** (neat,  $cm^{-1}$ ): 2953, 2854, 2360, 2340, 1595, 1523, 1493, 1468, 1451, 1416, 1342, 1309, 1221, 1119, 1036, 1007, 952, 927, 861, 756, 726.

**$R_f$**  = 0.2 (100% EtOAc)

**(E)-4-((3,5-dimethoxy-4-(2-morpholinoethoxy)phenyl)diazenyl)aniline (V.28)**

Nitroazobenzene **V.27** (480 mg, 1.15 mmol, 1.0 eq) and Na<sub>2</sub>S (270 mg, 3.46 mmol, 3.0 eq) were dissolved in dioxane/water (12:1, 35 mL) and heated to 90 °C for 3 h. After cooling to room temperature, the reaction mixture was diluted with EtOAc (200 mL) and washed with 1 M NaOH (4 x 100 mL), sat. NaCl (1 x 100 mL), dried over Na<sub>2</sub>SO<sub>4</sub> and the solvent was evaporated under reduced pressure. The crude material was purified by silica gel column chromatography (0% → 2% MeOH/DCM) to yield aniline **V.28** (395 mg, 1.02 mmol, 89%) as orange solid.

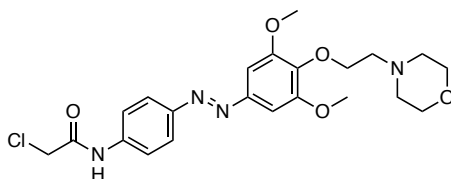
**<sup>1</sup>H NMR** (400 MHz, CDCl<sub>3</sub>): δ = 7.78 (d, *J* = 8.6 Hz, 2H), 7.16 (s, 2H), 6.74 (d, *J* = 8.6 Hz, 2H), 4.16 (t, *J* = 5.7 Hz, 2H), 4.05 (s, 2H), 3.93 (s, 6H), 3.79 - 3.73 (m, 4H), 2.80 (t, *J* = 5.8 Hz, 2H), 2.61 (s, 4H).

**<sup>13</sup>C NMR** (100 MHz, CDCl<sub>3</sub>): δ = 153.8, 149.6, 149.1, 145.5, 138.7, 125.1, 114.8, 99.8, 70.4, 67.1, 58.6, 56.2, 54.1.

**HRMS** (ESI): calcd for C<sub>20</sub>H<sub>27</sub>N<sub>4</sub>O<sub>4</sub><sup>+</sup> [M+H]<sup>+</sup>: 387.2017. found: 387.2024.

**IR** (neat, cm<sup>-1</sup>): 3453, 3351, 3224, 2957, 2855, 2362, 1626, 1598, 1506, 1495, 1465, 1425, 1402, 1327, 1268, 1215, 1116, 1069, 1035, 999, 949, 916, 844, 734.

**R<sub>f</sub>** = 0.4 (10% MeOH/DCM + 1% TEA)

**(E)-2-chloro-N-(4-((3,5-dimethoxy-4-(2-morpholinoethoxy)phenyl)diazenyl)-phenyl)acetamide (V.29)**

**V.28** (250 mg, 0.647 mmol, 1.0 eq) was dissolved in THF (20 mL) and cooled to 0 °C. DIPEA (280  $\mu$ L, 1.62 mmol, 2.5 eq) was added and chloroacetyl chloride (56.6  $\mu$ L, 0.712 mmol, 1.1 eq) was added dropwise. The reaction was stirred at 0 °C and allowed to warm to room temperature overnight. NaHCO<sub>3</sub> (80 mL) was added to the reaction, and the mixture was extracted with EtOAc (3 x 80 mL). The combined organic layers were washed with NaHCO<sub>3</sub> (3 x 100 mL), dried over Na<sub>2</sub>SO<sub>4</sub> and the solvent was removed *in vacuo*. The crude material was purified by silica gel flash column chromatography (1% → 3% MeOH/DCM) to yield **V.29** (283 mg, 0.611 mmol, 95%) as orange solid.

**<sup>1</sup>H NMR** (400 MHz, CDCl<sub>3</sub>):  $\delta$  = 8.41 (s, 1H), 7.93 (d, *J* = 8.7 Hz, 2H), 7.73 (d, *J* = 8.7 Hz, 2H), 7.23 (s, 2H), 4.23 (s, 2H), 4.18 (t, *J* = 5.7 Hz, 2H), 3.94 (s, 6H), 3.80 - 3.72 (m, 4H), 2.81 (t, *J* = 5.7 Hz, 2H), 2.61 (s, 4H).

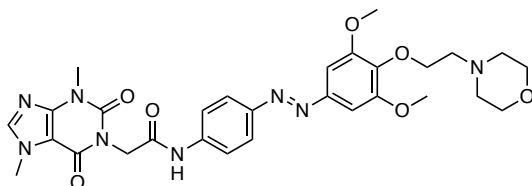
**<sup>13</sup>C NMR** (100 MHz, CDCl<sub>3</sub>):  $\delta$  = 164.0, 153.8, 149.6, 148.7, 139.7, 139.1, 124.0, 120.2, 100.4, 70.4, 67.1, 58.6, 56.3, 54.0, 43.0.

**HRMS** (ESI): calcd. for C<sub>22</sub>H<sub>28</sub>ClN<sub>4</sub>O<sub>5</sub><sup>+</sup> [M+H]<sup>+</sup>: 463.1673. Found 463.1742.

**IR** (neat, cm<sup>-1</sup>): 3307, 2944, 2859, 2808, 2361, 1686, 1597, 1525, 1496, 1465, 1451, 1438, 1412, 1369, 1328, 1296, 1270, 1218, 1151, 1125, 1111, 1067, 1037, 1025, 1000, 967, 940, 919, 891, 845, 826, 801, 772.

**R<sub>f</sub>** = 0.3 (3% MeOH/DCM)

**(E)-N-(4-((3,5-dimethoxy-4-(2-morpholinoethoxy)phenyl)diazenyl)phenyl)-2-(3,7-dimethyl-2,6-dioxo-2,3,6,7-tetrahydro-1H-purin-1-yl)acetamide (AzoCaffeine-7)**



Azobenzene **V.29** (50 mg, 0.108 mmol, 1.0 eq), theobromine (23.4 mg, 0.130 mmol, 1.2 eq),  $K_2CO_3$  (17.9 mg, 0.130 mmol, 1.2 eq) and KI (1.79 mg, 10.8  $\mu$ mol, 0.1 eq) were dissolved in DMF (2.0 mL) and heated to 60 °C for 2 h. After cool-down, the reaction mixture was diluted with EtOAc (20 mL) and washed with sat. NaCl (2 x 10 mL). The organic layer was dried over  $Na_2SO_4$  and the solvent was removed under reduced pressure. The crude material was purified by reverse phase  $C_{18}$  silica gel flash column chromatography (0%  $\rightarrow$  30% MeCN/ $H_2O$ ; + 0.1% FA) to yield AzoCaffeine-7 (42.9 mg, 70.7  $\mu$ mol, 66%) as an orange solid.

**$^1H$  NMR** (400 MHz,  $DMSO-d_6$ ):  $\delta$  = 10.63 (s, 1H), 8.09 (s, 1H), 7.88 (d,  $J$  = 8.7 Hz, 2H), 7.78 (d,  $J$  = 8.7 Hz, 2H), 7.22 (s, 2H), 4.73 (s, 2H), 4.05 (t,  $J$  = 5.7 Hz, 2H), 3.90 (s, 3H), 3.87 (s, 6H), 3.58 – 3.52 (m, 4H), 3.45 (s, 3H), 2.64 (t,  $J$  = 5.7 Hz, 2H), 2.46 (br s, 4H).

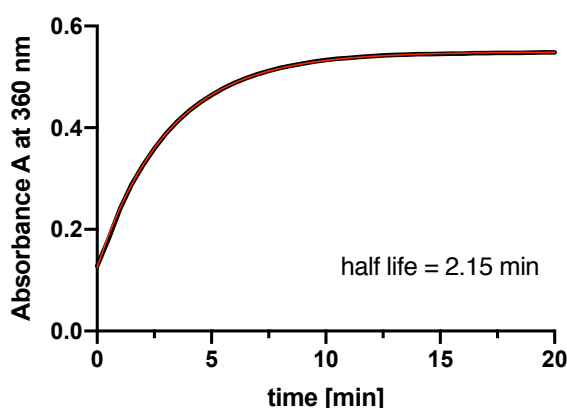
**$^{13}C$  NMR** (100 MHz,  $DMSO-d_6$ ):  $\delta$  = 166.3, 154.2, 153.4, 150.9, 148.6, 147.8, 147.5, 143.3, 141.6, 139.1, 123.6, 119.3, 106.6, 100.0, 70.3, 66.3, 57.8, 56.0, 53.6, 43.6, 33.3, 29.5.

**HRMS** (ESI): calcd for  $C_{29}H_{35}N_8O_7^+$   $[M+H]^+$  607.2623. Found: 607.2626.

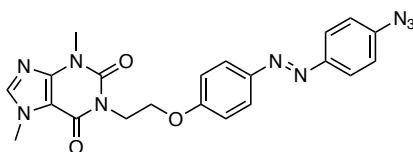
**IR** (neat,  $cm^{-1}$ ): 3542, 3280, 3116, 29554, 2855, 2360, 2340, 1702, 1650, 1597, 1545, 1494, 1466, 1414, 1368, 1328, 1302, 1245, 1219, 1192, 1150, 1127, 1070, 1036, 1003, 977, 951, 925, 852, 774, 743.

**R<sub>f</sub>** = 0.1 (10% MeOH/DCM)

**AzoCaffeine-7 in PBS**



Relaxation in the dark, 50  $\mu$ M in PBS, 25 C.

**(E)-1-(2-(4-((4-azidophenyl)diazenyl)phenoxy)ethyl)-3,7-dimethyl-3,7-dihydro-1H-purine-2,6-dione (V.32)**

Azobenzene **V.30** (100 mg, 0.418 mmol, 1.0 eq) was dissolved in DMF (2.0 mL),  $K_2CO_3$  (86.7 mg, 0.627 mmol, 1.5 eq), KI (6.94 mg, 41.8  $\mu$ mol, 0.1 eq) and brominated caffeine **V.31** (120 mg, 0.418 mmol, 1.0 eq) were added. The resulting suspension was heated to 65 °C for 3 h. After cool-down, the reaction was diluted with EtOAc (20 mL), washed with 10% NaCl (3 x 10 mL) and dried over  $Na_2SO_4$ . The solvent was removed *in vacuo* and the crude product was purified by silica gel flash column chromatography (70% → 100% EtOAc/hexanes) to yield **V.32** (83.0 mg, 0.186 mmol, 45%) as orange solid.

**$^1H$  NMR** (400 MHz,  $DMSO-d_6$ ):  $\delta$  = 8.04 (s, 1H), 7.88 (dd,  $J$  = 14.7, 8.8 Hz, 4H), 7.30 (d,  $J$  = 8.7 Hz, 2H), 7.14 (d,  $J$  = 8.9 Hz, 2H), 4.29 (t,  $J$  = 4.4 Hz, 4H), 3.89 (s, 3H), 3.43 (s, 3H).

**$^{13}C$  NMR** (100 MHz,  $DMSO-d_6$ ):  $\delta$  = 160.9, 154.4, 151.0, 149.1, 148.4, 146.2, 143.1, 141.8, 124.5, 124.1, 120.1, 115.1, 106.7, 64.7, 39.1, 33.3, 29.5.

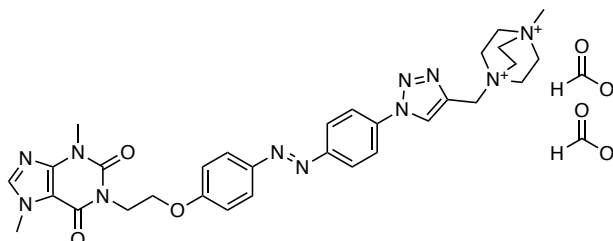
Note: The carbon signal at 39.1 was extracted from HSQC data.

**HRMS** (ESI): calcd for  $C_{21}H_{20}N_9O_3^+$  [ $M+H$ ] $^+$ : 446.1684. Found 446.1682.

**IR** (neat,  $cm^{-1}$ ): 2115, 1703, 1656, 1595, 1580, 1549, 1493, 1455, 1412, 1361, 1284, 1234, 1188, 1151, 1036, 842, 762, 735.



**(E)-1-((1-(4-((4-(2-(3,7-dimethyl-2,6-dioxo-2,3,6,7-tetrahydro-1H-purin-1-yl)ethoxy)phenyl)diazenyl)phenyl)-1H-1,2,3-triazol-4-yl)methyl)-4-methyl-1,4-diazabicyclo[2.2.2]octane-1,4-diium diformate (AzoCaffeine-8 diformate)**



The following reaction was performed under argon atmosphere. Azide **V.32** (50.0 mg, 0.112 mmol, 1.0 eq.) and alkyne **V.33** (147 mg, 0.393 mmol, 3.5 eq.) were dissolved in DMSO (10 mL) and the resulting solution was degassed. To this, a degassed solution of  $\text{CuSO}_4 \cdot 5\text{H}_2\text{O}$  (5.61 mg, 22.4  $\mu\text{mol}$ , 0.2 eq.) TBTA (11.9 mg, 22.4  $\mu\text{mol}$ , 0.2 eq) and sodium ascorbate (6.67 mg, 33.7  $\mu\text{mol}$ , 0.3 eq.) in water (5 mL) and acetonitrile (7.5 mL) was added. This mixture was sonicated at 40 °C for 4 h and more  $\text{CuSO}_4 \cdot 5\text{H}_2\text{O}$  (5.61 mg, 22.4  $\mu\text{mol}$ , 0.2 eq.) TBTA (11.9 mg, 22.4  $\mu\text{mol}$ , 0.2 eq) and sodium ascorbate (6.67 mg, 0.0337 mmol, 0.3 eq.) was added. Portion-wise addition and sonication was continued until full conversion was detected by LCMS. The reaction was diluted with water and the solvent was removed by lyophilization. The crude material was purified by reverse phase  $\text{C}_{18}$ -silica flash column chromatography (10% → 100% MeCN/ $\text{H}_2\text{O}$ ; + 0.1% FA), followed by HPLC (25% → 85% MeCN/ $\text{H}_2\text{O}$ ; + 0.1% FA) to yield AzoCaffeine-8 (29.0 mg, 41.3  $\mu\text{mol}$ , 37%) as orange solid.

**$^1\text{H NMR}$**  (400 MHz,  $\text{DMSO}-d_6$ ):  $\delta$  = 9.47 (s, 1H), 8.19 (s, 2H), 8.13 – 7.99 (m, 3H), 7.91 (d,  $J$  = 8.4 Hz, 2H), 7.17 (d,  $J$  = 8.5 Hz, 2H), 5.13 (s, 2H), 4.29 (s, 4H), 4.24 – 3.93 (m, 9H), 3.89 (s, 3H), 3.43 (s, 3H), 3.29 (s, 3H).

**$^{13}\text{C NMR}$**  (100 MHz,  $\text{DMSO}-d_6$ ):  $\delta$  = 161.4, 154.4, 151.6, 151.0, 148.4, 146.2, 143.2, 137.4, 135.3, 127.5, 124.9, 123.9, 121.1, 115.2, 106.7, 64.8, 57.2, 52.5, 51.4, 50.4, 33.3, 29.5.

**HRMS** (FAB): calcd for  $\text{C}_{31}\text{H}_{36}\text{N}_{11}\text{O}_3^+$   $[\text{M}-\text{H}]^+$ : 610.2997. Found: 610.3028.

**$R_t$**  = 2.42 min (5 → 10% MeCN/ $\text{H}_2\text{O}$  +0.1% FA, 5 min)



## VI. Optical Control of Myosin V



# **A Photoswitchable Inhibitor of Myosin V to Study the Interplay of Myosin V and Kinesin-2 in Skin Pigmentation**

## **Introduction**

The cytoskeleton is crucial for a cell's shape and function, as it provides structural support and organization within the cell. Motor proteins, which bind to elements of the cytoskeleton, are essential in moving cells and their organelles. They can be divided into three superfamilies, which distinguish themselves through the filament they are binding to. While members of the dynein and kinesin families bind to microtubules, myosin motors move along actin filaments. The myosin family is one of the largest and most diverse protein family in eukaryotes with many classes, based on phylogenetic analysis of the head domains.<sup>1-4</sup>

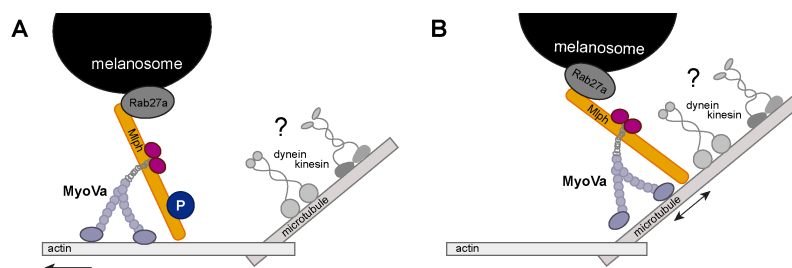
Myosins generally consist of three major domains, the head, neck and tail domain. While the head bears the actin-binding motor domain with ATPase activity, the class-specific tail can bind to various cargo, associated proteins and sometimes bears a coiled-coil motive for dimerization.<sup>2-4</sup> The neck (or lever arm) can bind calmodulin-like light chains and other associated proteins.<sup>4,5</sup> These diverse binding options make myosins essential for many cellular processes, such as cell division, cell motility and adhesion, endo- and exocytosis, and cellular signaling. They are also involved in muscle contraction, vision and hearing.<sup>2</sup>

The most studied class, myosin II is known as 'conventional' myosin. All other myosin classes are categorized as 'unconventional'.<sup>3,5</sup> Myosin V was initially discovered as calmodulin-binding protein, and is found in almost every eukaryotic genome sequenced to date.<sup>1,6</sup> Due to its unusually long neck domain, myosin V can be easily distinguished from other myosins.<sup>7</sup> With its two heads, its tasks include long-distance transport of cargo like lipids, mRNA, protein vesicles and organelles, like pigment granules. Gene mutations can result in diseases like Griscelli syndrome, which is characterized by pigmentary dilution of the skin, neurological disorders and, in some cases, immunodeficiency.<sup>6,8</sup>

In 2010, Kapoor and co-workers developed an inhibitor of myosin function, based on a 'privileged' scaffold known from kinase inhibitors, exploiting the structural similarity of the ATPase domain to GTPases.<sup>9</sup> The inhibition of movement is based on the inhibition the ATPase activity by specifically inhibiting ADP release from the actomyosin complex.

For our work, we chose MyoVIn-1, the most potent myosin V inhibitor from the series as a target to incorporate a photoswitch. In particular, we wanted to study the interaction between microtubule and actin-based transport of organelles, like the melanosome. Melanosomes are large granules, in which the skin pigment

melanin is synthesized and stored. They are responsible for skin pigmentation and therefore play a critical role in protection against UV irradiation and the occurrence of skin cancer.<sup>10</sup> Together with kinesin-2, myosin Va transports melanosomes from the center of the cell into the cytoplasm, which leads to a darkening of the skin color.<sup>11</sup>

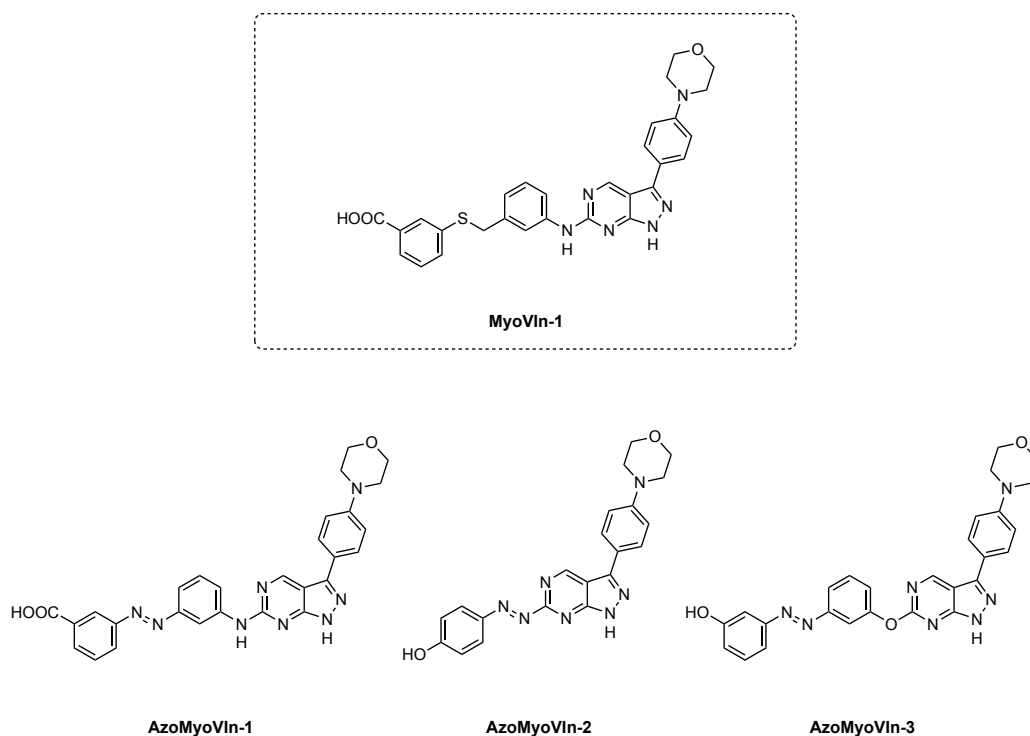


**Figure VI.1: The phosphorylation state of Mlph determines the track selection of myosin Va.** A: Phosphorylated Mlph walks along actin filaments. B: Dephosphorylation of Mlph through PKA leads to binding of myosin Va to microtubules. Figure adapted from Oberhofer et al. 2017.

Ökten and co-workers showed that the track selection of the Rab27a/melanophilin/myosin Va (Rab27a/Mlph/MyoVa) complex is determined by the phosphorylation state of the adaptor protein melanophilin (Mlph, Figure VI.1).<sup>12</sup> The discovered Mlph-microtubule interaction was mediated by the actin-binding domain of Mlph. While phosphorylated Mlph bound to actin, dephosphorylated Mlph preferentially bound to microtubules, even when actin was available. A similar mechanism has not yet been found for kinesin-2, suggesting that it might be a more passive player in the melanosome transport complex. Together with the Ökten lab, we wanted to investigate the interaction of kinesin-2 with myosin V. A photoswitchable myosin V inhibitor would enable us to study the kinesin-driven movement of melanosomes with and without the active participation of myosin V.

## Results and Discussion

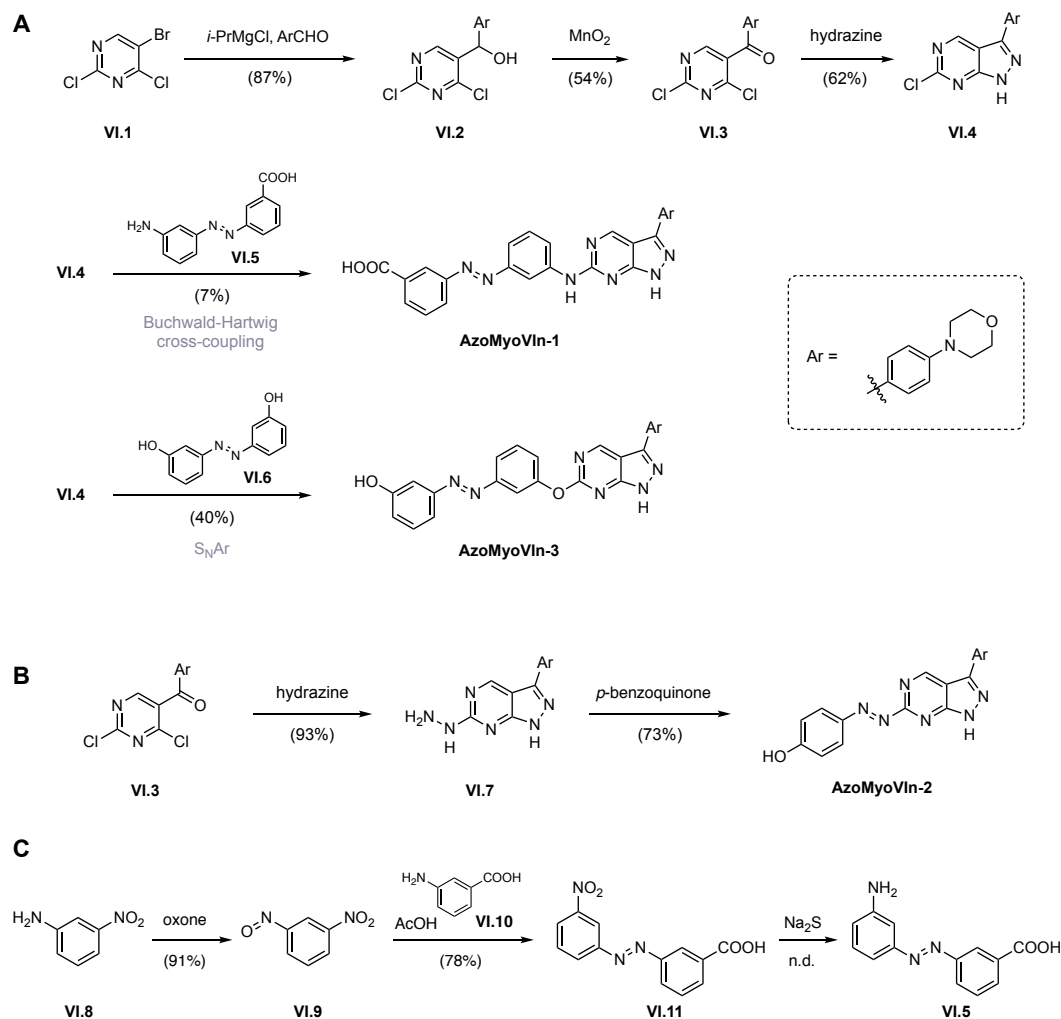
The most potent myosin V inhibitor reported by Kapoor and co-workers bears a benzyl-phenyl thioether, which can serve as an azologization motif (Figure VI.2).<sup>13,14</sup> The synthesis of AzoMyoVIn-1 was conducted similarly to the procedure reported.<sup>9</sup> The pyrazolopyrimidine core was synthesized in three steps and isolation was achieved by filtration. Careful addition of hydrazine monohydrate in the last step was crucial to prevent over-addition to hydrazine **VI.7** (Scheme VI.1). The synthesis of the azobenzene building block **VI.5** followed known procedures and was achieved through Baeyer-Mills reaction followed by reduction.<sup>15,16</sup>



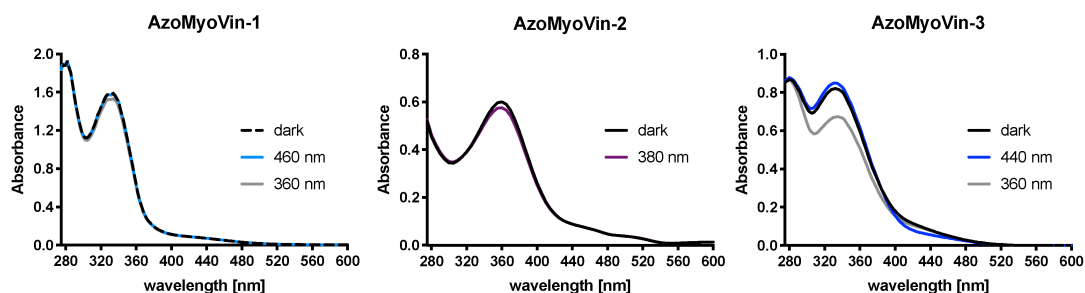
**Figure VI.2: MyoVIn-1 and photoswitchable analogues thereof.**

In contrast to the parent molecule MyoVIn-1, an  $S_NAr$  reaction in the last step proved to be unsuccessful with the azobenzene aniline **VI.5** (Scheme VI.1). The target molecule could instead be synthesized through a Buchwald-Hartwig cross-coupling, albeit in poor yield. The low yield might be due to remaining sulfides from the previous step (nitro to amine reduction), that could poison the catalyst.<sup>17</sup> Interestingly,  $S_NAr$  reaction between pyrazolopyrimidine **VI.4** and azobenzene phenol **VI.6** successfully yielded AzoMyoVIn-3. Additionally, AzoMyoVIn-2, a shorter version, was synthesized from hydrazine **VI.7** with *p*-benzoquinone.<sup>18</sup>

With three photoswitchable molecules at hand, we investigated their photophysical properties in DMSO (Figure VI.3). To our surprise, AzoMyoVIn-1 showed only little changes in the absorption spectrum upon irradiation. A similar behavior was observed for AzoMyoVIn-2, which showed a slightly red-shifted absorption spectrum and was subsequently best isomerized with 380 nm. With AzoMyoVIn-3, we observed the biggest changes upon illumination within this series of molecules and determined 360 nm as the best switching wavelength. While it was expected that the establishment of a good PSS would not be possible for AzoMyoVIn-2, we were surprised to see only little changes upon illumination with 360 nm light for AzoMyoVIn-1.



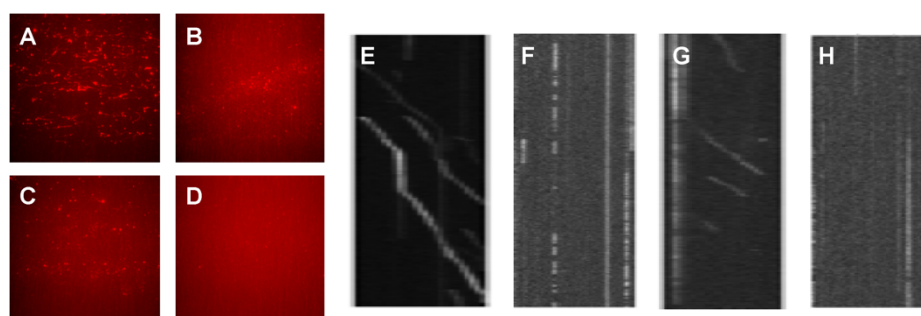
**Scheme VI.1: Synthesis of AzoMyoVin-1 to -3.** A: Synthesis of AzoMyoVin-1 and -3,<sup>9</sup> B: Excess of hydrazine forms the precursor for AzoMyoVin-2. C: Azobenzene synthesis following reported procedures.<sup>15,16</sup>



**Figure VI.3: UV Vis spectra of AzoMyoVin-1, -2 and -3.** Wavelengths between 480 nm and 320 nm were tested and the wavelengths, which gave the best PSSs are shown. Illumination: 3 min per wavelength. Spectra recorded in DMSO (50  $\mu$ m).



Due to the close similarity with the parent compound, we chose AzoMyoVIn-1 for our initial investigations in collaboration with the Ökten lab. Myosin Va and kinesin-2 were coupled through a DNA handle to study their interplay upon phosphorylation, dephosphorylation or the silencing of one of the individual components. The Rab27a/Mlph/MyoVa complex was labelled with AlexaFluor 488 or 647 on the SNAP-tagged MyoVa subunit for visualization. G-actin filaments were immobilized on a glass plate using biotinylated G-actin in the polymerization process. The Rab27/Mlph/MyoVa complex was mixed with vehicle, MyoVIn-1 or AzoMyoVIn-1 and incubated under the respective light conditions. Visualization with TIRF microscopy showed moving motors under control conditions (Figure VI.4A and E), and no movement using the inhibitor MyoVIn-1 (Figure VI.4B and F).



**Figure VI.4: Single molecule motility TIRF assays.** A-D: t-plane average stacks. A: Myosin Va motor movement is observed under control conditions, B: MyoVIn-1 inhibits motor movement. C: Reduced movement after application of AzoMyoVIn-1 under 460 nm light. D: no myosin Va movement after application of AzoMyoVIn-1 under 360 nm light. E-F: Kymographs for the data shown in A-D in the same order. MyoVIn-1 and AzoMyoVIn-1 were applied at 2  $\mu\text{M}$ . and 4  $\mu\text{M}$  respectively.

Application of AzoMyoVIn-1 under UV light fully inhibited movement of the myosin motors (Figure VI.4D and H). Incubation under blue light conditions, however, only partially inhibited motor movement (Figure VI.4C and G), leading to the conclusion that AzoMyoVIn-1 is a stronger inhibitor of MyoVa in its *cis* state, than in its *trans* state.

## Conclusion

Taken together, we have synthesized three photoswitchable versions of the known myosin V inhibitor MyoVIn-1. They can be operated with UV and blue light. Single molecule motility assays conducted in the Ökten lab indicate that AzoMyoVIn-1 is a *cis*-active inhibitor of myosin Va, which can be deactivated using blue light. Further evaluation of the ideal concentration to apply might result in more pronounced effects. Unfortunately, in these preliminary experiments, all kinesin-2

activity was suppressed. The reasons for this might be either unspecific coupling of myosin V to kinesin-2, or a dominant effect of myosin V over kinesin-2.

Currently, our collaborators at the Murrell lab are further evaluating AzoMyoVIn-1. Depending on their results the project will be discontinued or further pursued, possibly also including studies with AzoMyoVIn-2 and -3.

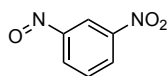
## References

- (1) Odrionitz, F.; Kollmar, M. Drawing the Tree of Eukaryotic Life Based on the Analysis of 2,269 Manually Annotated Myosins from 328 Species. *Genome Biol.* **2007**, *8*, R196.
- (2) Foth, B. J.; Goedecke, M. C.; Soldati, D. New Insights into Myosin Evolution and Classification. *Proc. Natl. Acad. Sci. U. S. A.* **2006**, *103*, 3681.
- (3) Hartman, M. A.; Spudich, J. A. The Myosin Superfamily at a Glance. *J. Cell Sci.* **2012**, *125*, 1627-1632.
- (4) Sweeney, H. L.; Houdusse, A. Structural and Functional Insights into the Myosin Motor Mechanism. *Annu. Rev. Biophys.* **2010**, *39*, 539-557.
- (5) Uyeda, T. Q.; Abramson, P. D.; Spudich, J. A. The Neck Region of the Myosin Motor Domain Acts as a Lever Arm to Generate Movement. *Proc. Natl. Acad. Sci.* **1996**, *93*, 4459-4464.
- (6) Reck-Peterson, S. L.; Provance, D. W.; Mooseker, M. S.; Mercer, J. A. Class V Myosins. *Biochim. Biophys. Acta BBA - Mol. Cell Res.* **2000**, *1496*, 36-51.
- (7) Vale, R. D. The Molecular Motor Toolbox for Intracellular Transport. *Cell* **2003**, *112*, 467-480.
- (8) Ménasché, G.; Ho, C. H.; Sanal, O.; Feldmann, J.; Tezcan, I.; Ersoy, F.; Houdusse, A.; Fischer, A.; Basile, G. de S. Griscelli Syndrome Restricted to Hypopigmentation Results from a Melanophilin Defect (GS3) or a MYO5A F-Exon Deletion (GS1). *J. Clin. Invest.* **2003**, *112*, 450-456.
- (9) Islam, K.; Chin, H. F.; Olivares, A. O.; Saunders, L. P.; De La Cruz, E. M.; Kapoor, T. M. A Myosin V Inhibitor Based on Privileged Chemical Scaffolds. *Angew. Chem. Int. Ed.* **2010**, *49*, 8484-8488.
- (10) Wasmeier, C.; Hume, A. N.; Bolasco, G.; Seabra, M. C. Melanosomes at a Glance. *J. Cell Sci.* **2008**, *121*, 3995-3999.
- (11) Aspengren, S.; Hedberg, D.; Sköld, H. N.; Wallin, M. Chapter 6 New Insights into Melanosome Transport in Vertebrate Pigment Cells. In *International Review of Cell and Molecular Biology*; Academic Press, 2008; Vol. 272, pp 245-302.
- (12) Oberhofer, A.; Spieler, P.; Rosenfeld, Y.; Stepp, W. L.; Cleetus, A.; Hume, A. N.; Mueller-Planitz, F.; Ökten, Z. Myosin Va's Adaptor Protein Melanophilin Enforces Track Selection on the Microtubule and Actin Networks in Vitro. *Proc. Natl. Acad. Sci.* **2017**, *114*, E4714-E4723.
- (13) Schoenberger, M.; Damijonaitis, A.; Zhang, Z.; Nagel, D.; Trauner, D. Development of a New Photochromic Ion Channel Blocker via Azologization of Fomocaine. *ACS Chem. Neurosci.* **2014**, *5*, 514-518.
- (14) Morstein, J.; Awale, M.; Reymond, J.-L.; Trauner, D. Mapping the Azolog Space Enables the Optical Control of New Biological Targets. *ACS Cent. Sci.* **2019**, *5*, 607-618.
- (15) Osorio-Planes, L.; Rodríguez-Eschrich, C.; Pericàs, M. A. Photoswitchable Thioureas for the External Manipulation of Catalytic Activity. *Org. Lett.* **2014**, *16*, 1704-1707.
- (16) Rück-Braun, K.; Kempa, S.; Priewisch, B.; Richter, A.; Seedorff, S.; Wallach, L. Azobenzene-Based  $\omega$ -Amino Acids and Related Building Blocks: Synthesis, Properties, and Application in Peptide Chemistry. *Synthesis* **2009**, *2009*, 4256-4267.
- (17) Hartwig, J. F. Evolution of a Fourth Generation Catalyst for the Amination and Thioetherification of Aryl Halides. *Acc. Chem. Res.* **2008**, *41*, 1534-1544.

- (18) Garcia-Amorós, J.; Díaz-Lobo, M.; Nonell, S.; Velasco, D. Fastest Thermal Isomerization of an Azobenzene for Nanosecond Photoswitching Applications under Physiological Conditions. *Angew. Chem. Int. Ed.* **2012**, *51*, 12820-12823.

## Experimental Procedures

### 3-nitronitrosobenzene (VI.9)



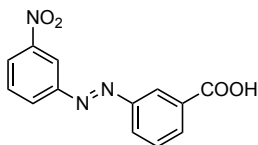
3-Nitroaniline (**VI.8**) (2.00 g, 14.5 mmol, 1.0 eq) was dissolved in DCM (50 mL). Oxone (17.9 g, 29.0 mmol, 2.0 eq) was dissolved in water (50 mL) and added to the DCM solution. The biphasic mixture was vigorously stirred, upon which the organic phase turned green. After 3 h, the phases were separated, the aqueous phase extracted with DCM (1 x 20 mL) and the combined organic phases were washed with sat. NaHCO<sub>3</sub> (3 x 40 mL), sat. NH<sub>4</sub>Cl (1 x 40 mL) and sat. NaCl (1 x 40 mL). The organic phase was dried over MgSO<sub>4</sub> and the solvent was removed *in vacuo*. The crude product was purified by silica gel column chromatography (20% DCM/hexanes) to yield **VI.9** (2.00 g, 13.1 mmol, 91%) as pale yellow solid.

**<sup>1</sup>H NMR** (400 MHz, CDCl<sub>3</sub>) δ = 8.58 (s, 2H), 8.34 (d, *J* = 7.6 Hz, 1H), 7.91 (t, *J* = 8.1 Hz, 1H).

**<sup>13</sup>C NMR** (100 MHz, CDCl<sub>3</sub>) δ = 163.4, 149.1, 131.0, 128.8, 126.7, 114.6.

**R<sub>f</sub>** = 0.23 (10%DCM/hexanes)

The analytical data matched those reported.<sup>15</sup>

**3-nitro-3'-carboxylic acid azobenzene (VI.11)**

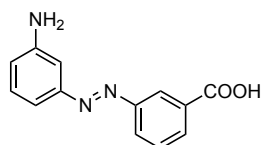
3-aminobenzoic acid (**VI.10**) (500 mg, 3.29 mmol, 1.0 eq) was dissolved in DCM (20 mL) and MeOH (1 mL) 3-nitronitrosobenzene (451 mg, 3.29 mmol, 1.0 eq) was added. Acetic acid (6.0 mL) was added and the reaction was stirred at room temperature overnight. The orange suspension was diluted with EtOAc and extracted with 1 M HCl (2 x 30 mL), sat. NH<sub>4</sub>Cl (1 x 30 mL), water (1 x 30 mL) and sat. NaCl (1 x 30 mL). The organic phase was dried over MgSO<sub>4</sub> and the solvent was removed *in vacuo*. The crude material was purified by silica gel column chromatography (0.1% AcOH + 50% → 75% EtOAc/hexanes) to yield **VI.11** (700 mg, 2.58 mmol, 78%) as orange solid.

**<sup>1</sup>H NMR** (400 MHz, DMSO-*d*<sub>6</sub>) δ = 13.41 (s, 1H), 8.56 (t, *J* = 2.0 Hz, 1H), 8.45 - 8.35 (m, 3H), 8.23 - 8.18 (m, 1H), 8.18 - 8.12 (m, 1H), 7.90 (t, *J* = 8.1 Hz, 1H), 7.76 (t, *J* = 7.8 Hz, 1H).

**<sup>13</sup>C NMR** (100 MHz, DMSO-*d*<sub>6</sub>) δ = 166.5, 152.0, 151.5, 148.7, 132.8, 132.3, 131.2, 130.1, 130.0, 127.9, 125.8, 122.6, 115.8.

**HRMS** (ESI): calcd. for C<sub>13</sub>H<sub>8</sub>N<sub>3</sub>O<sub>4</sub><sup>-</sup> [M-H]: 270.0520. Found: 270.0518

The analytical data matched the ones reported.<sup>16</sup>

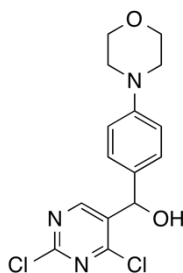
**3-amino-3'-carboxylic acid azobenzene (VI.5)**

**VI.11** was dissolved in dioxane/water (3:1, 60 mL) and  $\text{Na}_2\text{S}$  (432 mg, 5.53 mmol, 2.5 eq) was added. The solution was heated to 90 °C for 3h during which it turned dark red. After cooling down to room temperature, the solvent was removed *in vacuo* and the crude material was purified by reverse phase  $\text{C}_{18}$ -silica gel column chromatography (0.1% TFA + 10% → 50% MeCN/ $\text{H}_2\text{O}$ ) to yield **VI.5** (690 mg, calculated yield: 125% based on starting material **VI.11**) as a brown solid. The resulting product is likely containing sulfur impurities that were not removed during chromatography and not detected by NMR analysis and was used without further purification.

**$^1\text{H}$  NMR** (400 MHz,  $\text{DMSO-}d_6$ )  $\delta$  = 8.34 (s, 1H), 8.11 (d,  $J$  = 7.8 Hz, 2H), 7.73 (t,  $J$  = 7.8 Hz, 1H), 7.43 - 7.35 (m, 2H), 7.32 (s, 1H), 7.07 - 6.98 (m, 1H), 5.59 (s, 3H).

**$^{13}\text{C}$  NMR** (100 MHz,  $\text{DMSO-}d_6$ )  $\delta$  = 166.8, 152.8, 151.9, 145.4, 132.2, 131.8, 130.1, 130.0, 127.4, 122.2, 120.1, 115.9, 108.2.

**HRMS** (ESI): calcd. for  $\text{C}_{13}\text{H}_{12}\text{N}_3\text{O}_2^+$   $[\text{M}+\text{H}]^+$ : 242.0924. Found: 242.0923

**(2,4-dichloropyrimidin-5-yl)(4-morpholinophenyl)methanol (VI.2)**

5-Bromo-2,4-dichloropyrimidine (**VI.1**) (600 mg, 2.63 mmol, 1.0 eq) was dissolved in THF (1 mL) and *i*-propylmagnesium chloride (2 M in THF, 1.65 mL, 3.29 mmol, 1.25 eq) was added dropwise at  $-78\text{ }^{\circ}\text{C}$ . The reaction mixture was stirred for 50 min, while the temperature was allowed to rise to  $-40\text{ }^{\circ}\text{C}$ . A THF solution (1.3 mL) of 4-morpholinobenzaldehyde (504 mg, 2.63 mmol, 1.0 eq) was added dropwise at  $-40\text{ }^{\circ}\text{C}$  and the reaction was stirred at  $0\text{ }^{\circ}\text{C}$ . After 2.5 h it was quenched with sat.  $\text{NH}_4\text{Cl}$  (5 mL). The resulting mixture was extracted with EtOAc (3 x 3 mL) and the organic phase was washed with water (2 x 5 mL) and sat. NaCl (2 x 5 mL). After drying with  $\text{Na}_2\text{SO}_4$  the solvent was removed *in vacuo*. The crude material was purified by column chromatography (30%  $\rightarrow$  40% EtOAc/hexanes) to yield **VI.2** (777 mg, 2.63 mmol, 87%) as a colorless oil.

**$^1\text{H-NMR}$**  (400MHz,  $\text{CDCl}_3$ )  $\delta$  = 8.95 (s, 1H), 7.24 (d,  $J$  = 8.7 Hz, 2H), 6.88 (d,  $J$  = 8.7 Hz, 2H), 5.97 (d,  $J$  = 3.0 Hz, 1H), 3.88 - 3.82 (m, 4H), 3.19 - 3.14 (m, 4H), 2.30 (d,  $J$  = 2.8 Hz, 1H).

**$^{13}\text{C-NMR}$**  (100MHz,  $\text{CDCl}_3$ )  $\delta$  = 160.3, 159.2, 158.7, 151.7, 134.2, 130.9, 128.4, 115.7, 71.0, 66.9, 48.8.

**note:** the signals match those reported.<sup>9</sup>

**HRMS** (ESI): calcd. for  $\text{C}_{15}\text{H}_{16}\text{Cl}_2\text{N}_3\text{O}_2^+$   $[\text{M}+\text{H}]^+$ : 340.0614. Found: 340.0611.

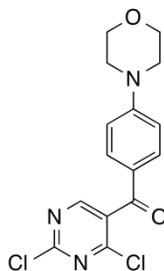
**IR:** (neat,  $\text{cm}^{-1}$ ): 3365, 3008, 2965, 2857, 1610, 1556, 1516, 1449, 1373, 1330, 1305, 1264, 1231, 1173, 1114, 1091, 1068, 1030, 962, 924, 869, 823, 785, 750, 685, 666.

**$R_f$**  = 0.25 (40% EtOAc/hexanes).



**MnO<sub>2</sub>**

Potassium permanganate (10.4 g, 65.8 mmol) was dissolved in water (65.0 mL) and heated to 80 °C. Two solutions, one of Manganese(II) sulfate monohydrate (9.14 g, 54.1 mmol) dissolved in dissolved in water (16.3 mL), and the other of aq. NaOH (40%, 12.7 mL), were simultaneously added dropwise to the heated permanganate solution at similar rate. The reaction mixture was stirred vigorously for 2 h, during which the temperature dropped to 50 °C. The warm reaction suspension was filtered through a hot glass frit, washed with warm water and dried at 120 °C for 48 h to yield MnO<sub>2</sub> as dark brown powder (9.02 g, 104 mmol, 96%).

**(2,4-dichloropyrimidin-5-yl)(4-morpholinophenyl)- methanone (VI.3)**

Alcohol **VI.2** (770 g, 2.26 mmol, 1.0 eq) was dissolved in DCM (45 mL) and divided in three portions. MnO<sub>2</sub> (635 g, 7.53 mmol, 3.3 eq) was added to each of the reaction vessels. The reaction mixtures were vigorously stirred at room temperature for 44 h and combined. The suspension was filtered over celite and washed with DCM. The yellow filtrate was concentrated *in vacuo* and purified by column chromatography (30% → 40% EtOAc/hexanes) and yielded **VI.3** (477 mg, 1.41 mmol, 62%) as a yellow solid.

**<sup>1</sup>H-NMR** (400MHz, CDCl<sub>3</sub>) δ = 8.57 (s, 1H), 7.70 (d, *J* = 9.0 Hz, 2H), 6.88 (d, *J* = 9.1 Hz, 2H), 3.91 - 3.82 (m, 4H), 3.44 - 3.36 (m, 4H).

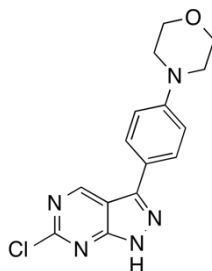
**<sup>13</sup>C-NMR** (100MHz, CDCl<sub>3</sub>) δ = 187.6, 161.0, 159.7, 159.1, 155.3, 132.6, 132.0, 125.4, 113.2, 66.5, 47.0.

**Note:** the signals match those reported in the literature.<sup>9</sup>

**HRMS** (ESI): calcd. for C<sub>15</sub>H<sub>14</sub>Cl<sub>2</sub>N<sub>3</sub>O<sub>2</sub><sup>+</sup> [M+H]<sup>+</sup>: 338.0458. Found: 338.0454.

**IR:** (neat, cm<sup>-1</sup>): 2975, 2856, 2016, 1645, 1593, 1551, 1515, 1456, 1433, 1374, 1352, 1332, 1273, 1240, 1228, 1192, 1173, 1118, 1107, 1090, 1068, 1049, 1026, 1001, 965, 924, 858, 830, 775, 759, 743, 693, 661.

**R<sub>f</sub>** = 0.36 (40% EtOAc/hexanes).

**4-(4-(6-chloro-1H-pyrazolo[3,4-d]pyrimidin-3-yl)phenyl) morpholine (VI.4)**

Ketone **VI.3** (150 mg, 0.44 mmol, 1.0 eq) was dissolved in THF (3.5 mL) and hydrazine monohydrate (42.2 mg, 0.84 mmol, 1.9 eq) was added dropwise over 15 min. The reaction mixture was stirred for 30 min at room temperature. The precipitated product was collected by filtration and washed with cold water. The resulting yellow solid was dried in a vacuum desiccator for 72 h to yield as a brown solid. **VI.4** (87.5 mg, 0.28 mmol, 62%).

**<sup>1</sup>H-NMR** (400MHz, DMSO-*d*<sub>6</sub>)  $\delta$  = 14.18 (s, 1H), 9.55 (s, 1H), 7.95 (d, *J* = 8.8 Hz, 2H), 7.08 (d, *J* = 8.8 Hz, 2H), 3.81 - 3.72 (m, 4H), 3.27 - 3.17 (m, 4H).

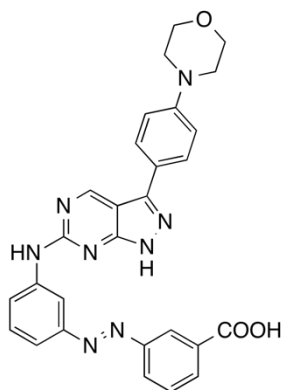
**<sup>13</sup>C-NMR** (100MHz, DMSO-*d*<sub>6</sub>)  $\delta$  = 156.7, 156.1, 155.3, 151.6, 144.6, 127.7, 121.9, 114.9, 110.6, 66.0, 47.7.

**Note:** the signals match those reported in the literature.<sup>9</sup>

**IR:** (neat,  $\text{cm}^{-1}$ ): 3322, 3204, 2961, 2850, 1594, 1573, 1555, 1484, 1443, 1431, 1375, 1319, 1291, 1271, 1239, 1185, 1120, 1070, 1053, 984, 955, 926, 899, 821, 803, 789, 766, 705, 677, 660.

**HRMS** (ESI): calcd. for  $\text{C}_{15}\text{H}_{13}\text{ClN}_5\text{O}$  [M-H]: 314.0814. Found: 314.0812.

**R<sub>t</sub>** = 3.40 min (0.1% FA, 10 → 90 % MeCN/H<sub>2</sub>O).

**AzoMyoVIn-1**

This reaction was performed under argon-atmosphere. *t*-Butanol (1 mL) was degassed three times by sonication under reduced pressure. BrettPhos (4.08 mg, 7.60  $\mu\text{mol}$ , 0.24 eq) and palladium(II)-acetate (0.853 mg, 3.80  $\mu\text{mol}$ , 0.12 eq) were added. The solution turned dark red within 10 min. After addition of **VI.4** (10.0 mg, 0.032 mmol, 1.0 eq), **VI.5** (7.64 mg, 31.7  $\mu\text{mol}$ , 1.0 eq) and  $\text{Cs}_2\text{CO}_3$  (33.0 mg, 101  $\mu\text{mol}$ , 3.2 eq.) the reaction mixture was degassed again and heated under microwave irradiation to 150  $^\circ\text{C}$  for 30 min. The resulting dark red suspension was concentrated under reduced pressure and the crude material was purified by column chromatography (1% MeOH, 0.06% AcOH, 0.06%  $\text{H}_2\text{O}/\text{DCM}$   $\rightarrow$  15% MeOH, 0.9% AcOH, 0.9%  $\text{H}_2\text{O}/\text{DCM}$ ). AzoMyoVIn-1 (1.33 mg, 2.22  $\mu\text{mol}$ , 7%) was obtained as orange solid.

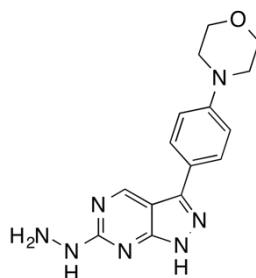
**$^1\text{H}$  NMR** (400 MHz,  $\text{DMSO}-d_6$ )  $\delta$  = 13.39 (s, 1H), 10.19 (s, 1H), 9.36 (s, 1H), 8.61 (s, 1H), 8.40 (s, 1H), 8.22 – 8.11 (m, 2H), 8.06 – 8.00 (m, 1H), 7.93 (d,  $J$  = 8.4 Hz, 2H), 7.76 (t,  $J$  = 7.8 Hz, 1H), 7.60 – 7.51 (m, 2H), 7.08 (d,  $J$  = 8.5 Hz, 2H), 3.81 – 3.74 (m, 4H), 3.24 – 3.17 (m, 4H).

**$^{13}\text{C}$  NMR** (200 MHz,  $\text{DMSO}-d_6$ )  $\delta$  = 167.1, 163.3, 157.8, 156.4, 154.1, 152.4, 151.9, 151.2, 144.0, 141.6, 131.8, 129.9, 129.4, 127.4, 123.1, 122.1, 121.9, 115.7, 115.0, 113.2, 106.1, 66.1, 47.9.

Note: for reasons of clarity, only *trans* signals are reported.

**HRMS** (ESI): calcd. for  $\text{C}_{28}\text{H}_{25}\text{N}_8\text{O}_3^-$   $[\text{M}+\text{H}]^+$ : 521.2044. Found: 521.2058. calcd. for  $\text{C}_{28}\text{H}_{23}\text{N}_8\text{O}_3^-$   $[\text{M}-\text{H}]^-$ : 519.1899. Found: 519.1905.

**R<sub>f</sub>** = 0.27 (2.5%  $\text{NH}_3$  (25% aq.)/7.5% MeOH/EtOAc).

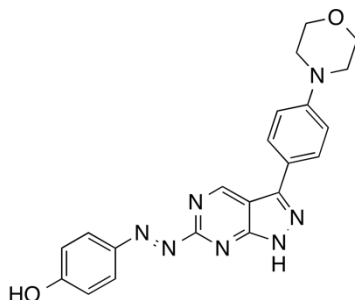
**4-(4-(6-hydrazinyl-1H-pyrazolo[3,4-d]pyrimidin-3-yl)-phenyl) morpholine**

Heteroaryl chloride **VI.3** (525 mg, 1.55 mmol, 1.0 eq) was dissolved in THF (15 mL) and hydrazine monohydrate (171 mg, 3.41 mmol, 2.2 eq) was added dropwise over 25 min. The reaction mixture was stirred for 75 min at 50 °C. The precipitate was collected by filtration and washed with cold water. The resulting light-yellow solid was dried in a desiccator for 24 h and the crude product **VI.7** (450 mg) was used without further purification.

**<sup>1</sup>H-NMR** (400 MHz, DMSO-*d*<sub>6</sub>)  $\delta$  = 9.98 (s, 1H), 8.87 (s, 1H), 8.12 (s, 1H), 7.45 (d, *J* = 8.4 Hz, 2H), 7.00 (d, *J* = 8.8 Hz, 2H), 4.71 (br s, 2H), 3.78 - 3.71 (m, 4H), 3.27 - 3.21 (m, 4H).

**R<sub>t</sub>** = 1.93 min (0.1 % FA, 10 → 90 % MeCN/H<sub>2</sub>O).

**HRMS** (ESI): calcd. for C<sub>15</sub>H<sub>18</sub>N<sub>7</sub>O<sup>+</sup> [M+H]<sup>+</sup>: 312.1567. Found: 312.1579.

**AzoMyoVIn-2**

1,4-Benzoquinone (52.1 mg, 0.48 mmol, 1.0 eq) was dissolved in water (5.4 mL) with perchloric acid (60%, 0.33 mL) and a suspension of **VI.7** (150 mg, 0.48 mmol, 1.0 eq) in water (6 mL) was added drop wise. The reaction solution turned dark red immediately and a precipitate formed. After 1 h the pH was set to 5 with ammonia (25% aq.) and  $\text{NH}_4\text{Cl}$ . The suspension was extracted with EtOAc (3 x 200 mL) and the combined organic phases purified by column chromatography (dry load; 2.5 %  $\text{NH}_3$  (25% aq.)/7.5% MeOH/EtOAc  $\rightarrow$  7.5%  $\text{NH}_3$  (25% aq.)/22.5% MeOH/EtOAc). AzoMyoVIn-2 (142 mg, 0.354 mmol, 68% yield over two steps) was obtained as light red solid.

**$^1\text{H-NMR}$**  (400 MHz,  $\text{DMSO-}d_6$ )  $\delta$  = 14.21 (s, 1H), 10.75 (s, 1H), 9.73 (s, 1H), 8.01 (d,  $J$  = 8.6 Hz, 2H), 7.94 (d,  $J$  = 8.7 Hz, 2H), 7.11 (d,  $J$  = 8.7 Hz, 2H), 7.02 (d,  $J$  = 8.7 Hz, 2H), 3.81 - 3.74 (m, 4H), 3.25 - 3.19 (m, 4H).

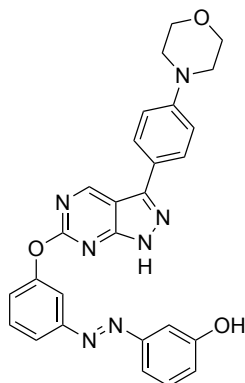
**$^{13}\text{C-NMR}$**  (100 MHz,  $\text{DMSO-}d_6$ )  $\delta$  = 164.6, 163.1, 154.6, 151.9, 145.9, 144.7, 128.1, 126.5, 116.7, 115.4, 66.5, 48.2.

**note:** Two quaternary carbons are not visible in the  $^{13}\text{C}$ -spectrum.

**IR:** (neat,  $\text{cm}^{-1}$ ): 3176, 2953, 2851, 1657, 1608, 1586, 1556, 1529, 1507, 1471, 1447, 1379, 1358, 1287, 1262, 1230, 1188, 1135, 1102, 1048, 985, 920, 843, 822, 801, 788, 740, 691.

**HRMS** (ESI): calcd. for  $\text{C}_{21}\text{H}_{20}\text{N}_7\text{O}_2^+$   $[\text{M}+\text{H}]^+$ : 402.1673. Found: 402.1674. calcd. for  $\text{C}_{21}\text{H}_{18}\text{N}_7\text{O}_2$   $[\text{M}-\text{H}]^-$ : 400.1527. Found: 400.1524.

**$R_f$**  = 0.27 (2.5 %  $\text{NH}_3$  (25% aq)/7.5 % MeOH/EtOAc).

**AzoMyoVIn-3**

Pyrazolopyrimidine **VI.3** (6.00 mg, 19.0  $\mu\text{mol}$ , 1.0 eq), diol<sup>a</sup> **VI.6** (20.4 mg, 95.0  $\mu\text{mol}$ ),  $\text{K}_2\text{CO}_3$  (2.89 mg, 10.9  $\mu\text{mol}$ , 1.1 eq) and KI (0.315 mg, 1.90  $\mu\text{mol}$ , 0.1 eq) were dissolved in DMF (0.2 mL) and heated to 110 °C for 7 h. Upon cooling, the reaction mixture was diluted with EtOAc (5 mL) and washed with 10% NaCl (2 x 2 mL). The organic solvent was removed *in vacuo* and the crude material was purified by preparative TLC (60% EtOAc/hexanes), followed by HPLC (0.1% FA + 40  $\rightarrow$  80%  $\rightarrow$  100% MeCN/ $\text{H}_2\text{O}$ , 45 nm) to yield AzoMyoVIn-3 (2.50 mg, 5.07  $\mu\text{mol}$ , 40%) as orange solid.

**$^1\text{H}$  NMR** (400 MHz,  $\text{DMSO-}d_6$ )  $\delta$  = 9.50 (s, 1H), 7.94 (d,  $J$  = 8.7 Hz, 2H), 7.83 (d,  $J$  = 8.0 Hz, 1H), 7.75 - 7.71 (m, 1H), 7.69 (d,  $J$  = 8.0 Hz, 1H), 7.50 (dd,  $J$  = 8.0, 2.0 Hz, 1H), 7.42 - 7.38 (m, 2H), 7.27 (s, 1H), 7.07 (d,  $J$  = 8.8 Hz, 2H), 7.01 - 6.96 (m, 1H), 3.79 - 3.74 (m, 4H), 3.24 - 3.18 (m, 4H).

**$^{13}\text{C}$  NMR** (100 MHz,  $\text{DMSO-}d_6$ )  $\delta$  = 163.4, 158.8, 157.4, 156.1, 154.2, 153.6, 153.5, 151.9, 144.7, 131.1, 130.7, 125.3, 122.9, 121.1, 119.6, 116.0, 115.4, 115.2, 109.3, 107.8, 66.5, 48.3.

**HRMS** (ESI): calcd. for  $\text{C}_{27}\text{H}_{24}\text{N}_7\text{O}_3^+$   $[\text{M}+\text{H}]^+$ : 494.1935. Found: 494.1939. calcd. for  $\text{C}_{27}\text{H}_{22}\text{N}_7\text{O}_3^-$   $[\text{M}+\text{H}]^-$ : 492.1790. Found: 492.1791.

<sup>a</sup>Diol was provided by the teaching laboratory at LMU.





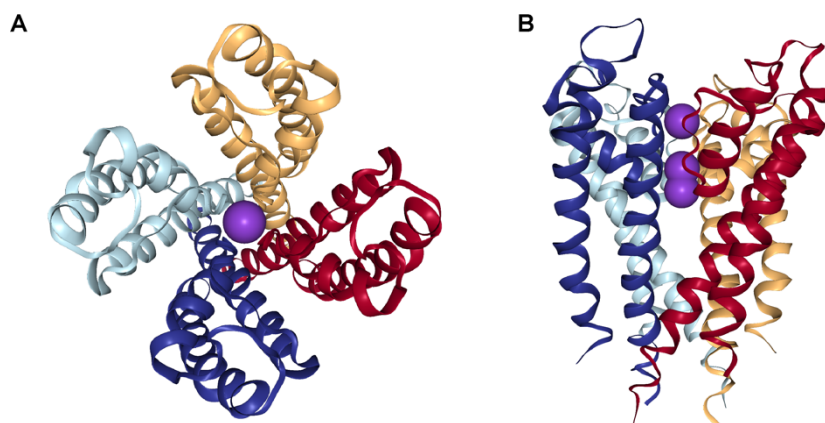
## VII. Open Channel Blockers for the Co-Crystallization with KcsA



## Arsenic-derivatives to Investigate the Interaction of Potassium Channels with *cis*-Azobenzenes

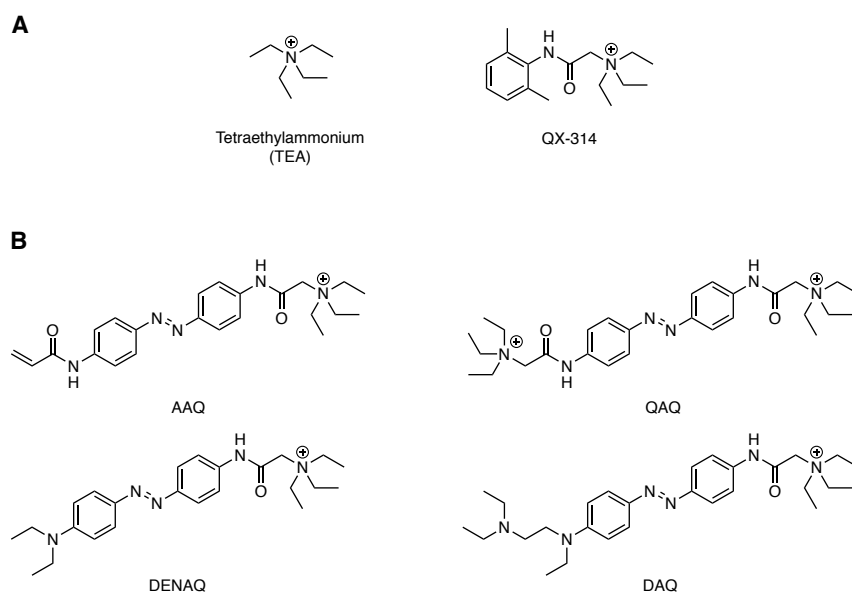
### Introduction

The voltage-gated potassium channel family is one of the largest transmembrane receptor families. In stark contrast to the mammalian voltage-gated sodium channel family with only 9 members ( $\text{Na}_v1.1$  –  $\text{Na}_v1.9$ ), there are 40 different human voltage-gated potassium channels in 12 subfamilies known to date.<sup>1,2</sup> Even though the channel subfamilies differ in gating mechanism and purpose (e.g. G protein-coupled inwardly-rectifying, voltage-gated, calcium-gated), the channel pore with selectivity filter is highly conserved. The homotetrameric channel is formed by four symmetrically arranged subunits (Figure VII.1). Each subunit comprises two membrane-spanning helices (inner and outer helix) and a third helix, which points towards the pore with its C-terminus.<sup>3</sup> In the conducting state, the channel occupied by two potassium ions in two different, distinct occupations. The negatively charged C-terminus of the above mentioned third helix and layers of carbonyl-oxygens and threonine-hydroxyl groups coordinate the potassium ions, similar to a hydration sphere.<sup>3</sup> This close binding of potassium, however, still enables high conductance rates, close to the diffusion limit, and is the structural reason for the astonishingly high selectivity of potassium over smaller mono-valent ions ( $\text{Na}^+$ ,  $\text{Li}^+$ ).<sup>3,4</sup>



**Figure VII.1 First X-Ray structure of the KcsA channel (Doyle et al. 1998).** A: top view, showing fourfold symmetry. B: side-view showing the set of two transmembrane helices and short helix pointing towards the pore (per subunit). Extracellular side on the top. Potassium ions shown as space-filling, purple spheres (pdb: 1BL8).

Blocking or modulating the gating-properties of potassium channels can be achieved through peptides, small molecules and ions.<sup>5</sup> While peptide toxins from sea anemones, cone snails, scorpions and snakes (for example charybdotoxin from the scorpion *Leiurus quinquestriatus var. hebraeus*) usually block the channel from the extracellular side through insertion of a lysine side chain into the channel pore, spider toxins bind to the voltage-sensor and shift the opening to more depolarized membrane potentials.<sup>6-8</sup> Small molecules (e.g. tetraethylammonium (TEA, Figure VII.2A), D-tubocurarine, 4-aminopyridine and verapamil) or metal ions (e.g. Ba<sup>2+</sup>, Cs<sup>+</sup>) can block the channel pore from the intracellular side.<sup>9</sup>



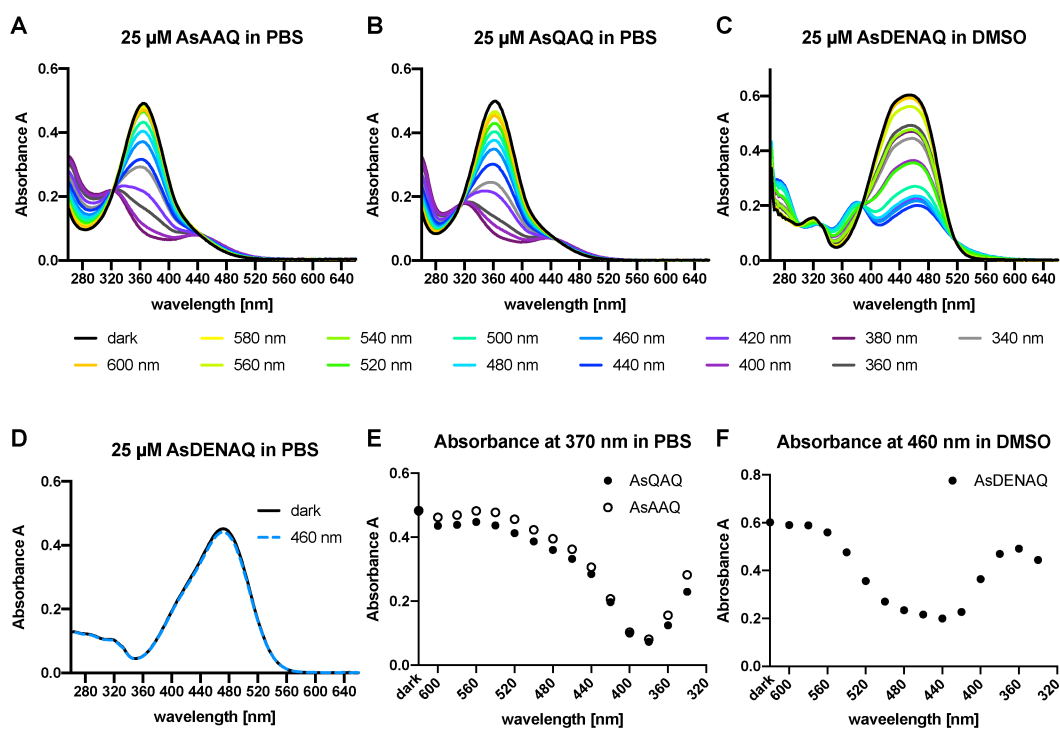
**Figure VII.2: Molecular structures of permanently charged ion channel blockers.** A: TEA can block potassium channels. QX-314 is a commercially available sodium channel blocker, which has served as design-template for photoswitchable open-channel blockers B: the photoswitchable ion channel blockers AAQ, QAQ, DENAQ and DAQ have found application in photopharmacology.

The TEA motif, which is also found in sodium channel blockers (e.g. QX-314, Figure VII.2A), has been used successfully to design photoswitchable open-channel blockers (Figure VII.2B).<sup>10</sup> Multiple generations of these open-channel blockers have been synthesized and have found application as research tools in vision restoration<sup>11</sup> or nociception.<sup>12</sup> Unlike their non-permanently charged congeners<sup>13</sup> they are not membrane permeable and rely on other channels, like P2X and TrpV1, for cell-uptake.<sup>12,14</sup> It has been established that azobenzene open-channel blockers block the pore from the intracellular side, and computational studies found explanations why the azobenzene photoswitch preferentially binds in its elongated *trans*-state.<sup>15</sup> However, it is not yet understood what happens upon isomerization to the *cis*-state and if the photoswitch fully diffuses out of the pore, if it remains in close proximity or if it even remains bound, but non-blocking.



Dianiline **VII.1** was reacted with chloroacetyl chloride (**VII.2**) to **VII.3**. Finkelstein reaction with NaI was followed by substitution reaction with triethylarsine to afford AsQAQ. Sequential reaction of **VII.1** with acryloyl chloride and **VII.2** yielded precursor **VII.6**, which was subjected to Finkelstein reaction and substitution reaction to yield AsAAQ. To synthesize AsDENAQ, aniline **VII.7** was reacted with chloroacetyl chloride (**VII.2**). Finkelstein reaction and substitution gave the target compound in good yield. In case of AsAAQ and AsDENAQ an aqueous work-up of the iodide instead of filtration was performed, which improved the yield of this sequence significantly.

Characterization of the switching properties of the arsenic analogues was conducted in PBS and DMSO (Figure VII.4). The best switching wavelengths for AsQAQ and AsAAQ in PBS were determined to be 380 nm. AsDENAQ did not show visible switching in PBS, but in DMSO and 440 nm was the optimal wavelength to enrich the *cis*-state.



**Figure VII.4: UV-Vis spectra of arsenic containing open-channel blockers.** A-C: wavelength scan to determine the best isomerization wavelengths for A: AsAAQ, B: AsQAQ and C: AsDENAQ. Scan was performed in 20 nm steps from higher to lower wavelengths with 5 min of illumination for each wavelength. D: photoisomerization of AsDENAQ could not be observed in PBS. E: Absorbance of AsQAQ and AsAAQ at 370 nm under different wavelengths of irradiation. F: Absorbance of AsDENAQ at 460 nm under different wavelengths of irradiation.

## **Conclusion**

We have synthesized three open channel blockers for the co-crystallization with potassium channels and determined their photophysical properties. The incorporated arsonium ion will serve as heavy atom to facilitate phasing. Crystallization attempts are currently undergoing in the lab of Prof Dr. Michael Kolbe in Hamburg.





## References

- (1) de Lera Ruiz, M.; Kraus, R. L. Voltage-Gated Sodium Channels: Structure, Function, Pharmacology, and Clinical Indications. *J. Med. Chem.* **2015**, *58*, 7093–7118.
- (2) Tian, C.; Zhu, R.; Zhu, L.; Qiu, T.; Cao, Z.; Kang, T. Potassium Channels: Structures, Diseases, and Modulators. *Chem. Biol. Drug Des.* **2014**, *83*, 1–26.
- (3) MacKinnon, R. Potassium Channels. *FEBS Lett.* **2003**, *555*, 62–65.
- (4) Hille, B. *Ionic Channels of Excitable Membranes*, 3rd ed.; Sinauer: Sunderland, 2001.
- (5) Wulff, H.; Castle, N. A.; Pardo, L. A. Voltage-Gated Potassium Channels as Therapeutic Targets. *Nat. Rev. Drug Discov.* **2009**, *8*, 982–1001.
- (6) MacKinnon, R.; Heginbotham, L.; Abramson, T. Mapping the Receptor Site for Charybdotoxin, a Pore-Blocking Potassium Channel Inhibitor. *Neuron* **1990**, *5*, 767–771.
- (7) Garcia, M. L.; Knaus, H. G.; Munujos, P.; Slaughter, R. S.; Kaczorowski, G. J. Charybdotoxin and Its Effects on Potassium Channels. *Am. J. Physiol.-Cell Physiol.* **1995**, *269*, C1–C10.
- (8) Huang, P.-T.; Shiau, Y.-S.; Lou, K.-L. The Interaction of Spider Gating Modifier Peptides with Voltage-Gated Potassium Channels. *Toxicon* **2007**, *49*, 285–292.
- (9) Kutluay, E.; Roux, B.; Heginbotham, L. Rapid Intracellular TEA Block of the KcsA Potassium Channel. *Biophys. J.* **2005**, *88*, 1018–1029.
- (10) Hüll, K.; Morstein, J.; Trauner, D. In Vivo Photopharmacology. *Chem. Rev.* **2018**, *118*, 10710–10747.
- (11) Tochitsky, I.; Kienzler, M. A.; Isacoff, E.; Kramer, R. H. Restoring Vision to the Blind with Chemical Photoswitches. *Chem. Rev.* **2018**, *118*, 10748–10773.
- (12) Mourot, A.; Fehrentz, T.; Le Feuvre, Y.; Smith, C. M.; Herold, C.; Dalkara, D.; Nagy, F.; Trauner, D.; Kramer, R. H. Rapid Optical Control of Nociception with an Ion-Channel Photoswitch. *Nat. Methods* **2012**, *9*, 396–402.
- (13) Laprell, L.; Tochitsky, I.; Kaur, K.; Manookin, M. B.; Stein, M.; Barber, D. M.; Schön, C.; Michalakis, S.; Biel, M.; Kramer, R. H.; et al. Photopharmacological Control of Bipolar Cells Restores Visual Function in Blind Mice. *J. Clin. Invest.* **2017**, *127*, 2598–2611.
- (14) Tochitsky, I.; Helft, Z.; Meseguer, V.; Fletcher, R. B.; Vessey, K. A.; Telias, M.; Denlinger, B.; Malis, J.; Fletcher, E. L.; Kramer, R. H. How Azobenzene Photoswitches Restore Visual Responses to the Blind Retina. *Neuron* **2016**, *92*, 100–113.
- (15) Morstein, J.; Awale, M.; Reymond, J.-L.; Trauner, D. Mapping the Azolog Space Enables the Optical Control of New Biological Targets. *ACS Cent. Sci.* **2019**, *5*, 607–618.
- (16) Doyle, D. A.; Cabral, J. M.; Pfuetzner, R. A.; Kuo, A.; Gulbis, J. M.; Cohen, S. L.; Chait, B. T.; MacKinnon, R. The Structure of the Potassium Channel: Molecular Basis of K<sup>+</sup> Conduction and Selectivity. *Science* **1998**, *280*, 69–77.
- (17) Schehr, M.; Ianes, C.; Weisner, J.; Heintze, L.; P. Müller, M.; Pichlo, C.; Charl, J.; Brunstein, E.; Ewert, J.; Lehr, M.; et al. 2-Azo-, 2-Diazocine-Thiazols and 2-Azo-Imidazoles as Photoswitchable Kinase Inhibitors: Limitations and Pitfalls of the Photoswitchable Inhibitor Approach. *Photochem. Photobiol. Sci.* **2019**, *18*, 1398–1407.
- (18) Weston, C. E.; Krämer, A.; Colin, F.; Yildiz, Ö.; Baud, M. G. J.; Meyer-Almes, F.-J.; Fuchter, M. J. Toward Photopharmacological Antimicrobial Chemotherapy Using Photoswitchable Amidohydrolase Inhibitors. *ACS Infect. Dis.* **2017**, *3*, 152–161.

- (19) Reiter, A.; Skerra, A.; Trauner, D.; Schiefner, A. A Photoswitchable Neurotransmitter Analogue Bound to Its Receptor. *Biochemistry* **2013**, *52*, 8972-8974.
- (20) Pangborn, A. B.; Giardello, M. A.; Grubbs, R. H.; Rosen, R. K.; Timmers, F. J. Safe and Convenient Procedure for Solvent Purification. *Organometallics* **1996**, *15*, 1518-1520.

## Methods

**General Experimental Techniques.** All reactions were conducted using flame dried glassware, under a positive pressure of nitrogen with magnetic stirring unless otherwise stated. Liquid reagents and solvents were added *via* syringe through rubber septa. Solids were added under inert gas counter flow or were dissolved in specified solvents prior to addition. Low temperature reactions were carried out in a Dewar vessel filled with the appropriate cooling agent e.g. H<sub>2</sub>O/ice (0 °C), acetone/dry ice (-78 °C). Reactions using temperatures above room temperature were conducted using a heated oil bath. Yields refer to spectroscopically pure compounds unless otherwise stated.

**Solvents and Reagents.** Anhydrous solvents were prepared with a solvent purification system by filtration of HPLC grade solvents through alumina according to the method of Grubbs<sup>20</sup> 1,2-dichloroethane (DCE), ethyl acetate (EtOAc) and dimethylsulfoxine (DMSO) were purchased from commercial suppliers (Acros Organics) and used as received. Solvents and additives for extraction and flash column chromatography were purchased in technical grade purity and distilled under reduced pressure prior to use. All other reagents and solvents were purchased from commercial suppliers and used as received, except stated otherwise.

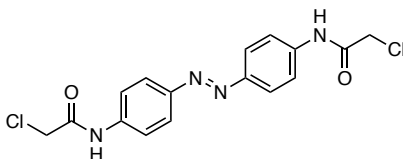
**Chromatography.** Reactions and chromatography fractions were monitored by qualitative thin-layer chromatography (TLC) on silica gel F<sub>254</sub> TLC plates from Merck KGaA. Analytes on the glass plates were visualized by irradiation with UV light and/or by immersion of the TLC plate in ninhydrin staining solution, followed by heating with a hot-air gun. Flash column chromatography was performed using silica gel, particle size 40–63 μM (eluents are given in parenthesis) Additives (FA and TEA) were added to all components of the eluent mixture and constantly kept at 0.1%, unless stated otherwise. Column chromatography was either performed manually or with an automated chromatography system (Teledyne Isco CombiFlash®). High-performance liquid chromatography (HPLC) was performed with HPLC grade solvents on an Agilent 1260 Infinity series system (Preparative Pump, Preparative Pump Gradient Extension, Preparative Autosampler, Infinity II Diode Array Detector WR, 1290 Infinity Valve Drive, Fraction Collector prep scale) equipped with a Phenomenex Gemini® LC Column (5 μm, C18, 110 Å, 150×30 mm, AXIA™ Packed) and Phenomenex Gemini® SecurityGuard™ Prep Cartridge (C18, 15×30mm ID).

**NMR Spectra.** NMR spectra were measured on a Bruker Avance III HD (400/100 MHz) spectrometer, both equipped with a CryoProbe™. The <sup>1</sup>H and <sup>13</sup>C NMR shifts are reported in ppm related to the chemical shift of tetramethylsilane. NMR shifts were calibrated to residual solvent resonances: CDCl<sub>3</sub> (7.26 ppm, 77.16 ppm), DMSO (2.50 ppm, 39.52 ppm) and MeOD (3.31 ppm, 49.00 ppm). <sup>1</sup>H NMR spectroscopic data are reported as follows: Chemical shift in ppm (multiplicity, coupling constants, integration). The multiplicities are abbreviated

with s (singlet), br s (broad singlet), d (doublet), t (triplet), q (quartet) and m (multiplet) and their respective combinations. Except for multiplets, the chemical shift of all signals is reported as the center of the resonance range. In addition to  $^1\text{H}$  and  $^{13}\text{C}$  NMR measurements, 2D NMR techniques as homonuclear correlation spectroscopy (COSY), heteronuclear single quantum coherence (HSQC) and heteronuclear multiple bond coherence (HMBC) were used to assist the compound identification process. Coupling constants  $J$  are reported in Hz. All raw fid files were processed, and the spectra analyzed using the program MestReNova 11.0 from Mestrelab Research S. L.

**Mass Spectra.** High-resolution mass spectra (HRMS) were recorded using an Agilent 6224 Accurate-Mass time-of-flight spectrometer with electrospray ionization (ESI) at the New York University Shared Instrumentation Facility (NYU-SIF).

**UV/Vis Spectra.** UV/Vis spectra were recorded on a Varian Cary 60 Scan UV/Vis spectrometer equipped with an 18-cell holder using Brandtech Scientific Inc. UV cuvettes (70-850  $\mu\text{L}$ , 10 mm light path. The stock solution was prepared at 50 mM in DMSO and diluted to 50  $\mu\text{M}$  in DMSO or PBS prior to the experiment. For the wavelength scan, photoswitching was achieved using an Optoscan Monochromator with an Optosource (75 mW lamp), which was controlled through a program written in Matlab. Irradiation to establish PSS took place from the top through a fiber-optic cable. Illumination was screened from 360-540 nm in 20 nm steps, going from higher to lower wavelengths, illuminating 5 to 10 min for each wavelength. Illumination conditions that afforded the highest *trans*-isomer and *cis*-isomer enrichment are shown. Spectra were processed using Microsoft Excel 16 and Prism 8 and the figures were generated in Adobe Illustrator 23.

**Experimental Procedures:****(E)-N,N'-(diazene-1,2-diylbis(4,1-phenylene))bis(2-chloroacetamide) (VII.3)**

**VII.1** (50.0 mg, 0.235 mmol, 1.0 eq.) was dissolved in THF (20 mL) and DIPEA (123  $\mu$ L, 707  $\mu$ mol, 3.0 eq.) was added. The solution was cooled to  $-78$   $^{\circ}$ C and chloroacetyl chloride (**VII.2**) (47.0  $\mu$ L, 0.589 mmol, 2.5 eq.) was added. The reaction mixture was stirred for 30 min and allowed to warm up to room temperature. The reaction was subsequently quenched with sat.  $\text{NaHCO}_3$  (10 mL) and extracted with EtOAc (3 x). The combined organic layers were washed with sat.  $\text{NaHCO}_3$  (3 x) and sat. NaCl and dried over  $\text{Na}_2\text{SO}_4$ . The solvent was evaporated under reduced pressure and the crude material **VII.3** (80.8 mg, 0.221 mmol, 94%) was used without further purification.

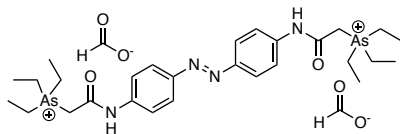
**$^1\text{H NMR}$**  (400 MHz,  $\text{DMSO-}d_6$ )  $\delta$  = 10.64 (s, 2H), 7.88 (d,  $J$  = 8.9 Hz, 4H), 7.81 (d,  $J$  = 8.9 Hz, 4H), 4.31 (s, 4H).

**$^{13}\text{C NMR}$**  (100 MHz,  $\text{DMSO-}d_6$ )  $\delta$  = 165.0, 148.0, 141.2, 123.5, 119.6, 43.6.

**HRMS:** (ESI) calcd. for  $\text{C}_{16}\text{H}_{15}\text{ClN}_4\text{O}_2^+$   $[\text{M}+\text{H}]^+$ : 365.0571, found: 365.0567.

**$R_f$**  = 0.4 (10% MeOH/DCM)

**$R_t$**  = 3.71 min (5  $\rightarrow$  100% MeCN/ $\text{H}_2\text{O}$  + 0.1% FA, 5 min)

**AsQAQ**

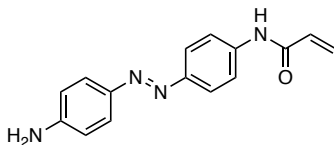
**VII.3** (20.0 mg, 55.0  $\mu\text{mol}$ , 1.0 eq.) was dissolved in acetone (2 mL) and NaI (49.3 mg, 0.329 mmol, 6.0 eq) was added. The reaction mixture was heated to 60 °C for 2 h. The solvent was removed under reduced pressure, the residual solid suspended in dichloromethane, filtered through a glass frit, and the filtrate was evaporated under reduced pressure. The resulting iodide was dissolved in THF and triethylarsine (231  $\mu\text{L}$ , 1.64 mmol, 30.0 eq.) was added. The reaction mixture was stirred at 90 °C in a pressure tube for 2 days. Upon cooling to room temperature, the solvent was evaporated, and the crude material was purified by preparative HPLC (5  $\rightarrow$  80% MeCN/H<sub>2</sub>O; + 0.1% FA; 12 min) to yield AsQAQ (8.3 mg, 0.012 mmol, 22%) as the formate salt as yellow solid.

**<sup>1</sup>H NMR** (400 MHz, DMSO-*d*<sub>6</sub>)  $\delta$  = 12.40 (s, 2H), 8.54 (s, 2H), 7.86 (s, 8H), 4.01 (s, 4H), 2.55 - 2.51 (m, 12H), 1.28 (t, *J* = 7.7 Hz, 18H). Note: The signal at 2.55 - 2.51 is overlapping with the solvent.

**<sup>13</sup>C NMR** (100 MHz, DMSO-*d*<sub>6</sub>)  $\delta$  = 165.6, 164.8, 148.0, 141.5, 123.4, 119.8, 28.2, 14.9, 7.1.

**HRMS:** (ESI) calcd. for C<sub>28</sub>H<sub>44</sub>As<sub>2</sub>N<sub>4</sub>O<sub>2</sub><sup>2+</sup> [M]<sup>2+</sup>: 309.0943, found: 309.0940

**R<sub>t</sub>** = 2.83 min (5  $\rightarrow$  100% MeCN/H<sub>2</sub>O + 0.1% FA, 5 min)

**(E)-N-(4-((4-aminophenyl)diazenyl)phenyl)acrylamide (VII.5)**

**VII.1** (100 mg, 0.471 mmol, 1.0 eq) was dissolved in THF (80 mL), DIPEA (98.0  $\mu$ L, 0.565 mmol, 1.2 eq) was added and the solution was cooled to  $-78$   $^{\circ}$ C. Acryloyl chloride (38.0 mL, 0.471 mmol, 1.0 eq) was added dropwise and the reaction was stirred for 30 min, before it was allowed to slowly warm up to room temperature. After 1h, the reaction was quenched with sat.  $\text{NaHCO}_3$  (30 mL). The mixture was extracted with EtOAc (2 x 50 mL), and the combined organic phases were washed with sat.  $\text{NaHCO}_3$  (50 mL) and sat.  $\text{NaCl}$  (50 mL) and dried over  $\text{Na}_2\text{SO}_4$ . The solvent was removed *in vacuo* and the crude material was purified by silica gel flash column chromatography (30  $\rightarrow$  80% EtOAc/hexanes) to yield **VII.5** (82.8 mg, 0.311 mmol, 66%) as light brown solid.

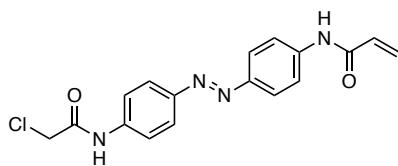
**$^1\text{H NMR}$**  (400 MHz,  $\text{DMSO-}d_6$ )  $\delta$  = 10.37 (s, 1H), 7.82 (d,  $J$  = 8.8 Hz, 2H), 7.74 (d,  $J$  = 8.8 Hz, 2H), 7.63 (d,  $J$  = 8.7 Hz, 2H), 6.66 (d,  $J$  = 8.7 Hz, 2H), 6.47 (dd,  $J$  = 16.9, 10.1 Hz, 1H), 6.29 (dd,  $J$  = 17.0, 1.7 Hz, 1H), 5.79 (dd,  $J$  = 10.1, 1.7 Hz, 1H).

**$^{13}\text{C NMR}$**  (100 MHz,  $\text{DMSO-}d_6$ )  $\delta$  = 163.2, 152.5, 148.3, 142.8, 140.2, 131.7, 127.3, 124.9, 122.5, 119.6, 113.4.

**HRMS:** (ESI) calcd. for  $\text{C}_{15}\text{H}_{15}\text{N}_4\text{O}^+$   $[\text{M}+\text{H}]^+$ : 267.1240, found: 267.1249

**$R_f$**  = 0.3 (50% EtOAc/hexanes)

**$R_t$**  = 3.19 min (5  $\rightarrow$  100% MeCN/ $\text{H}_2\text{O}$  + 0.1% FA, 5 min)

**(E)-N-(4-((4-(2-chloroacetamido)phenyl)diazenyl)phenyl)acrylamide (VII.6)**

**VII.5** (50.0 mg, 0.188 mmol, 1.0 eq) was dissolved in THF (32 mL), DIPEA (46.0  $\mu$ L, 0.264 mmol, 1.4 eq) was added and the reaction was cooled to  $-78$   $^{\circ}$ C. Chloroacetyl chloride (**VII.2**) (18.0  $\mu$ L, 0.225 mmol, 1.2 eq) was added and the reaction was stirred for 30 min before it was allowed to warm up to room temperature. After 1 h, the reaction was quenched with sat.  $\text{NaHCO}_3$  (20 mL) and the mixture was extracted with EtOAc (2 x 20 mL). The combined organic layers were washed with sat.  $\text{NaHCO}_3$  (20 mL) and sat.  $\text{NaCl}$  (20 mL), and dried over  $\text{Na}_2\text{SO}_4$ . The solvent was removed *in vacuo* and the crude material was purified by silica gel flash column chromatography (40% EtOAc/hexanes) to yield **VII.6** (59.2 mg, 0.173 mmol, 92%) as a brown solid.

**$^1\text{H NMR}$**  (400 MHz,  $\text{DMSO-}d_6$ )  $\delta$  = 10.65 (s, 1H), 10.50 (s, 1H), 7.94 - 7.78 (m, 8H), 6.49 (dd,  $J$  = 17.0, 10.1 Hz, 1H), 6.31 (dd,  $J$  = 17.0, 1.8 Hz, 1H), 5.82 (dd,  $J$  = 10.1, 1.8 Hz, 1H), 4.31 (s, 2H).

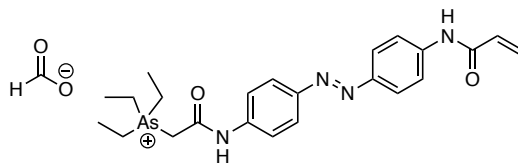
**$^{13}\text{C NMR}$**  (100 MHz,  $\text{DMSO-}d_6$ )  $\delta$  = 165.0, 163.4, 148.0, 147.8, 141.8, 141.1, 139.2, 131.6, 127.6, 124.9, 123.5, 119.6, 43.6.

**HRMS:** (ESI) calcd. for  $\text{C}_{17}\text{H}_{15}\text{ClN}_4\text{NaO}_2^+$  [ $\text{M}+\text{Na}$ ] $^+$ : 365.0776, found: 365.0788.

**$R_f$**  = 0.4 (10% MeOH/DCM)

**$R_t$**  = 3.64 min (5  $\rightarrow$  100% MeCN/ $\text{H}_2\text{O}$  + 0.1% FA, 5 min)



**AsAAQ**

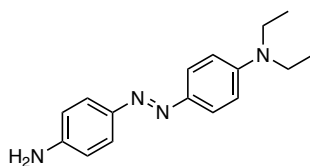
**VII.6** (25.0 mg, 73.0  $\mu\text{mol}$ , 1.0 eq) was dissolved in acetone (12 mL), NaI (32.8 mg, 0.219 mmol, 3.0 eq) was added and the reaction was heated to reflux for 1 h. The reaction mixture was diluted with EtOAc (30 mL), washed with sat. NaCl (20 mL) and dried over  $\text{Na}_2\text{SO}_4$ . The solvent was removed *in vacuo*. The resulting iodide was dissolved in THF (2.4 mL) and triethylarsine (308  $\mu\text{L}$ , 2.19 mmol, 30.0 eq) was added and the reaction was stirred at 80  $^\circ\text{C}$  in a pressure tube for 2 days. Upon cooling to room temperature, the solvent was evaporated, and the crude material was purified by reverse phase HPLC (5  $\rightarrow$  80% MeCN/ $\text{H}_2\text{O}$ ; +0.1% FA; 12 min) to yield AsAAQ formate (15.3 mg, 30.0  $\mu\text{mol}$ , 41%) as an orange solid.

**$^1\text{H NMR}$**  (400 MHz,  $\text{DMSO-}d_6$ )  $\delta$  = 12.13 (s, 1H), 10.66 (s, 1H), 8.54 (s, 1H), 7.89 (dd,  $J$  = 14.7, 7.8 Hz, 8H), 6.51 (dd,  $J$  = 17.0, 10.1 Hz, 1H), 6.35 – 6.27 (m, 1H), 5.81 (dd,  $J$  = 10.1, 1.7 Hz, 1H), 3.98 (s, 2H), 2.54 (d,  $J$  = 7.8 Hz, 3H), 1.28 (t,  $J$  = 7.8 Hz, 10H).

**$^{13}\text{C NMR}$**  (100 MHz,  $\text{DMSO-}d_6$ )  $\delta$  = 165.5, 164.7, 163.5, 148.1, 147.8, 141.9, 141.3, 131.7, 127.6, 123.5, 123.4, 119.6, 28.3, 14.9, 7.1.

**HRMS:** (ESI) calcd. for  $\text{C}_{23}\text{H}_{30}\text{AsN}_4\text{O}_2^+$   $[\text{M}]^+$ : 469.1579, found: 469.1584.

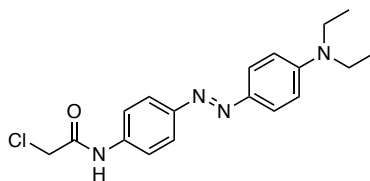
**$R_t$**  = 3.05 min (5  $\rightarrow$  100% MeCN/ $\text{H}_2\text{O}$  + 0.1% FA, 5 min)

**(E)-4-((4-aminophenyl)diazenyl)-N,N-diethylaniline (VII.7)**

**VII.7** was prepared according to Mourot, A.; Kienzler, M. A.; Banghart, M. R.; Fehrentz, T.; Huber, F. M. E.; Stein, M.; Kramer, R. H.; Trauner, D. Tuning Photochromic Ion Channel Blockers. *ACS Chemical Neuroscience* **2011**, 2, 536. Spectral data matched those reported.

**<sup>1</sup>H NMR** (400 MHz, CDCl<sub>3</sub>): δ = 7.79 (d, J = 9.1 Hz, 2H), 7.72 (d, J = 8.7 Hz, 2H), 6.72 (t, J = 8.6 Hz, 4H), 3.90 (s, 2H), 3.44 (q, J = 7.1 Hz, 4H), 1.22 (t, J = 7.1 Hz, 6H).

**<sup>13</sup>C NMR** (100 MHz, CDCl<sub>3</sub>): δ = 149.5, 148.1, 146.3, 143.4, 124.7, 124.1, 115.0, 111.2, 44.8, 12.8.

**(E)-2-chloro-N-(4-((4-(diethylamino)phenyl)diazenyl)phenyl)acetamide (VII.8)**

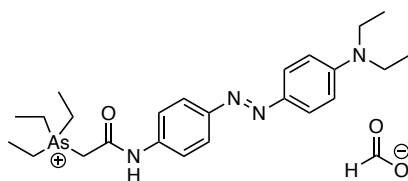
**VII.7** (100 mg, 0.373 mmol, 1.0 eq.) was dissolved in THF (80 mL), DIPEA (91.0  $\mu$ L, 0.522 mmol, 1.4 eq.) was added and the solution was cooled to  $-78$   $^{\circ}$ C. Chloroacetyl chloride (36  $\mu$ L, 0.448 mmol, 1.2 eq.) was added and the reaction was allowed to warm up to room temperature over 30 min. The reaction was quenched with sat.  $\text{NaHCO}_3$  (20 mL) and extracted with EtOAc (3 x). The combined organic layers were washed with sat.  $\text{NaHCO}_3$  and sat.  $\text{NaCl}$  and dried over  $\text{Na}_2\text{SO}_4$ . The solvent was removed *in vacuo* and the crude material was purified by silica gel column chromatography (40% EtOAc/hexanes) to yield **VII.8** (121 mg, 0.353 mmol, 94%) as an orange solid.

**$^1\text{H-NMR}$** : (400 MHz,  $\text{CDCl}_3$ )  $\delta$  = 8.33 (s, 1H), 7.85 (dd,  $J$  = 8.8, 4.5 Hz, 4H), 7.67 (d,  $J$  = 8.8 Hz, 2H), 6.72 (d,  $J$  = 8.6 Hz, 2H), 4.22 (s, 2H), 3.46 (q,  $J$  = 7.1 Hz, 4H), 1.23 (t,  $J$  = 7.2 Hz, 9H).  
 **$^{13}\text{C-NMR}$** : (100 MHz,  $\text{CDCl}_3$ )  $\delta$  = 163.8, 150.5, 150.3, 143.2, 137.51, 125.4, 123.2, 120.3, 111.12, 44.9, 43.1, 12.8.

**HRMS**: (ESI) calcd. for  $\text{C}_{18}\text{H}_{21}\text{ClN}_4\text{O}^+$   $[\text{M}+\text{H}]^+$ : 345.1477, found: 345.1590

**$R_f$**  = 0.6 (70% EtOAc/hexanes)

**$R_t$**  = 4.40 min (5  $\rightarrow$  100% MeCN/ $\text{H}_2\text{O}$  + 0.1% FA, 5 min)

**AsDENAQ**

**VII.8** (25.0 mg, 0.0720 mmol, 1.0 eq.) was dissolved in acetone (12 mL) and NaI (32.4 mg, 0.216 mmol, 3.0 eq.) was added. The reaction mixture was heated to 60 °C for 2 h. The solvent was removed under reduced pressure, the crude solid was dissolved in EtOAc (20 mL) and washed with and sat. NaCl (x 3). The organic layer was dried over Na<sub>2</sub>SO<sub>4</sub> and the crude material was used without further purification.

The resulting iodide (31.4 mg, 0.0720 mmol, 1.0 eq.) was dissolved in THF and triethylarsine (300 μL, 2.13 mmol, 29.6 eq.) was added. The reaction mixture was stirred at 90 °C in a pressure tube for 2 days. Upon cooling to room temperature, the solvent was evaporated, and the crude material was purified by reverse phase HPLC (5 → 80% MeCN/H<sub>2</sub>O; +0.1% FA; 12 min) to yield AsDENAQ (27.6 mg, 0.053 mmol, 74%) as the formate salt.

**<sup>1</sup>H NMR** (400 MHz, DMSO-*d*<sub>6</sub>) δ = 11.73 (s, 1H), 8.45 (s, 1H), 7.75 (q, *J* = 9.3 Hz, 6H), 6.77 (d, *J* = 9.1 Hz, 2H), 3.94 (s, 2H), 3.44 (q, *J* = 6.9 Hz, 4H), 2.55 - 2.49 (m, 6H), 1.27 (t, *J* = 7.7 Hz, 9H), 1.14 (t, *J* = 7.0 Hz, 6H). Note: the signal at 2.55 - 2.49 is partially overlapping with the solvent.

**<sup>13</sup>C NMR** (100 MHz, DMSO-*d*<sub>6</sub>) δ = 165.4, 164.4, 149.8, 148.6, 142.1, 139.6, 122.5, 119.8, 111.0, 44.0, 28.3, 14.9, 12.5, 7.1.

**HRMS:** (ESI) calcd. for C<sub>24</sub>H<sub>36</sub>AsN<sub>4</sub>NaO<sup>+</sup> [M]<sup>+</sup>: 471.2100, found: 471.2114

**R<sub>t</sub>** = 3.68 min (5 → 100% MeCN/H<sub>2</sub>O + 0.1% FA, 5 min)





## VIII. KCNQ Channel Modulators





# Photoswitchable and Non-Photoswitchable Retigabine Derivatives to Probe KCNQ Channel Function

## Introduction

Around 50 million people worldwide suffer from epilepsy and people with epilepsy bear a three times higher risk of premature death.<sup>1</sup> Epileptic seizures are caused by uncontrolled but rhythmic and synchronous firing of certain neurons in the central nervous system (CNS).<sup>2</sup> Most anti-epileptic drugs target voltage-gated sodium channels, T-type calcium channels, or GABA mediated neurotransmission. However, only two third of the patients respond to this kind of treatment, which emphasizes the need for novel approaches.<sup>3</sup>

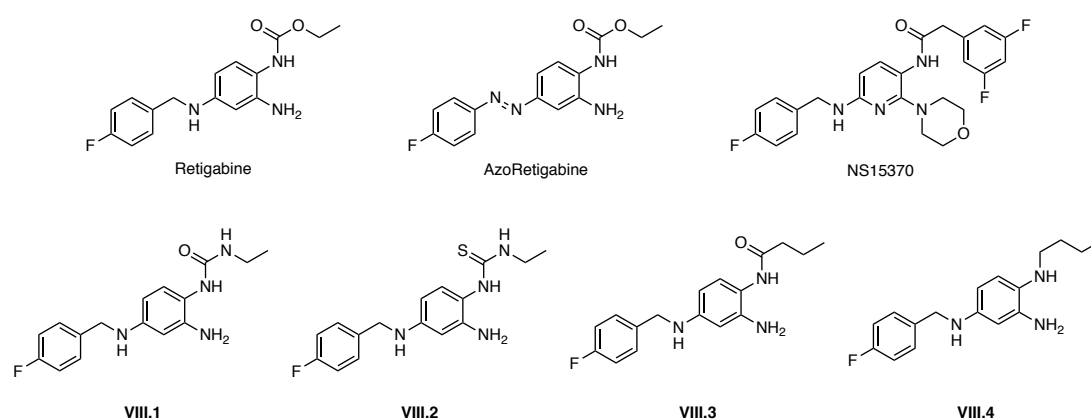
In 1980, when Brown and Adams detected a potassium current in frog neurons, which was evoked by the action of acetylcholine on muscarinic receptors (MRs), they called it the M-current.<sup>4</sup> Modulation of the M-current also modulates neuronal excitability. The slow activation and deactivation is crucial for its role as brake for neuronal firing.<sup>5</sup> In general, the regulation of the M-current can be achieved by many second messengers, like G proteins, lipids, and nucleotides. Dysregulation of the M-current has severe effects, as increased neuronal excitability leads to neuronal diseases like epilepsy. It is generally accepted that members of subfamily 7 voltage-gated potassium channels ( $K_V7$ ) form the so-called M-channel.<sup>6</sup> Some members of the  $K_V$  subfamily 7 ( $K_V7.1-7.5$ , also called KCNQ1-5) have therefore been recognized as potential targets.<sup>5</sup> KCNQ1 is mainly expressed in peripheral tissue and the heart muscle and has been identified as the channel whose mutation is responsible for the long QT-syndrome, a severe type of cardiac arrhythmia.<sup>7</sup> KCNQ2 and KCNQ3 are expressed in the brain, where they contribute to the M-current, KCNQ4 is linked to hearing defects and is found in auditory nerves of the inner ear and KCNQ5 is widely expressed in brain and muscle.<sup>5</sup> Hence, selectivity for neuronal over cardiac KCNQ channels is highly important for effective therapy.

KCNQ2 and 3 form a channel as a two-plus-two heteromer (the M-channel), but also combinations with other family members and homomeric channels have proven to be functional.<sup>5,6</sup> Block of the M-current can be achieved with tetraethylammonium (TEA), a standard potassium channel blocker.<sup>6</sup>

The resting potential of a neuron typically lies at -80 to -70 mV. Neuronal firing starts with membrane depolarization, which is usually achieved through opening of ligand-gated ion channels.<sup>8</sup> At -55 mV, voltage-gated sodium ( $Na_V$ ) channels open, and the membrane depolarizes further. At +30 to +40 mV members of the voltage-gated potassium ( $K_V$ ) channel family open and repolarize the membrane.

KCNQ channels are already partially open at resting potentials, A higher open probability of the channels leads to a decreased excitability. Retigabine (Figure VIII.1) is a KCNQ channel modulator, which is selective for KCNQ2 – 5 and stabilizes the open state.<sup>9,10</sup> Upon binding, retigabine shifts voltage-dependent opening of the channel to hyperpolarized potentials, which raises the open probability at resting potentials.<sup>11</sup> Overall, this dampens neuronal excitability. Retigabine was approved by the FDA in 2011 as an anti-epileptic drug, but its production and sale has been discontinued in 2017 due to safety concerns.<sup>12,13</sup> Nevertheless, it is still used as a tool compound.<sup>9,13</sup>

A conserved tryptophan (Trp) residue in the S5 segment of the channel is supposedly crucial for the effects of retigabine. This hypothesis is supported by its selectivity for KCNQ2 – 5 over KCNQ1, where the S5 Trp residue is absent.<sup>14</sup> In 2015 Pless and co-workers supported this hypothesis with their experiments using KCNQ mutants and different KCNQ channel modulators.<sup>15</sup> They demonstrated that the carbamate in retigabine is crucial, and probably acts as hydrogen bond acceptor to the conserved tryptophan.



**Figure VIII.1: Molecular structures of retigabine, AzoRetigabine, NS15370 (top) and retigabine derivatives with modified sidechain (bottom).**

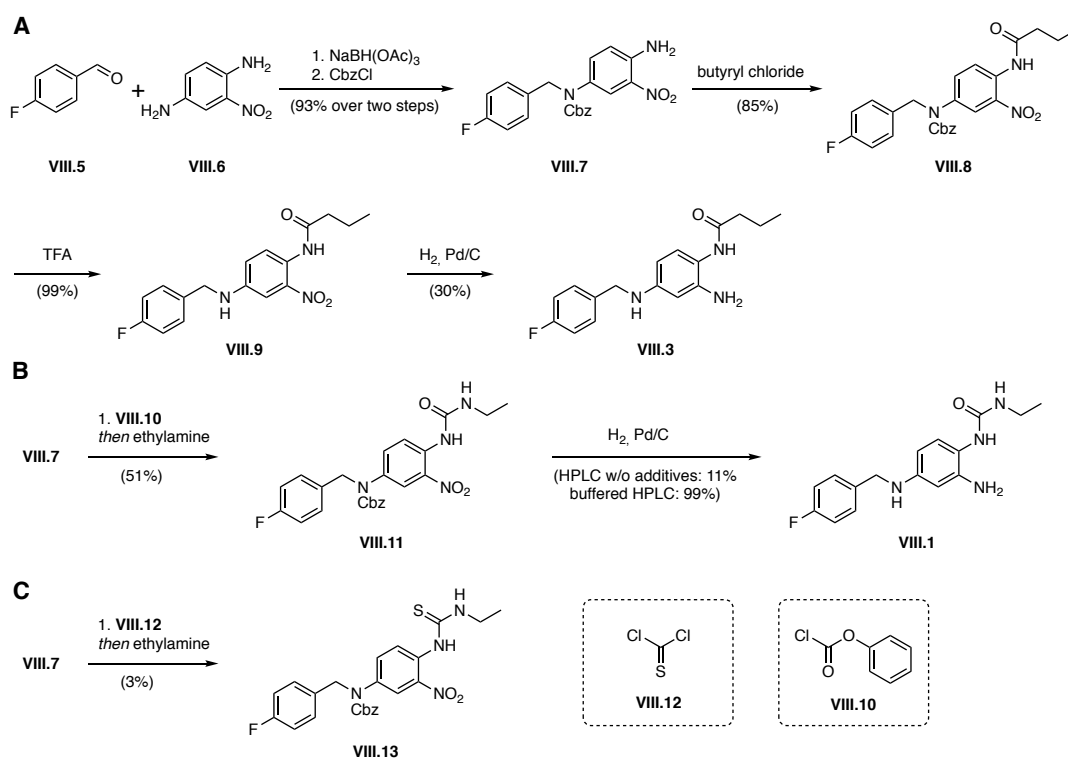
To deepen the understanding of the molecular basis of retigabine action, derivatives of retigabine, which can act as stronger or weaker hydrogen-bond acceptors, need to be synthesized. Together with the Pless lab, we envisioned to synthesize derivatives with altered hydrogen bond acceptor properties and evaluate their binding and potency. Possible molecules include a urea, a thiourea, an amide and an amine functionality (Figure VIII.1).

As a second goal within this project, we wanted to address the need for a photoswitchable tool to study KCNQ channels with high temporal precision. Due to their unique gating properties in the  $K_V$  family, a high-precision tool could be

crucial to gain a deeper understanding for neurological disorders and help finding novel treatments. A photoswitchable version of retigabine (AzoRetigabine, Figure VIII.1 top) has already been synthesized previously and preliminary results have been obtained.<sup>16</sup> Due to its decreased potency compared to retigabine, however, its biological evaluation was not conducted in depth. We now envisioned to azolog a more potent analogue of retigabine, NS15370 (Figure VIII.1).<sup>17</sup>

## Results and discussion

Synthesis of the common precursor **VIII.7** was achieved through a reductive amination of the more nucleophilic amine group in **VIII.6** with 4-fluorobenzaldehyde (**VIII.5**) and subsequent Cbz protection of the resulting secondary aniline (Scheme VIII.1A). Amide bond formation with commercially available butyryl chloride afforded **VIII.8**. Unlike in reported syntheses for retigabine,<sup>18,19</sup> one-pot reduction of the nitro group and Cbz deprotection was not successful. Therefore, we employed a two-step protocol consisting of TFA-mediated deprotection followed by reduction of the nitro group to synthesize **VIII.3**.

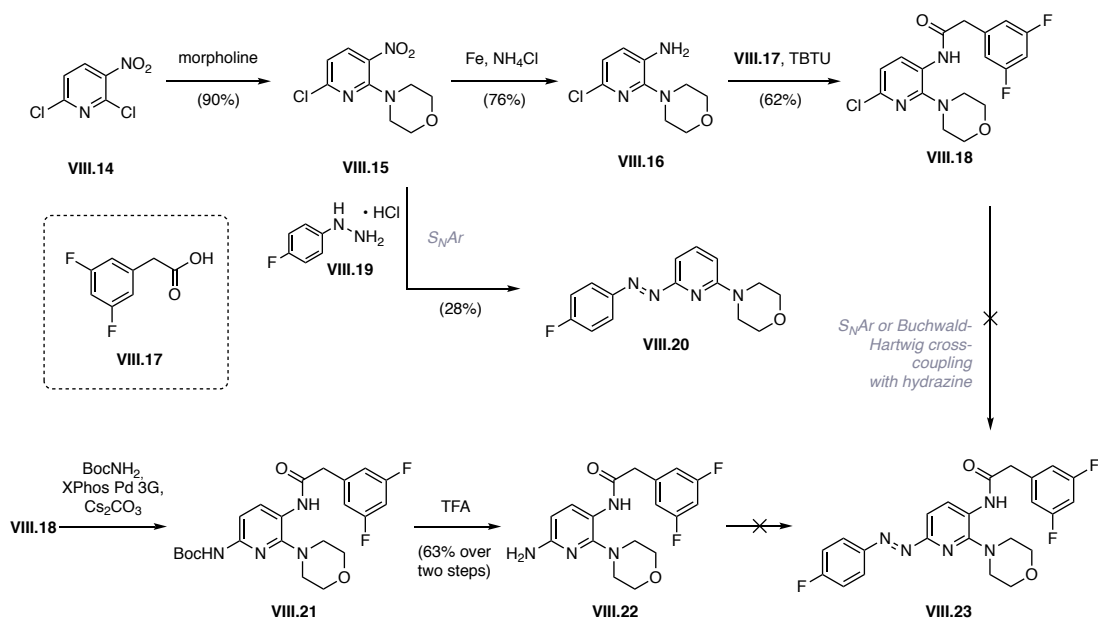


**Scheme VIII.1: Chemical synthesis of VIII.8, VIII.3, VIII.1 and precursor VIII.13.**

Formation of the urea functionality in **VIII.1** was achieved with phenyl chloroformate and ethylamine (Scheme VIII.1B). Reduction with H<sub>2</sub> and Pd/C gave the target compound **VIII.1**. Purification by ammonium acetate-buffered HPLC proved to be necessary, as complete decomposition was observed upon purification with 0.1% FA as an additive, and the majority of the compound decomposed without any additives.

For the synthesis of the thiocarbamate analogue **VIII.2**, reaction of **VIII.3** with either phenyl chlorothioformate and ethylamine or with ethyl isothiocyanate directly did not yield any product. In situ isothiocyanate formation on the aniline with thiophosgene (**VIII.12**), followed by thiourea formation with a large excess of ethylamine gave the product (Scheme VIII.1C). Unfortunately, the low yield did not allow us to advance enough material to carry out the remaining two steps (e.g. nitro group reduction and Cbz removal). Compounds **VIII.3** and **VIII.1** have been sent to the laboratory of Prof. Stefan Pless in Copenhagen, where they are currently under investigation.

The carbamate in retigabine is considered important for binding to KCNQ channels. However, a bulky amide in this position showed increased potency compared to the parent compound.<sup>17</sup> Azologization of the conserved 4-fluorobenzylamine in NS15370 (Figure VIII.1) would lead to **VIII.23**. We envisioned to follow reported protocols for the parent compound.<sup>17</sup> After regioselective nucleophilic aromatic substitution of **VIII.14** with morpholine, we attempted substitution with fluorophenyl hydrazine. Very unexpectedly, this reaction yielded **VIII.20** instead of the desired product, similar to a tele-substitution.<sup>20</sup> We therefore directly reduced the nitro group to the aniline with iron powder and ammonium chloride, followed by installation of the amide to furnish **VIII.18**. Unfortunately, the resulting pyridine was not electron-deficient enough to engage in S<sub>N</sub>Ar with 4-fluorophenylhydrazine. Buchwald-Hartwig cross-coupling reaction with multiple ligands/catalysts and pre-catalysts (e.g. MorDalPhos/[{Pd(cinnamyl)Cl}<sub>2</sub>]<sup>21</sup>, Pd(PtBu<sub>3</sub>)<sub>2</sub><sup>22</sup>) proved to be equally unsuccessful. Instead, a stepwise approach towards the formation of the azo group was investigated next: Buchwald-Hartwig cross-coupling of **VIII.18** to *tert*-butyl carbamate with the XPhos Pd 3G pre-catalyst enabled installation of the 2-amino group. The cross-coupling reaction gave an unidentifiable side product, which could only be removed after Boc-deprotection and the ensuing change in product polarity. All attempts to engage aniline **VIII.22** in a Baeyer-Mills reaction or an azo-coupling, however, failed. While no conversion could be observed under standard conditions with 4,4'-fluoronitrosobenzene in AcOH/DCM,<sup>23</sup> reaction under basic conditions<sup>24</sup> (1:1 50 w% aq. NaOH-toluene) yielded a prominent side-product. While the structure of this side product was not investigated in detail, HRMS data suggested that it is an oxidized version (azoxy or pyridine-N-oxide, calcd. [M+H]<sup>+</sup> for both: 472.1591, found: 472.1595) of compound **VIII.23**.



**Scheme VIII.2 Attempts towards a photoswitchable version of NS15370 (VIII.23).**

## Conclusions

We have successfully synthesized two retigabine derivatives which are currently being investigated for their binding properties in the laboratory of Stefan Pless. Synthesis of the thiourea derivative employing thiophosgene should be investigated further and conducted on larger scale. Another retigabine analogue, amine derivative **VIII.4**, could be synthesized by reductive amination of the common precursor **VIII.7** with butanal.

Additionally, we have synthesized advanced building blocks towards **VIII.23**, an azolog version of NS15370. To accomplish the synthesis, modification of the basic Mills reaction using milder and less oxidizing conditions, for example by slow and (sub)-stoichiometric addition of the nitroso component, could be promising.

## References

- (1) World Health Organization. *Epilepsy: A Public Health Imperative*; Geneva, 2019, Licence: CC BY-NC-SA 3.0 IGO.
- (2) McNamara, J. O. Emerging Insights into the Genesis of Epilepsy. *Nature* **1999**, 399, A15-A22.
- (3) Meldrum, B. S.; Rogawski, M. A. Molecular Targets for Antiepileptic Drug Development. *Neurotherapeutics* **2007**, 4, 18-61.
- (4) Brown, D. A.; Adams, P. R. Muscarinic Suppression of a Novel Voltage-Sensitive K<sup>+</sup> Current in a Vertebrate Neuron. *Nature* **1980**, 283, 673-676.
- (5) Jentsch, T. J. Neuronal KCNQ Potassium Channels: Physiology and Role in Disease. *Nat. Rev. Neurosci.* **2000**, 1, 21-30.
- (6) Hadley, J. K.; Passmore, G. M.; Tatulian, L.; Al-Qatari, M.; Ye, F.; Wickenden, A. D.; Brown, D. A. Stoichiometry of Expressed KCNQ2/KCNQ3 Potassium Channels and Subunit Composition of Native Ganglionic M Channels Deduced from Block by Tetraethylammonium. *J. Neurosci.* **2003**, 23, 5012-5019.
- (7) Wang, Q.; Curran, M. E.; Splawski, I.; Burn, T. C.; Millholland, J. M.; VanRaay, T. J.; Shen, J.; Timothy, K. W.; Vincent, G. M.; Jager, T. de; et al. Positional Cloning of a Novel Potassium Channel Gene: KVLQT1 Mutations Cause Cardiac Arrhythmias. *Nat. Genet.* **1996**, 12, 17-23.
- (8) Bean, B. P. The Action Potential in Mammalian Central Neurons. *Nat. Rev. Neurosci.* **2007**, 8, 451-465.
- (9) Kalappa, B. I.; Soh, H.; Duignan, K. M.; Furuya, T.; Edwards, S.; Tzingounis, A. V.; Tzounopoulos, T. Potent KCNQ2/3-Specific Channel Activator Suppresses In Vivo Epileptic Activity and Prevents the Development of Tinnitus. *J. Neurosci.* **2015**, 35, 8829-8842.
- (10) Gunthorpe, M. J.; Large, C. H.; Sankar, R. The Mechanism of Action of Retigabine (Ezogabine), a First-in-Class K<sup>+</sup> Channel Opener for the Treatment of Epilepsy. *Epilepsia* **2012**, 53, 412-424.
- (11) Brown, D. A.; Passmore, G. M. Neural KCNQ (Kv7) Channels. *Br. J. Pharmacol.* **2009**, 156, 1185-1195.
- (12) Stafstrom, C. E.; Grippon, S.; Kirkpatrick, P. Ezogabine (Retigabine). *Nat. Rev. Drug Discov.* **2011**, 10, 729-730.
- (13) Manville, R. W.; Abbott, G. W. Ancient and Modern Anticonvulsants Act Synergistically in a KCNQ Potassium Channel Binding Pocket. *Nat. Commun.* **2018**, 9, 1-14.
- (14) Lange, W.; Geißendörfer, J.; Schenzer, A.; Grötzinger, J.; Seebohm, G.; Friedrich, T.; Schwake, M. Refinement of the Binding Site and Mode of Action of the Anticonvulsant Retigabine on KCNQ K<sup>+</sup> Channels. *Mol. Pharmacol.* **2009**, 75, 272-280.
- (15) Kim, R. Y.; Yau, M. C.; Galpin, J. D.; Seebohm, G.; Ahern, C. A.; Pless, S. A.; Kurata, H. T. Atomic Basis for Therapeutic Activation of Neuronal Potassium Channels. *Nat Commun* **2015**, 6, 8116.
- (16) Kienzler, M. A. Total Synthesis of Smenochromene B and Halenaquinone and Studies on the Chemical and Biological Properties of Azobenzene Photoswitches. PhD Thesis, UC Berkeley, 2010.
- (17) Dalby-Brown, W.; Jessen, C.; Hougaard, C.; Jensen, M. L.; Jacobsen, T. A.; Nielsen, K. S.; Erichsen, H. K.; Grunnet, M.; Ahring, P. K.; Christophersen, P.; et al. Characterization of a Novel High-Potency Positive Modulator of Kv7 Channels. *Eur. J. Pharmacol.* **2013**, 709, 52-63.

- (18) Kinarivala, N.; Patel, R.; Boustany, R.-M.; Al-Ahmad, A.; Trippier, P. C. Discovery of Aromatic Carbamates That Confer Neuroprotective Activity by Enhancing Autophagy and Inducing the Anti-Apoptotic Protein B-Cell Lymphoma 2 (Bcl-2). *J. Med. Chem.* **2017**, *60*, 9739-9756.
- (19) Longoni, D.; Frigoli, S.; Alpegiani, M. Process and Intermediates for the Preparation of Retigabine. WO2013114315 (A1), August 8, 2013.
- (20) Suwiński, J. W. Cine- and Tele-Substitution Reactions: Review of Work from 2002-2016. *Arkivoc* **2017**, *2017*, 402-435.
- (21) Lundgren, R. J.; Stradiotto, M. Palladium-Catalyzed Cross-Coupling of Aryl Chlorides and Tosylates with Hydrazine. *Angew. Chem. Int. Ed.* **2010**, *49*, 8686-8690.
- (22) Barber, D. M.; Liu, S.-A.; Gottschling, K.; Sumser, M.; Hollmann, M.; Trauner, D. Optical Control of AMPA Receptors Using a Photoswitchable Quinoxaline-2,3-Dione Antagonist. *Chem. Sci.* **2017**, *8*, 611-615.
- (23) Jankowiak, A.; Obijalska, E.; Kaszynski, P. Cyclization of Substitued 2-(2-Fluorophenylazo)Azines to Azino[1,2-c]Benzo[d][1,2,4]Triazinium Derivatives. *Beilstein J. Org. Chem.* **2013**, *9*, 1873-1880.
- (24) Jankowiak, A.; Obijalska, E.; Kaszynski, P.; Pieczonka, A.; Young, V. G. Synthesis and Structural, Spectroscopic, and Electrochemical Characterization of Benzo[c]Quinolizinium and Its 5-Aza-, 6-Aza, and 5,6-Diaza Analogues. *Tetrahedron* **2011**, *67*, 3317-3327.

## Methods

**General.** Anhydrous solvents were prepared with a solvent purification system by filtration of HPLC grade solvents through alumina or distilled as followed: Tetrahydrofuran (THF) was distilled under a nitrogen atmosphere from Na/benzophenone prior to use. Triethylamine (Et<sub>3</sub>N) was distilled under a nitrogen atmosphere from CaH<sub>2</sub> prior to use. Dichloromethane (CH<sub>2</sub>Cl<sub>2</sub>), 1,2-dichloroethane (DCE), ethyl acetate (EtOAc), dimethylformamide (DMF) and methanol (MeOH) were purchased from commercial suppliers (Acros Organics) and used as received. Solvents for extraction and column chromatography were purchased in technical grade and distilled under reduced pressure prior to use. If necessary, solvents were degassed sonication in vacuo and backfilling with argon (three times). All other chemicals were purchased from commercial suppliers (Sigma-Aldrich, Acros Organics, TCI) and were used as received, unless stated otherwise. All reactions were magnetically stirred and carried out under inert gas atmosphere (N<sub>2</sub> or Ar). Glassware was oven dried at 120 °C or flame dried under vacuum prior to use. Solvents and liquid reagents were added by syringes or oven-dried stainless-steel cannulas through rubber septa. Solid reagents were dissolved in an appropriate solvent or were added under inert gas counter-flow. Reactions above room temperature were conducted in a heated silicon oil bath. Yields refer to isolated and spectroscopically pure materials, if not stated otherwise. Reaction progress was monitored by LC-MS and TLC. Reactions and chromatography fractions were monitored by qualitative thin-layer-chromatography (TLC) on silica gel F254 TLC-plates from Merk KGaA. Analytes on silica were visualized by UV light and an appropriate staining solution (ninhydrine, KMnO<sub>4</sub>) followed by heating with a hot-air gun (650 °C). LC-MS was performed on an Agilent 1260 Infinity HPLC System, MS-Agilent 1100 Series, Type: 1946D, Model: SL, equipped with a Agilent Zorbax Eclipse Plus C18 (100 x 4.6 mm, particle size 3.5 micron) reverse phase column with a constant flow-rate of 1 mL/min (gradient and time is reported in parentheses).

**Column Chromoatography.** Flash column chromatography was performed on Geduran<sup>®</sup> Si60 (40-63 μm) silica gel from Merk KGaA. All fractions containing the desired product were combined and solvents were removed under reduced pressure followed by drying in vacuo (10<sup>-2</sup> mbar).

**Purification by HPLC.** HPLC was performed on a Varian Prep Star HPLC System, Model SD-1 equipped with Varian Dynamax columns (RP-Analytical: Microsorb 60 C18, 250 x 4.6 mm, particle size 8 μm; RP-SemiPrep: Microsorb 60 C18, 250 x 21.4 mm, particle size 8 μm). Buffered RP-HPLC was performed on a Waters Alliance HPLC system equipped with a CC 250/4 Nucleosil N 120-3 C<sub>18</sub> column from Machery Nagel (250 x 4 mm, particle size 3 μm). The following buffer system was used: Buffer A (100 mM Et<sub>3</sub>NH<sup>+</sup>OAc<sup>-</sup> in H<sub>2</sub>O), buffer B (100 mM Et<sub>3</sub>NH<sup>+</sup>OAc<sup>-</sup> in 80% MeCN/H<sub>2</sub>O). Prior to injection, samples were filtered through a syringe filter (Chromafil Xtra GF100/25, pore size 1 μm).



**NMR spectroscopy.** NMR spectra were measured on a Bruker Avance III HD 400 MHz spectrometer equipped with a CryoProbe™ or Bruker Avance III HD 800 MHz with a CryoProbe™ operating at 400 MHz or 800 MHz for proton nuclei (100 MHz/400 MHz for carbon nuclei, respectively). <sup>1</sup>H-NMR shifts are reported in ppm related to the shift of TMS. <sup>1</sup>H-NMR shifts are calibrated to residual solvent resonances: CDCl<sub>3</sub> (7.26 ppm), CD<sub>2</sub>Cl<sub>2</sub> (5.32 ppm), MeOD (4.78 ppm), DMSO-d<sub>6</sub> (2.50 ppm) and acetone-d<sub>6</sub> (2.09 ppm). <sup>13</sup>C-NMR shifts are calibrated to residual solvent resonances: CDCl<sub>3</sub> (77.16 ppm), CD<sub>2</sub>Cl<sub>2</sub> (54.0 ppm), MeOD (49.2 ppm), DMSO-d<sub>6</sub> (39.5 ppm) and acetone-d<sub>6</sub> (29.9 ppm). <sup>1</sup>H-NMR shifts are reported as followed: Chemical shift in ppm (multiplicity, coupling constants J, integration intensity). The multiplicities are reported as followed: s (singlet), d (doublet), t (triplet), q (quartet), m (multiplet). 2D-NMR techniques such as homonuclear correlation spectroscopy (COSY), heteronuclear single quantum coherence (HSQC) and heteronuclear multiple bond coherence (HMBC) were used to assign signals. Coupling constants J are reported in Hz. All NMR-spectra were analyzed using MestReNova 11.0 from Mestrelab Research S. L.

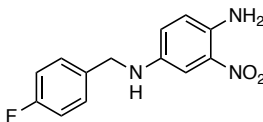
**Mass Spectra.** High-resolution mass spectra (HRMS) were recorded by the LMU Mass Spectrometry Service on a MAT 90 (ESI) spectrometer from Thermo Finnigan GmbH or using an Agilent 6224 Accurate-Mass time-of-flight spectrometer with electrospray ionization at the New York University Shared Instrumentation Facility (NYU-SIF).

**Infrared Spectra.** IR spectra were recorded on a Thermo Nicolet AVATAR FT-IR equipped with an ATR unit. The measured wave numbers are reported in cm<sup>-1</sup> or on a PerkinElmer Spectrum BX II FT-IR system. The measured wave numbers are reported in cm<sup>-1</sup>.



## Experimental Procedures

### ***N*<sup>1</sup>-(4-fluorobenzyl)-3-nitrobenzene-1,4-diamine (VIII.24)**



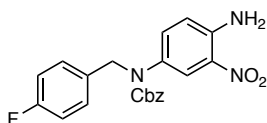
2-nitrobenzene-1,4-diamine (**VIII.6**) (440 mg, 1.70 mmol, 1.0 eq) and (4-fluorophenyl)-methanamine (**VIII.5**) (780  $\mu$ L, 6.80 mmol, 4.0 eq) were dissolved in DCM (25 mL) and AcOH (97.1  $\mu$ L, 1.70 mmol, 1.0 eq), followed by NaBH(OAc)<sub>3</sub> (504 mg, 2.38 mmol, 1.4 eq) were added. The red reaction mixture stirred overnight, at room temperature. The red suspension was poured into 1 M NaOH (100 mL), extracted with EtOAc (3 x 100 mL), washed with sat. NaCl (1 x 100 mL), dried over MgSO<sub>4</sub> and concentrated *in vacuo*. The crude material (476 mg) was used without further purification.

**<sup>1</sup>H NMR** (400 MHz, CDCl<sub>3</sub>)  $\delta$  = 7.33 (dd, *J* = 8.5, 5.5 Hz, 2H), 7.29 (d, *J* = 2.8 Hz, 1H), 7.03 (t, *J* = 8.7 Hz, 2H), 6.85 (dd, *J* = 8.9, 2.8 Hz, 1H), 6.70 (d, *J* = 8.9 Hz, 1H), 5.72 (s, 2H), 4.25 (s, 2H).

**<sup>13</sup>C NMR** (100 MHz, CDCl<sub>3</sub>)  $\delta$  = 162.3 (d, *J* = 245.6 Hz), 139.3, 138.4, 134.5 (d, *J* = 3.2 Hz), 132.5, 129.4 (d, *J* = 8.1 Hz), 125.5, 120.2, 115.7 (d, *J* = 21.4 Hz), 105.9, 48.3.

**IR** (neat, cm<sup>-1</sup>) = 3477, 3432, 3418, 3352, 3159, 3068, 2848, 1899, 1644, 1588, 1569, 1518, 1507, 1469, 1451, 1410, 1383, 1329, 1280, 1262, 1216, 1172, 1156, 1096, 1018, 961, 940, 859, 824, 760, 711, 681.

**HRMS (ESI)**: calcd. for C<sub>13</sub>H<sub>13</sub>FN<sub>3</sub>O<sub>2</sub><sup>+</sup> [M+H]<sup>+</sup>: 262.0986, found: 262.0990.

**benzyl (4-amino-3-nitrophenyl)(4-fluorobenzyl)carbamate (VIII.7)**

1-(4-fluorobenzyl)-3-nitrobenzene-1,4-diamine (**VIII.24**) (420 mg, 1.61 mmol, 1.0 eq) was dissolved in DCM (20 mL) and cooled to 0 °C, before Cbz-Cl (230  $\mu$ L, 1.61 mmol, 1.0 eq) was added. The reaction mixture was stirred for 1 h at 0 °C. Then, sat.  $\text{Na}_2\text{CO}_3$  (1.5 mL) was added and the reaction mixture was stirred for 2 h upon which it was allowed to warm up to room temperature. The reaction was quenched with  $\text{H}_2\text{O}$  (100 mL), extracted with EtOAc (3 x 100 mL). The combined organic layers were washed with sat. NaCl (1 x 100 mL), dried over  $\text{MgSO}_4$  and concentrated *in vacuo*. The crude product was purified by silica gel flash column chromatography (75% EtOAc/hexanes) to yield **VIII.7** (602 mg, 1.52 mmol, 93%) as red oil.

**$^1\text{H NMR}$**  (600 MHz,  $\text{CDCl}_3$ )  $\delta$  = 7.88 (s, 1H), 7.36 - 7.26 (m, 3H), 7.25 (s, 1H), 7.15 (s, 2H), 6.96 (t,  $J$  = 8.7 Hz, 2H), 6.68 (d,  $J$  = 8.9 Hz, 1H), 6.09 (s, 2H), 5.18 (s, 2H), 4.78 (s, 2H).

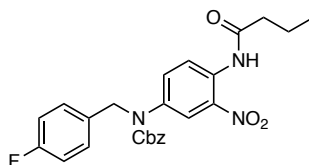
**$^{13}\text{C NMR}$**  (150 MHz,  $\text{CDCl}_3$ )  $\delta$  = 162.3 (d,  $J$  = 246.0 Hz), 155.7, 143.5, 136.3, 135.8, 133.1, 131.5, 130.0, 128.6, 128.3, 127.8, 124.5, 119.2, 115.6 (d,  $J$  = 21.4 Hz), 67.9, 53.7.

**IR** (neat,  $\text{cm}^{-1}$ ) = 3479, 3349, 3183, 3035, 2957, 2360, 1691, 1636, 1603, 1566, 1510, 1453, 1406, 1352, 1337, 1292, 1248, 1219, 1157, 1099, 1045, 1015, 971, 916, 825, 767, 755, 698.

**HRMS** (ESI): calcd. for  $\text{C}_{21}\text{H}_{17}\text{FN}_3\text{O}_4^-$  [M-H]: 394.1209, found: 394.1216.

**$R_t$**  = 8.23 min (10  $\rightarrow$  90% MeCN/ $\text{H}_2\text{O}$ ; +0.1% FA; 10 min).

**$R_f$**  = 0.20 (25% EtOAc/hexanes).

**benzyl (4-butyramido-3-nitrophenyl)(4-fluorobenzyl)carbamate (VIII.8)**

To a solution of **VIII.7** (50.0 mg, 0.126 mmol, 1.0 eq) in THF (1 mL) was added pyridine (20  $\mu$ L, 0.25 mmol, 2.0 eq) at room temperature. The clear solution was cooled to 0  $^{\circ}$ C, whereupon butyryl chloride (40  $\mu$ L, 0.39 mmol, 3.1 eq) was added dropwise. The yellow suspension was allowed to warm to rt and stirred overnight. Sat.  $\text{NH}_4\text{Cl}$  (5 mL) was added and the mixture was extracted with EtOAc (2 x 3 mL). The combined organic layers were washed with sat.  $\text{NaHCO}_3$  (2 x 5 mL) and sat.  $\text{NaCl}$  (5 mL), dried over  $\text{Na}_2\text{SO}_4$  and concentrated *in vacuo*. The crude product was purified via silica gel flash column chromatography (20% EtOAc/hexanes) to yield benzylamine **VIII.8** (50.0 mg, 0.107 mmol, 85%) as yellow oil.

**$^1\text{H NMR}$**  (400 MHz,  $\text{CD}_2\text{Cl}_2$ )  $\delta$  = 10.19 (s, 1H), 8.71 (d,  $J$  = 9.1 Hz, 1H), 7.99 (s, 1H), 7.40 (d,  $J$  = 8.4 Hz, 1H), 7.31 (d,  $J$  = 2.1 Hz, 3H), 7.26 (d,  $J$  = 7.6 Hz, 2H), 7.18 (dd,  $J$  = 8.6, 5.4 Hz, 2H), 6.98 (t,  $J$  = 8.8 Hz, 2H), 5.17 (s, 2H), 4.86 (s, 2H), 2.43 (t,  $J$  = 7.5 Hz, 2H), 1.74 (h,  $J$  = 7.4 Hz, 2H), 1.00 (t,  $J$  = 7.4 Hz, 3H).

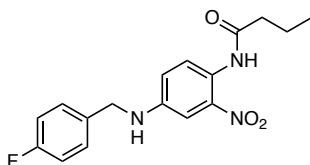
**$^{13}\text{C NMR}$**  (100 MHz,  $\text{CD}_2\text{Cl}_2$ )  $\delta$  = 171.9, 162.2 (d,  $J$  = 245.4 Hz), 155.0, 136.2, 135.9, 133.3, 133.0 (d,  $J$  = 3.2 Hz), 129.7, 128.5, 128.1, 127.8, 122.3, 115.4 (d,  $J$  = 21.6 Hz), 67.9, 40.4, 18.7, 13.4.

Note: the *N*-methylene carbon signal is overlapping with the solvent signal.

**HRMS** (ESI): calcd. for  $\text{C}_{25}\text{H}_{25}\text{FO}_5\text{N}_3$   $[\text{M}+\text{H}]^+$ : 466.1773, found: 466.1778.

**$R_f$**  = 0.7 (40% EtOAc/hexanes)

**$R_t$**  = 6.06 min (5  $\rightarrow$  100% MeCN/ $\text{H}_2\text{O}$ ; + 0.1% FA; 5 min)

**N-(4-((4-fluorobenzyl)amino)-2-nitrophenyl)butyramide (VIII.9)**

To a solution **VIII.8** (10.0 mg, 21.5  $\mu\text{mol}$ , 1.0 eq) in MeOH (100  $\mu\text{L}$ ) was added a of mixture of TFA in DCM (1:1, 1 mL) at rt. The pale, yellow solution was stirred overnight and sat.  $\text{NaHCO}_3$  solution (3 mL) was added. The resulting orange reaction mixture was extracted with EtOAc (3 x 2 mL) and the combined organic layers were washed sat.  $\text{NaHCO}_3$  solution (2 x 3 mL) and sat. NaCl solution (3 mL), dried over  $\text{Na}_2\text{SO}_4$  and concentrated *in vacuo*. The crude product was purified via silica gel flash column chromatography (1  $\rightarrow$  40% EtOAc/hexanes) to yield **VIII.9** (7.1 mg, 21  $\mu\text{mol}$ , 99%) as dark orange solid.

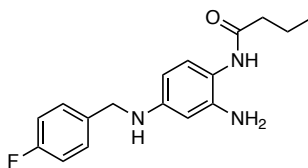
**$^1\text{H NMR}$**  (400 MHz,  $\text{CD}_2\text{Cl}_2$ )  $\delta$  = 9.75 (s, 1H), 8.42 (d,  $J$  = 9.1 Hz, 1H), 7.39 - 7.29 (m, 3H), 7.05 (t,  $J$  = 8.7 Hz, 2H), 6.95 (dd,  $J$  = 9.1, 2.9 Hz, 1H), 4.39 (s, 1H), 4.34 (s, 2H), 2.38 (t,  $J$  = 7.5 Hz, 2H), 1.73 (h,  $J$  = 7.4 Hz, 2H), 0.99 (t,  $J$  = 7.4 Hz, 3H).

**$^{13}\text{C NMR}$**  (100 MHz,  $\text{CD}_2\text{Cl}_2$ )  $\delta$  = 171.4, 162.1 (d,  $J$  = 244.7 Hz), 143.8, 137.9, 134.2, 129.1 (d,  $J$  = 8.1 Hz), 125.5, 123.9, 121.1, 115.5 (d,  $J$  = 21.5 Hz), 106.6, 47.3, 40.2, 29.7, 18.9, 13.4.

**HRMS** (ESI): calcd. for  $\text{C}_{17}\text{H}_{19}\text{FO}_3\text{N}_3$   $[\text{M}+\text{H}]^+$ : 332.1405, found: 332.1408.

**$R_f$**  = 0.6 (40% EtOAc/hexanes)

**$R_t$**  = 7.95 min (5  $\rightarrow$  100% MeCN/ $\text{H}_2\text{O}$ ; + 0.1% FA; 5 min)

**amide-retigabine (VIII.3)**

To a solution of benzyl **VIII.9** (20.0 mg, 43.0  $\mu\text{mol}$ , 1.0 eq) in MeOH (1.5 mL) was added palladium on activated charcoal (2.5 mg, 24  $\mu\text{mol}$ , 0.5 eq) at room temperature. The flask was purged with  $\text{H}_2$  and the yellow mixture was vigorously stirred for 30 min under  $\text{H}_2$  atmosphere, upon which time the red color dissipated. Thereafter, the reaction mixture was filtered through celite and concentrated *in vacuo*. The crude product was purified via reverse phase HPLC (30  $\rightarrow$  100% MeCN/ $\text{H}_2\text{O}$ ; no additives; 70 min), concentrated, and dried by lyophilization to yield the amide **VIII.3** (3.9 mg, 13  $\mu\text{mol}$ , 30%) as white powder.

**$^1\text{H NMR}$**  (400 MHz, MeOD)  $\delta$  = 7.35 (dd,  $J$  = 8.7, 5.5 Hz, 2H), 7.01 (t,  $J$  = 8.8 Hz, 2H), 6.76 (d,  $J$  = 8.5 Hz, 1H), 6.13 (d,  $J$  = 2.5 Hz, 1H), 6.08 (dd,  $J$  = 8.5, 2.5 Hz, 1H), 4.25 (s, 2H), 2.33 (t,  $J$  = 7.4 Hz, 2H), 1.72 (h,  $J$  = 7.4 Hz, 2H), 1.01 (t,  $J$  = 7.4 Hz, 3H).

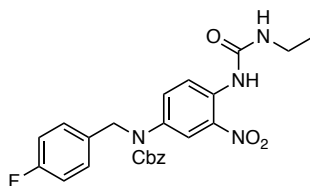
**$^{13}\text{C NMR}$**  (100 MHz, MeOD)  $\delta$  = 175.3, 163.2 (d,  $J$  = 242.8 Hz), 149.6, 144.2, 137.5, 130.1, 128.2, 116.0, 115.9 (d,  $J$  = 21.5 Hz) 105.7, 102.2, 47.9, 39.0, 20.5, 14.1.

**HRMS** (ESI): calcd. for  $\text{C}_{17}\text{H}_{21}\text{FON}_3$   $[\text{M}+\text{H}]^+$ : 302.1663, found: 302.1655.

**IR** (neat,  $\text{cm}^{-1}$ ): 3285, 2964, 2444, 1628, 1599, 1508, 1351, 1226, 1152, 1092, 840, 790.

**$R_f$**  = 0.21 (80% EtOAc/hexanes)

**$R_t$**  = 5.46 min (5  $\rightarrow$  100% MeCN/ $\text{H}_2\text{O}$ ; + 0.1% FA; 5 min)

**benzyl (4-(3-ethylureido)-3-nitrophenyl)(4-fluorobenzyl)-carbamate (VIII.11)**

To a solution of **VIII.7** (50.0 mg, 0.126 mmol, 1.0 eq) in THF (10 mL) were added phenyl chloroformate (**VIII.10**) (159  $\mu$ L, 1.26 mmol, 10 eq) and pyridine (153  $\mu$ L, 1.90 mmol, 15 eq) at room temperature. The pale, yellow mixture was stirred at 60  $^{\circ}$ C for 1 h and then cooled to room temperature, whereupon ethylamine (1.58 mL, 3.16 mmol, 25 eq) was added. The white suspension was stirred at room temperature for 2 h, before addition of sat.  $\text{NaHCO}_3$  (15 mL). The aq. phase was extracted with EtOAc (3 x 10 mL) and the combined organic layers were washed with sat.  $\text{NaHCO}_3$  (1 x 20 mL), NaOH (1 M, 1 x 20 mL) and sat. NaCl (1 x 20 mL), dried over  $\text{Na}_2\text{SO}_4$  and concentrated *in vacuo*. The crude product was purified by silica gel flash column chromatography (20  $\rightarrow$  30% EtOAc/hexanes). The product-containing fractions were combined, concentrated under reduced pressure and dissolved in MeCN (20 mL), washed with pentane (3 x 15 mL) and concentrated *in vacuo* to yield benzyl (4-(3-ethylureido)-3-nitrophenyl)(4-fluorobenzyl)-carbamate (**VIII.11**) (29.8 mg, 63.9  $\mu$ mol, 51%) as yellow oil.

**$^1\text{H NMR}$**  (400 MHz,  $\text{CD}_2\text{Cl}_2$ )  $\delta$  = 9.60 (s, 1H), 8.57 (d,  $J$  = 9.2 Hz, 1H), 7.94 (s, 1H), 7.40 - 7.23 (m, 6H), 7.18 (dd,  $J$  = 8.4, 5.5 Hz, 2H), 7.02 - 6.93 (m, 2H), 5.17 (s, 2H), 4.84 (s, 2H), 3.33 - 3.23 (m, 2H), 1.17 (t,  $J$  = 7.2 Hz, 3H).

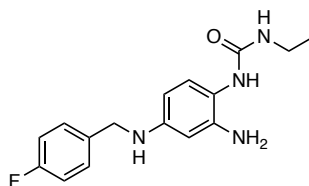
**$^{13}\text{C NMR}$**  (100 MHz,  $\text{CD}_2\text{Cl}_2$ )  $\delta$  = 162.8 (d,  $J$  = 245.3 Hz), 155.7, 154.1, 136.8, 136.3, 135.4, 133.7 (d,  $J$  = 3.2 Hz), 130.3, 129.0, 128.6, 128.3, 124.3, 122.1, 115.9 (d,  $J$  = 21.5 Hz), 68.3, 36.0, 31.2, 15.4.

**HRMS** (ESI): calc. for  $\text{C}_{24}\text{H}_{22}\text{FO}_5\text{N}_4$   $[\text{M}-\text{H}]^-$ : 465.1579, found: 465.1567.

**$R_f$**  = 0.47 (40% EtOAc/hexanes)

**$R_t$**  = 8.52 min (5  $\rightarrow$  100% MeCN/ $\text{H}_2\text{O}$ ; + 0.1% FA; 5 min)



**urea-retigabine (VIII.1)**

To a solution of **VIII.11** (23.6 mg, 50.6  $\mu\text{mol}$ , 1.0 eq) in MeOH (3.5 mL) was added palladium on activated charcoal (3.8 mg, 35.7  $\mu\text{mol}$ , 0.7 eq) at rt. The flask was purged with  $\text{H}_2$  and reaction was stirred 1 h under  $\text{H}_2$  atmosphere. After complete decolorization, the reaction mixture was filtered through celite and concentrated *in vacuo*. The crude product was purified *via* buffered reverse phase HPLC (buffer A/buffer B = 70/30  $\rightarrow$  0/100; 45 min), concentrated and dried by lyophilization to yield urea derivative **VIII.1** (15.1 mg, 49.9  $\mu\text{mol}$ , 99%) as white powder.

Buffer A: 100 mM  $\text{Et}_3\text{NH}^+\text{OAc}^-$  in  $\text{H}_2\text{O}$

Buffer B: 100 mM  $\text{Et}_3\text{NH}^+\text{OAc}^-$  in 80% MeCN/ $\text{H}_2\text{O}$

**$^1\text{H}$  NMR** (400 MHz,  $\text{DMSO}-d_6$ )  $\delta$  = 7.35 (dd,  $J$  = 8.6, 5.7 Hz, 2H), 7.19 – 7.04 (m, 3H), 6.66 (d,  $J$  = 8.4 Hz, 1H), 5.94 (d,  $J$  = 2.5 Hz, 1H), 5.85 (t,  $J$  = 6.2 Hz, 1H), 5.81 (dd,  $J$  = 8.4, 2.5 Hz, 1H), 5.76 (t,  $J$  = 5.3 Hz, 1H), 4.49 (s, 1H), 4.20 – 4.11 (m, 2H), 3.09 – 2.97 (m, 2H), 0.99 (t,  $J$  = 7.2 Hz, 3H).

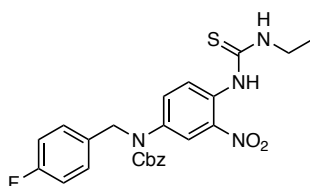
**$^{13}\text{C}$  NMR** (100 MHz,  $\text{DMSO}-d_6$ )  $\delta$  = 161.4 (d,  $J$  = 241.5 Hz), 157.2, 147.1, 144.1, 137.3, 129.3 (d,  $J$  = 8.0 Hz), 127.4, 115.3 (d,  $J$  = 21.1 Hz), 114.8, 102.3, 99.7, 46.4, 34.6, 16.1.

**HRMS (ESI)**: calcd. for  $\text{C}_{16}\text{H}_{20}\text{FON}_4$   $[\text{M}+\text{H}]^+$ : 303.1616, found: 303.1619.

**IR** (neat,  $\text{cm}^{-1}$ ): 3318, 1624, 1602, 1565, 1507, 1417, 1279, 1224, 837.

**$R_f$**  = 0.5 (10% MeOH/DCM)

**$R_t$**  = 5.10 min (5  $\rightarrow$  100% MeCN/ $\text{H}_2\text{O}$ ; + 0.1% FA; 5 min)

**benzyl (4-(3-ethylthioureido)-3-nitrophenyl)(4-fluorobenzyl)-carbamate (VIII.13)**

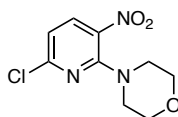
To a solution of **VIII.7** (20.0 mg, 50.6  $\mu\text{mol}$ , 1.0 eq in EtOAc (1.5 mL) was added thiophosgene (**VIII.12**) (8  $\mu\text{L}$ , 0.1 mmol, 2.0 eq) at room temperature. The pale, yellow solution was stirred at 75  $^{\circ}\text{C}$  for 1.5 h and then cooled to room temperature, whereupon ethylamine (126  $\mu\text{L}$ , 0.253 mmol, 5.0 eq) was added. The white suspension was stirred overnight at room temperature before the addition of sat.  $\text{NaHCO}_3$  solution (5 mL). The aq. phase was extracted with EtOAc (3 x 3 mL) and the combined organic layers were washed with sat.  $\text{NaHCO}_3$  (3 x 7 mL) and sat.  $\text{NaCl}$  (7 mL), dried over  $\text{Na}_2\text{SO}_4$  and concentrated *in vacuo*. The crude product was purified by silica gel flash column chromatography (20  $\rightarrow$  40  $\rightarrow$  60% EtOAc/hexanes) to yield **VIII.13** (0.7 mg, 1  $\mu\text{mol}$ , 3%) as yellow oil.

**$^1\text{H-NMR}$** : (400 MHz, Acetone- $d_6$ )  $\delta$  = 9.51 (s, 1H), 8.35-8.19 (m, 2H), 8.00 (d,  $J=2.6$ , 1H), 7.57 (dd,  $J=8.9, 2.6$ , 1H), 7.38-7.25 (m, 7H), 7.10-7.00 (m, 2H), 5.22 (s, 2H), 5.02 (s, 2H), 3.61 (dt,  $J=12.8, 6.2$ , 2H), 1.21 (t,  $J=7.2$ , 3H).

**HRMS (ESI)**: calcd. for  $\text{C}_{24}\text{H}_{24}\text{FO}_4\text{N}_4\text{S}$   $[\text{M}+\text{H}]^+$ : 483.1497, found: 483.1499.

**$R_f$**  = 0.6 (40% EtOAc/hexanes)

**$R_t$**  = 8.66 min (5  $\rightarrow$  100% MeCN/ $\text{H}_2\text{O}$ ; + 0.1% FA; 5 min)

**4-(6-chloro-3-nitropyridin-2-yl)morpholine (VIII.15)**

2,6-dichloro-3-nitropyridine (**VIII.14**) (1.00 g, 5.18 mmol, 1.0 eq) was dissolved in MeCN (100 mL) and triethylamine (2.87 mL, 20.7 mmol, 4.0 eq) was added. The light-yellow solution was cooled to 0 °C and morpholine (497  $\mu$ L, 5.70 mmol, 1.1 eq) was added dropwise at 0 °C. The solution turned bright yellow, was allowed to warm to room temperature and stirred overnight. The reaction mixture was diluted with 1M HCl (200 mL) and extracted with EtOAc (3 x 200 mL). The combined organic layers were washed with sat. NaCl, dried over MgSO<sub>4</sub>, concentrated *in vacuo* and the crude product was purified by silica gel flash column chromatography (0  $\rightarrow$  20% EtOAc/hexanes) to yield **VIII.15** (1.13 g, 4.64 mmol, 90 %) as yellow solid.

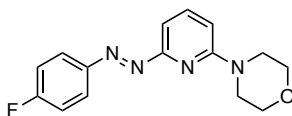
**<sup>1</sup>H NMR** (400 MHz, CDCl<sub>3</sub>)  $\delta$  = 8.10 (d, *J* = 8.4 Hz, 1H), 6.72 (d, *J* = 8.4 Hz, 1H), 3.83 - 3.76 (m, 4H), 3.50 - 3.46 (m, 4H).

**<sup>13</sup>C NMR** (100 MHz, CDCl<sub>3</sub>)  $\delta$  = 153.0, 152.2, 138.5, 131.2, 113.6, 66.6, 48.6.

**HRMS** (ESI): calcd. for C<sub>9</sub>H<sub>11</sub>ClO<sub>3</sub>N<sub>3</sub><sup>+</sup> [M+H]<sup>+</sup>: 244.0483, found: 244.0488.

**IR** (neat, cm<sup>-1</sup>): 3081, 2986, 2969, 2914, 2859, 2768, 2719, 2553, 2455, 2362, 2338, 1910, 1651, 1587, 1550, 1488, 1455, 1438, 1432, 1415, 1389, 1373, 1360, 1330, 1314, 1281, 1262, 1240, 1220, 1194, 1136, 1120, 1109, 1065, 1040, 1016, 962, 931, 868, 841, 811, 752, 728, 671.

**R<sub>f</sub>** = 0.8 (25% EtOAc/hexanes).

**4-(6-((4-fluorophenyl)diazenyl)pyridin-2-yl)morpholine (VIII.20)**

To a solution of 4-(6-chloro-3-nitropyridin-2-yl)morpholine (**VIII.15**) (100 mg, 0.411 mmol, 1.0 eq) in DMSO (5 mL) were added 4-fluorophenylhydrazine hydrochloride (201 mg, 1.23 mmol, 3.0 eq) and triethylamine (2.85 mL, 20.5 mmol, 50 eq) at room temperature. The reaction was heated to 95 °C. After 1.5 h, the orange reaction solution was allowed to cool down and then concentrated *in vacuo*. The crude product was purified *via* silica gel flash column chromatography (10 → 40% EtOAc/hexanes) to yield **VIII.20** (32.8 mg, 0.114 mmol, 28%) as dark orange solid.

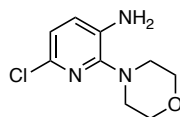
**<sup>1</sup>H NMR** (400 MHz, CDCl<sub>3</sub>) δ = 8.05 - 7.98 (m, 2H), 7.69 (t, *J* = 8.0 Hz, 1H), 7.24 - 7.16 (m, 2H), 7.09 (d, *J* = 7.5 Hz, 1H), 6.75 (d, *J* = 8.4 Hz, 1H), 3.89 - 3.83 (m, 4H), 3.67 - 3.62 (m, 4H).

**<sup>13</sup>C NMR** (100 MHz, CDCl<sub>3</sub>) δ = 165.0 (d, *J* = 253.2 Hz), 162.2, 159.4, 149.2, 139.6, 125.7 (d, *J* = 9.1 Hz), 116.2 (d, *J* = 23.0 Hz), 108.4, 103.9, 66.9, 45.6.

**Note:** for reasons of clarity, only *trans*-signals are reported.

**HRMS** (ESI): calcd. for C<sub>15</sub>H<sub>16</sub>FN<sub>4</sub>O [M+H]<sup>+</sup>: 287.1302, found: 287.1303.

**R<sub>f</sub>** = 0.13 (20% EtOAc/hexanes)

**6-chloro-2-morpholinopyridin-3-amine (VIII.16)**

To a solution of 4-(6-chloro-3-nitropyridin-2-yl)morpholine (**VIII.15**) (200 mg, 0.821 mmol, 1.0 eq) in dioxane/EtOH/H<sub>2</sub>O (2:1.5:1, 20 mL) were added iron powder (229 mg, 4.10 mmol, 5.0 eq) and NH<sub>4</sub>Cl (176 mg, 3.28 mmol, 4.0 eq) room temperature. The light-yellow suspension was stirred for 1.5 h at 70 °C, during which it turned green. The reaction was neutralized with sat. NaHCO<sub>3</sub> solution. The aq. phase was extracted with EtOAc (3 x 20 mL) and the combined organic layers were washed with sat. NaCl solution (25 mL), dried over Na<sub>2</sub>SO<sub>4</sub> and concentrated *in vacuo*. The crude purple product was purified by silica gel flash column chromatography (0 → 0.6 → 1% MeOH/DCM) to yield 6-chloro-2-morpholinopyridin-3-amine (**VIII.16**) (133 mg, 0.622 mmol, 76%) as white solid.

**<sup>1</sup>H-NMR:** (400 MHz, CDCl<sub>3</sub>) δ = 6.91 (d, J = 8.0 Hz, 1H), 6.83 (d, J = 8.1 Hz, 1H), 3.86 - 3.80 (m, 4H), 3.75 (s, 2H), 3.15 - 3.09 (m, 4H).

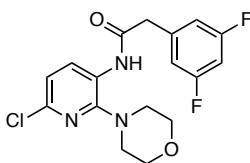
**<sup>13</sup>C-NMR:** (100 MHz, CDCl<sub>3</sub>) δ = 150.1, 137.7, 134.2, 124.7, 119.3, 67.2, 49.0.

**HRMS (ESI):** calcd. for C<sub>9</sub>H<sub>13</sub>ClN<sub>3</sub>O [M+H]<sup>+</sup>: 214.0742, found: 214.0743.

**R<sub>f</sub>** = 0.3 (40% EtOAc/hexanes)

**R<sub>t</sub>** = 5.91 min (5 → 100% MeCN/H<sub>2</sub>O; + 0.1% FA; 5 min)

**N-(6-chloro-2-morpholinopyridin-3-yl)-2-(3,5-difluorophenyl)-acetamide  
(VIII.18)**



2-(3,5-difluorophenyl)acetic acid (**VIII.17**) (123 mg, 0.576 mmol, 4.0 eq) was dissolved in DMF (3.0 mL) and TBTU (924 mg, 2.87 mmol, 5.0 eq) and triethylamine (742  $\mu$ L, 3.45 mmol, 5.0 eq) were added at room temperature. The solution was stirred for 30 min, before it was slowly added to a solution of 6-chloro-2-morpholinopyridin-3-amine (**VIII.16**) (123 mg, 0.576 mmol, 1.0 eq) in DMF (3.0 mL). The pale-yellow solution was stirred at room temperature overnight, before addition of  $\text{NaHCO}_3$  solution (20 mL). The aqueous phase was extracted with EtOAc (3 x 50 mL) and the combined organic layers were washed sat.  $\text{NaHCO}_3$  (2 x 50 mL) and sat. NaCl (50 mL), dried over  $\text{Na}_2\text{SO}_4$  and concentrated *in vacuo*. The crude product was purified by silica gel flash column chromatography (20% EtOAc/hexanes) to yield **VIII.18** (131 mg, 0.356 mmol, 62%) as colorless solid.

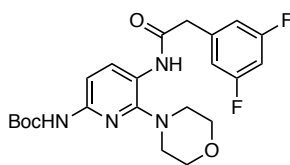
**$^1\text{H-NMR}$**  (400 MHz,  $\text{CDCl}_3$ )  $\delta$  = 8.60 (d,  $J$  = 8.5 Hz, 1H), 7.87 (s, 1H), 7.08 (d,  $J$  = 8.5 Hz, 1H), 6.96 - 6.82 (m, 3H), 3.77 (s, 2H), 3.65 - 3.55 (m, 4H), 2.93 - 2.83 (m, 4H).

**$^{13}\text{C NMR}$**  (100 MHz,  $\text{CDCl}_3$ )  $\delta$  = 163.6 (dd,  $J$  = 251.0, 12.8 Hz), 151.9, 143.8, 137.6 (t,  $J$  = 9.2 Hz), 130.4, 126.5, 120.9, 112.8 (dd,  $J$  = 18.4, 7.0 Hz), 103.9 (t,  $J$  = 25.0 Hz), 66.7, 50.5, 44.8.

**HRMS** (ESI): calcd. for  $\text{C}_{17}\text{H}_{15}\text{ClF}_2\text{N}_3\text{O}_2^-$  [ $\text{M-H}$ ]: 366.0826, found: 366.0828.

**$R_f$**  = 0.4 (40% EtOAc/hexanes)

**$R_t$**  = 7.71 min (5  $\rightarrow$  100% MeCN/ $\text{H}_2\text{O}$ ; + 0.1% FA; 5 min)

**tert-butyl (5-(2-(3,5-difluorophenyl)acetamido)-6-morpholinopyridin-2-yl)-carbamate (VIII.21)**

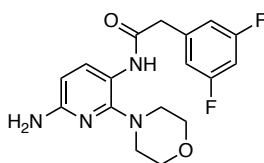
<sup>t</sup>BuOH (5 mL) was degassed and backfilled with argon three times. To a pressure tube, **VIII.18** (204 mg, 0.555 mmol, 1.0 eq), <sup>t</sup>BuNH<sub>2</sub> (65.0 mg, 0.55 mmol, 1.0 eq), Cs<sub>2</sub>CO<sub>3</sub> (253 mg, 0.777 mmol, 1.4 eq), XPhos (13.2 mg, 277 μmol, 0.05 eq) and XPhosPd3G (47.0 mg, 55.5 μmol, 0.1 eq) were added sequentially. The tube was sealed and the reaction was heated to 110 °C for 4 h. The reaction was allowed to cool down to room temperature and diluted with EtOAc (20 mL). The organic layer was washed with sat. NaHCO<sub>3</sub> (2 x 10 mL) and sat. NaCl (1 x 10 mL), dried over Na<sub>2</sub>SO<sub>4</sub> and all volatiles were removed under reduced pressure. The crude material was purified by silica gel flash column chromatography (20% EtOAc/hexanes) to yield **VIII.21** (174 mg) as colorless solid contaminated with inseparable impurities. It was used without further purification for the next step.

**<sup>1</sup>H NMR** (400 MHz, DMSO-*d*<sub>6</sub>) δ = 9.41 (s, 1H), 9.30 (s, 1H), 7.75 (d, *J* = 8.5 Hz, 1H), 7.31 (d, *J* = 8.5 Hz, 1H), 7.15 (t, *J* = 9.4 Hz, 1H), 7.08 (d, *J* = 6.8 Hz, 2H), 3.72 (s, 2H), 3.66 - 3.59 (m, 4H), 3.02 - 2.94 (m, 4H), 1.45 (s, 9H).

**HRMS** (ESI): calcd. for C<sub>22</sub>H<sub>27</sub>F<sub>2</sub>N<sub>4</sub>O<sub>4</sub> [M+H]<sup>+</sup>: 449.1995, found: 449.1996.

**R<sub>f</sub>** = 0.32 (40% EtOAc/hexanes)

**R<sub>t</sub>** = 6.7 min (10 → 100% MeCN/H<sub>2</sub>O; +0.1% FA; 7 min)

***N*-(6-amino-2-morpholinopyridin-3-yl)-2-(3,5-difluorophenyl)acetamide  
(VIII.22)**

**VIII.22** (118 mg, 0.263 mmol, 1.0 eq) was dissolved in DCM (5.0 mL) and TFA (5.0 mL) was added at room temperature. The reaction mixture was stirred for 30 min. The reaction was basified to pH = 10 with NaOH (1 M) and the mixture was extracted with EtOAc (3 x 25 mL). The combined organic layers were washed with sat. NaHCO<sub>3</sub> (1 x 30 mL) and sat. NaCl (1 x 30 mL), dried over Na<sub>2</sub>SO<sub>4</sub> and all volatiles were removed under reduced pressure. The crude material was purified by silica gel flash column chromatography (50 → 80% EtOAc/hexanes) to yield **VIII.22** (82.0 mg, 0.235 mmol, 63% over two steps) as a white solid.

**<sup>1</sup>H NMR** (400 MHz, DMSO-*d*<sub>6</sub>) δ = 9.04 (s, 1H), 7.34 (d, *J* = 8.4 Hz, 1H), 7.19 - 7.10 (m, 1H), 7.06 (d, *J* = 6.7 Hz, 2H), 6.04 (d, *J* = 8.4 Hz, 1H), 5.70 (s, 2H), 3.65 (s, 2H), 3.61 - 3.55 (m, 4H), 2.92 - 2.86 (m, 4H).

**<sup>13</sup>C NMR** (100 MHz, DMSO-*d*<sub>6</sub>) δ = 167.9, 162.2 (dd, *J* = 245.8, 13.5 Hz) 156.1, 154.2, 140.5 (t, *J* = 9.8 Hz), 136.9, 112.9, 112.3 (dd, *J* = 18.3, 6.6 Hz), 102.2 (t, *J* = 25.6 Hz), 101.0, 66.1, 49.1, 42.2.

**HRMS** (ESI): calcd. for C<sub>17</sub>H<sub>19</sub>F<sub>2</sub>N<sub>4</sub>O<sub>2</sub> [M+H]<sup>+</sup> = 348.1471, found: 349.1475.

**R<sub>f</sub>** = 0.45 (100% EtOAc)

**R<sub>t</sub>** = 2.6 min (10 → 100% MeCN/H<sub>2</sub>O; +0.1% FA; 7 min)







## IX. Appendix



## General List of Abbreviations

®	registered
°C	degree Celsius
Alpha2A	alpha-2A adrenergic receptor
aq.	aqueous
atm	atmosphere
AR	adenosine receptors
br	broad (IR)
calc	calculated
Cbz	carboxybenzyl
CNS	central nervous system
cAMP	Cyclic Adenosine Monophosphate
COSY	homonuclear correlation spectroscopy (NMR)
d	doublet (NMR)
DAT	Dopamine transporter
DCM	dichlormethane
DMSO	dimethyl sulfoxide
eq	equivalent(s)
ESI	electron spray ionisation (MS)
FA	formic acid
FDA	Food and Drug Administration
GABA	γ-aminobutyric acid
GIRK	G Protein-Coupled Inwardly Rectifying Potassium Channel
h	hour(s)
5-HT <sub>2</sub>	5-Hydroxytryptamine receptor 2
HMBC	heteronuclear multiple bond coherence (NMR)
HPLC	high performance liquid chromatography
HRMS	high resolution mass spectroscopy
HSQC	heteronuclear single quantum coherence (NMR)
IR	infrared

---

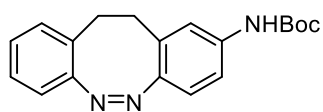
J	coupling constants
K <sub>v</sub>	voltage-gated ion channels
LC	liquid chromatography
m	medium (IR), multiplet (NMR)
M	molar
MHz	megahertz
min	minute(s)
MS	mass spectroscopy
MW	molecular weight
NET	norepinephrine transporter
NMR	nuclear magnetic resonance spectroscopy
Na <sub>v</sub>	Voltage-Gated Sodium Channel
o.n.	overnight
P2X	ATP-Gated Purinoreceptor
ppm	parts per million (NMR)
q	quartet (NMR)
r.t.	room temperature
R <sub>f</sub>	retardation factor
RP	reverse phase
R <sub>t</sub>	retention time
s	singlet (NMR)
sat.	saturated
t	triplet (NMR)
T	temperature
TBTA	Tris(benzyltriazolylmethyl)amine
TEA	triethylamine or tetraethylammonium
TFA	trifluoroacetic acid
THF	tetrahydrofuran
TLC	thin-layer-chromatography
TM	transmembrane
™	Unregistered trademark

TMS	trimethylsilane
TMSCl	trimethylsilyl chloride
TMSI	trimethylsilyl iodide
Trp	tryptophan
TRP	Transient Receptor Potential
UV	ultraviolet
Vis	visible
w	weak (IR)
$\delta$	chemical shift (NMR)

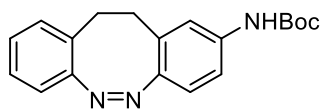
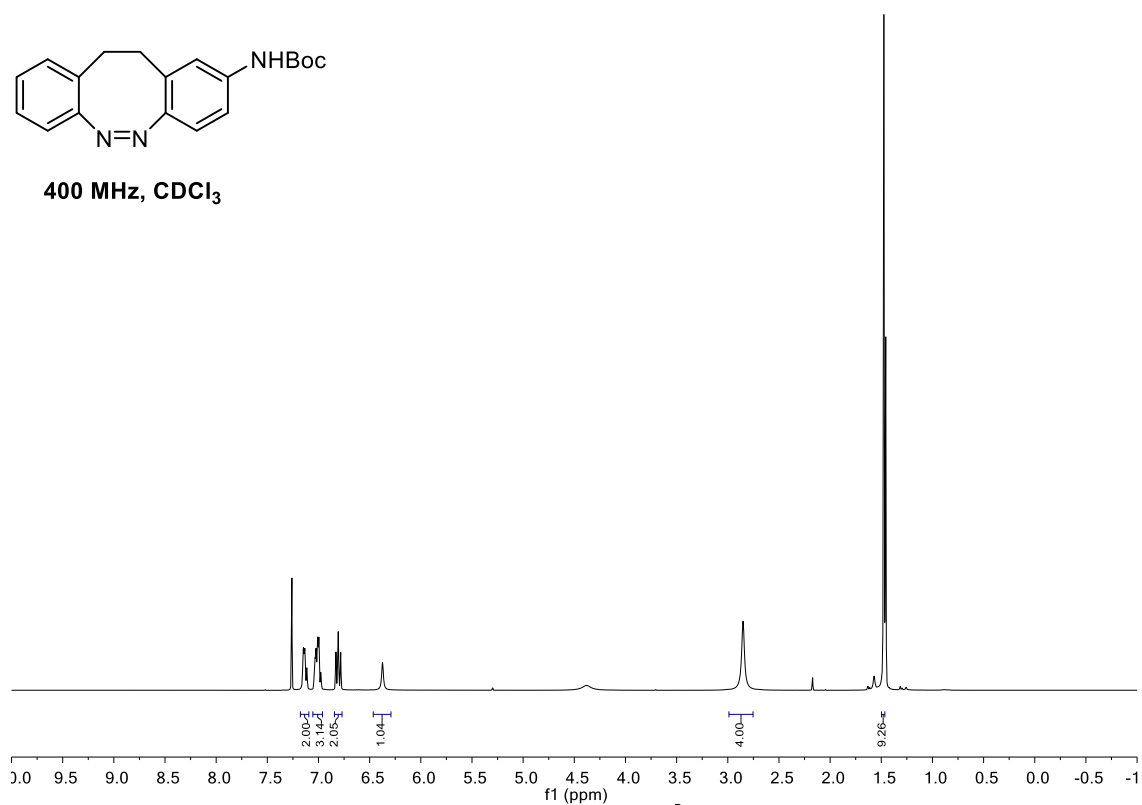




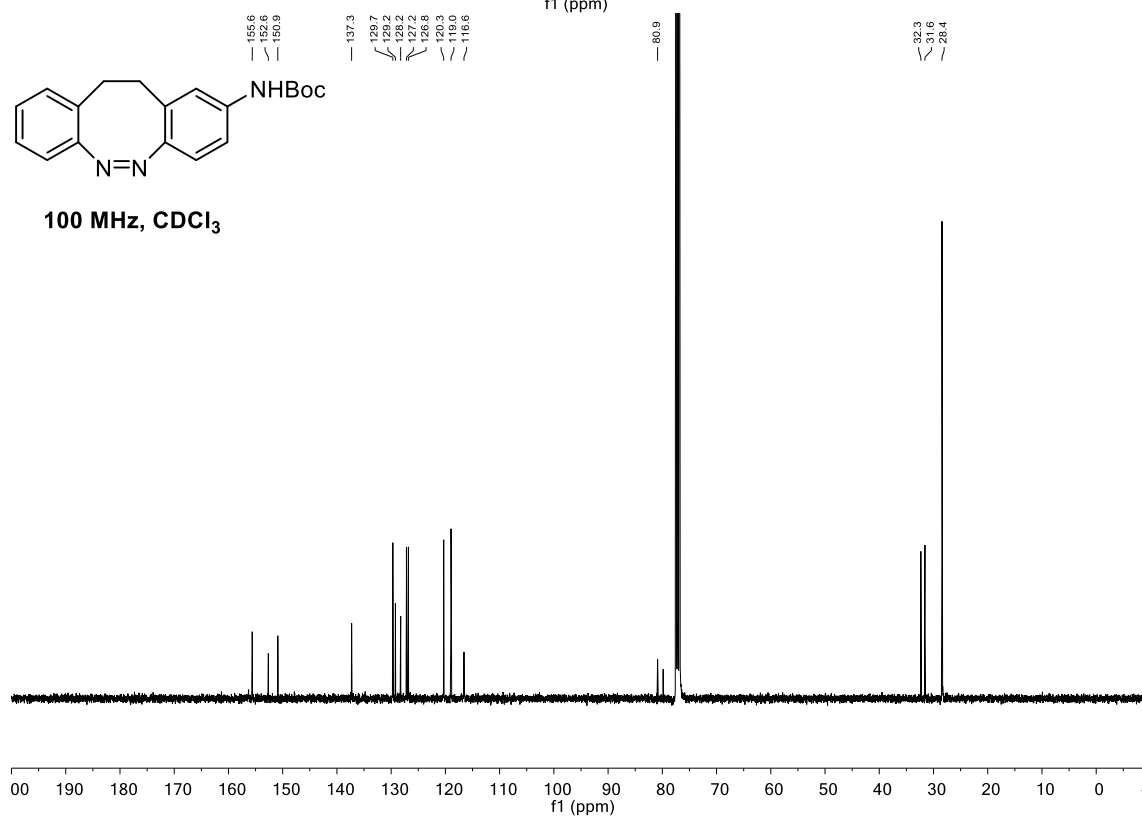
## NMR Spectra

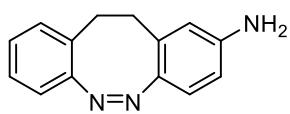


400 MHz, CDCl<sub>3</sub>

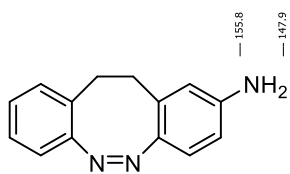
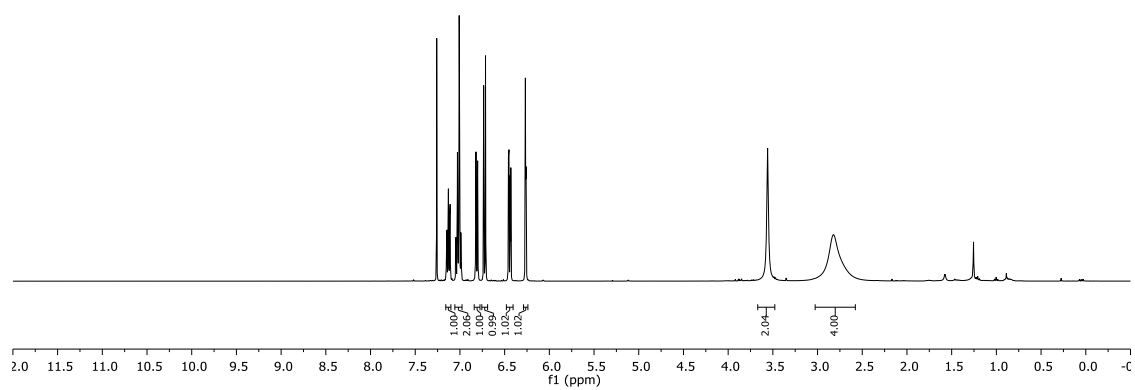


100 MHz, CDCl<sub>3</sub>

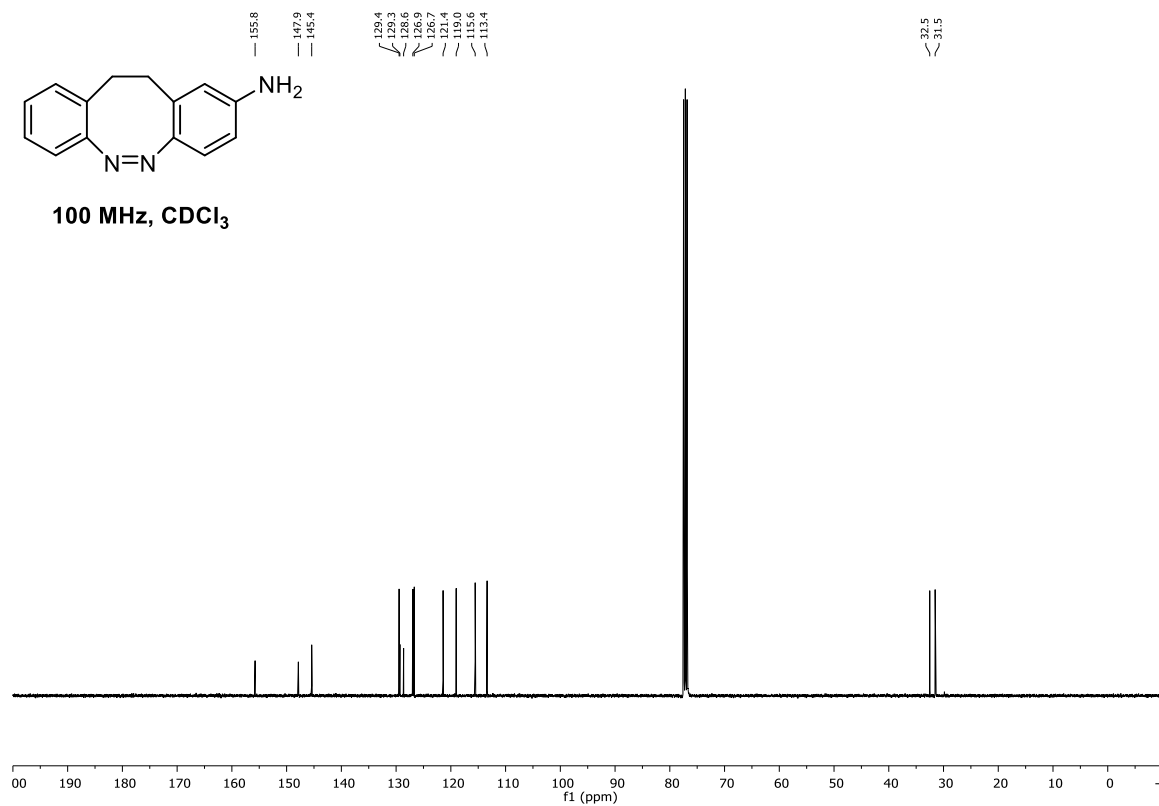


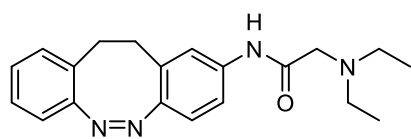
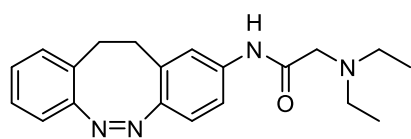
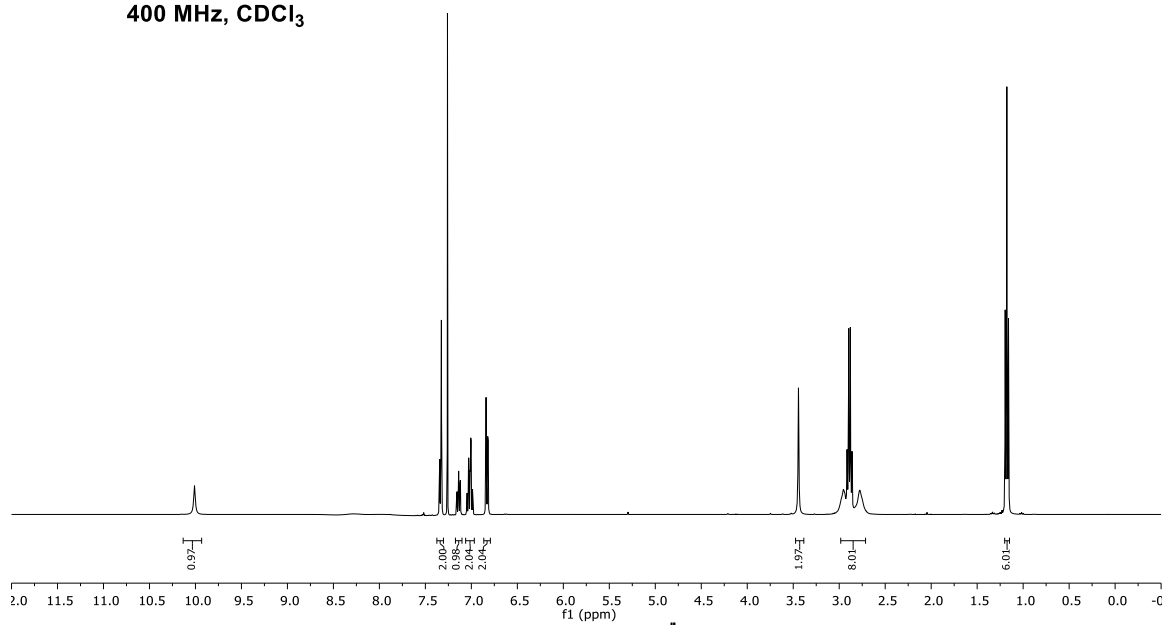
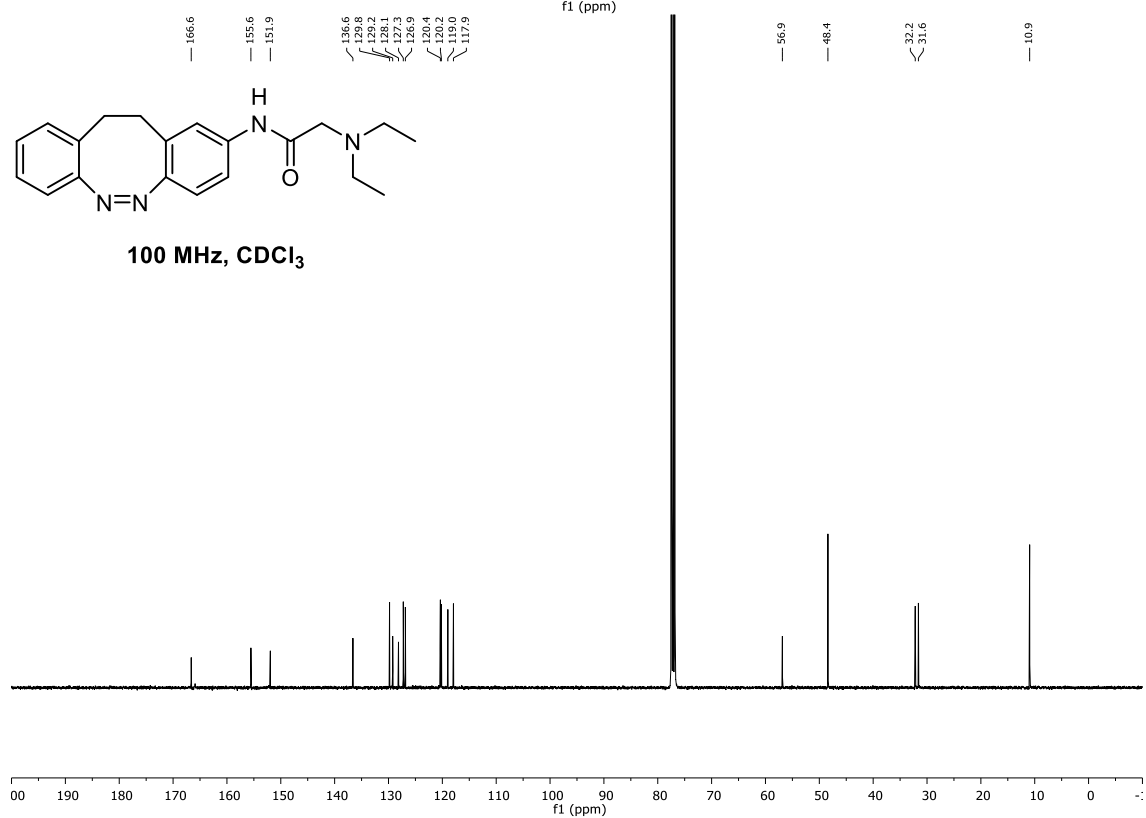


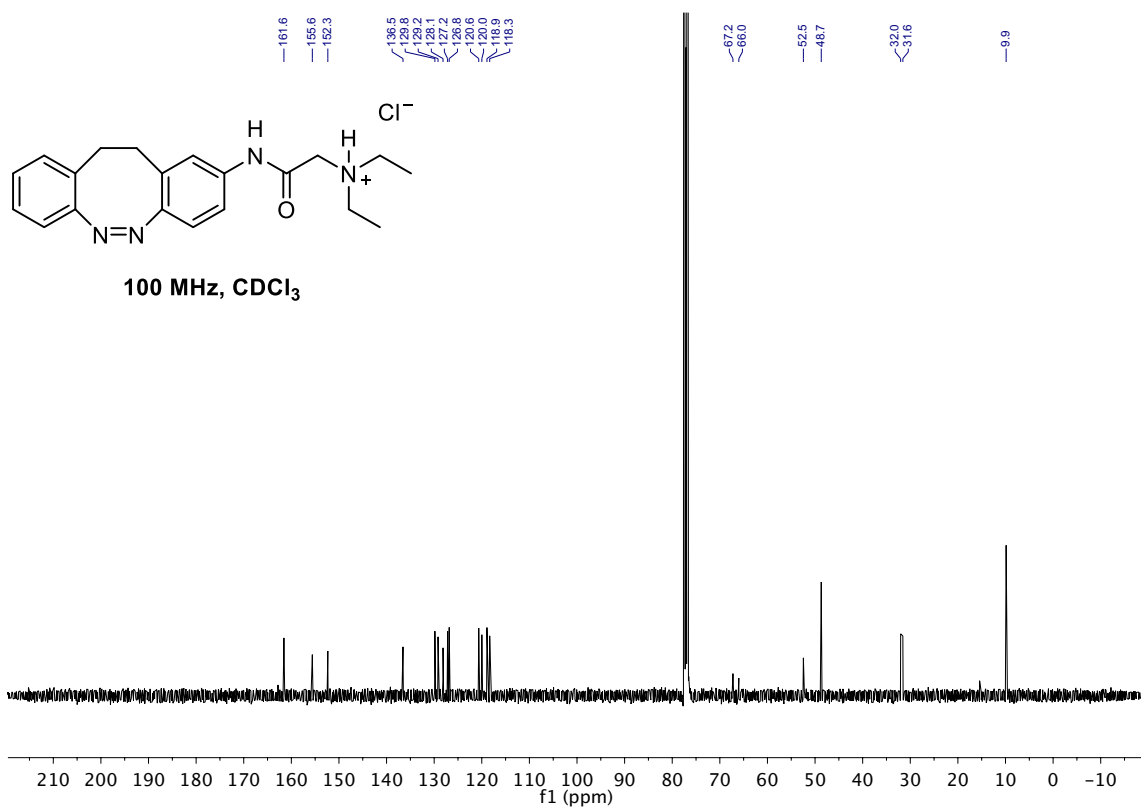
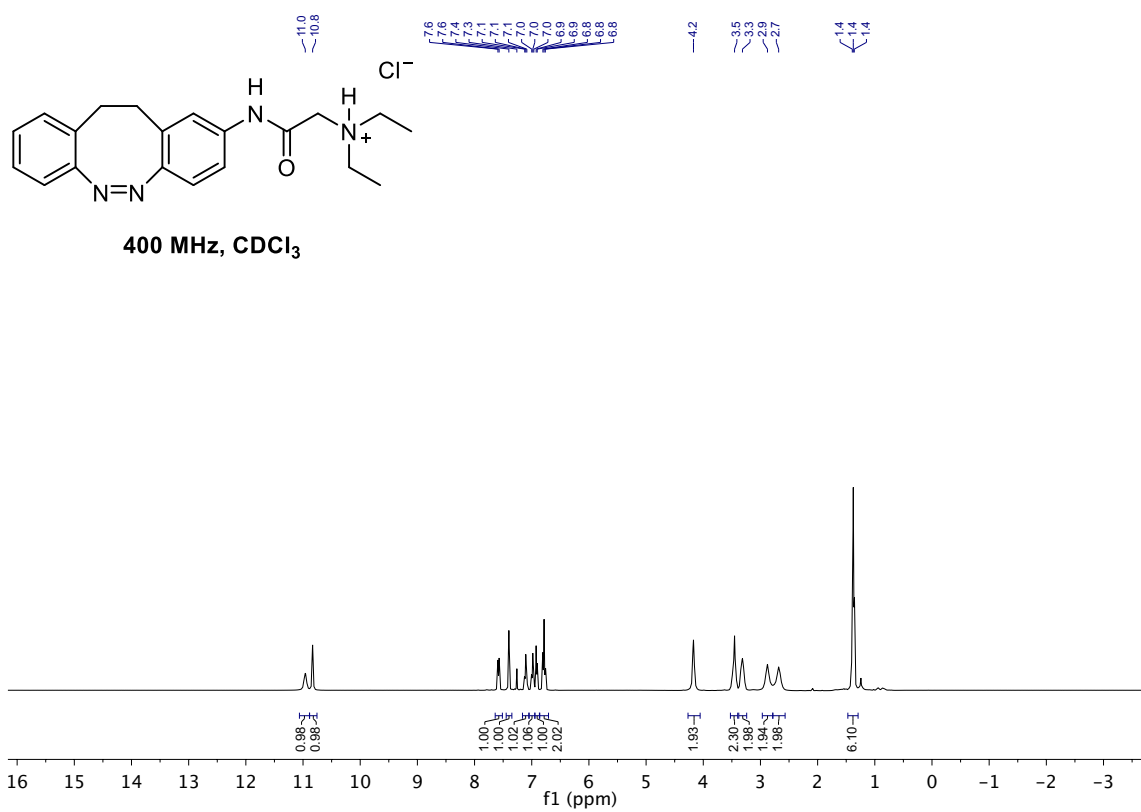
400 MHz, CDCl<sub>3</sub>

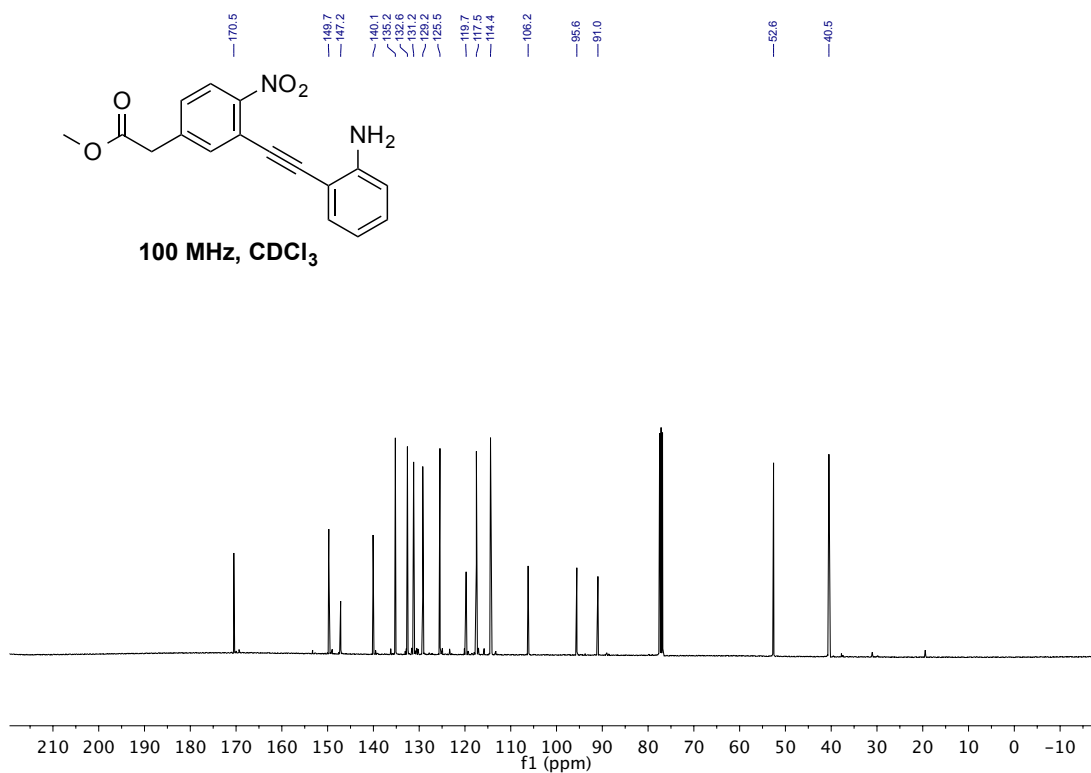
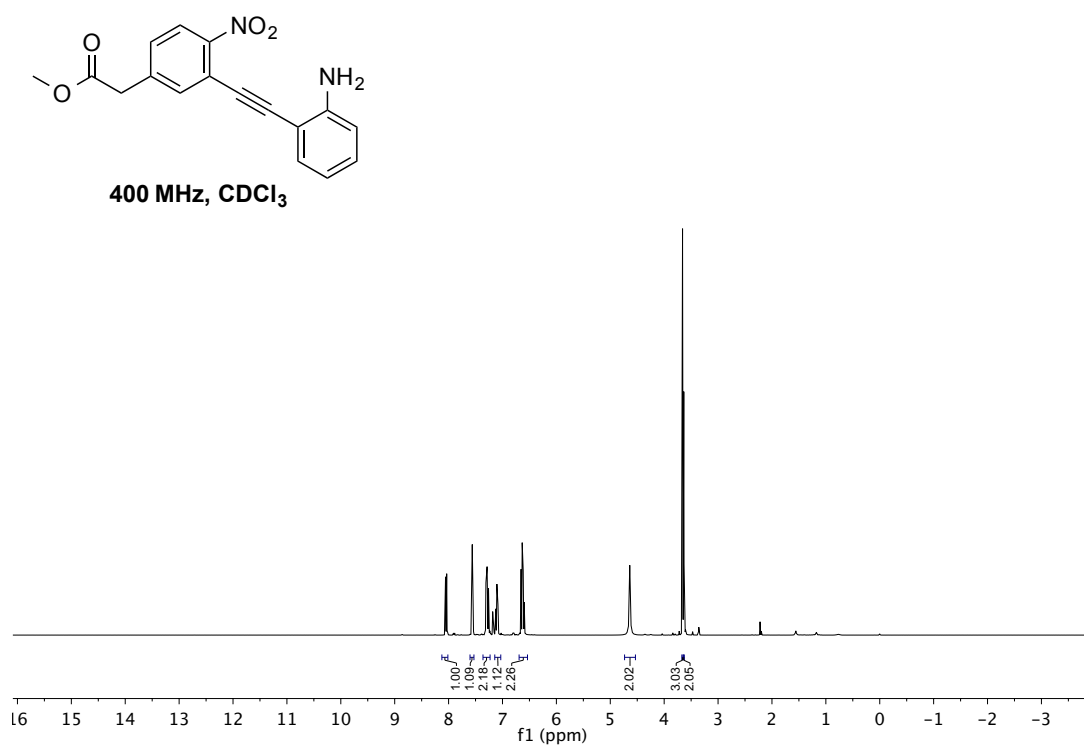


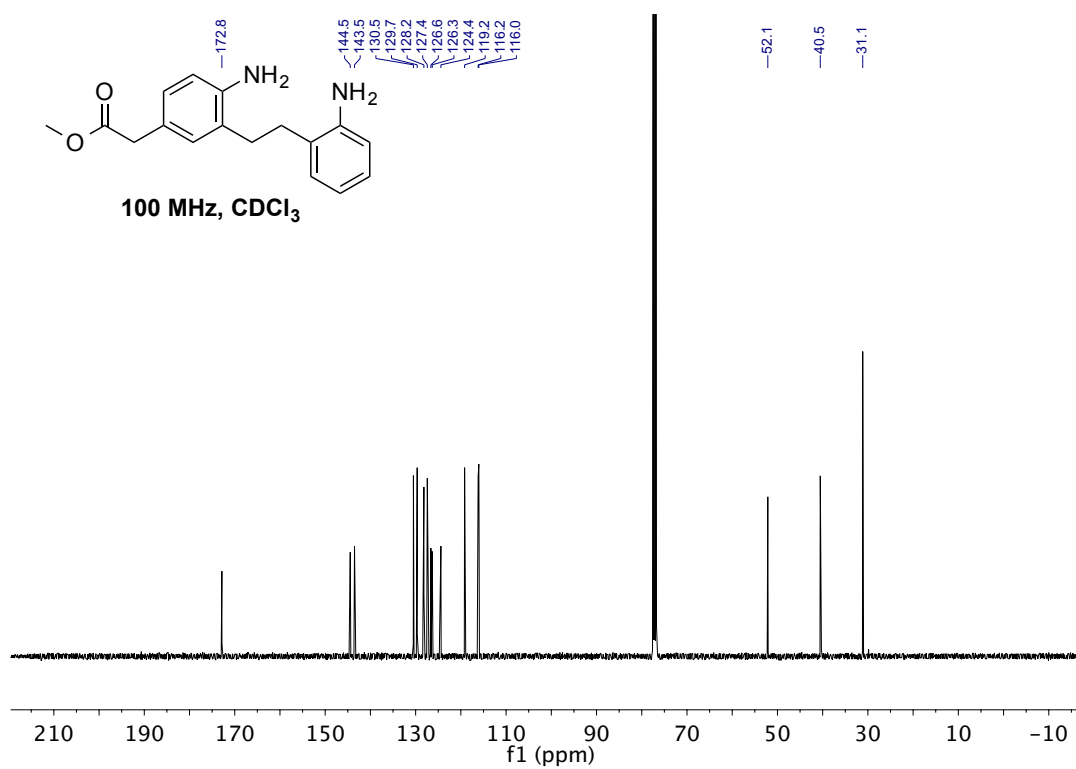
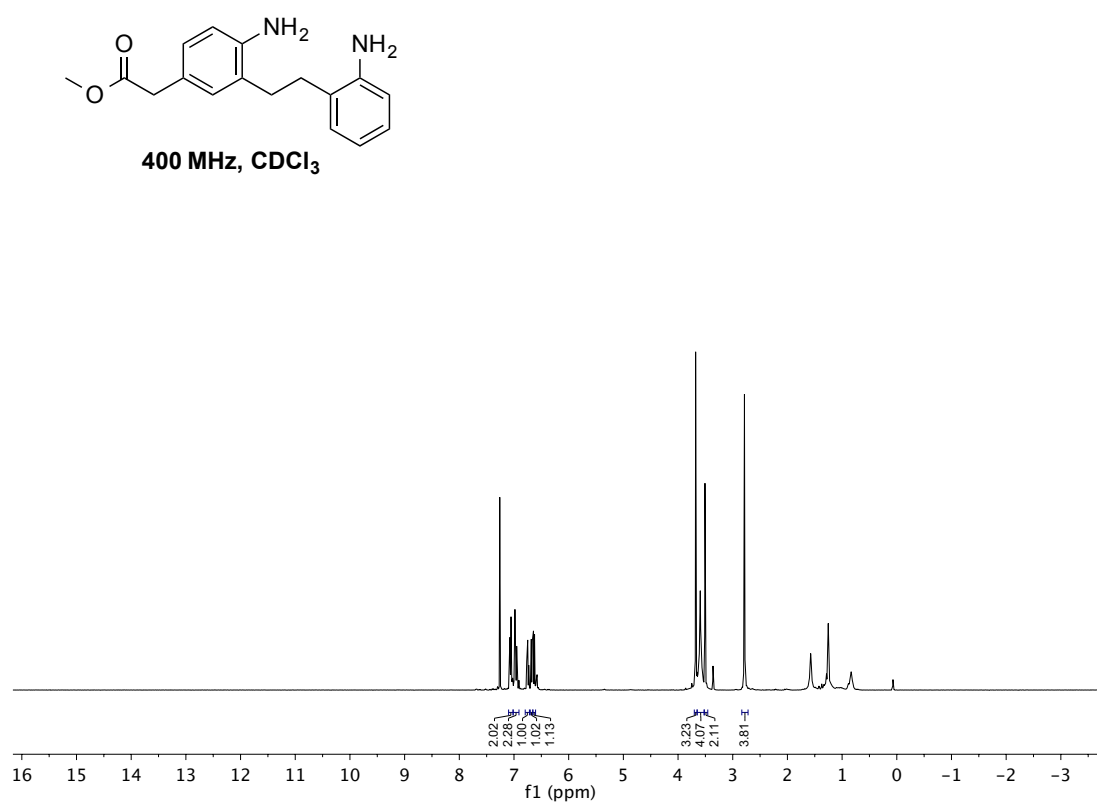
100 MHz, CDCl<sub>3</sub>

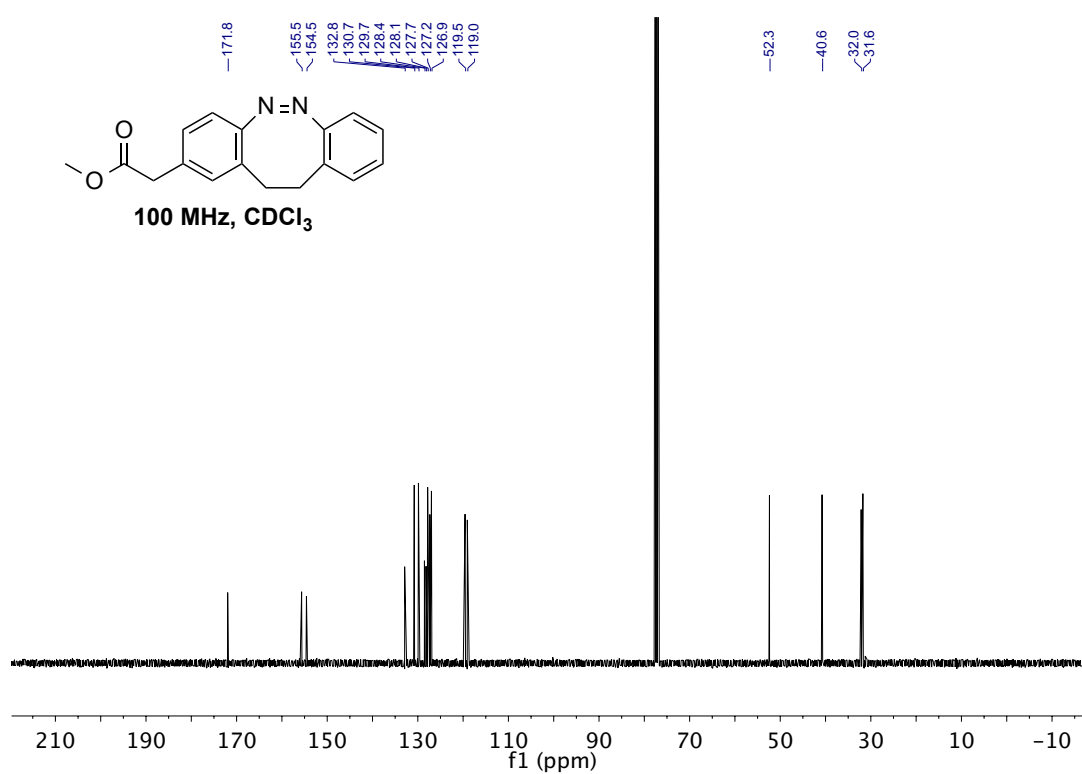
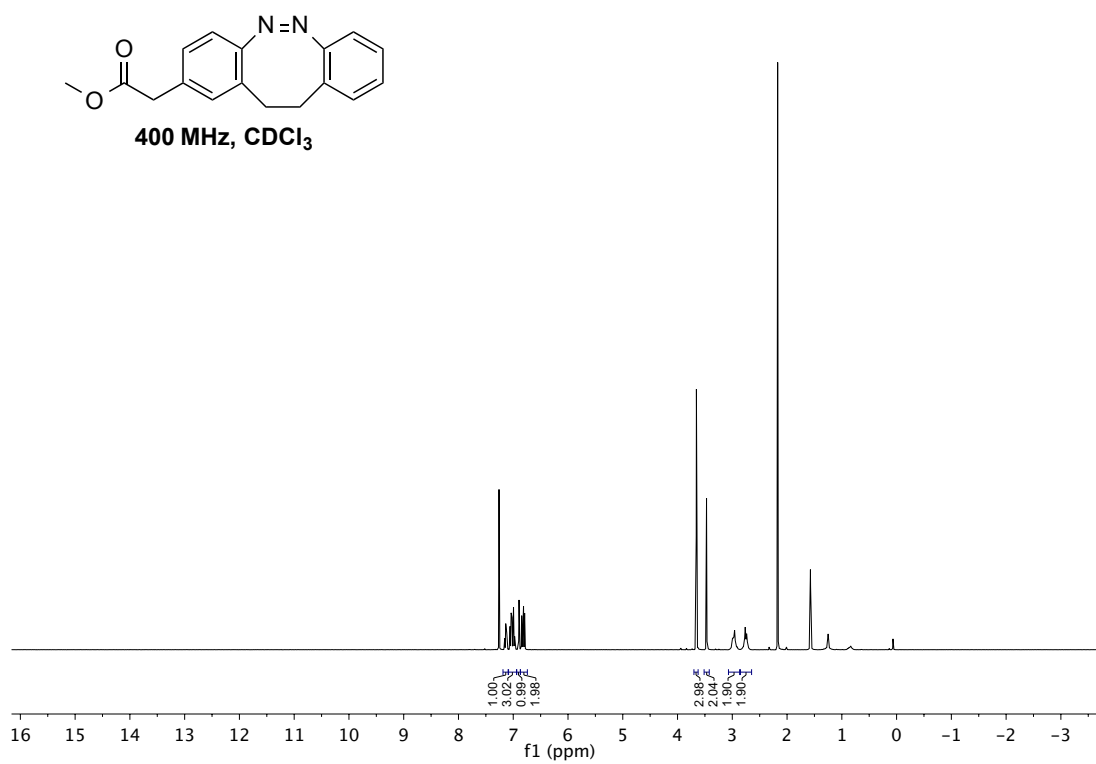


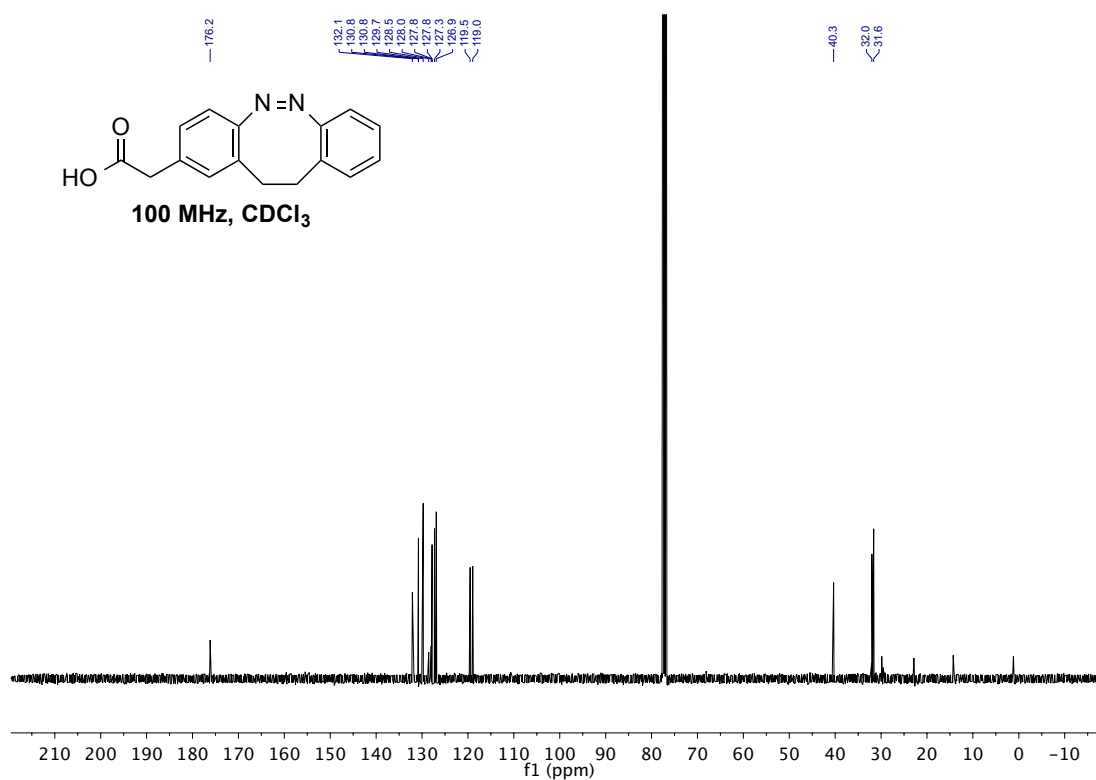
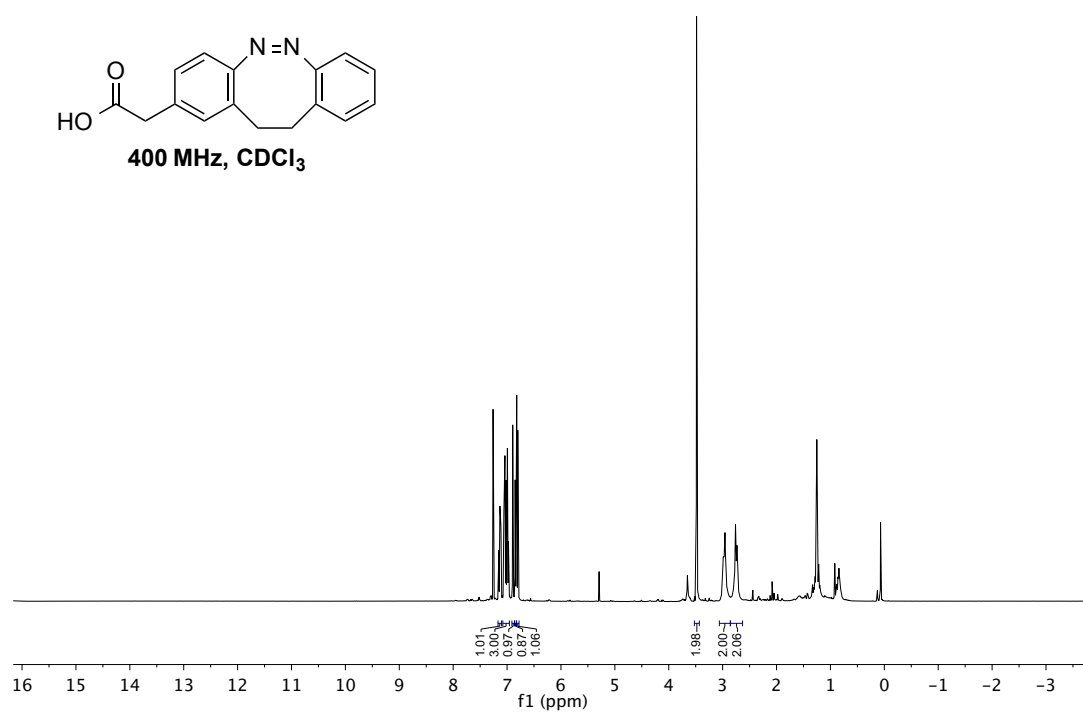
400 MHz, CDCl<sub>3</sub>100 MHz, CDCl<sub>3</sub>



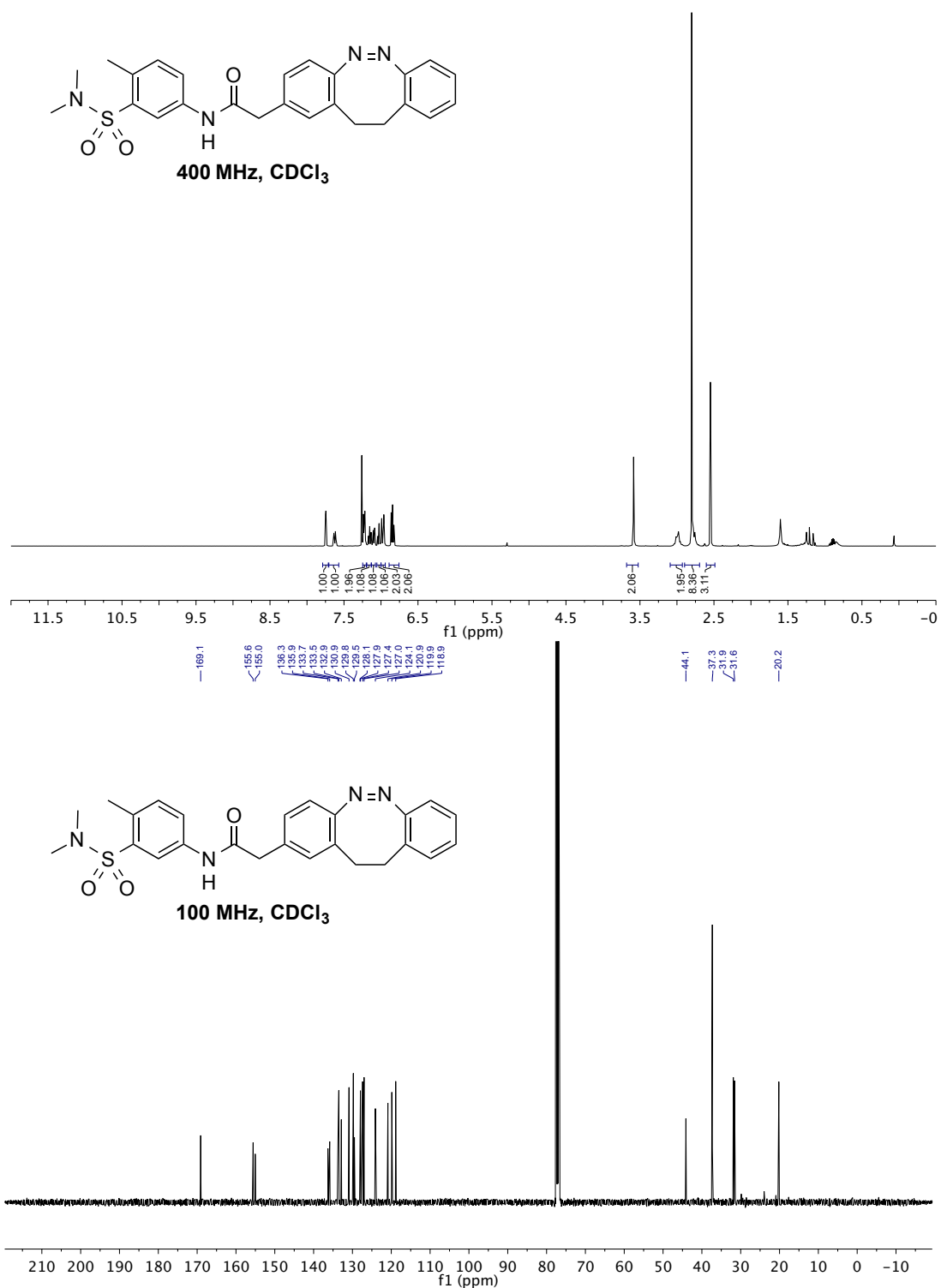


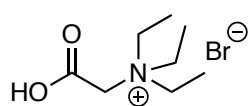




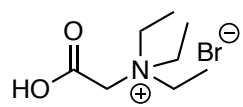
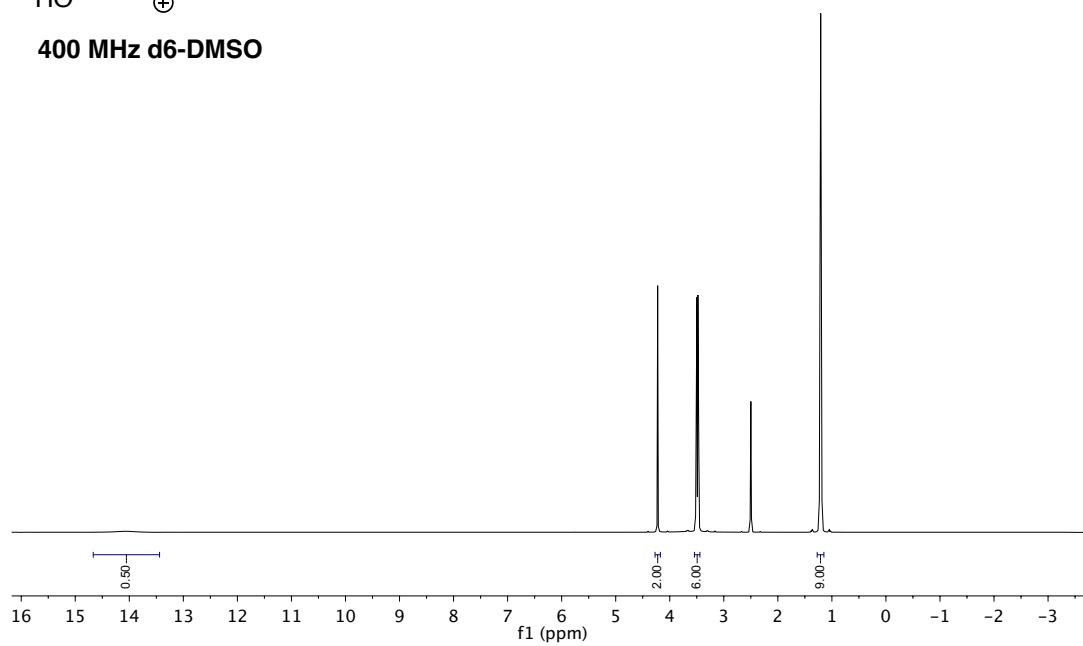




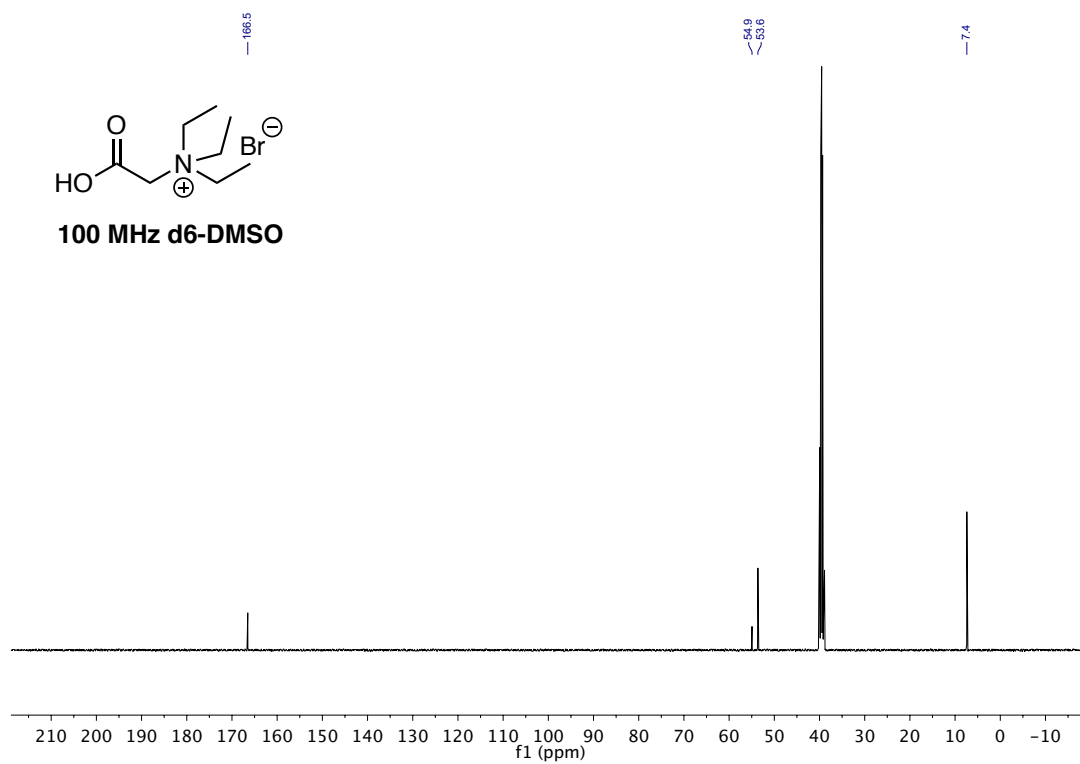


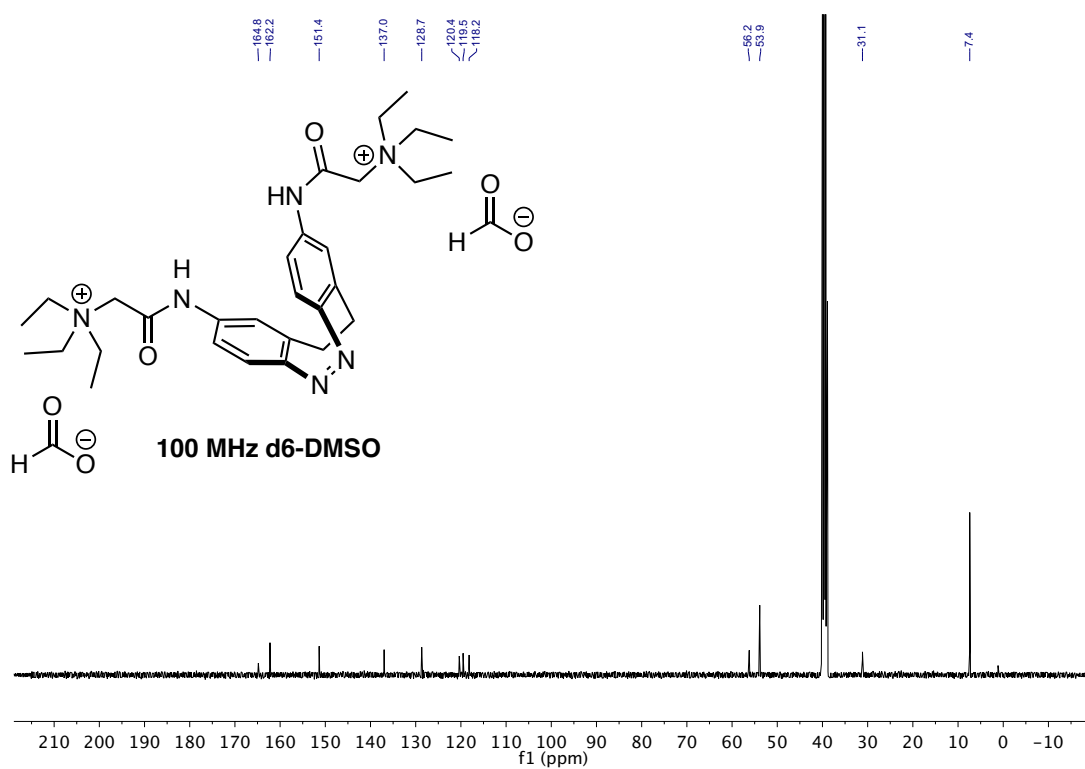
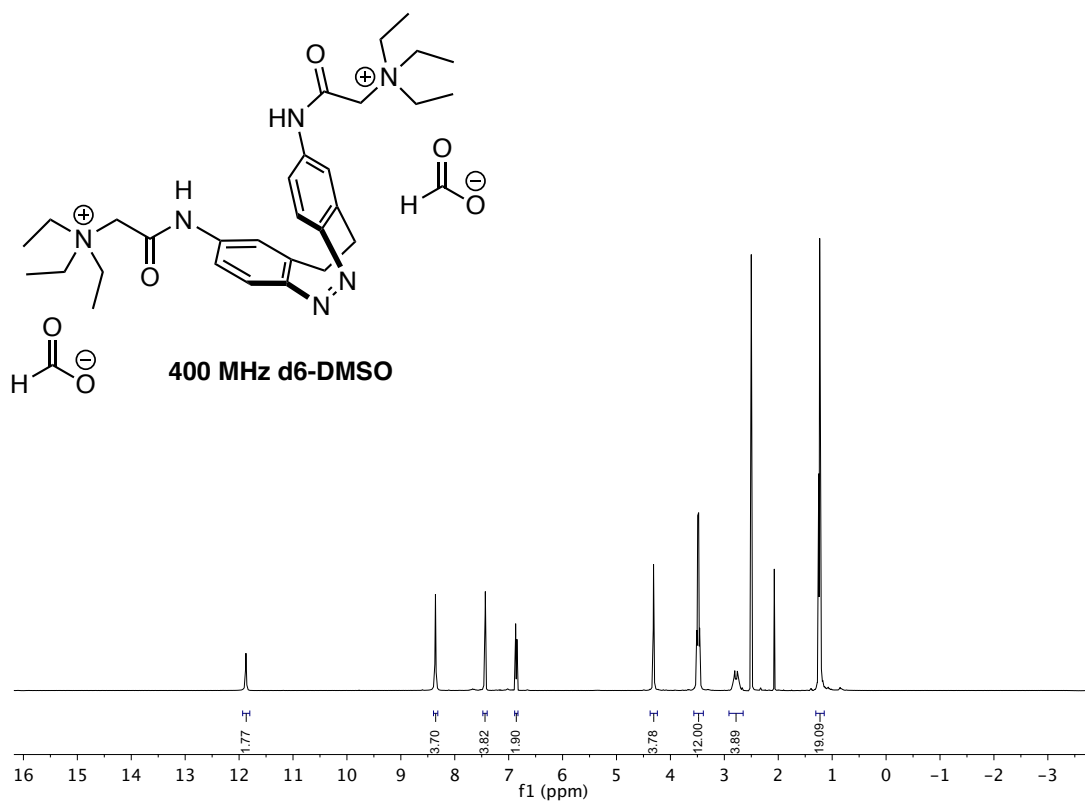


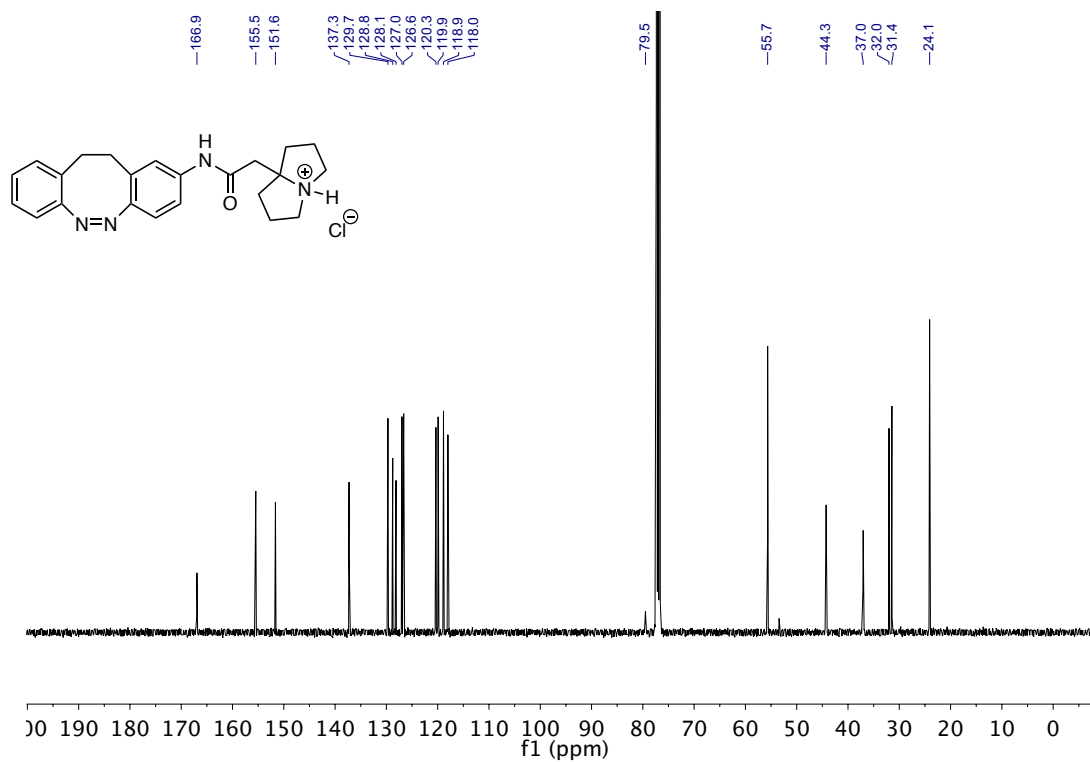
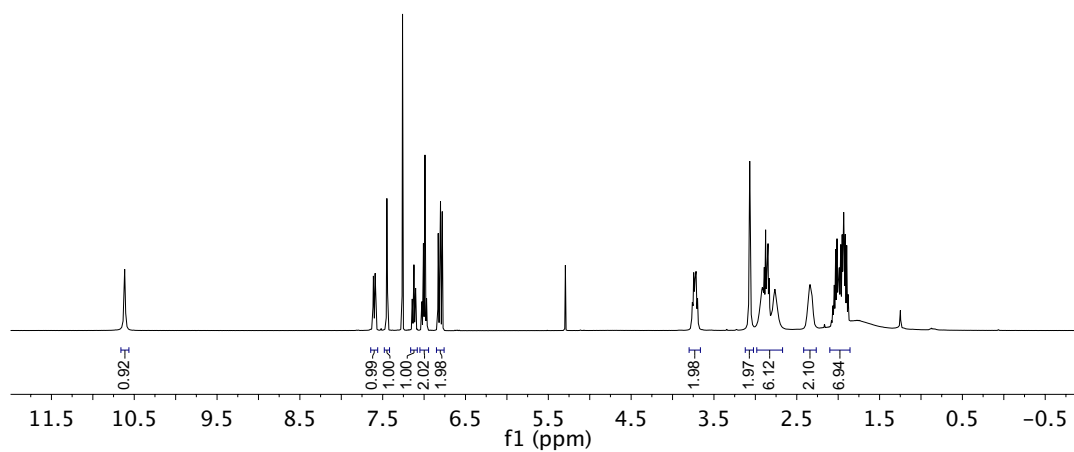
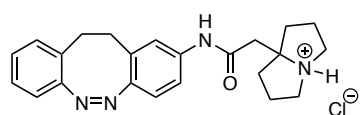
400 MHz d6-DMSO

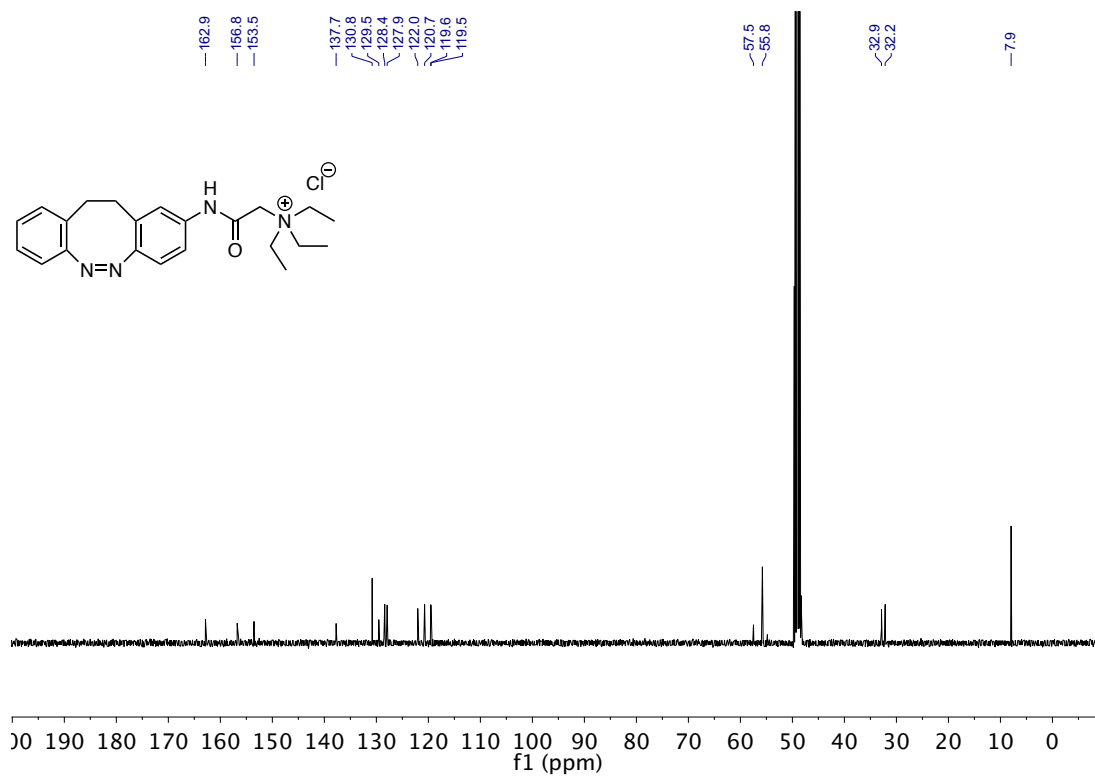
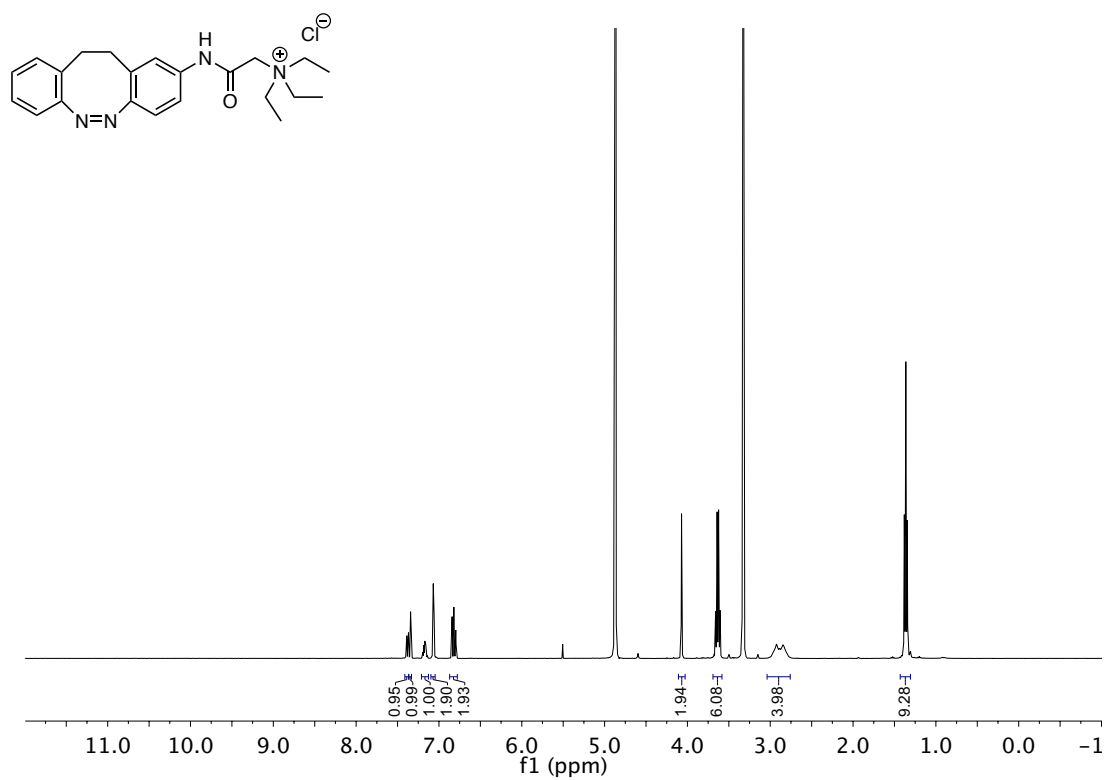


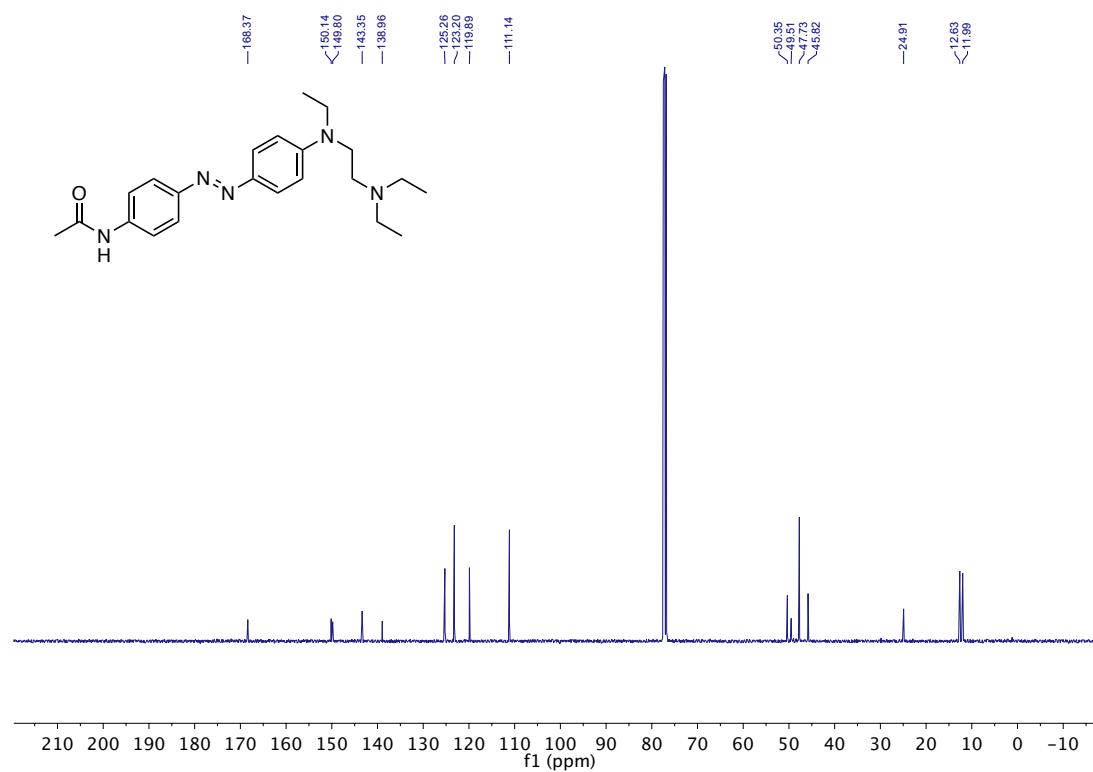
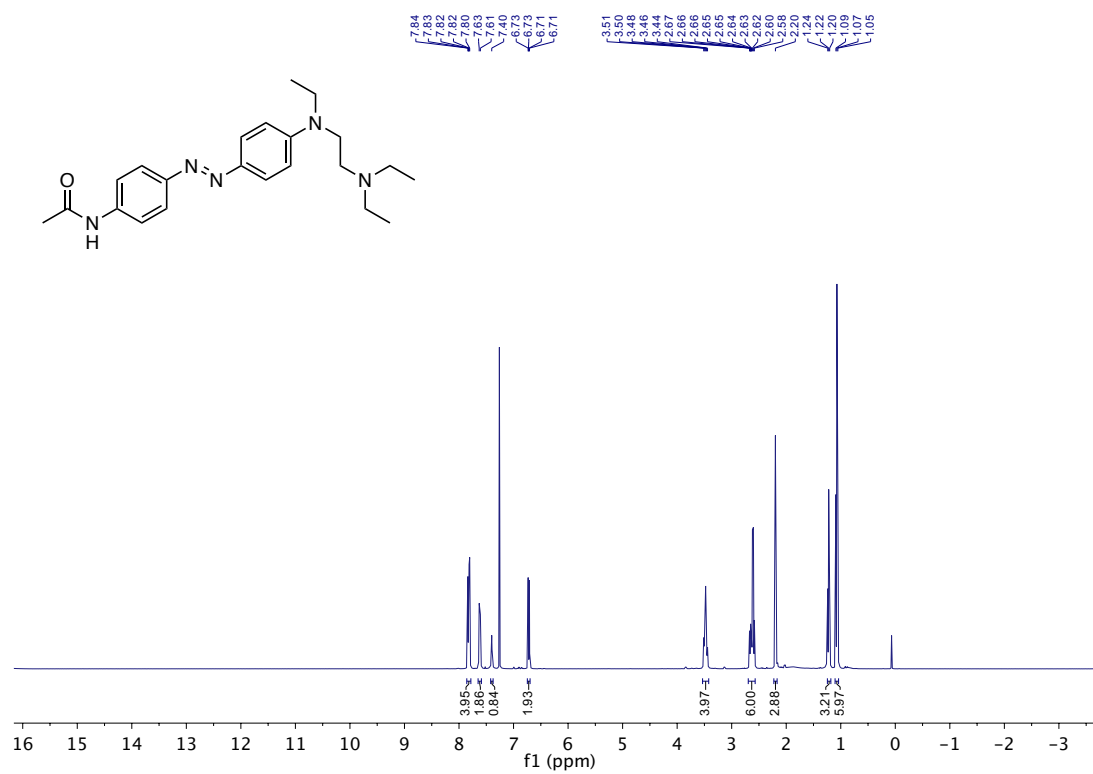
100 MHz d6-DMSO

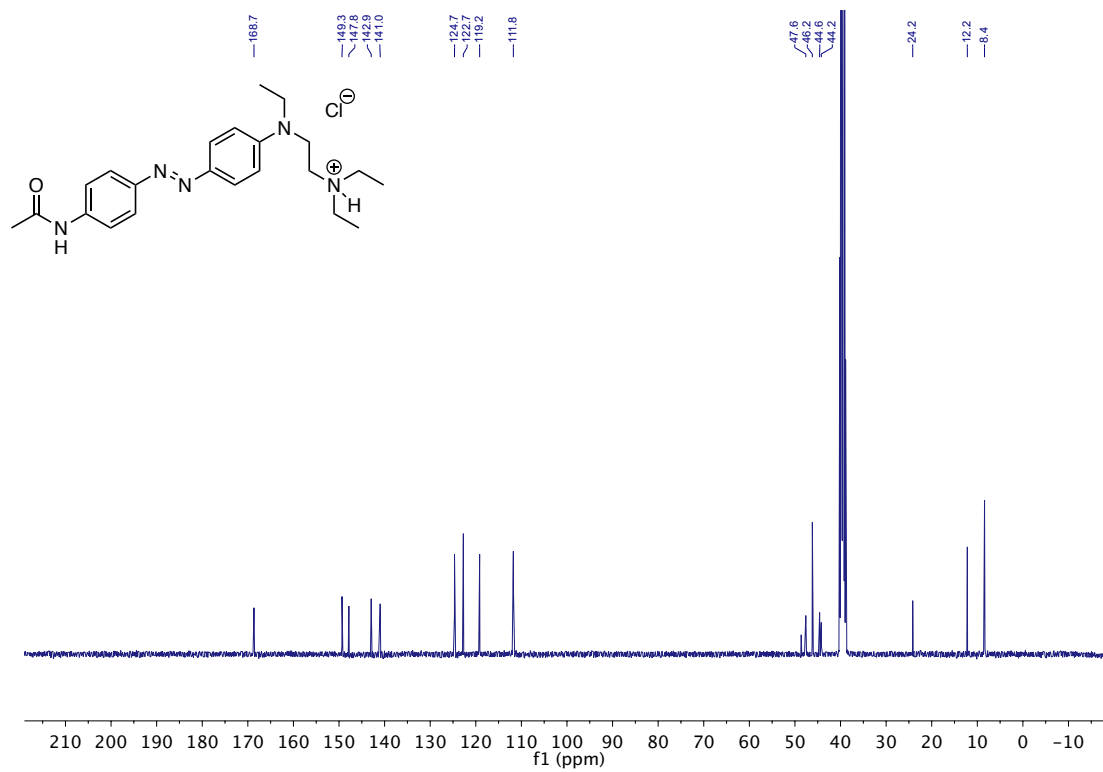
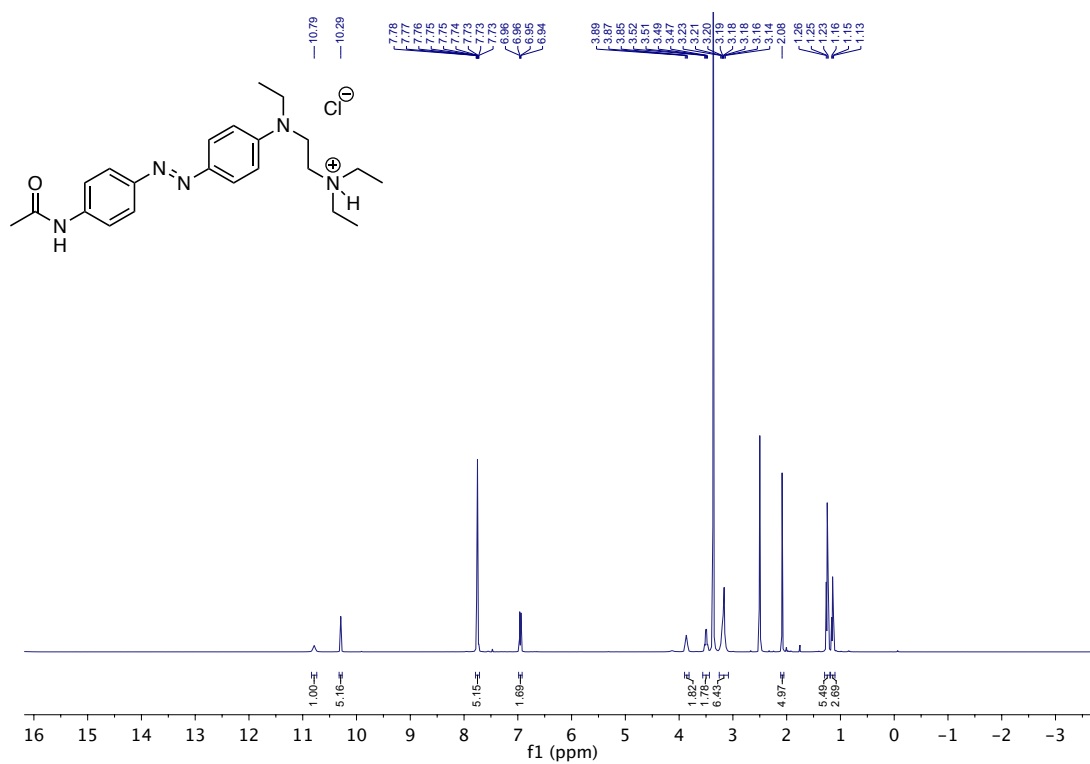


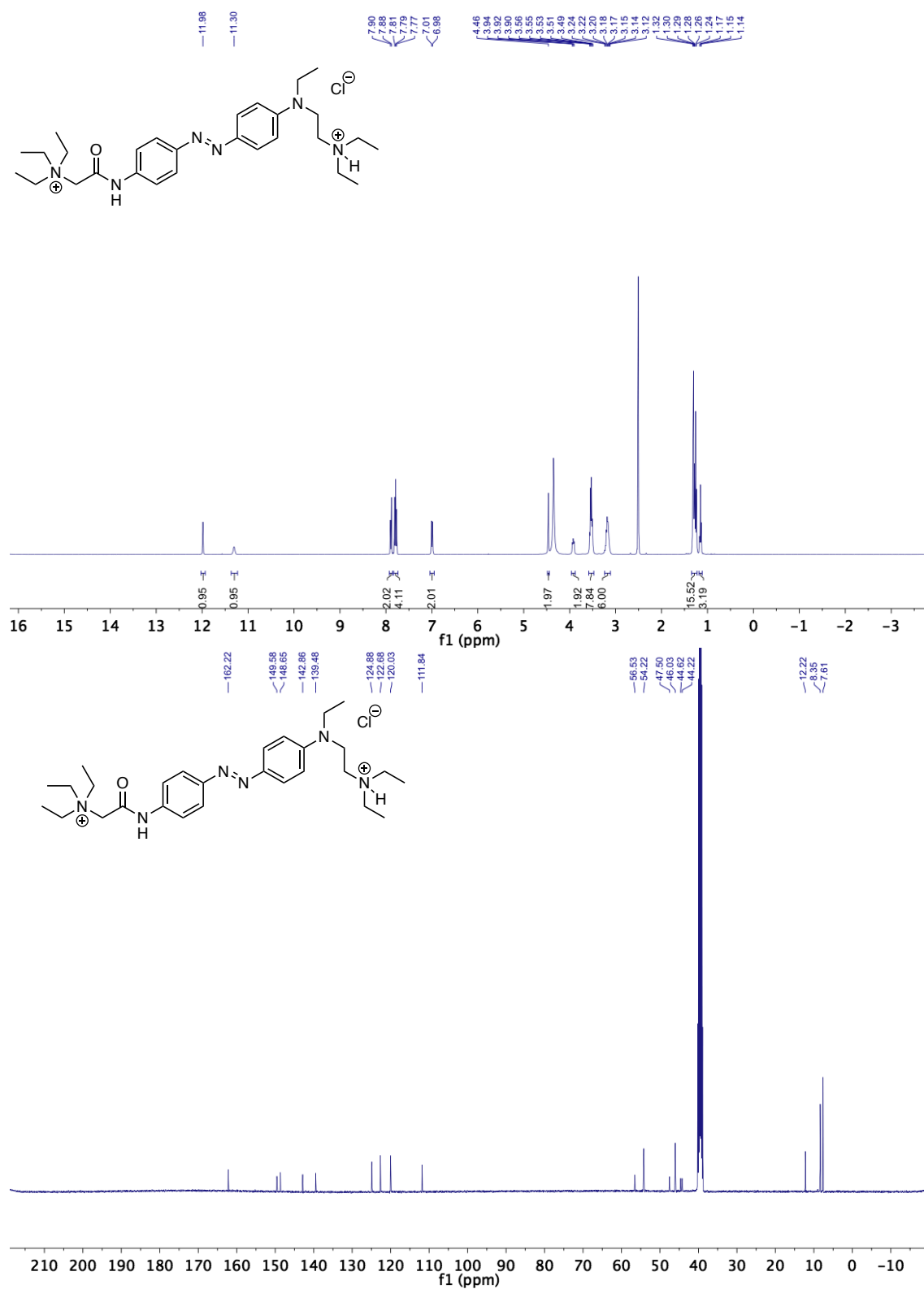




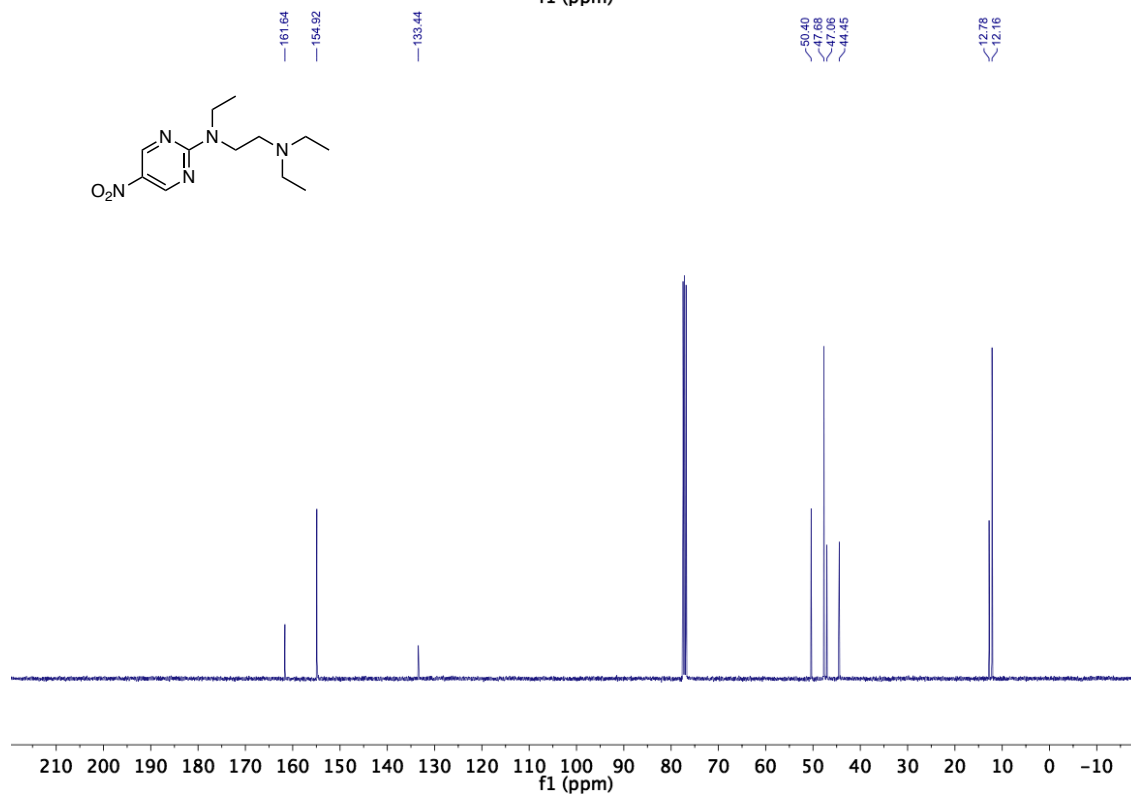
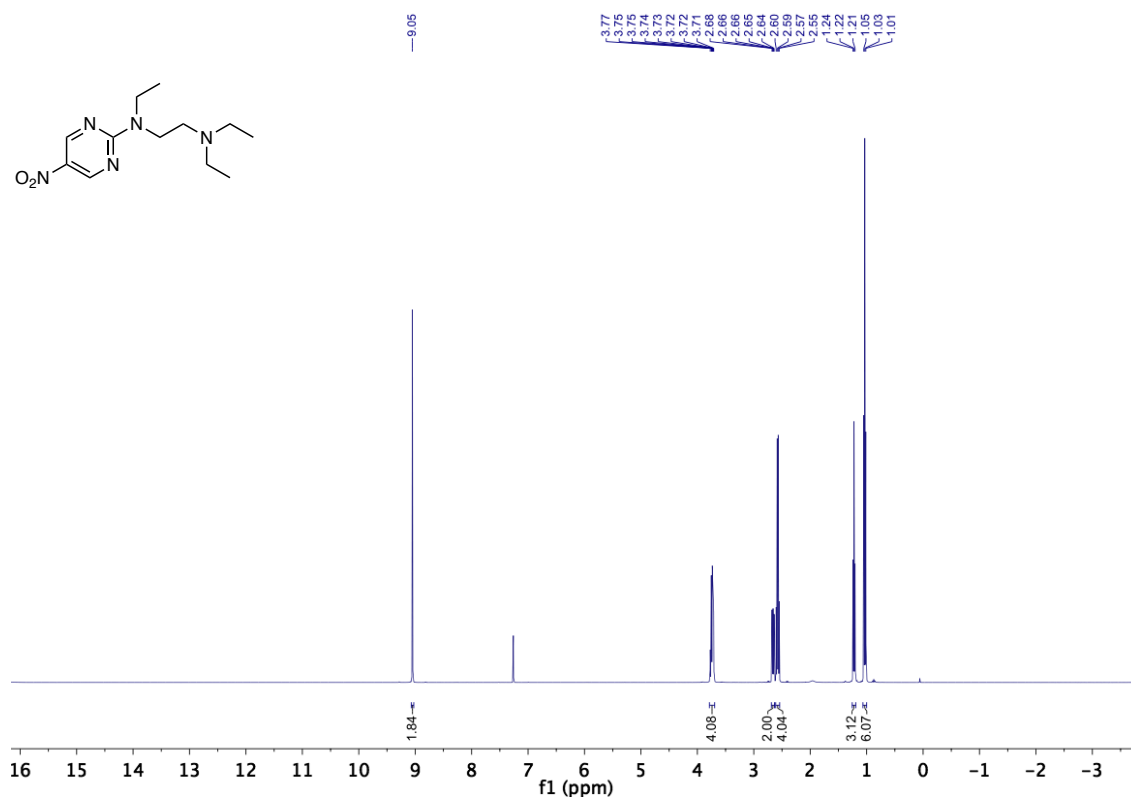


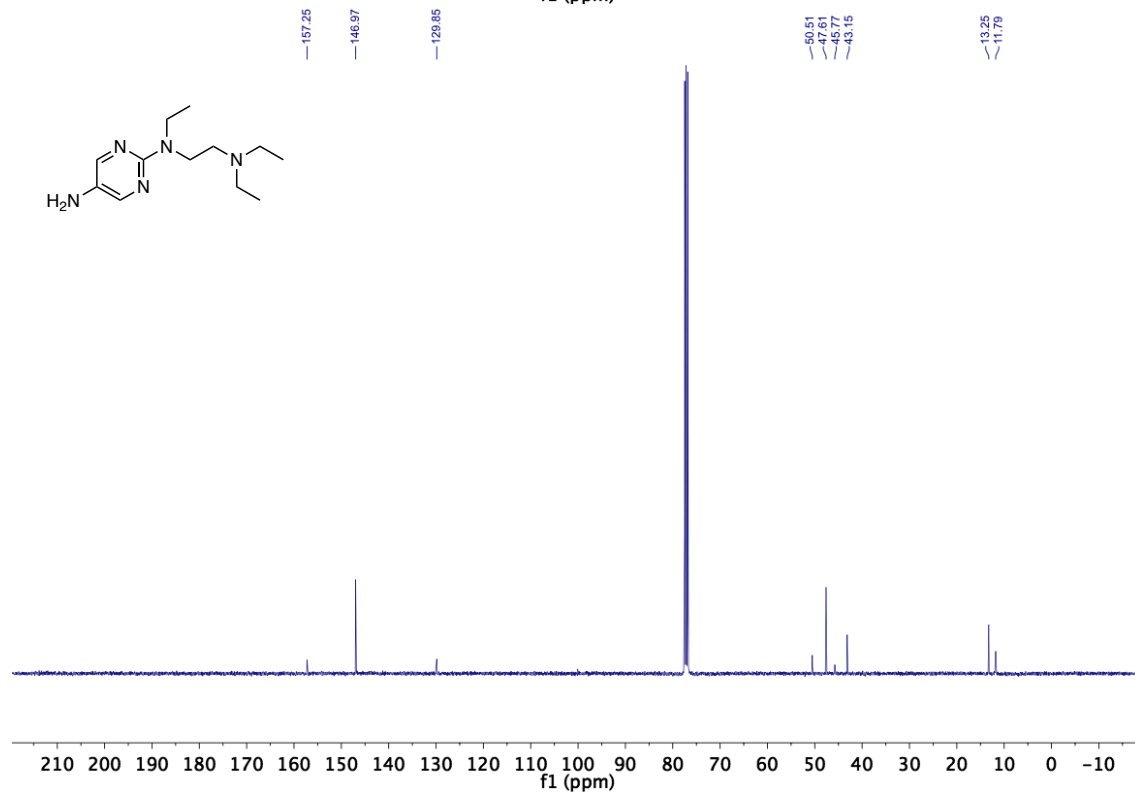
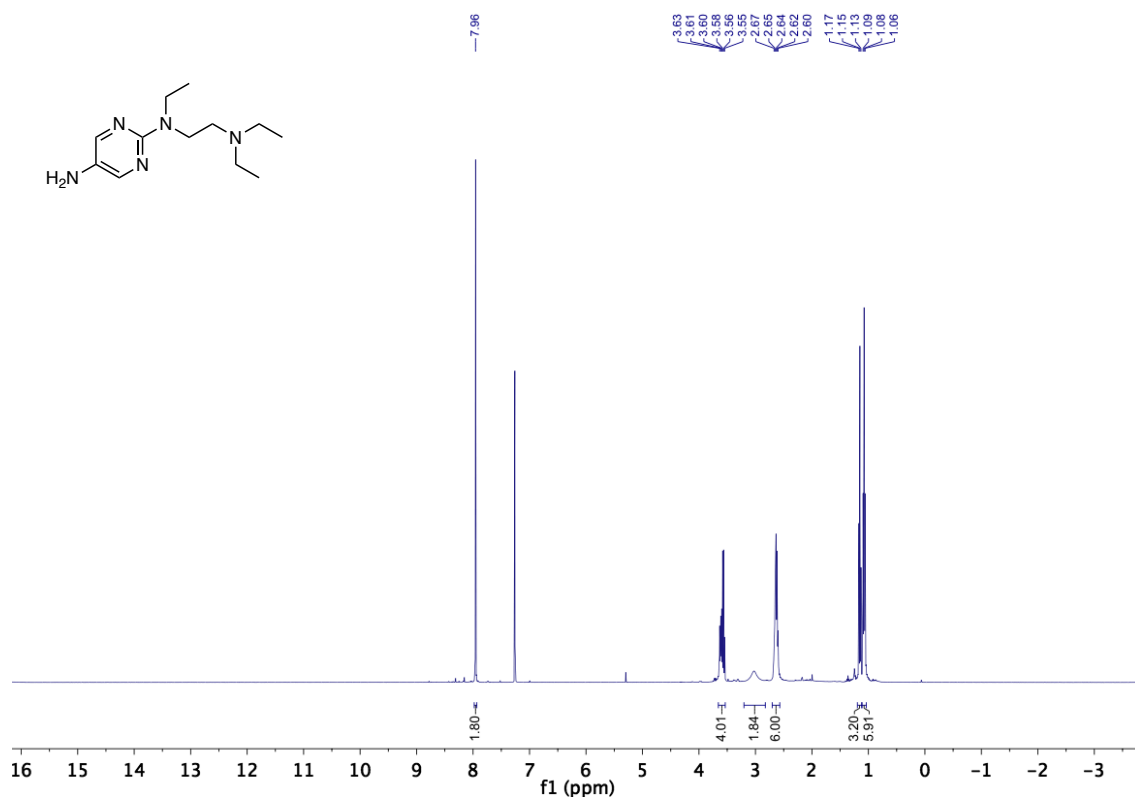


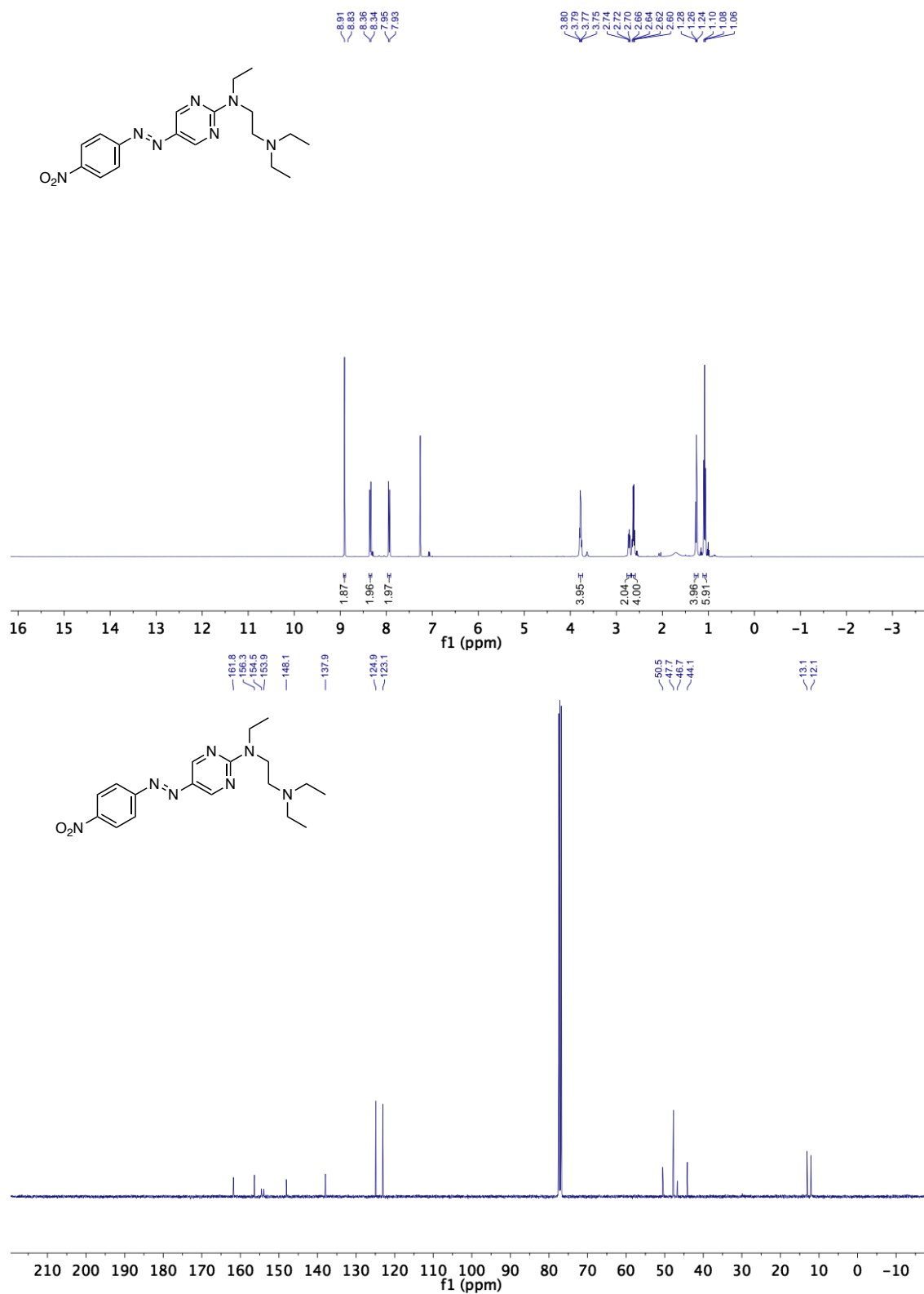


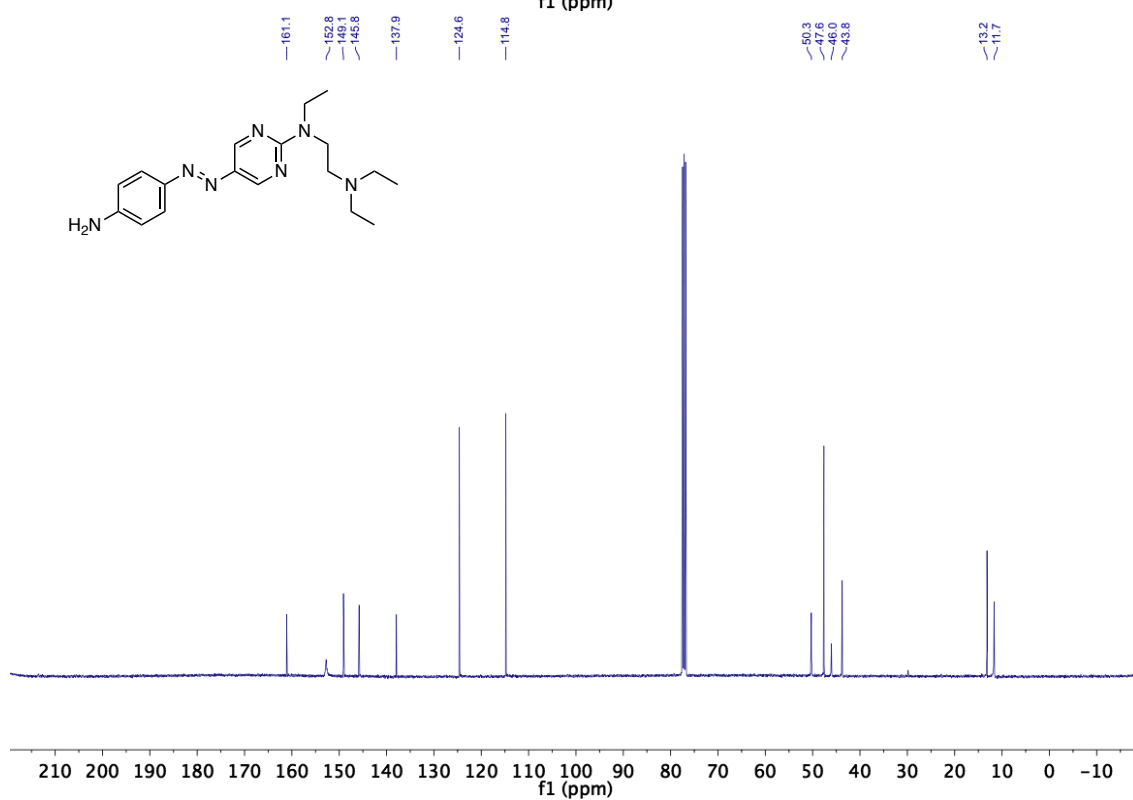
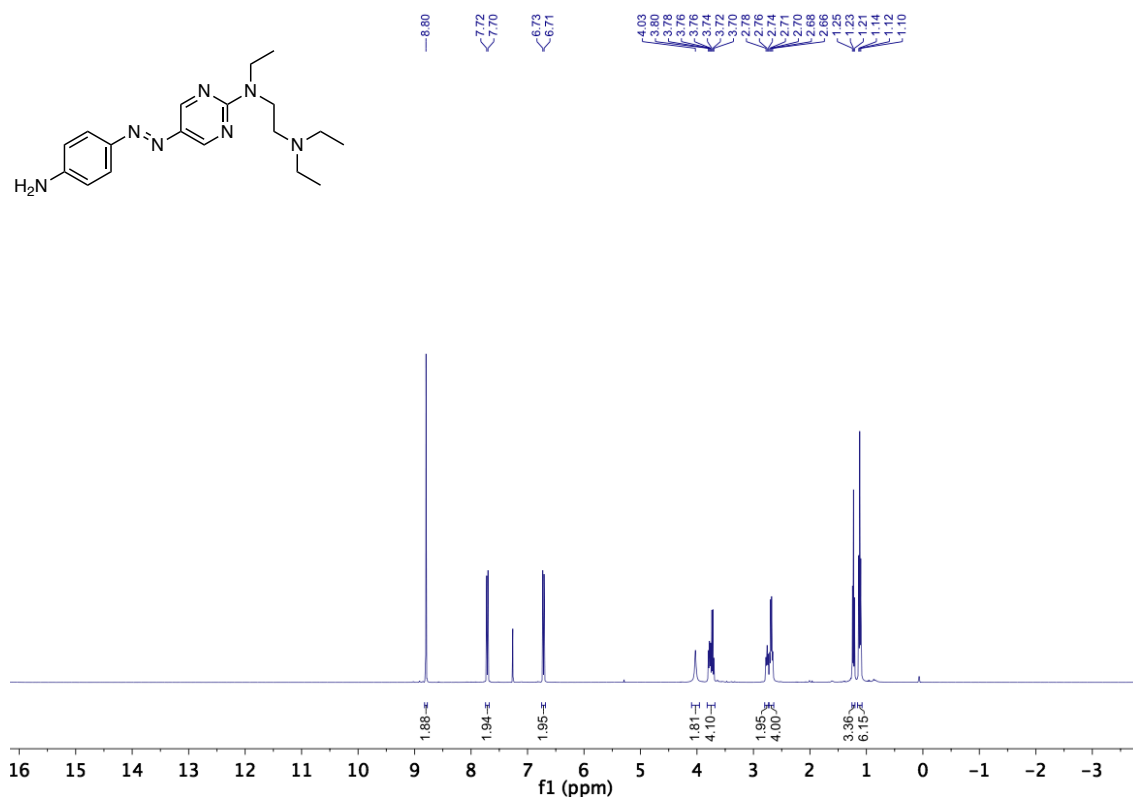


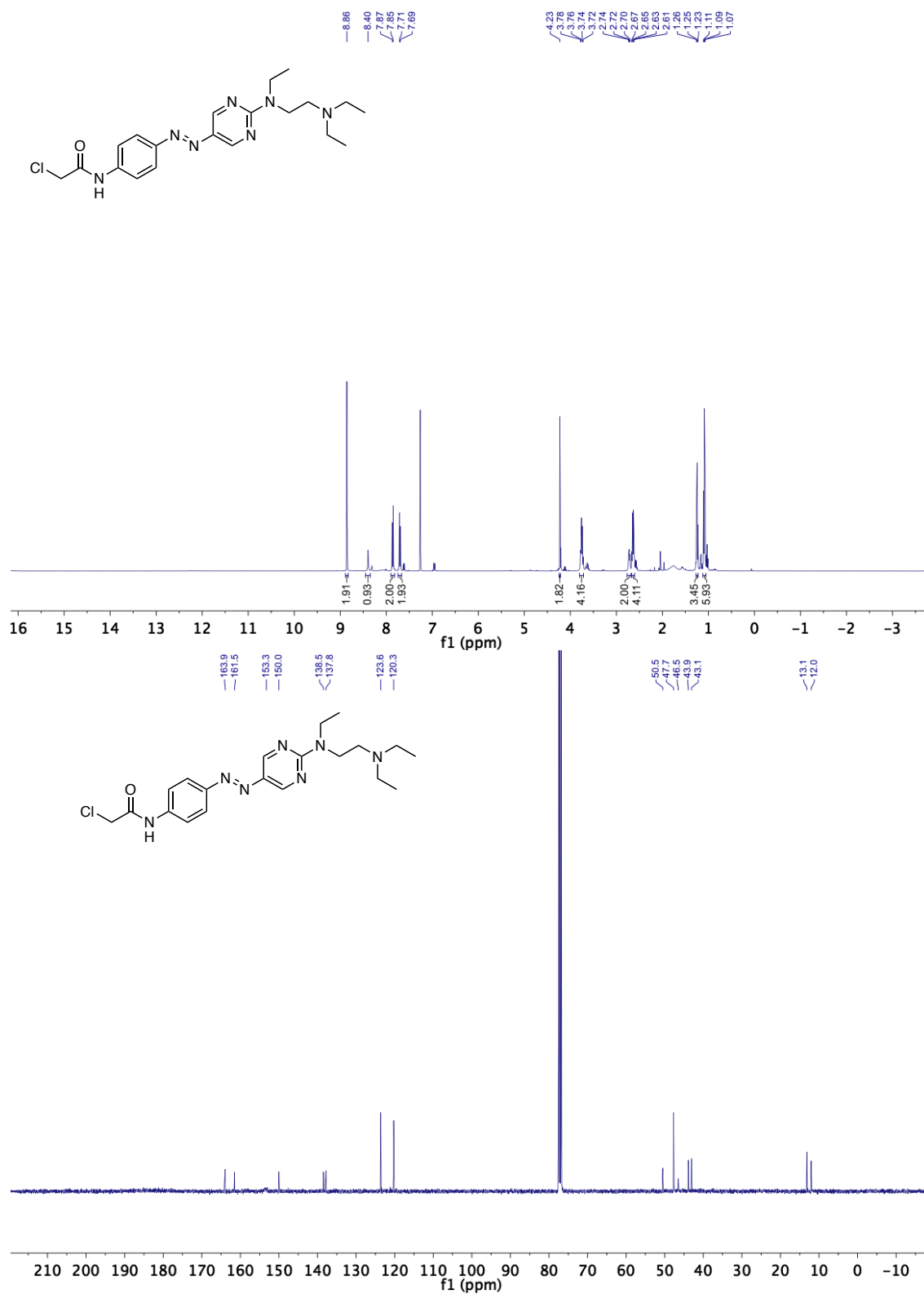


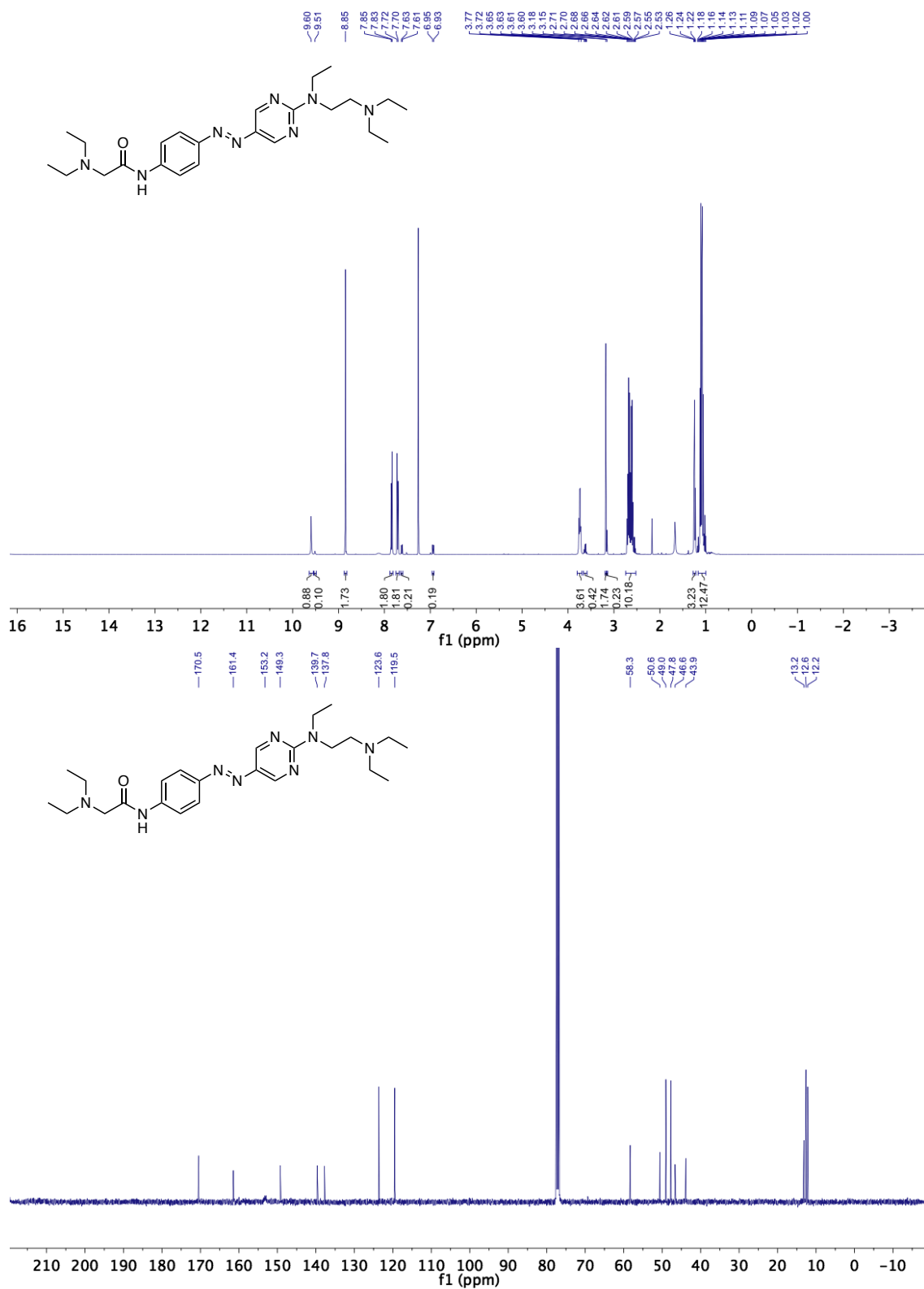


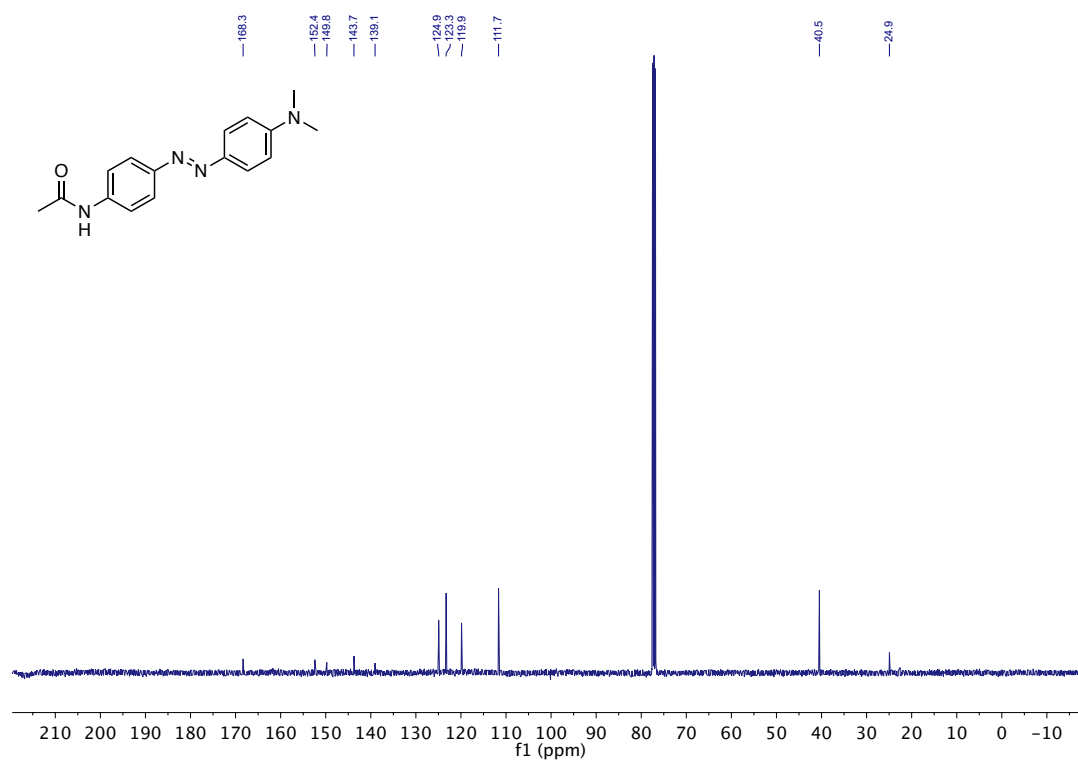
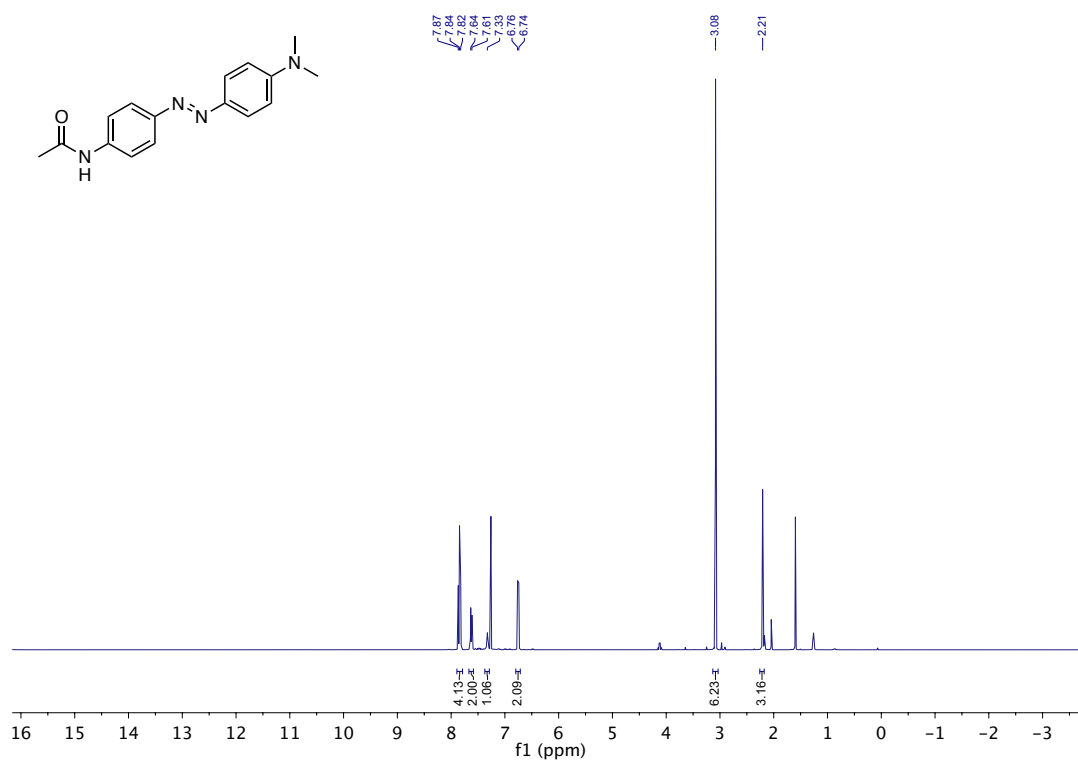


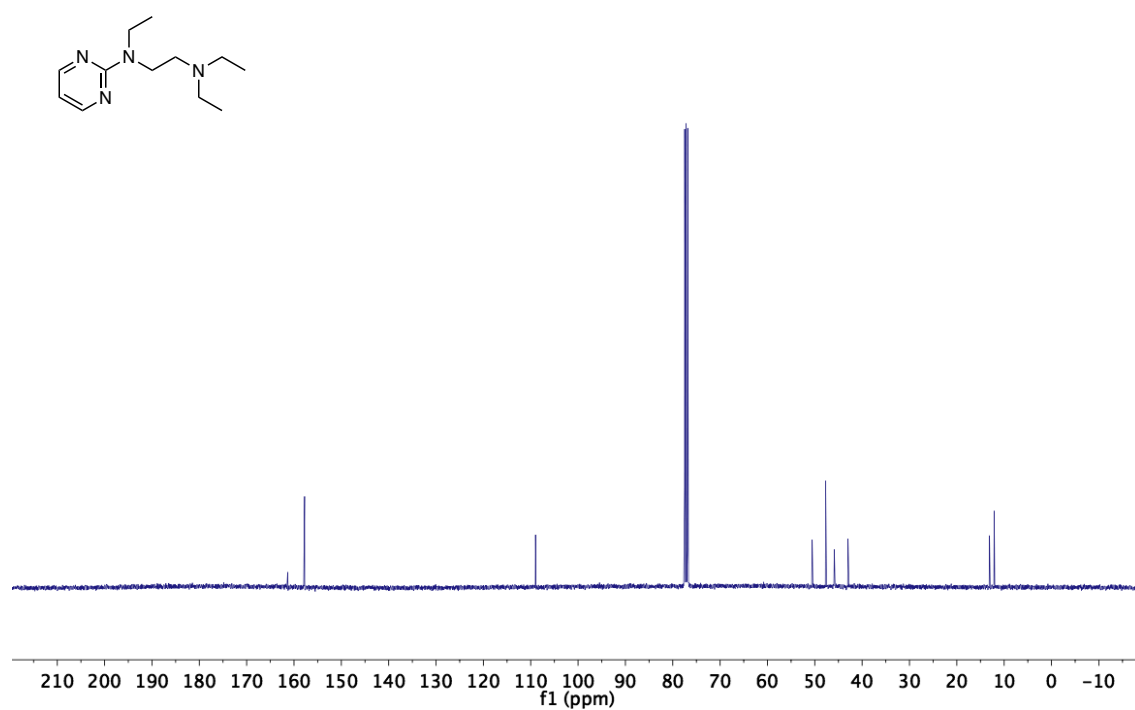
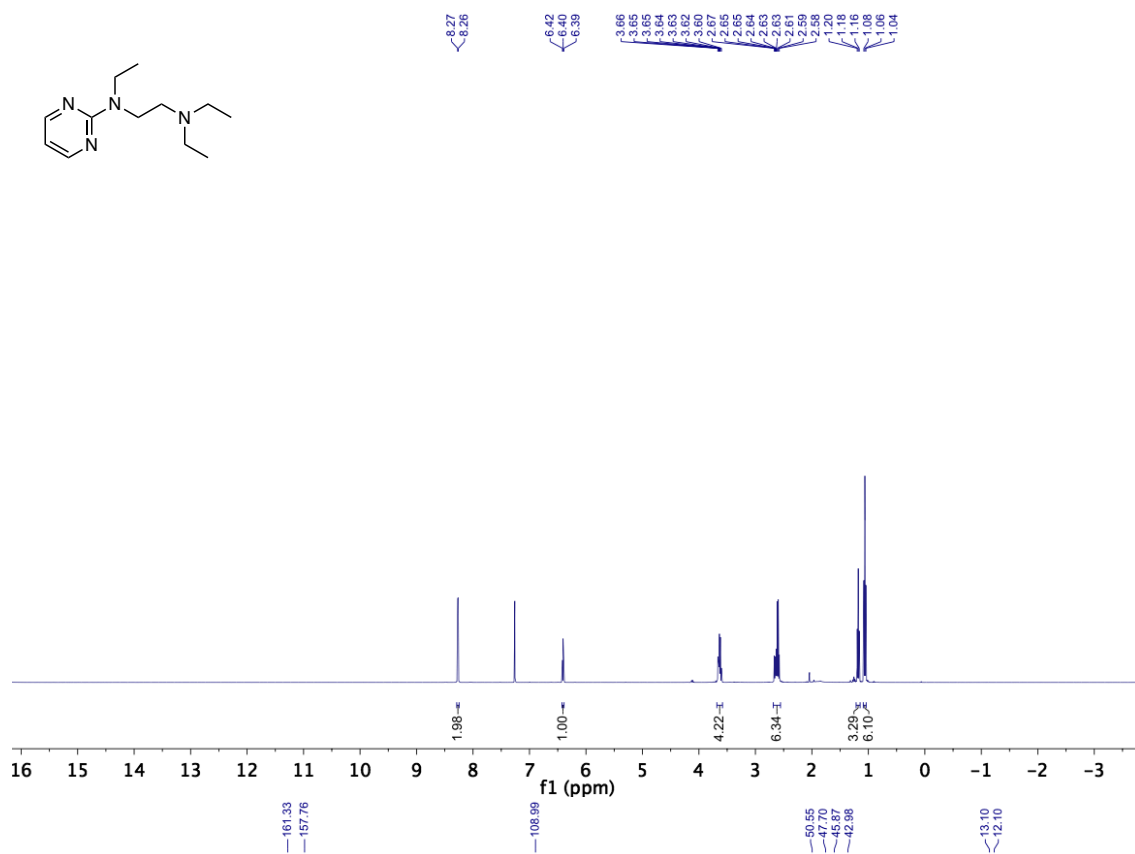




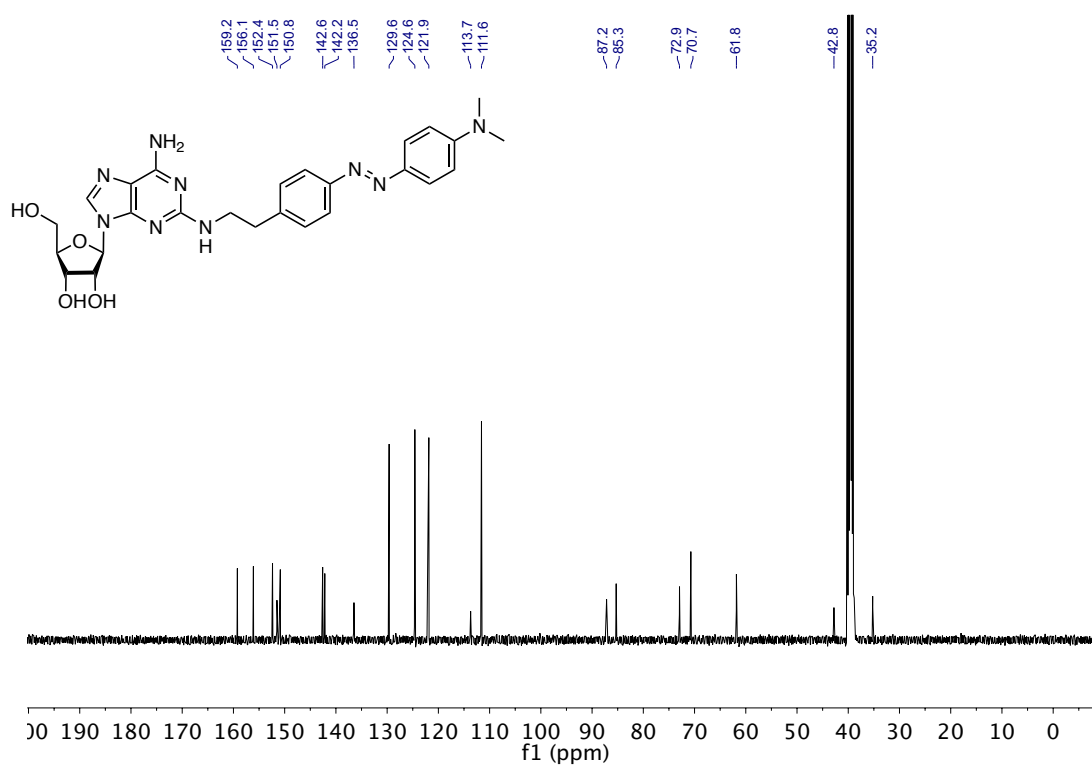
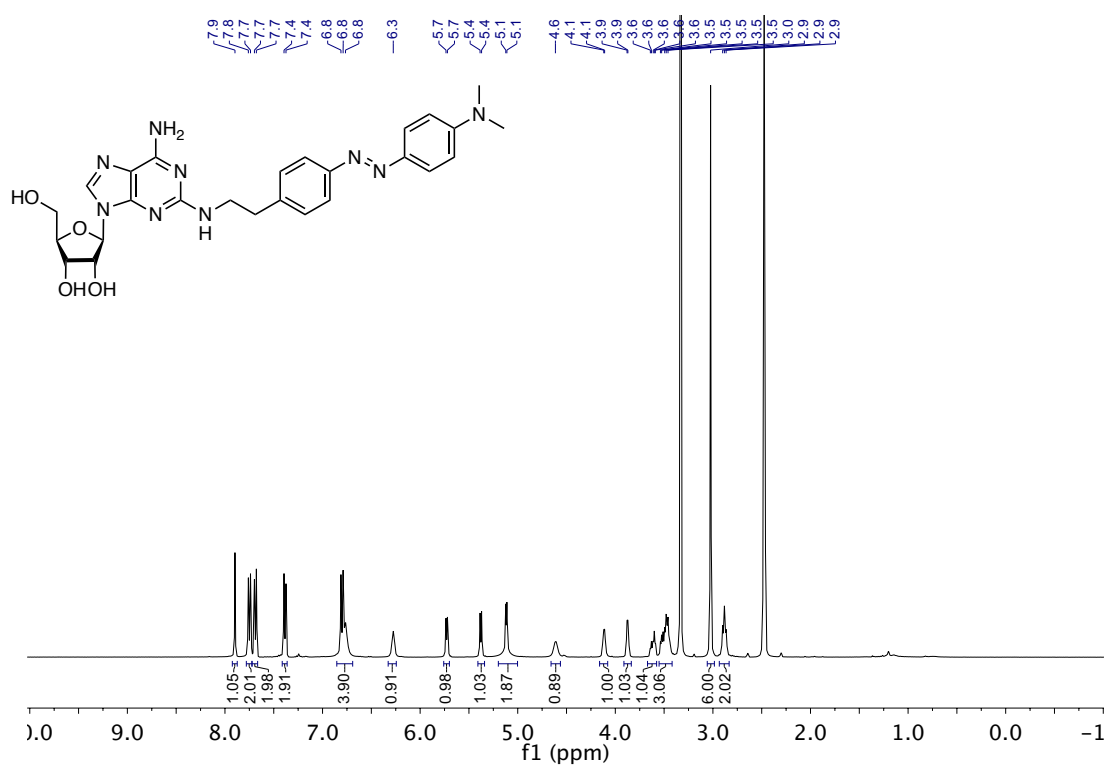


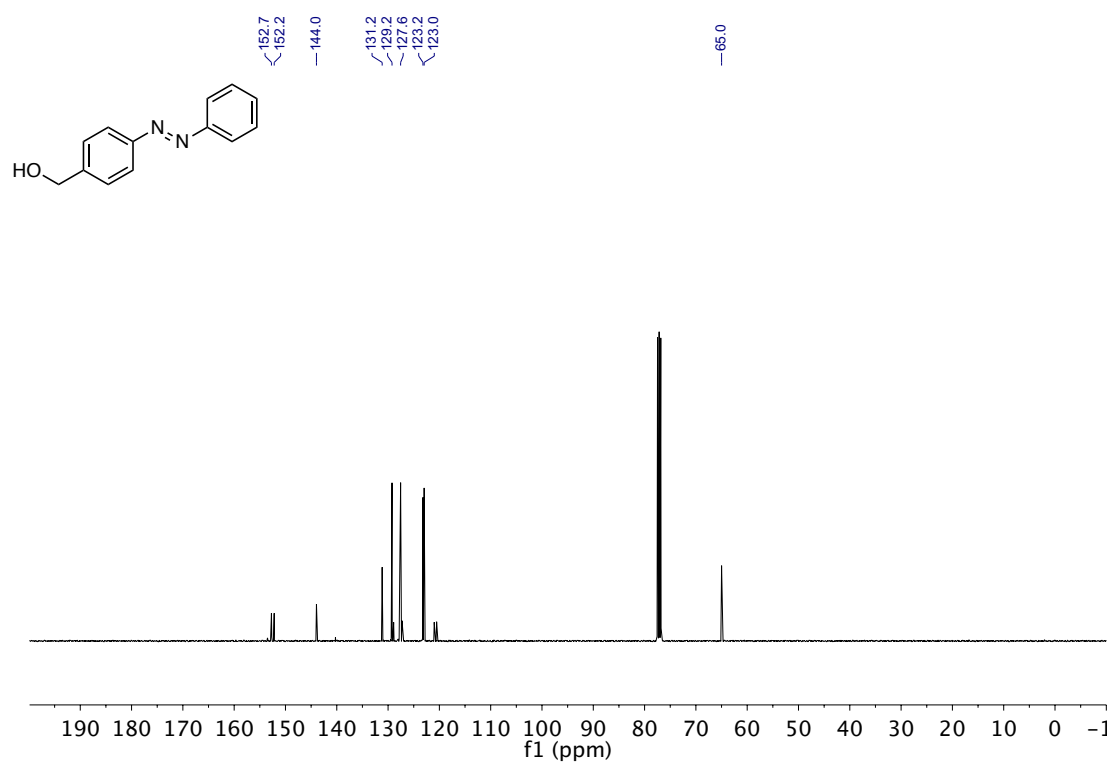
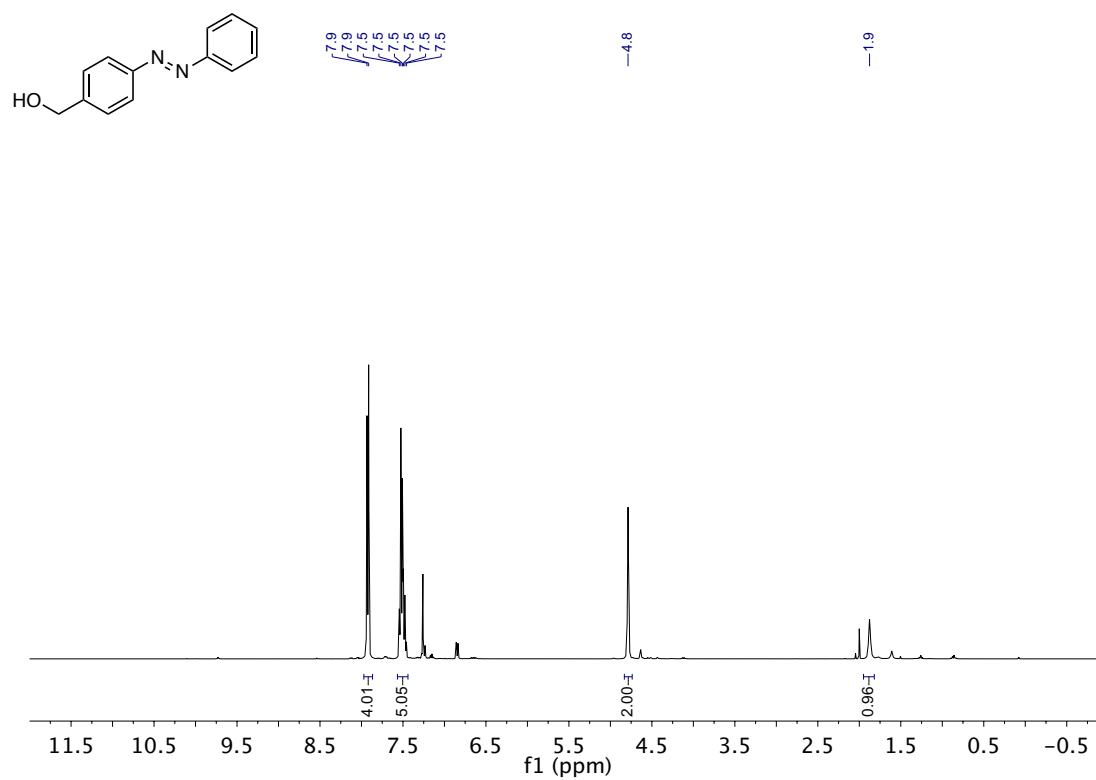


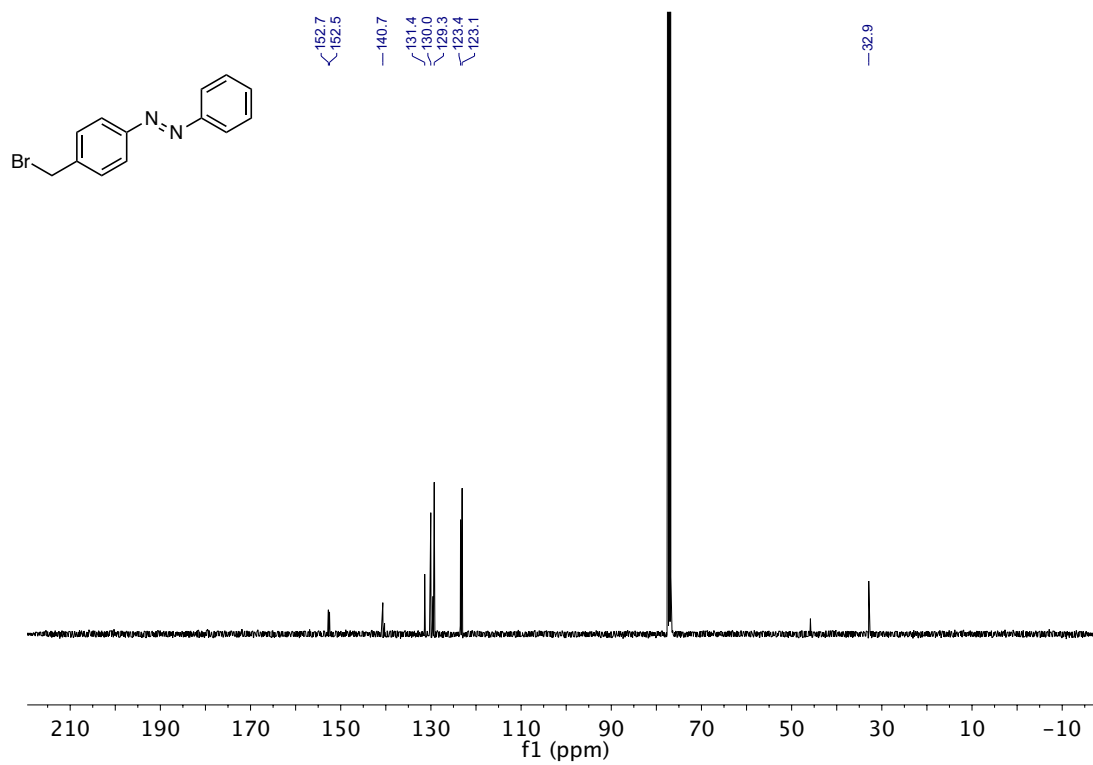
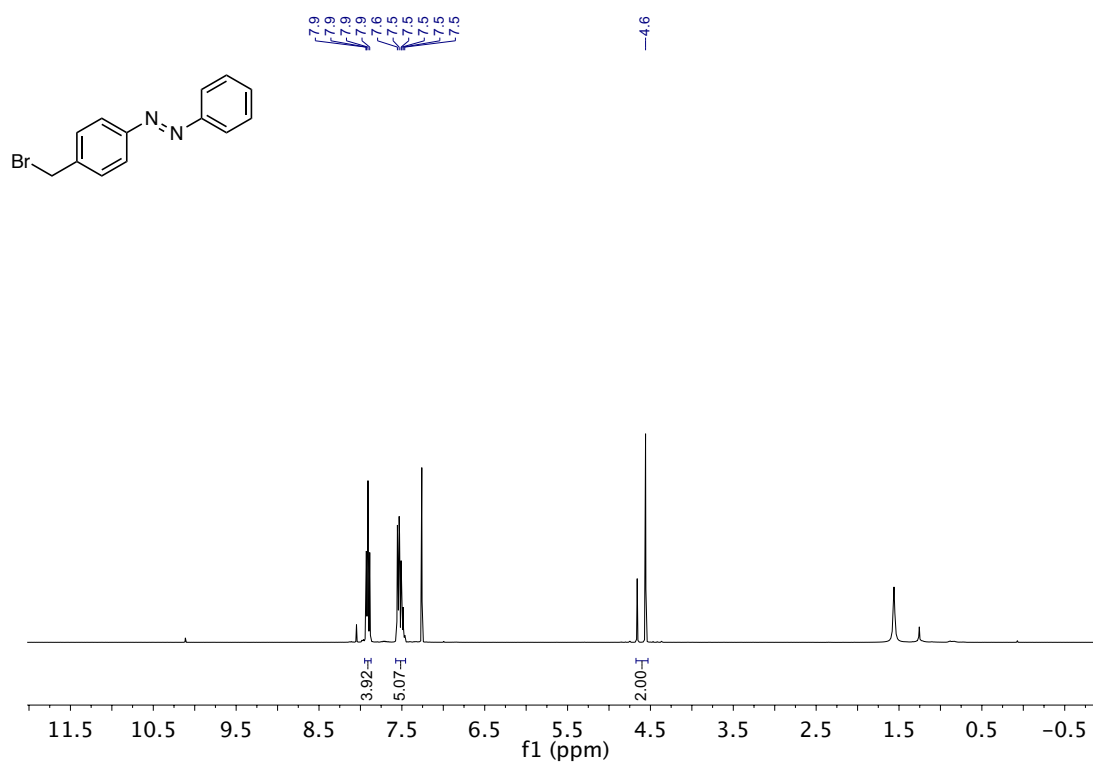


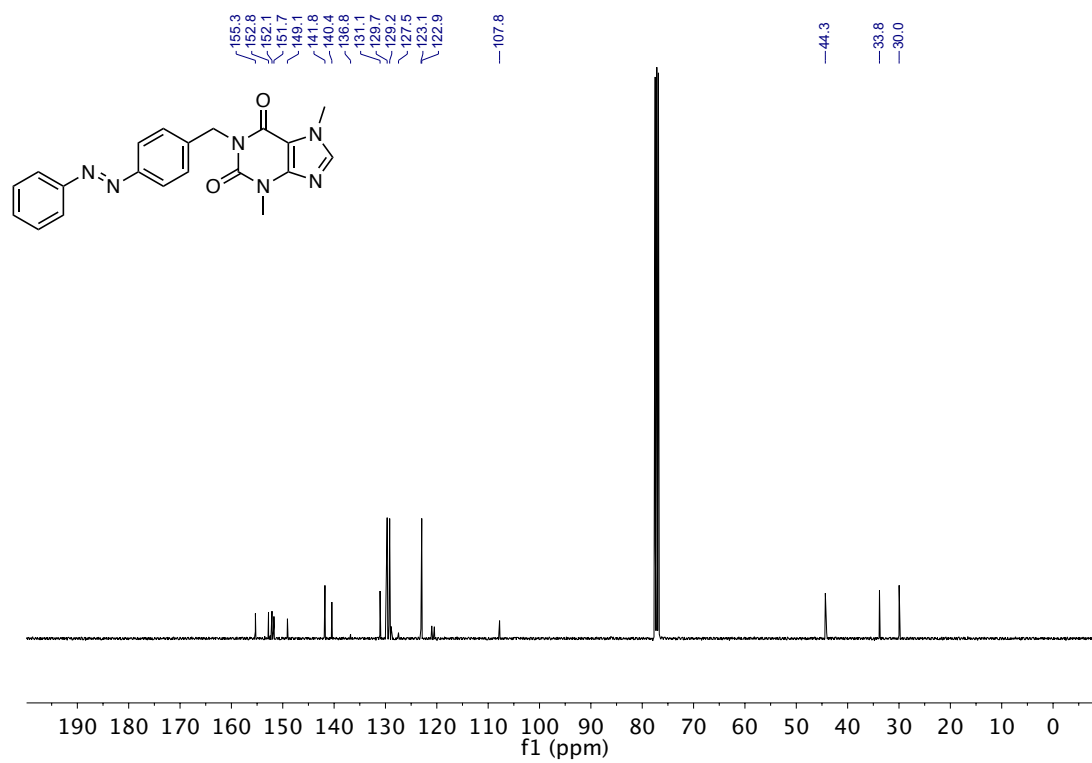
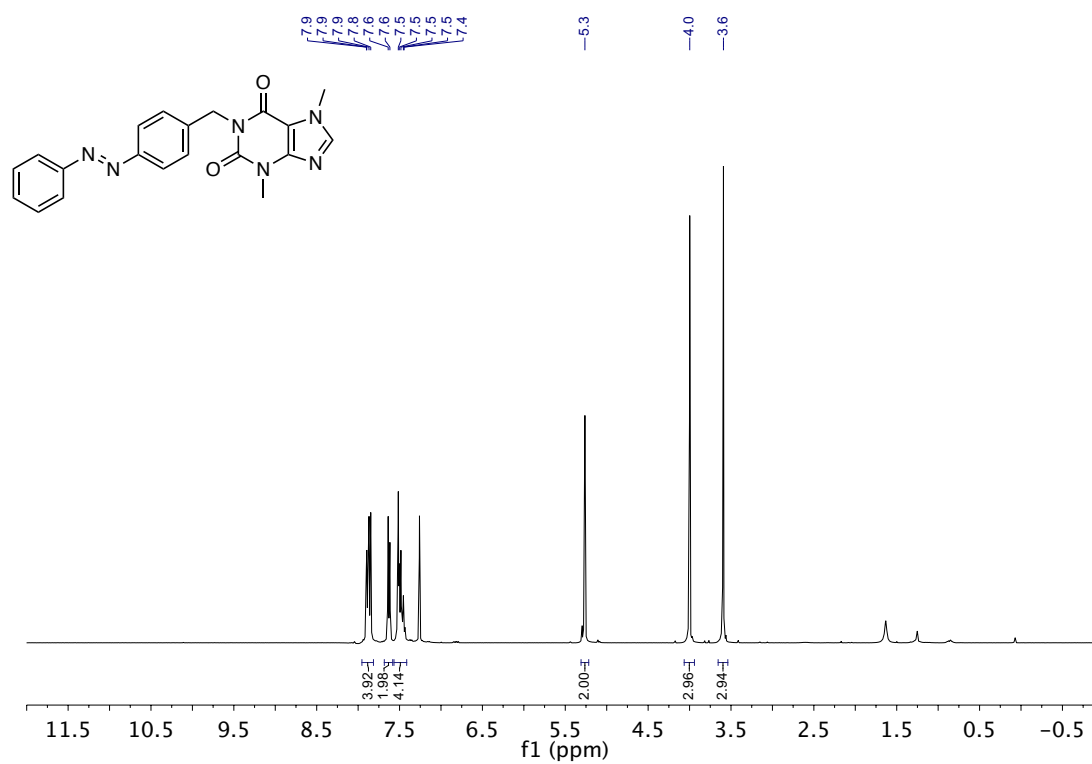




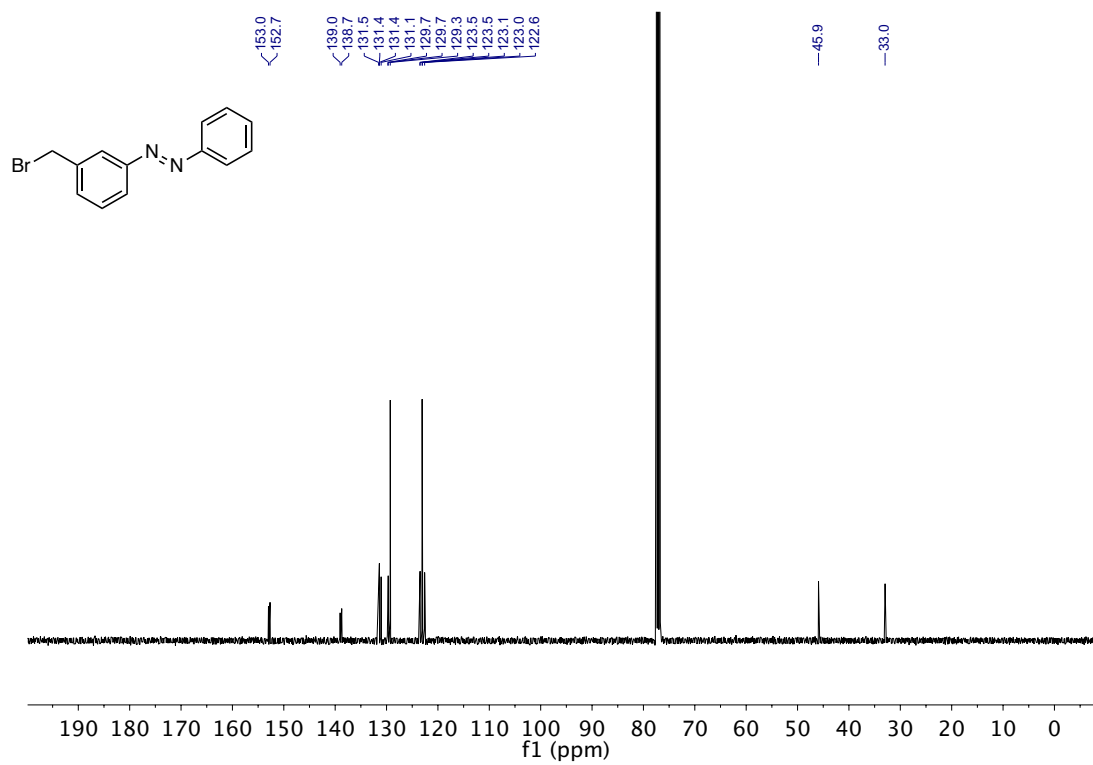
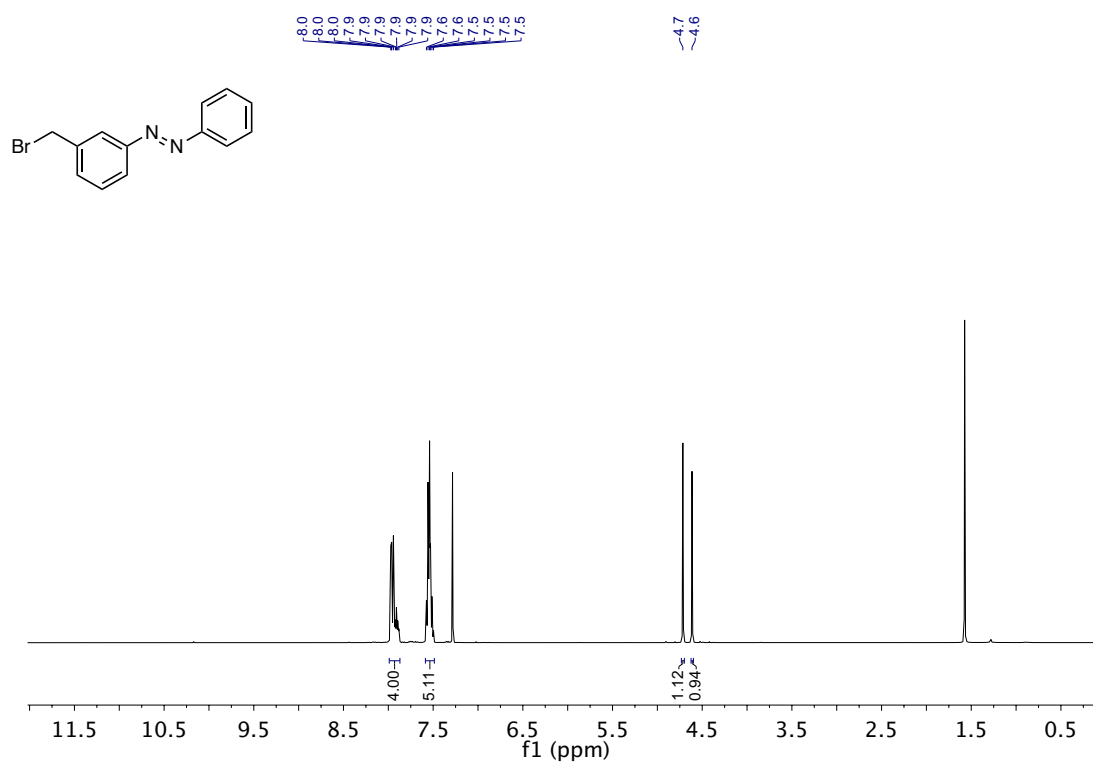


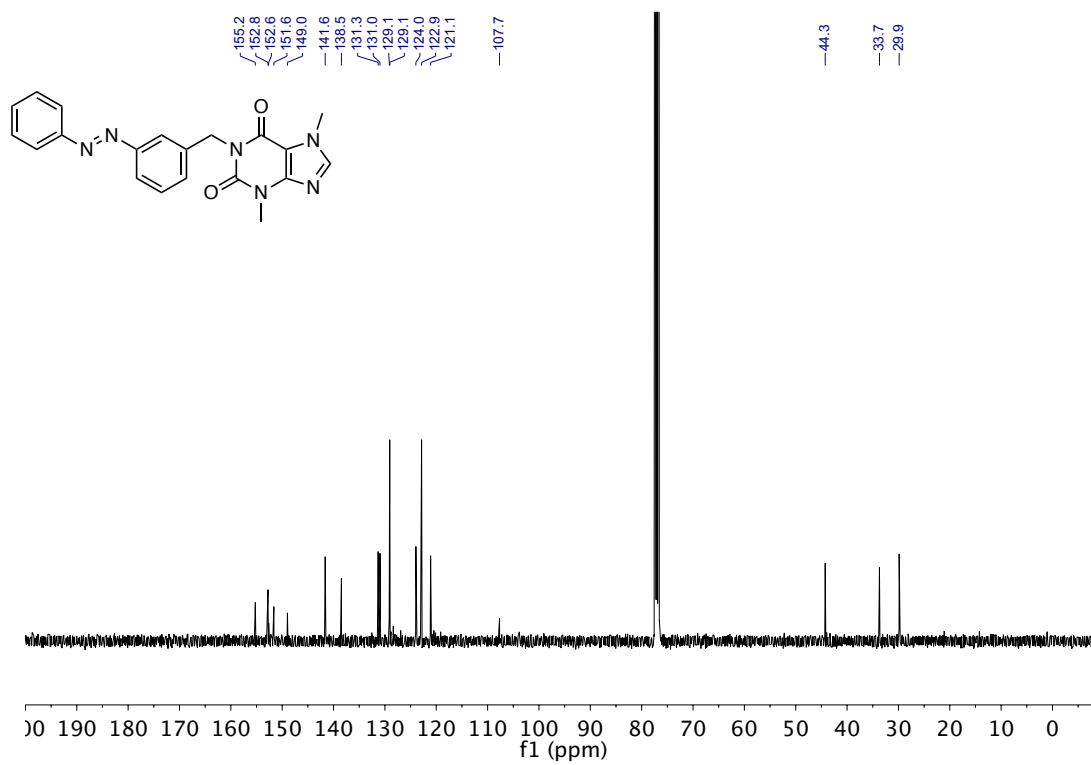
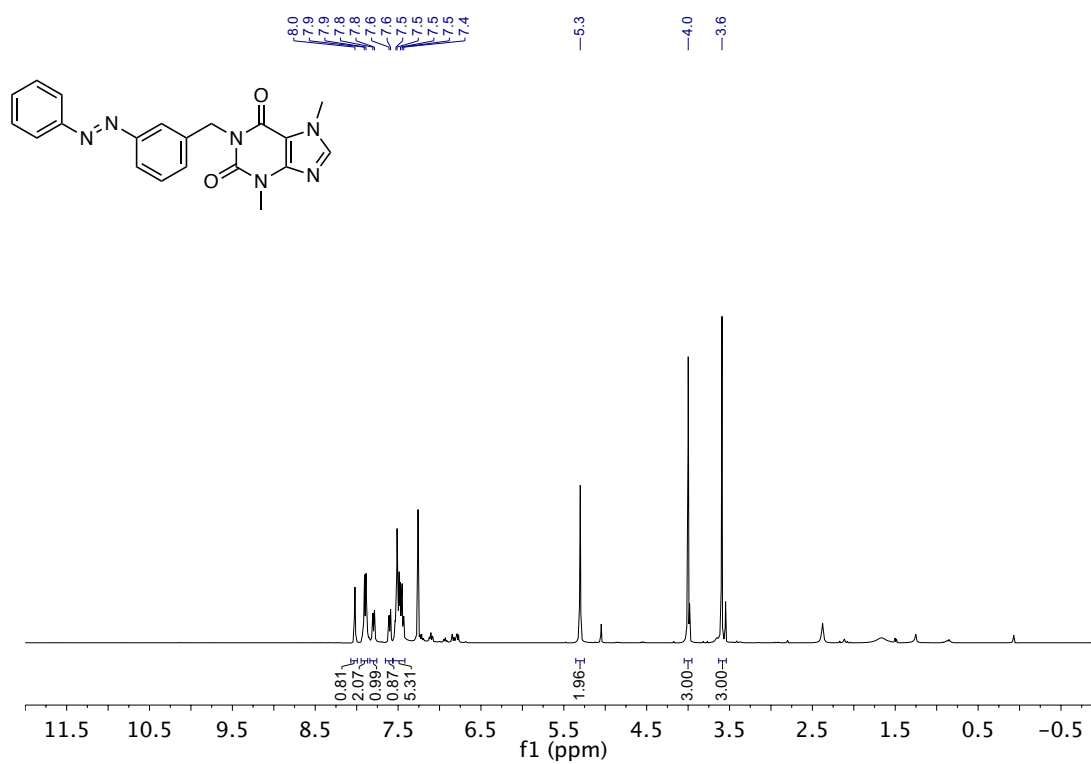


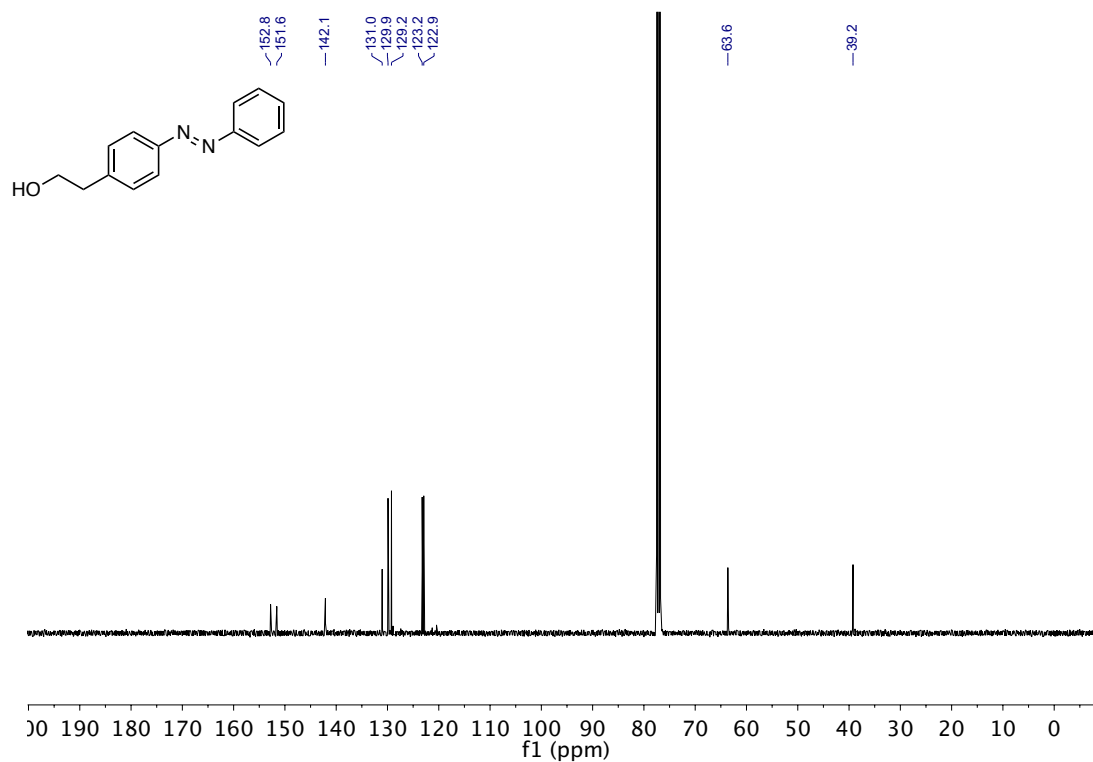
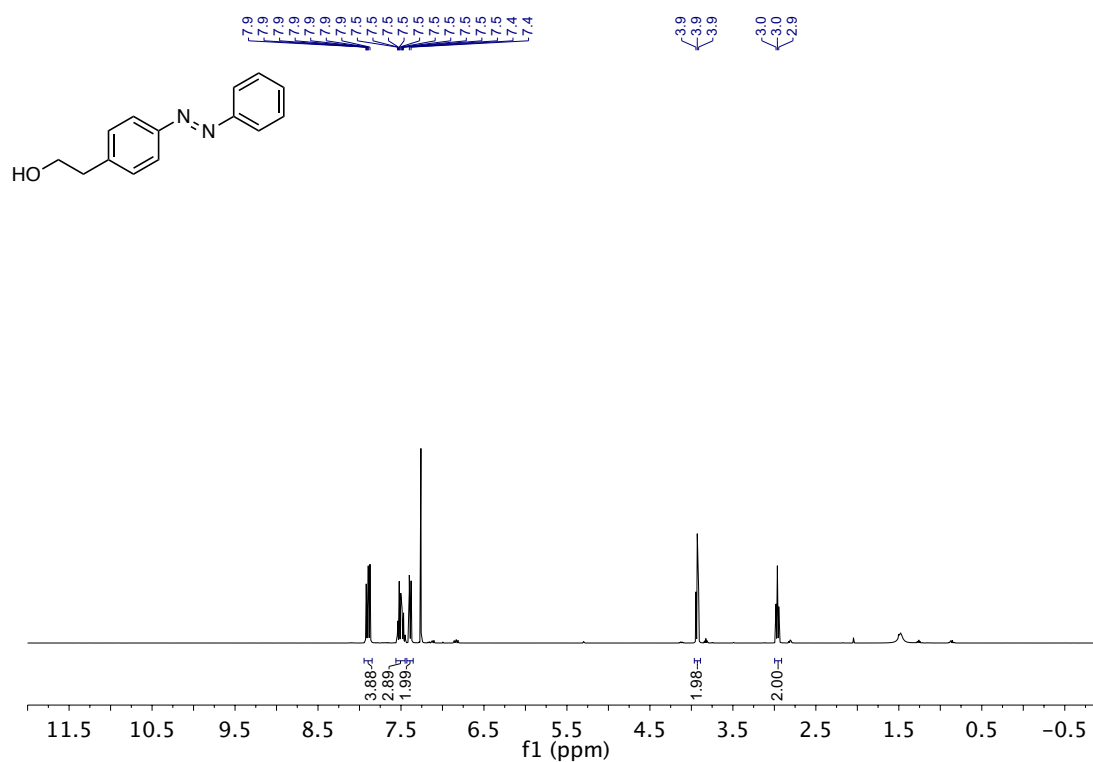




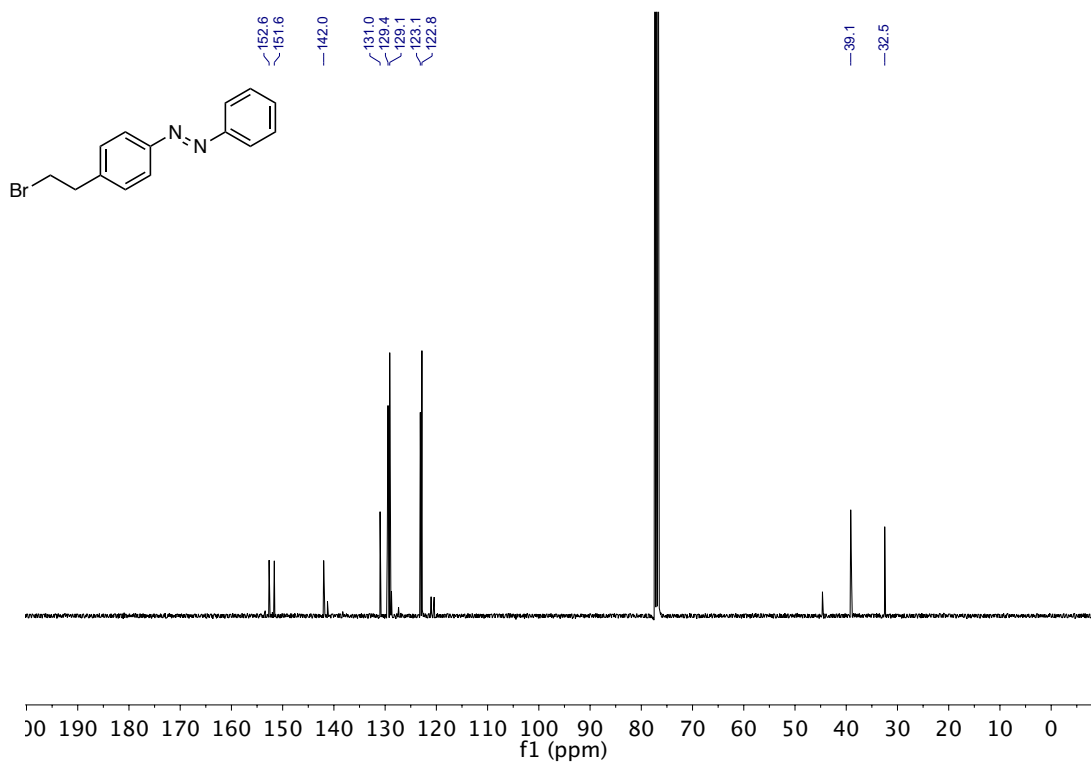
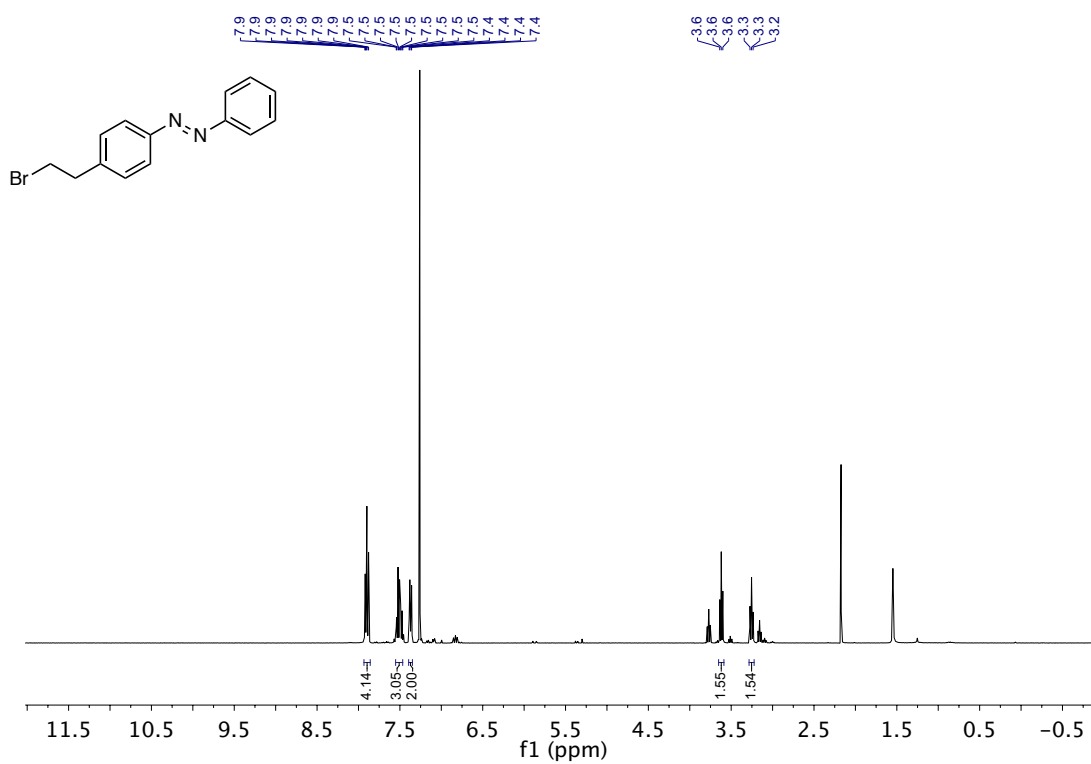


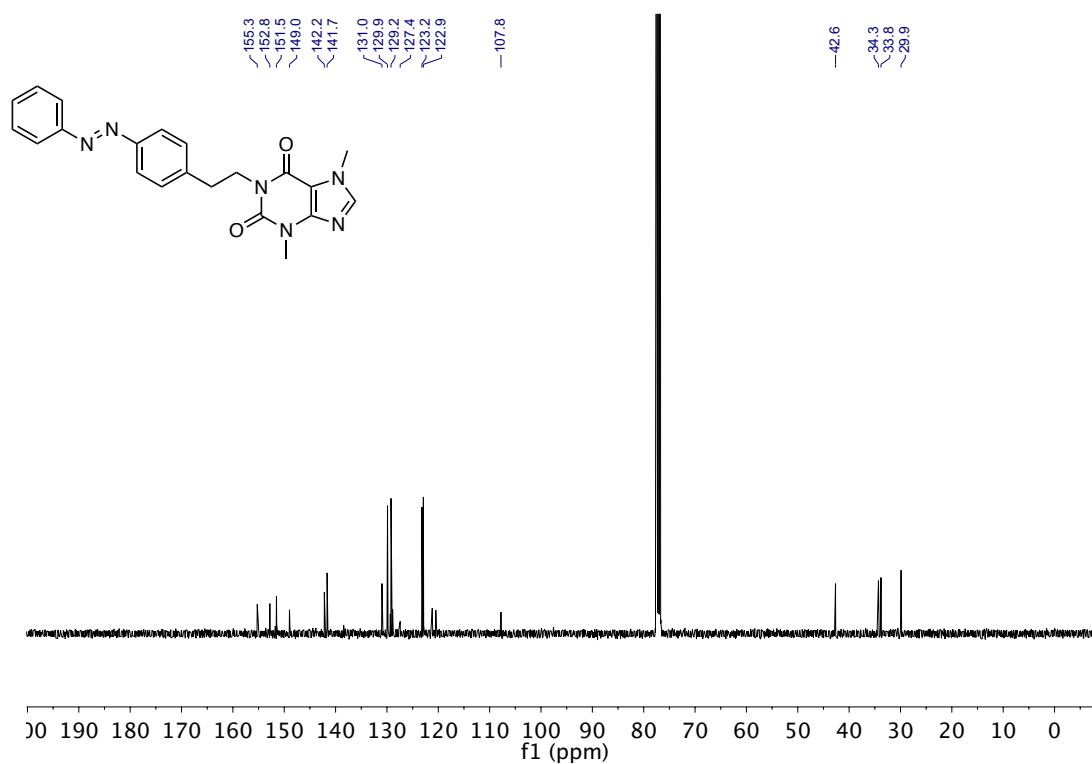
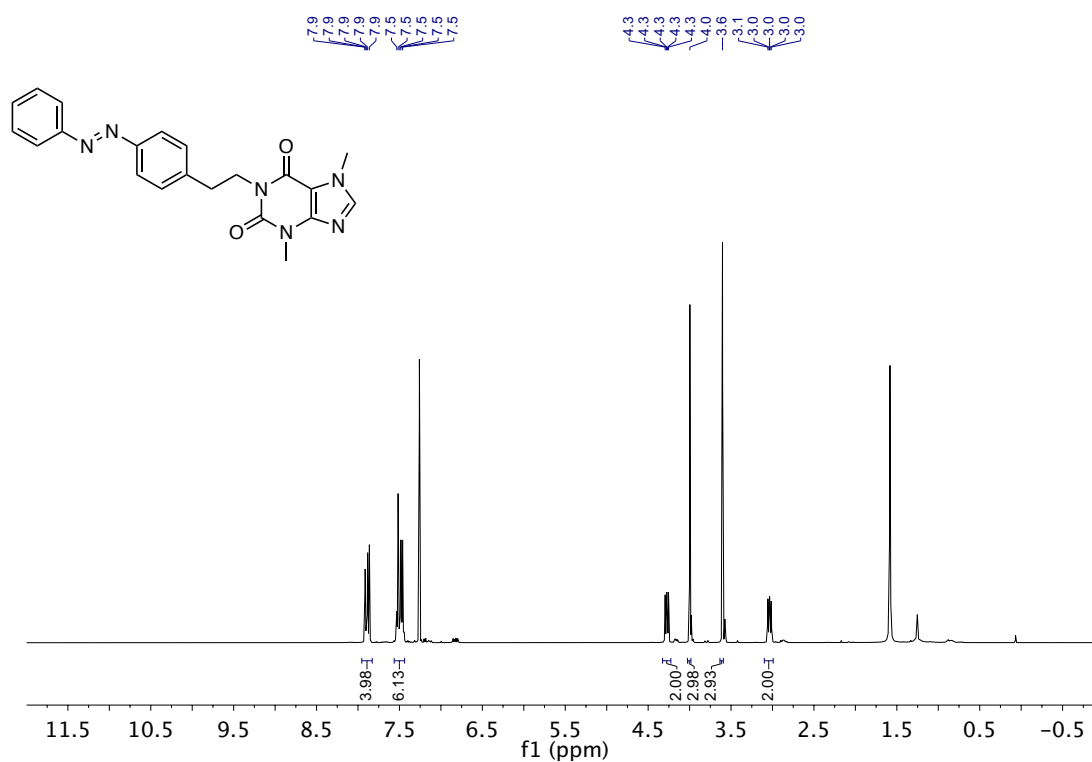


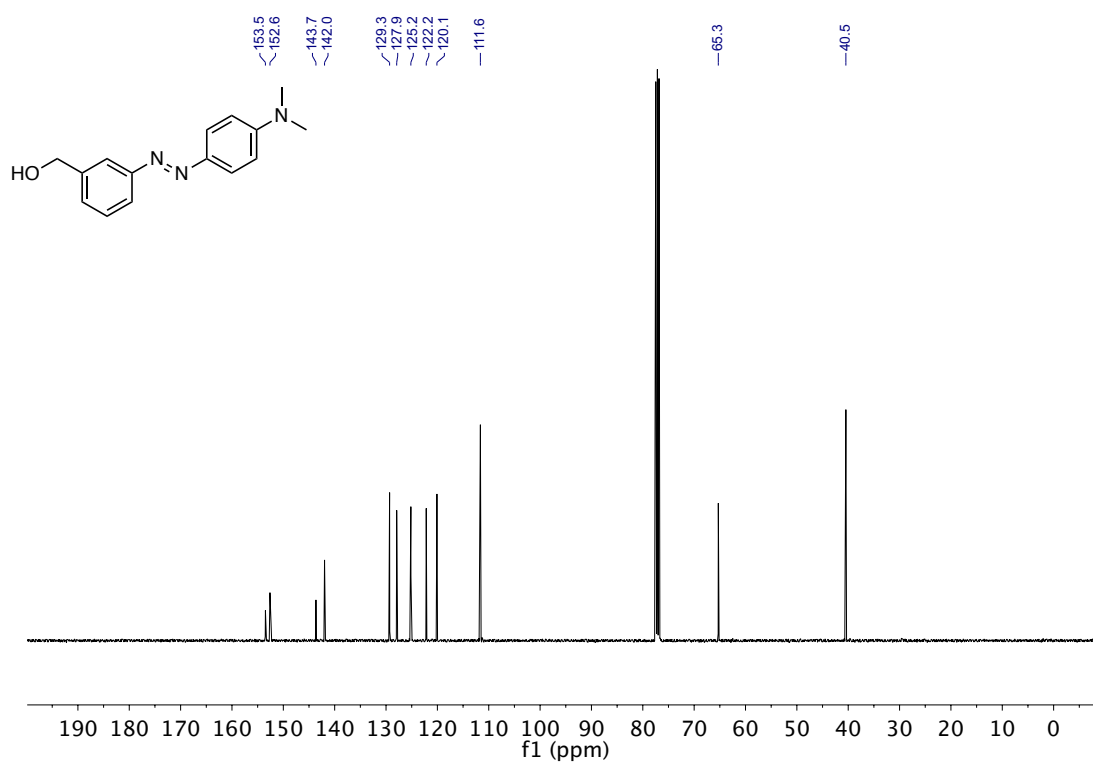
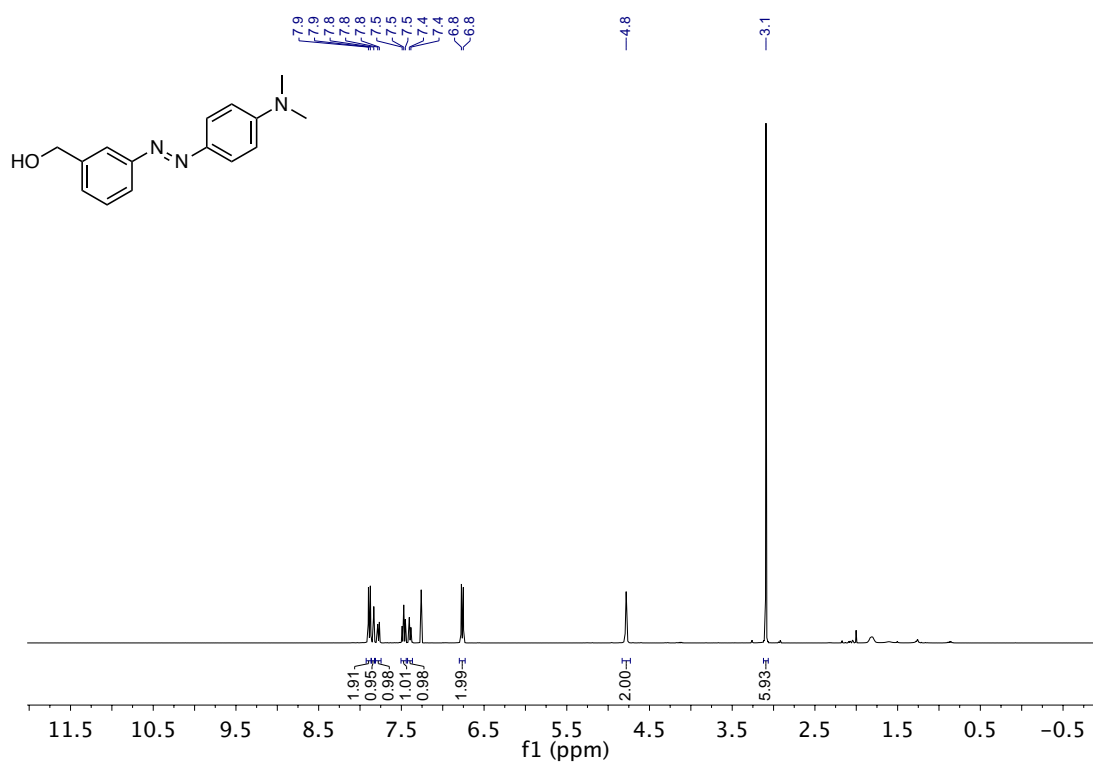


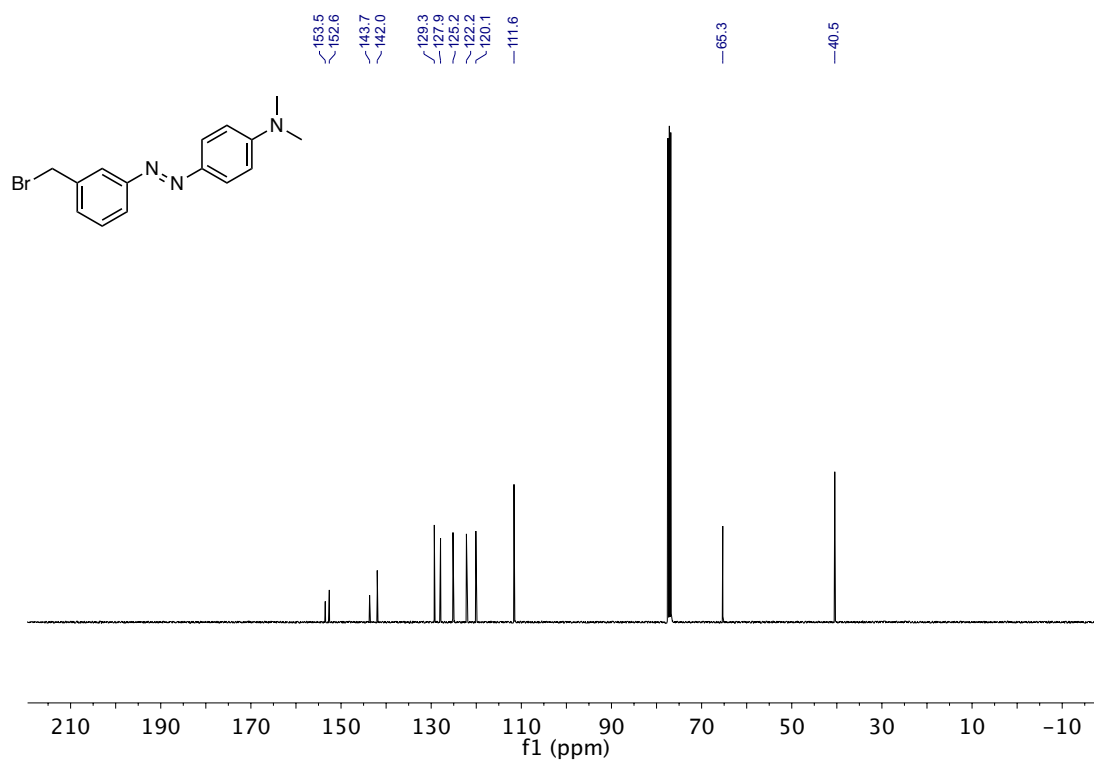
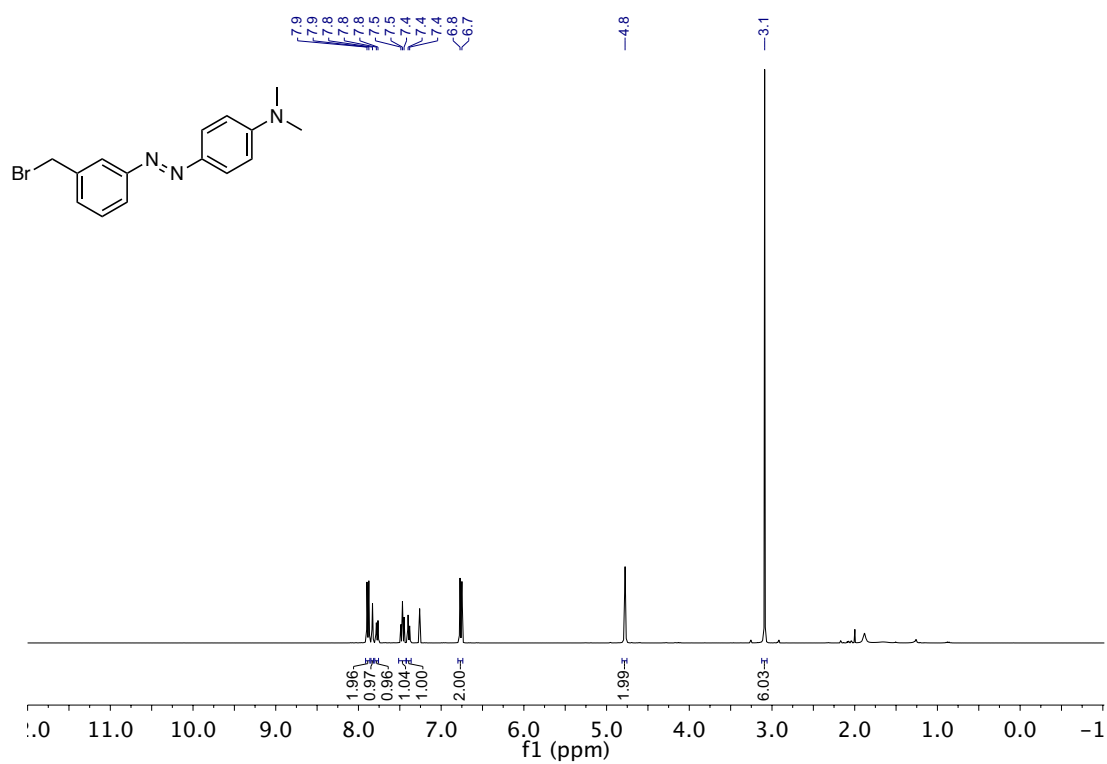


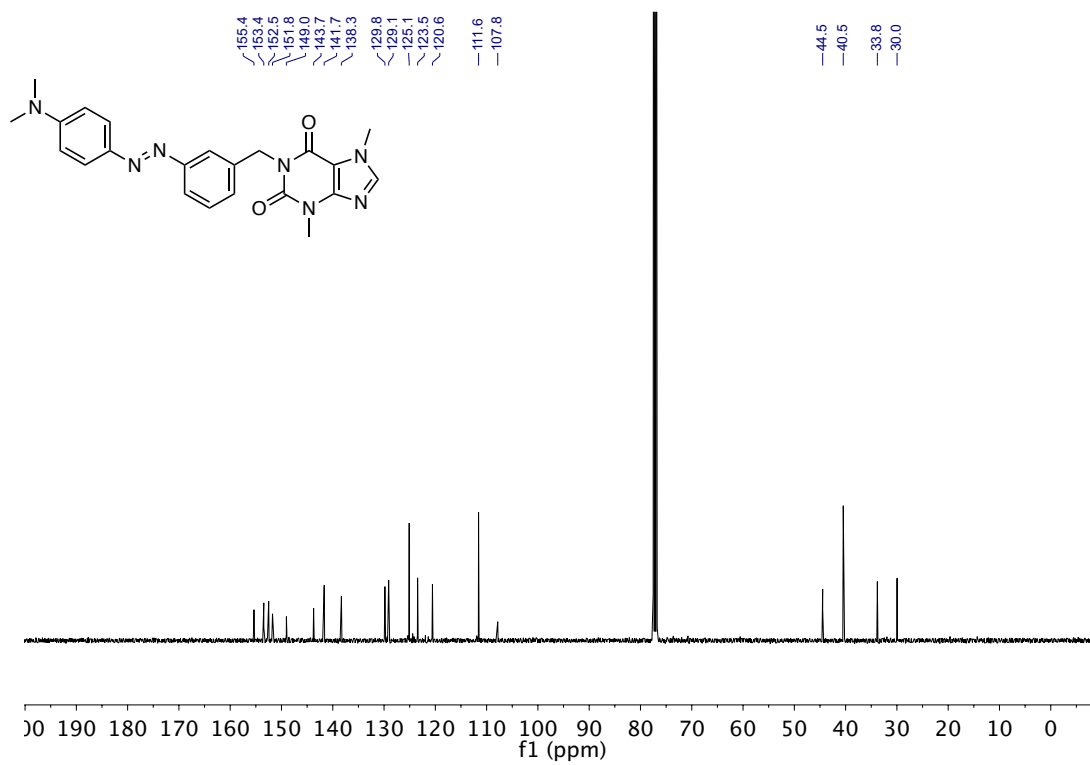
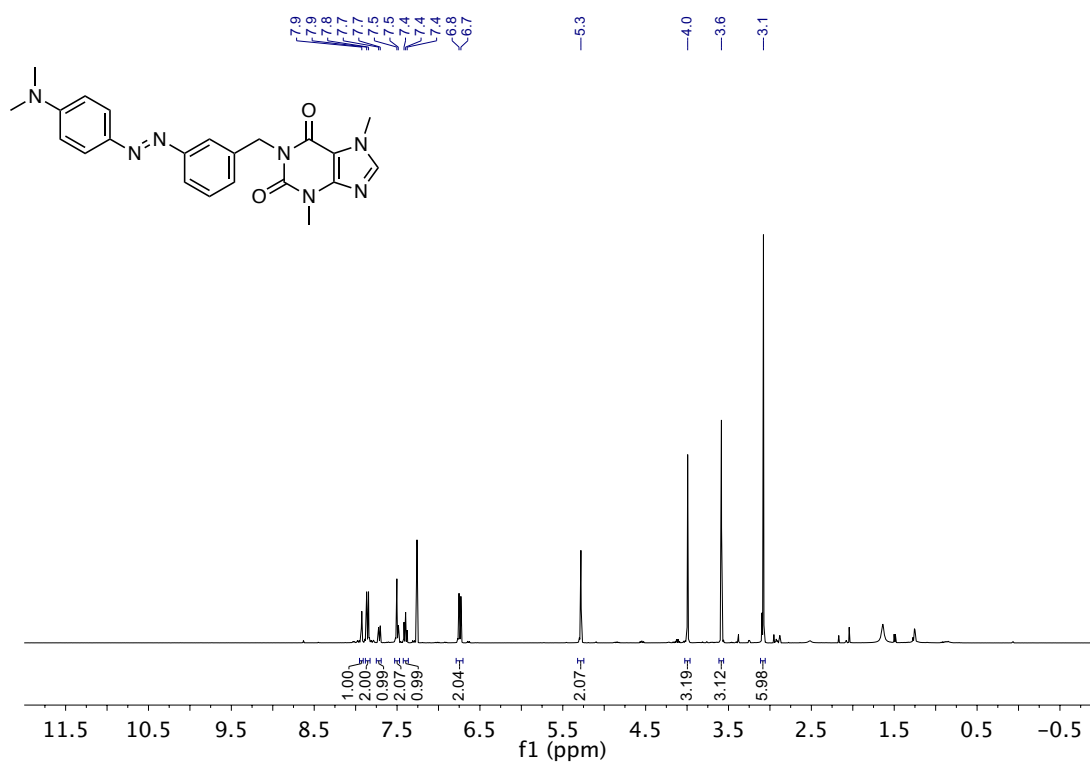


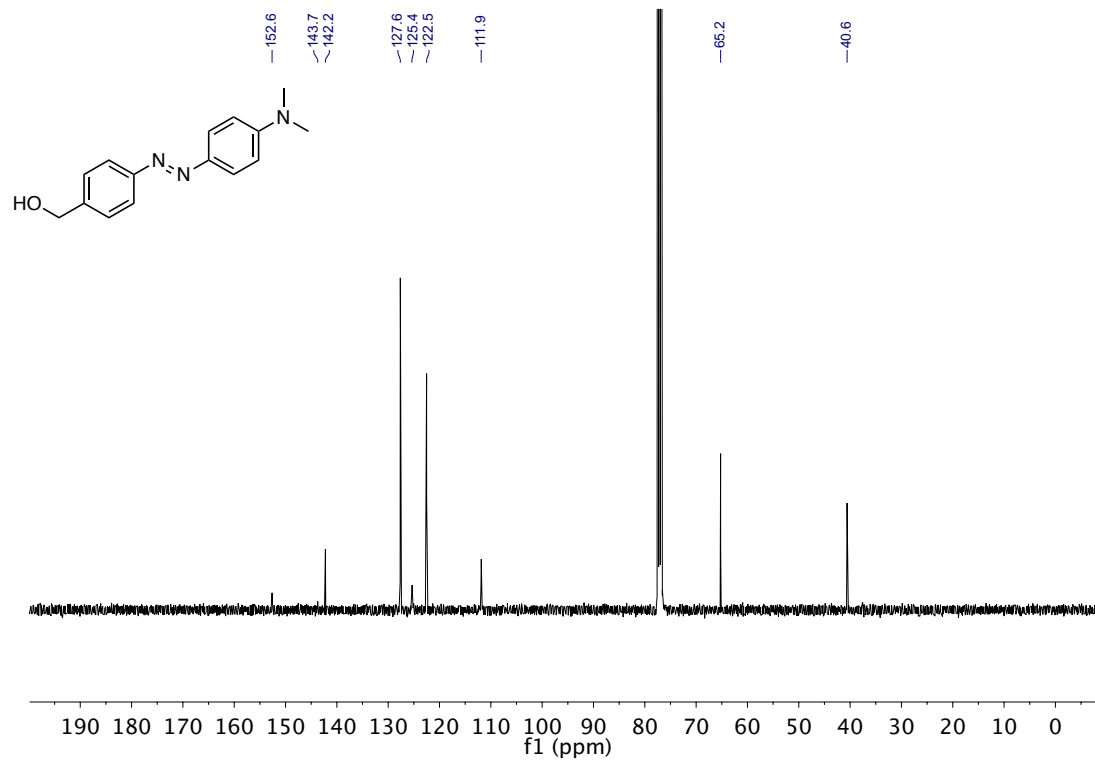
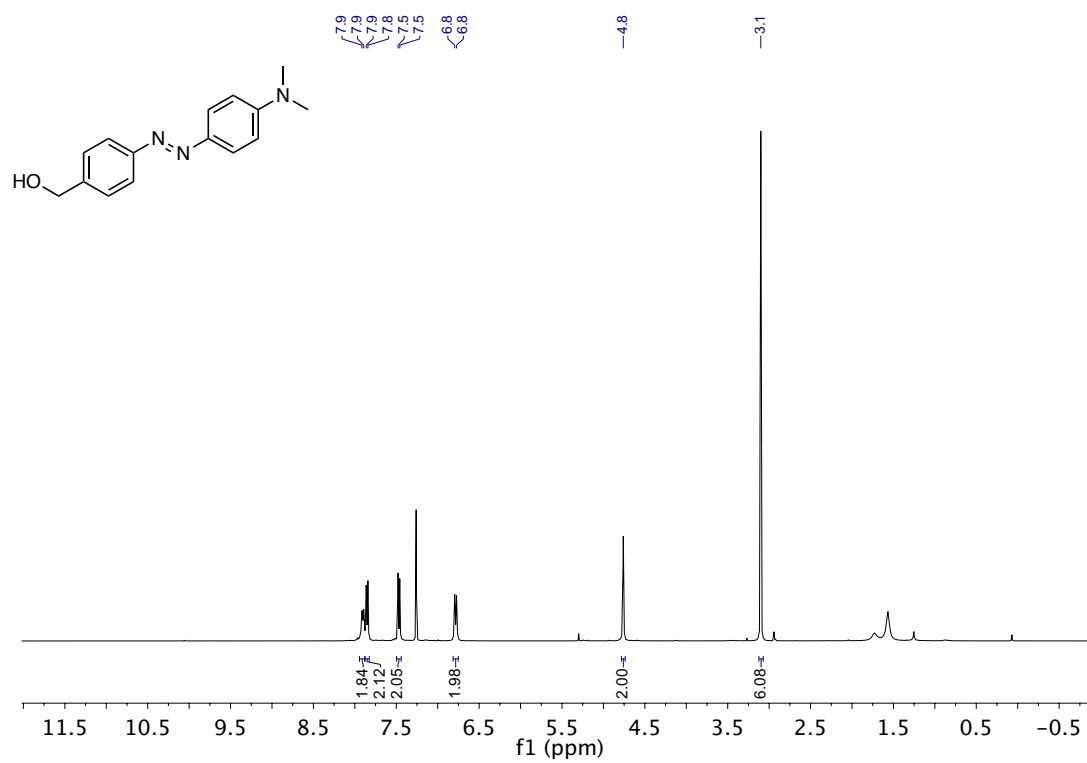


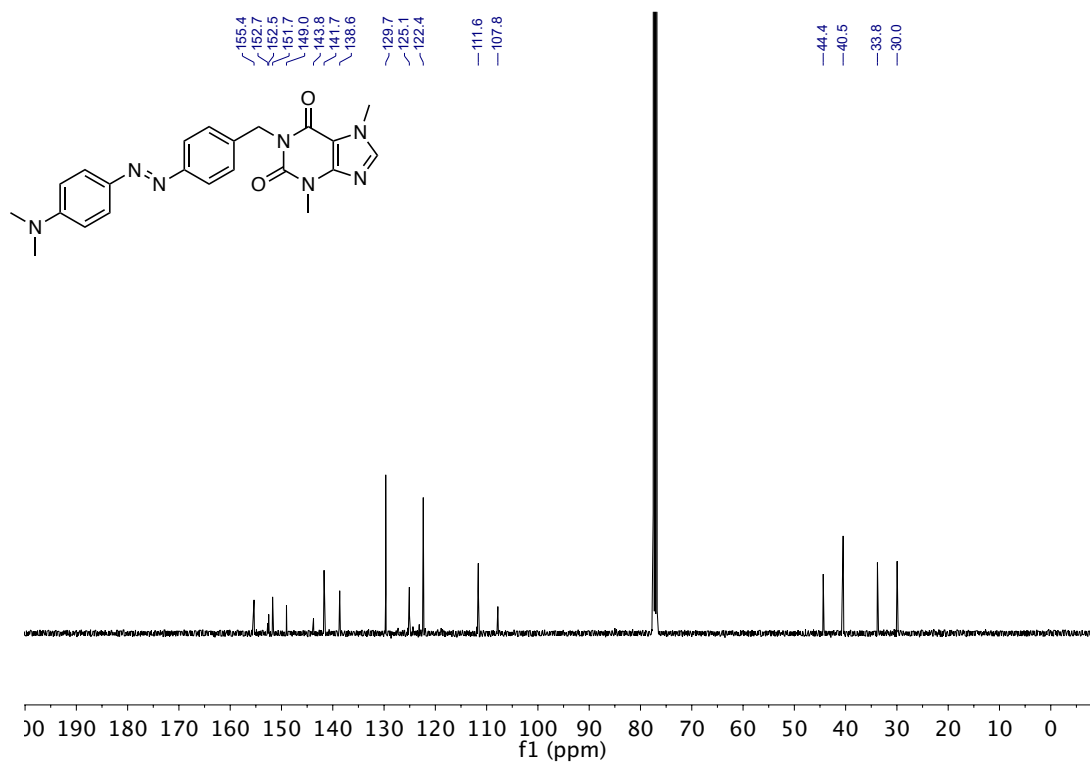
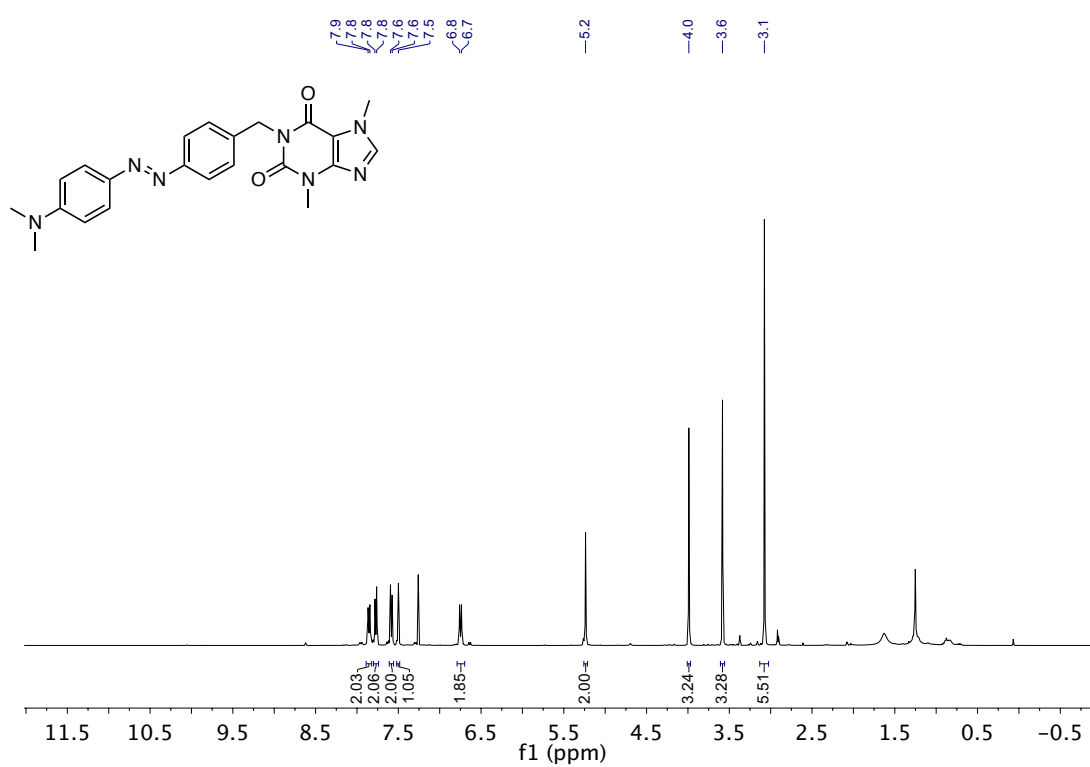


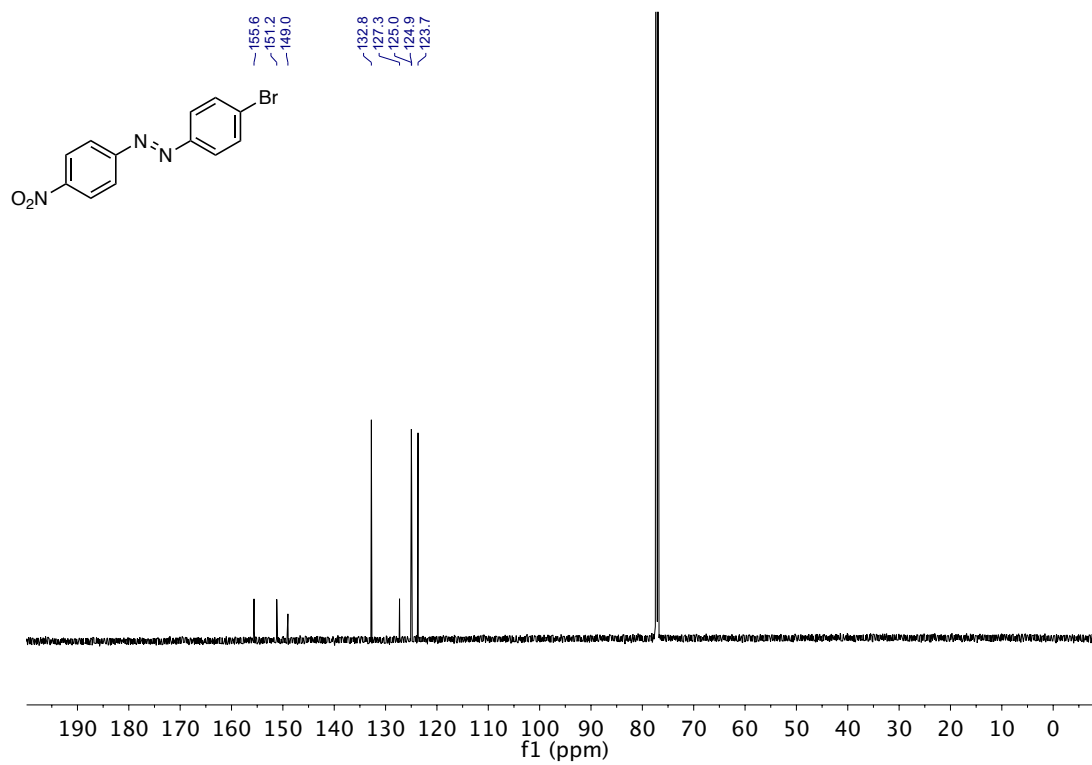
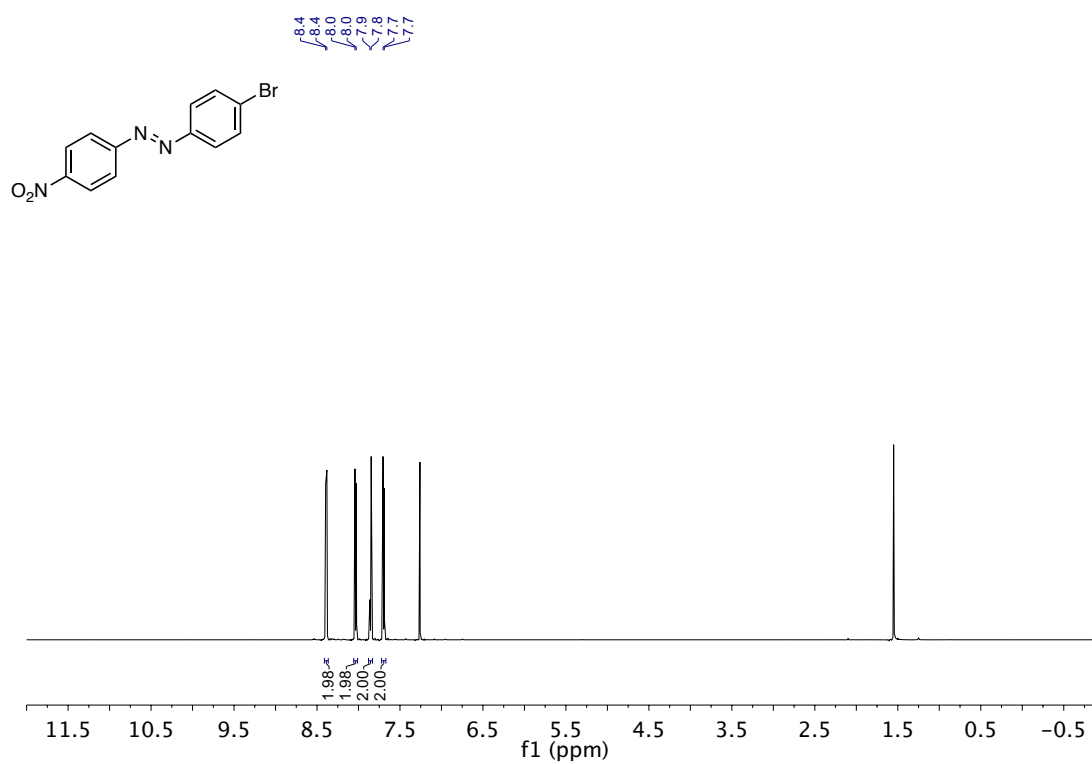




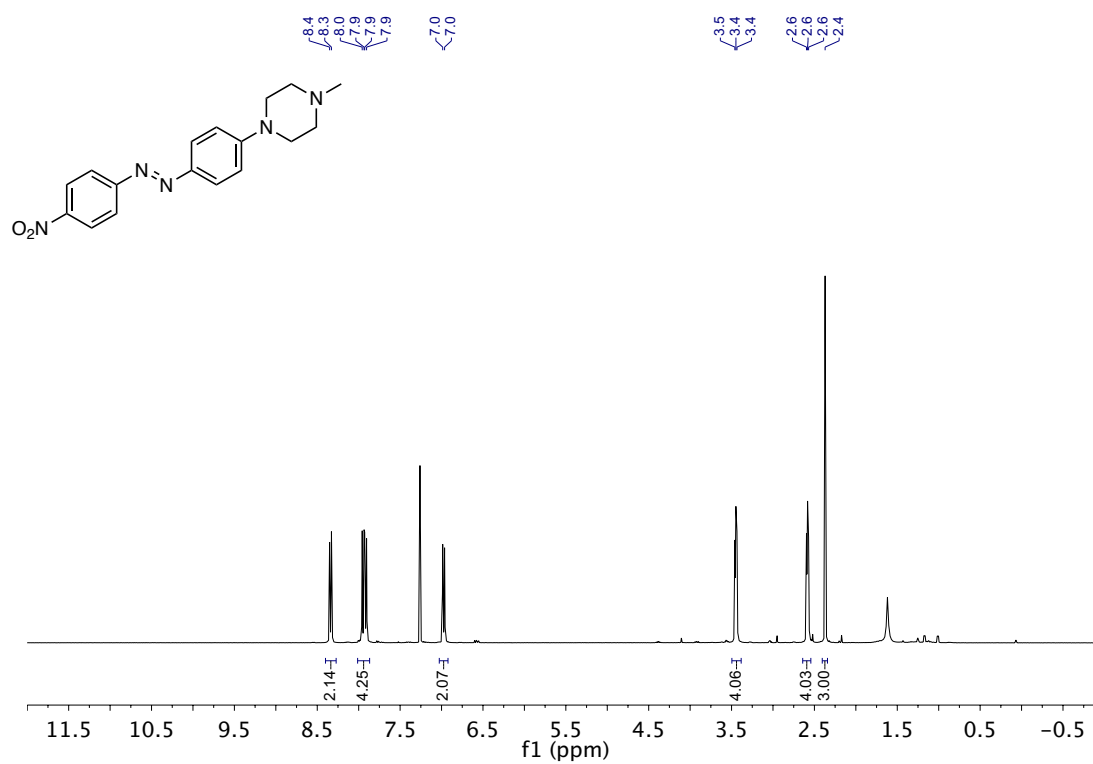


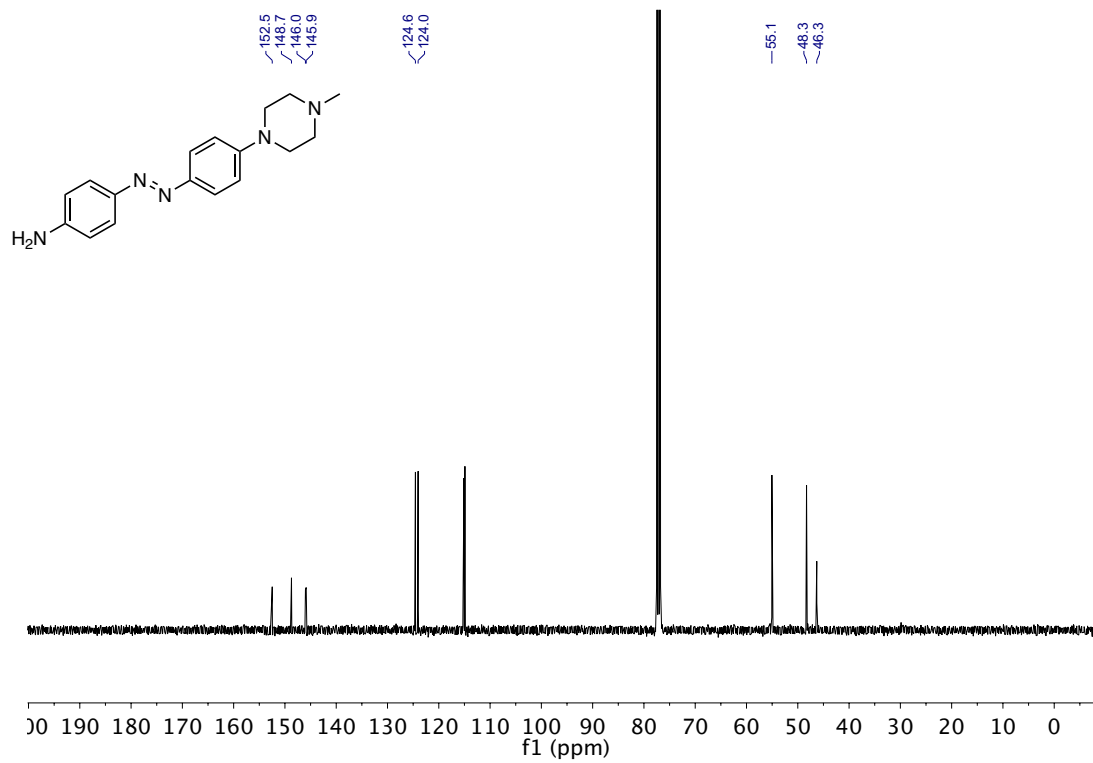
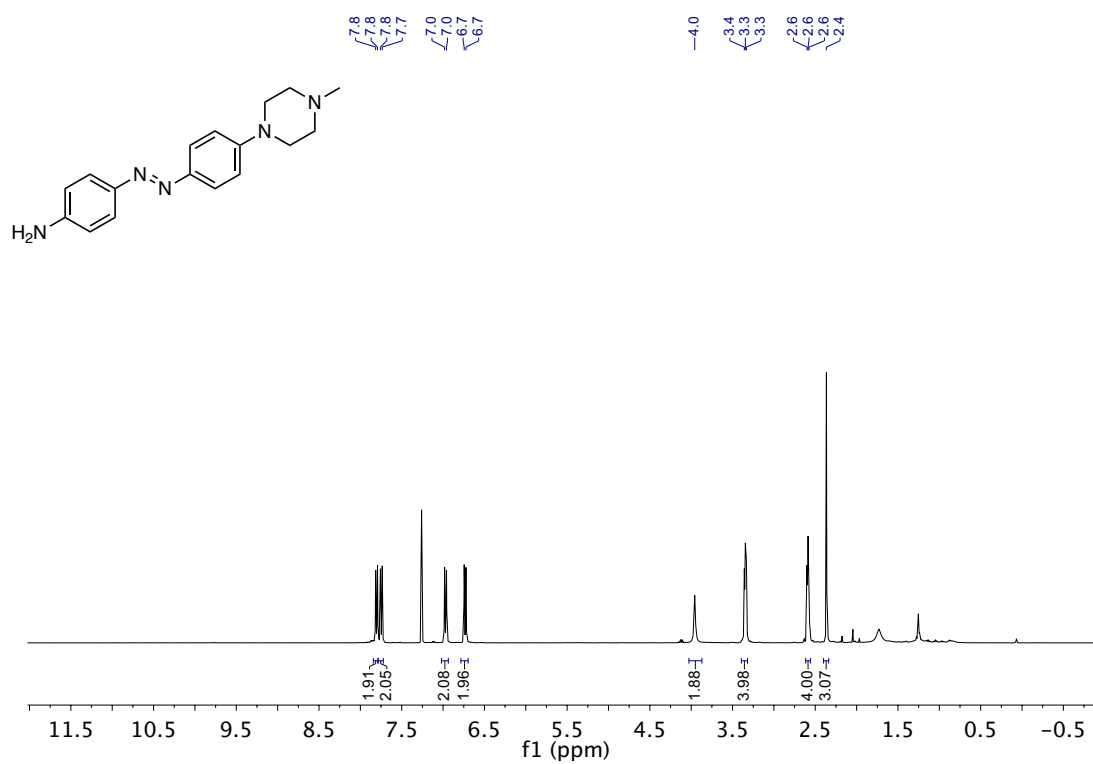


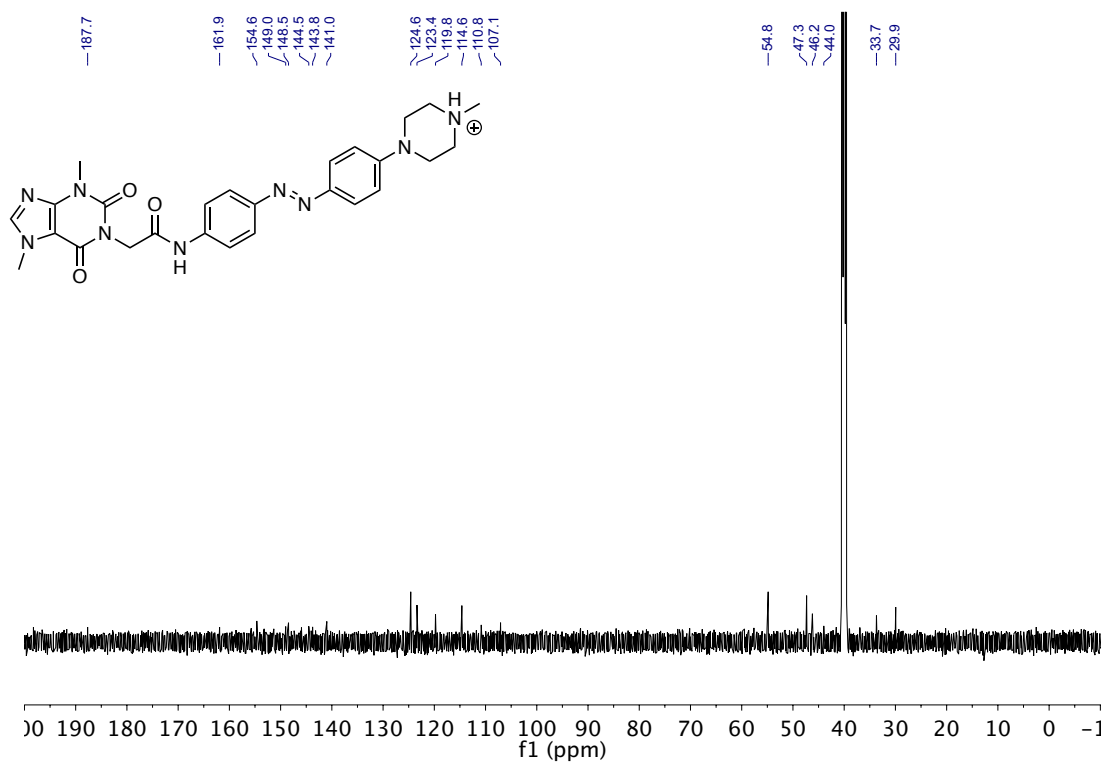
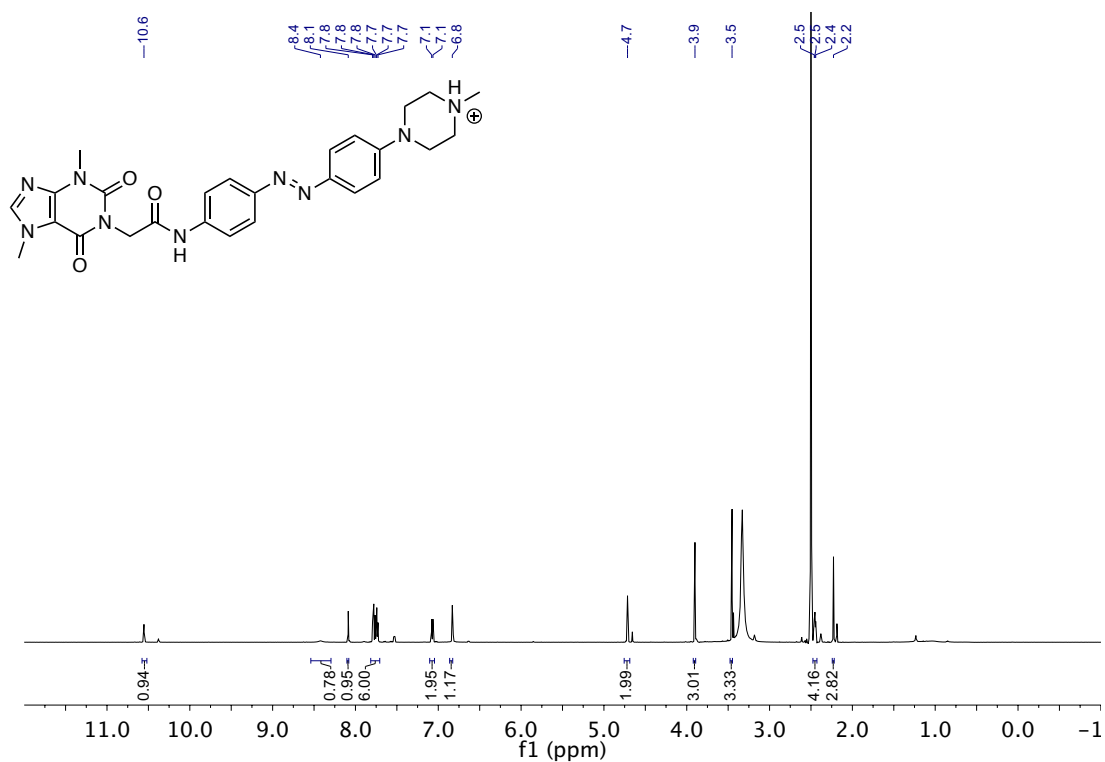


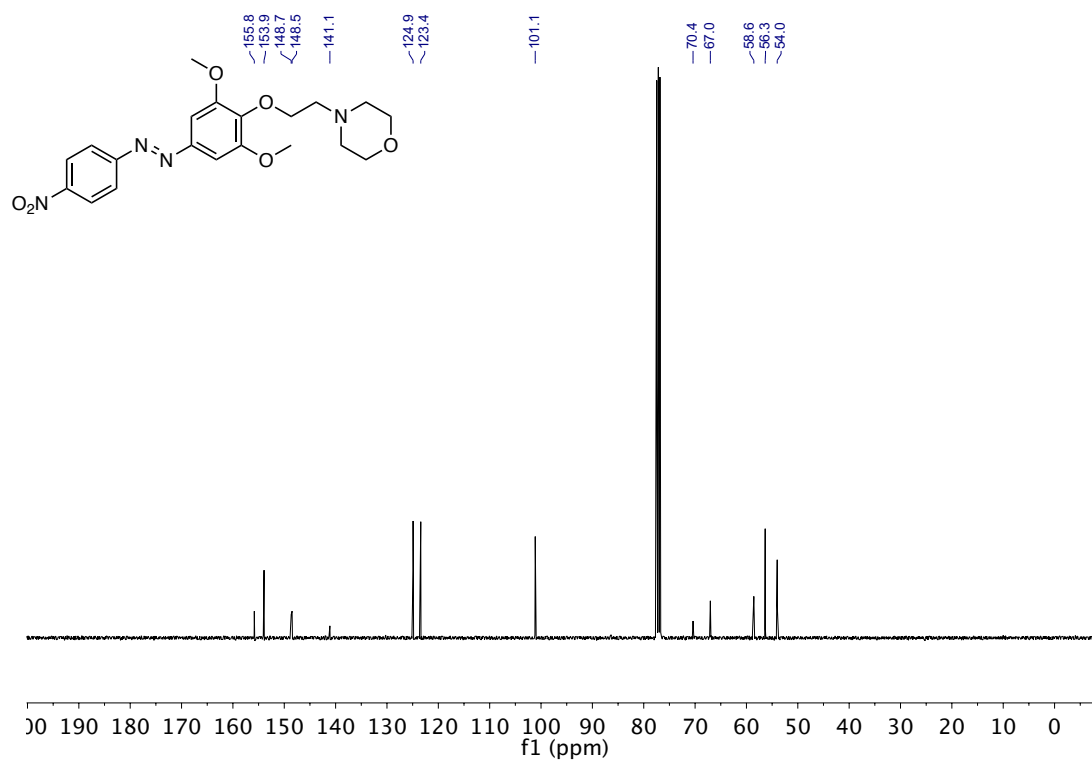
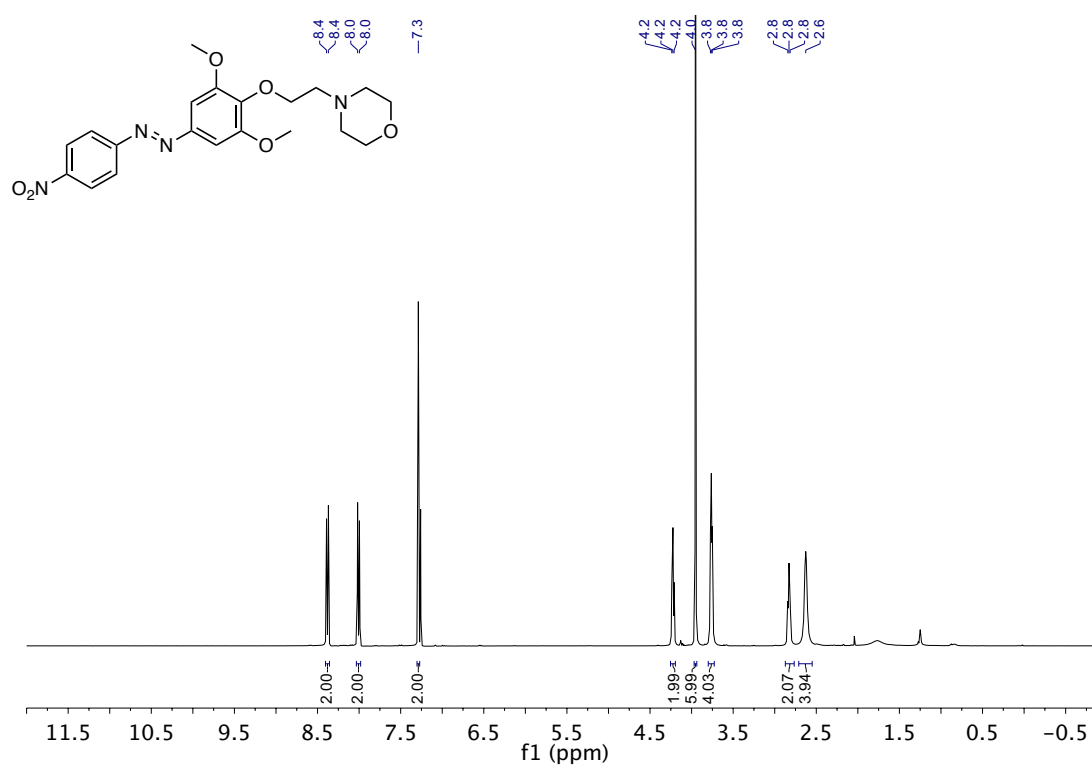


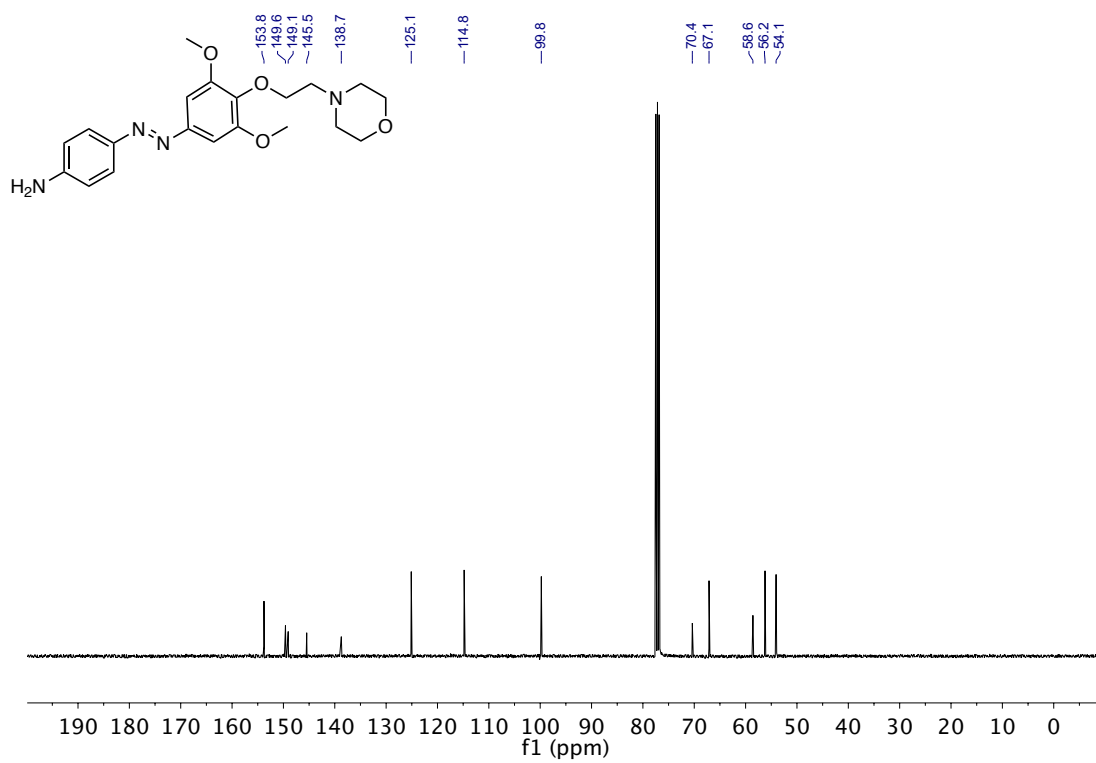
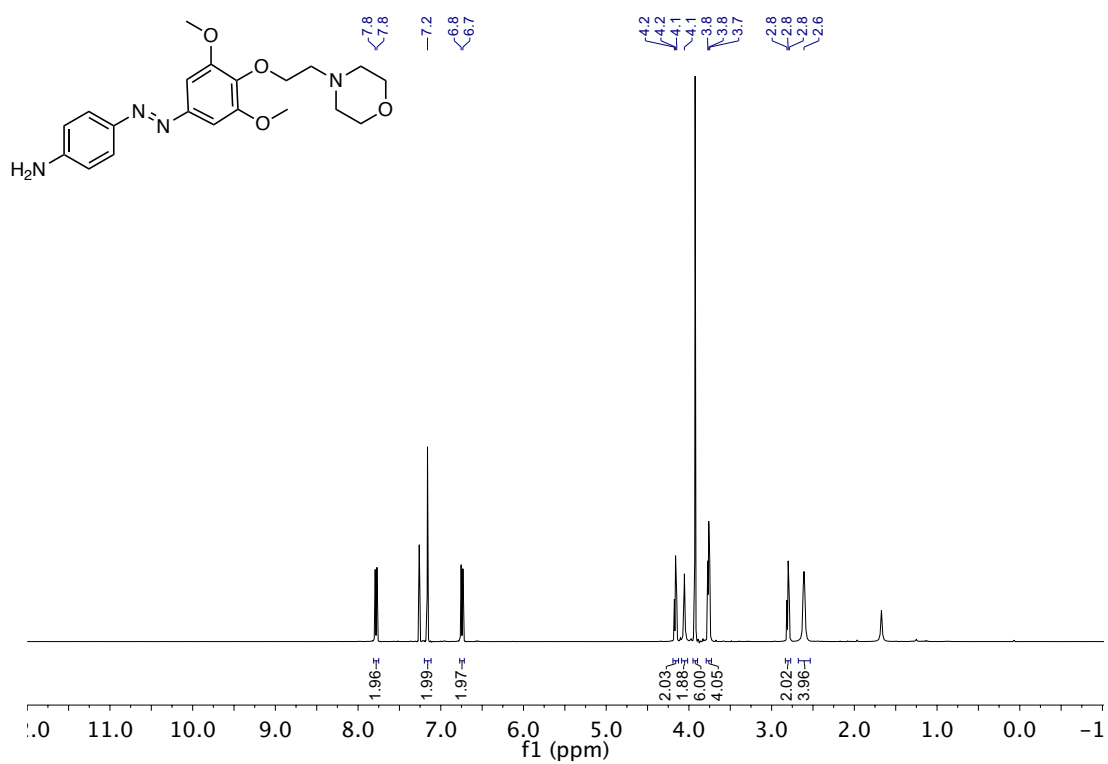


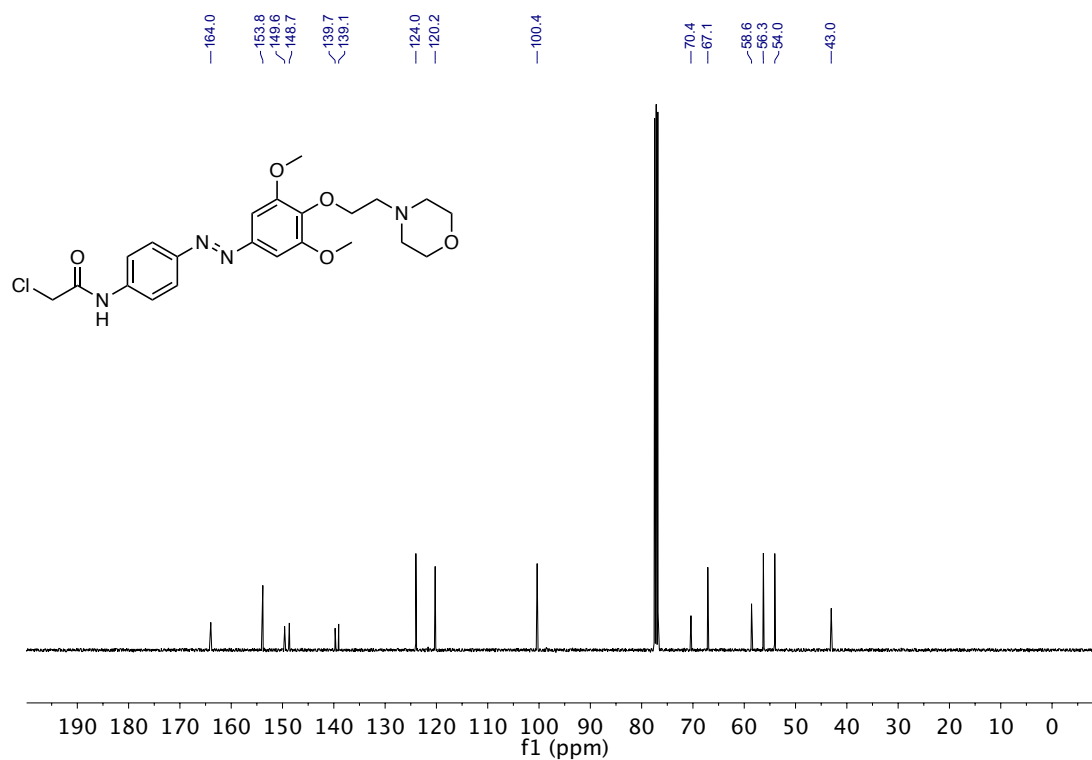
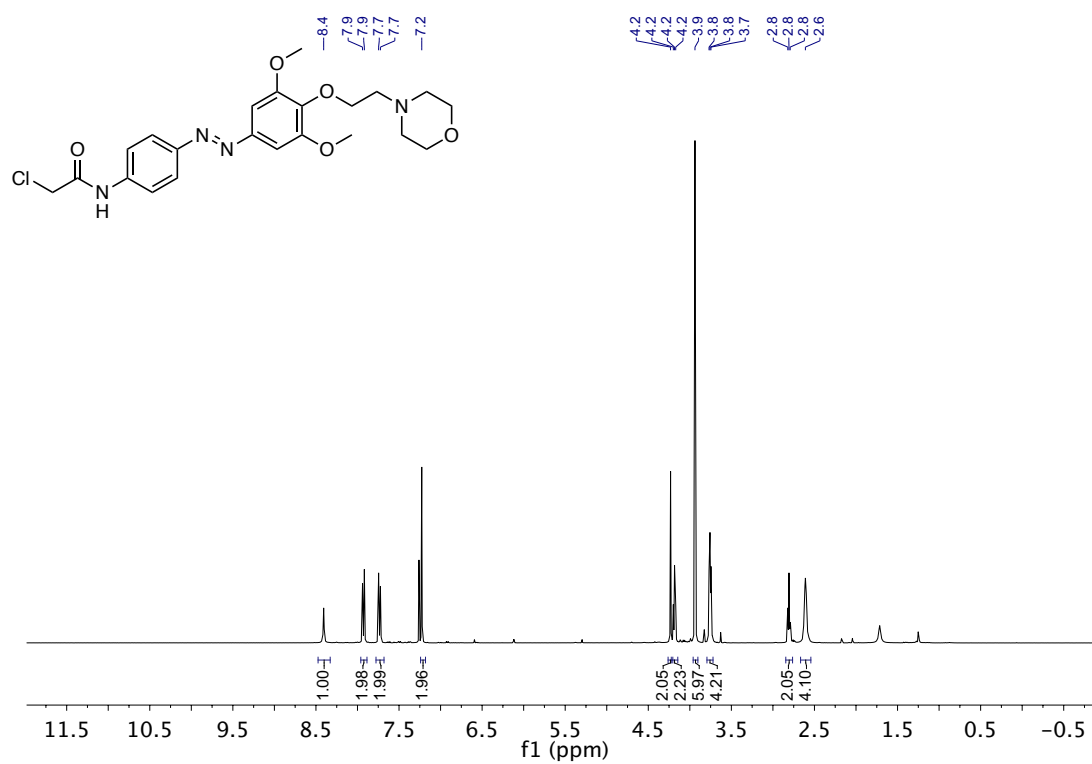


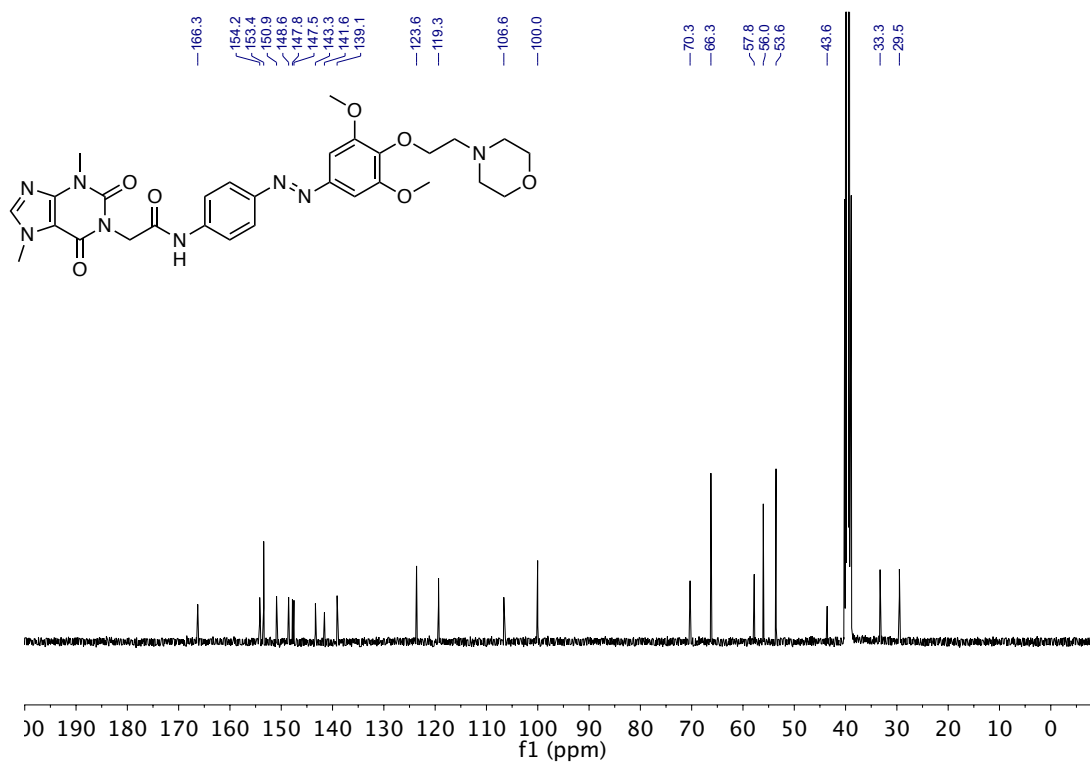
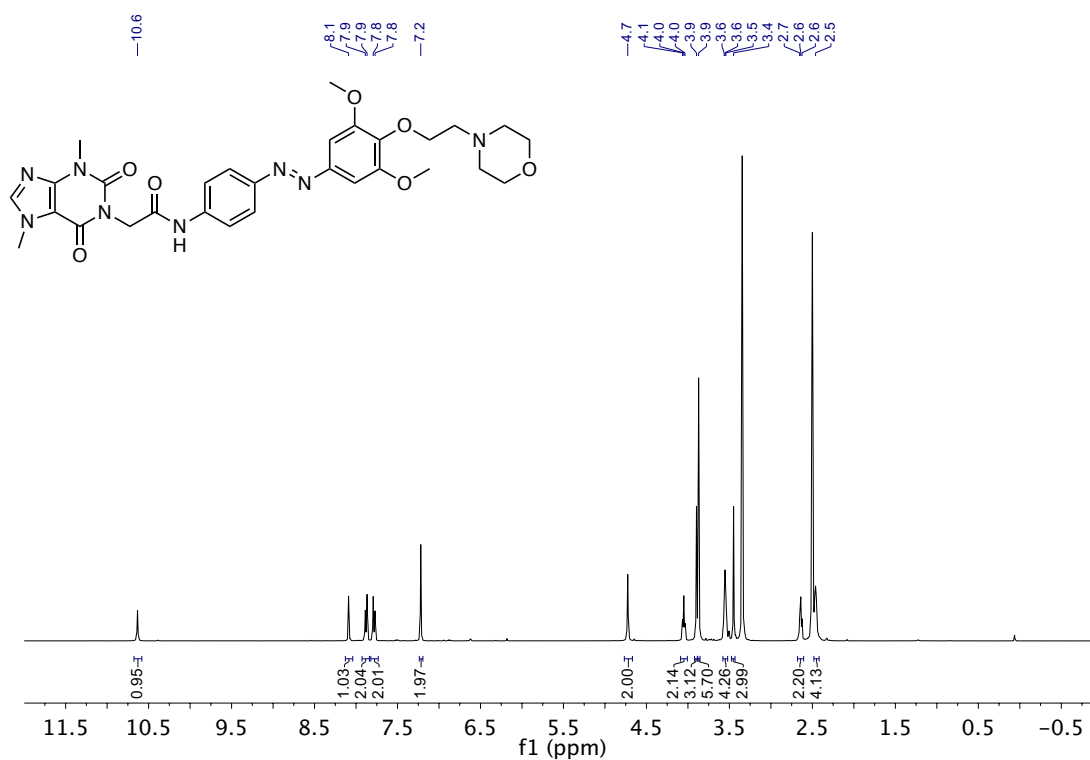


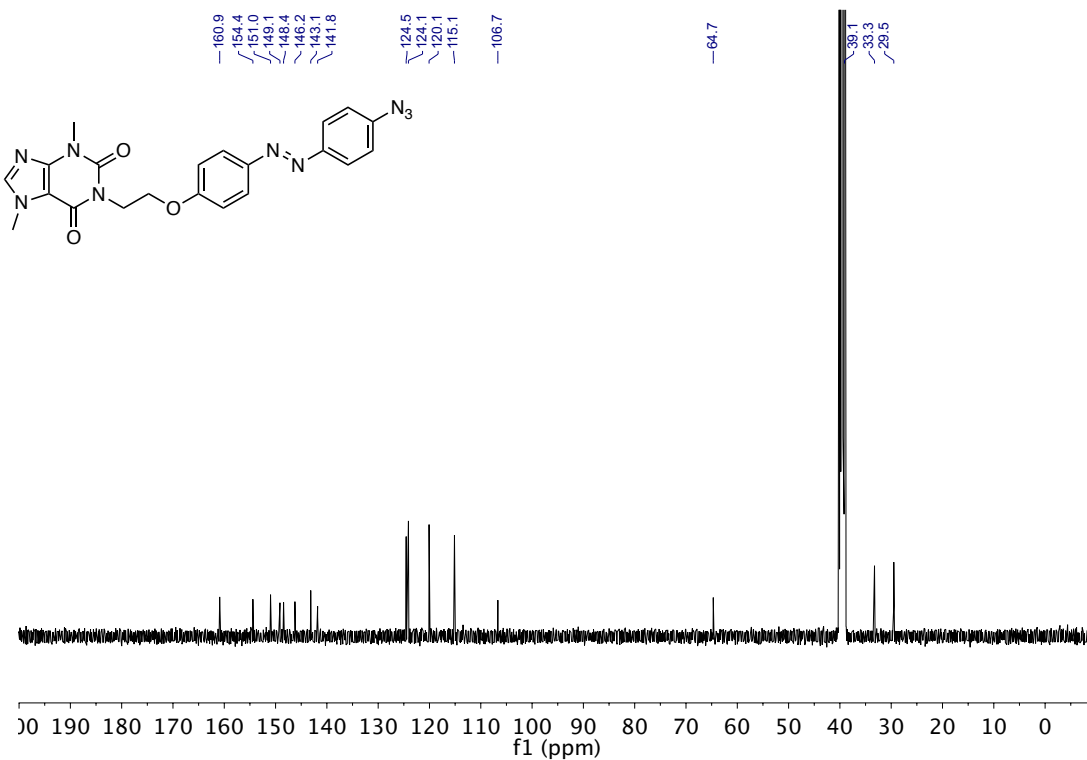
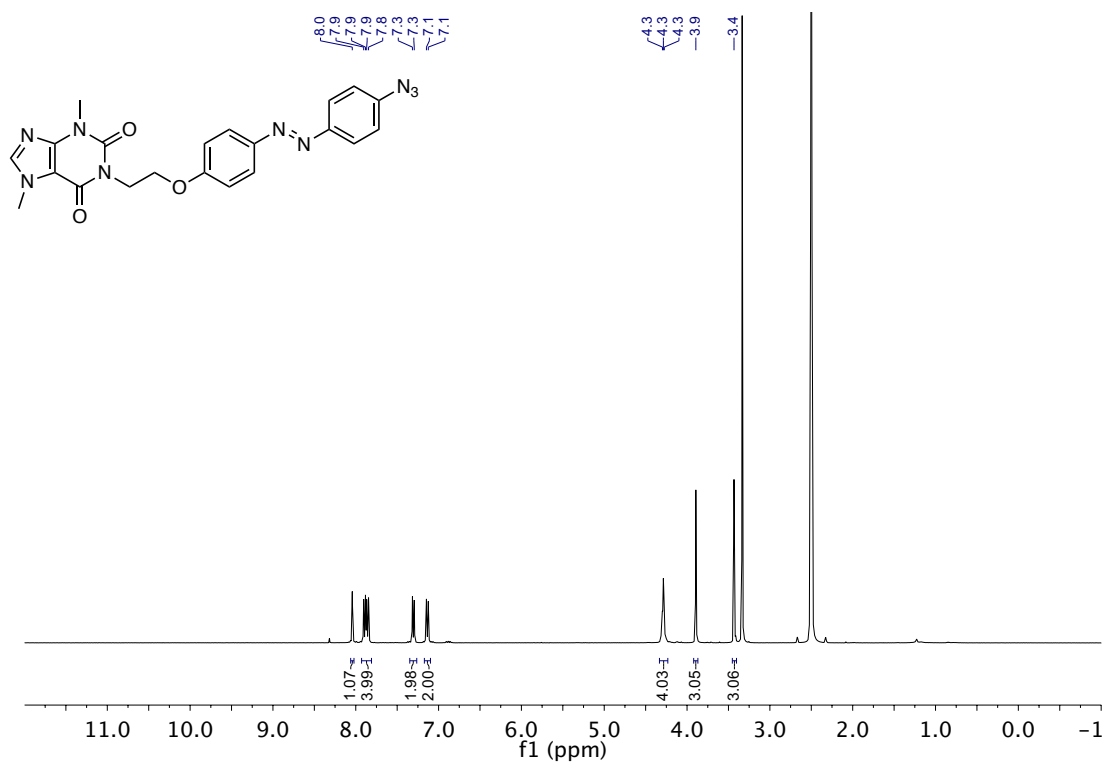




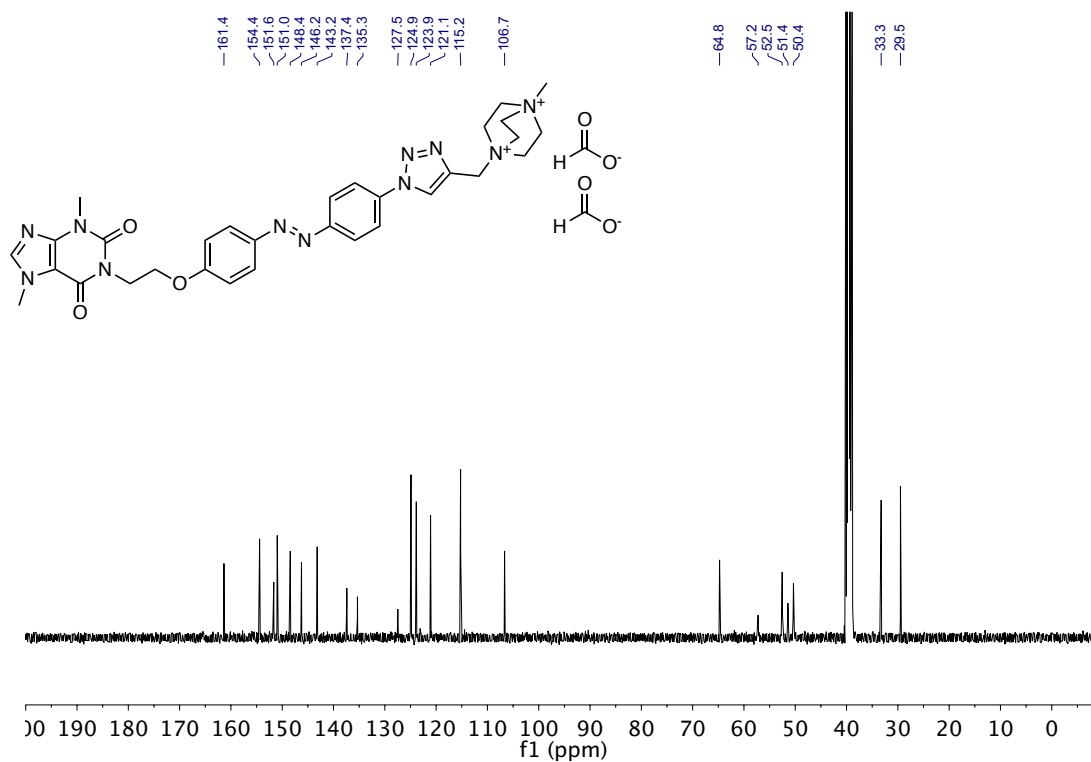
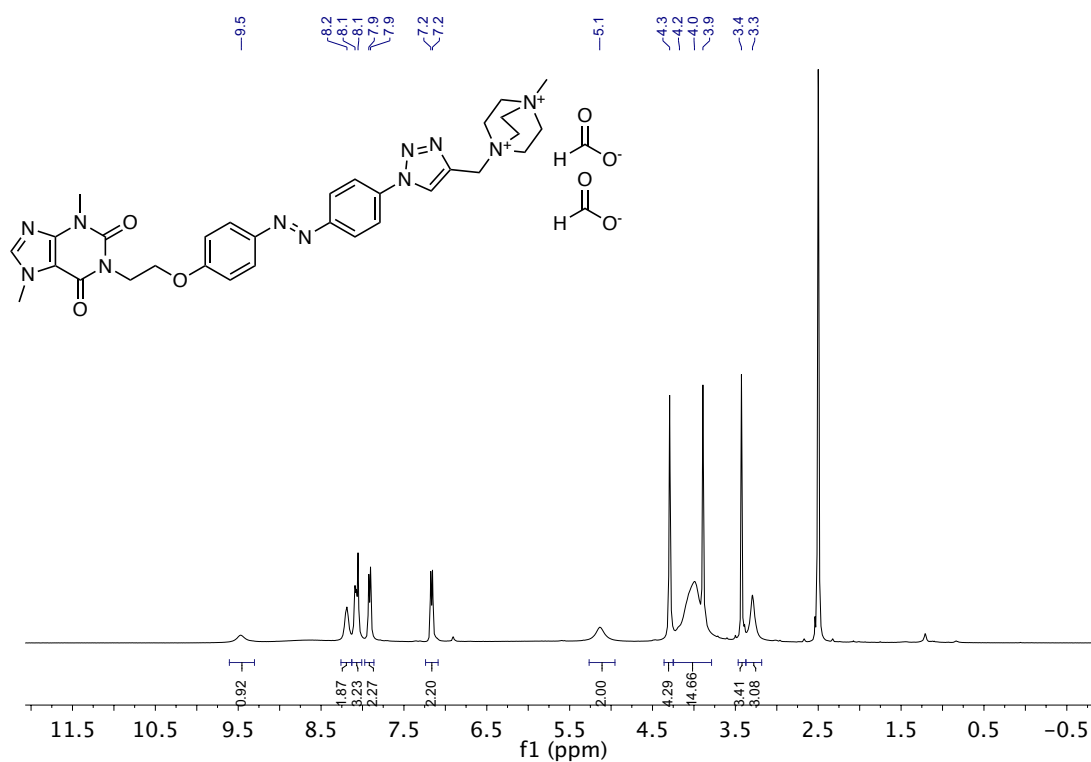


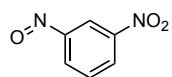




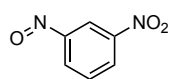
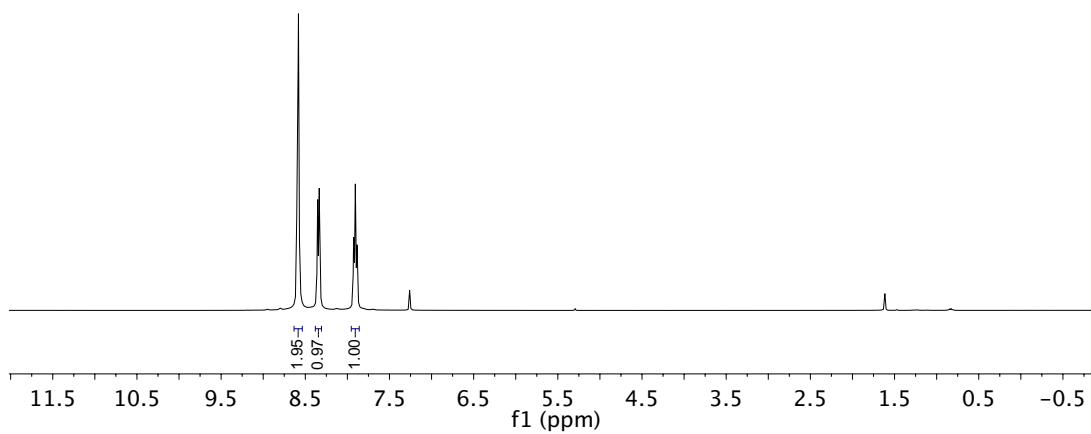








8.6  
8.4  
8.3  
7.9  
7.9



163.4  
149.1  
131.0  
128.8  
126.7  
114.6

